THE UNIVERSITY
of ADELAIDE

Manufacturing Processes Leading to Improved High pH SCC Resistance in Pipes

School of Mechanical Engineering

The University of Adelaide

A thesis submitted in fulfilment of the requirements for the degree of Doctor of Philosophy

Candidate:

Anthony Joseph Roccisano

Supervisors:

Reza Ghomashchi

Shahrooz Nafisi

Erwin Gamboa

April 2020

Contents

Abstract

Stress Corrosion Cracking (SCC) is a damaging form of environmental corrosion found in pipeline steels that forms in the presence of a high pH environment. SCC forms at the surface of gas pipes under damaged coatings and propagates towards the inner wall of the pipe until a critical depth is reached and the internal pressure ruptures the pipe. Prior to considering the role that crystallographic texture had on SCC, the accepted SCC mechanism was unable to explain why adjacent sections of pipe suffered differing levels of SCC damage. When comparing the crystallographic textures of adjacent pipes that suffered differing levels of SCC damage, it was observed that crystallographic texture, produced during manufacturing, was markedly different.

The primary aim of this thesis was to analyse the influence that manufacturing has on the crystallographic texture development in pipeline steels and to investigate the effect that has on the subsequent SCC susceptibility. The project was executed in three main phases; the first phase involved laboratory rolling pipeline steel under different rolling schedules and characterising the resulting mechanical and microstructural properties. The second phase consisted of characterising the crystallographic texture of the produced steels. The final stage involved testing the SCC susceptibility of the produced steels and determining which material properties influenced the susceptibility.

During laboratory scale rolling, recrystallized, hot and warm rolling processes were undertaken with the influence these manufacturing processes had on the steel investigated. Of the three rolling schedules, only recrystallized rolling met the minimum specifications

necessary for an API 5L X70 grade steel whilst the other two resulted in suboptimal mechanical properties. All three rolling schedules produced bainitic structures with upper bainite dominant in the recrystallized rolling whilst granular bainite and polygonal ferrite mixtures, typical of X70 steels, were observed in the hot and warm rolled steels.

When investigating the crystallographic texture of the produced steels, all three rolling schedules produced crystallographic textures reminiscent of those identified in steel rolling literature. Recrystallized rolling resulted in $(001)[1\bar{1}0]$, $(001)[110]$, $(110)[1\bar{1}0]$ and $(110)[001]$ textures in the quarter plane. Hot rolling resulted in $(112)[1\bar{1}0]$ textures joined along the γ-fibre to $(554)[\bar{2}\bar{2}5]$ along the quarter plane. Warm rolling produced textures between recrystallized rolling and hot rolling.

SCC testing was undertaken in a cyclic LIST apparatus where samples were loaded in a $1NNa_2CO_3 + NaHCO_3$ solution for 10 cycles with the resulting cracks investigated. It was observed that recrystallized rolling had the worst SCC susceptibility with a crack velocity of 2.27×10^{-7} mm/s followed by hot rolling with a crack velocity of 1.16×10^{-7} mm/s and finally warm rolling with the lowest susceptibility of 8.70×10^{-8} mm/s. It was identified that SCC susceptibility was strongly linked to the grain size and yield strength with larger grains and higher yield stresses resulting in higher crack velocities. With regards to crystallographic texture, increases in $\{111\}\langle112\rangle$, $(332)[\bar{1}\bar{1}3]$, $(554)[\bar{2}\bar{2}5]$, $(112)[1\bar{1}0]$ and $(113)[1\bar{1}0]$ textures and decreasing the proportion of $(110)[1\bar{1}0]$ corresponded to lower crack velocities.

List of Publications

1. Lavigne O, Gamboa E, Griggs J, Luzin V, Law M, Roccisano A. (2016). High-pH inclined stress corrosion cracking in Australian and Canadian gas pipeline X65 steels. Materials Science and Technology, 32: 684-690.
   DOI: 10.1080/02670836.2015.1132030

2. Roccisano, A., Nafisi, S. and Ghomashchi, R. (2018). Texture Study of Stress Corrosion Cracking in Ex-Service Pipeline Steels, In Iron and Steel Technology Conference, AISTech 2018.
   DOI: TBC

3. Cornish, N., Kurji, R., Roccisano, A. and Ghomashchi, R. (2019). Techno-economic Feasibility of Modified Pulse Arc Deposition on Thick Section of Quenched and Tempered Steel. In MATEC Web of Conferences (Vol. 269, p. 01012). EDP Sciences.
   DOI: 10.1051/matecconf/201926901012

4. Nafisi, S., Roccisano, A., Ghomashchi, R., Vander Voort, G. (2019) A Comparison between Anodizing and EBSD Techniques for Primary Particle Size Measurement. Metals 2019, 9, 488.
   DOI: https://doi.org/10.3390/met9050488

5. Roccisano, A., Nafisi, S. & Ghomashchi, R. (2019) Correlation between EBSD Quantification and Dilatometry Examination of An X70 Steel. Contributed Papers from Materials Science and Technology 2019, MS&T19.
   DOI: 10.7449/2019/MST-2019-423-430

6. Roccisano, A., Nafisi, S. & Ghomashchi, R. 2019. Stress Corrosion Cracking Observed in Ex-service Gas Pipelines: A Comprehensive Study. Metallurgical and Materials Transactions A.
DOI: 10.1007/s11661-019-05496-3

Declaration of Authorship

I certify that this work contains no material which has been accepted for the award of any other degree or diploma in my name, in any university or other tertiary institution and, to the best of my knowledge and belief, contains no material previously published or written by another person, except where due reference has been made in the text. In addition, I certify that no part of this work will, in the future, be used in a submission in my name, for any other degree or diploma in any university or other tertiary institution without the prior approval of the University of Adelaide and where applicable, any partner institution responsible for the joint-award of this degree.

I acknowledge that copyright of published works contained within this thesis resides with the copyright holder(s) of those works.

I also give permission for the digital version of my thesis to be made available on the web, via the University's digital research repository, the Library Search and also through web search engines, unless permission has been granted by the University to restrict access for a period of time.

I acknowledge the support I have received for my research through the provision of an Australian Government Research Training Program Scholarship.

Anthony Joseph Roccisano

Date

Acknowledgements

I'd like to take the opportunity to thank all of those who helped make completing this thesis a reality and show my appreciation.

First and foremost I need to thank my principal supervisor Associate Professor Reza Ghomashchi. Reza, I can't overstate your role in getting this thesis completed. Thank you for your tireless effort and support.

To my supervisor Dr. Shahrooz Nafisi, thank you for all the after-hours time you have put in to teach and support me through the duration of the project. Supervising a project in person is difficult enough without adding the separation of the Pacific Ocean and inconvenient time-zone differences. I could not have finished this project without your guidance.

To my supervisor Dr. Erwin Gamboa, thank you for the opportunity to carry out a PhD, I can't thank you enough for the opportunities you have given me.

I would like to express my thanks to Geoff Callar for all the work and the support he has given me as industry advisor. His willingness to look into my obscure requests and provide guidance and support was greatly appreciated.

The tireless efforts of the Energy Pipelines CRC and those who work there is greatly appreciated for all the help, support and understanding you have given me. This work was funded by the Energy Pipelines CRC, supported through the Australian Govern-

ments Cooperative Research Centres Program. The funding and in-kind support from the APGA RSC is gratefully acknowledged.

I wish to thank various people for their contribution to this project; Dr. Olivier Lavigne for being an unofficial supervisor to me, Dr. Codrington for the help and training, all the workshop and technical staff who have supported me in particular Pascal Symons, Simon Golding, Dale Hodson and Mike Keeble. I'd also like to take the opportunity to thank Professor Zhengyi Jiang and Mr. Nathan Hodges of Wollongong University for providing me access to vital equipment necessary for the completion of this project and the expertise to use it. I'd like to thank Dr. Jason Gascooke and Dr. Animesh Basak for their microscopy support and going above and beyond to help me during the course of the project. I'd also like to thank Mr Iain Adair and Bureau Veritas for carrying out chemical composition testing for me.

I need to thank my family, friends and colleagues for their support, encouragement and assistance provided during the course of this PhD. I couldn't have done it without you and I'll always appreciate your support.

List of Figures

List of Tables

List of Abbreviations

AMMRF	**A**ustralian **M**icroscopy and **M**icroanalysis **R**esearch **F**acility
APF	**A**tomic **P**acking **F**actor
API	**A**merican **P**etroleum **I**nstitute
ASTM	**A**merican **S**ociety for **T**esting and **M**aterials
ASXXXX	**A**ustralian **S**tandard XXXX
BCC	**B**ody **C**entred **C**ubic
CCT	**C**ontinuous **C**ooling **T**ransformation
CEPA	**C**anadian **E**nergy **P**ipeline **A**ssociation
CERT	**C**onstant **E**xtension **R**ate **T**est
CI	**C**onfidence **I**ndex
CP	**C**athodic **P**rotection
CSE	**C**opper **S**ulphate **E**lectrode
CSL	**C**oincidence **S**ite **L**attice
EBSD	**E**lectron **B**ack**S**catter **D**iffraction
EDS/ EDX	**E**nergy-**D**ispersive **X**-ray **S**pectroscopy
EMAT	**E**lectro**M**agnetic **A**coustic **T**ransducers
ERW	**E**lectrical **R**esistance **W**elding
ESEM	**E**nvironmental **S**canning **E**lectron **M**icroscope
FBE	**F**usion **B**onded **E**poxy
FCC	**F**ace **C**entred **C**ubic
FEG	**F**ield **E**mission **G**un
HAB	**H**igh **A**ngle **B**oundary

HAZ	**H**eat **A**ffected **Z**one
HCP	**H**exagonally **C**lose **P**acked
HIC	**H**ydrogen **I**nduced **C**racking
HV	**V**ickers **H**ardness
ILI	**I**n **L**ine **I**nspection
IPF	**I**nverse **P**ole **F**igure
IR	**I**nfra**R**ed
kN	**K**ilo**N**ewton
LAB	**L**ow **A**ngle **B**oundary
LIST	**L**inearly **I**ncreasing **S**tress **T**est
LRD	**L**ongitudinal to **R**olling **D**irection
MA	Retained Austenite
MOP	**M**aximum **O**perating **P**ressure
MPa	**M**ega**Pa**scal
MPI	**M**agnetic **P**article **I**nspection
ND	**N**ormal **D**irection
NDT	**N**on-**D**estructive **T**esting
ODF	**O**rientation **D**istribution **F**unction
OES	**O**ptical **E**mission **S**pectrometry
PSL	**P**roduct **S**pecification **L**evels
RD	**R**olling **D**irection
RP	**R**olling **P**lane
RPM	**R**evolution **P**er **M**inute
RT	**R**oom **T**emperature
SCC	**S**tress **C**orrosion **C**racking
SEM	**S**canning **E**lectron **M**icroscope
SHE	**S**tandard **H**ydrogen **E**lectrode
SMYS	**S**pecified **M**inimum **Y**ield **S**tress

SSC	**S**tress **S**ulfide **C**racking
SSRT	**S**low **S**train **R**ate **T**est
$\boldsymbol{T_{NR}}$	**N**on-**R**ecrystallization **T**emperature
TD	**T**ransverse **D**irection
TRD	**T**ransverse to **R**olling **D**irection
TTT	**T**ime **T**emperature **T**ransformation
UOE	**U**-ing, **O**-ing and **E**xpanding
UT	**U**ltrasonic **T**esting
UTS	**U**ltimate **T**ensile **S**trength
UTS	**U**ltimate **T**ensile **S**tress
XRD	**X**-**R**ay **D**iffraction
YS	**Y**ield **S**tress

This is fine, KC Green 2013, `www.gunshowcomic.com/648`

Chapter 1

Introduction

Stress Corrosion Cracking (SCC) is a common environmental cracking process that causes cracks to form in a stressed engineering structure such as a gas transmission pipeline. If a crack grows to a sufficient depth, the fracture toughness of the material may be exceeded leading to sudden mechanical failure [1]. SCC is caused by the interaction of three factors: an applied stress or residual tensile stress, a corrosive environment and a susceptible material. SCC presents as a series of branched cracks growing perpendicular to the direction of the stress, where given sufficient time, can cause failure of engineering structures and components. One such engineering structure where SCC is frequently identified is in buried high pressure gas transmission pipelines. SCC has been identified in gas pipelines since the 1960's [2] and has been responsible for numerous failures around the world; resulting in loss of life, product, and confidence in the integrity of pipeline infrastructure. As SCC originates from the outer surface of the pipe, coating technology has been immensely important in preventing the initiation of SCC. However, when coatings are damaged or breached, SCC can still occur unhindered leading to failure in pipelines previously thought of as being free of SCC.

SCC defects form in steel pipelines when coating disbondment occurs in cathodically protected pipes. Cathodic protection develops a passive oxide layer on exposed surfaces of the pipe leading to improved protection from general corrosion in the event of a coating disbondment. If a sufficiently high cathodic potential is applied, water is dissociated to form

hydroxide ions, (OH^-). The hydroxide ions create a localized high pH region by combining with CO_2 dissolved in groundwater present in the surrounding soil to form carbonate and bicarbonate ions [3]. Solutions with a pH greater than 9.3 cause the intergranular, high pH form of SCC, whereas a lower pH between 5.5 and 7.5 tends to encourage the transgranular, near neutral form of SCC [3–5]. The primary propagation mechanism for high pH SCC (SCC hereafter) is film fracture followed by anodic dissolution [6, 7]. SCC forms when an applied or residual stress fractures the passive oxide layer, exposing it to the corrosive environment, where anodic dissolution corrodes grain boundaries. Anodic dissolution continues to corrode grain boundaries until cathodic protection reforms the passive film that prevents further corrosion until an applied or residual stress fractures the film.

In an effort to minimise the damage caused to the pipe in the event of coating failure, research regarding the material properties of pipeline steel identified that different manufacturing processes could slow or even prevent the propagation of SCC. Areas of research including the effect of surface roughness [8], chemical composition [9–12], microstructure [4, 13–16] and grain size [17–19] have all given some insight as the factors that influence SCC. However, they are not able to definitively predict or control crack growth. This deficiency in the literature is highlighted when comparing SCC in a run of pipe from the same manufacturer, made to the same specifications [20]. When accounting for sections with similar levels of coating disbondment and soil conditions, some sections of pipe were more susceptible to SCC than others [20]. It was identified that the main difference between these pipes was the crystallographic texture present due to slight differences in manufacturing that influenced the susceptibility behaviour. Control of crystallographic texture, produced during rolling processes, could therefore enhance or degrade the resistance to SCC in pipeline steels [20]. Crystallographic texture or simply texture refers to the non-random distribution of grain (crystal) orientations within a polycrystalline material, with respect to an external frame of reference. Grains align themselves in a preferred direction with respect to the maximum strain direction, due to either an external or internal force

during the manufacturing. Controlled rolling, used in the manufacturing of pipeline steel, can be manipulated to develop different grain orientations by altering process parameters such as rolling temperatures, cooling rates and reduction ratios [21–23]. Through the manipulation of rolling schedules it is possible to develop different textures to assess the effect of manufacturing on crystallographic texture and the eventual SCC susceptibility.

It has been identified in open literature that intergranular SCC is more likely to propagate through High Angle Boundaries (HAB's) with misorientation $\theta \geqslant 15^{\circ}$ as compared to Low Angle Boundaries (LAB's) with misorientation $\theta < 15^{\circ}$ [24]. In addition, there is some evidence that grains with orientations belonging to the {111}//Rolling Plane (RP) and {110}//RP fibres are more resistant to SCC than randomly oriented grains [20, 24, 25]. In comparison, when cracking occurred between grains with similar angular misorientation, there was a tendency for cracks to grow between grains that had {100}<110> orientations [20, 24, 25]. It has been predicted that increasing the proportion of resistant boundaries through control of the manufacturing process can reduce SCC susceptibility of the final product [26].

Controlled rolling of pipeline steels is the main process used to develop the microstructure and mechanical properties necessary for use in industry. Whilst there is a narrow band of material and physical properties allowable in pipe grades [27], numerous rolling procedures can be undertaken to achieve the desired properties. There are two main rolling regimens utilised in mid-grade pipeline steels, hot rolling and warm rolling. Hot rolling is conducted when the steel phase is entirely austenitic, whereas warm rolling is finished in the dual phase region where austenite and ferrite coexist. As finish rolling temperature is reduced from hot rolling into warm rolling, the crystallographic textures also changes through the interaction between recrystallisation and deformation textures [21]. By rolling the steel in different temperature regimens, different textures can be produced and the resulting samples investigated for SCC susceptibility.

The following chapter presents a review of available literature on the topic of SCC and manufacturing processes, and what is currently understood regarding the effect of manufacturing on SCC susceptibility in pipeline steels. The aims and objectives are outlined in Chapter 3 and the overall scope of the project is defined. The overarching aim of the project is to investigate the effect controlled rolling has on texture development and the subsequent effect on SCC susceptibility. The experimental procedures for manufacturing steel pipe samples, texture analysis and SCC testing are outlined in Chapter 4. A combined results and discussion of controlled rolling, texture analysis and SCC susceptibility are presented in Chapters 5, 6 and 7, respectively. Concluding remarks and implications to industry are reported in Chapter 8 summarising how controlled rolling can impact SCC susceptibility in pipeline steels.

Chapter 2

Literature Review

2.1 Introduction

Stress Corrosion Cracking (SCC) is a form of environmentally induced corrosion that is common to gas pipelines. Whilst SCC has been observed in pipelines for more than half a century, managing SCC can still provide challenges to pipeline owners. Tight control of pipe coating integrity and regular inspection is industry best practice for preventing SCC. However, coatings can fail and inspection is a costly endeavour that is often postponed in pipes where SCC has not been previously identified. It has been observed in pipeline sections where cracking is rampant, certain pipe sections are more susceptible to intergranular SCC than others [20]. When accounting for other factors (microstructure, chemical composition, coating condition) it became evident that crystallographic texture differences caused by slight variations in manufacturing procedures could account for these differences [20]. Recent observations have identified that crystallographic texture, the overall measure of grain orientation in polycrystalline structures, can have an influence on the SCC susceptibility [24]. The crystallographic texture is strongly influenced by the manufacturing process and for materials with the same chemical compositions, altering the manufacturing process results in different textures [21].

This chapter contains a review of the factors that influence the occurrence of SCC, the manufacturing processes used to produce pipes and the development of crystallographic

texture through those processes. As SCC is a highly complex corrosion phenomenon, this review will cover an overview of the SCC mechanism followed by a review of the factors that influence SCC susceptibility. Crystallographic texture development is heavily dependent on the manufacturing process, hence, an overview of steel properties is provided followed by a review on the development of crystallographic texture during controlled rolling. The overarching theme of this review is to investigate the effect of crystallographic texture on SCC susceptibility with a focus on high pH SCC and pipeline steels. Some literature from related mechanisms and materials is substituted when deficiencies in pipeline steel literature are identified but are clearly identified as such.

2.2 What is Stress Corrosion Cracking?

SCC describes the phenomenon of brittle intergranular cracking in typically ductile materials due to being exposed to a corrosive media whilst in the presence of a tensile stress. SCC formation relies on the concurrent presence of three elements for it to form: the material must be experiencing a tensile stress (either applied or residual); the material must be exposed to a corrosive environment; and the material must have a microstructure that is susceptible to SCC in the said environment. The removal of any of the three elements prevents SCC from forming, although other corrosion mechanisms are not necessarily prevented as is presented in Figure 2.1.

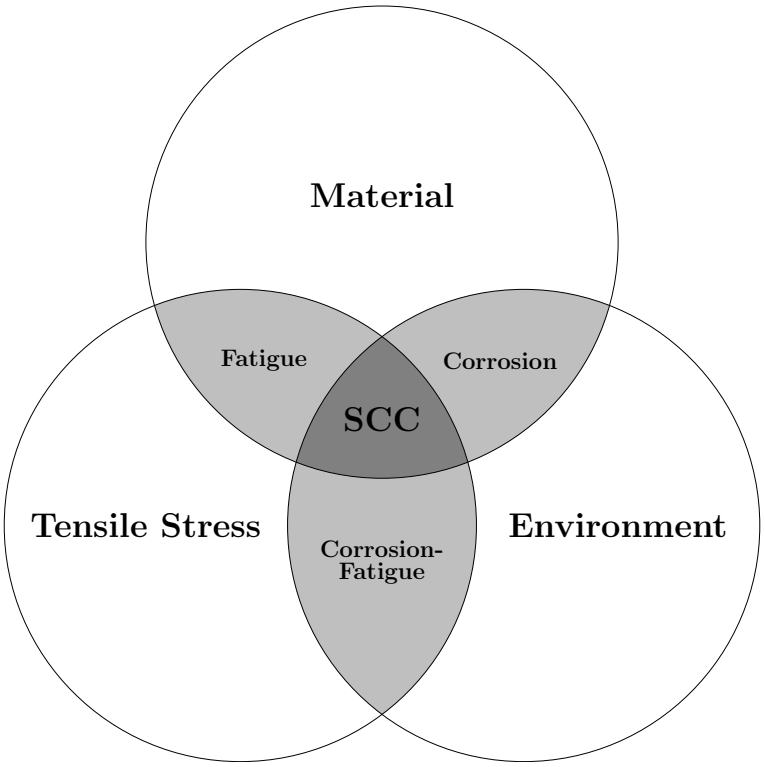

Figure 2.1: Venn diagram of SCC development.

In gas pipelines, SCC can appear in two main forms depending on the pH of the soil the pipe is exposed to. The intergranular form of SCC is produced when the pH of the surrounding soil is above 9.3 whilst the transgranular form is observed when the surrounding pH is between 5.5 and 7.5 [3–5]. The high pH is formed in ground water surrounding a pipe when a high cathodic potential is applied to the pipe causing water to dissociate and form hydroxide ions (OH^-). The localised high pH solution then combines with CO_2, dissolved in groundwater, to form carbonate and bicarbonate ions [1, 6].

High pH SCC grows axially along the pipe initiating from the outer surface propagating towards the inner surface. The SCC cracks on the outer surface of the pipe is shown schematically in Figure 2.2. In practice, high pH SCC forms cracks too fine to see with the naked eye and require the use of non-destructive testing (NDT) visualisation techniques such as magnetic particle inspection (MPI) to observe. When sectioned, the beginning of a crack is referred to as the crack mouth whilst the body of the crack is referred to as the crack path. As high pH SCC follows grain boundaries, the crack path often appears

jagged and grows either perpendicular to the surface or inclines depending on the material properties [28–30].

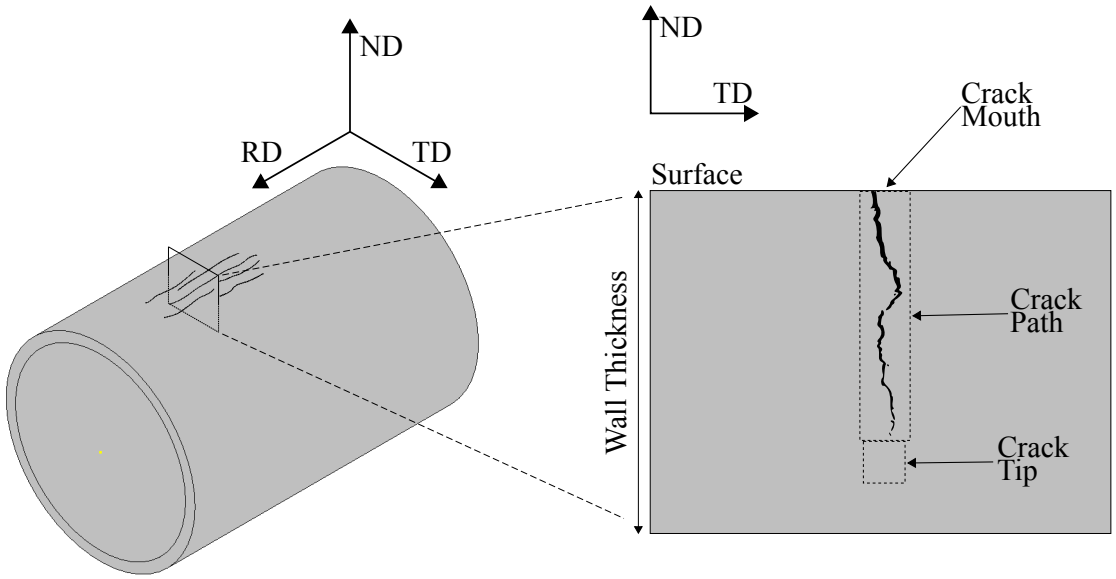

Figure 2.2: The appearance of SCC cracks in gas pipelines where a transverse section is cut to reveal the cross-section of the crack. Reprinted from [31].

2.3 Formation of SCC

As explained in the previous section, SCC is the result of a susceptible material being exposed to a tensile stress in the presence of a corrosive medium. The initiation of SCC occurs in pipeline steel where surface defects such as pits or fractured mill scale become exposed to the corrosive environment and localised anodic dissolution of exposed susceptible grain boundaries occurs. Without the presence of a tensile stress these initiated cracks are not able to propagate further as the formation of a passive oxide layer prevents further chemical attack [1]. Hence, SCC propagates through the combination of anodic dissolution of susceptible grain boundaries and film fracture. At the crack tip, tensile stress fractures the impervious oxide layer (film) which allows anodic dissolution to occur between the now unprotected grain boundaries [7, 32]. SCC forms perpendicular to the direction of largest acting stress. In gas pipelines, this is the hoop direction and hence cracks form along the rolling direction of the pipe as seen in Figure 2.2. While SCC tends

to form along the rolling direction of the pipe, improper welding or physical defects can cause cracks to form in different orientations [33].

As a corrosion mechanism, SCC requires materials that form passive oxide layers for it to occur. The low carbon steel used in pipelines does not develop a passive oxide layer without the use of Cathodic Protection (CP) that produces an oxide layer on the steel surface when exposed to the environment. The aim of CP is to cathodically polarise the pipeline in the range of -850 to -1200 mV vs. $Cu/CuSO_4$ (CSE) such that general corrosion of the pipeline is unable to form [34]. The range in which SCC forms is typically between -600 to -750 mV vs. CSE [35]. Whilst the two ranges do not intersect, as SCC requires coating defects to initiate, potential shielding occurs where the CP potential is lower under the coating defect such that the potential is shifted into the SCC forming range [35]. Figure 2.3 shows the narrow range of potentials that SCC requires for its formation when comparing polarization scans with fast and slow scan rates [1].

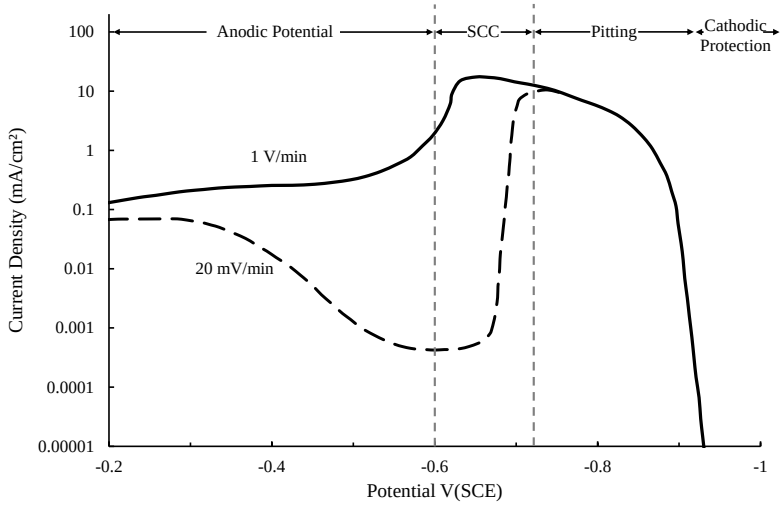

Figure 2.3: Fast and slow sweep rate polarization curves for line pipe steel showing the range in which SCC forms. Adapted from [1].

Anodic dissolution occurs at the rate limited by Faraday's law which in pipeline steels is on the order of 10^{-6} mm/s [7]. Due to the effect of film formation, in practice the actual

crack velocity for an SCC crack is usually orders of magnitude slower, commonly in the range of $10^{-9} - 10^{-7}$ mm/s [7, 36]. SCC forms between the active and passive potential ranges for pipeline steel where both anodic dissolution and passive film formation can occur [37]. SCC remains an intergranular mechanism due to the formation of the passive film layer which prevents anodic dissolution of the crack walls once the crack front has passed, forcing the crack to continue propagating further into the material [38]. The growth of SCC tends to follow the relationship depicted in Figure 2.4 [39]. Stage 1 exists before the conditions necessary to generate SCC. In Stage 2 a breakdown of the coating and sufficient levels of carbonate/ bicarbonate ions are produced causing rapid crack initiation. Stage 3 comprises of the period of slow, steady crack growth by extension and coalescence of nearby cracks. Near the end of the SCC crack life cycle (Stage 4) cracks begin to reach the critical length where the threshold stress of the material is reached and fast fracture occurs leading to the eventual failure of the gas pipe.

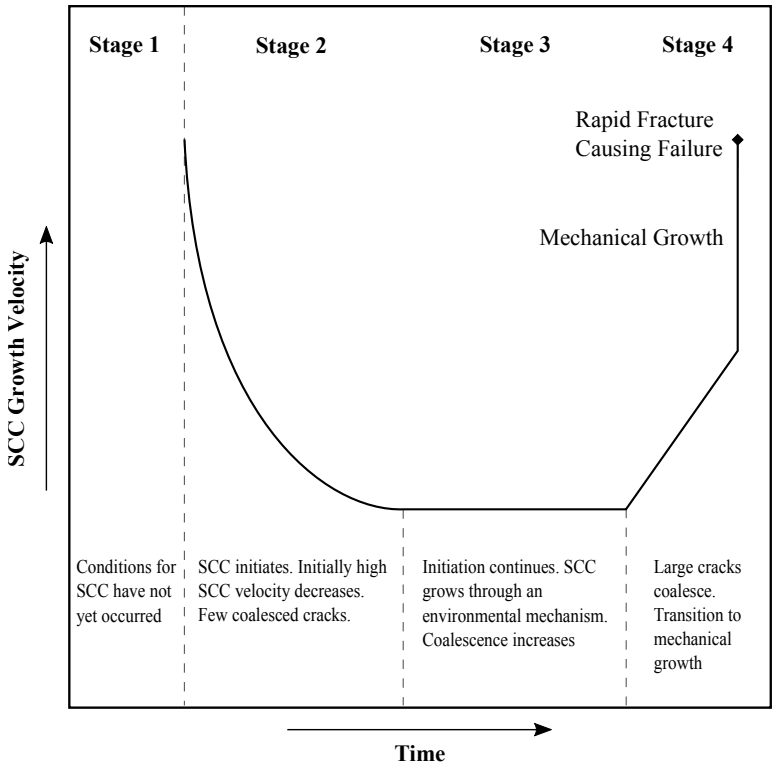

Figure 2.4: Bathtub model of SCC formation. Adapted from [39].

Occurrence of SCC can be somewhat predicted based on the environmental conditions the pipes are exposed to. There is an increased risk of SCC development in pipe down-

stream from compressor stations where the product temperature is significantly increased [5]. In addition to temperature, the soil type, CO_2 level or moisture content can inform pipeline owners of the potential to SCC formation [40]. Aside from a failure, SCC is often discovered in pipelines after a hydrotesting or non-destructive investigation of the pipe walls. Buried pipes at a high risk of SCC formation or sections known to contain SCC are inspected regularly through "In-Line Inspection", (ILI), or 'pigging' as it is known in industry. Ultrasonic Testing (UT) is one of the most common techniques used to find SCC and other pipe defects. Of the UT technologies shear wave UT and ElectroMagnetic Acoustic Transducers (EMAT) are capable of finding pipe defects with high certainty. ILI, however, is expensive to carry out and often can not be used in small diameter pipes [40]. Field inspections and rehabilitation of sections likely to fail are the likely result of ILI.

The management procedure surrounding SCC is dependent on the severity of SCC based on how likely it is to fail under standard operating conditions. The Canadian Energy Pipeline Association (CEPA) outlined the categories for SCC severity as shown in Table 2.1 which outlines the required response from pipeline operators when cracks are identified. Based on the physical conditions of a crack i.e. the length and depth, a crack is categorised based on the likelihood it has to causing a failure. As the severity increases the magnitude of the internal pressure that will cause a rupture $P_{F,SCC}$ is classified and the pipe owners response is provided. Although CEPA SCC severity categories are primarily concerned with transgranular SCC, the crack ratings are mechanism agnostic and only provide guidance to failure resulting from crack defects in a pressurised pipe wall.

Table 2.1: CEPA SCC severity categories. Adapted from [40].

Category		**Definition**	**Description**
I	$P_{F,SCC} \geqslant$ 110%×MOP×SF	A failure pressure greater than or equal to 110% of the product of the MOP (Maximum Operating Pressure) and a company defined safety factor (SF). The failure pressure for Category I SCC typically equals 110% of SMYS.	SCC in this category does not reduce pipe pressure containing properties relative to the nominal pipe properties. Toughness dependent failures are not expected for this category of SCC.
II	110%×MOP×SF> $P_{F,SCC} \geqslant$ ×MOP×SF	A failure pressure less than 110% of the product of the MOP and a company defined safety factor, but greater than or equal to the product of the MOP and a company defined safety factor.	No reduction in pipe segment safety factor.
III	MOP × SF > $P_{F,SCC}$ > MOP	A failure pressure less than the product of the MOP and a company defined safety factor but greater than the MOP.	A reduction in the pipe segment safety factor.
IV	$P_{F,SCC} \leqslant$ MOP	A failure pressure equal to or less than MOP.	An in-service failure becomes imminent as the MOP is approached.

2.4 Factors Controlling SCC Susceptibility

SCC susceptibility may be defined as how likely a material is to begin cracking and how rapidly cracks are able to propagate through the material once initiated. As there are three factors required for the development of SCC, each factor contributes to the overall SCC susceptibility in a system. The following section will highlight the effects of the environment, tensile stress and material properties on SCC susceptibility.

2.4.1 Environmental Factors

Chemical Composition of Soil

The presence of HCO_3^- and CO_3^{2-} ions in the surrounding soil is vital to the development of SCC in pipeline steels [1]. When a pipeline is polarized through a CP system, and ground water comes into contact with the pipe surface through a defect in the coating, H_2O breaks down into hydroxide ions (OH^-). The hydroxide ions are then combined with CO_2 dissolved in ground water to form HCO_3^- and CO_3^{2-} ions [1, 3–6]. SCC does not typically start to form until the concentration of carbonate and bicarbonate ions reaches $0.25N$ (normal concentration)[41]. When water is first split, there are insufficient levels of carbonate and bicarbonate ions to begin SCC, however, wet and dry cycles cause the concentration to gradually increase to levels that can sustain SCC [6]. An important factor in the occurrence of SCC is that cracking likely only occurs in-between the extremes of wet and dry seasons. This is because, if it is too dry the electrolyte dries up and if it is too wet the concentration of carbonate-bicarbonate ions is reduced to levels below the SCC forming threshold.

Whilst the importance of carbonate and bicarbonate ions is evident, without the presence of highly soluble sodium or potassium ions, SCC will not occur [6, 42]. Without the presence of sodium and potassium ions, to balance the high anion concentrations caused by the presence of carbonate and bicarbonate ions, SCC is unable to occur [6]. Field investigations have linked sodium ions as being the most present cation around SCC cracks [43]. The magnitude of sodium and potassium ions in the soil is a statistically significant indicator to high pH SCC formation [42]. The migration of sodium ions to defect locations is caused by the external cathodic protection system which attracts the positively charged ions to balance the negatively charged carbonate and bicarbonate ions [6]. As the formation of carbonate and bicarbonate ions outstrips the diffusion of Cl^- ions (commonly found dissolved in ground water) within disbonded regions, the pH can increase to a level conducive to SCC with the continued diffusion of sodium ions to balance the charge [6].

When carrying out laboratory testing of SCC on a Linearly Increasing Stress Test (LIST) apparatus or a Slow Strain Rate Test (SSRT), the typical electrolyte used to simulate the environmental conditions is a solution consisting of $1N\ NaHCO_3$ and $1N\ Na_2CO_3$ [1]. A $1N - 1N$ solution at 75°C gives a current density of 10^{-2} A/cm^2 which results in cracking behaviour very similar to those found in pipelines [44]. Whilst carbonate-bicarbonate solutions tend to be the most commonly used solutions to simulate cracking under laboratory conditions, other nitrate and sulphate containing solutions have been used to simulate intergranular SCC, although they are not as widely accepted for pipeline steels [45].

Temperature

As SCC propagates through the combined mechanisms of anodic dissolution and film fracture at the crack tip, temperature can dramatically increase the corrosion rate as anodic dissolution is temperature dependent governed by the Arrhenius equation ($k = Ae^{\frac{-E_a}{RT}}$) where k is the rate constant, A is a constant, E_a is the activation energy, T is the temperature in Kelvin and R is the universal gas constant [46]. Accordingly, higher temperatures result in faster SCC propagation. Systematic experimentation by Beavers et al. (1998) [47] with a $1N\ NaHCO_3$ and $1N\ Na_2CO_3$ solution at temperatures from 15°C to 90°C found that the rate of SCC propagation increased with the increased temperature, observed in Figure 2.5. Figure 2.5 shows that while SCC can occur over a wide temperature range, higher temperatures result faster crack velocities and hence, larger cracks over a given duration. The increase in crack velocity due to increased test temperature is a common observation [33, 48].

[1] $1N\ NaHCO_3$ and $1N\ Na_2CO_3$ corresponds to $0.5M\ Na_2CO_3$ and $1M\ NaHCO_3$.
($1M\ NaHCO_3$ is 84.006 g/L and $1M\ Na_2CO_3$ is 105.998 g/L)

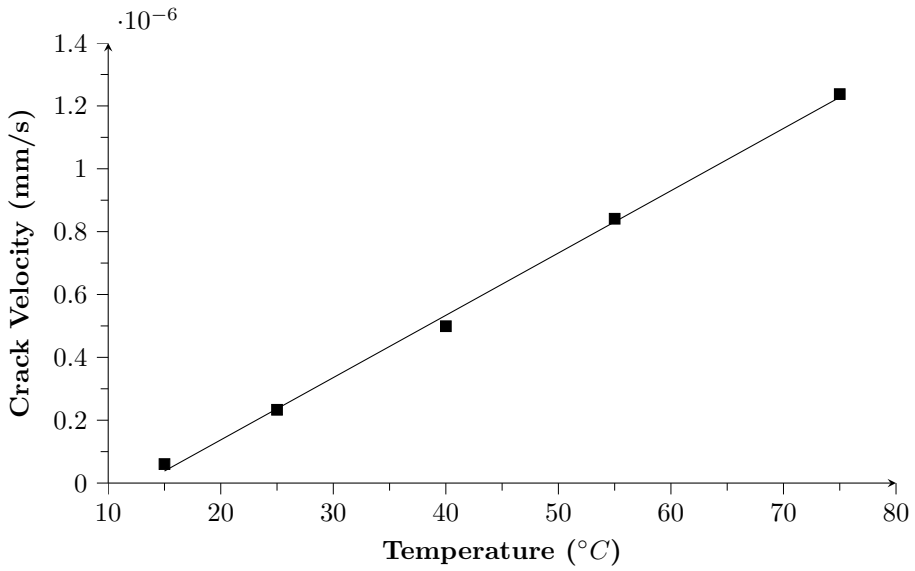

Figure 2.5: The effect of temperature on SCC crack velocity in a 1N-1N solution. Adapted from [47].

In gas pipelines the vast majority of cracking occurs close downstream from gas compressor stations where the temperature is increased as a side effect of the pressure increase [5]. In high pH SCC, most cracking occurs within 20 km of the compressor station where temperature can often be in excess of 70°C [49]. The effect of temperature is the same for near neutral pH SCC, where a strong affinity to high temperatures is reported with up to 65% of instances discovered within 30 km distance from compressor stations [5].

Effect of Coatings on SCC

As SCC requires direct contact between the outer surface of the pipe and the soil where electrolyte ingress can occur, intact coatings prevent SCC from forming. As improvements in pipeline coating occur, pipe operators tend to move away from the older coating systems to those that offer better protection when commissioning new pipelines or when carrying out any repairs on pipes coated with older systems. SCC failure is often linked to legacy coating systems such as coal tar enamel and polyethylene tape while new technology such as fusion bonded epoxy (FBE), urethanes, liquid epoxy and other composite materials have shown much greater resistance to SCC formation [5].

Coating disbondment where the coating detaches from the pipe surface leaving a region

exposed to the environment is the most common form of pipeline coating failure [50]. When a coating disbonds from the surface of a pipe, the defect that forms allows ingress of soil and electrolyte to come in contact with the pipe wall [51]. Whilst CP is generally able to protect the exposed region of the pipe wall, a shielded crevice can form and the effectiveness of the CP is greatly reduced [51]. The regions that CP is not able to penetrate can cause shielding that shifts the applied potential into a range that promotes SCC [35].

The degree of cathodic shielding is related in part to the coating system used with some coatings being more susceptible to shielding than others [52]. While some early generation coatings such as polyethylene tape cause shielding, modern FBE coatings tend to allow cathodic protection to penetrate the coating and protect the pipe even under disbondment [52, 53]. It is noted that whilst coal tar epoxy coatings are not typically found to cause shielding, SCC has formed in these pipes frequently [5, 52]. A key factor in determining whether a coating is adequately protecting a pipe via cathodic protection whilst disbonded, is an increase in pH [51]. Under those conditions a net cathodic current is detected and hence cathodic protection can be considered active under the disbondment. As SCC requires an increase in pH to occur, if the CP current drops due to having to permeate through the coating, it may still produce conditions that allow the growth of SCC which could explain SCC in coal tar enamel coatings [54].

Summary of the Effect of Environmental Conditions

The investigated literature about the effect of environmental conditions on SCC susceptibility can be summarised as follows:

1. SCC forms when the cathodic protection splits water forming OH^- ions which combine with CO_2 forming carbonate and bicarbonate ions that raise pH and corrode grain boundaries

2. The presence of sodium or potassium ions is necessary for the pH surrounding defects to rise to the levels necessary for SCC

3. The propagation rate of SCC is defined by temperature through the Arrhenius equation. Higher temperatures result in faster cracking rates. As a result SCC tends to occur downstream from compressor stations where the temperature is increased as a result of the increased pressure

4. A correctly applied coating is in general resistant to SCC, however, when disbondment occurs coatings can shield the CP potential resulting in pH increases and SCC

2.4.2 Effect of Stress on SCC Susceptibility

Surface Condition

The surface condition of the pipe has a large impact on the susceptibility behaviour of the pipeline material. As SCC is a stress based corrosion process, the introduction of stress raisers can increase the likelihood of SCC initiating from the surface of an exposed section of pipe. The overall increase in pitting locations corresponds to an overall increase in SCC [55]. SCC is often found at the base of surface pits where the electrochemical conditions and stress are favourable to crack initiation; so more initiations sites, the greater the chance SCC will form [56]. One method of controlling pitting is to ensure the surface is as smooth as possible. Surface roughness in stainless steel has been linked by Burstein and Pistorius (1995) [57] to an electrochemical potential conducive to pitting, hence, pitting is more likely on a rough surface as seen in Figure 2.6, where the number of metastable pit sites (N_o) is plotted against the potential vs. saturated calomel electrode ($E(V_{SCE})$).

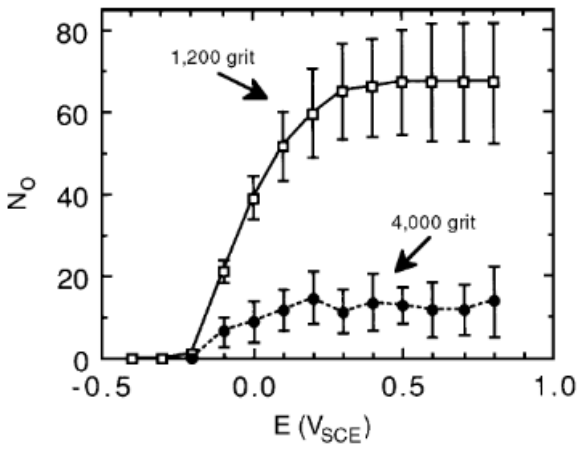

Figure 2.6: The effect of surface roughness and potential on pitting. Reprinted from [57].

Best industry practice is to coat pipelines prior to installation to prevent contact with the soil and to reduce the risk of general corrosion. As low carbon steels are susceptible to rust, the pipes are often coated in the factory where surfaces are grit blasted prior to being coated to both remove oxides and roughen the surface for better adhesion. As discussed previously, rougher surfaces result in a higher chance of SCC initiation sites hence grit blasting may initially be thought to increase SCC susceptibility. As seen in Figure 2.7, the effect that surface roughness has on SCC susceptibility is not as clearly defined. Whilst increasing surface roughness resulted in a lower Time To Failure (TTF) Figure 2.7a, the average crack depth did not appear to increase for the grit blasted surfaces Figure 2.7b. Whilst a rougher surface may fail faster due to the increased; likelihood of SCC initiation, this is because the rough surface has more potential stress raisers than the smooth surface[8]. As grit blasting results in better coating adhesion, SCC initiation is less likely hence grit blasting is expected to have a net positive impact on SCC susceptibility. Grit blasting can also induce residual compressive stress into the surface of the pipe which has been found beneficial in delaying the onset of SCC [3].

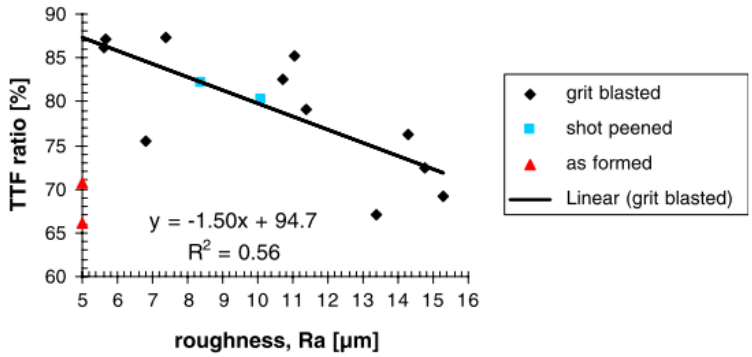

(a) Surface roughness vs. time to failure

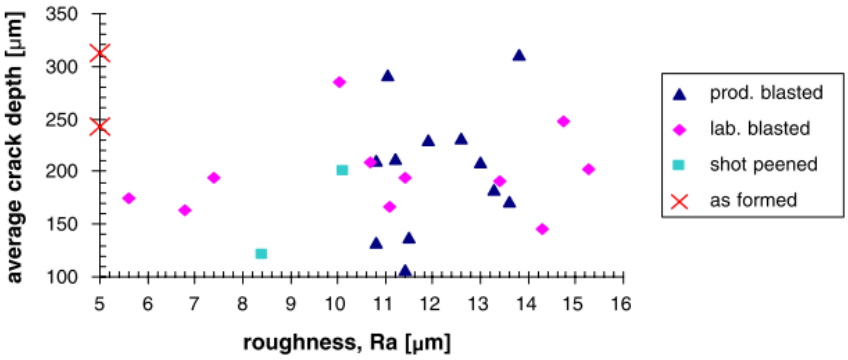

(b) Laboratory crack velocity pre-crack specimens

Figure 2.7: The effect of surface roughness on SCC. Reprinted from [8].

Another aspect of surface condition is the effect that mill scale has on the initiation of SCC. Mill scale is an oxide layer formed during the manufacturing process where hot rolled steel can oxidise at the surface between rolling passes forming a surface scale. Seasoned pipes (mill scale covered pipe surfaces) are more susceptible to SCC than machined pipes, however, this is not necessarily because mill scale covered surfaces were more susceptible [55]. Mill scale protects the surface from SCC whilst it is intact, however, mill scale is brittle and fractures readily. When mill scale fractures, the steel surface is exposed to the soil allowing the conditions necessary for SCC to develop [55, 58]. The lower fracture toughness of the mill scale can cause mill scale covered pipes to develop SCC at a higher rate than polished surfaces [3, 37].

Effect of Applied Stress

SCC crack propagation occurs through the combined action of film fracture at the crack tip and localized anodic dissolution of the exposed grain boundaries. Without sufficient applied stress, the protective film will not fracture and SCC propagation will halt. SCC typically occurs perpendicular to the hoop stress direction (greatest stress direction) when the internal pressure of the pipe is at 60% of its SMYS (specified minimum yield stress) [59]. However, SCC has occurred at pressures as low as 46% SMYS but this was usually attributed to a stress concentrator [59]. Australia has a maximum acceptable operating pressure of 72% SMYS which is more than sufficient for SCC formation to occur in susceptible line pipe [60]. SCC usually occurred in regions without significant secondary stresses but SCC has been found in locations of branch connections and where large dents and other surface defects have introduced stress concentrators [44]. Two different defects are shown in Figure 2.8 from pipelines where failure had occurred. As seen in Figure 2.8a a manufacturing defect caused the wall thickness on the right side of the weld to be lower than required, thus increasing the stress experienced in that side of the pipe causing SCC to occur [30]. Similarly, in Figure 2.8b the pipe was exposed to a significant bending stress at the failure location due to being bent to travel under the canal. The combined bending stress and stress from the internal pressure lead to accelerated SCC in the ruptured section where the bending stress was most severe [61].

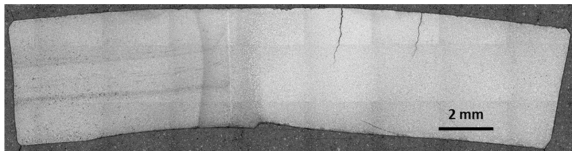

(a) Cross-section of defective pipe. Reprinted from [30].

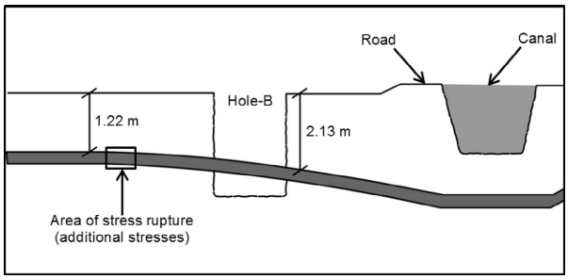

(b) Environmental conditions leading to SCC failure. Reprinted from [61].

Figure 2.8: Two examples of stress concentrators leading to SCC.

The nature of the applied stress can have a large influence on the rate of SCC initiation [1, 39, 62]. Whilst pipelines are designed as statically operating structures, they are subjected to pressure fluctuations due to differences in daily demand, temperature fluctuations and production output. In a statically loaded SCC case, the SCC growth is heavily influenced by the creep rate [1]. It has been observed by Parkins (2000) [1] that if a specimen is statically loaded in a carbonate-bicarbonate solution while held at a non-cracking potential, once creep had been exhausted, the application of a cracking potential did not cause SCC crack growth. As pipeline SCC is thought to initiate in a cyclic stress environment, research into the effect of cyclic loading on SCC has been undertaken [62]. There is evidence that cyclic loading can considerably reduce the threshold stress necessary for SCC to initiate and form [1]. This can be due to micro plastic deformation that allows sustained film fracture even when the creep is exhausted [1]. When attempting to simulate the crack growth behaviour witnessed in the field, by introducing cyclic loading to standard SCC testing procedure (load fluctuation of approximately $\pm 1.5\%$ over the course of a day) the developed cracks closely approximated those found in the field [39].

Under lab conditions, when carrying out cyclic loading of SCC specimens, the maximum crack depth levelled off after approximately 15 cycles as seen in Figure 2.9a [39]. When measuring the crack velocity, a measure of the susceptibility to SCC, the actual crack velocity as highlighted in Figure 2.9b is more closely represented by 10 cycles [39].

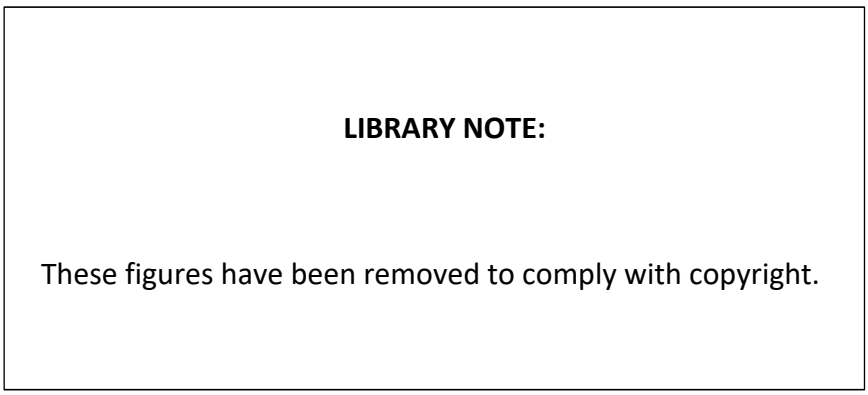

(a) Laboratory crack velocity of uncracked specimens

(b) Laboratory crack velocity pre-crack specimens

Figure 2.9: SCC crack velocity vs. number of cycles. Reprinted from [39].

Effect of Residual Stresses

The residual stresses created during manufacturing and processing can have a particularly devastating effect on otherwise unloaded samples. A classic example is the season cracking of brass cartridges prior to 1921 where the residual stress in cold drawn brass mixed with the corrosive agent ammonia caused SCC without an applied stress [63]. During the forming of pipe from plate, the material undergoes both coiling and uncoiling along with pipe forming and welding that creates residual stress in the material. The significance of this is residual stress in addition to the applied stress, hence a residual tensile stress can increase the overall stress experienced leading to higher SCC rates.

The result of numerous SCC inspections has determined that SCC frequently occurs in the vicinity of seam welds. The reason behind this is likely due to the increase in residual stress as well as the change in microstructure that occurs in the heat affected zone (HAZ). Corrosion studies carried out on weld metal and the HAZ have determined that there is an increased susceptibility to corrosion in the HAZ and weld metal as compared to the parent metal which would likely increase the regions susceptibility to SCC [64–66]. As the weld heat input can result in different expansion and contraction rates between the weld metal and the parent metal, residual stresses are created during the cooling in a seam weld [67]. In addition, increased heat input from multipass welding during simulated girth

welding of a 304 stainless pipe increased the SCC susceptibility and decreased the time to failure as seen in Table 2.2 [68].

Table 2.2: Time and pressure table of SCC generation. Adapted from [68].

Specimen No.	**Pass**	**Through-Wall Crack Time (min)**	**Max Inner Pressure (bar)**
W1	1	787	192
W2	5	646	120
W3	10	132	127
W4	12	323	144
W5	15	294	157

In addition to welds creating stress concentrators, the pipe forming process also produces residual stresses in the pipe. During the coiling process, flat plate is bent into a coil to facilitate easier transport and storage prior to pipe forming. The process of coiling results in the outer surface being stretched leading to tensile residual stresses and the inner surface being compressed leading to compressive residual stress [67]. The pipe forming process where the uncoiling plate is cold deformed into a pipe results in similar tensile and compressive residual stresses to be created in the outer and inner walls respectively [67]. The residual tensile stress at the outer surface increases the risk of SCC by combining with the applied stress.

The processes which have been discussed as imparting residual stresses have been detrimental to the SCC susceptibility, however, grit blasting and shot peening for instance can improve the SCC susceptibility. Grit blasting, which is used commonly in modern coated pipes not only removes scale from the pipe surface to improve adhesion, also imparts a slight compressive residual stress in the surface which may be beneficial to SCC formation [3, 15].

Summary of the Effect of Stress on SCC Susceptibility

The investigated literature about the effect of stress on SCC susceptibility can be summarised as follows:

1. The surface can heavily influence the SCC susceptibility
   (a) Surfaces with intact mill scale prevents SCC but when the scale is cracked it can shield potential leading to SCC
   (b) Surfaces with pitting are more susceptible to SCC than those without the surface defect
   (c) Grit blasting the surface ensured better coating adhesion and introduced a slight compressing residual stress leading to decreased SCC susceptibility
2. The magnitude of stress applied to the material is strongly linked to SCC susceptibility with higher stresses resulting to faster crack propagation
3. Cyclic loads result in worsening SCC susceptibility than static or linear loading patterns
4. Residual tensile stresses introduced into the pipe surface result in higher SCC susceptibility

2.4.3 Effect of Material Properties on SCC Susceptibility

Effect of Chemical Composition on SCC

When designing a low carbon steel for use in pipeline steels, the API 5L standard governs certain chemical composition limits, there is a fair degree of latitude provided to pipe manufacturers to tweak the properties to suit the requirements. The alteration of the chemical composition in steel can lead to improved microstructure development and mechanical properties.

There have been limited investigations carried out on the role of microalloying elements on SCC susceptibility. There is some evidence that in martensitic and austenitic stainless steels an increase in the manganese content can increase susceptibility to corrosion [9, 10]. However, there have not been any systematic reviews on the role of chemical composition to SCC susceptibility in pipeline steels. More research has focussed on the role of carbon on SCC susceptibility and hence will be the focus of this section.

Effect of Carbon Content

The relationship between SCC susceptibility and carbon content is not linear and is not well understood. When comparing the effect of carbon content on SCC susceptibility (in a nitrate solution) in very low carbon steels (carbon content ranged from 0.001-0.16 wt.%), the observed SCC susceptibility increased with decreasing carbon content [46]. In addition, very low carbon wire loaded in a nitrate solution with carbon content ranging from (0-0.1 wt.%) determined that the susceptibility initially peaked at 0.009% before decreasing with increased carbon content [69].

In two linked studies of higher carbon content steels conducted by Eaglesham, et al. (1988) [11] and Bulloch (1991) [12], three steels with carbon contents of 0.4%, 0.6% and 0.8% saw that an increase in carbon content tended to result in a decrease in $K_{I_{SCC}}$ (increased SCC susceptibility) as seen in Figure 2.10. Whilst the 0.4% and 0.8% carbon steels experienced a linear increase in $K_{I_{SCC}}$ with increasing temper, there was a plateau associated with the 0.6% carbon steel. The difference in susceptibility is likely becasue of the difference fracture mechanisms observed with different tempers and carbon contents shifting from transgranular to intergranular [12]. These findings are similar to those observed by Sandoz (1971) [9] who found the highest SCC resistance was with a carbon content of 0.2% and that the highest SCC susceptibility occurred with a carbon content just below 0.4% as seen in the $K_{I_{SCC}}$ graph in Figure 2.11. It is noted that no error bars were included in any of the results so while the average trend is presented it is uncertain

whether the results are of statistical significance.

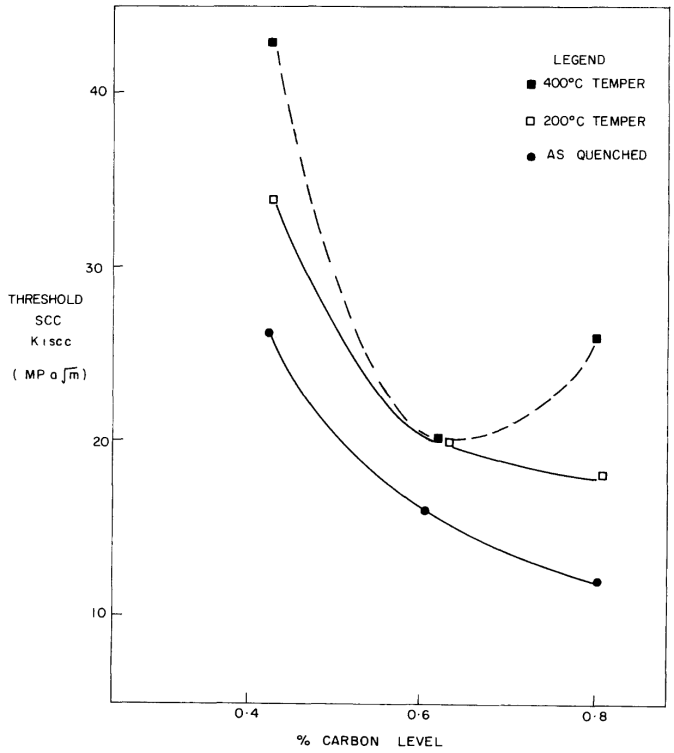

Figure 2.10: The effect of carbon content and temper on SCC. Reprinted from [12].

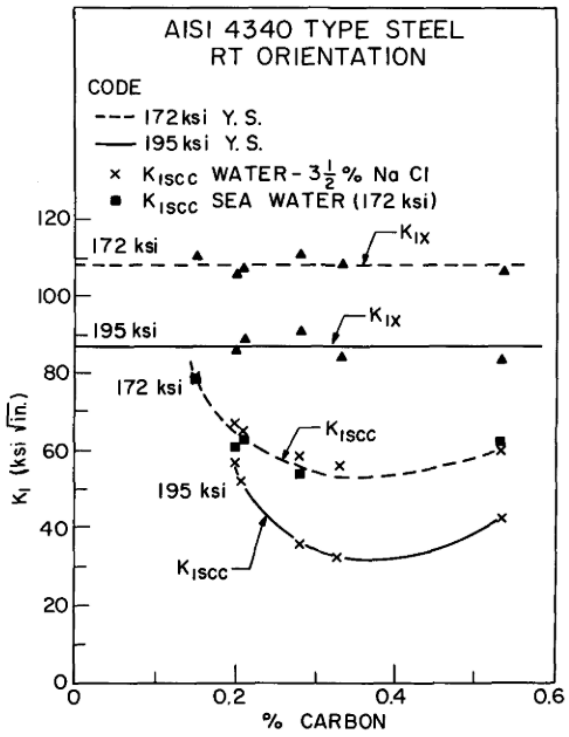

Figure 2.11: The effect of carbon content on SCC. Reprinted from [9].

Based on the above results, increasing the carbon content up to 0.2% tends to result in increased resistance to SCC and any subsequent increase has a net negative effect. The role of carbon content appears to be linked most strongly to the precipitation of Fe_3C (iron carbide). The carbon in solution associated with the Fe_3C particles may be involved in SCC due to ferrite acting as efficient points for cathodic discharge where carbon is less reactive than ferrite and encourages anodic dissolution [70].

Effect of Microstructure

During the pipe making process, aside from the chemical composition, there is significant latitude provided to pipe manufacturers regarding the developed microstructure (provided the mechanical properties are achieved for the grade). As each microstructure carries with it different physical characteristics, they too have different susceptibilities to SCC. The microstructures that have been investigated are ferritic, ferritic-pearlitic, bainitic and quench-tempered, examples of which can be seen in Figure 2.12.

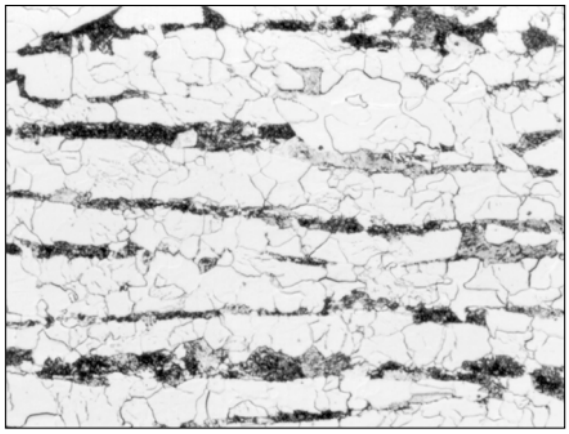

(a) Banded ferritic-pearlitic microstructure. Reprinted from [15].

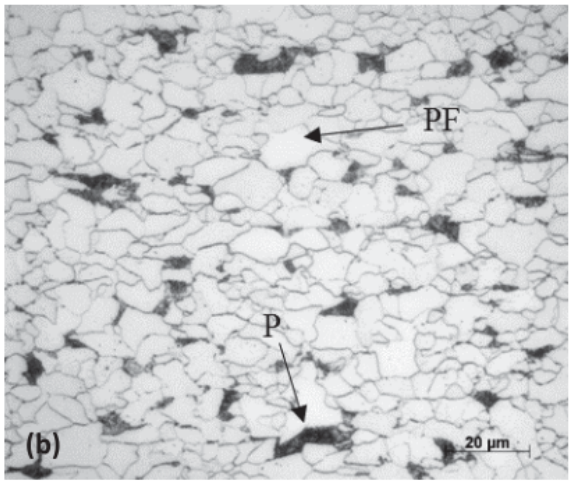

(b) Ferritic-pearlitic microstructure. Reprinted from [71].

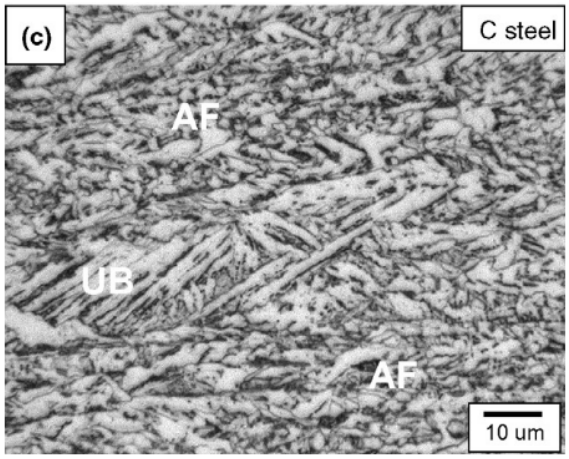

(c) Bainitic microstructure. Reprinted from [72].

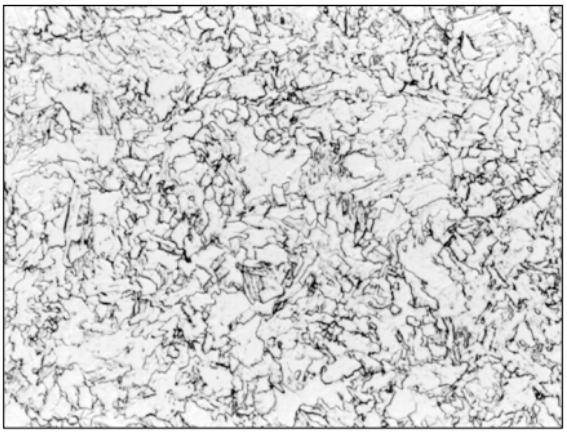

(d) Quench-tempered microstructure. Reprinted from [15].

Figure 2.12: Series of common pipeline steel microstructures. P:Pearlite, PF:Polygonal Ferrite, UB:Upper Bainite and AF:Acicular Ferrite.

In terms of microstructure, in a range of SCC solutions, quenched samples along with quenched and tempered microstructures (typically consisting of bainite in low carbon steels) tend to be more susceptible to SCC than typical control rolled steels with ferrite matrix and bainite or pearlite interspersed [4, 13, 14]. The studies carried out heat treatment on samples of either X70 or X80 pipe, so the chemical composition is the same between the different microstructures.

When comparing the microstructures in a series of different pipe samples, all different

grades and pipe manufacturing processes, bainite and bainitic-ferrite microstructures were found to be more resistant to SCC initiation than ferritic or ferritic-pearlitic structures [15, 16]. These studies were carried by the same group in both high pH and near neutral pH environments and only tested low carbon pipeline steels. It is apparent that differences in susceptibility were the result of not only microstructure but also manufacturing procedure. Bainite that formed through quench-tempering [4, 13, 14] was more susceptible than bainite formed through thermomechanical rolling [15, 16]. Martensite was often present in the quenched samples so the inhomogeneity of the microstructures could have also contributed to the lower SCC susceptibility. Homogeneous microstructures were identified as more resistant to SCC than mixed microstructures [15, 16].

There appears to be consensus that microstructure has a strong influence on SCC susceptibility, however, there is more to SCC susceptibility than just microstructure. As bainite formed through controlled rolling has a different susceptibility as compared to bainite formed through quench-tempering, the role of microstructure can not be sufficiently clear to predict SCC susceptibility in low carbon steels.

Effect of Grain Size on SCC

The grain size of an alloy subjected to a corrosive media controls the number of boundaries potentially exposed and the overall area of the boundary to be fractured. There have not been any studies concerned with the role of grain size on SCC in pipeline steels. Although there are no specific studies concerning the role of grain size on SCC susceptibility in pipeline steels, the role of grain size on SCC susceptibility has been investigated in other susceptible materials. The role of grain size on SCC may not be directly comparable between different materials, however, it can provide some indication on the expected role that grain size has on SCC in pipeline steel.

To determine the role of grain size on SCC susceptibility in a 7475 aluminium alloy, a

series of temper treatments were performed to alter the grain size of the as received material [17]. Grain refinement resulted in a more homogeneous slip mode and smaller grain boundary precipitate size that improved SCC susceptibility. When refinement caused the grain boundary precipitates to reduce below the critical size (approximately 25 nm), SCC susceptibility was increased as hydrogen was now able to nucleate at the precipitates [17]. In aluminium alloys, the vast majority of literature pertaining to corrosion in general advise reducing grain size for improving corrosion resistance [18]; however, as reported by Tsai and Chuang (1997)[17], excessive reduction of grain size can have unintended effects that increase susceptibility. In general, grain refinement stabilises the passive oxide layer of light alloys which could reduce the likelihood of SCC by reducing the time the oxide layer takes to reform after being fractured [18].

In addition to aluminium alloys, some studies have been undertaken to determine what role grain size has on SCC susceptibility in stainless steel. In a series of tests on heat treated samples, an increase in experimental austenitic stainless steel grain size resulted in higher $NaCl$ SCC susceptibility [19]. The authors suggested that the increase in SCC susceptibility for larger grain sizes may be due to the reduction in mechanical properties combined with decreased stability of the passive film [19]. It is noted that grain boundary precipitation can encourage hydrogen to precipitate under certain electrochemical circumstances hence encouraging their presence through poor heat treatment is expected to degrade the SCC resistance of the stainless steel alloys.

In SCC, the stress limit under which no SCC will occur is called the threshold stress [73]. Increasing the threshold stress of a material improves the SCC resistance by increasing the force needed to be applied before SCC can initiate. It has been demonstrated that refining grain size improves the yield strength which corresponded to an increase in the threshold stress for SCC to form[73]. Hence, in this manner, refining grain size should result in a net improvement of SCC susceptibility.

Effect of Yield Strength

The yield strength of materials undergoing SCC seems to play a significant role on the susceptibility to SCC. As API 5L pipeline steels are essentially differentiated by grade due to their tensile properties, the role of yield strength on the SCC behaviour can help to illuminate the role grade has on SCC susceptibility.

The effect of tensile properties such as yield strength on SCC susceptibility is given in Figure 2.13. According to Eaglesham et al. (1988) [11] in Figure 2.13 an increase in yield strength tends to corresponded to a decrease in $K_{I_{SCC}}$ up until yield strengths of 1400 MPa where it levels off. $K_{I_{SCC}}$ corresponds to the fracture toughness of the passive film layer developed during cathodic protection. If the value of $K_{I_{SCC}}$ reduces, SCC susceptibility increases because the load required to fracture the oxide layer and allow anodic dissolution to occur is reduced, i.e. smaller loads can result in SCC. When comparing that to pipeline steel literature, in near neutral SCC, there appears to be a similar trend in that an increase in yield strength tends to come with a subsequent decrease in SCC resistance [74].

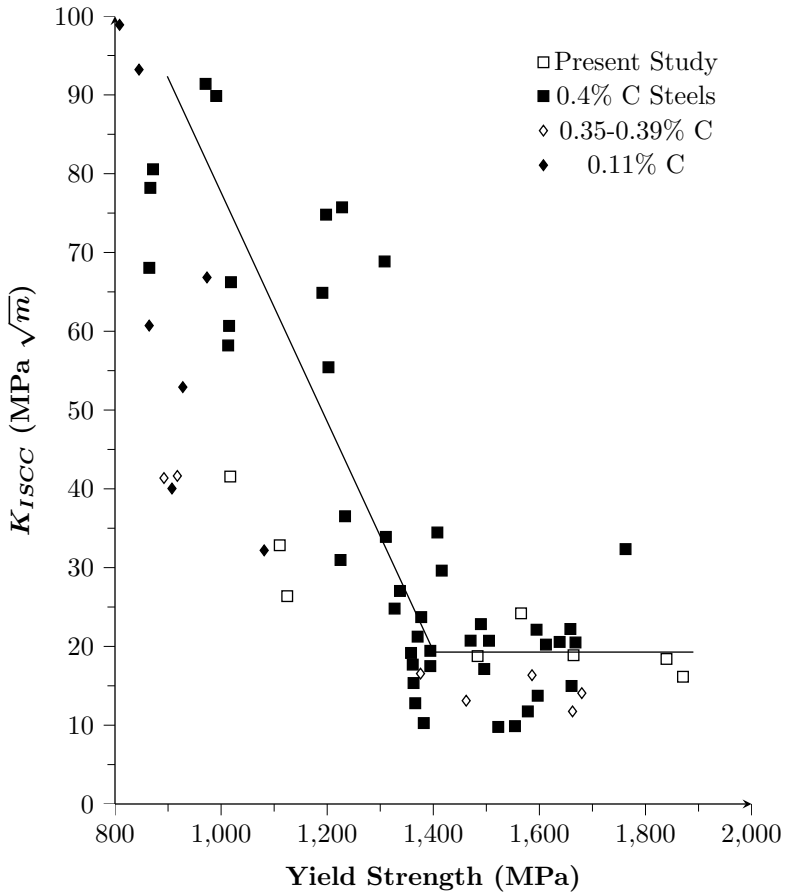

Figure 2.13: The effect of yield strength on $K_{I_{SCC}}$ of steel samples. Adapted from [11].

Increases in yield strength appear to result in a decrease in the value of $K_{I_{SCC}}$. The result of this is a weaker fracture toughness of the passive oxide layer at the crack tip of SCC cracks resulting in higher potential crack rates. It is expected that higher grade pipeline steels should be more susceptible to SCC due to their greater yield strengths and associated lower value of $K_{I_{SCC}}$.

Summary of the Effect of Material Properties

The investigated literature about the effect of material properties on SCC susceptibility can be summarised as follows:

1. In general, the chemical composition is not thought of as an especially important parameter in determining the resistance to SCC in pipeline steels. Whilst the carbon content has been shown to improve the resistance to SCC up to 0.2%, but becomes

detrimental past this point. The maximum carbon content allowed in modern, thermomechanical formed pipes is only 0.12% [27]. The higher the grade of the pipe steel the lower the carbon content. Hence increasing carbon content of a pipe steel is not a realistic method to reduce SCC susceptibility.

2. A decrease in grain size seems to have a net positive effect on SCC susceptibility because the passive film strength is improved with a reduction in grain size.

3. There is no clear data regarding the influence of microstructure on the SCC susceptibility except that quenched steels tend to have the worst SCC susceptibility. There are some issues with the methodology carried out in these studies as there was no residual stress measurements conducted after heat treatment where the quenched samples likely has higher residual stress than normalised samples.

4. Increased yield strength appear to negatively affect the SCC susceptibility in steel samples by reducing the fracture toughness value of the passive film. This means a lower stress or load is required for SCC to propagate.

2.5 SCC Testing

As SCC requires the three conditions of 1) a corrosive medium, 2) susceptible material and 3) and tensile stress to form, laboratory testing is essentially a method of creating conditions for SCC to occur. In laboratory testing, materials are subjected to a corrosive environment and either a fixed or dynamic load to determine the susceptibility. Fixed load tests such as the u-bend, c-ring and bent beam tests provide inexpensive qualitative testing whereas dynamic testing such as the Slow Strain Rate Test (SSRT) or Linearly Increasing Stress Test (LIST) provide quantitative susceptibility behaviour [75].

2.5.1 Fixed Load Testing

Whilst SCC susceptibility testing using either the SSRT or the LIST provides quantitative results for SCC susceptibility, the apparatuses are expensive to purchase and are limited to only conducting a single test at a time. Whilst only able to provide qualitative results for SCC susceptibility, fixed load SCC tests such as the U-bend, C-ring and bent beam are inexpensive and simple to conduct [75]. Examples of each test are provided in Figure 2.14. A variety of samples are loaded to different percentages of their yield stress and give a failure/ no-failure result that can provide an estimation for the critical load necessary for SCC to develop in a particular system. Fixed load tests are simple tests that can provide loading conditions below which SCC is highly unlikely to form.

Fixed load testing relies on creep for film fracture and as creep rate diminishes with time, unless sustained by crack growth, the rate of SCC growth will stall [1]. A dynamic system with varying loading conditions may not be adequately represented by a fixed load test. When testing a material with unknown susceptibility there is no indication of when SCC has formed and the test is complete. If after an extended period of time no cracks form, it is uncertain whether they will form if given more time or if the material is not truly not susceptible [76]. Fixed load testing is primarily a qualitative testing method and should not be used for determining the susceptibility of material to SCC if an SSRT or LIST apparatus is available.

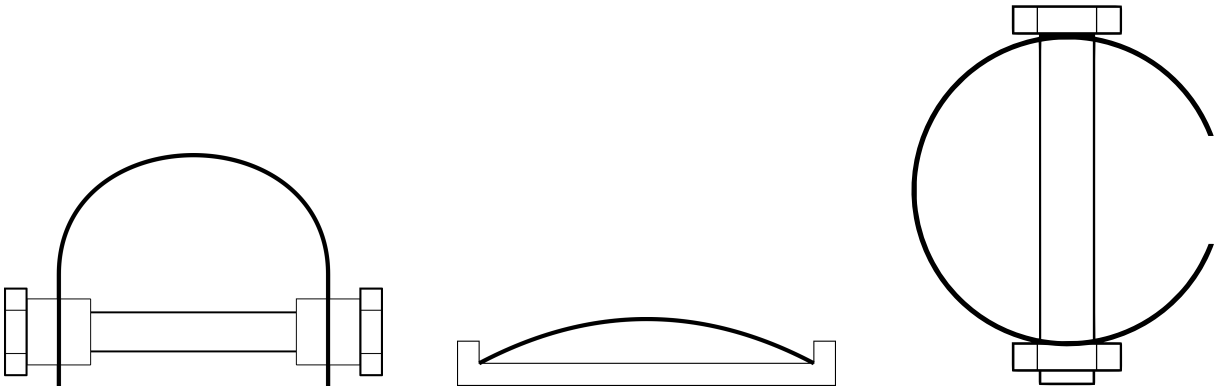

(a) U-Bend Test (b) Bent Beam Test (c) C-Ring Test

Figure 2.14: Fixed load SCC tests. Adapted from [75].

2.5.2 Dynamic Load Testing

The most effective tests for determining the susceptibility of materials to SCC are either SSRT or LIST tests. While different apparatuses, they operate essentially the same and apply a changing load to a specimen until the specified end point of the test. The applied load can either increase until failure (which marks the end of the test) or cycle between two loads for a predetermined number of cycles with both apparatuses capable of performing either loading condition. Each method has advantages and both are used to test SCC susceptibility.

When the load is increased until failure, the main advantage is that the test will always have an endpoint defined by fracture, so it is certain to develop cracks as the stress increases to failure. Cyclic loading is advantageous since the test piece does not fracture during testing, cracks can be measured from any cross section; not only from the fracture surface as is the case when continuously loading to failure. As the sample does not fracture at the conclusion of testing, EBSD analysis of cracks is far simpler because the sample does not deform and the orientation data is preserved. As a result, crystallographic texture measurements surrounding the SCC cracks are simpler.

SSRT

The SSRT or as it is also known as the Constant Extension Rate Test (CERT), is the most commonly used dynamic SCC test currently. The SSRT is essentially a specialised tensile testing unit with an environmental chamber that can operate at extension rates as low as $2.54 \times 10^{-4} - 2.54 \times 10^{-6}$ mm/s [77]. The SSRT is governed by three international standards ASTM G129 [77], ISO 7539-7 [78] and NACE TM-198 [79]. The SSRT is the most widely used apparatus in literature regarding the failure of gas pipelines in low carbon steel [38, 39, 44, 48, 49, 55, 80–83]. As a result, most research outcomes come from this test. A typical SSRT apparatus is displayed in Figure 2.15 where a gearbox lies underneath the frame providing the slow extension rates required for the test and a sealed chamber for the environmental cell.

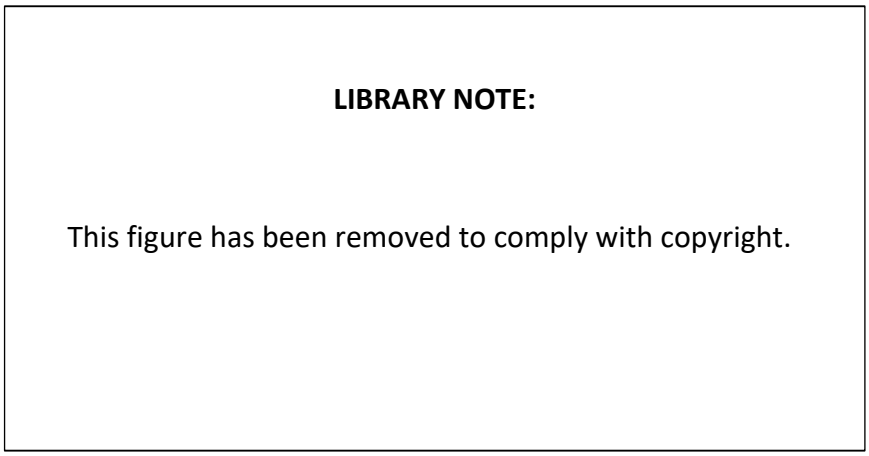

Figure 2.15: Commercial SSRT apparatus manufactured by Cortest Inc. Reprinted from Cortest [84].

To test the susceptibility of a material to SCC in an SSRT test, a specimen is initially

tested to failure in a non-corrosive environment (usually air) to determine baseline material properties. Samples are then sealed in the environmental test chamber and strained until failure. The mechanical properties of the run in the corrosive environment are then compared to the baseline test. If the material properties are significantly worsened when exposed to the solution, it is a good indication that SCC has occurred. After failure, the fracture surface is examined under SEM to determine the length of the SCC crack and a crack velocity is determined to indicate the susceptibility of the test piece to SCC. One limitation of the SSRT and in fact all SCC testing is that the sample that do not produce their own passive oxide layer (i.e. aluminium, titanium, stainless steel etc.) need to have a potential applied to them for SCC to occur. Gas pipelines are polarized through CP in the field and therefore a similar condition is required to be applied to the pipe during the SCC test otherwise susceptible materials will not develop SCC [76].

LIST

The Linearly Increasing Stress Test (LIST) is a newer form of dynamic test devised by Atrens et al. (1993) [36] of the University of Queensland in the early 1990's. The LIST is similar to the SSRT in that it applies an increasing load to a test specimen whilst in a corrosive environment. Where they differ is that the SSRT is extension controlled while the LIST is load controlled. The benefit of the LIST as compared to the SSRT is the test duration using the LIST is often shorter because once SCC initiates the test specimen fails much faster than SSRT testing [85]. Measuring SCC susceptibility is similar for the SSRT and the LIST, since crack velocity determined by measuring the length of the SCC crack divided by the time taken to grow the crack for both tests [36].

Whilst load controlled tests can also be carried out in an SSRT apparatus, the LIST apparatus is a simpler mechanism consisting of a cantilever beam with a sliding weight attached to the test specimen to control the applied load. An example of the LIST apparatus used in this thesis can be seen in Figure 2.16. The LIST is a widely accepted

form of SCC testing and is the basis of many fundamental studies into the behaviour of SCC on a wide variety of materials and corrosive mediums [37, 85–91]. A cyclic loading condition will be used to measure SCC susceptibility in this thesis which could be carried out on either device with equal accuracy and repeatability. As the LIST is a simpler device, there is less chance of electronic signal failure during testing and hence may be more repeatable in the load controlled condition than the SSRT. It is for that reason the LIST will be the apparatus used when testing the SCC susceptibility of the laboratory rolled samples.

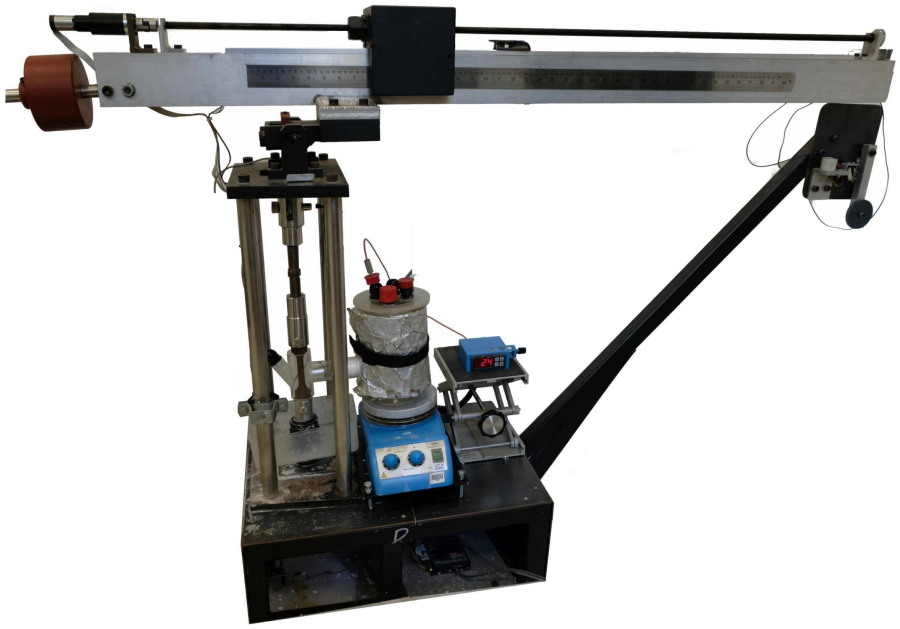

Figure 2.16: LIST apparatus manufactured at University of Adelaide.

Oscillating Loads

In their original test specifications, both the SSRT and the LIST apply an increasing load to a test specimen until failure is observed. This loading condition does not exist in gas pipelines; there are oscillations in the load due to pressure fluctuations of the gas going through the pipe depending on demand and temperature [39]. To better mimic the operating conditions researchers have altered the loading pattern to include a triangular loading pattern such that the applied stress oscillates around a mean stress.

The stress at which SCC forms is typically below the yield stress due to the fact that for the crack to form, it does not need to fracture the material, but the passive oxide layer allowing anodic dissolution to occur [7, 32]. The fracture toughness of the passive oxide layer ($K_{I_{SCC}}$) is lower than that of the parent metal (K_{I_C}) so applied stresses that would not normally cause fracture in the parent metal will cause fracture of the passive oxide layer [92, 93] i.e.

$$K_{I_C} > K_{I_{SCC}} \tag{2.1}$$

Oscillating loads can generate cracks below yield stress provided it is higher than the critical stress necessary for film fracture [39].

When utilising oscillating loads in an SSRT or LIST apparatus there is reduced likelihood of producing cracking from general failure mechanisms and as the test is halted prior to failure, crack length can be measured through standard optical microscopy without the need for SEM analysis.

2.6 Crystallographic Texture

Within polycrystalline materials, atoms are arranged as discreet crystals known as grains which are formed during the manufacturing process. Crystallographic texture is a statistical parameter that measures the overall orientation of grains within a polycrystalline solid with reference to an external frame of reference [94]. Crystallographic texture is statistical in nature, hence, the more grains that share the same orientation the stronger the crystallographic texture is said to be [94]. It is important to note that crystallographic texture does not refer to the local grain orientation revealed through etching but the orientation of the crystal plane within the grains.

Crystallographic texture is developed through the interplay between the material and the manufacturing process (operation, % deformation, temperature range etc.). Since crystallographic texture is related to the entire processing history of the material, its development is therefore controlled through the manufacturing process [94, 95]. Manufacturing processes such as rolling, forging or drawing result in differences in strain at the surface compared to the centre. This could generate different textures through thickness with the surface often left with textures indicative of higher shear stress whilst the centre shows the result of plane stress [96]. Similar to other material properties discussed in previous sections, texture is also reported to have some influence on the line pipe steel susceptibility to SCC [20, 24, 25].

2.6.1 Quantification of Crystallographic Texture

Texture measurements can be carried out by diffraction methods based on the interaction of high energy beams of x-ray, electron or neutron with the material. The resolution of the measurement depends on the size of the beam-material interaction volume and as compared in Table 2.3. Neutron diffraction and x-ray diffraction have far larger gauge volumes as compared to electron diffraction. When conducting neutron or x-ray diffraction, the materials bulk texture is discerned because of the large number of grains sampled whereas electron microscopy is only able to indicate microtexture because the number of grains able to be sampled is lower. The latest application of electron diffraction in the frame work of a scanning electron microscope is termed Electron BackScatter Diffraction (EBSD). Whilst EBSD is unable to give a true indication of the bulk texture, an upwards sampling size of 10,000 grains can give a good approximation of the bulk texture [97].

Table 2.3: Gauge volumes of different diffraction methods. Adapted from [98].

Beam Type	Laboratory X-Rays (6.4-17.4 keV)	Hard X-Rays (35-250 keV)	Electrons (100-500 keV)	Neutrons (1-100 MeV)
Typical Gauge Volume	$1 \times 5 \times 0.01$ mm^3	$50 \times 50 \times 1000$ μm^3	$5 \times 5 \times 100$ nm^3	$1 \times 1 \times 1$ mm^3

The analysis of texture is somewhat dependant on the purpose of measuring crystallographic texture. For an overview of textures present in a specimen, analysis is often undertaken through graphical means [99, 100]. The main plot used to analyse texture is the Orientation Distribution Function (ODF) plot. The ODF is a function whereby orientation data is mapped to Euler space with the frequency of a particular orientation being shown with contour lines. Whilst pole figures are still used in analysis, ODF plots offer a simpler method of analysing datasets without having to rely on known textures to compare to. An example of Euler space (Bunge notation) as produced by Ray et al. (1992) is presented in Figure 2.17 with the important (in steel) $\varphi_2 = 45°$ slice highlighted. As ODF's are produced through a simple transformation of orthogonal axes, different nomenclature and order of operations lead to different final axes. The Euler space pictured utilised Bunge notation as opposed to Roe notation [21]. Whilst early texture studies in steels showed both Bunge and Roe notations, Bunge notation (ϕ_1,Φ,ϕ_2) appears to have taken over as the dominant method in contemporary research [21, 101, 102].

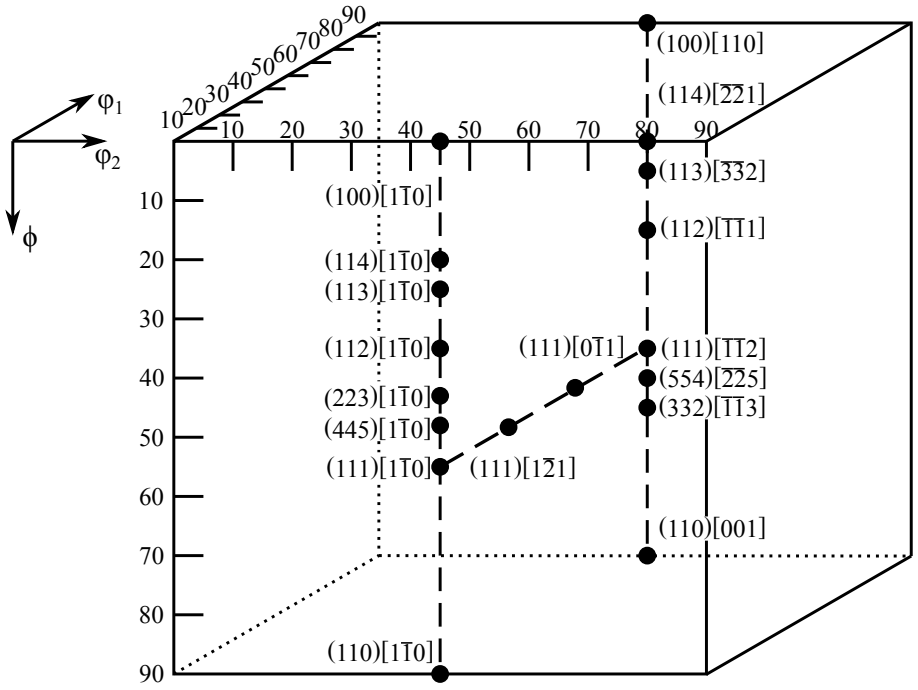

Figure 2.17: A three-dimensional view of euler space (Bunge notation) with important orientations highlighted. Adapted from [103].

When measuring texture it is common to use graphical means such as contour plots that show the concentration of a specific orientation above random orientation of grains. The most commonly used texture plotting tool is the Orientation Distribution Function plot or ODF plot. The ODF is a mathematical function that describes the frequency of different orientations present in a three-dimensional Euler space whose coordinates are defined by three Euler angles. The Euler angles are determined by calculating the angle of extrinsic rotation required to align the inclined crystal with the external coordinate system. The concentration of textures is described in ODF plots through contours showing similar concentrations of texture with the greater magnitude corresponding to stronger texture. A key of the important orientations and fibre textures in Bunge notation at $\phi_2 = 45°$ is presented in Figure 2.18 [2]. Texture is typically described in terms of strength and weakness with a strong texture correlating to a high density of contours and a weak texture correlating to a low density of contours. Physically this relationship describes the likelihood of a particular orientation being present in a sample. Textureless correlates to

[2]The authors acknowledge that fibre textures, such as those presented in Figure 2.18b, are typically labelled {hkl}//ND. Arafin and Szpunar (2009) [24] labels fibre textures per Figure 2.18b and because they are an important benchmark for determining the role of texture on SCC in low carbon steels, their nomenclature was adopted.

a completely random distribution of orientations.

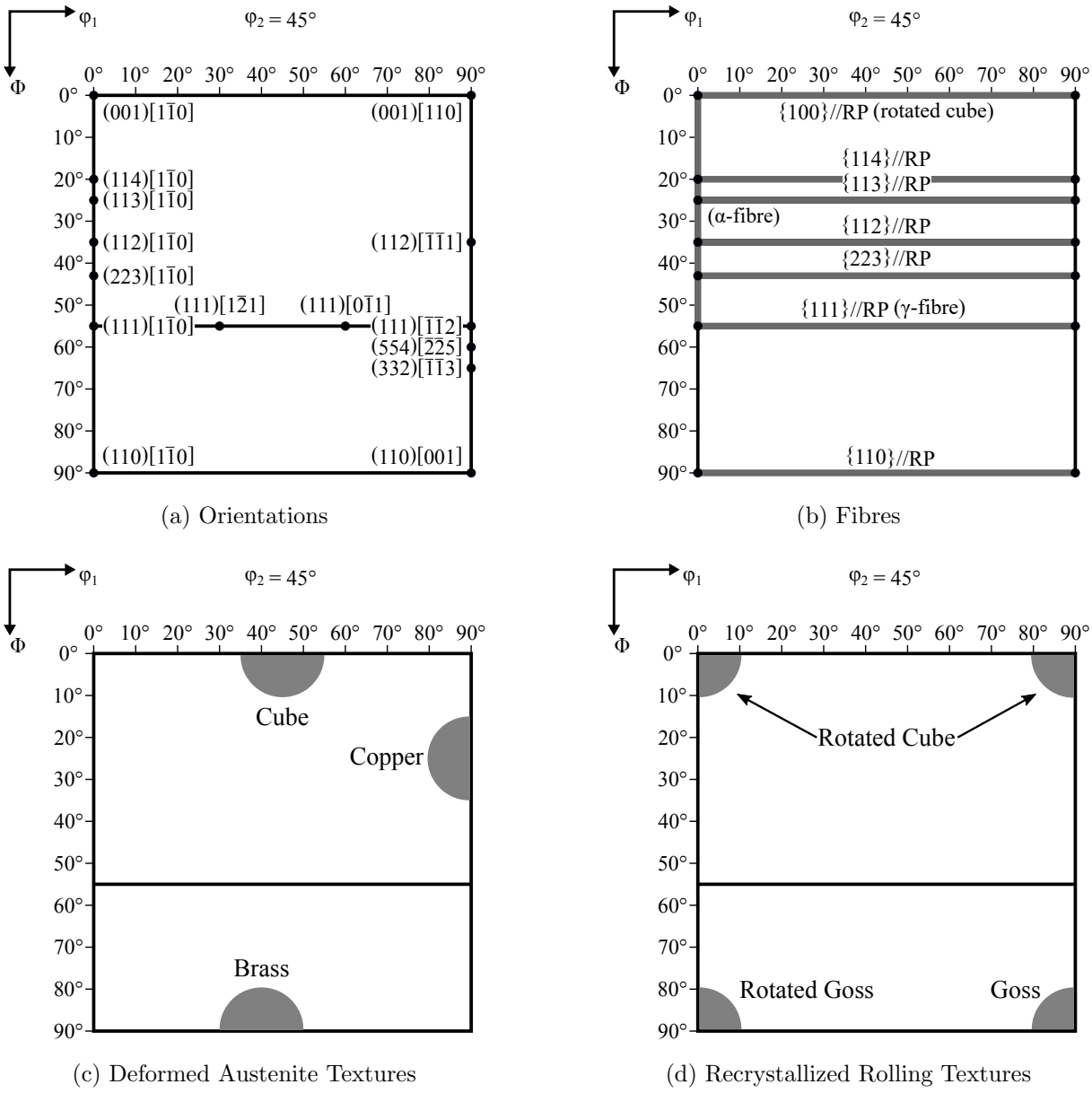

(a) Orientations

(b) Fibres

(c) Deformed Austenite Textures

(d) Recrystallized Rolling Textures

Figure 2.18: ODF at $\phi_2 = 45°$ showing important fibres and orientations. Adapted from [21, 24].

Grain Boundaries

There has been some significant discussion about intergranular cracking, however, the very nature of a grain boundary has not been elucidated. If a grain is a discreet collection of aligned atoms, a grain boundary is the region between grains where dissimilar crystal orientations border one another [104, 105]. The grain boundary represents the geometric

surface created at the interface of two grains where atoms are not orderly spaced and result in localised regions of tension and compression [104]. Grain boundaries have higher energies than the parent grains due to the poor mismatch between neighbouring grains with energy depending on the degree of misorientation between the adjacent grains [106, 107]. The differences in energy between the boundary and within the grain is exploited during metallographic etching where boundaries are more reactive and hence dissolve at a higher rate.

Visually, grain boundaries are trivial to distinguish through correct metallographic etching but the classification of boundaries is less trivial. Grain boundaries are characterised by five degrees of freedom that are in essence the transformation parameters necessary to rotate one crystal plane into the other [108]. The degrees of freedom relates to three rotations with one describing the misorientation and two others describing the normal to the boundary plane [108]. Through EBSD it is possible to classify all three misorientation parameters which can be represented by the angular misorientation and the crystal direction.

Grain boundaries are classified based on their angular misorientation which separates boundaries, broadly, between High Angle grain Boundaries (HAB's) and Low Angle grain Boundaries (LAB's) due to physical differences between the structure of the boundaries. High angle boundaries are borders between grains of different orientations whilst low angle grain boundaries are a series of aligned dislocations within a grain [109]. The misorientation that separates LAB's from HAB's is typically cited as between $10 - 20^{\circ}$ with the most commonly used value being 15° [110, 111]. The critical misorientation depends on not only the material but also the tilt axes (crystal orientation) with different axes corresponding to different transition angles. When discussing intergranular cracking, high angle grain boundaries are being fractured whereas transgranular cracking refers to the breaking of grains themselves.

Whilst grain boundaries are created due to the dissimilarity in the crystallographic orien-

tation of adjoining grains, occasionally the grains are aligned such that a pseudo-lattice is created from the coincidence of atoms within the separate grains. The name for this lattice is called the Coincident Site Lattice (CSL) boundary [110]. The creation of a CSL boundary can be visualised by the illustration in Figure 2.19. Two crystal lattices meeting at a boundary are depicted by the red and yellow points, when an atom is common to both the red and yellow planes it is depicted as green. CSL boundaries are denoted by Σ and a number corresponding to the proportion of coincident atoms between the two crystal planes. As seen in Figure 2.19, the $\Sigma 5$ boundary is characterised by coincidence of one in five atoms, similarly in $\Sigma 13a$ boundaries, one in 13 atoms are coincident to both lattices.

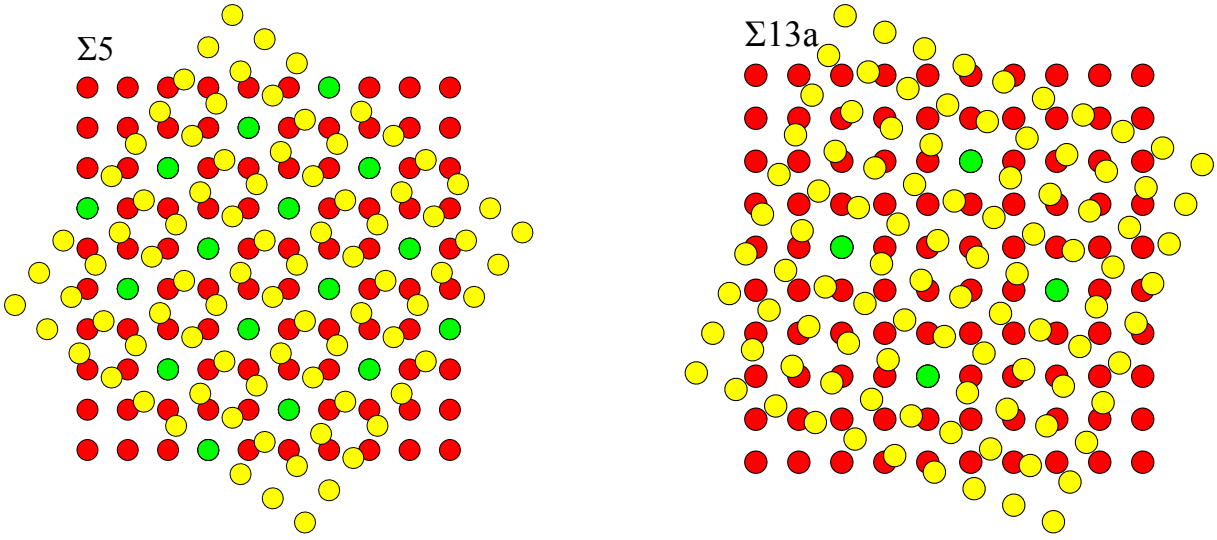

(a) $\Sigma 5$ Boundary (b) $\Sigma 13a$ Boundary

Figure 2.19: Depiction of coincident site lattice boundaries and how they are defined. Adapted from [112].

Table 2.4 is a summary of the misorientation angle and tilt axis characteristic of all CSL boundaries. With the exception of the $\Sigma 41a$ boundary, all CSL boundaries are high angle grain boundaries (transition angle 15°) with the majority having misorientations greater than 30°. *N.B. The suffix a, b and c in Table 2.4 denotes a difference in both misorientation and axis between CSL boundaries that have the same fraction of coincident atoms.*

Table 2.4: CSL boundary angle and axis requirements. Adapted from [112].

Σ Type	**Angle**	**Axis**	**Σ Type**	**Angle**	**Axis**
1	00.00	111	33a	20.05	110
3	60.00	111	33b	33.56	311
5	36.86	100	33c	58.99	110
7	38.21	111	35a	34.05	211
9	38.94	110	35b	43.23	331
11	50.47	110	37a	18.92	100
13a	22.62	100	37b	43.14	31-
13b	27.79	111	37c	50.57	111
15	48.19	210	39a	32.20	111
17a	28.07	100	39b	50.13	321
17b	61.92	221	41a	12.68	100
19a	26.53	110	41b	40.88	210
19b	46.83	111	41c	55.88	110
21a	21.78	111	43a	15.18	111
21b	44.41	211	43b	27.91	210
23	40.45	311	43c	60.77	332
25a	16.26	100	45a	28.62	311
25b	51.68	331	45b	36.87	221
27a	31.59	110	45c	53.13	221
27b	35.43	210	47a	37.07	331
29a	43.60	100	47b	43.66	320
29b	46.40	221	49a	43.57	111
31a	17.90	111	49b	43.57	511
31b	52.20	211	49c	49.23	322

Controlling the concentration of CSL boundaries has been shown to improve corrosion

resistance [113–116], creep resistance [117–120] and fatigue strength [121, 122] in a variety of materials. Grain boundary engineering is the field that is related to controlling boundaries for the benefit of improving the material properties.

2.7 Crystallographic Texture Development in Steel

Crystallographic texture is developed through the combination of manufacturing process and the initial material characteristics. In order to understand the development of crystallographic texture in pipeline steels, a background on both the physical characteristics of steel and manufacturing processes is necessary.

2.7.1 Steel Background

Steel is one of the most commonly used materials in the world and has wide application because of the low cost and the range of possible mechanical properties. Through the alteration of manufacturing process and chemical composition, steel can be altered to suit a wide range of applications. The key factor behind the variability of steel properties stems from the crystal structure (microstructure) and the ability to alter microstructures based on processing temperatures and times (cooling rates).

Microstructure Development

Upon transformation from austenite $\longrightarrow$ ferrite, the austenitic microstructure undergoes a series of changes as the crystal structure reorders itself from an FCC to BCC structure. Depending on the carbon content and the kinetics of transformation, different microstructure are developed upon transformation. The two main modes of transformation from austenite $\longrightarrow$ ferrite are displacive and reconstructive. In a displacive transformation the changes in crystal lattice is due to collaborative displacement of atoms initiated by shear

which results in a new orientation whilst in a reconstructive transformation diffusion and atomic mobility is necessary for transformation to occur. In essence, the level of diffusion permitted controls the microstructure produced. In pipeline steels, the most common microstructures present are ferritic-pearlitic structures typically found in sub X70 grades whilst X70 and above contains bainitic structures.

Pearlite

Pearlite is a common microstructure in steel that consists of grains of interpenetrating bicrystals of ferrite and cementite that, when sectioned, appears as lamellae of iron and cementite. Pearlite forms through a reconstructive transformation where carbon diffuses out of ferrite and is absorbed by cementite reinforcing the alternating layers. In hypoeutectoid (lower than eutectoid, $C < 0.8$ wt.%) compositions, pearlite exists in a matrix of often polygonal ferrite as seen in Figure 2.20 whilst hypereutectoid (higher than eutectoid, $C > 0.8$ wt.%) compositions consist of pearlite matrix with cementite at the grain boundaries.

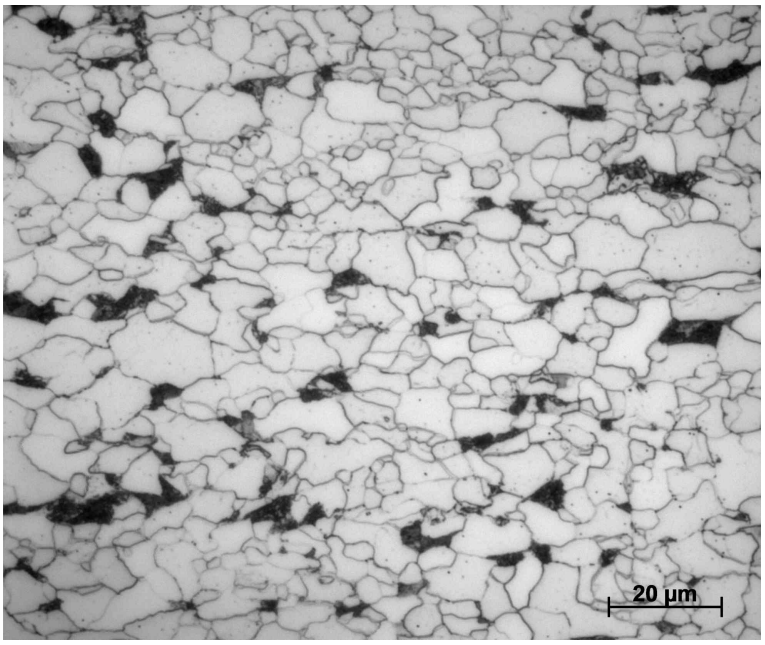

Figure 2.20: Ferrite-pearlite structure present in a sample of X65 steel. Adapted from [31]

Bainite

Bainite, is a microstructure that forms layers of ferrite with some cementite dispersion. Unlike pearlite, bainite transformation is displacive and grows without diffusion, after which carbon diffuses rapidly into the austenite; cementite subsequently forms from the carbon enriched austenite [123]. The two common forms of bainite are upper bainite and lower bainite [123]. Upper bainite is the high temperature form of bainite and is characterised by lath like structure with cementite particles present between individual laths [123]. Lower bainite is the low temperature form of bainite and consists of laths of ferrite and cementite the same as upper bainite, however, the subunits of ferrite contain carbide precipitate [124]. In addition to lath morphology (upper and lower bainite), granular bainite is another form that is found in low carbon steels formed through continuous cooling [123, 125]. When the carbon is partitioned from the bainitic ferrite the high carbon content stabilises the austenite which upon transformation can produce any transformation product possibly formed from carbon enriched austenite including pearlite and degenerate pearlite, cementite debris, bainite and cementite, and martensite-austenite (M/A) constituents [125]. An example of a bainitic microstructure is shown in Figure 2.21 where samples of upper bainite and granular bainite can be observed. In addition, SEM micrographs of degenerated pearlite and M/A constituents are presented in Figure 2.22.

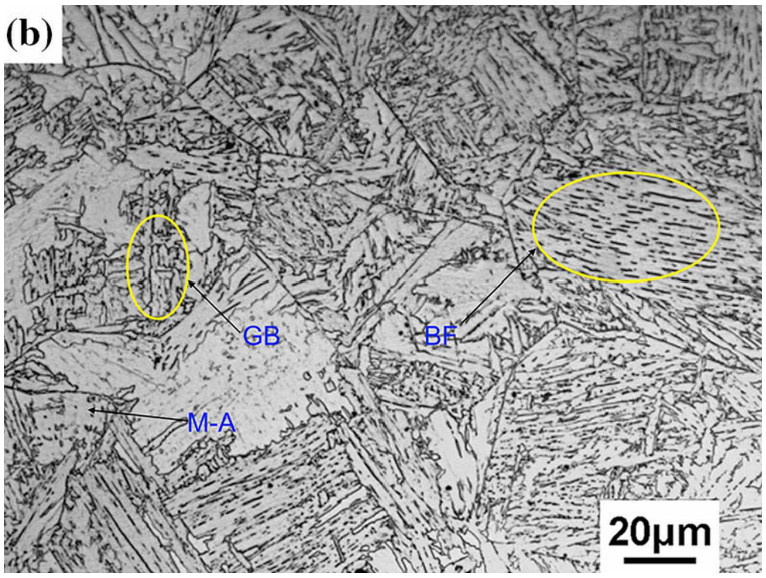

Figure 2.21: Bainitic structures present in low carbon steel showing both upper (BF) and granular bainite (GB). Reprinted from [126].

(a) Degenerate Pearlite (b) M/A constituent

Figure 2.22: Degenerate pearlite and MA constituents present in low carbon bainitic steels. Reprinted from [125].

In low carbon steels the appearance of discontinuous yielding appears to be linked to the microstructure developed with ferritic-pearlitic microstructures where diffusion permits the migration of interstitial atoms, increasing the appearance of discontinuous yielding [127, 128]. Discontinuous yielding or the Portevin-Le Chatelier effect is a phenomenon observed in many materials, especially low carbon steels. It occurs as a result of Lüders bands propagating through the material, localised along the Lüders front [129]. Lüders bands are caused by dislocations being pinned down by interstitial solute/ impurity atoms,

such as carbon and nitrogen, that prevent slip from occurring until a sufficiently high applied force can mobilise the dislocations [129].

In contrast, bainitic microstructures tend to suppress discontinuous yielding as reported by Kim et al. (2008) [127], especially those that are produced under continuous cooling conditions as determined by Shibata and Asakura (1995) [130]. The presence of fine intergranular precipitates under these conditions reduces the amount of carbon in solution able to pin down dislocations, hence, discontinuous yielding is suppressed [130]. The appearance of secondary phases such as M/A constituents tends to remove discontinuous yielding when present in concentrations greater than 5% [131].

2.7.2 Manufacturing of Pipeline Steel

Manufacturing of pipes for use in gas transmission is undertaken in the following broad stages:

Stage 1: Slab Casting

Stage 2: Rolling

Stage 3: Cooling and Coiling

Stage 4: Pipe forming and welding

Stage 5: Coating

Each stage contributes to the final characteristics of the pipe and how likely they affect SCC. Whilst slab casting and coating are beyond the scope of this review the effect of rolling and cooling during coil production along with pipe forming have direct effects on the pipeline steel properties leading to SCC development and will be discussed further. Whilst pipe can be manufactured through seamless methods, the lower unit cost and availability of welded pipe often outweighs the benefits of seamless pipes (except for certain cases when required by a standard [132]). As the majority of pipe used in gas

transmission is welded pipe, that will be the focus of the review.

Rolling

Rolling is the main process used to develop the microstructure and mechanical properties necessary for pipe steels. Whilst there is a quite narrow band of properties allowed in higher pipe grades (lower grades are more accommodating in terms of strength requirements) there is a multitude of rolling procedures that can be used to achieve the desired properties. Conventional Rolling (CR) is insufficient to develop the high strength requirements for modern, high grade steels and has been replaced with the ThermoMechanical Controlled rolling Process (TMCP). The main difference between conventional rolling and the thermomechanical controlled rolling process is that TMCP finish rolls at lower temperatures than CR, thereby refining the microstructure and favouring bainitic microstrucutres over ferritic/ pearlitic [133]. A comparison of CR and TMCP can be seen in Figure 2.23 where additional rolling after rough rolling can be observed.

Figure 2.23: Conventional rolling (CR) compared to thermomechanical controlled rolling process (TMCP). AcC: Accelerated Cooling. Reprinted from [133].

The two rolling regimes commonly used in TMCP manufacturing of pipeline steels are hot rolling and warm rolling. Hot rolling is rolling that occurs when the steel crystal structure has completely transformed into austenite whilst warm rolling is carried out below the A_3 temperature in the dual phase region where austenite and ferrite coexist. Hot rolling typ-

ically relies on high initial temperatures to undertake the bulk of the thickness reduction in a minimal number of passes as well as to refine the grain size of the material during rolling through repeated recrystallization (dynamic during rolling and static between rolling passes) [134]. In a hot rolling regime the temperature below which no complete static recrystallization can occur between rolling passes is called the non-recrystallization temperature (T_{NR}) [135]. When rolling above the T_{NR}, between rolling passes, grains can undergo complete static recrystallization so new grains are formed between passes. Deformation below the T_{NR} causes accumulation of deformation to occur resulting in elongated grains and deformation bands. The resulting transformation from austenite to ferrite occurs by nucleation at both austenite grain boundaries and within austenite grains at deformation bands, hence, increased nucleation sites generated by rolling below the T_{NR} promotes the formation of finer ferrite grain sizes [135, 136].

Rolling Schedules Used in Industry

As pipelines are primarily designed to meet a series of mechanical and physical properties, the exact rolling schedule is not heavily regulated and is left to the pipe manufacturer to develop. In the strictly controlled PSL 2 pipe designation in the API 5L standard [27], material can be manufactured by four processes with restrictions placed on what grades can use what process. The four processes available to pipe manufacturers are as rolled, normalized rolling, quench and tempered rolling and thermomechanical controlled rolling. As seen in Table 2.5 each increasingly complex manufacturing process has a higher allowable maximum grade as the process can be better controlled. As thermomechanical rolling is the most complex of the four potential pipe making processes, it can be used to manufacture all the current grades of pipe whilst normalised rolling, for instance, can only produce up to X60 grade steel.

X70 pipeline steel is typically manufactured through thermomechanical rolling (Masoumi et al. (2015) [137] for instance investigated the quench and tempered method of X70 pro-

duction) with schedules changed depending on requirements. X70 is a moderate strength pipe grade that does not have as strenuous strength requirements as higher grade pipes. As the primary requirement for determining whether a pipe meets the minimum grade is the yield strength and the tensile strength, provided a manufactured pipe meets the minimum requirements, it is within specifications. Studies carried out to research the role of changing the rolling schedule on the mechanical and microstructural properties of X70 pipe found that the rolling schedule was not particularly important if the main goal was to produce pipe that was within specifications for X70 [72, 138, 139]. In the study by Hwang et al. (2007) samples of plate were rolled through both hot and warm rolling processes with each producing pipe that had a yield strength within the specified range for X70 (485-635 MPa) [27]. Refer to Appendix A for the full range of specifications of API 5L steels. Similarly, Shin et al. (2007) [72] carried out hot and warm rolling on samples of X70 plate with both samples producing plate that had tensile properties within the range required for X70 pipe. The study of X70 manufacturing carried out by Kim et al. (2002) [139] was the one exception where the manufacturing process produced plate with tensile properties below the required range. As the aim of the study was to determine the impact of microstructure on tensile properties, the pipes with primarily ferritic and pearlitic microstructres did not meet the minimum required strength levels that would have been achieved had bainite been a constituent. The role of strength development in pipeline steel is linked strongly to the microstructure developed and not necessarily the cooling rate utilised. In a study by Olivares et al. (2008) [140] a sample of X70 grade steel was rolled under identical conditions with air cooling, nitrogen cooling and water quenching. The resulting steels showed that a cooling rate of 3°C/s with Nitrogen resulted in a higher strength material than a cooling rate of 5°C/s with a water spray. X70 grade pipe steel is not especially sensitive to the manufacturing process and as has been displayed in literature, both hot and warm rolling processes have been undertaken to produce X70 pipeline steel [72, 138, 139]. Provided the samples have tensile properties within the specified range they will be considered X70 grade pipe.

Table 2.5: API 5L permissible manufacturing methods for PSL2 grade pipeline steel. Adapted from [27].

Delivery Condition	**Pipe/ Steel Grade**
As Rolled	L245R or BR
Normalizing rolled, normalizing formed,	L245N or BN
normalized or normalized and tempered	L290N or X42N
	L320N or X46N
	L360N or X52N
	L390N or X56N
	L415N or X60N
Quenched and tempered	L245Q or BQ
	L290Q or X42Q
	L320Q or X46Q
	L360Q or X52Q
	L390Q or X56Q
	L415Q or X60Q
	L450Q or X65Q
	L485Q or X70Q
	L555Q or X80Q
Thermomechanical rolled or	L245M or BM
thermomechanical formed	L290M or X42M
	L320M or X46M
	L360M or X52M
	L390M or X56M
	L415M or X60M
	L450M or X65M
	L485M or X70M
	L555M or X80M
Thermomechanical rolled	L625M or X90M
	L690M or X100M
	L830M or X120M

Cooling and Coiling

After the bulk of the deformation has been accounted for, the finish rolling temperature and coiling temperatures are the next critical parameters for developing the required strength levels; lower finishing temperatures usually correspond to higher strength products at the cost of higher rolling loads [141]. Due to the thermal inertial of the plate after hot rolling low carbon steels in commercial rolling mills, transformation tends to occur during coiling. Therefore the coiling temperature is important in industrial steel rolling. As the coiling temperature affects the transformation kinetics, microstructure that is developed, the grain size and, the resulting mechanical properties are all influenced by the coiling temperature [142].

It is noted that the more modern rolling techniques tend to leverage greater control of rolling temperatures as well as increased incidence warm rolling and accelerated cooling to further improve the microstructure [143]. Pushing the transformation mechanism further away from the diffusion controlled ferrite-pearlite microstructure allows for the development of high strength microstructures consisting of lower bainite and tempered martensite, necessary for X100 grade steels and beyond [143–145].

Pipe Forming and Welding

Whilst pipe can be manufactured through seamless methods, the lower unit cost and availability of welded pipe often outweighs the perceived benefits of seamless pipe. Welded pipe is manufactured by forming flat plate into the shape of pipe and then welding the seam. The pipe forming and welding process is altered depending on the desired final dimensions of the pipe with large diameter, heavy (thick) wall pipe being manufactured through different methods compared to small diameter, thin walled pipe. Pipe forming processes are broadly separated into two categories, roll forming and press forming whilst welding is separated into resistance welding and fusion welding [146]. Whilst there are different processes that take advantage of both sets of roll forming and welding process,

the most commonly used processes in Australian pipelines are roll formed pipes utilizing Electric Resistance welding (ERW) and press formed pipes welded through Submerged Arc Welding (SAW) which will be investigated below.

Roll Formed Pipe

Roll formed pipe is one of the most commonly used pipe forming processes for pipes and can form pipe up to 600 mm in diameter [146]. The roll formed pipe utilises a continuous stream of flat plate that is rolled through successive rollers of different shapes to form pipes. Figure 2.24 shows an example roll forming schedule where the skelp is initially gently rounded in stages 1-3 before stages 4-7 brings in the edges to form a rough circle. Stages 8-10 is where the circularity of the pipe is refined and a bevel for welding is formed into the edges of the plate through the use of a finned top roller. Stage 11 is where the circular pipe is welded through some Electrical Resistance Welding (ERW) method that utilizes the electrical resistance of the material to heat the edges to a temperature where fusion welding is possible [146]. Roll formed pipe is often called ERW pipe after the welding process, however, there are different processes through which ERW is carried out including DC, low frequency and high frequency depending on the diameter of pipe being produced. One issue with ERW welded pipe is that it is more sensitive to centreline segregation (an issue controlled during slab continuous casting) when manufactured using centre slit coil. To prevent welding defects, higher levels of steel cleanliness are required and manganese content has to be managed during slab casting to reduce the formation of centreline segregation [147].

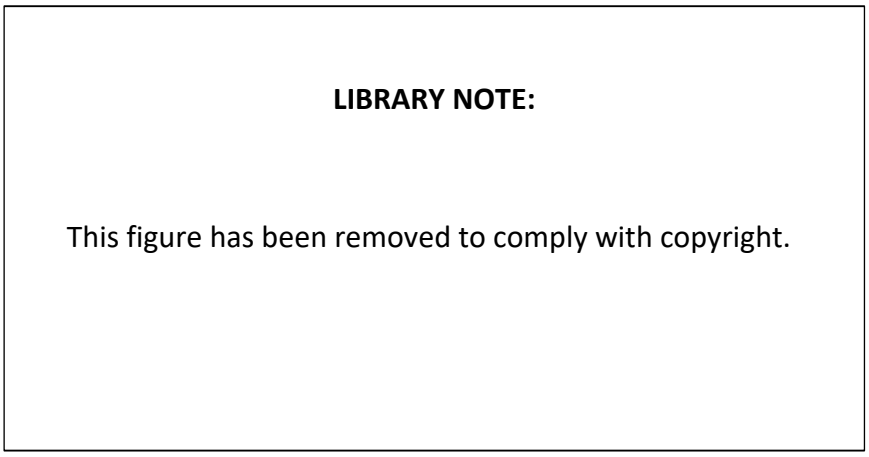

Figure 2.24: Roll forming process showing roller shape progression. Reprinted from [146].

Press Formed Pipe

Press formed pipe is a method of producing heavy wall pipes of various grades through the use of hydraulic presses and dies. Common press forming processes are shown in Figure 2.25 [146]. As seen in Figure 2.25 the two main press forming processes are UOE pipe as well as C-ing pressed pipe with three-roll bending and spiral tube existing between roll formed pipe and press formed pipe.

UOE pipe tends to be the most common process used to generate large diameter, heavy wall gas pipe out of the press formed pipe types [146]. UOE pipe is named after the three stages of pressing used in the manufacturing process, U-ing, O-ing and Expanding. The UOE process is a four step process through which a trimmed steel skelp has its edges crimped before being pressed into a "U" shape and subsequently an "O" shape as observed in Figure 2.25. The circular pipe is then welded before being expanded from the inside to final dimensions with hydraulically actuated mandrels [148]. Pipe formed through this method uses Submerged Arc Welding (SAW) where filler wire submerged under solid flux fusion-welds the two sides of the pipe together. The weld leverages filler material with a higher strength than the parent material such that there is no weakening

of the material in the Heat Affected Zone (HAZ) and no heat treatment is required post welding. UOE pipe has the distinct disadvantage compared to roll formed pipe in that it is not a continuous operation so production volumes are lower for UOE than ERW pipe.

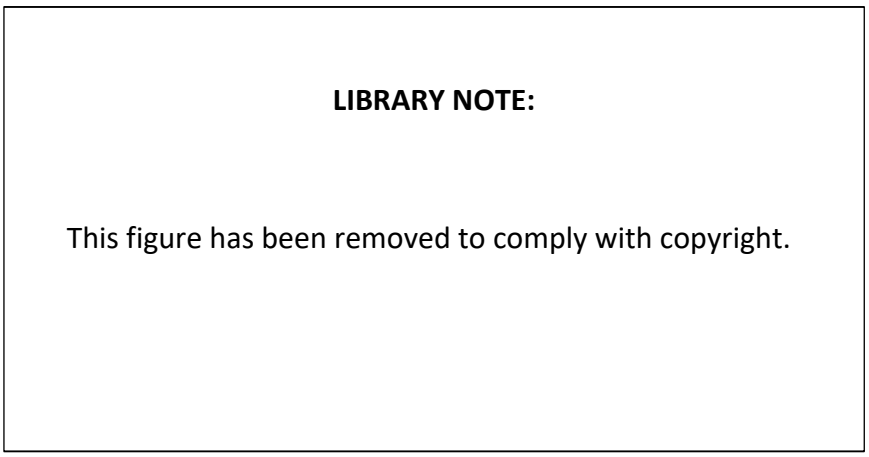

Figure 2.25: Tube forming processes utilising presses and simple forming rolls. Reprinted from [146].

2.7.3 Rolling Schedule Parameters

In order to create steel products with properties that can withstand the conditions expected for high pressure gas pipelines, the rolling schedule needs to be designed such that the desired microstructures and hence properties are achieved.

Transformation Diagrams

The decomposition of austenite upon cooling is an area of immense importance to industry. Knowing the behaviour of alloys on cooling is vital to developing manufacturing schedules that result in products with the required microstructural characteristics and material properties. Transformation diagrams are composition specific and, for common alloys, are readily available, often directly from the manufacturer [149, 150]. Austenite can

decompose into ferritic microstructures under two different conditions, isothermal (constant temperature) and continuous cooling (constant cooling rate), both of which give information on what phases are produced and at what temperature ranges [151, 152]. Transformation diagrams are used to quantify the transformation of austenite into ferritic microstructures. Transformation diagrams produced under isothermal conditions are referred to as Time Temperature Transformation (TTT) diagrams whilst those produced under constant cooling conditions are referred to as Continuous Cooling Transformation (CCT) diagrams. Both transformation diagrams are produced using dilatometers which are devices that can measure very small changes in length due to both the temperature and the transformation from austenite to ferrite. To control temperature thermocouples are fused to the surface while induction coils and inert cooling gasses maintain temperature/ cooling rates.

Time Temperature Transformation (TTT) Diagrams

A TTT diagram displays the phases that develop during isothermal transformation. TTT diagrams such as the ones presented in Figure 2.26 of different steel alloys show the possible phases that can be generated depending on the cooling rates and holding temperature. As seen in Figure 2.26 two distinct curves are present in each alloy with the higher temperature curve denoting pearlite formation and the lower temperature curve denoting the bainite transformation [123]. The final series of flat lines beginning below 400°C is the martensite start temperature [123]. TTT diagrams are useful tools in planning isothermal heat treating processes and are able to highlight to entire austenite decomposition range and show every microstructure able to be produced in the material [152].

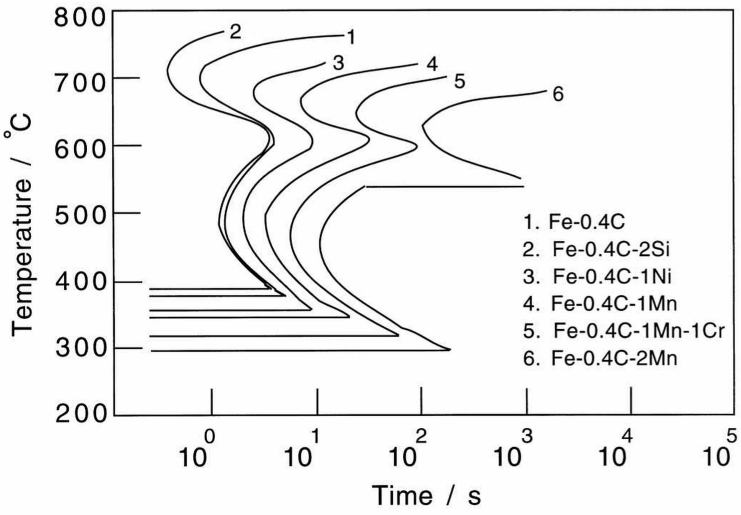

Figure 2.26: TTT diagram of different steel alloys. Reprinted from [123].

Continuous Cooling Transformation (CCT) Diagrams

As industrial cooling tends to be carried out at a constant rate, the use of TTT diagrams is not able to give information on complex, mixed microstructures produced during these regimes. CCT diagrams, like the one presented in Figure 2.27 of a low carbon steel, show the intersection of microstructures produced at different cooling rates. Like the TTT diagram, a CCT diagram is alloy specific and any change in chemical composition results in different cooling diagrams.

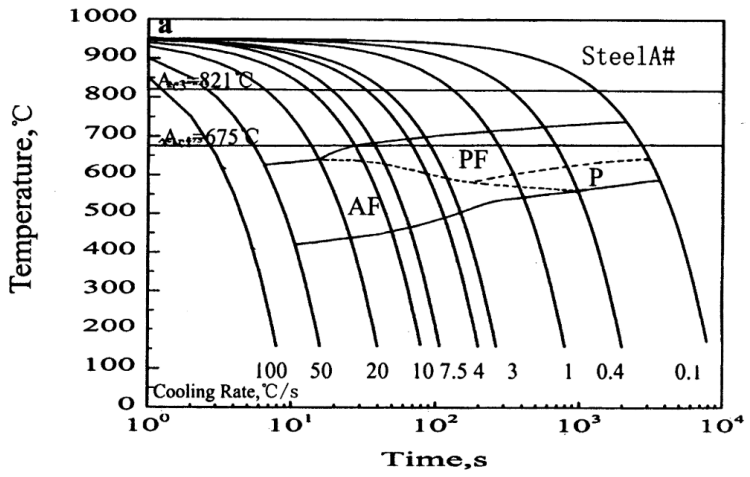

Figure 2.27: CCT diagram of a pipeline steel. Reprinted from [153].

Upon transformation from austenite to ferrite, recalescence can occur in both TTT and

CCT diagrams which is a temporary temperature rise due to the FCC $\longrightarrow$ BCC transformation. This can be observed in TTT diagrams as a slight increase in average holding temperature that averages out shortly after it begins [154]. TTT diagrams are less sensitive to this phenomenon than CCT diagrams as recalescence is observed directly on the resulting CCT diagram as a knee at the start of transformation as seen in Figure 2.28. It is likely that modern CCT diagrams remove the knee through data processing or, potentially, they use a more efficient cooling gas such as helium as opposed to nitrogen.

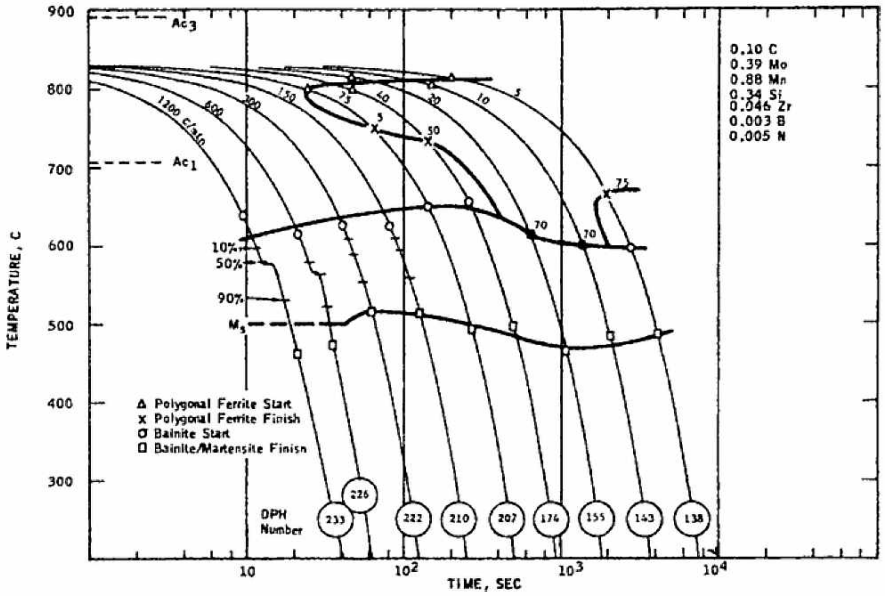

Figure 2.28: CCT diagram showing recalescence at 1200°C/min cooling rate. Reprinted from [155].

Non-Recrystallization Temperature T_{NR}

During hot rolling of steel, equiaxed austenite grains are deformed by the rollers to produce elongated austenite grains. During deformation, dynamic recrystallization occurs where equiaxed grains begin to grow from the grain boundaries of the elongated grains [156]. It is noted that prior to recrystallization, recovery occurs where the dislocations, which are uniformly distributed within the deformed grains, begin to migrate and annihilate forming sub-grains [156]. Recrystallization kinetics are a vitally important parameter to consider when carrying out hot deformation of steel structures as grain structure is directly influenced by the phase transformation [157]. Recrystallization occurs typically at

50% of the melting temperatures in most materials so heavy deformation typically occurs in hot rolling above this temperature [157].

The temperature below which complete static recrystallization in the interval between rolling passes can no longer occur is called the non-recrystallization temperature (T_{NR}) [158]. When deformation occurs below the T_{NR}, elongated austenite grains do not completely recrystallize prior to successive rolls. During phase change in steel from austenite to ferrite, new ferrite grains initiate from prior austenite grain boundaries and regions of high dislocation density, hence, it can be beneficial for deformation to occur below T_{NR} so the number of nucleation sites increases such that fine ferrite grains are produced upon transformation.

T_{NR} can be determined through either empirical formulae or through laboratory methods. In terms of the experimental methods, one of the most commonly used methods of determining the T_{NR} is through double hit deformation testing. Double hit deformation testing is when a small cylindrical sample is deformed at a set temperature and then deformed again after a set interpass time whilst holding at that temperature to measure the amount of softening due to recrystallization [159]. Softening is a measurement of the reduction in strength over the strain range applied to the cylindrical specimens which indicates recrystallization due to the applied deformation. When the level of softening at all interpass times is below 20%, the temperature used during those series of tests is the T_{NR}. T_{NR} is determined when softening reaches 20% as 20% softening accounts for recovery [160, 161]. Other methods such as torsion testing are similar but a single test consists of multiple torsion passes in a single specimen at set interpass times [162]. The T_{NR} is determined by calculating the temperature when the slope of the mean flow stress vs. temperature plot changes. The results are similar to the double hit deformation test and as there is not currently a standard method for determining the T_{NR} of a material through experimental methods each are used.

There has been a number of empirical formulae derived that could give an approximation of the T_{NR} in steel specimens based on the chemical composition. One of the earliest and well known equations was devised by Boratto et al. (1988) [163] and is shown in Equation (2.2). The Boratto equation neglects Nitrogen and as a result tends to over-estimate the value of T_{NR} [159]. Equation (2.3) devised by Bai et al. (1993) [162] and Equation (2.4) devised by Fletcher (2008) [164] are able to give better approximations of the T_{NR} despite their apparent neglect of the impact of some elements included in the Boratto equation.

$$T_{NR} = 887 + 464C + \left(6445Nb - 644\sqrt{Nb}\right) + \left(732V - 230\sqrt{V}\right) + 890Ti + 363Al - 357Si \tag{2.2}$$

$$T_{NR} = 174 \log\left[Nb\left(C + \frac{12}{14}N\right)\right] + 1444 \tag{2.3}$$

$$T_{NR} = 849 - 349C + 676\sqrt{Nb} + 337V \tag{2.4}$$

The empirical formulae can give results very close to the actual T_{NR} found through experimental data, however, the addition of other alloying elements that encourage or retard recrystallization, or vastly different strain rates from those carried out in the development of the formulae can render them ineffective; experimental data is required for accurate determination of T_{NR} [162, 165, 166].

2.7.4 Texture Development

Transformation Textures

The transformation of austenite to ferrite produces a shift in the crystal plane from an FCC to a BCC crystal structure when both ferrite and martensite are formed. The crys-

tal lattice structure of the FCC contains the structure of the BCC material within itself (and vice versa) as seen in Figure 2.29 where in the centre of two FCC unit cells exists a BCC crystal. The shift from an FCC $\longrightarrow$ BCC crystal structure, is governed by correspondence relationships which model the orientation shift that occurs due to the new crystal structure. Five orientation relationships have been identified when austenite (γ-FCC) transforms to ferrite (α-BCC). They are called the Bain, Kurdjumov-Sachs (KS), Nishiyama-Wasserman (NW), Pitsch and the Greninger-Troiano (GT) orientation relationships. The Kurdjumov-Sachs, Nishiyama-Wasserman and Pitsch orientation relationships are the most commonly considered when studying the transformation of austenite to ferrite [167].

N.B. as highlighted in Figure 2.29 no physical rotation of the crystal structure is observed in the austenite $\longrightarrow$ ferrite transformation [168]. The BCC unit cell is not coincident to the FCC unit cell, hence the orientation (and direction) is mapped to a different origin leading to an observed rotation.

Figure 2.29: The Kurdjumov-Sachs orientation relationship. Reprinted from [167].

The three main orientation relationships can be summarised in Table 2.6 where the lattice relationship shows the rotation in crystal structure observed after the austenite to ferrite transformation. The number of variants refers to the symmetry of the planes and directions in the transformed orientation hence according to the Kurdjumov Sachs orientation relationship a {111}<110> crystal could transform into any one of 24 equivalent {110}<111> planes with equal likelihood. The Bain relationship is the simplest and the

first model which existed for predicting the transformation from austenite to martensite [169]. Although the Bain transformation is not observed in steel, it can be used as a general analogue of FCC $\longrightarrow$ BCC orientations and a first approximation to phase transformation in steel [167]. The transformation in steel tends to follow the Kurdjumov-Sachs (KS) and Nishiyama-Wasserman orientation relationships during the austenite to ferrite or martensite transformation although there is still debate over which is more dominant [168, 170–172]. Whilst important in explaining the behaviour of transformed austenite, the transformation relationships are not applicable when deformation occurs such as when rolling below the T_{NR}.

Table 2.6: Orientation relationships between γ-steel and α-steel.

Orientation Relationship	**Lattice Relationship**	**Number of Variants**
Bain	$\{100\}\gamma//\{100\}\alpha$	3
[169]	$<100>\gamma//<110>\alpha$	
Kurdjumov-Sachs	$\{111\}\gamma//\{110\}\alpha$,	24
[173]	$<110>\gamma//<111>\alpha$	
Nishiyama-Wasserman	$\{111\}\gamma//\{110\}\alpha$,	12
[174, 175]	$<112>\gamma//<110>\alpha$	

Hot Rolling Above T_{NR}

Recrystallized rolling is the process through which steel is rolled above T_{NR} where complete static recrystallization between rolling passes can occur. Recrystallized rolling typically takes place between the temperature range of 840-1100°C depending on strain rate and chemical composition of the steel [162, 166, 176]. When austenite is rolled above T_{NR} the most dominant texture to form is the cube texture $(100)[0\bar{1}0]$ [21–23, 101]. The cube is a typical texture developed when rolling FCC materials and upon transformation tends to transform into the rotated cube texture $\{100\}<110>$ and the Goss $(110)[001]$ and rotated Goss $(110)[1\bar{1}0]$ textures [21, 177]. This can be better visualised in the Figure 2.30

where the cube texture located at $(100)[0\bar{1}0]$ is transformed by 45° into the rotated cube textures at $\varphi_1 = 0°$ and 90°. As the cube is transformed into three components, the intensity of each remaining component is 1/3 the original cube intensity [168]. The rotated cube is a very stable texture which strengthens in intensity with subsequent deformation shown experimentally through the increased intensity of the rotated cube with subsequently lower final rolling temperatures [23]. In contrast, the rotated Goss $(110)[1\bar{1}0]$ orientation rotates along the RD fibre to the {111}<110> texture with additional deformation [177]. It is important to note that due to the mechanism of rolling, the surface undergoes a shear deformation whereas the centre undergoes nearly plane strain with the Goss texture (110)[001] making up a majority of the shear texture [178, 179].

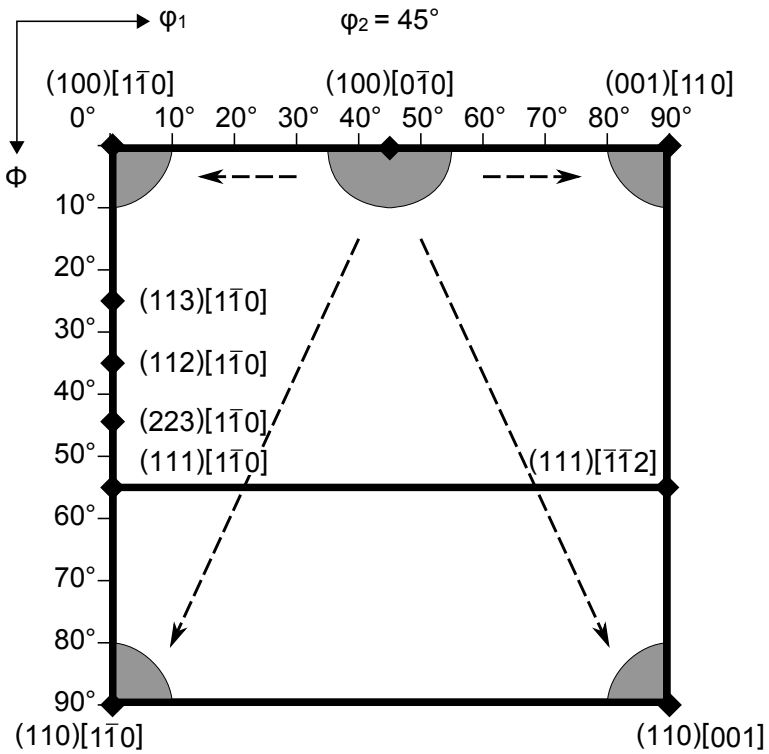

Figure 2.30: The rotation of crystal orientations from recrystallized austenite. Adapted from [168].

In practice, recrystallized rolling is not commonly used in pipeline steels and hence, limited literature surrounding the texture developed due to recrystallized rolling exists. The limited literature that exists shows that for low carbon steels rolled above the T_{NR} reports strong rotated cube textures ($(001)[1\bar{1}0]$ and (001)[110]) and weak $(332)[\bar{1}\bar{1}3]$ textures [21,

180].

Hot Rolling Below T_{NR}

During hot rolling below the T_{NR}, elongated grains post rolling are not able to fully recrystallize between rolling passes. As the deformation is accumulated, there is a marked texture change when compared to hot rolling above the T_{NR}. The main deformation textures associated with austenite deformation are the Brass {110}<112>, Copper {112}<111>, {123}<614> and occasionally a weak Goss texture. These textures are temporary features in the steel and upon transformation can form a number of different ferrite textures. The Brass {110}<112> texture upon transformation forms the {332}<113> texture which is not stable and upon subsequent deformation rotates to form the {554}<225>, {111}<112> and the {111}<110> textures [21]. The {112}<110> texture upon transformation to ferrite forms the {113}<110> texture. This texture is fairly stable although it can rotate upon subsequent cold rolling toward the ND fibre by forming the {223}<110> texture [21].

Due to the interaction between the material and the rollers, in practice, texture does not form uniformly from the surface to the centre of a rolled plate; variation of the through-thickness texture is often observed [179, 181–183]. As mentioned previously in Section 2.7.4, the interaction between the rollers and the material can lead to different deformation profiles being subjected to the surface as compared to the centre leading to different textures. The surface of hot rolled steels tends to be dominated by textures along the {110}//RP fibre [183–185]. Other surface textures in hot rolled steels have been reported consisting of strong {100}//RP fibre textures [137, 181]. The quarter thickness and centre plane texture of samples in literature tend to consist of strong (001)[110] and (112)[$1\bar{1}0$]/ (113)[$1\bar{1}0$] textures that extend along the {111}//RP fibre and finish at between the {332}<113> and {554}<225> textures [96, 137, 180, 181, 184, 185]. A summary of what these textures presented in ODF plots is observed in Figure 2.31.

(a) Hot rolled surface texture [184].

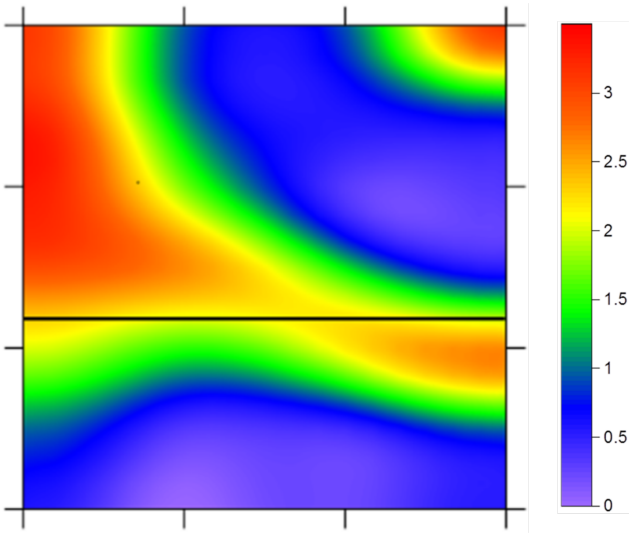

(b) Hot rolled centre texture [183].

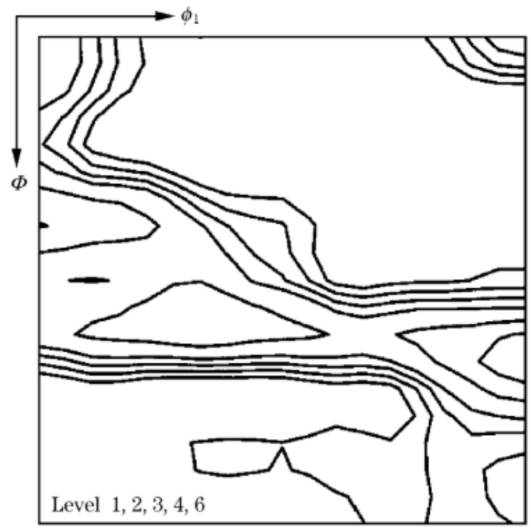

(c) Hot rolled centre texture [185].

(d) Hot rolled centre texture [184].

Figure 2.31: ODF's of hot rolled steels at various depths through thickness. Reprinted from [183–185].

Warm Rolling

There is a large amount of overlap regarding which austenitic textures can form a particular ferritic texture. This is due to the multitude of relationships that exist when changing geometry from an FCC to a BCC crystal structure as described by K-S and other relations. Deformed ferrite crystals on the other hand are somewhat simpler to research as neither recrystallization nor transformation occur as a result of ferrite deformation.

Deformation of ferrite grains at either room temperature or above A_1 (723°C) temperature tends to shift the present texture to more stable orientations [23, 102]. This results in the stable recrystallized texture: the rotated cube and the stable deformed austenite texture: {113}<110> to be strengthened while other textures such as the other main deformed austenite derived ferrite texture {332}<113> shifts towards the {111}<110> texture giving the characteristic strong ND fibre of steels finish rolled in ferrite [186].

Warm rolled texture is typically very similar to that of hot rolled textures, however, there are some slight differences reported in literature. The surface texture of warm rolled steel is similar to that of hot rolled steel with the main texture component present the {110}//RP fibre as reported by Engler et al. (2000) [182]. The bulk texture of warm rolled steels appear very similar to that of hot rolled steels with strong (112)[1$\bar{1}$0]/ (113)[1$\bar{1}$0] textures continuing along the {111}//RP fibre and finishing at between the {332}<113> and {554}<225> [21, 187, 188]. Some differences between hot rolled steels and warm rolled steels can occur with the texture of warm rolled steels finish rolled at successively lower temperatures shifting the (112)[1$\bar{1}$0] texture towards the (001)[1$\bar{1}$0] [187]. A summary of warm rolled textures in ODF plots are observed in Figure 2.32.

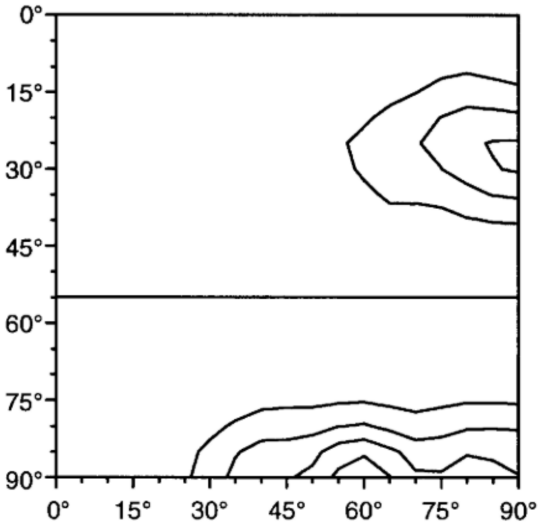

(a) Warm rolled centre texture [182].

Intensity levels: 1,2,4,7

(b) Warm rolled bulk texture [188].

Intensity levels: 2,3,4,...

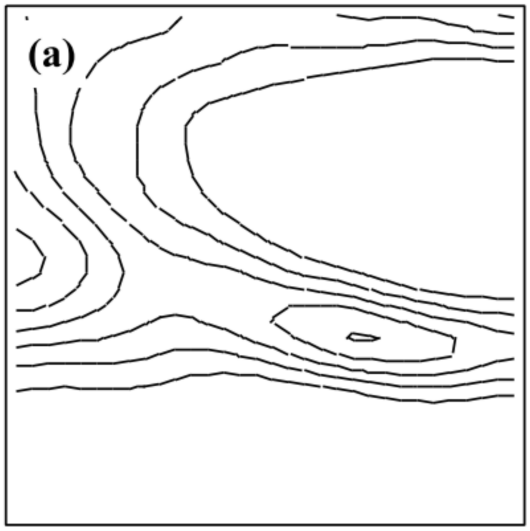

(c) Warm rolled bulk texture at 810°C [187].

Intensity levels: 1,2,3,...

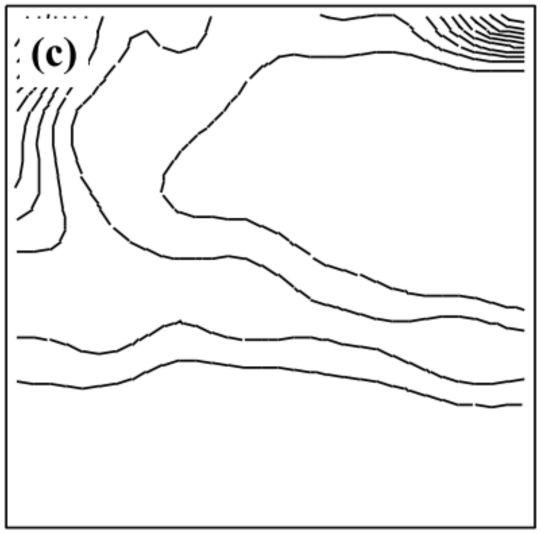

(d) Warm rolled bulk texture at 750°C [187].

Intensity levels: 1,2,3,...

Figure 2.32: ODF's of warm rolled steels at various depths through thickness. Reprinted from [182, 187, 188].

2.7.5 Effect of Crystallographic Texture on SCC in Pipeline Steel

Based on the role of material properties on SCC, it remains unclear as to what is the driving mechanism behind SCC susceptibility. Whilst there is some evidence that altering the carbon content, grain size and even the tensile strength can alter susceptibility, it

does not explain why adjacent pipes made by the same manufacturer experience different levels of susceptibility when exposed to the same conditions. Recent investigation on SCC in pipeline steels has found that there may be a link between SCC and the materials crystallographic texture. Presented below is a critical review of crystallographic texture and its role in SCC and other corrosion mechanisms where relevant.

With the advent of x-ray diffraction techniques, the direct investigation of crystallographic orientation in polycrystalline materials was made possible. One of the earliest study on the effect of crystallographic orientation on intergranular corrosion rates in steel, conducted by Rath & Bernstein (1971) [189], found that corrosion rates were linked to both the angular misorientation of adjacent grains as well as the crystallographic texture. Rath & Bernstein (1971) [189] found that corrosion rarely occurred with misorientation below 20° and that low index crystallographic orientations were far less susceptible to intergranular attack than random high index orientations. Later work building on the findings of Rath & Bernstein (1971) lead to grain boundary engineering where it was considered that corrosion rates between adjacent grains would vary based on the grain boundary energy with higher grain boundary energies corresponding to a higher corrosion rate [107].

Early investigations studied the effect that different crystallographic texture and grain boundary properties could have on the susceptibility behaviour of materials to intergranular cracking [107, 189–191] . For pipeline steels, the effect of crystallographic texture was initially investigated on Hydrogen Induced Cracking (HIC). Initial studies conducted by Venegas et al. (2005)[192] determined that HIC occurred intergranularly through high angle grain boundaries (HABs) and transgranular cracking occurred primarily through cleavage of {100}//<ND> oriented grains and, through slip in {112}<111> and {123}<111> oriented grains. This work was followed up again by Venegas et al. (2007) [193] where the authors confirmed the intergranular cracking mechanism of HIC in pipeline steels. Venegas et al. found, based on comparison of cracked grains and uncracked grains, that there was a higher presence of $\Sigma 11$, $\Sigma 13b$ and $\Sigma 29a$ coincident site lattice (CSL) bound-

aries in uncracked grains. It was hypothesised that the high presence of CSL boundaries correlated with the high concentration of {111}//ND orientations more than an intrinsic resistance of CSL boundaries to intergranular cracking. Indeed, subsequent publications by Venegas et al. [194] suggested that there was no statistical significance on the role played by CSL boundaries to increasing intergranular cracking resistance.

In a similar methodology to Venegas et al. [192–194], Mohtadi-Bonab et al. (2013) [195] found in X70 that cracking occurred when there were low proportions of {111}//ND grains and when there were strong {100}//ND grains surrounding the crack. There was also strong proportions of grains with other textures including {322}//ND, {332}//ND and {112}//ND through the material but their effect was not mentioned. In the subsequent papers by Mohtadi-Bonab, et al. (2015a) [196] and (2015b) [197], the result show that just increasing the proportions of {111}//ND, {322}//ND, {332}//ND or {112}//ND grains does not necessarily prevent intergranular cracking as cracking was observed through all of these orientations.

It is important to mention the work by Venegas on the role of texture on HIC susceptibility as it inspired subsequent investigations linking the role of crystallographic texture to SCC [20, 24, 25, 29]. Arafin and Szpunar (2009) [24] investigated a field-cracked sample of X65 and found that overall, cracks propagated between HAB's typically following the path of greatest misorientation or the direction most favourably oriented to the stress direction i.e. perpendicular to stress direction. When the cracks went in an unfavourable direction it was postulated that it was due to the presence of $\Sigma 11$, $\Sigma 13b$ or $\Sigma 5$ boundaries or due to unaffected grain boundary being formed by two {110}//RP grains, however, it was not fully discussed. Arafin and Szpunar (2009) [24] later examined the crack path and adjacent area ahead of the crack to see if there was any significant difference in texture. They determined that cracks tended to bypass grain boundaries that were associated with {110}//RP and {111}//RP boundaries and propagated through grain boundaries associated with {100}//RP textures. Whilst this methodology was able to distinguish

between grains that did and did not fracture, it is not clear whether the areas ahead of the crack the authors scanned were actually associated with crack arrest locations as the cracks they investigated were not the result of a failure and it is likely that if the pipe was placed back in the ground, the cracks would continue to grow. In addition, when analysing the magnitude of textures they reported on, it becomes clear that they very selectively sampled individual grains along the crack path. As there was no overall texture reported surrounding the crack, the texture identified may not be representative of the texture found along the entire crack path. There is still some uncertainty regarding the textures that are associated with cracking in pipeline steel based on this paper [24].

The concentration of crystallographic texture was found to be important to SCC susceptibility in work conducted by Lavigne, et al. (2014) [20]. They found that the concentration of crystallographic texture was important for the susceptibility of SCC and when the surface of a pipe samples contained a strong ($\sim 3\times$ random) {110}<110> texture no cracking initiated, however, a weaker ($\sim 1.5\times$ random) concentration of {110}<110> developed SCC cracks. The work conducted by Arafin and Szpunar [24, 25] also found that that grains with {110}//RP and {111}//RP fibre textures were more resistant to cracking than grains with other major fibre textures. There is a difference in methodology with how the two authors came to their conclusions. Whilst Arafin and Szpunar (2009) used EBSD of individual grains to determine the texture present in cracked regions, Lavigne et al. (2014) utilised neutron diffraction to sample large sections of through thickness texture. Arafin and Szpunar (2009) may have sampled too few grains to develop a statistically sound finding and Lavigne et al. (2014) may have sampled too many grains; an exact map of which grains were preferentially fractured was not able to be developed.

The importance of CSL boundaries was touched on previously but there is still some debate regarding the resistance of CSL boundaries to cracking. Direct measurement of CSL boundaries to fracture undertaken by Lin and Pope (1993) [191] found that only $\Sigma 1$ (LAB's) and $\Sigma 3$ boundaries have any special resistance to fracture based on them

being closely related to the ideal lattice structure. This finding is somewhat supported by Lin et al. (1995) [114] who found increasing the overall proportion of CSL boundaries reduced the crack susceptibility, however, the main increase was the Σ3 boundary type and the other higher energy CSL boundary proportions remained mostly the same. Similar results are found by Kurishita et al. (1983) [190] who conducted four point bending tests on single crystals of molybdenum along the <110> twist axis. The resulting crystal was sectioned at different orientations to create different misorientations which were then fractured in a four-point bend test. The results showed that of all the CSL boundaries present, the Σ3 and Σ17*b* had the highest strength and other CSL boundaries along the <110> axis were significantly weaker, including the Σ11 boundary.

Whilst most literature suggests that Σ3 boundaries are resistant to intergranular cracking, in the literature by Venegas et al. (2007) and subsequently Arafin and Szpunar (2009) [24, 193] considered Σ3 boundaries to be regular HAB's as they are *"texture induced non-coherent high energy grain boundaries since true twinning/ multiple twinning does not occur in these steels"* [24]. The origin of this consideration is from the 1987 ASM Metals Handbook Volume 13 [198] and is no longer included in the current versions.

2.8 Summary

Stress Corrosion Cracking in pipeline steels can lead to premature pipe failure without prior warning by reducing the nominal pipe thickness to below the minimum required for containment. SCC propagates through steel pipes through the combined effort of anodic dissolution and film fracture. As the cathodic protection system develops a passive oxide layer on the surface of the pipe, pressure fluctuations cause the pipe to deform slightly and fracture the film. When the film is fractured the metal below is unprotected and anodic dissolution between the grain boundaries occurs. As the grain boundaries are more susceptible to cracking than the grains themselves in high pH SCC, altering the grain boundaries to make them more resistant to cracking is thought to be beneficial to

decreasing SCC susceptibility. The introduction of grain boundary engineering to SCC research determined that in samples of X65 pipe, SCC seems to be more active between high angle grain boundaries, particularly those boundaries associated with {100}//RP textures. Conversely, there is more resistance to SCC between low angle grain boundaries as well as high angle boundaries associated with grains having {110}//RP and {111}//RP textures. As explored above there are some shortcomings in the methodologies used to come to those conclusions as the number of grains sampled between studies was not consistent and the selection of crack arrest locations was unconvincing.

In terms of manufacturing, the exact rolling schedule is developed based on the required strength level, the climate and the physical dimensions of the pipe with the chemical composition introducing more complexity. Both hot and warm rolling has been carried out to produce X70 pipe with the specified requirements therefore, both rolling schedules should be evaluated for their SCC resistance.

Texture formation in pipeline steels as a result of the rolling schedule is a comprehensively studied area with the effect that hot, warm and cold rolling has on the texture development in low carbon steels. The development of texture in pipeline steels is the result of the complex interaction between deformation, recrystallisation and transformation textures that occur in different concentrations depending on the specifics of the rolling schedule utilised. In the simplest rolling procedure with hot rolling above the T_{NR}, the austenitic recrystallisation texture, the cube texture ((100)[001]) dominates. Upon transformation to ferrite the cube undergoes a rotation due to the change from FCC to BCC crystal structures to form rotated cube {100}<110>, Goss (110)[001] and rotated Goss textures $(110)[1\bar{1}0]$.

When introducing hot rolling below the T_{NR}, deformation textures start to develop as deformed austenite no longer undergoes complete dynamic recrystallisation in the interpass interval. Deformed austenite is a more complex texture production process with Brass

{110}<112>, Copper {112}<111>, {123}<614> and weak Goss texture primarily forming. As deformation texture can be deformed further prior to transformation, the final texture can be highly complex. In general the Brass textured grains produces {332}<113> texture that can be further deformed to form either the {554}<225>, {111}<112> or {111}<110> textures. Copper textured grains can form {113}<110> grains upon deformation. Each of the deformed textures transform into different textures upon cooling to ferrite which shows where the complexity arrives. Warm rolling and cold rolling further complicates the texture production as the transformation textures developed through hot rolling below T_{NR} and those developed through deforming ferrite form. In general warm rolling strengthens the deformed austenite textures as well as strengthening the {111}//RP texture.

When evaluating the available literature, some gaps in the current understanding of the manufacturing processes affecting SCC in pipeline steels become apparent. In terms of the effect of crystallographic texture on SCC, there are no EBSD studies linking SCC to crystallographic texture in pipeline steels in grades other than X65 or similar ferritic/ pearlitic steels. In addition, the methodology appears to have some short-comings that does not take into account long sections of the crack isolated from the surrounding material. As new pipes being installed are typically high strength with bainitic microstructures, it is unknown whether the recommendations from previous research are applicable for these different microstructures. The manufacturing methods used in the creation of X70 grade pipeline steel is a well studied area with many papers having previously been published providing guidelines for the production of X70 steel through thermomechanical processing; for the intents of this project there are no gaps that need to be addressed. In terms of texture production, there exists a wealth of literature linking the effect of rolling on the final texture development in low carbon steels. Although the exact crystallographic texture produced through different manufacturing processes on an arbitrary material is not able to be calculated directly, recrystallized rolling, hot rolling and warm rolling each have fundamental textures produced that can be altered by changing minor elements of

the schedule. There exists a major gap in the literature where there is no strong link between the manufacturing process and the effect that it has on the texture production and the subsequent effect on the SCC resistance in X70 grade pipe.

Chapter 3

Scope

3.1 Aims

The primary aim of this thesis is to investigate the effect of manufacturing schedules on the crystallographic texture of gas pipelines, and the subsequent effect on pipeline stress corrosion cracking (SCC) susceptibility. The data presented can be utilised by pipeline manufacturers for the development of pipes with greater inbuilt resistance to SCC.

The specific aims of this project are to determine the effect of:

1. different rolling schedules on the crystallographic texture development in pipeline steel.

2. crystallographic texture on high pH SCC susceptibility.

The aims of the project were narrowed to exclude verifying the role crystallographic texture had on high pH SCC propagation in field-generated SCC samples. Prior to this, a conference and a journal article were published, investigating the role of crystallographic texture on field-generated SCC samples and are included in Appendix I.

3.2 Objectives

To achieve the aims of the project, the measurable objectives that have been evaluated are as follows:

1. The design of a series of rolling schedules to generate different crystallographic textures in pipeline steel.

2. Characterisation of the microstructure of the selected pipeline steel generated from the different rolling schedules, including analysis of the resulting crystallographic texture.

3. The assessment of the effect of different rolling schedules on SCC susceptibility through SCC testing, and the correlation of susceptibility with changes in crystallographic textures.

3.3 Exclusions

1. This project is primarily aimed at determining the role of texture on SCC susceptibility and, as such, other parameters that affect SCC susceptibility, such as steel chemistry, will not be investigated. To prevent different chemistry between the samples, all rolling samples will be manufactured from the same raw material.

2. The intention of this project is not to develop rolling schedules for use in industry, rather to assess what effect changing the rolling schedule will have on the SCC susceptibility. Hence, the rolling schedules used are specifically designed for achieving this goal. The author wants to reiterate that the schedules are representative of rolling carried out in industry, however, are specific to the material and equipment available.

3. The susceptibility of low carbon pipeline steel, in particular API 5L X70, is being tested in this project. While it may have similar characteristics to other steel pipeline grades, the results may not necessarily translate.

4. Only high pH SCC will be considered in this project. Near neutral SCC is beyond the scope of this project.

Chapter 4

Experimental Procedure

The aim of the study was to investigate the role of controlled rolling on the formation of crystallographic texture in pipeline steel and the effect it had on stress corrosion cracking susceptibility. As the development of texture is primarily due to controlled rolling schedules implemented prior to pipe forming, a series of rolling schedules to produce different textures is necessary for developing materials for the purpose of testing SCC susceptibility. This chapter provides a brief overview of the industry supplied materials used, and summarises all experimental procedures and equipment used in the various controlled rolling schedules. Subsequently, equipment and methods utilised for the characterisation of material properties and SCC susceptibility post controlled rolling are outlined.

4.1 Industry Supplied Materials

This section contains an overview of the industry supplied materials used during this study. The supplied materials were for both controlled rolling experiments as well as to compare properties with the laboratory rolled plate. The industry supplied samples acted as a benchmark of expected X70 mechanical, microstructural, and crystallographic properties such that the laboratory rolled samples could be compared to materials currently used in industry. Three samples of X70 were supplied for use in the project: a 20 mm X70 plate manufactured by BAOSTEEL (Baoshan Iron and Steel Co., Ltd.); a 10 mm X70 pipe section of 500 mm external diameter supplied by pipeline operator SGSP Assets

Pty Ltd, trading as Jemena; and a 6.4 mm X70 plate manufactured by Shougang Qian'an Iron & Steel Company and supplied by pipeline operator Jemena.

The 20 mm X70 plate was delivered as an approximately 1 m^2 section and had not been used in any pipe forming operations with the mill scale attached to the top and bottom surfaces. The rolling direction was provided but neither the rolling schedule or processing temperatures were supplied. The 20 mm X70 plate used in this investigation was initially cut from the 900 × 1035 mm plate with a section of plate seen in Figure 4.1. The material was further sectioned into 120 × 200 mm sections for the rolling trials.

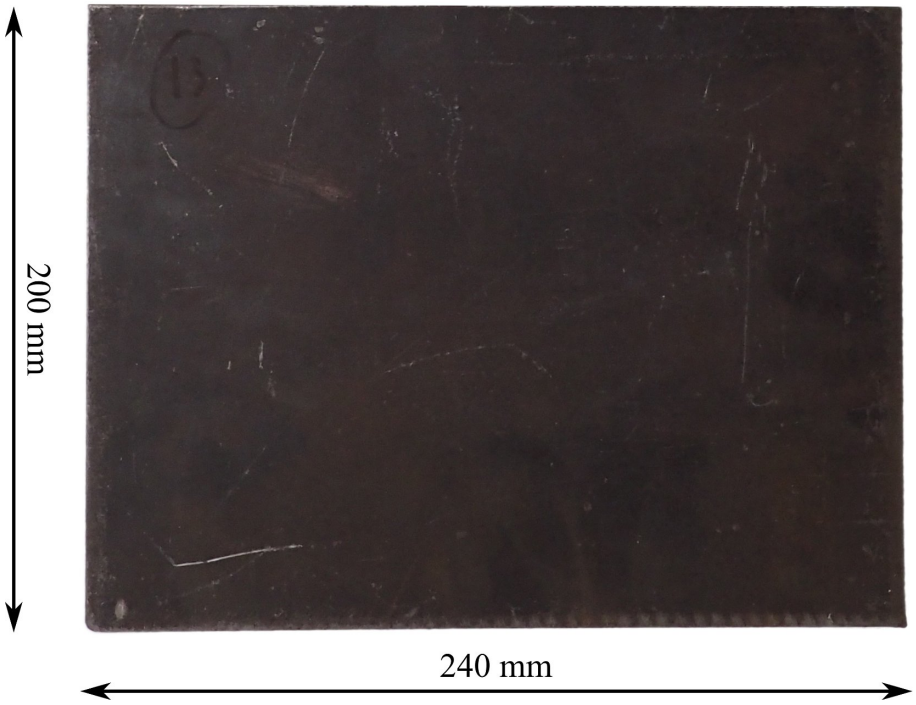

Figure 4.1: 20 mm X70 plate used during this investigation.

The 10 mm X70 pipe section was supplied by Jemena from their collection of spare pipe. The pipe had a wall thickness of 10 mm and an outer diameter of 500 mm. The pipe was supplied fully coated but had not been placed in service previously. A small wedge of the pipe cut for metallography is seen in Figure 4.2a. The section was sourced from the 3 o'clock position to avoid the weld material and the centre of the roll where segregation concentrates. Neither the original manufacturer nor the rolling schedule was provided

and chemical composition was similarly unknown. The 6.4 mm thick plate was supplied in two 400 × 1000 mm plates, as seen in Figure 4.2b, and had not yet been used in any pipe forming operations. The plate did have a residual curve in it as it was coiled after cooling, and no efforts were made to flatten the supplied material.

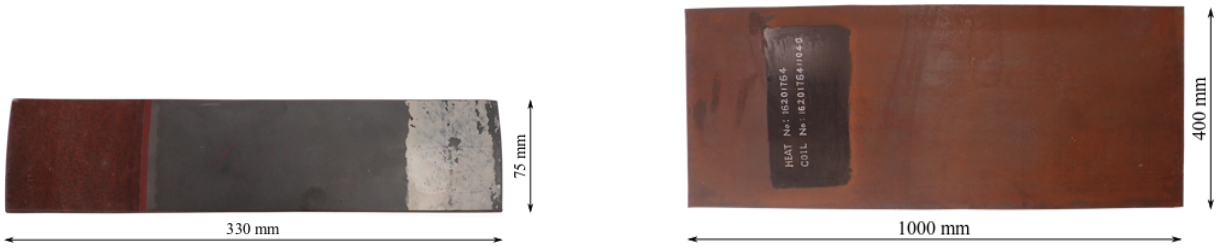

(a) 10 mm X70 pipe section

(b) 6.4 mm X70 plate

Figure 4.2: Pipe and plate samples supplied by Jemena.

4.1.1 Chemical Composition

The chemical compositions of the three industry supplied materials are presented in Table 4.1. The chemical composition of all the samples were analysed by Bureau Veritas [1] using Optical Emission Spectrometry (OES) and combustion analysis for Carbon and Nitrogen content. This was undertaken on all samples, irrespective of the provision of chemical composition from the manufacturer, to ensure accuracy of the results. The results are within the range allowed for X70 steels set by the API 5L standard [27], and are compared in Appendix A.

Table 4.1: Chemical Composition of industry supplied materials (w.t. %). *Fe* Balance.

	C	***Mn***	***Si***	***Ni***	***Cu***	***Al***	***Mo***	***V***	***Nb***	***Ti***	***Cr***	***Ca***	***P***	***S***	***B***	***N***
20 mm X70	0.059	1.57	0.19	0.19	0.16	0.05	0.17	0.03	0.05	0.01	0.03	0.002	0.01	0.002	0.0005	0.004
10 mm X70	0.080	1.48	0.21	0.007	0.006	0.03	0.002	0.03	0.05	0.01	0.14	0.004	0.009	0.001	0.0004	0.005
6.4 mm X70	0.073	1.53	0.19	0.006	0.010	0.03	0.13	0.002	0.05	0.01	0.02	0.004	0.01	0.0003	0.0003	0.011

[1] Bureau Veritas Whyalla
Phone: 08 8647 6500
Address: 4-6 Jacobs St, Whyalla SA 5600

4.2 Development of Rolling Schedules

The primary aim of this project was to investigate the effect of manufacturing procedures on the crystallographic texture in pipeline steels and the subsequent SCC susceptibility. In controlled rolling, steel is processed under different regimens depending on the desired properties where regimes are determined by the phases present during rolling. The three controlled rolling regimes that exist are recrystallized rolling, hot rolling and warm rolling as explored in Chapter 1. These three regimes can produce different crystallographic textures in the final product due to the different responses to deformation and recrystallization mode of each regime. *N.B. while the material used as feed stock for controlled rolling has its own crystallographic texture, soaking the steel causes the grain structure to change due to phase transformation to austenite and grain growth, hence the crystallographic texture produced in the laboratory rolled specimens will not be influenced by the material's initial texture significantly.*

The development of the rolling schedules was dependent on being able to develop a refined microstructure that would have material properties similar to those found in industry. Therefore, it is required to accurately determine the temperature range within which the desired phases are formed. To determine the temperature range of the rolling regimes for our rolling feed stock, the development of a Continuous Cooling Transformation (CCT) diagram was necessary. In addition, to ensure that rolling would adequately refine the grain size, it was necessary to study the prior austenite grain size developed from different soaking temperatures and times.

4.2.1 Development of the CCT Diagram

To develop rolling schedules that would be comparable to those currently used in industry, the transformation temperatures and microstructure development in the as-received 20 mm X70 plate (used for laboratory rolling) needed to be determined. A CCT diagram was constructed rather than a Time Temperature Transformation (TTT) diagram

because, as explored in Chapter 1, industrial processes tend to utilise continuous cooling treatments rather than isothermal transformation to develop steel microstructures. Hence a CCT diagram is more applicable in the development of a rolling schedule.

Equipment

The CCT diagram was produced using a TA Instruments DIL 805 A/D quenching and deformation dilatometer as seen in Figure 4.3. The dilatometer required cylindrical samples with dimensions of $\varnothing 4 \times 10$ mm. Dilatometer samples were sourced from the 20 mm X70 plate, with the long axis aligned with the rolling direction. The centre of the diameter was coincident to the quarter thickness plane of the 20 mm plate. Samples were conventionally machined on a lathe. A schematic diagram of this sample orientation and dimensions can be seen in Figure 4.4.

Figure 4.3: TA Instruments DIL 805 A/D Dilatometer.

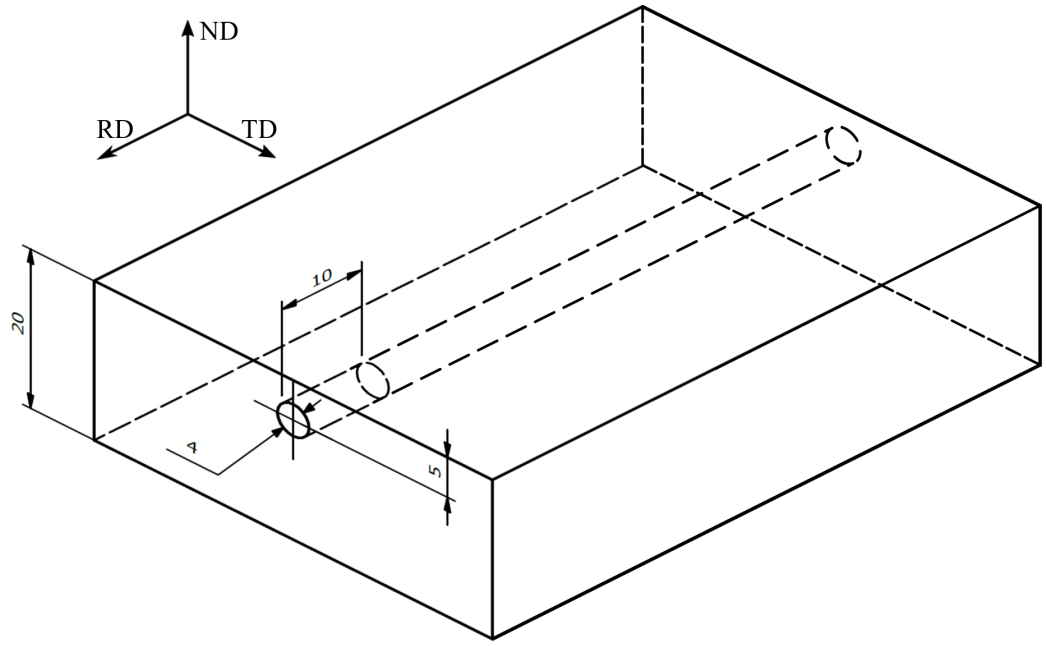

Figure 4.4: Dilatometer sample dimensions and orientation with respect to the 20 mm X70 plate.

Procedure

Dilatometer samples were polished briefly with 1200 grit sand paper to remove any surface rust that had formed during transit. Samples were then degreased and washed with ethanol. A Type S (90% Pt/ 10% Rh-Pt) thermocouple was spot welded to the dilatometer sample and placed between the fused silica grips of the dilatometer, where the atmosphere was evacuated. Samples were heated with an induction coil at 3°C/s to a temperature of 1100°C. The specimens soaked for 5 minutes to allow the internal temperature to homogenise and allow all ferrite to transform to austenite. The samples were then quenched with compressed nitrogen gas at specified rates while the change in extension due to transformation was recorded. To determine equilibrium transformation temperatures, a sample was heated and cooled at a rate of 2°C/min such that Ac_1 and Ac_3 temperatures were identified during the heating phase and Ar_1 and Ar_3 identified during the cooling phase.

The transformation temperatures were developed by plotting the temperature against the elongation and finding regions where the linear slope changes to a cubic function, as seen

in Figure 4.5. The transformation temperatures during cooling are determined by finding the exact temperature the curve changes from linear to cubic as highlighted in Figure 4.6.

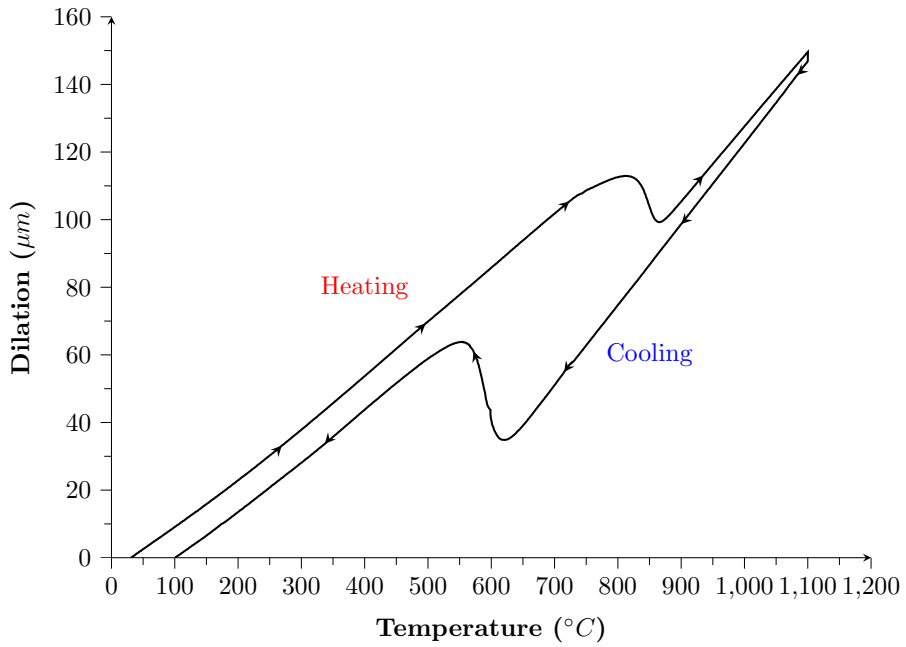

Figure 4.5: Dilation vs. temperature plot.

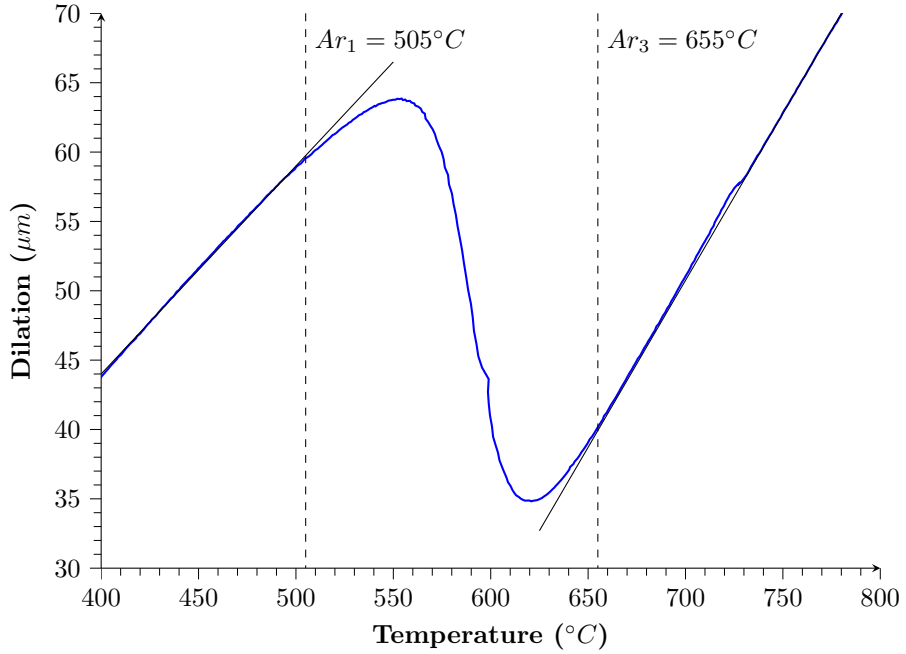

Figure 4.6: The change in extension exhibited in a dilation curve due to changes in microstructure.

To identify the microstructures produced during the different cooling rates to complete

the CCT diagram, the dilatometer samples were mounted longitudinally to the rolling direction and ground to the mid-point and polished, as shown in Figure 4.7. The specimens were etched with 2% Nital according to ASTM E407-07 and five Vickers microhardness indents were made according to ASTM E384 in the pattern, shown in Figure 4.7, to get an average hardness of each cooling rate. The central hardness indent served to locate a common region for optical and Scanning Electron Microscopy (SEM) characterisation, such that the microstructure of each cooling rate could be identified and compared using both techniques concurrently. The CCT diagram was produced by plotting all cooling rates from 1000°C to room temperature, highlighting transformation regions and filling each region with the microstructure produced.

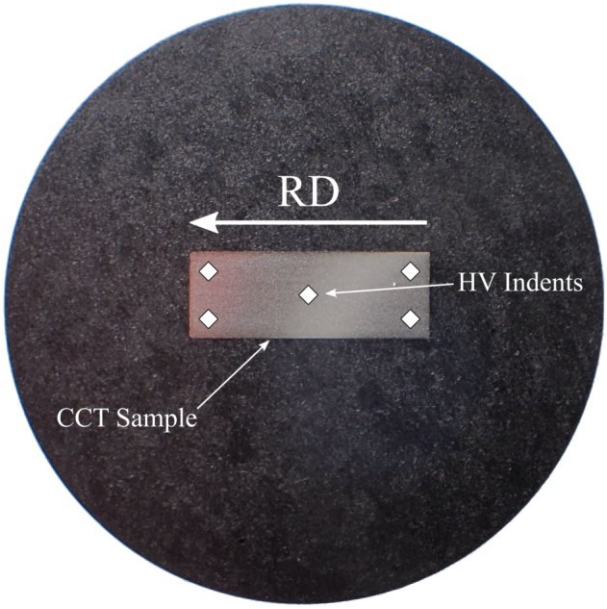

Figure 4.7: Mounted and polished CCT specimen showing the rolling direction (RD) and location of microhardness indents.

4.2.2 Determination of Prior Austenite Grain Size

Since the process of controlled rolling is based on the transformation of γ-iron to α-iron, such as ferrite-pearlite and bainite mixtures depending on steel composition, a knowledge of prior austenite grain size is an important parameter to consider. Finer prior austenite grain size leads to finer grain sizes in the transformed microstructures including bainite

and ferrite, however, fine prior austenite grain size increases the roll force necessary to deform the plate during hot rolling [199]. A balance between transformed microstructure grain size and required roll force on the laboratory scale mill must be made.

In order to study the effect of soaking time on the prior austenite grain size, four samples with dimensions as shown in Figure 4.8 were placed into a resistance heating furnace at 1180°C. Once the internal furnace temperature stabilised at 1180°C, samples were removed and quenched in water after 60, 120, 150 and 180 minutes. Specimens were sectioned transverse to the rolling direction, prepared conventionally down to 1 μm diamond paste and etched in saturated aqueous picric acid for 10 minutes. The etchant details are found in Section 8.2.2. Prior austenite grain size was then determined through the intercept method outlined in ASTM E112 [200].

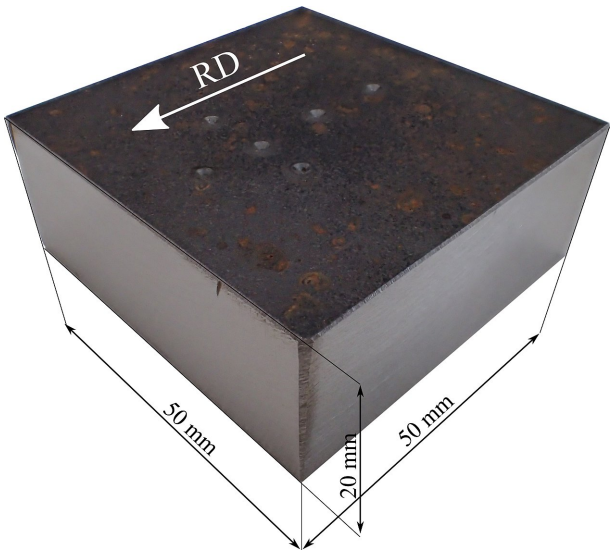

Figure 4.8: Dimensions of the prior austenite grain size specimens.

4.3 Controlled Rolling

Crystallographic texture in steels is developed through a combination of the manufacturing process, the crystal structure, and chemical composition. Whilst small scale plane strain compression testing may be used to simulate controlled rolling and development of different crystallographic textures, the dimensions of the final specimens are not compati-

ble for subsequent SCC testing [201]. Laboratory scale hot rolling is a close approximation to commercially produced samples and offers similar manufacturing flexibility and size benefits that commercially produced products offer. In addition, the specimens produced through laboratory rolling allows mechanical and corrosion test specimens to be produced from a single plate reducing the need for multiple test specimens.

A fundamental aspect of rolling schedule design is determining the final thickness of the material. X70 pipelines in Australia have been produced with wall thicknesses of both 6.4 mm and 7 mm so either thickness is a valid option when designing the rolling schedules. Upon consultation with Australian pipeline operators, 7 mm wall thickness X70 pipe is more attractive because it enables slightly higher operating pressures leading to increased product throughput. A final nominal thickness of 7 mm was selected to better align with the current and future industry needs.

4.3.1 Rolling Equipment

Rolling Mill

Laboratory rolling of X70 plate was undertaken on a Hille 100 experimental rolling mill, shown in Figure 4.9. The Hille 100 experimental rolling mill was a laboratory scale, two high mill with hardened steel rollers. The rolls were 220 mm wide and a diameter of ⌀250 mm, with a maximum roll gap of 20 mm. For the adjustment of the rollers, the mechanical screws adjusted the top rollers height, and hydraulic pistons controlled the lower roller to adjust the roll gap. The hydraulic system allowed for rapid adjustment of the roll gap of up to 6 mm before reconfiguration of the top roll was required. Adjusting the roll gap over 6 mm resulted in the rolls disengaging from the hydraulic system and prevented a constant roll gap from being maintained. Hence, reduction of the roll gap by more than 6 mm required a break for the system to be adjusted through the mechanical screws. This roll gap limitation strongly influenced the reduction per pass of the developed rolling schedules. The rolling mill was powered by a 56 kW electric mo-

tor and provided a maximum roll force of 1500 kN. Through initial trials with test pieces of X70 plate, the optimised roller speed was set to 30 RPM for the most consistent results.

Figure 4.9: Hille 100 rolling mill used for laboratory rolling.

Furnaces

Two furnaces were used during rolling, one for soaking the samples prior to rough rolling and another furnace maintained at the finish rolling temperature. The soaking furnace was a Tetlow K6 FL kiln, Figure 4.10a, with a maximum temperature of 1300°C and internal dimensions of 380 × 380 × 460 mm ($W \times D \times H$) allowing four 200 mm long samples to fit simultaneously. A series of built in ports are present in the front of the furnace which facilitated access for nitrogen shielding gas to prevent the build-up of excessive scale on the surface of the specimens. A Labec 4TF35/2 was used as the holding furnace and could achieve a maximum temperature of 1200°C. The Labex furnace was larger than the Tetlow furnace with internal dimensions of $300 \times 300 \times 500$ mm ($W \times H \times D$) Figure 4.10b. Not visible in the Labec furnace is the port at the rear for the shielding gas. The shielding gas used was Coregas grade 4 nitrogen which was pumped into both chambers at a rate of 15 L/min. Compositional details of grade 4 nitrogen are provided in Appendix H.

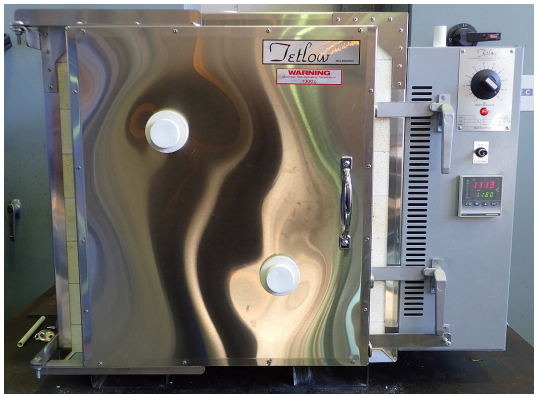

(a) Tetlow K6 FL soaking furnace.

(b) Labec 4TF35/2 holding furnace.

Figure 4.10: Furnaces used during hot rolling experiments.

Rolling Mill Pyrometers

To measure the temperature of rolling samples prior to and after rolling, two pyrometers, one placed at the entrance to the rolling mill and the other at the exit, were utilised. The pyrometers were Calex PUA2-751-HT, with a temperature range of 450-2000°C and an accuracy of ± 2°C or 1%, whichever was greater.

The spectral response [2] was 2.2 μm and a spot size of 27 mm at 400 mm away from the surface of the plate. The pyrometer attached to the front of the rolling mill, as seen in Figure 4.11, has an adjustable bracket to orient it directly above the entrance to the mill. The temperature was recorded with CalexSoft 2 software, allowing both logging and display of the temperature simultaneously for instant feedback on when to push the sample through the rollers. Approximately three measurements per second are recorded with the CalexSoft 2 software.

[2] Spectral response is the wavelength of the infrared light used by the pyrometer to measure temperature. 2.2 μm is the wavelength commonly used for measuring the temperature of metals

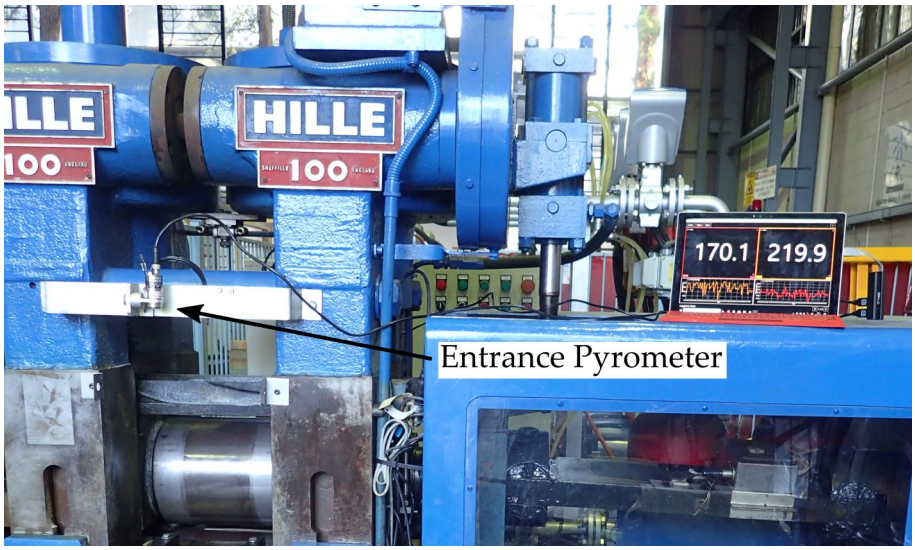

Figure 4.11: Calex PUA2-751-HT pyrometer attached to the rolling mill. *One important point to note is that the temperatures presented on the pyrometer screen is measuring room temperature but because it is below the minimum threshold temperature it outputs noise.*

Runout Table

The runout table is an essential piece of equipment that is used to cool sections of steel plate at constant rates to ensure correct microstructure development. The runout table used in this rolling trial is an Ultra Fast Cooling System for Test Rolling Mill manufactured by the State Laboratory of Rolling and Automation, Northeastern University, China, as seen in Figure 4.12. This system was directly connected to the Hille 100 rolling mill such that upon exiting, steel specimens were conveyed directly into the runout table. The system cools from both the top and bottom using straight nozzles (240 total) with a maximum pressure of 600 kPa and is capable of delivering water volumes of up to 0.85 m^3/h from each nozzle. As a cooling rate of 10°C/s was desired, the speed of the travel through the runout table was constrained based on the initial and final temperatures required of each schedule. For example to cool a sample 200°C at 10°C/s the sample needed to spend 20 seconds in the runout table, whereas, to cool a sample 100°C at 10°C/s the sample needed to spend 10 seconds in the runout table.

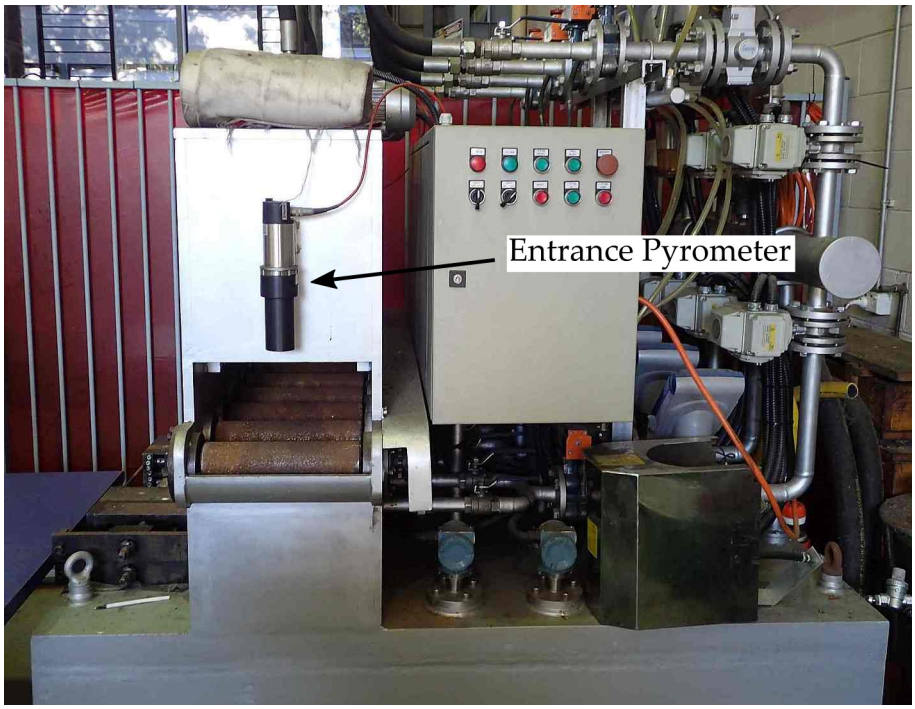

Figure 4.12: Ultra Fast Cooling System for Test Rolling Mill.

Runout Table Pyrometers

To measure the temperature at the start and end of the runout table, two pyrometers fixed to the table were used. The entrance pyrometer was a Raytek RAYMM1MLSF2 which has a temperature measurement range of 400-1470°C and an accuracy of $\pm 0.3\% + 1°C$. The spectral response was 1 μm and a spot size of 27 mm at 300 mm. The exit pyrometer was a Raytek RAYMM2MLSF2 which has a measurement range of 300-1100°C and an accuracy of $\pm 0.3\% + 2°C$. The spectral response was 1 μm and a spot size of 27 mm at 300 mm. The entrance pyrometer is shown in Figure 4.12 and the exit pyrometer is shown in Figure 4.13.

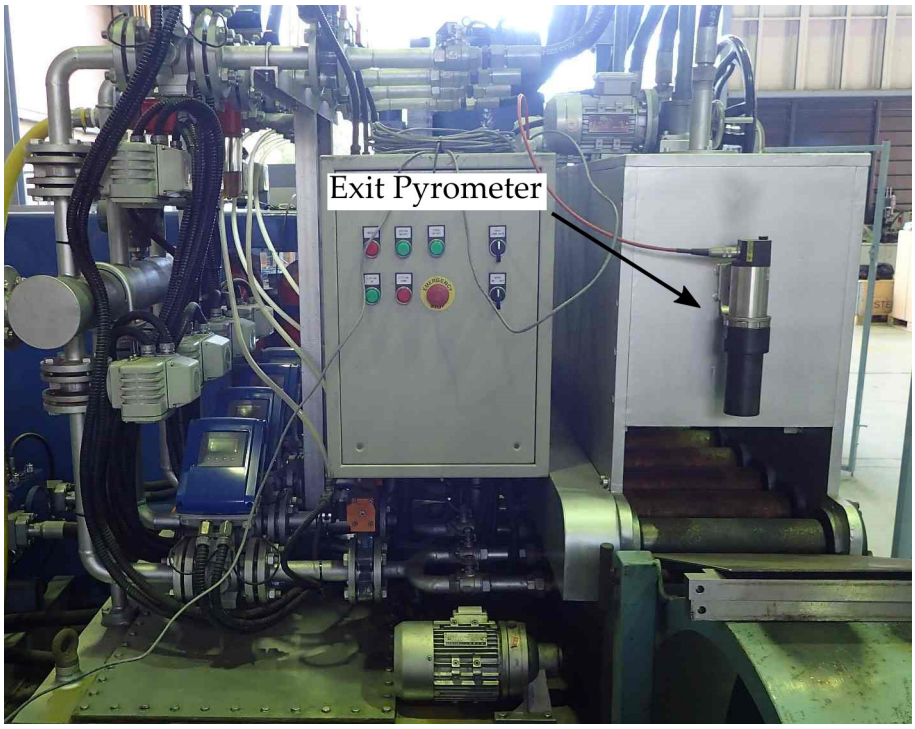

Figure 4.13: Runout table exit pyrometer.

Thermocouples

K-type thermocouples, sourced from Temperature Controls Pty Ltd [3], were used to confirm / calibrate the pyrometer temperature measurements. The thermocouples were 500 mm long and had a diameter of 1 mm. The reported accuracy of the thermocouples were ±2.20°C or ±0.75% whichever was greater. Thermocouples were placed on the surface of the steel plates and the temperature between pyrometer and thermocouple was compared and the emissivity of the pyrometer was changed until temperature measurements were the same for the expected temperature range.

4.3.2 Rolling Sample

The rolling specimens, as shown schematically in Figure 4.14, had an overall width of 120 mm and total length of 200 mm including a 50 mm long lead. Dimensions of the rolling specimen were determined by the physical constraints of the rolling equipment and the dimensions the rolled plate had to have to fit all test pieces within it. Whilst the

[3]Temperature Controls Pty Ltd
Website: `https://www.temperature.com.au/`

rolling mill was equipped with rollers 220 mm wide, when rolling specimens with widths greater than 120 mm the rolling mill tended to stall, hence a maximum width of 120 mm was selected. The 50 mm lead was necessary due to the rollers being used for both hot rolling and cold rolling, hence, they were polished to produce a better surface finish in cold rolled products. As a result, the lack of friction prevented samples without a lead from being pulled into the rollers. There was no maximum length of the specimen from the rolling mills perspective, however, to fit all the test specimens on the final rolled plate, the minimum plate length required was 400 mm.

A fundamental characteristic of metal working is that the volume of metal remains constant after deformation processes. In addition, since rolling is in the plane strain condition, change in width due to rolling is assumed to be negligible such that the initial width is equal to the final width. This leads to the relationship:

$$\begin{aligned} V_{initial} &= V_{final} \\ V &= L \times W \times T \\ \therefore L_i \times W_i \times T_i &= L_f \times W_f \times T_f \\ W_i &= W_f \\ \therefore L_f &= \frac{L_i \times T_i}{T_f} \end{aligned} \tag{4.1}$$

where V = Volume of plate

L = Length of plate

W = Width of plate

T = Thickness of plate

Hence, elongation is only a function of length and thickness. Rearranging the equation for an initial thickness of 20 mm and a final length and thickness of 400 mm and 7 mm, respectively, gives an initial length of 140 mm. Adding a 50 mm lead and a 10 mm safety

factor resulted in a 200 mm long sample.

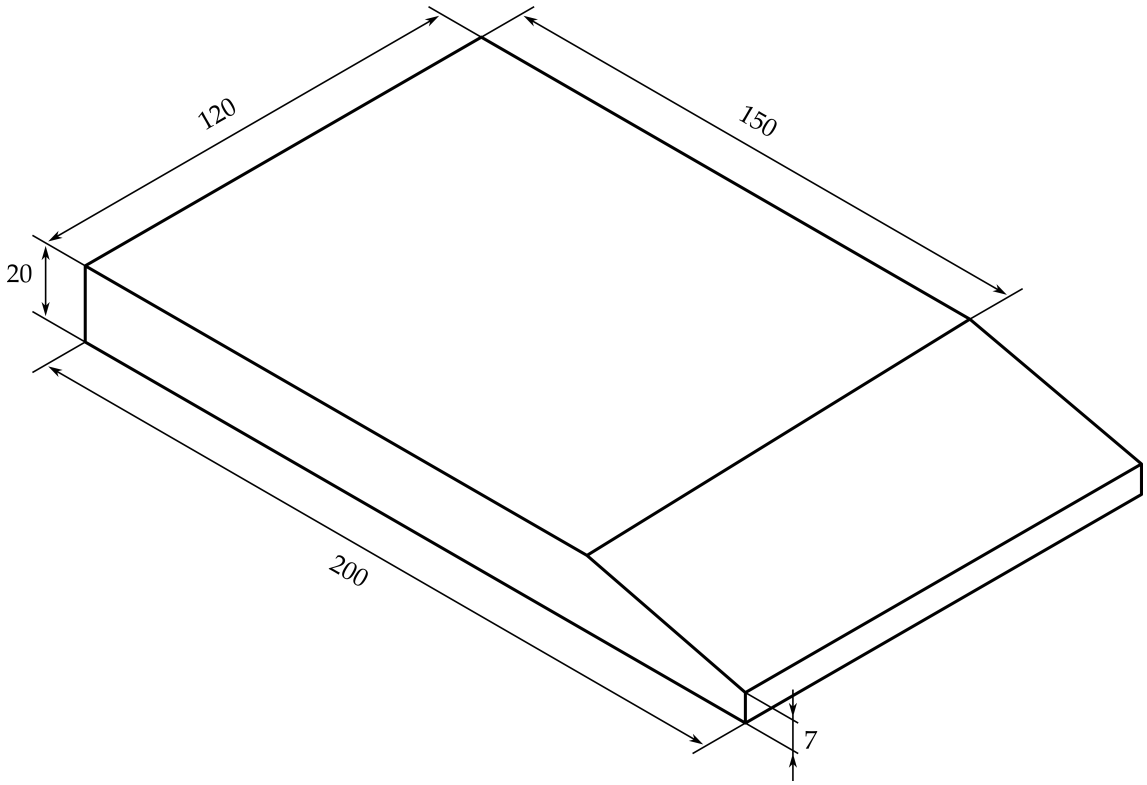

Figure 4.14: Schematic diagram of the rolling specimens used in this investigation.

A representation of the rolled specimens output from the final rolled plate is presented in Figure 4.15, which shows the final length of the rolled plate with an overview of the test specimens cut from it. *Note: the final length is 500 mm and that no specimens are included 100 mm from the lead.* This 100 mm space accounts for the length of the lead that was machined into the rolling specimen. 100 mm was calculated as being the length the lead contributes to the final length of the rolled specimen, as follows:

$$\begin{aligned} V_{Initial} &= V_{Final} \\ W \times \left(\left(\frac{T_1 + T_2}{2} \times L_i \right) \right) &= W \times (L_f \times T_f) \\ 120 \times \left(\left(\frac{7 + 20}{2} \times 50 \right) \right) &= 120 \times (L_f \times 7) \\ L_f &= 96.43\, mm \end{aligned} \tag{4.2}$$

Each specimen was positioned to maximise space (i.e. longitudinal impact specimens

located in the space between Linearly Increasing Stress Testing (LIST) specimens) with any region not used able to be salvaged in the event more test specimens were needed. In addition, the locations considered the natural bend in each plate, and the test specimens were positioned such that any bending was minimised or was isolated to the grip section.

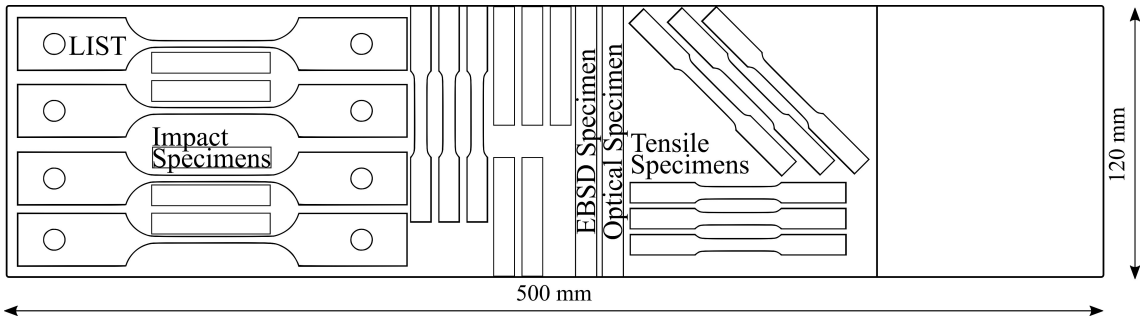

Figure 4.15: Summary of test specimens produced from the rolled plate.

A summary of the test specimens and the total number produced from each rolled plate is as follows:

1 × Optical Strip

1 × EBSD Strip

9 × Tensile Samples (3 × RD, 45° and TD)

10 × RD Charpy Impact Specimens (5 × RD and TD)

4 × LIST Specimens

4.3.3 Procedure

The procedure to run the rolling mill was driven by two key factors: 1) the roll gap adjustment of the hot rolling mill, and 2) the cooling rate of the steel plate. As the hydraulic system controlling the roll gap of the Hille 100 experimental rolling mill had a maximum extension of 6 mm, a holding furnace was required to isothermally hold the temperature while the mill was adjusted between passes. In addition, as continuous rolling in industry is carried out with steel slabs upwards of 200 mm thick, the high thermal inertia prevents cooling before rolling has finished. As the steel plate used in this investigation was only

20 mm thick initially, it cooled much faster to accommodate continuous rolling. The holding furnace prevented the plate from cooling below the critical rolling temperatures between passes.

For each rolling schedule, four samples were selected to be rolled, two dummy samples and two test samples. The dummy samples were of the same material as the test samples but had defects that made them unsuitable for analysis after rolling. The dummy samples were used to assess parameters such as roll gap, roll speed and lubrication. The four samples were placed in the Tetlow K6 FL furnace that was preheated to 1180°C where they soaked for 2.5 hours (150 minutes) after they reached the desired temperature, with the nitrogen purge running at 15 L/min to prevent excess scale formation. Once the samples were placed in the soaking furnace, the second Labec furnace was heated to the required holding temperature to enable an isothermal hold while the roll gap was adjusted.

Prior to each pass, the rollers were sprayed with a synthetic lubricant to prevent excessive bending in the samples. Once the samples had soaked for the required time, the roll gap was set, and the rolling mill started. A dummy sample was used to test the apparatus and ensure the roll gap was correct. The sample was then placed into the holding furnace. Adjustments were made and the procedure carried out with a second dummy sample to ensure everything was set correctly. Following the success of the dummy samples, the test samples were rolled and the process was repeated until final thickness was achieved.

Prior to the final roll, the runout table was turned on and the flow rate of the sprays allowed to reach steady-state. An image of the flow rate of water in the runout table is seen in Figure 4.16. Once the sample was within the temperature range required, it was pushed through the rolls as before. The runout table was connected to the exit rolls which automatically pulled the sample through, where it was cooled at the specified rate. Once the samples emerged from the runout table they were removed and allowed to air cool to room temperature.

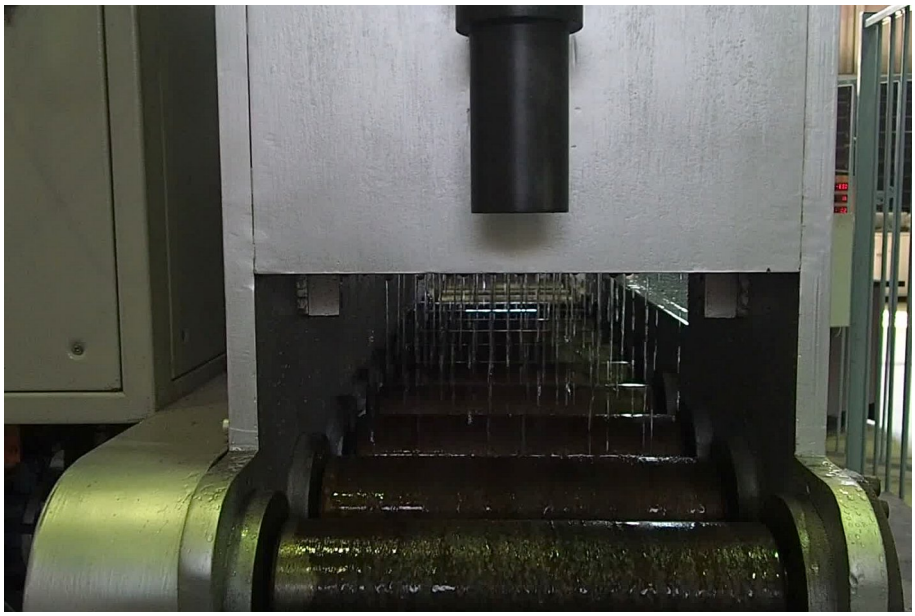

Figure 4.16: Water flow inside the runout table.

4.4 Material Characterisation

4.4.1 Specimen Preparation

Sectioning

Samples were sectioned on a Struers Unitom 50 metallographic saw, Figure 4.17, equipped with a Rappold Winterthur 172477/01A abrasive disk. The samples were then hot mounted in a Struers Citopress 5 with phenolic resin for optical only microscopy and conductive LECO 811-138 copper filled diallyl phthalate powder, for SEM, and EBSD analysis.

Figure 4.17: Struers Unitom 50 metallographic saw.

Polishing

Polishing took place on a Struers Tegramin 25 automatic polisher, as seen in Figure 4.18. Rough grinding was carried out on 220, 500 and 1200 grit diamond-impregnated disks. Polishing was carried out successively using 9 μm, 3 μm, 1 μm diamond and 0.04 μm colloidal silica abrasives with a short colloidal silica polishing time used for optical microscopy or SEM analysis, and upwards of 25 minutes used for EBSD. For full polishing procedure see Appendix B.

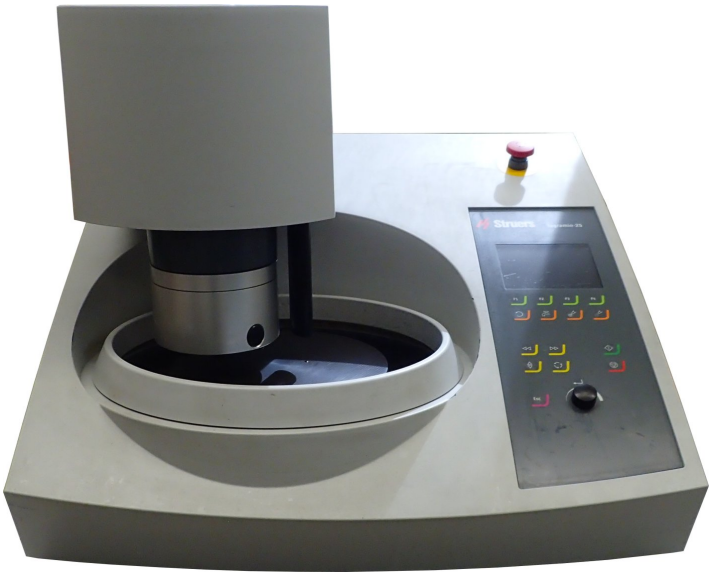

Figure 4.18: Struers Tegramin 25 polisher.

4.4.2 Optical Microscopy

Optical microscopy was undertaken on a Zeiss AXIO Imager.M2m reflected light optical microscope, Figure 4.19, equipped with bright field, dark field and cross-polarization filters. The microscope has a 10× ocular, and 5×, 10×, 20×, 50×, and 100× objectives. Images were analysed with Axiovision software version 4.9.1.

Figure 4.19: Zeiss AXIO Imager.M2m optical microscope.

4.4.3 Electron Microscopy

Electron microscopy was undertaken at both Adelaide Microscopy and Finders Microscopy; branches of Australian Microscopy and Microanalysis Research Facility (AMMRF), South Australia. Electron microscopy was used to generate SEM images of steel microstructure, energy-dispersive X-ray spectroscopy analysis of inclusions within the steel microstructure, and to develop EBSD maps for texture analysis.

SEM

General SEM imaging was undertaken at on an FEI Quanta 450 FEG Environmental Scanning Electron Microscope (ESEM), Figure 4.20. The microscope contained both sec-

ondary and backscatter electron detectors and is fitted with an Oxford Ultim Max Large Area SDD EDS detector. An accelerating voltage of 20 keV was used in conjunction with a spot size of between 4 and 5, dependent on the resulting image quality (determined based on level of polish, mounting substrate and severity of etching). Samples were typically mounted with conductive epoxy which used carbon tape to bridge the connection from the conductive resin to the stub.

Figure 4.20: Quanta 450 FEG ESEM.

EBSD

To determine the crystallographic texture of both the laboratory rolled and industry supplied specimens, Electron BackScatter Diffraction (EBSD) was utilised as it enabled a very localised measurement of texture over a short time period. EBSD was undertaken on an FEI Inspect F50 FEG SEM equipped with an EDAX Hikari EBSD detector, Figure 4.21. Samples were affixed to standard ⌀25 mm stubs using a low temperature hot glue to prevent mechanical drift. A conductive path from the the polished steel to the stub was made with carbon tape. Samples were tilted to 70° with a fixed angle stub

aligned to the EBSD detector for rapid and accurate sample orientation.

Figure 4.21: Inspect F50 FEG SEM.

Through a series of trials, the highest quality EBSD maps were generated using an accelerating voltage of 25 keV, a spot size of 5 and a 50 μm aperture. The spot size is a dimensionless value used by FEI SEMs and corresponds to the diameter of the electron beam at the sample surface. Increased spot size correlates to a larger electron beam diameter so more backscattered electrons are produced. EBSD was carried out using TSL OIM Data Collection 7 using a gain of 500, a camera exposure time of 4 ms and a camera binning of 5×5, which allowed for 250 EBSD patterns to be sampled per second. On the recommendation of EDAX software engineers, 500 frames were taken for background acquisition and the pattern signal was cleaned using the recipe consisting of background subtraction, dynamic background subtraction, and finally by normalising intensity. A summary of the Hough settings are given in Figure 4.22. The settings were confirmed with technicians at EDAX to provide accurate analysis of the EBSD patterns. For uncracked EBSD scans, three frames with a size of 450×450 μm with a step size of 0.5 μm were analysed for each sample. EBSD of SCC cracks grown through LIST testing

were carried out on two frames with a size of 110 × 110 μm with a step size of 0.2 μm each.

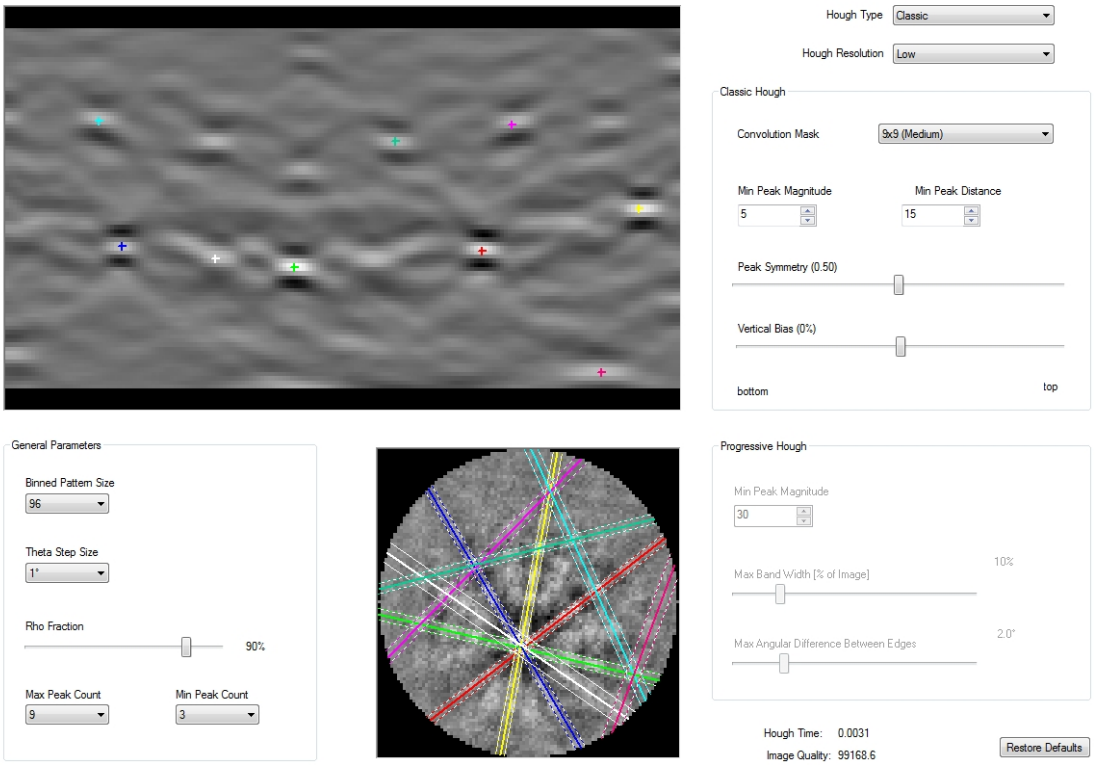

Figure 4.22: Hough settings for low carbon steel EBSD acquisition.

Analysis of EBSD data was undertaken using OIM Analysis 7 where a series of corrections to the data was made prior to analysis of texture. Prior to analysis, the data was processed using Confidence Index (CI) standardisation where the CI of each grain was standardised to remove any poor internal indexing. The data was then further cleaned by removing all points with CI less than 0.1, on the recommendation of EDAX software engineers. The result of this was especially important for SCC cracks as it removed all unindexed points from within the crack resulting in a clear boundary between the grains surrounding the crack. To ensure consistent grain size determinations, the threshold between low angle and high angle grain boundaries was defined as 15° and no edge grains were counted when determining statistics. In addition, according to ASTM E2627 [202] the minimum pixel count for considering what constitutes a grain was set to 100 (with the exception of EBSD scans at the surface which, due to smaller grain size required a less strict minimum pixel count).

ODF plots were created with Bunge notation (ϕ_1, Φ, ϕ_2), the main focus being the section $(\phi_1 = 1 - 90°, \Phi = 1 - 90°, \phi_2 = 45°)$. The ODF is produced using a harmonic series expansion with a series rank of 10 and Gaussian Half-Width of 5°. EBSD scans of the surface plane were rotated by an angle of $-90°$ around the Normal Direction (ND) as labelled in OIM Analysis to align the orientation of the sample to that required by the software. This rotation was confirmed as necessary, with EDAX software engineers, ensuring the external reference frames were in alignment between the system defaults and the sample orientation, so the ODF plot produced was from the correct plane.

To measure the texture of the X70 steel specimens, three pieces were sectioned, per Figure 4.23, for the analysis of the surface, quarter and centre planes. The surface plane was scanned at a different orientation to the quarter and centre planes to ensure details at the very surface were included in the scan. The data was rotated in software to the correct orientation for subsequent EBSD analysis. Three EBSD analyses were conducted on each plane, with the three scans combined to determine the average texture of each depth.

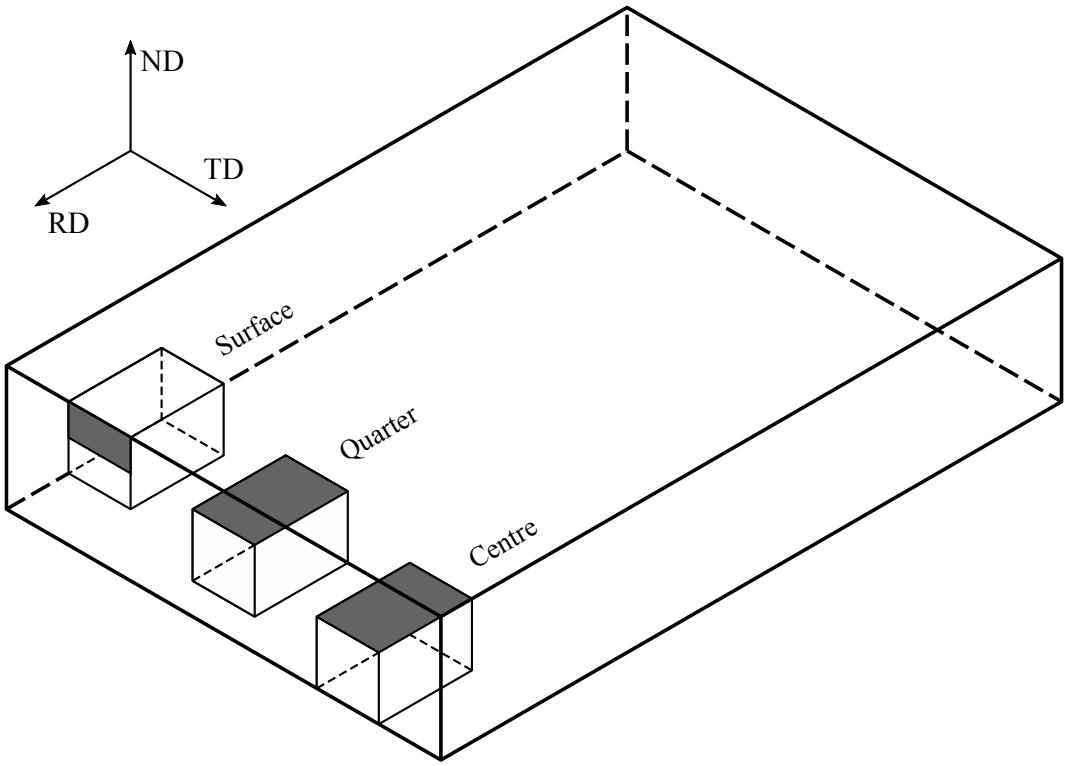

Figure 4.23: Sample sectioning for the production of EBSD specimens; Investigated planes highlighted.

4.5 Mechanical Testing

4.5.1 Tensile Testing

Tensile testing was carried out on both the as-received X70 steel and the laboratory rolled steel to: 1) confirm the strength of the materials, and 2) to determine the parameters for carrying out the SCC testing. The tensile specimens were made according to ASTM E8 [203]. Tensile test were carried out on 6 mm wide sheet-type subsize specimens, sectioned in three orientations, the LRD (0°), 45° to the rolling direction and TRD (90°), to evaluate anisotropy. In addition, 12.5 mm wide sheet-type tensile specimens were produced from the 20 mm X70 plate to compare the measured properties of the standard and subsize specimens. The dimensions of the 6 mm subsize specimens are provided in Figure 4.24. The maximum allowable thickness of the 12.5 mm and 6 mm wide sheet-type specimens is 19 mm and 6 mm, respectively. As the final thickness of the rolled specimens was 7 mm, 0.5 mm was removed from each side to conform to the standard. The 20 mm plate

required 0.5 mm to be removed from each side of the standard tensile specimen and, in the case of the subsize specimen, samples were sourced from the quarter thickness plane, hence 2 mm was removed from the surface and 12 mm was removed from the bottom. The 10 mm sample was sectioned as close to the quarter plane as possible whilst also removing all curvature from the samples. The 6.4 mm plate only required 0.2 mm to be removed from each side to conform to the standard. Prior to testing, all surfaces were finished with 500 grit sandpaper to remove all major scratches. The gauge width and thickness were measured using a micrometer at three locations, with the cross-sectional area determined from the averaged dimensions.

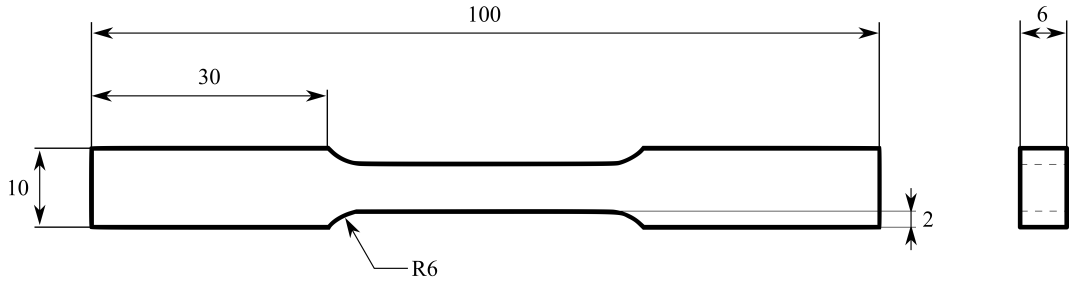

Figure 4.24: Dimensions of sheet-type tensile specimens ASTM E8. Adapted from [203].

Tensile testing was carried out on a MTS Criterion Model 45 universal testing machine, as seen in Figure 4.25, equipped with an A-grade MTS LPS.305 300 kN load cell which has a calibrated accuracy of better than 1% from 1 kN. The load cell is calibrated annually for effective loading. Prior to loading, gauge lengths were lightly scribed into the surface of the tensile specimens to facilitate fracture elongation measurements. The 12.5 mm and 6 mm gauge width specimens have gauge lengths of 50 mm and 25 mm, respectively. The samples were placed in wedge style grips, with one MTS 632.11F-90 extensometer attached to the specimen with rubber bands. The specimens were elongated at a cross-head speed of 5 mm/min until failure. Once the extensometer had elongated past 5%, it was was removed and the extension measured from the built-in extension meter of the MTS universal testing machine.

Figure 4.25: MTS Criterion Model 45 tensile tester.

Three samples for each rolling schedule and each orientation were tested to provide statistical significance. Engineering stress and strain were calculated from the extension and load measurements and plotted against each other. The Yield Stress (YS) was calculated using the 0.5% total elongation method, as is required by the API 5L standard [27]. The Yield, Ultimate Tensile Stress (UTS), uniform elongation, total elongation and the ratio of YS:UTS were calculated and presented for each sample. An image of where each of these values lie on the the Stress vs. Strain curve is presented in Figure 4.26.

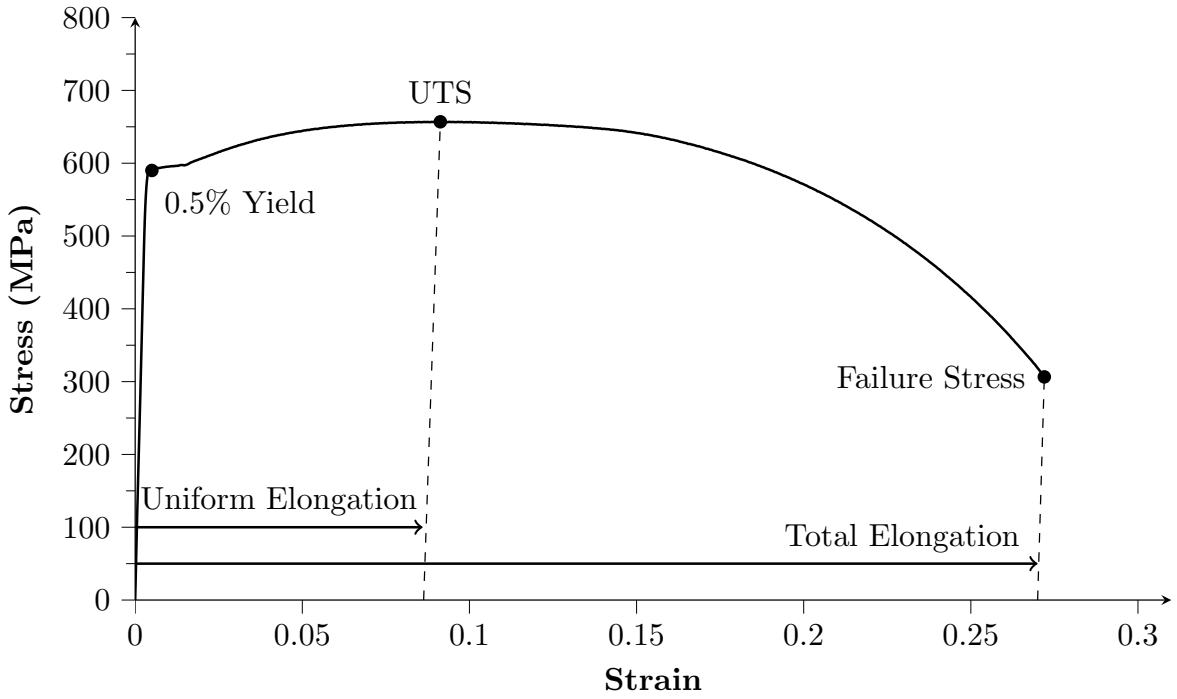

Figure 4.26: An example of a typical low carbon steel stress vs. strain plot showing the important properties.

4.5.2 Hardness Testing

Vickers hardness testing was carried out on a LECO LM700AT microhardness tester Figure 4.27, according to ASTM E384-17 [204]. Through-thickness measurements were carried out with a force of 500 g (4.9 N). In accordance to ASTM E384-17 [204], subsequent hardness indents were spaced greater than 3× the diagonal length of the indent (typically 500 μm intervals) to ensure previous indents do not influence the results due to material deformation. The indent diagonals were measured using the optical microscope to ensure the highest accuracy, and the Vickers hardness calculated from the equation $HV \approx \frac{0.1891 \times F}{d^2}$ [N/mm^2]. The full derivation of the equation is presented in Appendix G.

Figure 4.27: LECO LM700AT vickers microhardness tester.

4.6 Stress Corrosion Cracking Testing

To test the SCC susceptibility of the industry supplied and laboratory rolled samples, the LIST, devised by Atrens et al. (1993) [36] was utilised. The LIST is a load controlled dynamic SCC test that is widely accepted by industry and academia for testing the susceptibility of materials to SCC, as discussed in Section 2.5.2. The LIST is a loaded cantilever beam with an environmental cell connected to the loaded sample that applies a set potential to the steel sample to mimic the cathodic protection (CP) found in the field. The components and the method for running the LIST are provided in this section.

4.6.1 Linearly Increasing Stress Test

Electrodes

To simulate the environmental conditions that lead to SCC in pipeline steels, the test specimen is connected to an environmental cell, with a three-electrode cell used to simulate the CP connected to the buried pipeline. The three-electrode cell is a standard corrosion tool, where a working electrode (in this case the LIST specimen) connected to

the reference electrode supplies a fixed potential to the system whilst the counter electrode balances the charge observed at the working electrode. The reference electrode was a Pine RREF0021 Silver Chloride ($Ag/AgCl$) reference electrode (0.199 V vs. Standard Hydrogen Electrode (SHE)) and the counter electrode was a platinised titanium mesh, Figure 4.28. The silver chloride reference electrode is a commonly used reference in electrochemistry. It is stable at the temperatures experienced during LIST testing and, as such, minimal drift is likely to occur due to temperature effects. Although SCC testing utilises both platinum and graphite counter electrodes in literature, platinum was selected as the counter electrode as graphite has the propensity to degrade and contaminate the carbonate-bicarbonate solution. Platinised titanium mesh provides the benefits of using platinum as the counter electrode whilst increasing the surface area due to the rough surface finish, minimising charging effects. Due to contamination of iron oxide in the solution as dissolution occurs, the platinum counter electrode became coated in an oxide layer. The electrode was sonicated briefly in a dilute solution of HCl after each run to remove the iron bearing contamination rapidly without damaging the platinum coating.

(a) Pine RREF0021 silver chloride ($Ag/AgCl$) reference electrode.

(b) Platinised titanium counter electrode.

Figure 4.28: Reference and counter electrodes used in the LIST apparatus.

Potentiostat

To apply a fixed potential over the course of the LIST experiment a Gamry Interface 1000 general purpose potentiostat was used, Figure 4.30. The Interface 1000 potentiostat is capable of delivering constant potential over the course of the LIST experiment, whilst simultaneously logging the applied potential. The potentiostat was connected with the

working lead connected to the steel specimen, the counter lead to the platinum electrode and the reference lead to the reference electrode. The applied potential was logged through the working sense lead connected to the working electrode. A schematic diagram of the connections are seen in Figure 4.29.

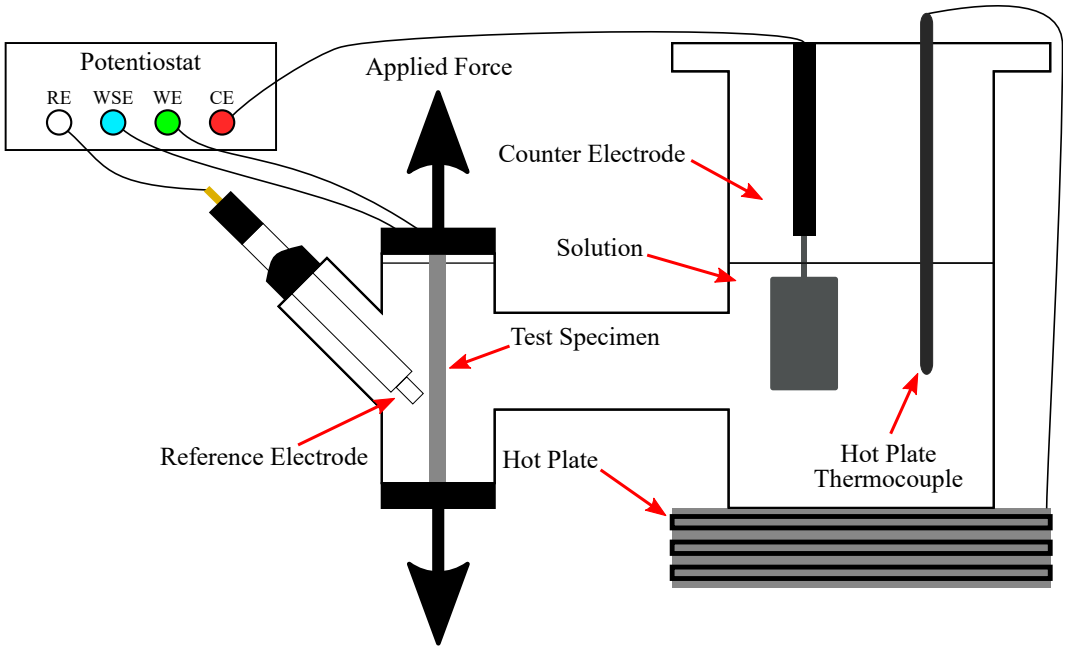

Figure 4.29: Schematic diagram of the LIST corrosion cell.

The potentiostat was calibrated prior to use, using the supplied dummy cell carried out inside a Faraday cage. Re-calibration was carried out periodically at the interval specified by the manufacturer.

Figure 4.30: Gamry Interface 1000 potentiostat.

4.6.2 Polarization Scans

As SCC only forms within a tight electrochemical potential range of approximately 150 mV, Section 2.3, the determination of the cracking range is necessary for SCC to form during LIST testing. As explored in Section 2.3, the use of fast and slow potentiodynamic scans enables the cracking potential range to be identified. The potentiodynamic scan range was conducted from -1000 mV to -0.2 mV vs. E_{ref} at two scan rates to determine the domain in which SCC would form. The fast scan carried out a linear sweep of the potential range at a rate of 5 mV/s, whilst the slow scan carried out a linear sweep at a rate of 0.17 mV/s. As explored in Section 2.3, the potential corresponding to the greatest difference in current between fast and slow polarization scans is the highest SCC forming potential, as seen in Figure 4.31.

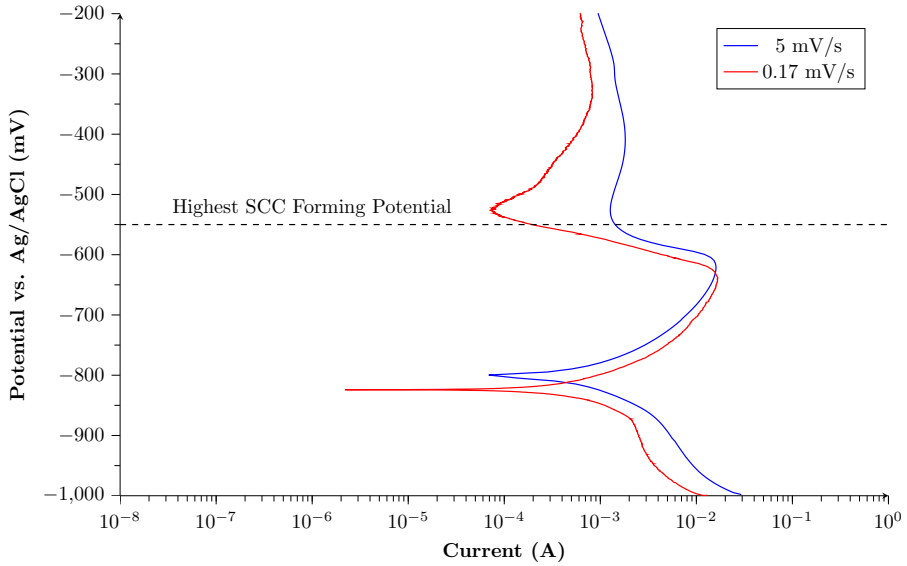

Figure 4.31: Determination of potential that provides the highest rate of SCC formation.

4.6.3 LIST Test Apparatus

As explored in Section 2.5.2, the use of dynamic load testing enables quantification of SCC severity in a range of materials whilst static load testing can only be used for qualitative testing. Whilst the SSRT is the industry standard for SCC testing, the LIST can carry out the same tests. In addition, when used to fracture samples with a linearly increasing

load, the LIST finishes the test faster than the SSRT. The LIST, much like the SSRT, has been used in literature to determine the SCC susceptibility of a variety of materials as explored in Section 2.5.2, and is accepted by both industry and academia as a quantitative test for determining SCC susceptibility. In order to test the SCC crack rate in the rolled specimens, an oscillating loading pattern used in the LIST. It was established in Section 2.5.2 that the oscillating load produced cracks faster than with linear testing and, from a testing perspective, prevents failure of the specimen such that the texture of the grains surrounding the crack can be examined with EBSD.

The LIST apparatus used during testing was manufactured by Fletcher and Gunawardena (2006) [205] with control system improvements made by Liew (2011) [206] at the School of Mechanical Engineering, University of Adelaide. The LIST has a maximum axial load of 14,430 N and a maximum rate of loading of 24 N/h, corresponding to the mass (dead weight on the horizontal arm) moving at 1.63 mm/h. An image of the apparatus is presented in Figure 4.32a, along with a detailed schematic diagram of the apparatus in Figure 4.32b.

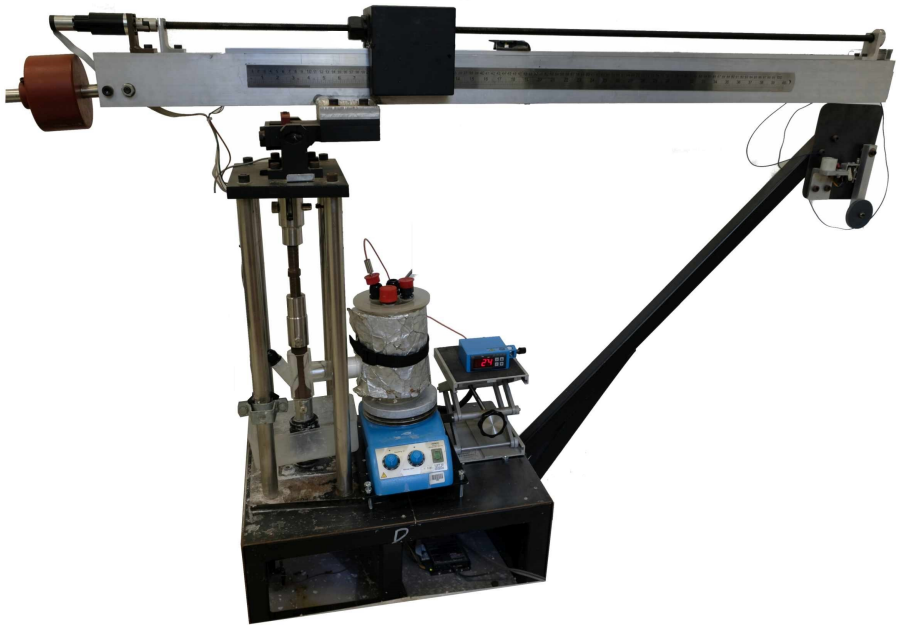

(a) LIST used for experimental work in the project.

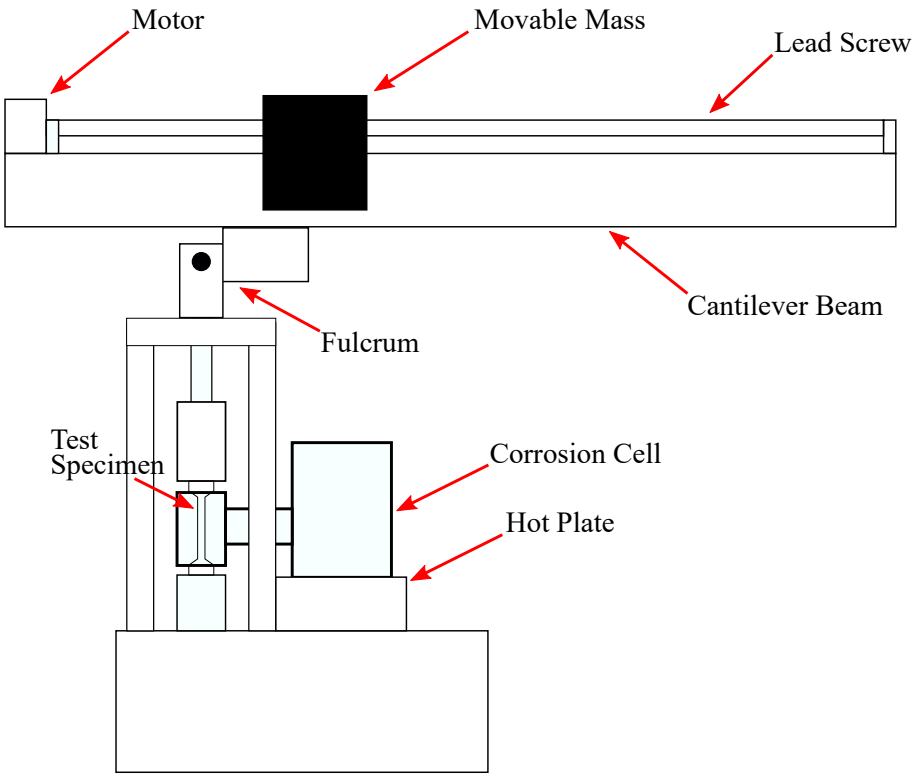

(b) Schematic diagram of the LIST apparatus.

Figure 4.32: Image and schematic diagram of the LIST apparatus.

A schematic diagram of the LIST specimen is presented in Figure 4.33a. To prepare the LIST specimen for use, it was sanded with successively finer grits of SiC sandpaper to

remove all randomly oriented scratches. The final grit utilised was 600 grit correlating to a surface roughness of approximately 0.1 μm per Wang and Atrens (1996) [37]. The specimens were loaded into the apparatus and oscillated from $90 - 95\%$ of the measured 0.5% yield stress [4] for 10 cycles at a rate of 24 N/h. Once the final cycle completed, the specimens were unloaded and removed from the apparatus. The moving mass transmits load through the straight beam, with the maximum load transmission occurring when the beam is parallel to the ground. To ensure accurate load transmission, the beam is positioned parallel to the ground with the aid of a level. Periodic adjustments were made if the length of the sample increased due to temperature or loading effects.

As explored in Section 2.4.2, SCC occurs in pipelines loaded below their yield stress with the maximum allowable pressure equal to 72% of the Specified Minimum Yield Stress (SMYS). In laboratory testing, the addition of a stress concentrator lowered the cracking threshold to as low as 40% of their yield stress; plain samples were observed to crack at as low as 60% of their yield stress [59]. As laboratory testing takes place over far shorter time frames than is experienced in the field, as determined by Baker et al. (1986) [39], cyclic loading maximises the crack growth rate especially high stress cycling at $90 - 95\%$ SMYS.

LIST specimens were sectioned from the laboratory rolled plate in the orientation shown in Figure 4.15 and machined down to the quarter thickness plane. Whilst SCC initiated from the surface of pipes, as will be made evident in Chapter 6, the surface textures of the three laboratory rolled samples is nearly identical due to the rolling process and there was not enough variation in texture present to test the impact that texture would have on SCC.

After testing, the LIST specimens were sectioned with a saw per the schematic diagram in Figure 4.33b, with the samples mounted as labelled. SCC cracks grow perpendicular to the direction of applied load and from the outer surface towards the centre of the spec-

[4] The 0.5% yield stress was specified in the API 5L standard for determining yield stress of pipe steel [27]

imen, with the highest penetration at the centreline. To accurately determine the depth of the grown cracks, the sample is ground to the centreline (identified in Figure 4.33) such that the maximum crack length can be accurately measured.

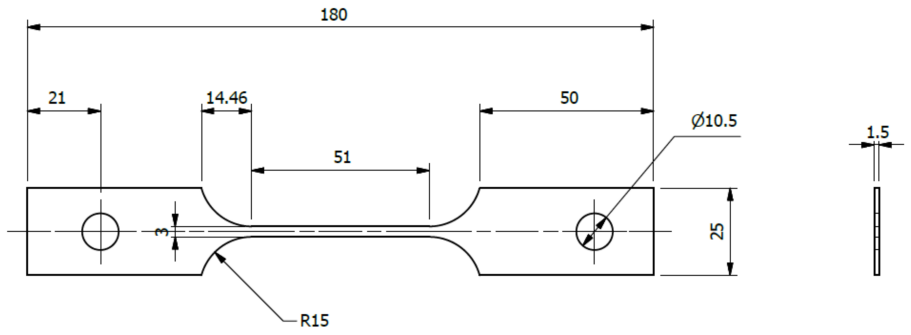

(a) LIST sample schematic diagram.

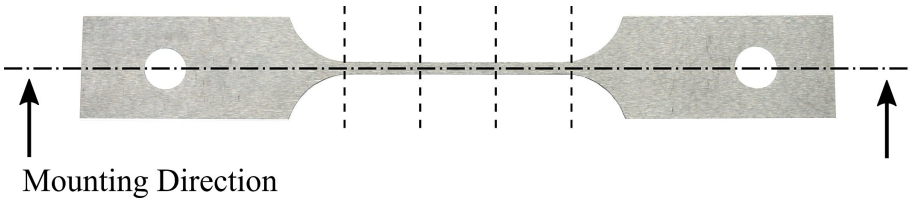

(b) Sectioning schematic diagram of LIST specimens.

Figure 4.33: LIST schematic diagram and sectioning diagram.

The length of all significant cracks is measured using optical microscopy and the total number of cracks counted with the crack velocity (v) found by dividing the length of the longest crack (l) by the total time (t) of the LIST experiment, as seen in Equation (4.3). The number of cracks in the LIST specimen were tallied, with any defect having an aspect ratio greater than 10, as observed at 1000× optical magnification, considered a crack.

$$v = \frac{l}{t} \tag{4.3}$$

An example of the cracks produced through LIST experimentations is presented in Figure 4.34. The length of the crack is the distance parallel to the surface of the LIST specimen to the tip of the crack, not including all the crack branches. SCC cracks produced through LIST testing are only visible against the unetched steel and show the

characteristic crack branching expected of high pH SCC.

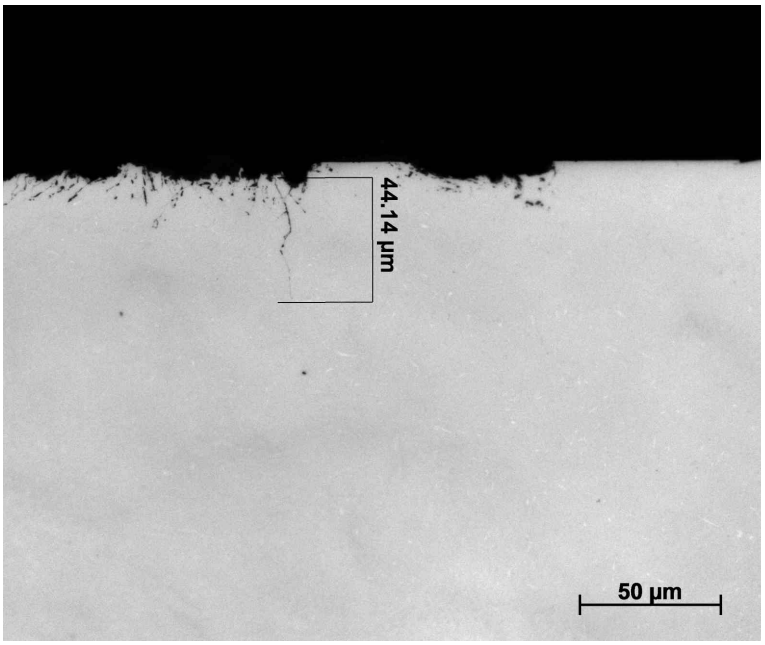

Figure 4.34: Cracks in pipeline steel grown using the LIST.

Once the cracks were observed optically, EBSD of samples of each rolling schedule and industry supplied samples was undertaken to determine the crystallographic texture properties of the cracked sections. The results were compared with the crack velocity and the number of cracks that formed during LIST testing to determine which factors controlled SCC susceptibility.

4.7 Summary

This chapter encompassed the experimental procedure for developing and testing steel plate rolling schedules for the purpose of creating different crystallographic textures to test their susceptibility to SCC. In addition, the procedure to roll the material and subsequently characterise the microstructure, mechanical properties, crystallographic texture and corrosion resistance were detailed. The following chapter, Manufacturing Processes, encompasses the development of the rolling schedules and the resulting microstructures and mechanical properties.

Chapter 5

Results and Discussion - Controlled Rolling

The aim of the study was to investigate the role of controlled rolling on the formation of crystallographic texture in pipeline steel and the effect it had on stress corrosion cracking susceptibility. To generate sufficiently different crystallographic textures, different rolling regimens were required, as explained in Chapter 1. Controlled rolling schedules were developed around the thermomechanical controlled rolling process such that the material would have microstructures and mechanical properties similar to X70 steels currently in use. As a result, the SCC susceptibility could be directly compared to the susceptibility of industry supplied samples.

This section describes the process of designing the rolling schedules followed by a review of the microstructural and mechanical properties that developed. To develop steel with the desired microstructure and strength, it is critical that rolling temperatures and reduction ratios are monitored to ensure they are within the specified limits. The rolling schedules were designed for use in laboratory scale equipment and while all efforts were made to produce material with similar properties to those manufactured on full scale equipment, some differences were noted.

The primary aim of this chapter is to investigate the microstructure and mechanical properties of the laboratory rolled specimens, produced under different rolling schedules. The microstructures of the industry supplied samples are first investigated to both aid in the design of the rolling schedules and serve as a benchmark of the results. The factors critical to the development of the rolling schedules are investigated with the final regimes presented. The microstructures and mechanical properties of the laboratory rolled samples are investigated with the results compared to industry supplied samples of X70 pipe and plate.

5.1 Materials

As discussed in Section 4.1, three industry supplied X70 steels were utilized in this study to investigate the role of controlled rolling on the formation of crystallographic texture and the subsequent stress corrosion cracking susceptibility:

1. 20 mm thick X70 plate, used for controlled rolling trials and to benchmark against laboratory produced samples.

2. 10 mm thick X70 pipe, used to benchmark against laboratory produced samples.

3. 6.4 mm thick X70 plate, used to benchmark against laboratory produced samples.

The 20 mm thick X70 plate was manufactured and supplied by BAOSTEEL [1], the section of 10 mm thick, ⌀500 mm X70 pipe sourced from pipe operator Jemena [2] and the 6.4 mm thick plate sourced by Jemena, and manufactured by Shougang Steel [3]. The microstructures of the industry supplied samples are investigated to benchmark against the laboratory rolled samples; examined in later sections.

[1] Baoshan Iron and Steel Co., Ltd.
Website: `http://bg.baosteel.com/en/`
[2] Jemena
Website: `https://jemena.com.au/`
[3] Shougang Group
Website: `https://www.shougang.com.cn/en/ehtml/index.html`

5.1.1 20 mm X70 Plate

The 20 mm thick X70 steel plate was the raw material used to produce the laboratory rolled samples. The plate was manufactured by BAOSTEEL (Baoshan Iron and Steel Co., Ltd.) and supplied in 1 m^2 sections. The plate was supplied as-rolled, uncoated with the factory mill scale attached. A section of the 20 mm thick X70 steel plate is presented in Figure 5.1. No material properties were provided with the plate and had to be determined prior to rolling. The as-received 20 mm X70 plate was sectioned into appropriate sized pieces dimensions for the laboratory mill (200 × 120 × 20 mm). The samples were of sufficient thickness (20 mm) to allow for the development of a refined grain structure whilst enabling hand loading into the rolling mill.

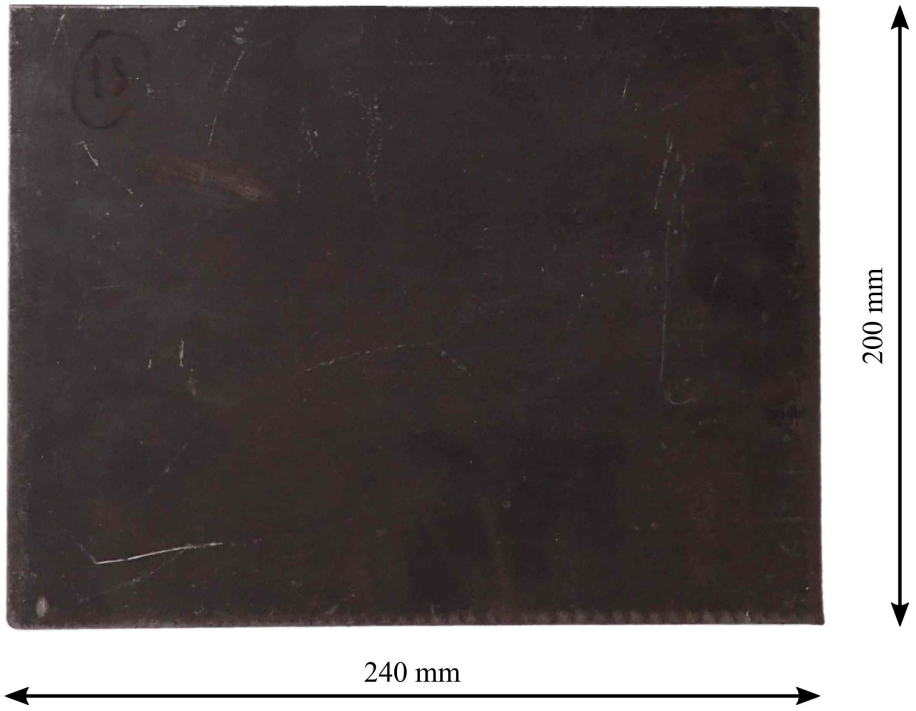

Figure 5.1: As-received 20 mm X70 plate.

Microstructure of as-received 20 mm X70 Plate

The microstructure of the as-received 20 mm X70 plate was comprised of primarily granular bainite and polygonal ferrite as seen in Figure 5.2 in both Longitudinal (LRD) and Transverse to Rolling Directions (TRD). The surface plane of the as-received 20 mm X70

plate shows the development of an approximately 20 μm thick layer of oxidation and possible decarburisation due to the presence of large ferrite grains, as observed in Figure 5.2a and Figure 5.2b. The decarburised surface extended for approximately 250 μm after which the microstructure was more akin to that found in the quarter plane. There appears to be some degree of banding in the microstructure near the surface in the LRD direction (Figure 5.2a), although it is less obvious in the TRD direction (Figure 5.2b). The quarter plane, as observed in Figure 5.2c and Figure 5.2d, has a microstructure consisting of primarily granular bainite with instances of polygonal ferrite interspersed evenly through the entire structure. There is a very slight elongation of the grain structure in the LRD direction (Figure 5.2c), primarily observed in the polygonal ferrite grains. The TRD direction (Figure 5.2d) displays grains with more uniform aspect ratios. The microstructure of the centre plane in the as-received 20 mm X70 plate, in Figure 5.2e and Figure 5.2f, was very similar to that of the quarter plane and contained primarily granular bainite with some instances of polygonal ferrite. When comparing the microstructures of the quarter and centre planes, the centre plane contains large, highly elongated grains of bainite, particularly in the LRD direction in Figure 5.2e. Additionally, a lower fraction of polygonal ferrite is observed at the centre compared with the quarter plane.

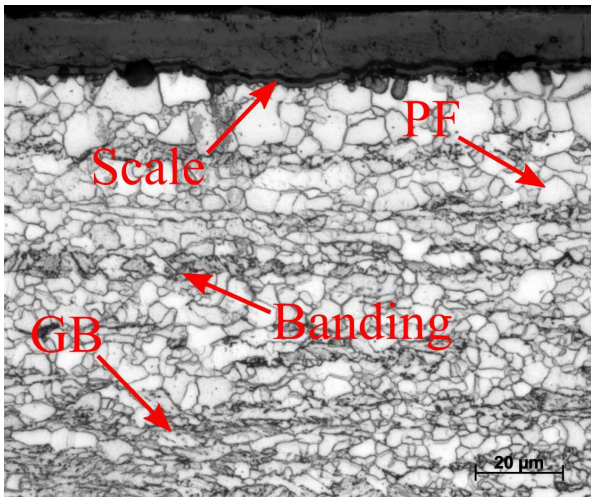

(a) 20 mm X70 plate surface 1000x LRD.

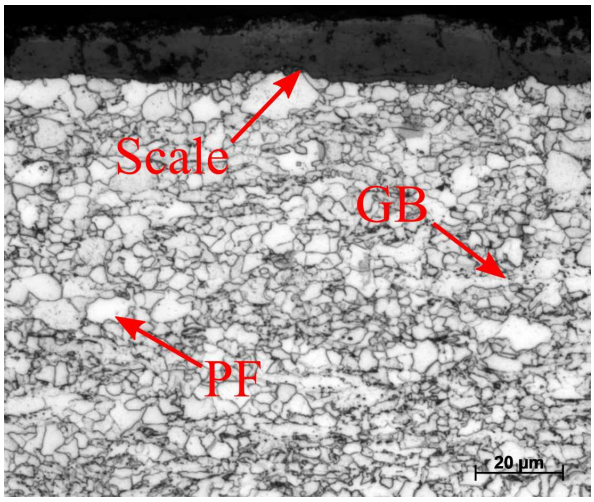

(b) 20 mm X70 plate surface 1000x TRD.

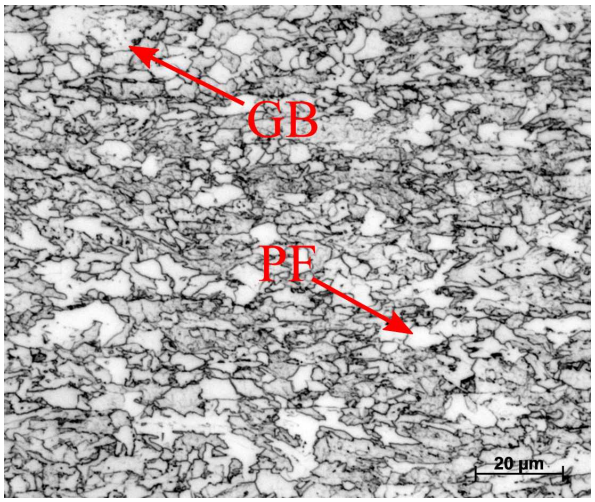

(c) 20 mm X70 plate quarter 1000x LRD.

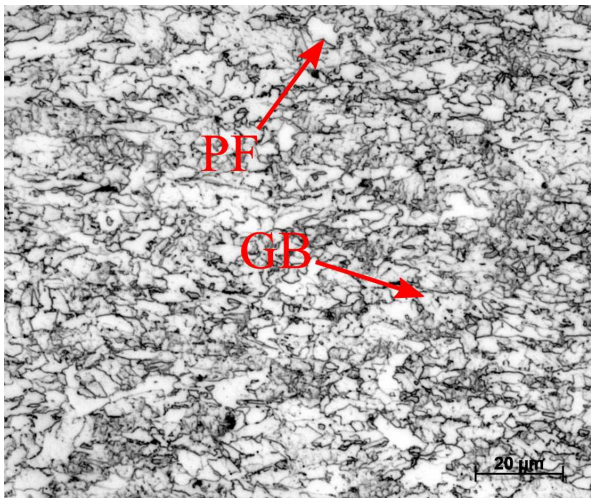

(d) 20 mm X70 plate quarter 1000x TRD.

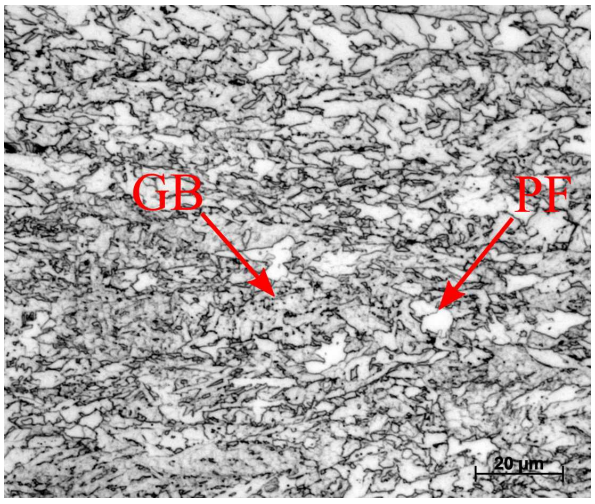

(e) 20 mm X70 plate centre 1000x LRD.

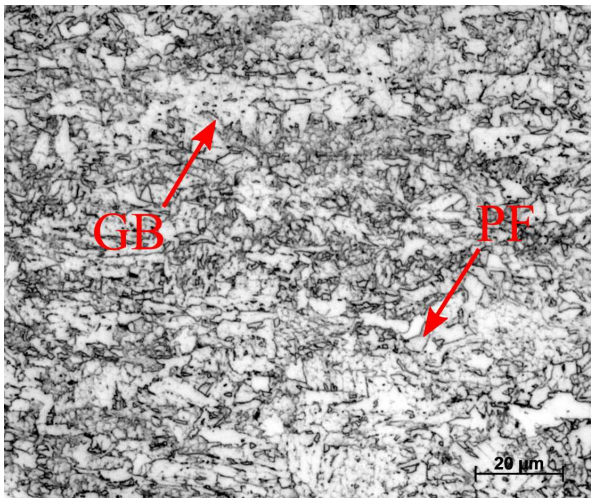

(f) 20 mm X70 plate centre 1000x TRD.

Figure 5.2: Through-thickness optical microstructure of 20 mm X70 plate taken from 1/4 width. PF: Polygonal Ferrite, GB: Granular Bainite.

SEM Microscopy

Scanning Electron Microscopy (SEM) of the dark regions not able to be resolved through optical microscopy are presented in Figure 5.3. The optical micrograph in Figure 5.3a shows the three features investigated with SEM. The phases present in Figure 5.3b, Figure 5.3c and Figure 5.3d are Martensite-Austenite (M-A) constituents and Degenerate Pearlite (DP). Some instances of solely M-A constituents and degenerate pearlite were observed, however, they were typically interspersed as observed in Figure 5.3. M-A constituents are formed because austenite stabilizing elements, such as nickel, allow austenite to exist at room temperature [207]. Note in Table 4.1, the 20 mm X70 plate contains a high concentration of nickel, a strong austenite stabilizer [141]. It is expected that the 20 mm X70 plate will show higher proportions of M-A constituents than the other two steel specimens because of this higher nickel content.

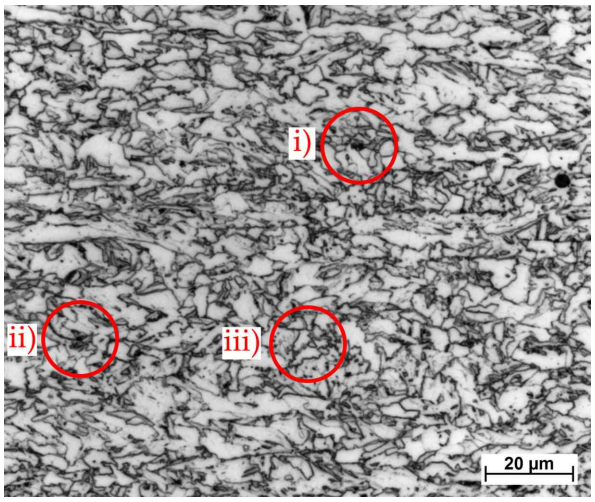

(a) 20 mm X70 plate optical image.

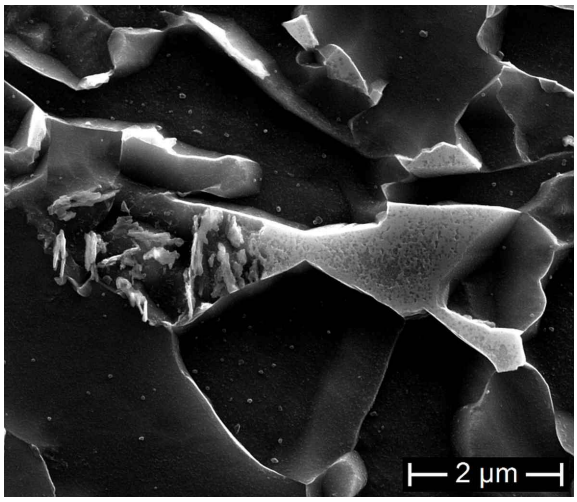

(b) Location i: M-A and DP.

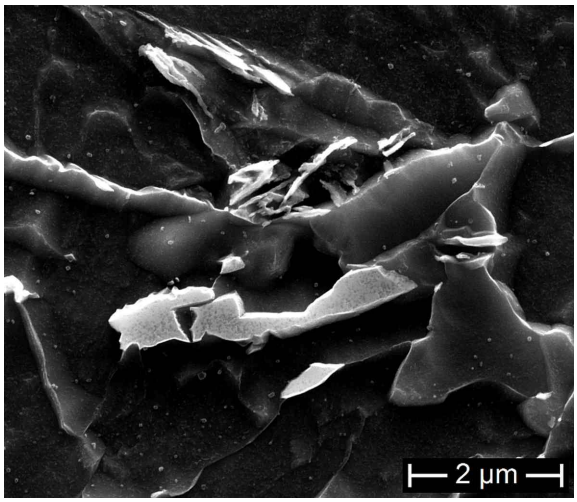

(c) Location ii: M-A and DP.

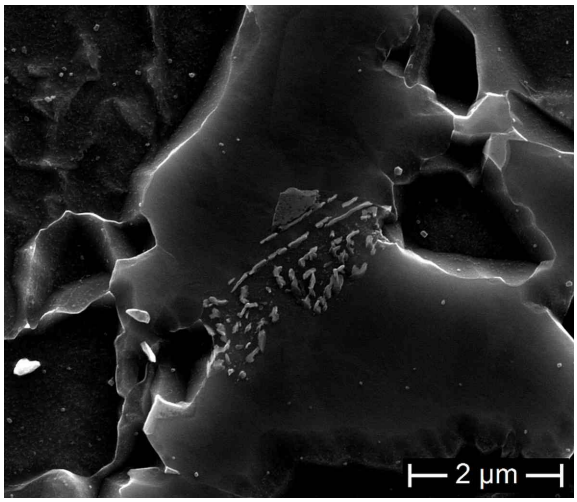

(d) Location iii: M-A and DP.

Figure 5.3: SEM micrographs of the dark regions in (a) present in the 20 mm X70 pipe (LRD).

Through-thickness Hardness of the as-received 20 mm X70

Hardness indents were performed in the TRD plane of the X70 specimen from the outer surface to the inner surface at increments of 500 μm. The micro Vickers hardness is presented in Figure 5.4. No strong trends were identified in the through thickness hardness and it appeared to have a near uniform hardness. Despite this, the outer surfaces appeared to be slightly harder than the centre of the plate, possibly due to the smaller grain size observed at the surface of the plate (see Figure 5.2a and Figure 5.2b). The average hardness of the as-received 20 mm X70 was measured to be 197.8 $\pm$ 2.4 HV0.5.

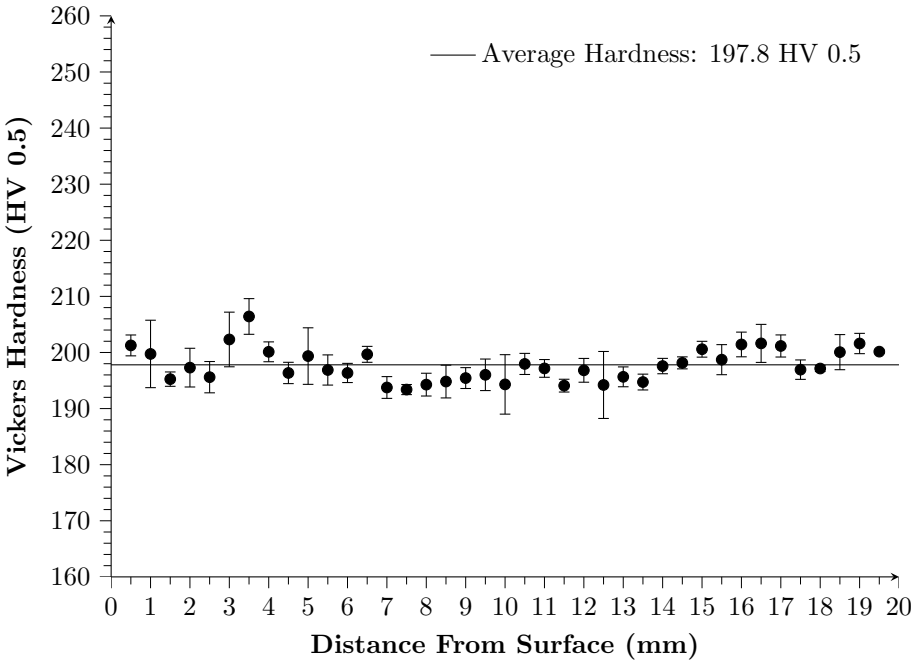

Figure 5.4: Through-thickness hardness of 20 mm X70 plate.

Tensile Properties of 20 mm X70

Full thickness tensile properties of the as-received 20 mm X70 plate were measured on a standard dimensioned specimen according to ASTM E-8 [203]. The specimen had a gauge width of 12.5 mm, a gauge length of 50 mm and a maximum thickness of 19 mm. Tensile properties of the full thickness samples were measured in both the LRD and TRD directions prior to the sub size tensile testing explored in Section 5.3.4 as the difference in thickness needed to be evaluated to ensure the reduction in thickness did not drastically alter the results.

The results of the tensile testing are summarised in Table 5.1. As expected, the tensile results adhere to the limits set by the API 5L standard in both LRD and TRD orientations. *Note: although both the 0.5% and 0.2% proof stresses (yield stresses) are evaluated, the strength requirements of pipeline steels per the API 5L standard are evaluated based on the 0.5% yield stress [27].* These results are within the expected range of X70 plate and similar results have been presented in literature [138, 208, 209].

Table 5.1: Full thickness tensile strength of the 20 mm X70 plate.

	LRD	***TRD***
0.2% Yield (MPa)	542 ± 5.7	538 ± 17
0.5% Yield (MPa)	543 ± 3.6	550 ± 9
UTS (MPa)	620 ± 5	648 ± 5
Failure Stress (MPa)	321 ± 10	371 ± 11
Elongation (%)	28 ± 0.5	26 ± 1

Distinct upper and lower yielding were observed in both LRD and TRD samples as seen in Figure 5.5. Upper and lower yielding can be observed in some X70 steels, depending on the processing conditions and microstructures that develop [72, 131, 208].

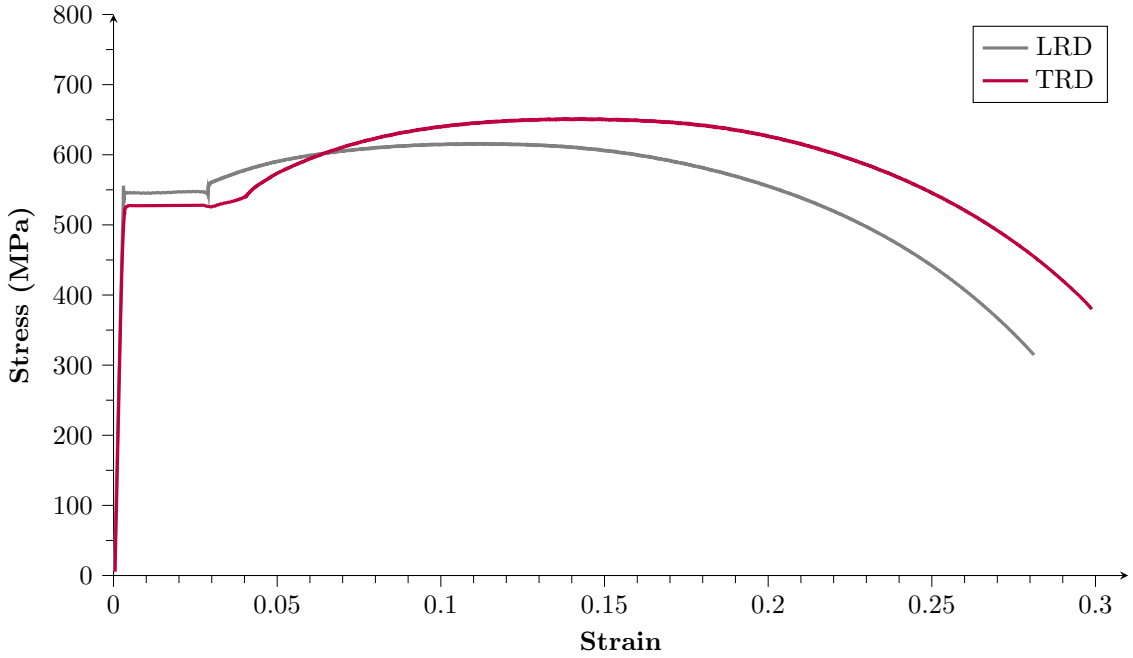

Figure 5.5: Stress-strain curve of the full-thickness 20 mm X70 plate.

5.1.2 10 mm X70 Pipe

The 10 mm thick X70 pipe samples, sourced from SGSP Assets Pty Ltd (Jemena), came from a 500 mm long section of ⌀500 mm pipe from their stock of spare pipe sections. The

manufacturer of the pipe was not provided by Jemena. The material was supplied flame cut from one end of the pipe and was supplied factory coated in two layers of epoxy with the ends bare and bevelled to facilitate welding in the field. A wedge was removed from the pipe to facilitate cutting and mounting and shown in Figure 5.6. The uncoated end shows severe oxidation from extended storage time and was not used for any microstructure observations or testing of mechanical properties. Whilst the intended final thickness of the laboratory rolled samples was 7 mm, the 10 mm thick sample still provides a good sample to benchmark the final mechanical properties and microstructure.

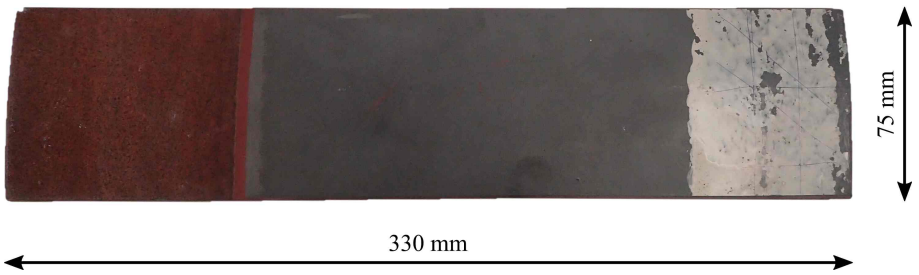

Figure 5.6: Section of 10 mm X70 pipe in the as supplied state (wall thickness = 10 mm, pipe diameter = 500 mm).

Microstructure of 10 mm Wall-thickness X70 Pipe

The microstructure of the 10 mm X70 pipe is observed in Figure 5.7 and displays the microstructure from the surface, quarter and centre planes in both LRD and TRD orientations. As the pipe was supplied factory coated with epoxy, the surface grains appear highly deformed with no scale or oxide present due to the grit blasting prior to coating as observed in Figure 5.7a and Figure 5.7b. The microstructure consists of primarily granular bainite with polygonal ferrite through-thickness.

The microstructure appears to be consistent through-thickness with no obvious signs of oxidation or decarburisation present at the surface of the pipe. The microstructure present at the quarter plane in Figure 5.7c and Figure 5.7d is composed of primarily granular bainite with some minor occurrences of polygonal ferrite in both the LRD and TRD orientations. The microstructure of the centre plane in Figure 5.7e and Figure 5.7f

is similar to that observed in the quarter plane, with the exception of severe centreline segregation observed in both LRD and TRD orientations. The grain size at the centre appears larger than that observed at the surface or quarter planes. The steel grains appear more equiaxed in the TRD sections with grain size increasing from the surface to centre plane. This is expected due to cooling inhomogeneity through-thickness during casting and rolling. The severe centreline segregation shown in Figures 5.7e and 5.7f is deleterious to the properties of the finished pipe. Its origin, during continuous casting of billets, is beyond the scope of the current study.

The grains in the LRD sections are slightly elongated at the surface Figure 5.7a, quarter plane Figure 5.7c and in the centre plane Figure 5.7e. The grains are more equiaxed in the TRD sections with grains size increasing from the surface to centre plane.

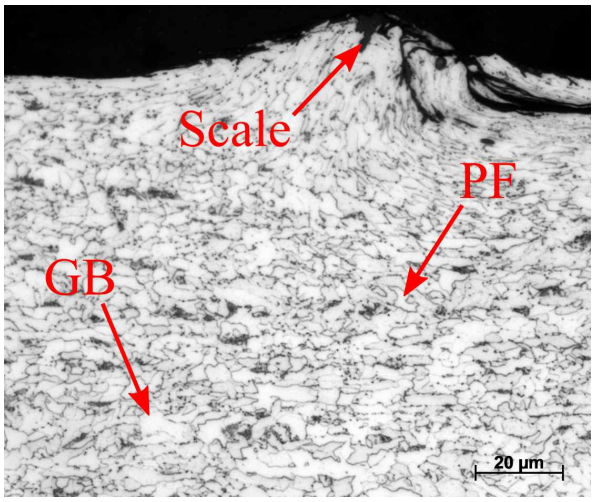

(a) 10 mm X70 pipe surface 1000x LRD.

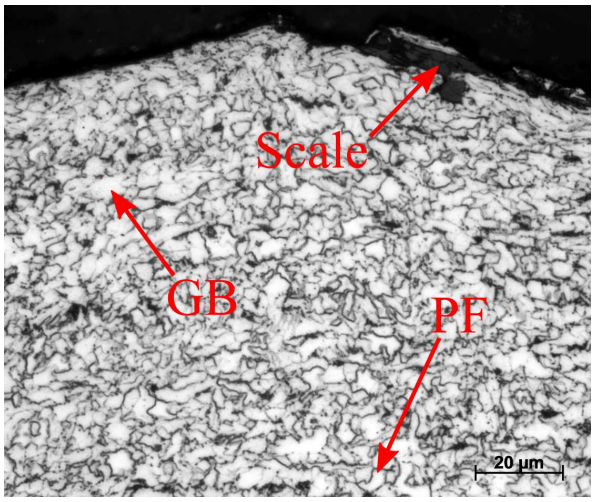

(b) 10 mm X70 pipe surface 1000x TRD.

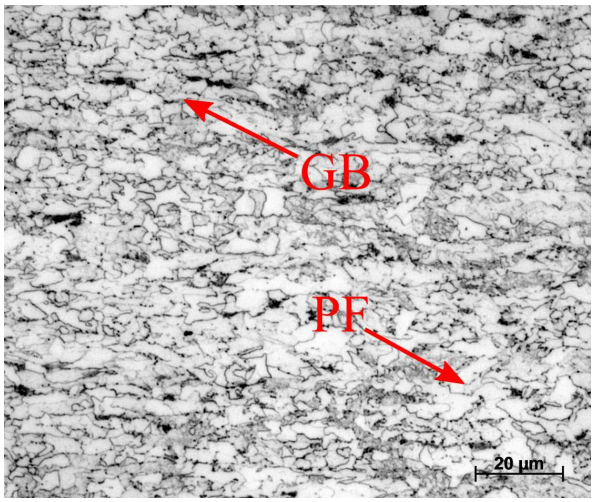

(c) 10 mm X70 pipe quarter 1000x LRD.

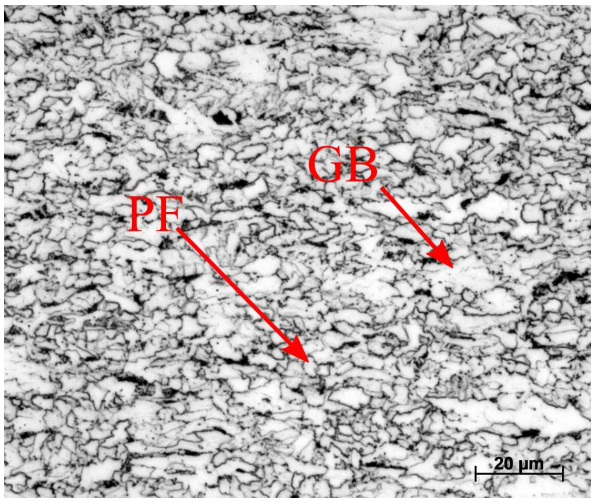

(d) 10 mm X70 pipe quarter 1000x TRD.

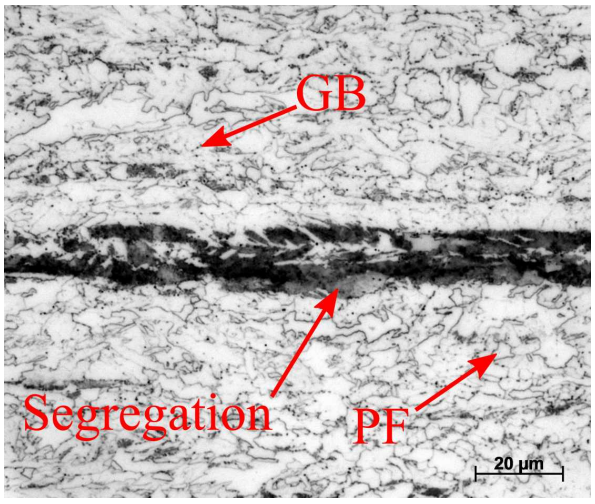

(e) 10 mm X70 pipe centre 1000x LRD.

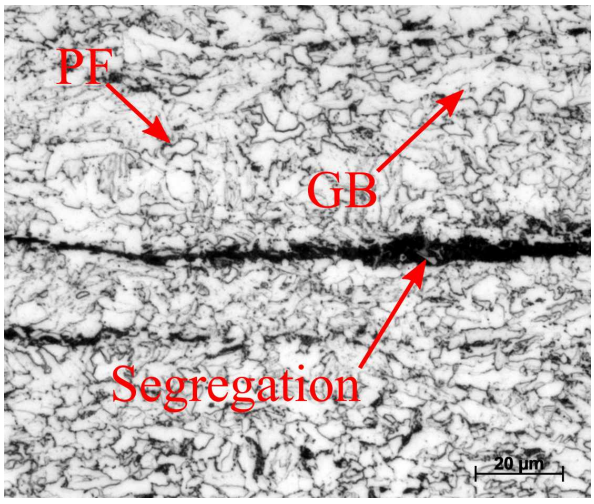

(f) 10 mm X70 pipe centre 1000x TRD.

Figure 5.7: Through-thickness optical microstructure of 10 mm X70 pipe taken from 3 o'clock position of the pipe.

SEM Microscopy

The 10 mm X70 SEM micrographs are presented in Figure 5.8 with an optical micrograph in Figure 5.8a highlighting the three features investigated with SEM. The secondary microconstituents in Figures 5.8b to 5.8d were all identified as degenerate pearlite. No M-A constituents were detected in the 10 mm X70 pipe, unlike the 20 mm X70 plate. This difference is likely due to the lower nickel content present in the 10 mm X70 pipe, observed in Table 4.1, compared to the 20 mm X70. The nickel content is likely insufficient to stabilise austenite, disallowing M-A constituents to exist at room temperature [141, 207].

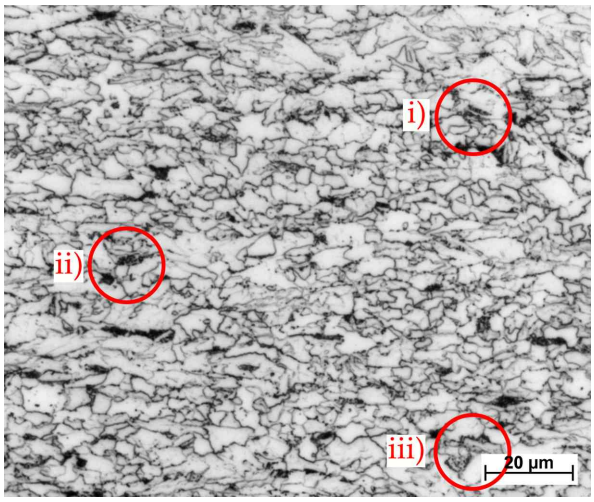

(a) 10 mm X70 pipe optical image.

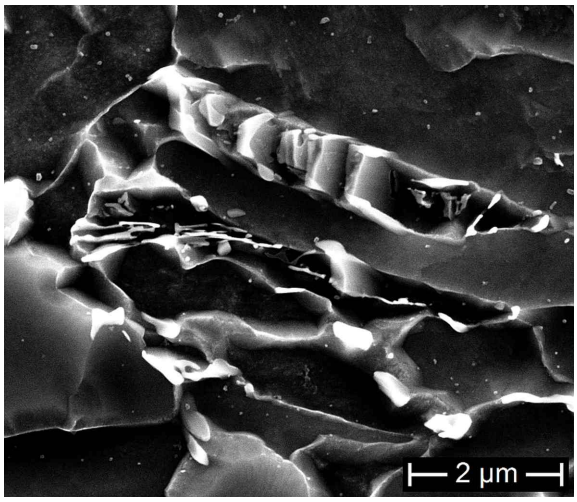

(b) Location i: DP.

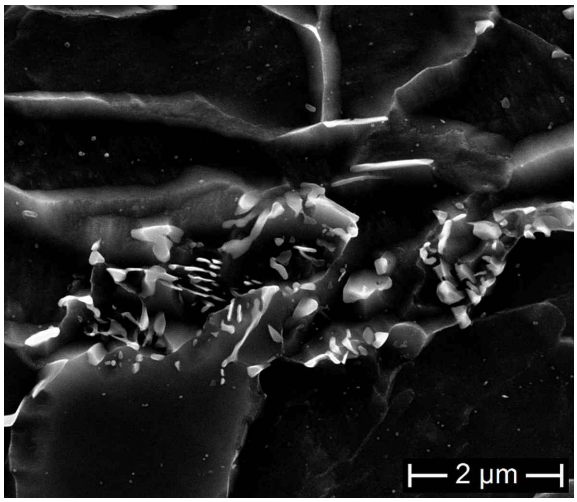

(c) Location ii: DP.

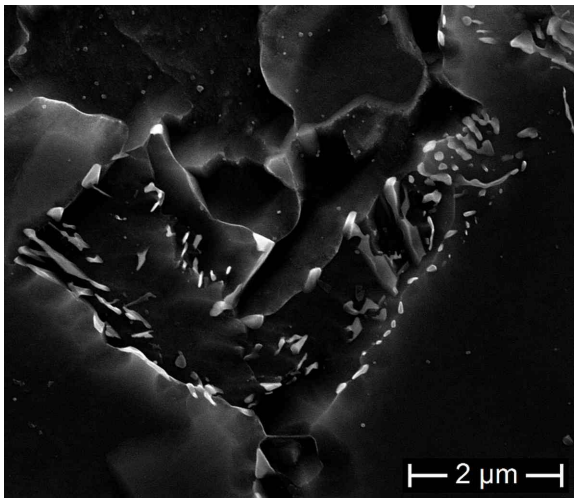

(d) Location iii: DP.

Figure 5.8: SEM micrographs of the dark regions in (a) present in the 10 mm X70 pipe (LRD).

Through-thickness Hardness of 10 mm wall-thick X70 pipe

The through thickness hardness of the 10 mm X70 is presented in Figure 5.9. It had an average hardness of 221 ± 4.7 HV0.5 with a peak hardness of 280 HV0.5. The peak hardness is associated with the centreline segregation that is significantly harder than the surrounding metal. This is due to the higher manganese and carbon content of the segregated region that lead to the formation of harder microconstituents [210]. The outer surface is softer than the inner surface of the pipe, likely the result of the pipe forming process that increased compressive residual stress at the inner surface compared with

residual tensile stresses formed at the outer surface.

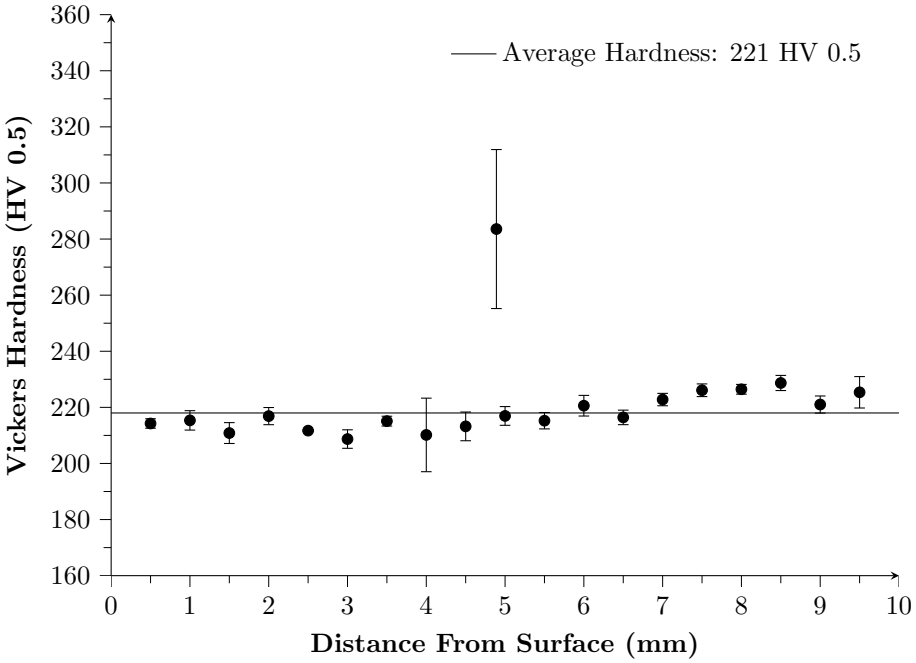

Figure 5.9: Through-thickness hardness of 10 mm X70 pipe.

5.1.3 6.4 mm X70 Plate

The 6.4 mm X70 plate manufactured by Shougang Steel in China was supplied in a 400 mm × 1000 mm plate. The supplied section was flame cut from an approximately 1000 mm wide plate at approximately 1/4 of the total width of the plate. An image of the material as supplied is shown in Figure 5.10 where light surface oxidation is observed. The 6.4 mm plate specimen was sourced to benchmark against the laboratory rolled material. This is because the 6.4 mm plate had a very similar final thickness to the intended laboratory rolled samples. Pipe with both 6.4 mm and 7 mm wall thicknesses are commonly used in Australia. Whilst the full rolling schedule of the 6.4 mm plate was not provided, the finish rolling temperature and coiling temperatures, 840°C and 551°C respectively, were disclosed.

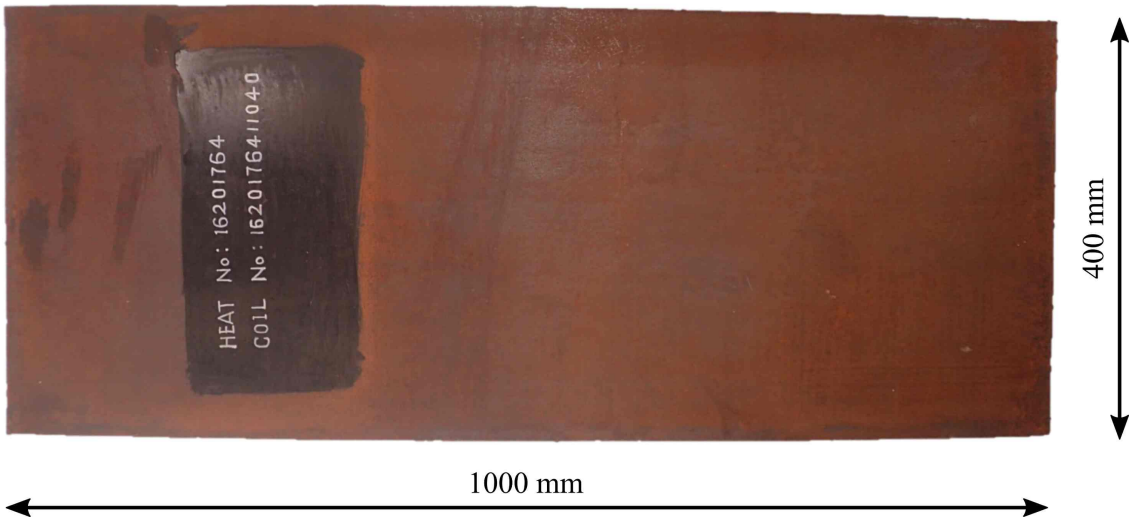

Figure 5.10: 6.4 mm X70 plate in the as-received condition.

Microstructure of 6.4 mm X70

The microstructure of the 6.4 mm Shougang X70 plate is presented in Figure 5.11 and displays the microstructure from the surface, quarter and centre planes taken in both LRD and TRD orientations. The through-thickness microstructure is primarily composed of granular bainite and polygonal ferrite with the darkly etched regions consisting of degenerated pearlite as determined in Figure 5.12. The surface microstructure in Figures 5.11a and 5.11b appears to be slightly decarburised for approximately 20-50 μm below the surface and has a higher proportion of polygonal ferrite as compared to the quarter and centre planes. The grain structure is more equiaxed as compared to the quarter and centre planes and has a lower proportion of the darkly etched regions. As the plate was supplied uncoated, an oxide layer is present at the surface of the plate. The oxide has adhered to the surface and has a nominal thickness of approximately 10 μm. In the quarter plane, Figures 5.11c and 5.11d the microstructure is mainly composed of granular bainite with a small fraction of polygonal ferrite, observed readily in the TRD orientation. The microstructure in the centre plane, Figures 5.11e and 5.11f, is very similar to that observed in the quarter plane except the grain size appears coarser in the LRD direction and less polygonal ferrite.

The grains in the LRD sections are highly elongated, particularly in the centre plane, with

very coarse granular bainite visible. The grain size tends to increase from the surface to the centre plane with grains at the centre plane considerably larger than at the surface. Grain sizes in the TRD orientations are more uniform at all depths compared with the LRD orientations.

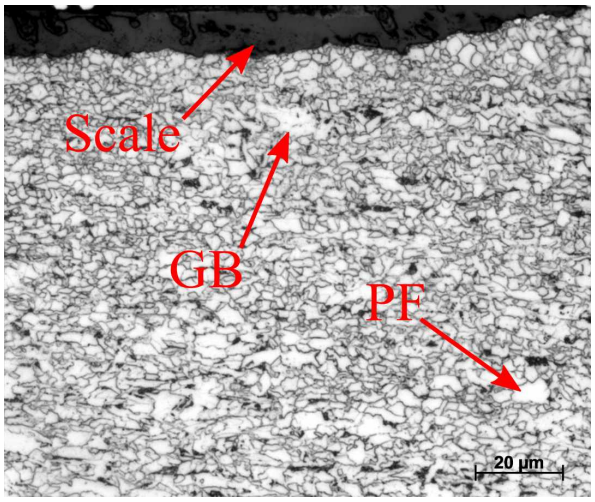

(a) 6.4 mm X70 plate surface 1000x LRD.

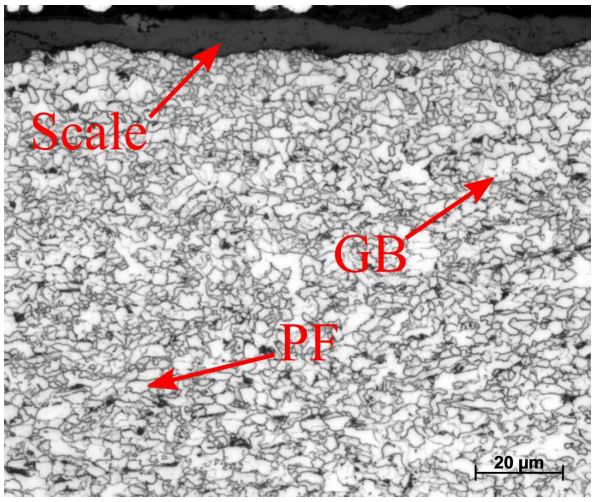

(b) 6.4 mm X70 plate surface 1000x TRD.

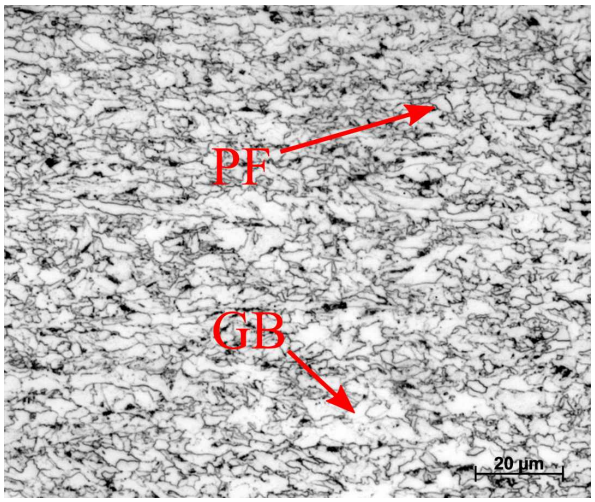

(c) 6.4 mm X70 plate quarter 1000x LRD.

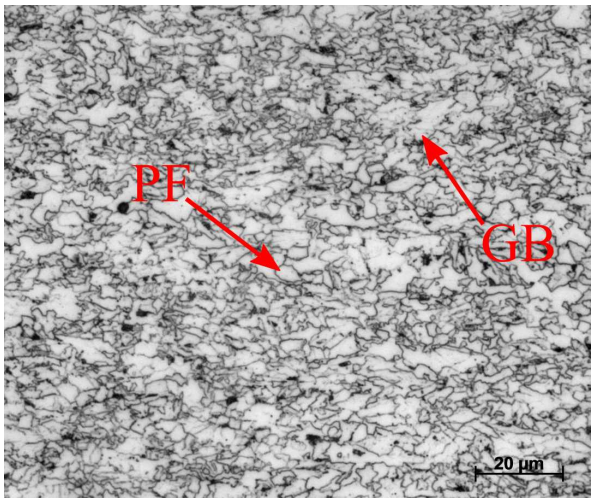

(d) 6.4 mm X70 plate quarter 1000x TRD.

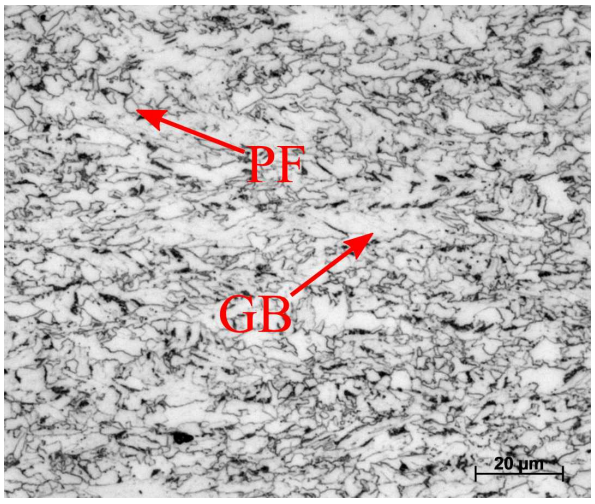

(e) 6.4 mm X70 plate centre 1000x LRD.

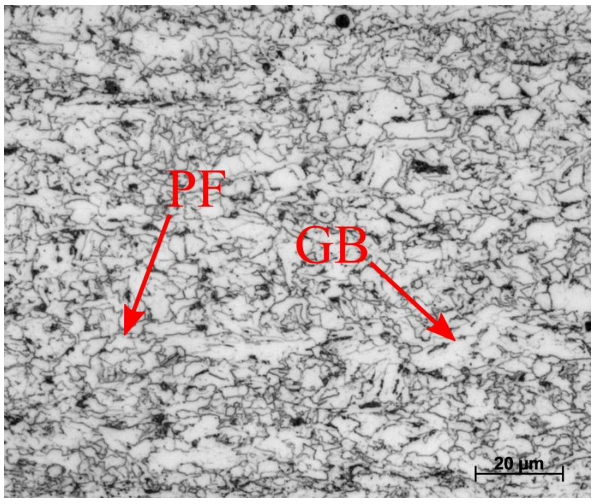

(f) 6.4 mm X70 plate centre 1000x TRD.

Figure 5.11: Through-thickness optical microstructure of 6.4 mm X70 plate.

SEM Microscopy

The 6.4 mm X70 SEM micrographs are presented in Figure 5.12 with an optical micrograph in Figure 5.12a showing the location of the SEM images in Figures 5.12b to 5.12d. The microconstituents in the 6.4 mm X70 are identified as degenerate pearlite. No M-A constituents were identified in the 6.4 mm X70 plate. This finding is similar to the 10 mm X70 pipe and likely because neither the 6.4 mm X70 plate or the 10 mm X70 pipe have sufficient concentrations of nickel to act as an austenite stabilizer. The presence of nickel has been found to allow M-A constituents to be exist in room temperature microstructures [141, 207].

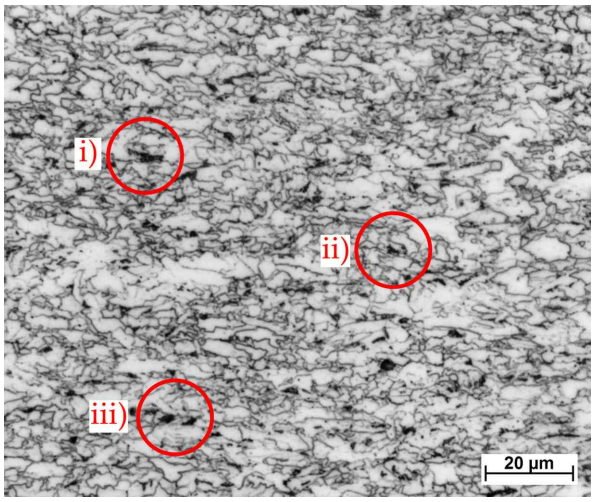

(a) 6.4 mm X70 plate optical image.

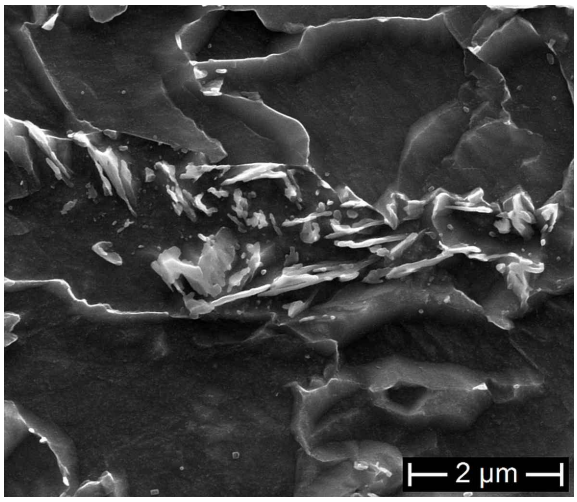

(b) Location i: DP.

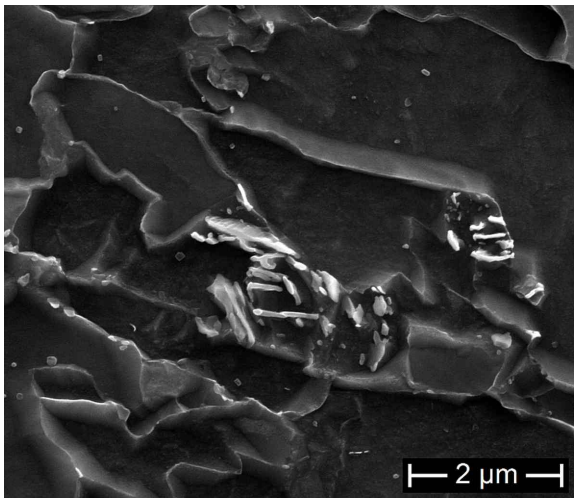

(c) Location ii: DP.

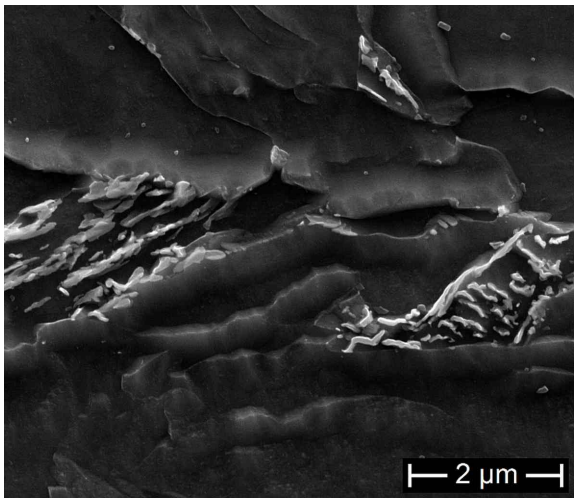

(d) Location iii: DP.

Figure 5.12: SEM micrographs of the dark regions in (a) present in the 6.4 mm X70 pipe (LRD).

Through-thickness Hardness of 6.4 mm X70

The through-thickness hardness of the 6.4 mm X70 steel plate is presented in Figure 5.13. The average hardness was measured to be 202 ± 3 HV0.5 with a peak hardness of 207 HV0.5 was observed at the outer surface of the plate. The through-thickness hardness of the plate, excluding the inner and outer surfaces, were uniform and with minimal variation in hardness observed from the outer surface towards the inner surface of the pipe. The higher average hardness of the 10 mm X70 pipe and 6.4 mm X70 plate as compared to the 20 mm X70 plate is likely due to the higher carbon content of the 10 mm X70

pipe and 6.4 mm X70 plate. In addition, as the 10 mm X70 pipe and 6.4 mm X70 plate contain pearlite as a secondary microconstituent as opposed to the M-A constituent of the 20 mm plate, the higher hardness of the cementite may account for the higher average hardness identified in Figure 5.13 and Figure 5.9 compared to Figure 5.4.

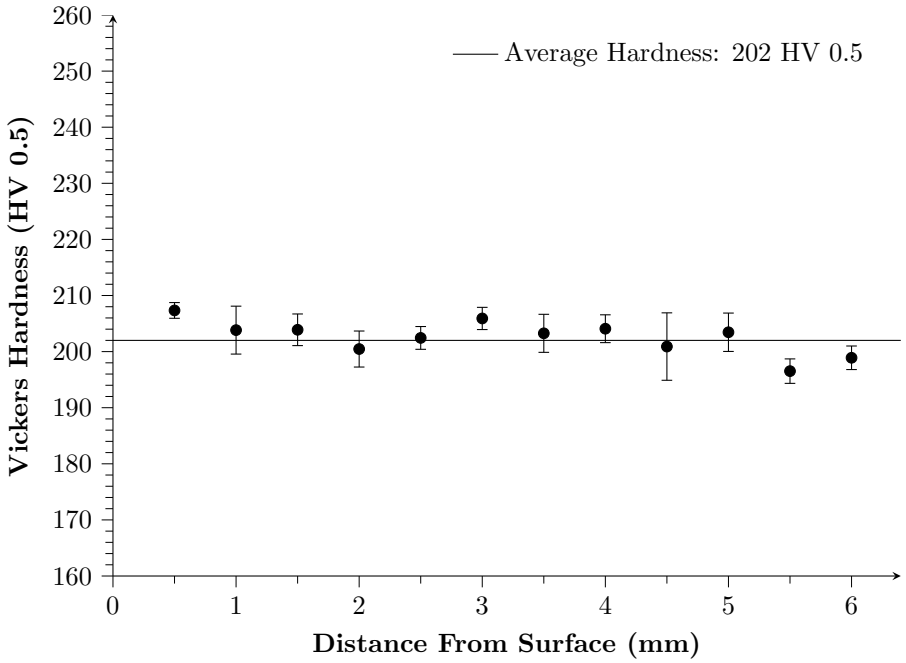

Figure 5.13: Through-thickness hardness of 6.4 mm X70 plate.

5.1.4 Summary of Industry Supplied Material

Microstructure Comparison

The microstructure of the three industry supplied samples consisted of primarily granular bainite with varying amounts of polygonal ferrite. The grain size increases in each sample from the surface towards the centre plane with the largest grain size observed in the centre plane of each sample. The grain size in each of the three materials was similar, however, the 10 mm X70 pipe appeared to have the largest average grain size of the three industry supplied samples.

The microstructure at the surface of the 20 mm, 10 mm and 6.4 mm X70 contained a mixture of polygonal ferrite and granular bainite, each having a higher proportion of

polygonal ferrite than bainite at the very surface. The plate samples (20 mm and 6.4 mm X70) were uncoated and have scale produced through manufacturing still attached to the surface whilst the 10 mm X70 was grit blasted and does not have a continuous layer of scale. Another consequence to being grit blasted was the 10 mm X70 pipe had some scale embedded into the surface of the steel unsurprisingly not observed in the 6.4 mm or 20 mm X70 plate.

The microstructure of the quarter thickness plane was similar in all three industry supplied samples and contained primarily granular bainite with grains of polygonal ferrite interspersed throughout. The 20 mm X70 plate and 10 mm X70 pipe show almost equal levels of granular bainite and polygonal ferrite whilst the 6.4 mm X70 plate has higher proportions of granular bainite. Similarities between the microstructure of the three industry supplied samples were expected as they have very similar chemical compositions and were the same X70 grade. Quarter thickness microstructures containing primarily granular bainite and polygonal ferrite, like those identified in the industry supplied samples were also observed in the relevant literature [138, 208, 211]. Some elongation was observed in the LRD directions of each industry supplied sample with the degree of elongation increasing as the wall thickness decreased. The steel grains in the TRD orientation were observed to have lower aspect ratios and approached unity.

The microstructure of the centre plane of the three industry supplied samples were very similar to those observed in the quarter plane, although the average grain size increased in all specimens. The centre plane of the 10 mm thick X70 pipe displayed prominent centreline segregation, not observed in the other X70 samples. The centreline segregation is believed to have its origins in continuous casting of billets/ slabs. Further elaboration of this casting defect is beyond the scope of the current study.

Microhardness Comparison

A comparison of the average through-thickness micro-hardness of the industry supplied samples is presented in Figure 5.14. The 20 mm X70 plate, 10 mm X70 pipe and 6.4 mm X70 plate had average hardnesses of 197.8 ± 2.4 HV0.5, 221 ± 4.7 HV0.5 and 202 ± 3 HV0.5, respectively. The 20 mm X70 had the lowest average hardness of the three samples with the 10 mm X70 had the highest average hardness. The high average hardness of the 10 mm X70 is likely the result microstructure as there was a higher proportion of pearlite colonies in the 10 mm X70 compared with the 6.4 mm X70 plate or the 20 mm X70 plate.

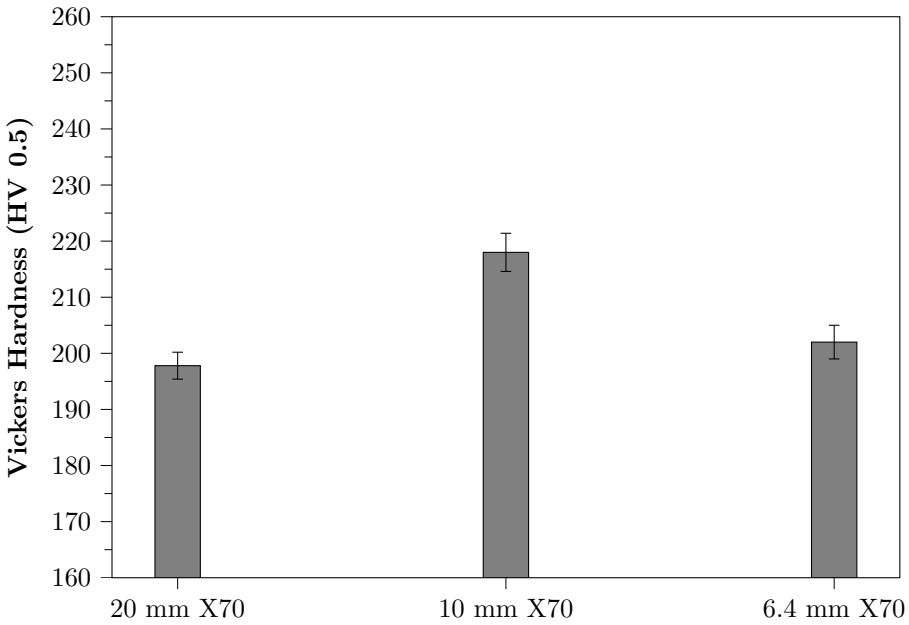

Figure 5.14: Comparison of average through-thickness micro-hardness of the industry supplied material.

5.2 Schedule Design

The primary aim of laboratory controlled rolling was to develop test specimens with different crystallographic textures. As has been highlighted in Section 2.7, texture is developed in steel during thermomechanical treatment at elevated temperatures. It was aimed to develop rolling schedules that produced different textures whilst producing similar microstructures to prevent additional factors from influencing the SCC susceptibility. In

order to develop the rolling schedules, transformation temperatures as well as the overall transformation behaviour of the as-received material (20 mm X70 plate) needed to be determined through CCT diagram development. Additionally, since the prior austenite grains size influences the effectiveness of controlled rolling schedules, as reported by Militzer et al. (1996) [212], it was necessary to investigate the prior austenite grain size development during soaking.

5.2.1 Prior Austenite Grain Size Determination

As explored in Section 4.2.2, the prior austenite grain size was determined by soaking samples of as-received 20 mm X70 plate at 1180°C for 60, 120, 150 and 180 minutes followed by quenching in water to prevent further grain growth. The grain size was then revealed through etching and measured with optical microscopy. The grain sizes was determined according to ASTM E112 [200] through the intercepts method as described in Section 4.2.2. An example of the grain morphology and size at each investigated temperature is presented in Figure 5.16 showing the grain size and, the length and location of intercepts used to calculate the average prior austenite grain size.

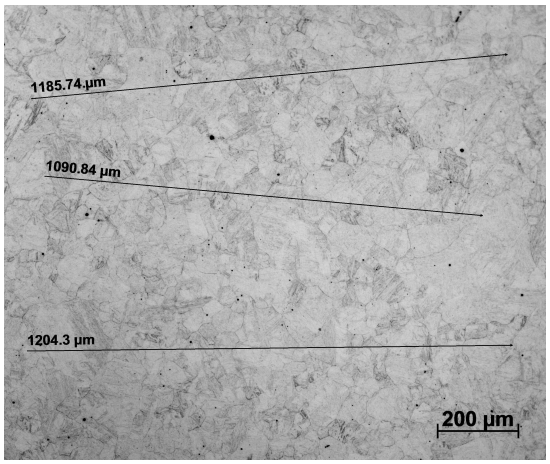

(a) 60 minute soak.

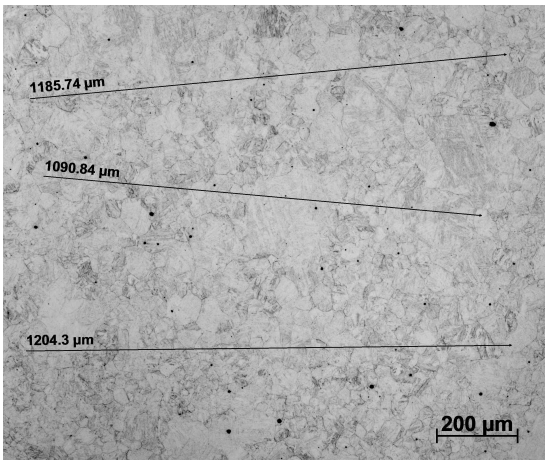

(b) 120 minute soak.

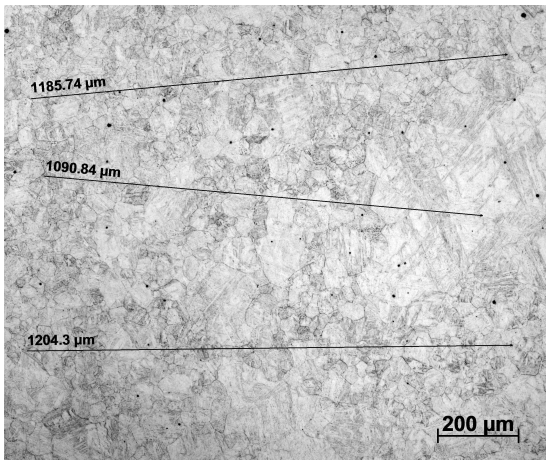

(c) 150 minute soak.

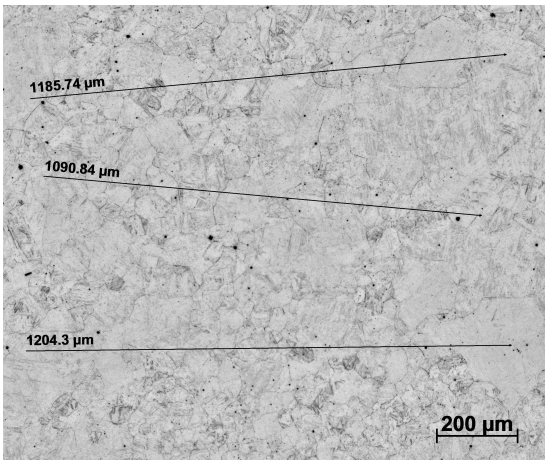

(d) 180 minute soak.

Figure 5.15: Prior austenite grain size revealed through aqueous picric acid etching.

The results for the average prior austenite grain size are provided in Table 5.2. As seen in Figure 5.16, the grain size after soaking at 1180°C for 120 minutes was only 3.5 μm larger than the average grain size identified after soaking for 60 minutes. The average prior austenite grain size increased to 61.6 μm after 150 minutes and further increased to 71.3 μm after 180 minutes.

Table 5.2: Prior austenite grain size of the 20 mm X70 plate.

Soaking Time	Grain Diameter
60 Minutes	49.4 ± 8 μm
120 Minutes	52.5 ± 8.7 μm
150 Minutes	61.6 ± 18.6 μm
180 Minutes	71.3 ± 12 μm

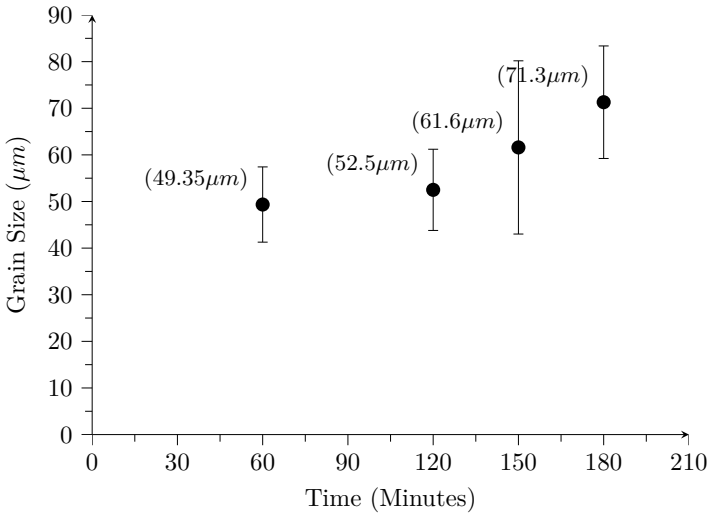

Figure 5.16: Prior austenite grain size of the 20 mm X70 plate.

The soaking time and temperature are critical factors for commercial hot rolling and must be undertaken at a sufficiently high temperature and long duration such that some degree of homogenization is achieved [213]. This is undertaken to ensure the material is uniform prior to rolling and to reduce the likelihood of hard precipitates to achieve uniform deformation [213]. The soaking time and temperature also influence the prior austenite grain size with longer soaking times and/ or higher soaking temperatures producing larger prior austenite grain sizes [214].

Soaking at temperatures greater than 1200°C enables faster dissolution of alloying elements without segregated regions, however, there is a higher risk of surface oxidation [213]. Industry and laboratory testing described in the literature typically conduct soaking at 1180 or 1200°C [137, 138, 180, 215–217]. At soaking temperatures lower than approximately 1150°C, non-metallic inclusions may pin down austenite grain boundaries and retard uniform deformation upon rolling hence, it is important to soak at sufficiently high temperatures [218].

Summary

A soaking time of 150 minutes at a temperature of 1180°C was chosen to soak the samples prior to hot rolling as it corresponded with an increase in prior austenite grain size,

likely indicating all non-metallic inclusions had entered solid solution whilst keeping the oxidation at the surface to a minimum.

5.2.2 Calculating Non-Recrystallization Temperature T_{NR}

During recrystallization and transformation, nucleation of new grains initiates preferentially at grain boundaries. To enable grain refinement during transformation to ferrite, the prior austenite grain size should be refined such that the grain boundary area is increased. As detailed in Section 2.7.3 when rolling above the non-recrystallization temperature (T_{NR}), between rolling passes, complete static recrystallization can occur and equiaxed grains form; resulting in a lower grain boundary area. Upon transformation, coarse ferrite grains are produced due to less nucleation. Conversely, rolling below the non-recrystallization temperature leads to strain accumulation because complete static recrystallization can not occur between rolling passes. Upon transformation, fine ferrite grains are formed as there are a large number of nucleation sites available for ferrite formation due to strain accumulation [156].

The determination of the T_{NR} was undertaken using empirical formulae calculated from steels chemical composition as described in Section 2.7.3. Three common equations used for the determination of the T_{NR} in low carbon steels are: Equation (5.1) devised by Boratto et al. (1988) [163] in Equation (5.1), Equation (5.2) devised by Bai et al. (1993) [162] and Equation (5.3) devised by Fletcher (2008) [164]. As discussed in Section 2.7.3 whilst the Boratto equation tends to overestimate the value of T_{NR}, the Bai and Fletcher equations (Equation (5.2) and Equation (5.3)) give much better approximations experimentally determined T_{NR}. Any error identified between the empirical equations and experimentally determined values were within the margin of error of the temperature measurement equipment. Hence, the empirical equations are sufficient for determining the value of T_{NR} for use in developing the rolling schedules.

Table 5.3: Chemical composition of the 20 mm X70 plate (w.t. %). Fe Balance.

	C	***Mn***	***Si***	***Ni***	***Cu***	***Al***	***Mo***	***V***	***Nb***	***Ti***	***Cr***	***Ca***	***P***	***S***	***B***	***N***
20 mm X70	0.059	1.57	0.19	0.19	0.16	0.05	0.17	0.03	0.05	0.01	0.03	0.002	0.01	0.002	0.0005	0.004

$$T_{NR} = 887 + 464C + \left(6445Nb - 644\sqrt{Nb}\right) + \left(732V - 230\sqrt{V}\right) + 890Ti + 363Al - 357Si \tag{5.1}$$

$$T_{NR} = 174 \log\left[Nb\left(C + \frac{12}{14}N\right)\right] + 1444 \tag{5.2}$$

$$T_{NR} = 849 - 349C + 676\sqrt{Nb} + 337V \tag{5.3}$$

The value of T_{NR} as calculated through each of the listed equations and chemical composition from Table 5.3 are as follows:

- Boratto Equation: $T_{NR} = 1034.5°C$
- Bai Equation: $T_{NR} = 1008°C$
- Fletcher Equation: $T_{NR} = 989.7°C$

As discussed in Section 2.7.3, the Boratto equation tends to consistently overestimate the T_{NR} whilst the Bai and Fletcher Equations are closer to experimentally determined T_{NR} in low carbon steels, as investigated by Homsher (2013) [159]. The steels investigated in the study by Homsher (2013) [159] had similar chemical compositions to the 20 mm X70 plate used in the current study and hence, can benchmark the validity of the two equations. It was observed by Homsher (2013) [159] that the Bai equation slightly overestimated the experimentally derived T_{NR} whilst the Fletcher equation consistently under estimated the experimentally determined T_{NR}. The true T_{NR} was found by Homsher (2013) [159] to be almost the exact average of the Bai and Fletcher equations and hence, the experimentally determined T_{NR} value for the 20 mm X70 will likely be close to the

average of the Bai and Fletcher equations. The average value of T_{NR} from the Bai and Fletcher equations was calculated to be 998.9°C. The value of 998.9°C was within the range suggested by Al Shahrani et al. (2010) [219] and Schambron et al. (2009) [220] for experimentally determined T_{NR} of X70 specimens. One important point to consider is that neither Al Shahrani et al. (2010) [219] or Schambron et al. (2009) [220] provided the exact concentration for all elements so verifying the empirical equations was not possible.

The T_{NR} of the 20 mm X70 plate for use in developing the rolling schedules was empirically calculated to be 998.9°C. Above this temperature, complete static recrystallization can occur between rolling passes resulting in recrystallization textures. Finish rolling below this temperature does not allow complete static recrystallization to occur, thus allowing deformation textures to develop.

5.2.3 CCT Diagram

The CCT diagram was developed from dilation data produced from a DIL 805 A/D dilatometer. A dilation curve was developed under quasi-equilibrium conditions to approximate the temperature that the as-received 20 mm X70 plate would transform from ferrite to austenite upon heating and austenite to ferrite upon cooling. Nine cooling rates ranging from 0.5°C/s to 100°C/s (0.5, 1, 3, 5, 10, 20, 30, 50 and 100°C/s), after being held at 1100°C [4] for 5 minutes, were tested to determine what phases developed. The specific phase transformation temperatures microstuctures that developed were identified to construct the CCT diagram. The method used to develop the CCT diagram is provided in Section 4.2.1.

[4] 1100°C was the temperature limit for the configured system

Transformation Temperature Determination

The determination of the critical temperatures was carried out on a specimen heated and cooled at a rate of 2°C/min (holding temperature was five minutes, the same as the other specimens) where the slow heating and cooling rate was able to give an approximation of equilibrium conditions. The quasi-equilibrium heating transformation temperatures Ac_1 (the beginning of ferritic transformation to austenite upon heating) and Ac_3 (the end of ferritic transformation to austenite upon heating) and the quasi-equilibrium cooling transformation temperatures Ar_3 (the temperature austenite begins to transform to ferrite during cooling) and Ar_1 (the temperature when the austenite to ferrite transformation is completed during cooling) were determined from the graphs presented in Figure 5.17. As can be seen in Figure 5.17a, the Ac_1 temperature was found to be 702°C whilst the Ac_3 temperature is 913°C. Similarly in Figure 5.17b, the Ar_1 temperature was found to be 660°C whilst the Ar_3 temperature was found to be 767°C.

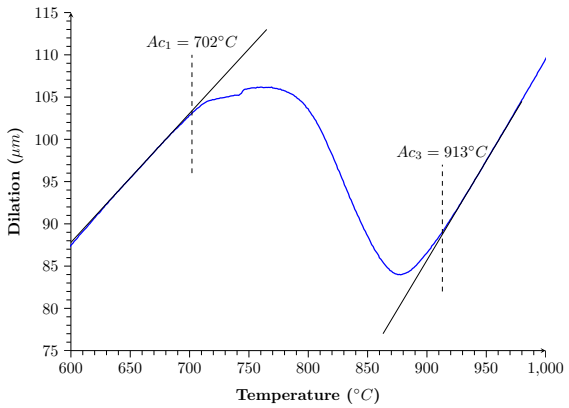

(a) Heating dilation curve showing Ac_1 and Ac_3 temperature determination.

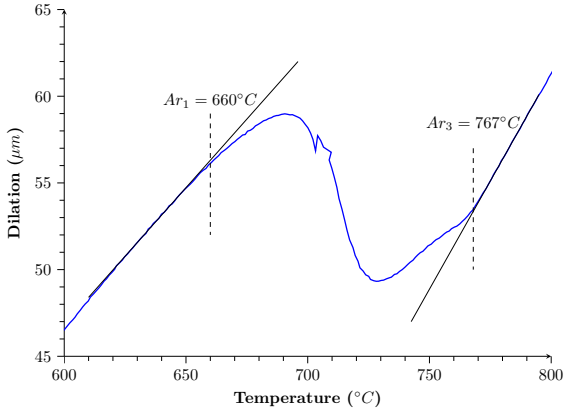

(b) Cooling dilation curve showing Ar_1 and Ar_3 temperature determination.

Figure 5.17: Dilation curves showing the determination of the critical transformation temperatures in the as-received 20 mm X70 plate.

Effect of Cooling Rate on Microstructure

As the primary purpose of the current study was to determine the role of crystallographic texture of the pipeline steel on its susceptibility to SCC, keeping the microstructure of the

test specimens consistent was important to prevent additional factors influencing SCC susceptibility. As X70 pipe microstructure primarily consists of bainite, it was important that the laboratory prepared X70 steel also had a primarily bainitic structures that matched the industry manufactured samples. As detailed in Section 4.2.1 once the specimens were cooled, they were mounted and polished to the centre plane and the microstructure analysed through both optical and SEM analysis to determine the microstructures that developed.

As the cooling rate increases, a change in microstructure is expected due to the changing kinetics of the transformation from austenite to ferrite in steels. The transformation from austenite to ferrite in steels develops by either displacive or reconstructive transformation depending on the cooling rate/ isothermal transformation temperature as detailed in Section 2.7.1. Three distinct regions developed, distinguished by microstructure, due to different cooling rates in the 20 mm X70 plate. Region 1 contained cooling rates between 0.5-3°C/s, Region 2 contained cooling rates between 5-20°C/s and Region 3 consisted of cooling rates between 30-100°C/s.

CCT Diagram - Region 1

Region 1 cooling rates consisted of the slowest cooling CCT specimens, 0.5, 1 and 3°C/s. As seen in the optical micrographs, Figure 5.18 the three cooling rates developed similar microstructures consisting primarily of granular bainite and quasi-polygonal ferrite. Some dark secondary phases not able to be resolved through optical microscopy were also produced. A selection of the dark secondary microconstituents were viewed under SEM at high magnification to aid in the identification of the microstructures that formed during cooling.

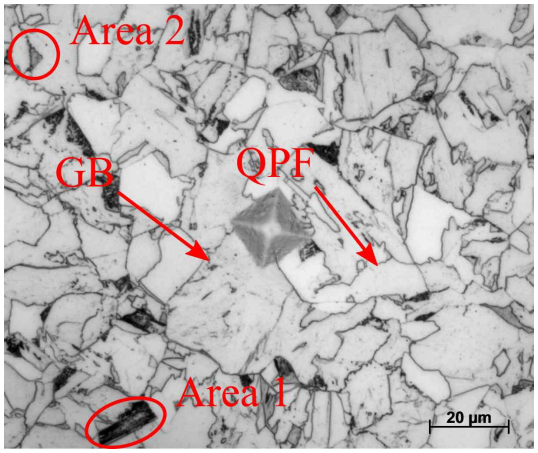

(a) Optical microscopy of the 0.5°C/s cooling rate CCT sample.

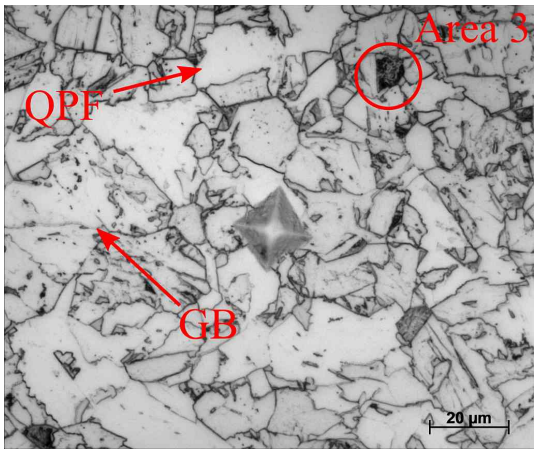

(b) Optical microscopy of the 1°C/s cooling rate CCT sample.

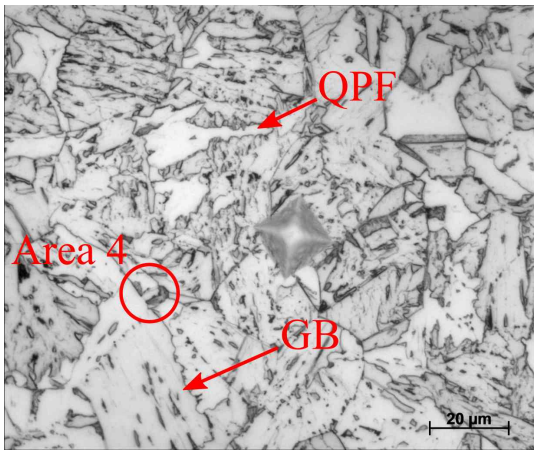

(c) Optical microscopy of the 3°C/s cooling rate CCT sample.

Figure 5.18: Optical microstructure of Region 1 cooling rate CCT samples.

SEM images of the circled areas from Figure 5.18 are presented in Figure 5.19. The dark secondary microconstituents present in Region 1 cooling rates were degenerate pearlite and M-A constituents. Both degenerate pearlite and M-A constituent were present in the 0.5°C/s cooling rate specimen in almost equal proportions (Figures 5.19a and 5.19b). In the 1°C/s cooling rate specimen Figure 5.19c, there was significantly more M-A constituent than degenerate pearlite, likely owing to the faster cooling rate limiting diffusion, required for degenerate pearlite to form. There was minimal degenerate pearlite identified in the 3°C/s cooling rate specimens with the main secondary constituent being comprised of M-A constituents.

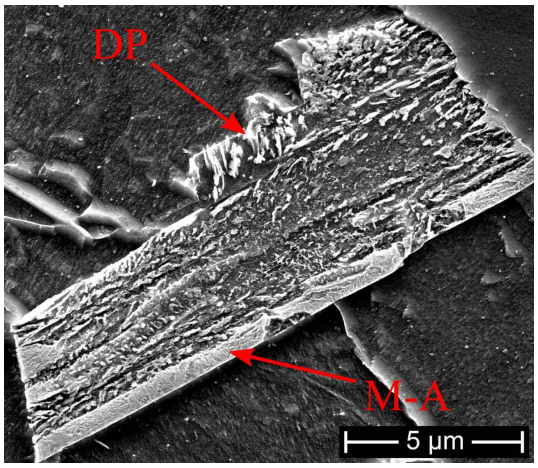

(a) DP present in Area 1.

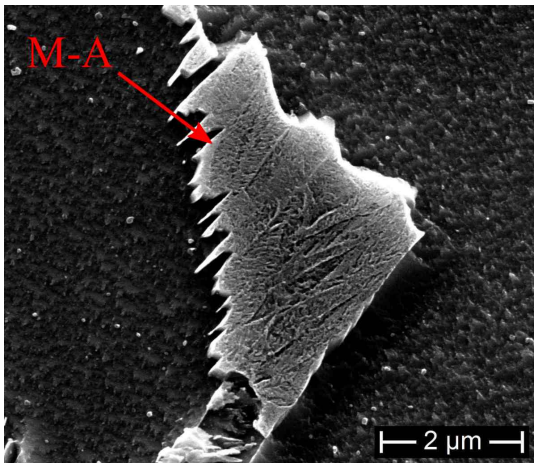

(b) M-A Constituent present in Area 2.

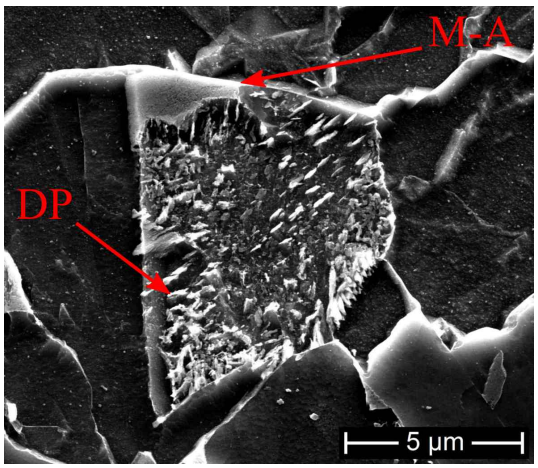

(c) DP present in Area 3.

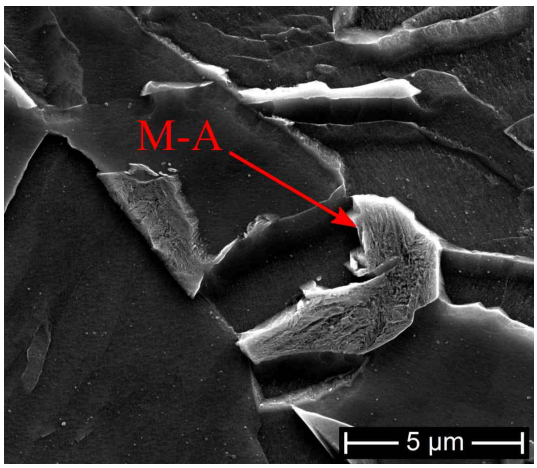

(d) M-A Constituent present in Area 4.

Figure 5.19: SEM images of secondary phases present in Figure 5.18.

The slow cooling rates in region 1 appear to be more influenced by diffusion controlled transformation mechanisms, owing to the prevalence of degenerate pearlite and quasi-polygonal ferrite [221]. The observed microstructures align well with other CCT diagrams developed for X70 grade steels. As seen in Cizek et al. (2015) [222] the slow cooling rates tended to produce irregular quasi-polygonal ferrite and granular bainite with M-A constituent as a secondary phase. The degenerate pearlite forms from the enriched austenite due to the presence of alloying elements that decrease carbon activity in austenite [125]. The presence of degenerate pearlite is closely linked to M-A constituents and as seen in Figure 5.19a can occasionally be present within the same grain.

CCT Diagram - Region 2

Region 2 cooling rate CCT specimens consist of moderate cooling rates including 5, 10 and 20°C/s. The cooling in these specimens, as with Region 1, occurred after soaking at 1100°C for 5 minutes before cooling with nitrogen at the specified rate. As seen in the optical micrographs in Figure 5.20, the three cooling rates generate microstructures primarily consisting of granular bainite with increasing proportions of upper bainite with increasing cooling rates. Granular bainite forms in low carbon steels through a mechanism that is identical to that of upper bainite, however, due to the slower transformation speed, the sheaves of bainite can appear coarse giving granular bainite a block-like appearance[141]. In addition, as the diffusion of carbon out of the transformed austenite is slower, it does not form cementite between sheaves, but instead stabilises the austenite such that M-A constituents are present both within and bordering granular bainite grains [125]. As the cooling rate increases coarse upper bainite grains begin to form as the thermodynamics of the transformation being to favour cementite production and upper bainite begins to emerge [141].

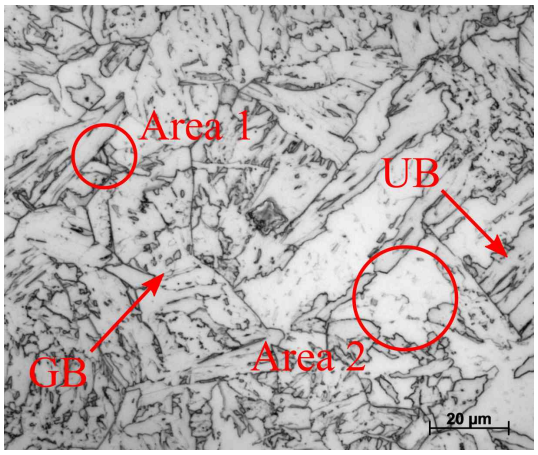

(a) Optical microscopy of the 5°C/s cooling rate CCT sample.

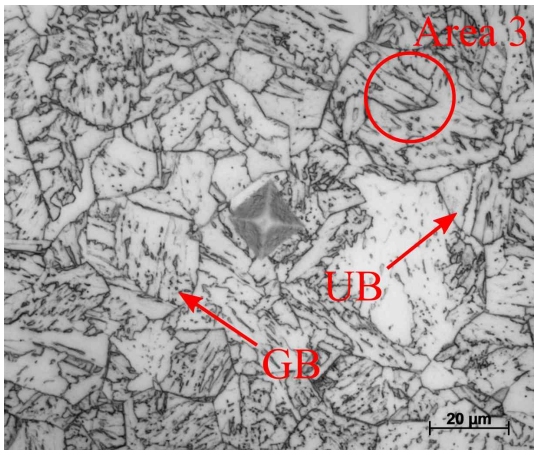

(b) Optical microscopy of the 10°C/s cooling rate CCT sample.

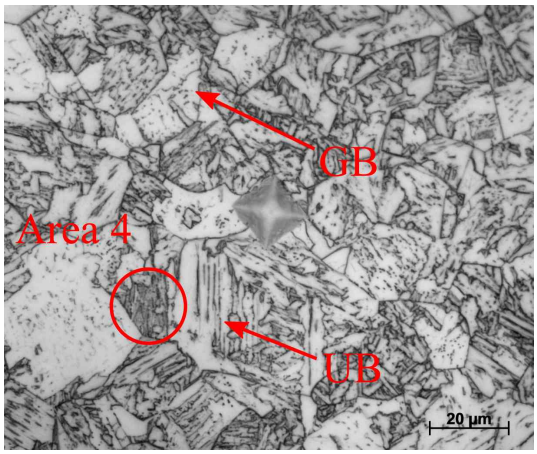

(c) Optical microscopy of the 20°C/s cooling rate CCT sample.

Figure 5.20: Optical microstructure of Region 2 cooling rate CCT samples.

A selection of the dark secondary phases circled in Figure 5.20 were viewed with SEM under high magnification to aid in the identification of the microstructures that formed during cooling, presented in Figure 5.21. The secondary phase identified in Area 1 of the 5°C/s cooling rate CCT sample, as shown in Figure 5.21a, is degenerate pearlite formed from enriched austentie. The degenerate pearlite appears to have grown intergranularly and shows the beginnings of an upper bainite grain. Granular bainite, as seen in Figure 5.21b, appears as bainitic ferrite with small islands of M-A constituent within the grain. M-A constituent are formed within the grain because carbon partitioned out of the bainite during transformation stabilises the remaining austentie islands within bainite to

exist at room temperature. In Figure 5.21c the M-A constituent present in Area 3 appears to be present between coarse sheaves of ferrite giving it the appearance of degenerated upper bainite. Degenerated upper bainite forms when cementite formation is prevented and carbon rich austenite remains after transformation [125]. This microstructure appears as an intermediary between granular bainite and upper bainite and is expected within this intermediate cooling range. The first true upper bainite appears in the 20°C/s cooling rate CCT specimen as seen in Area 4 in Figure 5.21d. At the higher cooling rates, transformation of enriched austenite to cementite is favoured and upper baintie permitted to form [141].

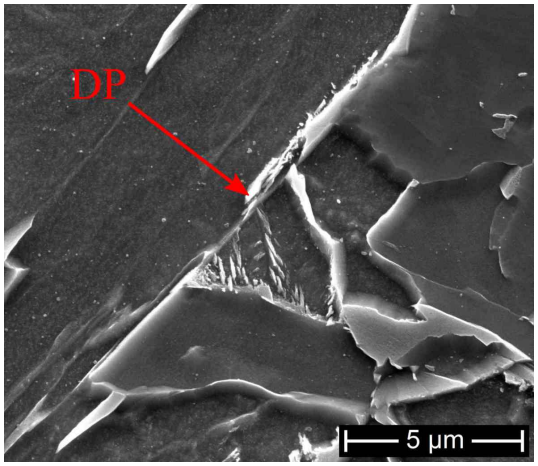

(a) DP present in Area 1.

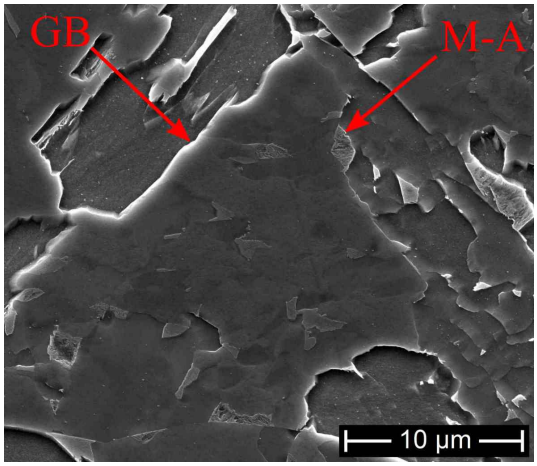

(b) GB present in Area 2.

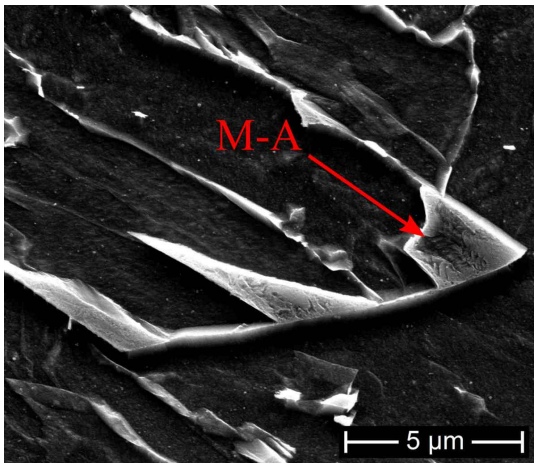

(c) M-A Constituent present in Area 3.

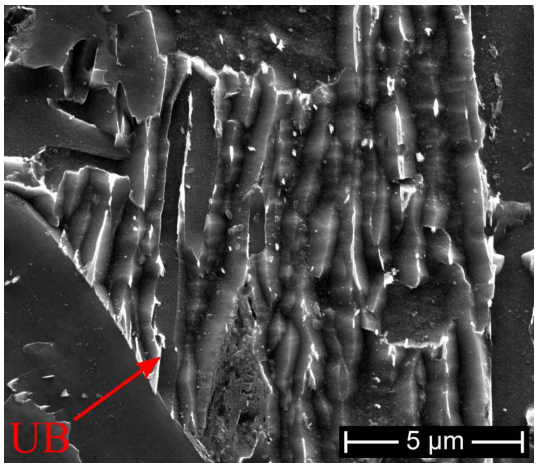

(d) UB present in Area 4.

Figure 5.21: SEM images of secondary phases present in Figure 5.20.

The intermediate cooling rates of Region 2 allow for the formation of granular bainite and coarse upper bainite with the typical secondary phases also identified in Region 1. As cooling rate increases, displacive driven transformations dominate at the expense of diffusion dominant transformations as is evident in Region 2 with the absence of quasi-polygonal ferrite and introduction of upper bainite.

CCT Diagram - Region 3

Region 3 cooling rate CCT specimens consist of fast cooling rates 30, 50 and 100°C/s. The cooling in these specimens, as with regions 1 and 2, occurred after being soaking at 1100°C for 5 minutes before cooling with nitrogen at the specified rate. As seen in the optical micrographs in Figure 5.22, the three cooling rates result in the formation of upper bainite with very small proportions of granular bainite dispersed occasionally throughout the microstructure. Upper bainite forms in two discreet steps through a diffusion controlled displacive mechanism [141]. The first step in upper bainite formation is the displacive transformation of austenite into a bainitic ferrite lath. As the solubility of carbon in the newly formed lath is low (< 0.02 wt%) excess carbon diffuses out into the parent austenite [141]. The newly enriched austenite rejects the increased carbon through the formation of cementite, hence, upper bainite appears as laths of bainitic ferrite separated by cementite precipitate [125, 141, 221]. There appears to be a lack of martensite even at the fastest cooling rate indicated by the presence of cementite between the bainitic laths [141, 221]. This is likely due to the low carbon content of the steel leading to near complete bainite transformation prior to reaching the martensite start temperature upon cooling.

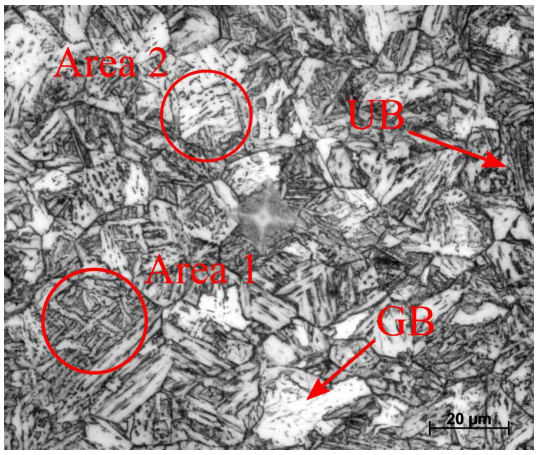

(a) Optical microscopy of the 30°C/s cooling rate CCT sample.

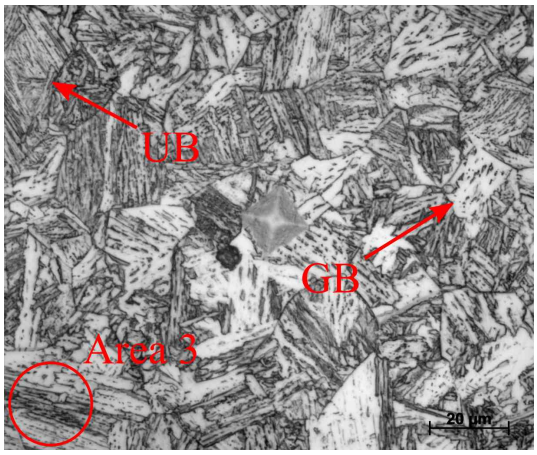

(b) Optical microscopy of the 50°C/s cooling rate CCT sample.

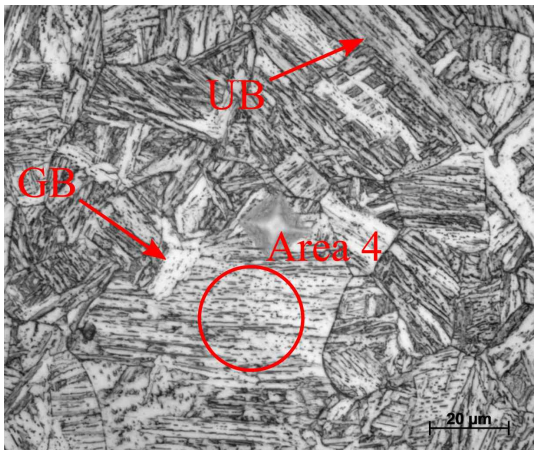

(c) Optical microscopy of the 100°C/s cooling rate CCT sample.

Figure 5.22: Optical microstructure of Region 3 cooling rate CCT samples.

A selection of grains circled in Figure 5.22 were viewed under high magnification using SEM to aid the identification of microstructures that formed during cooling with the results presented in Figure 5.23. The microstructure identified in Figure 5.23a of Area 1 appears to be a collection of upper bainite laths, characterised by laths of ferrite separated by cementite particles. The cementite particles between the laths appear discrete as expected from a low carbon steel [125]. As seen in Area 2, Figure 5.23b, the laths are approximately 1 μm thick and appear far coarser than those produced in Areas 3 and 4. The difference in upper bainite lath width is related to the cooling rate, faster cooling rates and subsequently lower transformation temperatures result in thinner lath width

[223]. As seen in Area 3, Figure 5.23c, the grain is comprised of uniform upper bainite with discrete cementite particles separating the bainitic ferrite laths. The overall lath width is approximately 0.5 μm with no trace of M-A constituents. The final SEM image of Area 4, Figure 5.23d, shows a grain comprised of primarily upper bainite although there appears to be inter-lath cementite indicative of lower bainite that has been circled. The lath width is slightly larger than that observed in Area 3, although it is still less than 1 μm observed in Area 1.

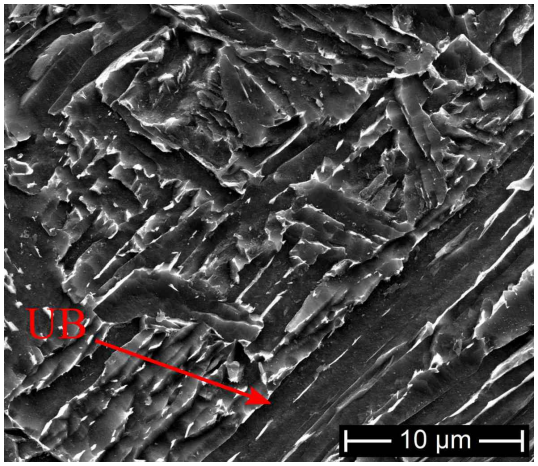

(a) UB present in Area 1.

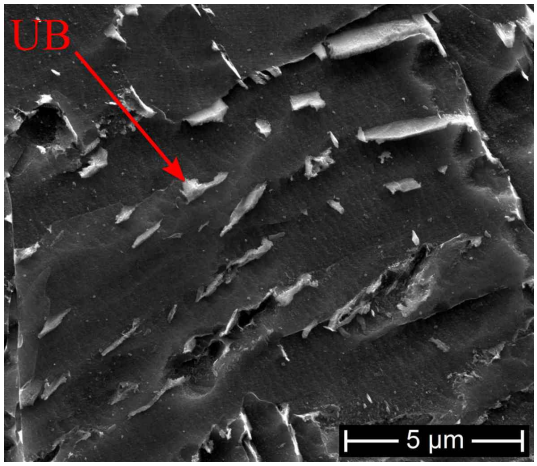

(b) UB present in Area 2.

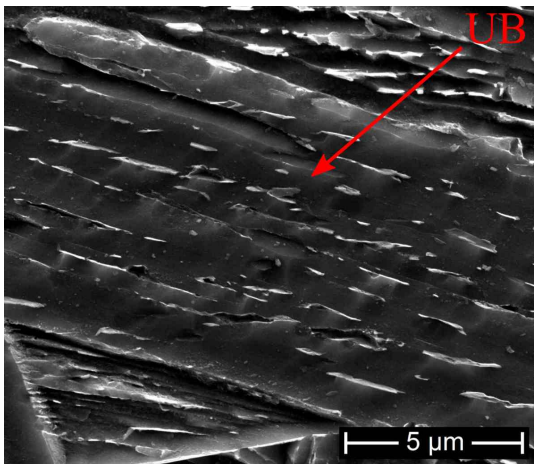

(c) UB present in Area 3.

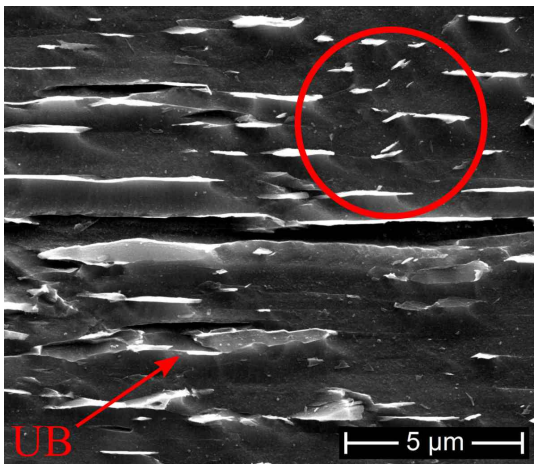

(d) UB present in Area 4.

Figure 5.23: SEM images of secondary phases present in Figure 5.22.

The microstructures of the CCT specimens in Region 3 were dominated by upper bainite with low presence of M-A constituent and degenerate pearlite. As stated above, upper

bainite is expected to form rather than granular bainite under faster cooling rates. The lack of secondary phases like M-A constituent or degenerate pearlite are because there is no carbon enriched austenite for them to be formed from, as is the case of granular bainite production, observed in the slower cooling rates.

Hardness Measurements

Hardness measurements were carried out on each CCT specimen to to aid microstructure determination as hardness is strongly influenced by microstructure. The micro Vickers hardness of the CCT specimens is presented in Figure 5.24, plotted against a logarithmic x axis for ease of reading, showing the logarithmic increase in hardness as a linear function of cooling rate. The overall change in hardness with cooling rate is 87 HV0.5 when comparing the lowest hardness 0.5°C/s cooling rate to the highest hardness 100°C/s cooling rate. As the cooling rate increases, the microstructure shifts from coarse granular bainite dominant to the finer upper bainitic dominant structures that typically have harder microhardnesses [224]. Cementite associated with upper bainite has a much higher hardness than MA associated with granular bainite, in addition, as the cooling rate increases, the bainitic laths become finer which also contributes to a higher hardness [224, 225].

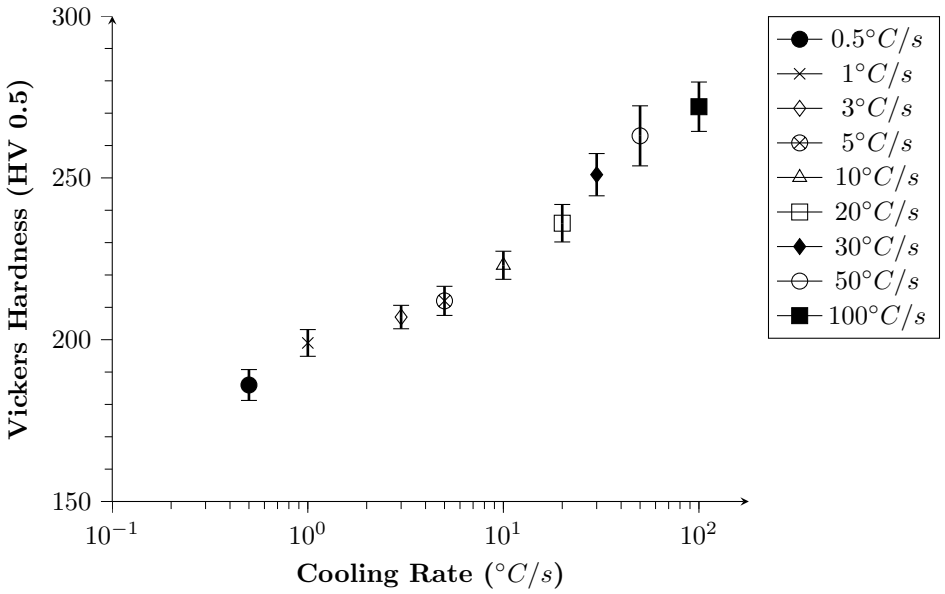

Figure 5.24: Vickers microhardness of CCT specimens.

The industry supplied samples had hardness values of between 197.8 HV0.5 to 221 HV0.5. To develop a steel that closely approximated the mechanical properties of industry manufactured X70, the hardness would need to be in a similar range. A desired range of hardnesses above 200 HV0.5 and below 240 HV0.5 leaves a range of possible cooling rates between 5°C/s and 20°C/s.

CCT Diagram

The CCT diagram developed from the cooling data is presented in Figure 5.25. The CCT diagram displays each constant cooling rate with the transformation start and end temperatures joined together to form a region of microstructure development. As can be seen in the CCT diagram, above 1°C/s the only microstructures that developed were bainitic. Below 1°C/s a mixed microstructure of bainite with ferrite and pearlite is formed due to the slow cooling rate allowing greater diffusion of carbon out of austenite. It is important to note that the CCT diagram developed did not take into account deformation. Whilst the current CCT diagram is a good approximation, rolling introduces a number of other factors that will influence the final microstructure. To develop rolled material with a microstructure and hardness that most closely matches those found in industry supplied

samples, the 10°C/s cooling rate was selected.

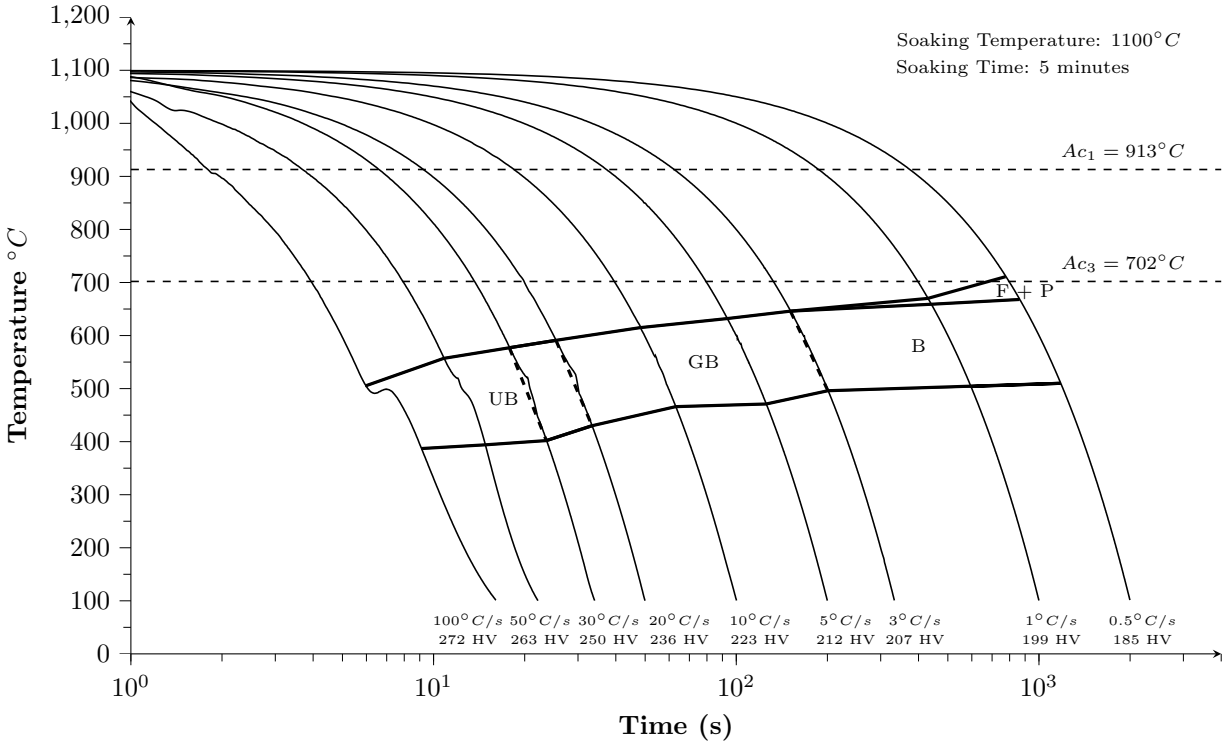

Figure 5.25: CCT diagram of the 20 mm X70 plate.

5.2.4 Rolling Schedules

As the primary intention of performing controlled rolling was to develop different textures and different concentrations of textures, the rolling schedules were required to be devised such that different temperature regimes were targeted. As explored in Section 2.7.4, the development of different crystallographic textures during controlled rolling is strongly dependent on the rolling temperature. The three main regimens that steel is rolled are classified as recrystallised rolling, hot rolling and warm rolling. Recrystallised rolling involves finish rolling above the T_{NR} as described in Section 2.7.2, and takes advantage of the strong cube {100}<001> texture formed in austenite prior to transformation [21–23, 101]. After transformation the cube rotates into either rotated cube {100}<110>, Goss {110}<001> or Rotated Goss {110}<110> textures [21, 177].

Hot rolling is defined as rolling below the T_{NR} and defined by strong recrystallized cube

textures. However, due to being rolled below the steels T_{NR}, strain accumulation occurs in the grains and deformation textures begin to form. Hot rolling tends to be defined by the introduction of Brass {110}<112> and Copper {112}<111>, {123}<614> textures that upon transformation develop into {554}<225>, {111}<112> and {113}<110> textures [21].

Warm rolling occurs when rolling takes place at temperature range where both austenite and ferrite are present, i.e. elongation occurs in both austenite and ferrite. The higher levels of strain accumulation in this temperature range results in strengthening of the γ-fibre and deformed austenite textures [23, 102, 186]. Recrystallised rolling, hot rolling and warm rolling should enable the production of different textures such that the role that texture has on SCC testing can be determined. Whilst different processes cold drawing would likely develop more dissimilar textures, the results would not be as useful for the production of control rolled pipeline steel.

Schedule 1

Schedule 1 is a recrystallised rolling schedule where all the rolling was undertaken above T_{NR}. The aim of rolling in this temperature range was for static recrystallization to occur between rolling passes. Rolling under these conditions would result in the development of equiaxed grains with minimal elongation, along with the development of recrystallization textures. Due to rolling above the T_{NR}, strain accumulation of the austenite is not expected, hence post-transformation, equiaxed ferrite grains would result. The details of rolling Schedule 1 is outlined in Table 5.4 where the rolling temperature range, initial and final thickness (t_i and t_f) reduction ratio, sample length and cooling rate are provided.

All rolling was carried out between 1010-1180°C using the high temperature furnace to both soak the samples and hold them at temperature between rolling passes. As the intention of this rolling regimen is to develop recrystallization textures, rolling was carried

out above the non-recrystallization temperature that was empirically determined to be 998.9°C.

Prior to water cooling, Schedule 1 was air cooled from approximately 1010°C to 785°C to ensure all three rolling schedules were water cooled from approximately the same starting temperature. Schedule 1 was water cooled to 450°C and subsequently allowed to air cool to room temperature. In industrial rolling mills, specimens are typically cooled to approximately 550°C (depending on the final plate thickness) and then coiled to permit transport to pipe forming operations.

Table 5.4: Schedule 1 rolling parameters.

Schedule 1	**Temperature**	t_i	t_f	**Reduction**	**Length**	**Cooling Rate**	**Medium**
	$°C$	mm	mm	%	mm	$°C/s$	
Rough Rolling:	1180-1010	20	17	15	216		
	1180-1010	17	13.6	20	270		
	1180-1010	13.6	10.2	25	360		
	1180-1010	10.2	7	31.4	525		
Cooling:	1010-785					$\sim 1°C$	Air
	785-450					$10°C$	Water
	450-RT					$\sim 1°C$	Air

Schedule 2

Schedule 2 is a hot rolling schedule where the rough rolling occurs above T_{NR} and finish rolling below T_{NR}. The aim of rolling in this temperature range is for static recrystallization to occur after rough rolling to develop stronger recrystallization textures and refine the grain size. Finish rolling should then be undertaken below the T_{NR} (empirically determined to be 998.9°C) such that strain accumulation in the austenite would occur and hot rolling deformation textures develop. The microstructure of this schedule was expected to be slightly elongated along the rolling direction. The details of Schedule 2 are

provided in Table 5.5. Schedule 2 is expected to have the highest elongation of the three rolling schedules due to rough rolling only accounting for 12.5% of deformation with the three finish rolling passes occurring below T_{NR} accounting for 30, 25 and 23.8% rolling reduction. The microstructure of Schedule 2 was expected to most closely match those of industrially prepared X70 as it was identified in literature that X70 steels are typically rolled under similar conditions [138, 211].

Sample rolled under Schedule 2 were initially soaked at 1180°C in the soaking furnace before being rough rolled at between 1010-1125°C. The rolled samples were then placed into a second holding furnace maintained at a temperature between 785-860°C such that the samples would not transform to ferrite between finish rolling passes when the rolling mill was adjusted. Following finish rolling, the sample is immediately cooled from 785°C to 450°C under water, cooling at a rate of 10°C/s (same as schedule 1) before being air cooled to room temperature.

Table 5.5: Schedule 2 rolling parameters.

Schedule 2	**Temperature** $°C$	t_i mm	t_f mm	**Reduction** %	**Length** mm	**Cooling Rate** $°C/s$	**Medium**
Rough Rolling:	1125-1010	20	17.5	12.5	210		
Finish Rolling:	860-785	17.5	12.25	30	300		
	860-785	12.25	9.2	25	400		
	860-785	9.2	7	23.8	525		
Cooling:	785-450					$\sim 1°C$	Water
	450-RT					$\sim 1°C$	Air

Schedule 3

Schedule 3 was a warm rolling schedule where the rough rolling occurs above T_{NR} and finish rolling occurs in the two-phase region where both austenite and ferrite are present. The aim of finish rolling in the two-phase region is for warm rolling textures developed.

The details of rolling Schedule 3 are observed in Table 5.6. Samples were soaked at 1180°C in the soaking furnace before being rough rolled between 1010-1125°C. The samples experienced a deformation of 30% during rough rolling leaving only 7 mm of deformation remaining before reaching the desired thickness. As almost half the deformation was undertaken above the T_{NR} (empirically determined to be 998.9°C) it is expected that lower pancaking would occur in the finish rolling passes resulting in a coarser grain size than that observed in Schedule 2.

Finish rolling was carried out in three passes (26, 20.5 and 15% deformation respectively) at a temperature range beginning at 860°C in the austenite and finishing at 690°C within the two phase region. Due to the addition of rolling within the two phase region, the microstructure is expected to appear different compared to the hot rolled industry supplied samples [72, 138]. Following finish rolling, the sample was immediately cooled from 690°C to 450°C under water cooling at a rate of 10°C/s (same as schedule 1) before being air cooled to room temperature.

Table 5.6: Schedule 3 rolling parameters.

Schedule 3	**Temperature** $°C$	t_i mm	t_f mm	**Reduction** %	**Length** mm	**Cooling Rate** $°C/s$	**Medium**
Rough Rolling:	1125-1010	20	14	30	263		
Finish Rolling:	860-690	14	10.36	26	355		
	860-690	10.36	8.2	20.5	446		
	860-690	8.2	7	15	525		
Cooling:	690-450					$\sim 1°C$	Water
	450-RT					$\sim 1°C$	Air

Rolling Schedule Summary

A rolling schedule diagram is presented in Figure 5.26. Rolling start and finish temperatures are represented by the diagonal lines along the temperature plot with rough

rolling beginning from 1180°C (Schedules 2 and 3 begin rough rolling at 1125°C) and finish rolling starting at 860°C. The diagram clearly shows the different rolling regimens of the three rolling schedules based on the start and finish temperatures. Schedule 1 was rolled at temperatures above the empirically calculated T_{NR} to ensure only recrstallization textures would develop. Schedule 1 was cooled to 785°C in air prior to water cooling to align Schedule 1 with the other two schedules.

Schedule 2 was rough rolling above the T_{NR} and finish rolling below T_{NR} to ensure deformed austenite textures would form upon transformation, differentiating it from Schedule 1. Schedule 3 was rough rolled above the T_{NR} and finish rolled in the two-phase region such that both deformed austenite and deformed ferrite textures would develop upon transformation.

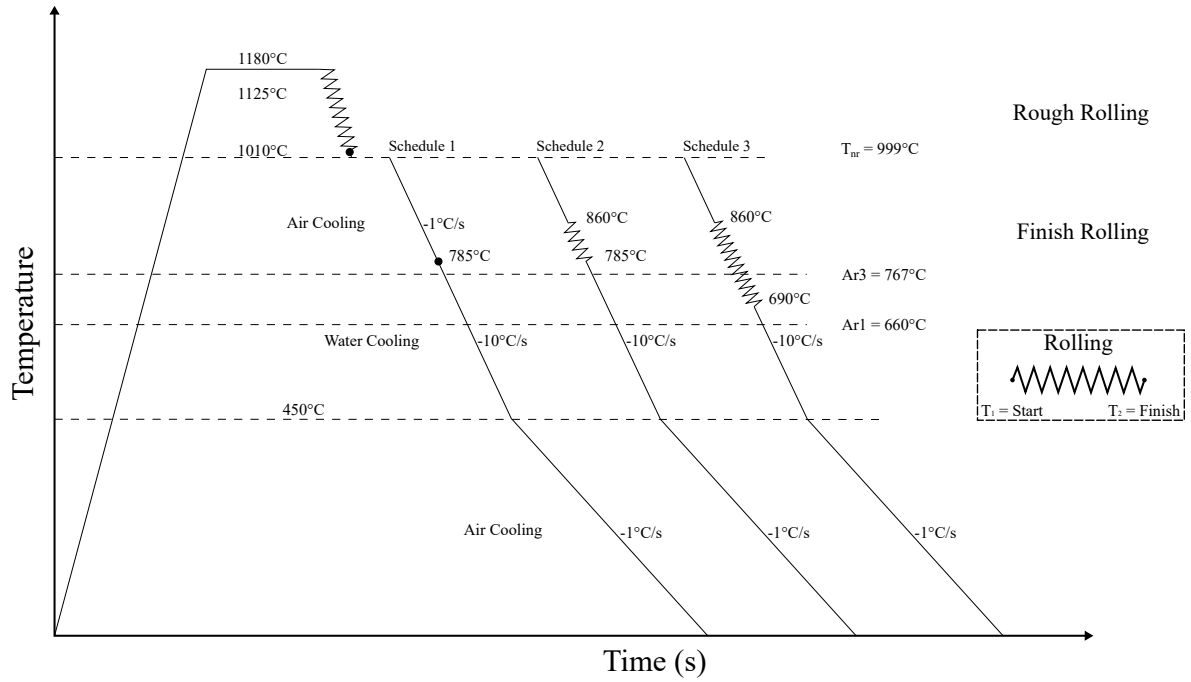

Figure 5.26: Summary of the rolling schedules.

5.3 Rolling Results

Once the samples were rolled the microstructure and mechanical properties were investigated to determine the effect of the rolling process. This section investigates the effect the

different rolling schedules had on the through-thickness microstructure development and compares them to the industry supplied samples. Following this the mechanical properties including through-thickness hardness and tensile strength were investigated and compared with the industry supplied materials.

5.3.1 Temperature Observations of Rolled Material

Controlled rolling was carried out on the as-received 20 mm X70 plates applying the designed schedules with the temperatures and rolling reductions recorded. The rolling temperature for each pass was recorded on pyrometers attached to the rolling mill entrance and exit, Table 5.7. The results were within the temperature range specified by the desired rolling schedules with only slight deviations. In Schedule 1, the initial temperature of Pass 1 and Pass 3 were noted to be significantly lower than the required value. This is because a thick surface scale developed during soaking of the as-received 20 mm X70 plates, despite a high ($> 15L/min$) nitrogen purge. The scale interfered with the ability of the pyrometer to accurately measure the surface temperature due to the non-contact nature of IR pyrometers. Scale build-up was alleviated by knocking the scale off the material prior to rolling where possible, however, the temperature drop was rapid after exiting the furnace so if the scale was not removed after two attempts, the samples were rolled regardless of scale. Rolling removed scale from the surface which allowed the exit temperature to be accurately determined. When scale was not adhered to the sample surface, the exit temperature was lower than the entrance temperature. The typical temperature drop was observed to be less than 100°C, hence, it is expected that the initial temperature of Schedule 1 was within the required range despite the temperature not being accurately measured.

In Schedule 2 and 3, whilst some temperature passes caused the temperature to drop below the specified temperatures range at the exit, the accuracy of the pyrometer was approximately ±2% so the deviation was within the allowable range for the measurement

equipment. In addition, as the rolled material was placed inside the intermediate furnace between passes, the temperature drop was temporary and heated to within the required range before subsequent passes.

Table 5.7: Rolling schedule temperature results.

Schedule 1	**Entrance Temperature**	**Exit Temperature**	**Final Thickness**	**Cooling Rate**
Pass 1	$852°C$ (surface scale)	$1079°C$	17	
Pass 2	$1046°C$	$1032°C$	13.6	
Pass 3	$995°C$ (surface scale)	$1102°C$	10.2	
Pass 4	$1145°C$	$1080°C$	7	
Cooling	$770°C$	$403°C$	7	$11.5°C/s$
Schedule 2	**Entrance Temperature**	**Exit Temperature**	**Final Thickness**	**Cooling Rate**
Pass 1	$1145°C$	$1113°C$	17.5	
Pass 2	$860°C$	$816°C$	12.2	
Pass 3	$778°C$	$774°C$	9.2	
Pass 4	$791°C$	$781°C$	7	
Cooling	$770°C$	$449°C$	7	$10°C/s$
Schedule 3	**Entrance Temperature**	**Exit Temperature**	**Final Thickness**	**Cooling Rate**
Pass 1	$1004°C$	$1102°C$	14	
Pass 2	$724°C$	$738°C$	10.4	
Pass 3	$760°C$	$773°C$	8.2	
Pass 4	$697°C$	$691°C$	7	
Cooling	$720°C$	$464°C$	7	$10.7°C/s$

5.3.2 Microstructural Characterisation

The laboratory rolled samples (Schedules 1, 2 and 3) were sectioned from one quarter of the plate width for consistency and to ensure any edge effects from rolling were avoided. The samples were then mounted both longitudinal (LRD) and transverse (TRD) to the rolling direction for microstructure investigation. Microscopic analysis was undertaken to determine what microstructures developed during rolling. Samples were polished per

the procedure outlined in Section 4.4.1 and examined at the surface, quarter and the centre planes. Laboratory rolled samples were compared to industry supplied samples to compare microstructure with those currently used in industry.

Schedule 1

Through-thickness microstructure of samples manufactured though Schedule 1 are presented in Figure 5.27. As seen in Figure 5.27a and Figure 5.27b, some decarburisation and oxidation of the steel is present near the surface. Despite a nitrogen purge during soaking and between passes, the high temperature of the soaking furnace appears to have caused some decarburisation. The microstructure near the surface consists of granular bainite with an overall grain size of approximately 20 μm. The microstructure at quarter thickness in Figure 5.27c and Figure 5.27d, is equiaxed and contains a mixture of upper bainite and granular bainite. The microstructure at the centre plane in Figure 5.27e and Figure 5.27f, is similar to that of the quarter plane, with no discernible change in grain size or microstructure identified. The grain sizes at the quarter and centre planes are larger than those observed at the surface. The cause for the smaller grain size at the surface may be due to the faster cooling rate experienced at the surface as compared to the quarter and centre planes. Slower cooling rates allows more time for grain growth, both prior to and after phase change, hence, the slower cooling rate at the quarter and centre planes result in larger grain sizes. The equiaxed grains observed in Schedule 1 is due to the rolled sample being processed entirely above T_{NR}. Above T_{NR}, complete static recrystallization of deformed austenite after rolling passes occurs and equiaxed, recrystallized grains form. Upon cooling, as ferrite grains typically nucleate at prior austenite grain boundaries, the equiaxed austenite grains give rise to equiaxed bainitic grains.

The microstructure observed in Schedule 1 is significantly different compared to the industry supplied samples, with regards to both grain size and phases that are present. With regards to microstructure, deformation below the T_{NR} likely occurred in the indus-

try supplied samples, resulting in pancaking of prior austenite grains and higher grain boundary area. The higher grain boundary area produces smaller transformed grains as more grains nucleate [222]. The microstructure observed in the industry supplied samples was granular bainite and polygonal ferrite whilst the microstructure of Schedule 1 consisted of granular bainite and upper bainite. The difference in microstructure was likely due to the industry supplied samples being finish rolled in a different temperature range compared to Schedule 1. Increasing the levels of strain in austenite below the T_{NR} results in enhanced ferrite nucleation rate and expands the cooling rates over which it can form [222]. The lack of deformation below the T_{NR} in Schedule 1 is the reason for the difference in microstructure compared to the industry supplied samples.

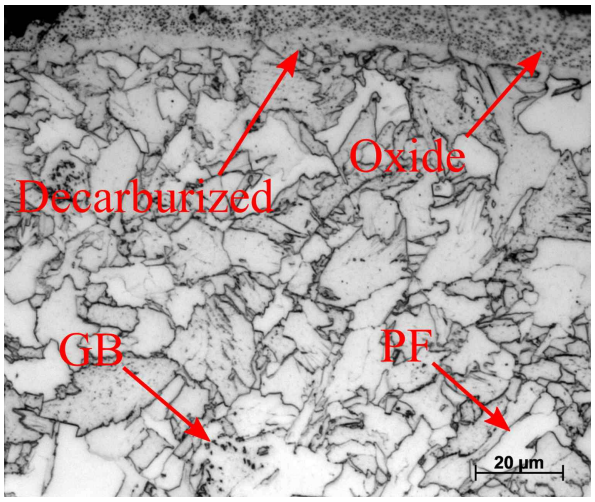

(a) Schedule 1 surface 1000x LRD.

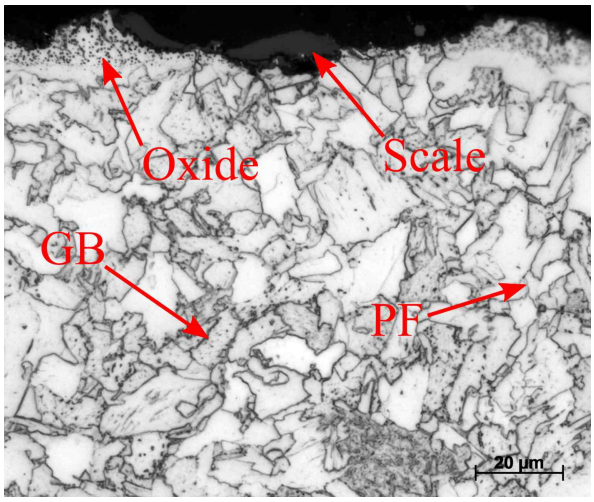

(b) Schedule 1 surface 1000x TRD.

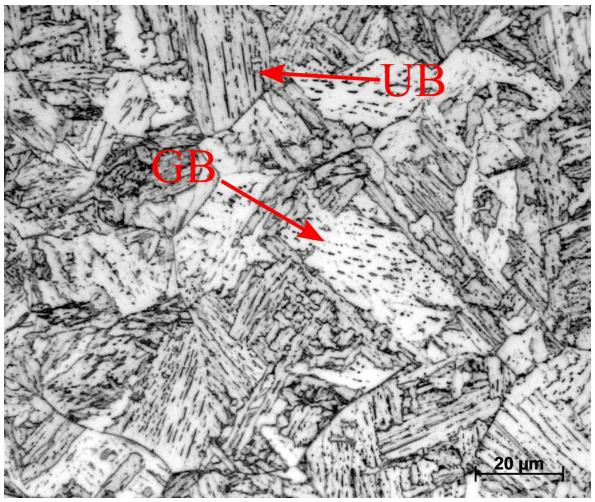

(c) Schedule 1 quarter 1000x LRD.

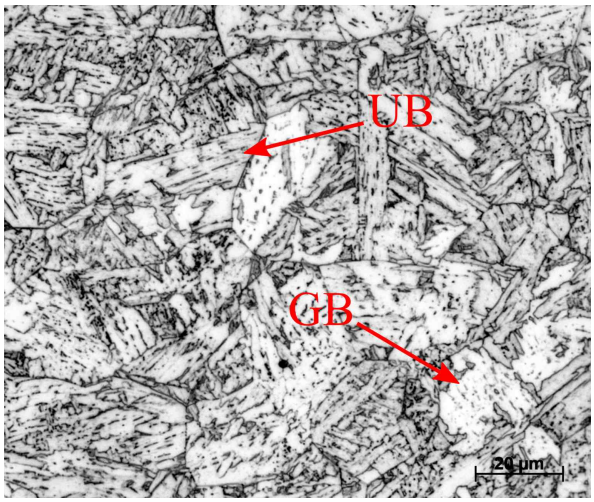

(d) Schedule 1 quarter 1000x TRD.

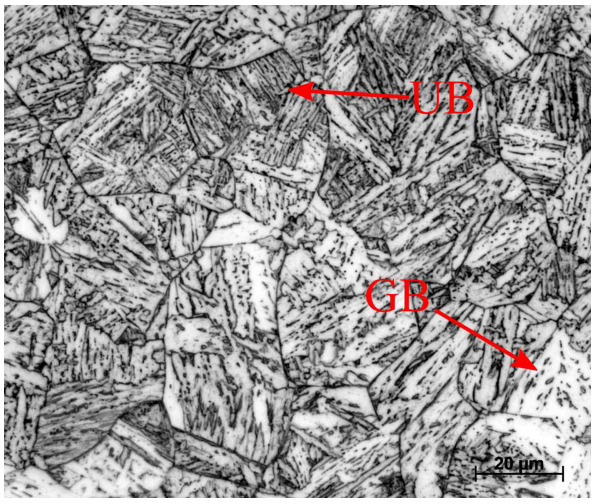

(e) Schedule 1 centre 1000x LRD.

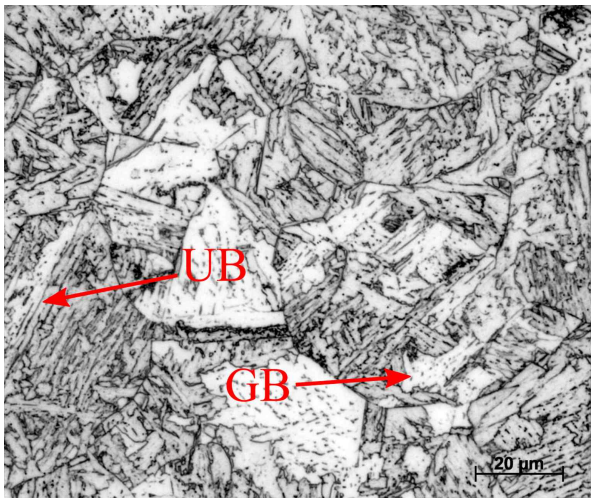

(f) Schedule 1 centre 1000x TRD.

Figure 5.27: Through-thickness optical microstructure of Schedule 1.

SEM Microscopy

An analysis of microstructures present in Schedule 1, are presented in Figure 5.28. An optical image of the investigated section is presented in Figure 5.28a and shows the primarily granular and upper bainite microstructure produced from Schedule 1 rolling. Three circled sections are viewed using secondary electron SEM to classify the microstructures present. The phase identified in Figure 5.28b was M-A constituent, present between ferrite laths. As laths are present, the microstructure of this location can be considered degenerate upper bainite as classified by Zajac et al. (2005) [125]. Granular bainite was identified in Figure 5.28c as the M-A constituents were present within the large ferrite grain, typical of classic granular bainite. In Figure 5.28d upper bainite is the dominant microstructure, identified by cementite particles between distinct ferrite laths.

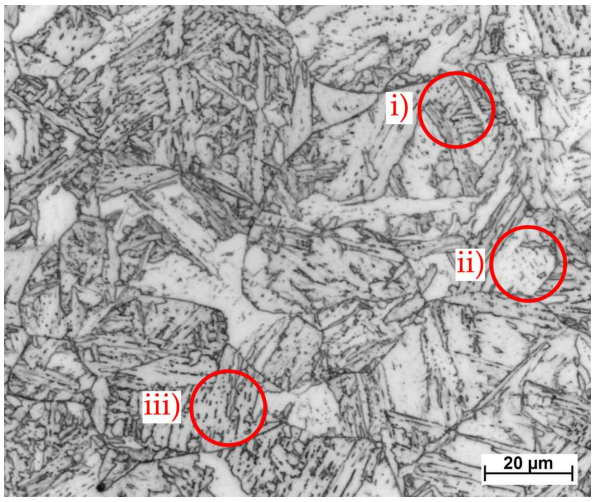

(a) Schedule 1 optical.

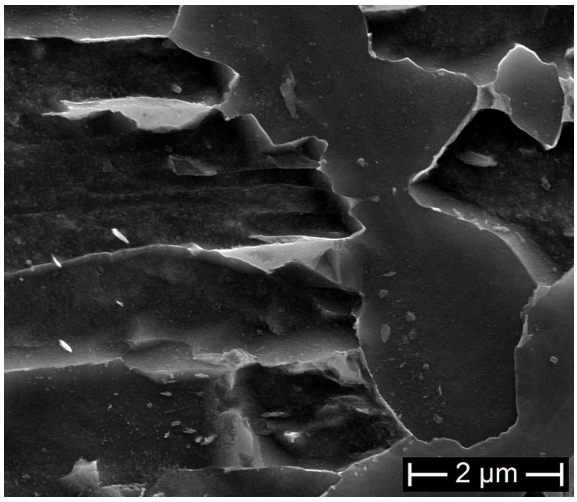

(b) Location i: M-A.

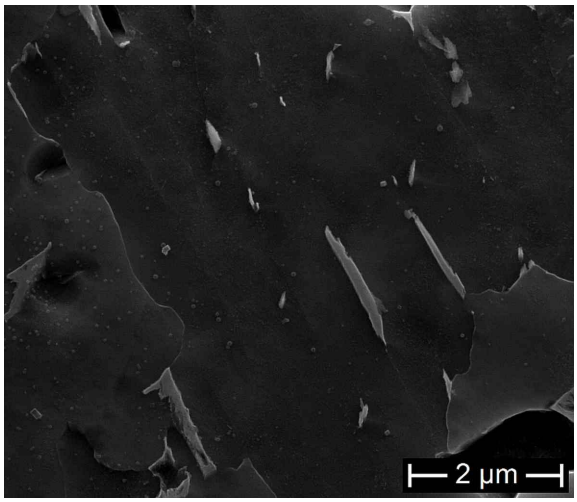

(c) Location ii: GB.

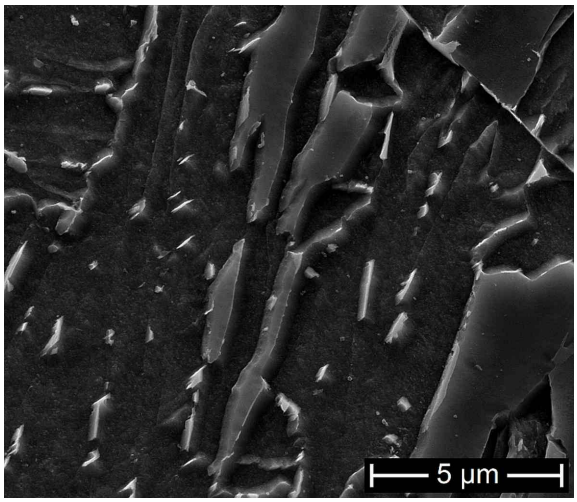

(d) Location iii: UB.

Figure 5.28: SEM micrographs of the dark regions in (a) present in Schedule 1 (LRD).

Schedule 2

The through-thickness microstructure of samples produced though Schedule 2 is presented in Figure 5.29. In Figure 5.29a and Figure 5.29b, similar to Schedule 1, there is some degree of decarburisation and oxidation at the surface of samples produced through Schedule 2. The level of decarburisation in Schedule 2 is lower than in Schedule 1, likely due to the lower finish rolling temperatures. The surface microstructure observed in Figure 5.29a and Figure 5.29b, consists of primarily polygonal ferrite with sparse instances of granular bainite. The microstructure at the quarter plane, Figures 5.29c and 5.29d, is very similar to the X70 microstructures seen in the industry supplied 6.4 mm X70 plate,

10 mm X70 pipe and initial 20 mm X70 plate, observed in Figures 5.2, 5.7 and 5.11 respectively. When compared to the surface, the grain size of the quarter plane appears to be coarser with a higher proportion of granular bainite. The microstructure in the centre plane, Figures 5.29e and 5.29f, is similar to that of the quarter plane and is composed of primarily granular bainite with some instances of polygonal ferrite. The LRD direction, Figure 5.29e, has a larger grain size than the TRD direction, Figure 5.29f, although both orientations show larger grain sizes than both the quarter plane and surface.

The microstructure of this schedule consists of primarily polygonal ferrite and granular bainite at the quarter plane. Whilst the CCT diagram determined that granular bainite and upper bainite would form at a continuous cooling rate of 10°C/s, the appearance of polygonal ferrite is not unexpected. As the CCT diagram was produced without straining the sample prior to cooling, it could not reproduce the impact strain accumulations would have on microstructure development. As discussed by Cizek et al. (2015) [222], strain accumulation in the austenite, results in enhanced ferrite nucleation upon cooling and expands the cooling rates over which it can form. This is the likely reason polygonal ferrite exists in this rolling schedule despite being cooled at a rate that should preclude it. The elongation and refinement of the microstructure is again likely due to pancaking of the austenite prior to transformation. Pancaking of the microstructure results in a larger grain boundary area and more initiation sites for new phases to nucleate [226]. The difference in phases present at the surface compared to the quarter and centre planes is likely due to the carbon content deficit at the surface due to decarburisation and oxidation. The altered chemical composition of the steel at the surface would likely alter the transformation behaviour.

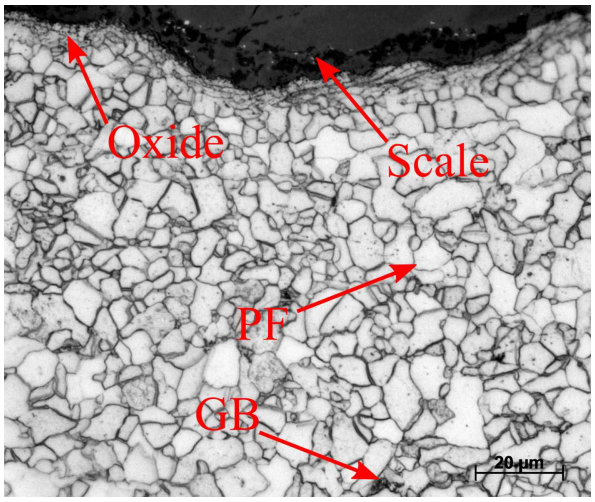

(a) Schedule 2 surface 1000x LRD.

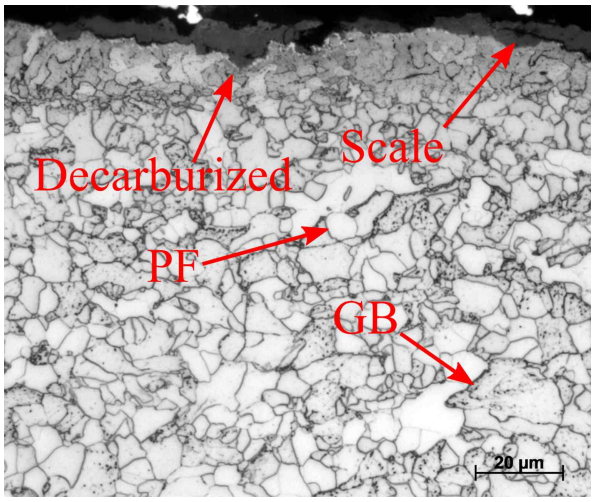

(b) Schedule 2 surface 1000x TRD.

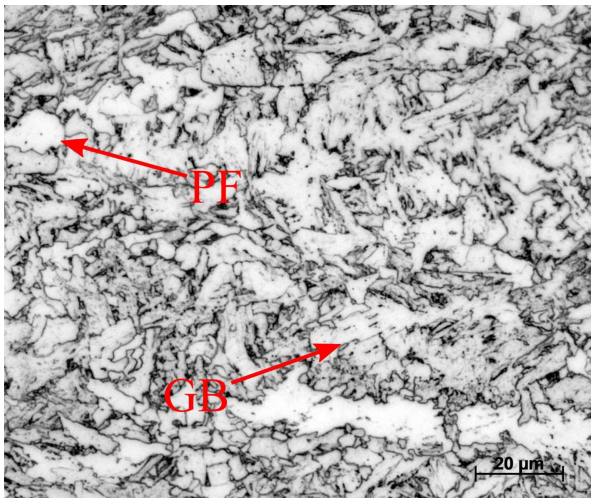

(c) Schedule 2 quarter 1000x LRD.

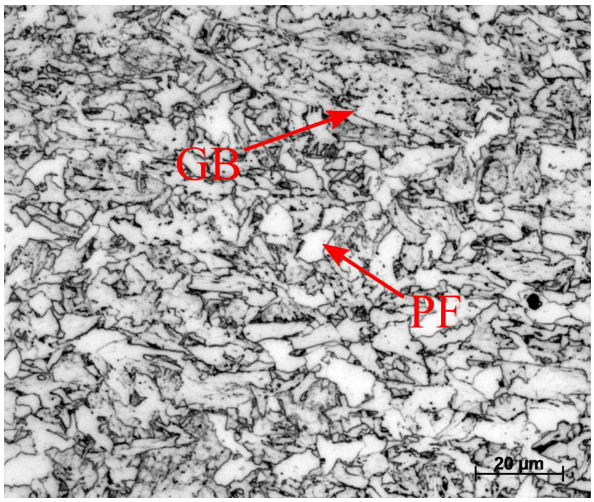

(d) Schedule 2 quarter 1000x TRD.

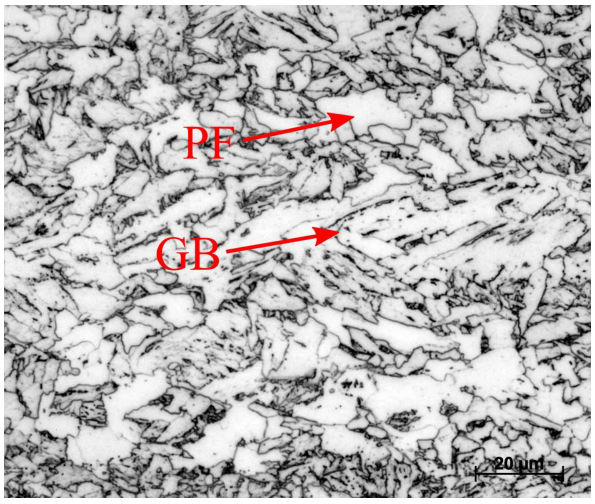

(e) Schedule 2 centre 1000x LRD.

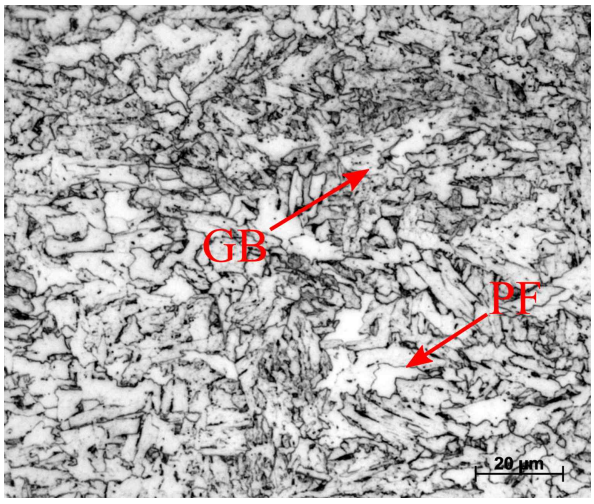

(f) Schedule 2 centre 1000x TRD.

Figure 5.29: Through-thickness optical microstructure of Schedule 2.

SEM Microscopy

SEM investigation of Schedule 2 was undertaken to determine the microstructure of finer phases not able to be distinguished through optical means, Figure 5.30. An optical overview of the microstructure in question is presented in Figure 5.30a with areas of interest circled and labelled. The dark secondary phase identified in Location i in Figure 5.30b, appears to be primarily M-A constituent although there is some cementite debris present on the side of the grain, indicative of partial transformation from the carbon enriched austenite. Location ii, in Figure 5.30c, appears to show both an M-A constituent and a small region of degenerate pearlite. As both inclusions are within a ferrite grain, it would be classified as granular bainite [125]. Location iii, in Figure 5.30d, has the same morphology as Location ii, and shows a granular bainite grain with secondary phases of M-A constituent and degenerate pearlite.

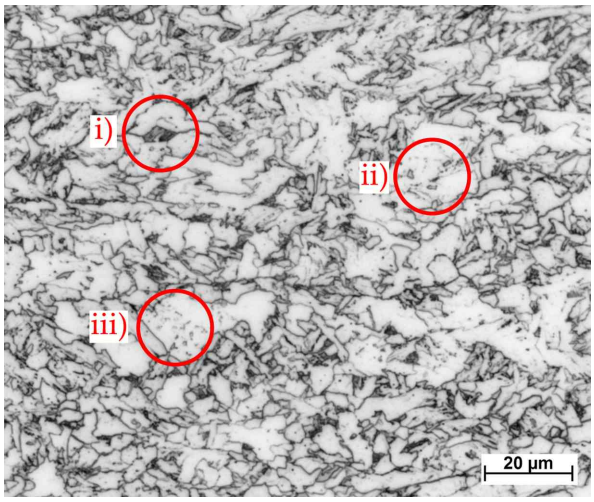

(a) Schedule 2 optical.

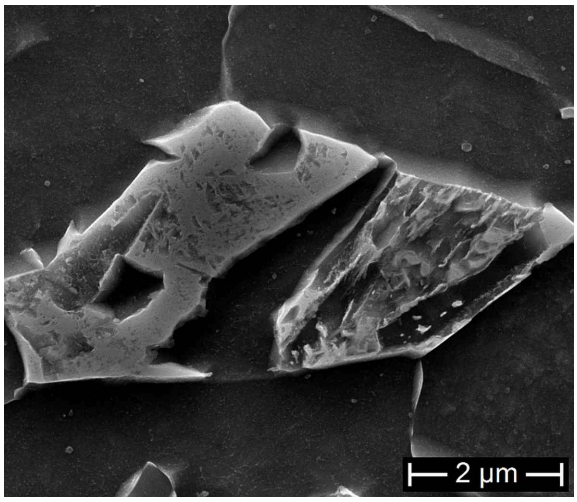

(b) Location i: M-A constituent.

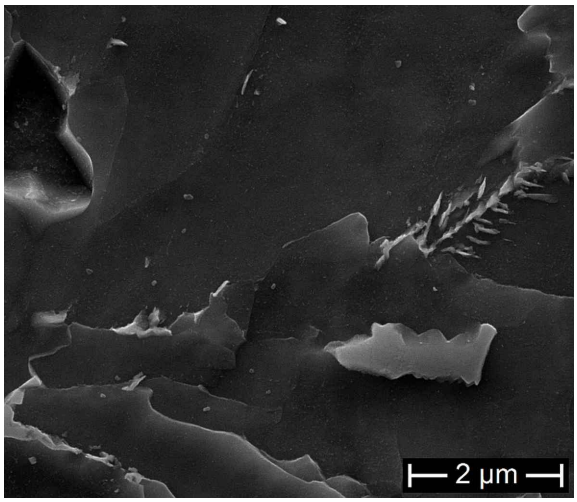

(c) Location ii: GB and DP.

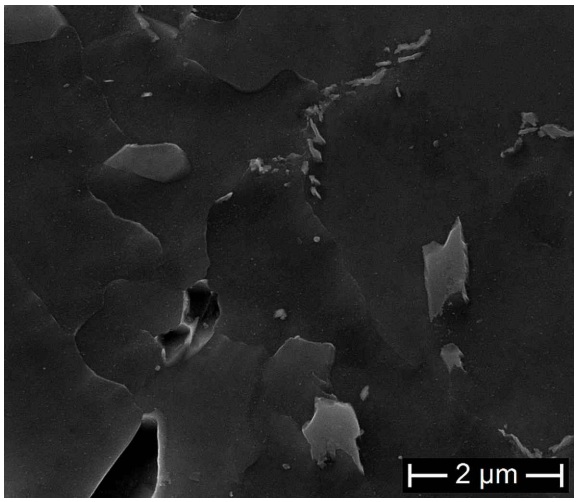

(d) Location iii: GB and DP.

Figure 5.30: SEM micrographs of the dark regions in (a) present in Schedule 2 (LRD).

Schedule 3

The through-thickness microstructure of Schedule 3 is presented in Figure 5.31. As seen in Figure 5.31a and Figure 5.31b, decarburisation and heavy oxidation of the steel is present at the surface of Schedule 3. The surface microstructure consists of ferrite and granular bainite with no consistent grain size. Observe the localised massive ferrite grains at the surface in Figure 5.31a. The microstructure of the quarter plane in Figure 5.31c and Figure 5.31d, is predominantly ferrite and granular bainite, similar to that observed at the surface, however, the grain size is more uniform with higher proportions of dark etching secondary phases. The microstructure observed at the centre plane in Figure 5.31e and

Figure 5.31f, consists of predominantly ferrite and granular bainite, similar to that observed at the quarter plane, however, there appears to be a higher proportion of polygonal ferrite at this depth as compared to the quarter plane. The microstructure produced is dissimilar to those of the industry supplied X70 samples in Figures 5.2, 5.7 and 5.11 due to the higher polygonal ferrite concentration, likely due to the difference in finish rolling temperature.

There is a significantly higher proportion of polygonal ferrite in Schedule 3 compared to the industry supplied samples in Figures 5.2, 5.7 and 5.11, and even Schedules 1 and 2 in Figures 5.27 and 5.29. One possible reason for this is the high levels of deformation undertaken just above the transformation temperature. Substructures of deformed austenite retard bainite transformation by impeding the growth of ferritic laths. As deformation of austenite occurred within the temperature range where austenite and ferrite existed, any residual austenite would be further deformed during transformation, further retarding bainite growth [227, 228]. While the microstructure is not found in industry supplied samples, studies of laboratory rolled X70, under similar conditions have produced steel containing primarily polygonal ferrite structures as observed in Schedule 3 [211].

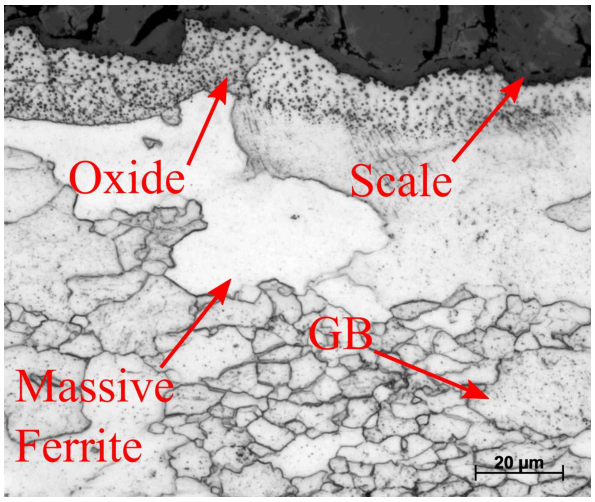

(a) Schedule 3 surface 1000x LRD.

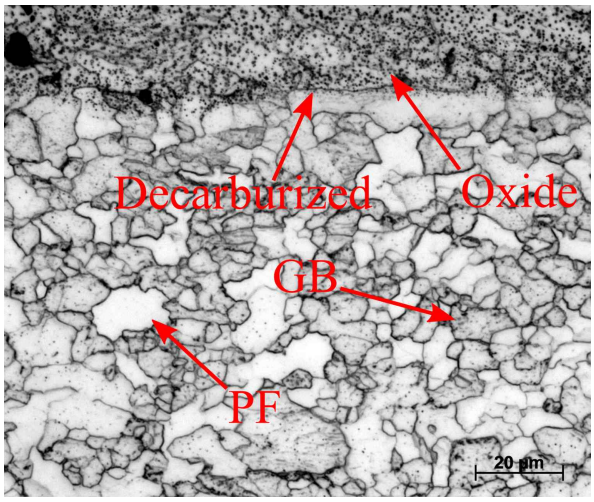

(b) Schedule 3 surface 1000x TRD.

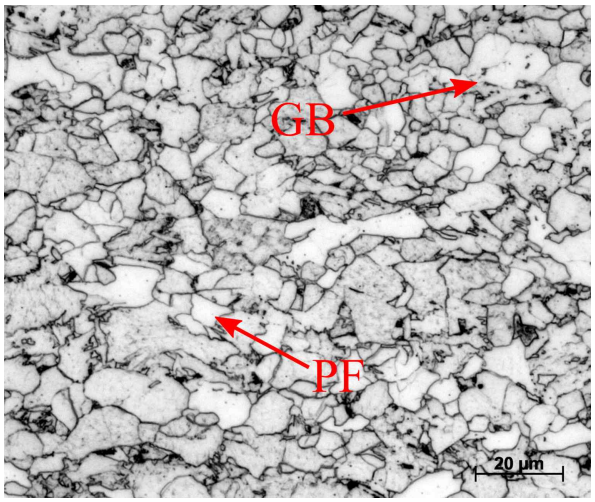

(c) Schedule 3 quarter 1000x LRD.

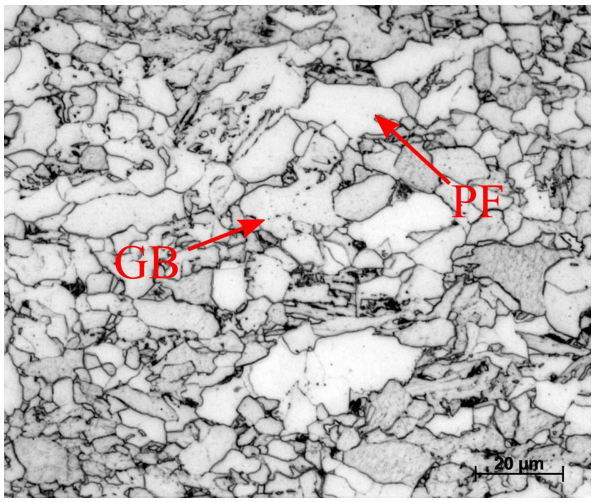

(d) Schedule 3 quarter 1000x TRD.

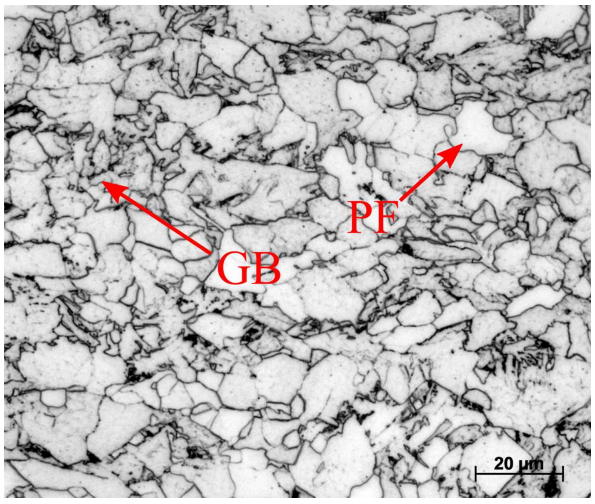

(e) Schedule 3 centre 1000x LRD.

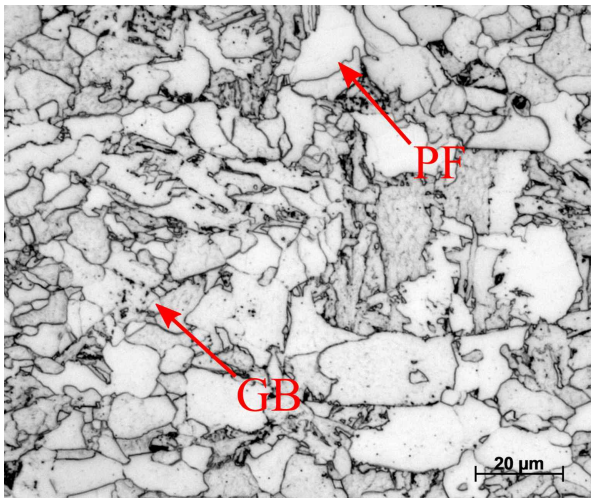

(f) Schedule 3 centre 1000x TRD.

Figure 5.31: Through thickness optical microstructure of Schedule 3.

SEM Microscopy

Selected SEM micrographs of Schedule 3 were taken to determine the microstructure of finer phases not able to be determined through optical means, presented in Figure 5.32. An optical overview of the microstructure is presented in Figure 5.32a with areas of interest circled and labelled. The secondary phase identified in Location i in Figure 5.32b appears to be a mixture of degenerate pearlite and M-A constituents. As explained previously, the degenerate pearlite forms from carbon enriched austenite retained after transformation. The secondary phase identified in Location ii in Figure 5.32c, shows islands of M-A constituents within a large ferrite grain so the overall grain is classified as granular bainite [125]. The secondary phase identified in Location iii, Figure 5.32c, is the same as that found in Location i, degenerate pearlite growing from M-A constituent. The overall grain appears to be granular bainite as classified by Zajac et al. (2005) [125] where granular bainite can contain a variety of secondary phases.

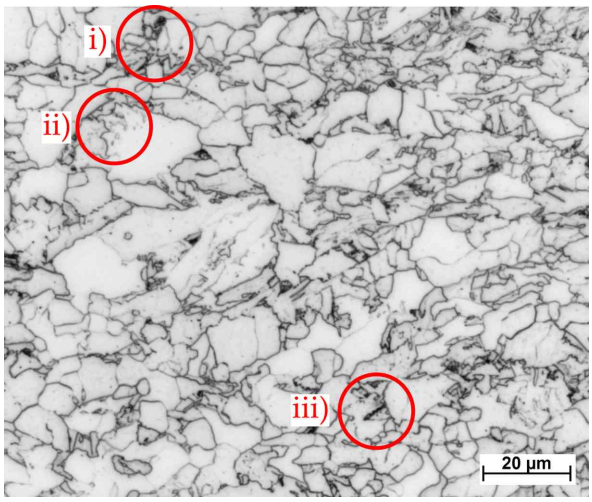

(a) Schedule 3 optical.

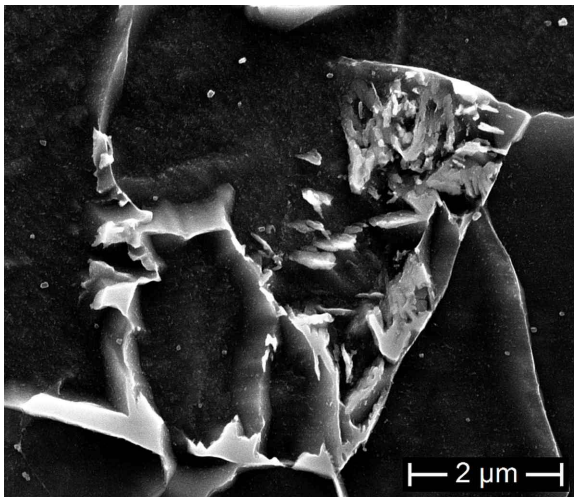

(b) Location i: DP.

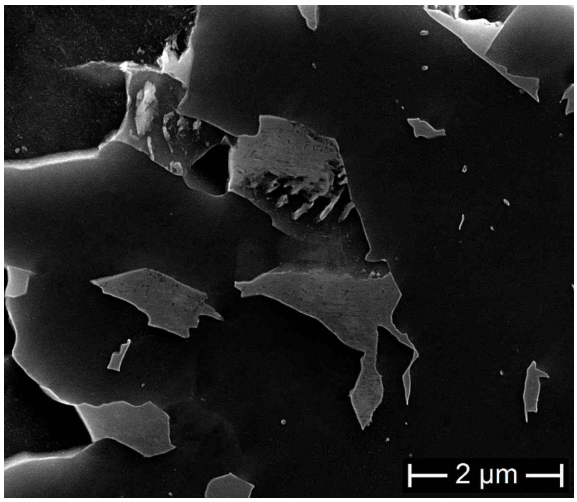

(c) Location ii: GB.

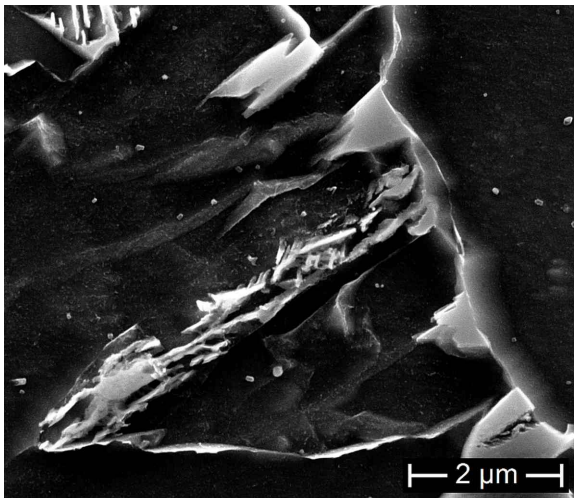

(d) Location iii: M-A consitituent and DP.

Figure 5.32: SEM micrographs of the dark regions in (a) present in Schedule 3 (LRD).

Summary of Microstructural Characterisation

When comparing the microstructure of the laboratory rolled samples with the industry supplied samples, it is evident that while similar, there were some distinct differences between them. In terms of microstructure, Schedule 2 was the closest approximation of the industry supplied X70 microstructure. Schedule 2 contained a primarily granular bainite and polygonal ferrite microstructure, akin to the industry supplied samples, albeit coarser. Industrially rolled X70 steels are typically finish rolled above the Ar3 temperature (hot rolling regimen) as it results in lower roll pressures and can produce steel with the desired mechanical properties [138, 211, 229]. Warm rolling in conjunction with different cooling

rates can produce pipeline steels for certain applications, although, some properties, such as low temperature impact toughness, were degraded with warm rolling schedules [138, 230]. Recrystallization rolling tended to be used as a comparison with more standard rolling processes in manufacturing literature due to its simplicity as a rolling schedule [137, 180].

The overall grain size of the laboratory rolled samples are significantly higher than those found in the industry supplied samples. This can be attributed to the reheating temperature and time. As the initial material thickness was only 20 mm, there was insufficient thickness to carry out austenite refinement through successive rough rolling passes. To develop finer grain sizes, a shorter soaking time could have been utilized to produce finer prior austenite grain sizes. The risk to shorter soaking times is the presence of undissolved, non-metallic precipitates influencing rolling. As laboratory rolling was intended to develop different textures, slightly large grain sizes were not a large concern provided it was consistent between rolling schedules. The microstructures developed in the three schedules were a by-product of requiring three different textures to be produced through control rolling so as they are all similar, they achieve their purpose.

5.3.3 Hardness Testing

The through-thickness hardness of the samples rolled under each schedule were carried out in the TRD plane from 500 μm below the top surface to the bottom surface in increments of 500 μm.

Schedule 1

The micro Vickers hardness of Schedule 1 is presented in Figure 5.33. Schedule 1 has the highest hardness of the three schedules with an average hardness of 235 $\pm$ 11 HV0.5 and a peak hardness of 248 HV0.5. The hardness of the samples rolled by Schedule 1 has two

main peaks located approximately 2 mm from each surface with a dip in hardness at the centre. The high hardness of schedule 1 is due to the high proportion of upper bainite present that has a higher hardness than granular bainite and ferrite found in Schedule 2 and 3. The hardness at the bottom of the plate is significantly lower than the hardness at the top of the plate. This may be attributed to the runout table cooling the top at a higher rate than the bottom. The initial material did not experience a difference in hardness from the top to the bottom so it is likely that the difference is the result of the rolling process.

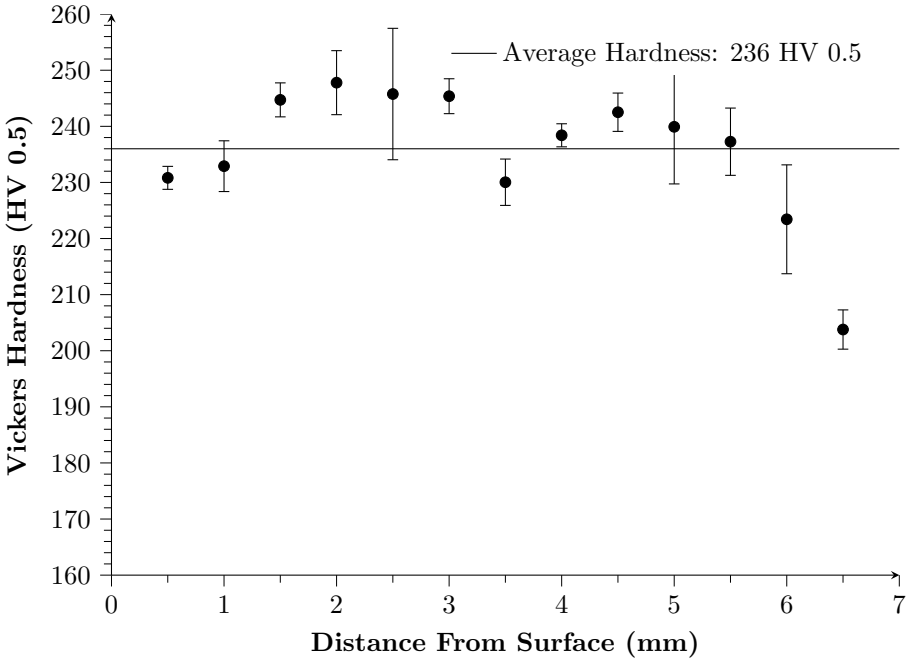

Figure 5.33: Through-thickness hardness of Schedule 1.

Schedule 2

The hardness observed in Schedule 2 in Figure 5.34 is the second highest of the three rolled schedules with an average of 190 ± 9 HV0.5 and a peak hardness of 202 HV0.5 1.5 mm below the top surface of the plate. The microhardness initially increases from the top surface towards the centre where it levels off until it reaches the centre. Beyond the centre, the hardness decreased with the bottom 2 mm softer than the surface. This phenomenon is likely due to differences in water spray at the top and bottom of the runout

table that cooled the plate unevenly.

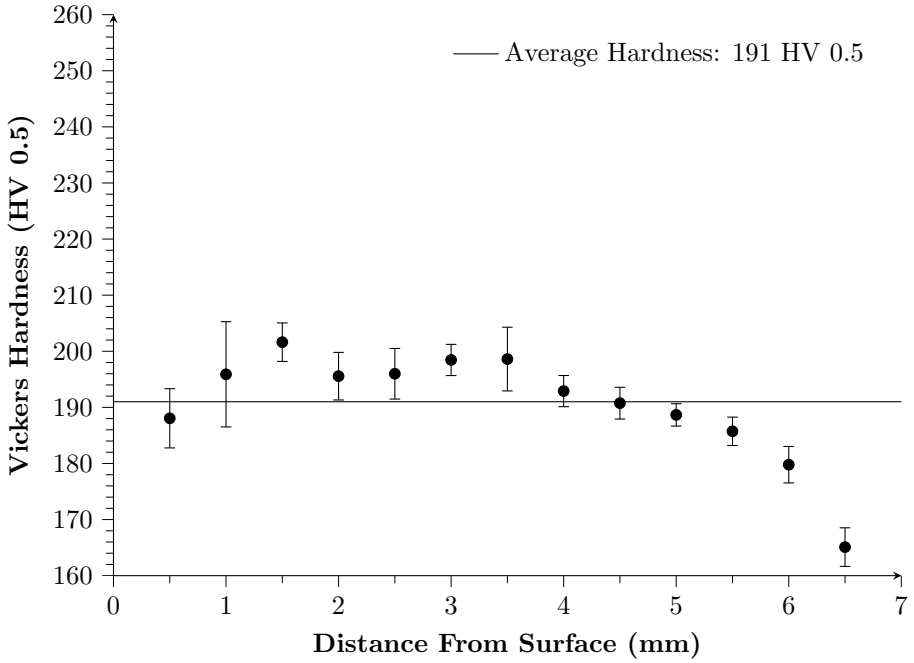

Figure 5.34: Through-thickness hardness of Schedule 2.

Schedule 3

The hardness observed in Schedule 3 in Figure 5.35 is the softest of the three rolled schedules with an average hardness of 175 ± 3 HV0.5 and a peak hardness of 179 HV0.5, 2 mm below the top surface of the plate. No strong trends in the hardness of Schedule 3 were observed, with the hardness is relatively consistent through-thickness. Whilst there is a slight dip in hardness at the bottom surface of the rolled plate, the overall low hardness is not dramatically influenced by it. The low uniform hardness in Schedule 3 was likely due to samples manufactured through Schedule 3 having a higher proportion of ferrite in the microstructure, Figure 5.31, which is less impacted by cooling rate than bainite.

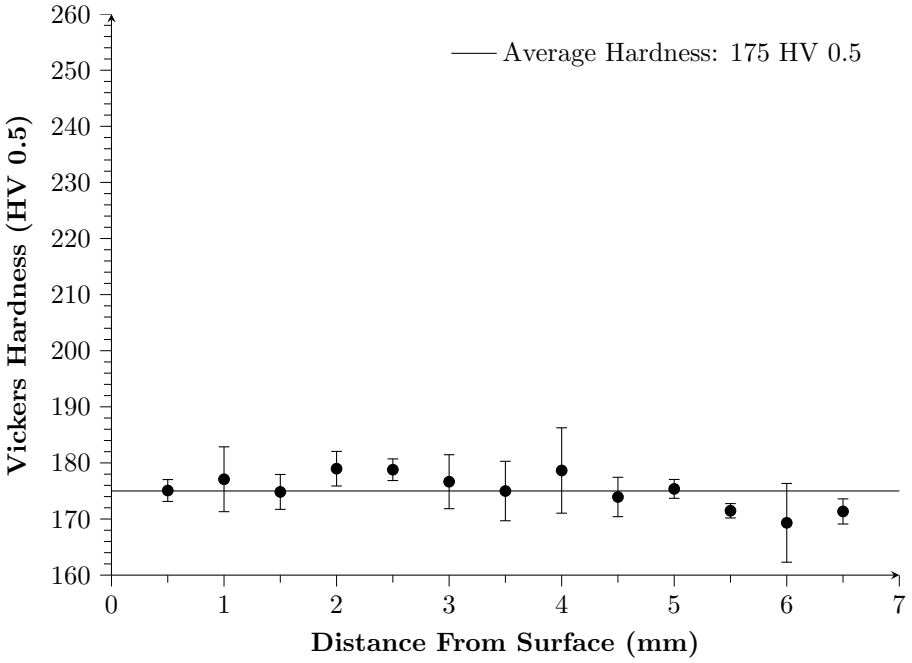

Figure 5.35: Through-thickness hardness of Schedule 3.

Summary of Hardness Testing

The reason for differences in average hardness between Schedules 1-3 is due to microstructural differences. Upper bainite tends to have a much higher hardness compared to granular bainite and polygonal ferrite due to the very hard cementite particles present within upper bainite grains. Whilst M-A constituents have very high hardnesses akin to cementite, they are more dispersed within granular bainite and have less impact on the overall hardness of the microstructure than cementite laths in upper bainite [231].

In the laboratory rolled samples the hardness tended to drop from the upper surface towards the lower surface in part due to the uneven cooling from the runout table of the laboratory rolling mill. Schedule 2 had the closest average hardness to the industry supplied samples at 190 ± 9 HV0.5 compared to 198 ± 2.4 HV0.5, 221 ± 4.7 HV0.5 and 202 ± 3 HV0.5 of the 20 mm X70 plate, 10 mm X70 pipe and 6.4 mm X70 plate, respectively. This is expected because the microstructure of Schedule 2 was most similar to the the industry supplied samples. The lower hardness can likely be explained by the larger grain size observed in Schedule 2 compared with the industry supplied samples.

5.3.4 Tensile Properties

The tensile properties of the laboratory rolled samples and the industry supplied samples were measured on subsize specimens, according to ASTM E-8 [203], to keep results consistent and avoid comparing different size test specimens. Tensile testing was conducted in three different orientations for each of the analysed specimens, the LRD (0°), 45° to the rolling direction and TRD (90°) such that anisotropy in the steel could be evaluated. The 10 mm X70 was the only exception as it was a pipe and hence, the curvature did not allow for samples to be sectioned from orientations other than the LRD (0°) without flattening the pipe.

The maximum allowable thickness of ASTM E8 [203] subsize specimens was 6 mm hence, all samples were machined to the maximum allowable thickness. The laboratory rolled specimens and the 6.4 mm X70 plate were essentially through-thickness specimens with surface removal occurring symmetrically on both sides. The tensile test pieces for the as-received 20 mm X70 plate were machined from the quarter thickness as it had the most representative microstructure. The 10 mm pipe was sectioned as close to the quarter thickness plane as possible whilst eliminating curvature from the surface. A table of results is presented in Table 5.8 where standard properties governed by the API 5L standard [27] were compared to see how the schedules compared to industry supplied samples and industry requirements. A graph showing the 0° stress-strain curves of the industry supplied and laboratory rolled samples is presented in Figure 5.36.

Table 5.8: Combined tensile properties of industry supplied and laboratory rolled samples.

Sample		$\sigma_{0.5\%}$ **(MPa)**	**UTS (MPa)**	$\sigma_{0.5}$ **/ UTS**	**EL (%)**	**uEL (%)**
20 mm	0°	499.3 ± 4.3	627.5 ± 6.9	0.80 ± 0.007	28.0 ± 0.22	13.3 ± 0.11
	45°	495 ± 3.7	622.5 ± 8.3	0.80 ± 0.012	27.7 ± 0.25	13.1 ± 0.12
	90°	543.8 ± 1.2	649.5 ± 0.5	0.84 ± 0.003	27.0 ± 0.12	11.9 ± 0.01
10 mm	0°	616.7 ± 5.6	649.4 ± 4.1	0.95 ± 0.003	23.6 ± 0.9	7.4 ± 0.2
6.4 mm	0°	555.7 ± 4.9	623.9 ± 1.8	0.89 ± 0.01	26.5 ± 1.0	10.1 ± 0.3
	45°	557.8 ± 3.3	610.3 ± 2.4	0.91 ± 0.002	28.4 ± 0.1	10.3 ± 0.01
	90°	590.0 ± 4.8	651.8 ± 3.8	0.91 ± 0.002	26.8 ± 0.2	9.1 ± 0.1
Schedule 1	0°	559.6 ± 8.4	715.3 ± 11.9	0.78 ± 0.006	17.7 ± 1.2	5.4 ± 0.6
	45°	555.4 ± 18.8	716.1 ± 13.1	0.78 ± 0.01	20.4 ± 1.2	6.9 ± 0.8
	90°	543.7 ± 1.8	702.0 ± 13.4	0.77 ± 0.01	18.1 ± 0.6	5.3 ± 0.5
Schedule 2	0°	409.8 ± 20.5	569.8 ± 13.4	0.72 ± 0.02	27.1 ± 0.3	12.9 ± 0.1
	45°	416.1 ± 0.1	576.3 ± 5.8	0.72 ± 0.01	27.2 ± 0.2	12.5 ± 0.5
	90°	409.7 ± 4.4	558.5 ± 1.7	0.73 ± 0.006	28.2 ± 0.5	13.1 ± 0.1
Schedule 3	0°	377.6 ± 12.5	540.2 ± 1.9	0.70 ± 0.02	29.5 ± 0.1	16.7 ± 0.5
	45°	377.3 ± 3.5	535.9 ± 2.5	0.70 ± 0.01	29.4 ± 0.1	16.7 ± 0.3
	90°	386.1 ± 10.5	559.9 ± 3.6	0.69 ± 0.01	28.3 ± 0.8	15.8 ± 0.9

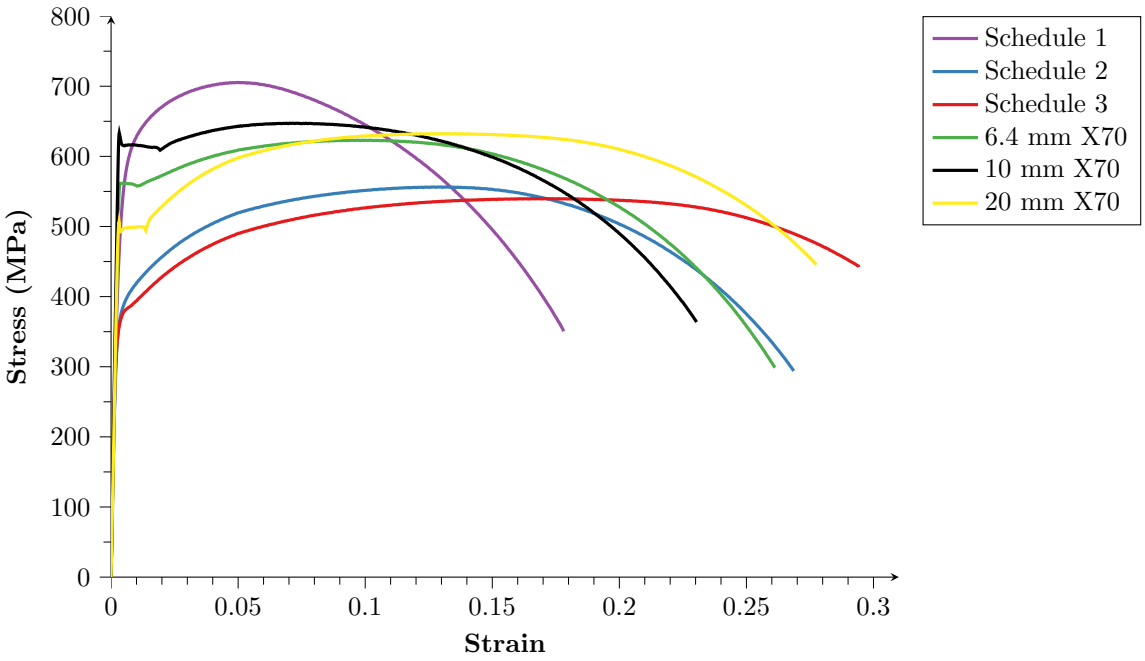

Figure 5.36: Combined 0° stress vs. strain graphs of the industry supplied and laboratory rolled samples.

0.5% Yield

In order to standardise the determination of the yield point in materials that don't have well defined yield points, arbitrary limits are imposed to give repeatable values for the boundary between elastic and plastic deformation behaviour. The 0.5% yield stress was specified in the API 5L standard [27] for use in determining the yield stress of pipeline samples. Hence, the 0.5% yield stress was evaluated for the industry supplied specimens and the laboratory rolled samples. The 0.5% yield stress is the stress associated with the 0.5% strain.

As seen in Figure 5.36, discontinuous yielding, distinct upper and lower yield points, was observed in the industry supplied samples of X70, however, all of the laboratory rolled schedules displayed continuous yielding. As explored in Section 2.7.1, the appearance of secondary phases such as M/A constituents tends to remove discontinuous yielding when present in concentrations greater than 5% [131]. Many instances of M-A Constituents were observed in the laboratory rolled samples as seen in Figures 5.28, 5.30 and 5.32, however, no M-A constituents were observed in either the 6.4 mm X70 plate or 10 mm

X70 pipe (Figures 5.8 and 5.12). While small amounts of M-A constituents were identified in the 20 mm X70 plate (Figure 5.3) they may not be present at sufficient concentrations to suppress discontinuous yielding. It is likely that discontinuous yielding is suppressed in the laboratory rolled samples due to the higher proportion of M-A constituents as compared to the industry supplied samples.

As can be seen in Figure 5.37, all industry supplied samples have 0.5% yield stresses in the specified range required for X70 steel [27]. When comparing the full thickness 20 mm X70 plate samples in Table 5.1 with the subsize samples in Table 5.8, the full thickness 20 mm specimen had slightly higher LRD (0°) 0.5% yield stress than the subsize samples, however, the full thickness TRD (90°) yield stress was more in line with the subsize specimen.

Of the laboratory rolled specimens, only Schedule 1 achieved the minimum required strength level for an X70 grade steel (485 MPa). Schedules 2 and 3 were both below the required strength requirements for an X70 steel. Whilst the laboratory rolled specimens have insufficient mechanical properties for an X70 steel, the aim of the project was to develop different crystallographic textures for testing the role of texture on the SCC susceptibility. As raw material for the laboratory rolled samples was only 20 mm thick as compared to the approximately 200 mm thick slabs found in industry, the grain size was not able to be refined enough with the limited reduction per pass. As a result of the coarse microstructure, the yield strength was below the desired level.

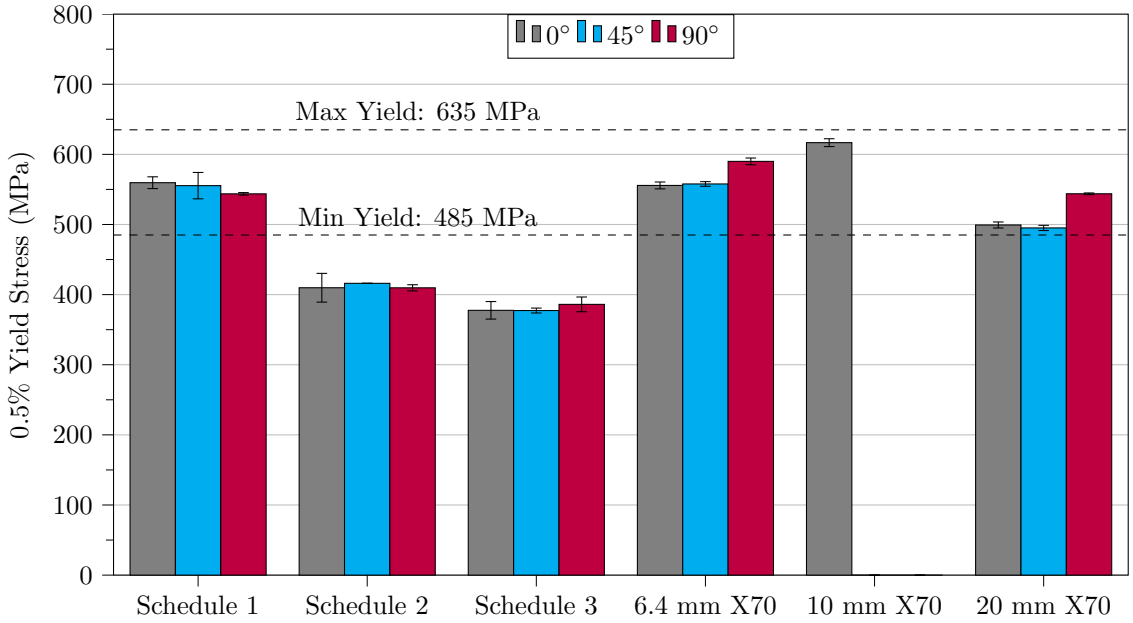

Figure 5.37: Combined 0.5% yield stress of industry supplied and laboratory rolled samples.

Ultimate Tensile Stress

Each grade of pipeline steel has a Ultimate Tensile Stress (UTS) range that must by met. According to the API 5L standard [27], an X70 PSL2 pipeline steel must have a minimum UTS of 570 MPa and a maximum UTS of 760 MPa. As can be seen in Figure 5.38 all orientations of the industry supplied samples met the minimum requirements for UTS of an X70 steel. Of the laboratory rolled specimens, only Schedule 1 met the minimum requirements for an X70 steel in all orientations. Of Schedule 2 and 3, only the 45° orientation of Schedule 2 achieved the minimum requirements.

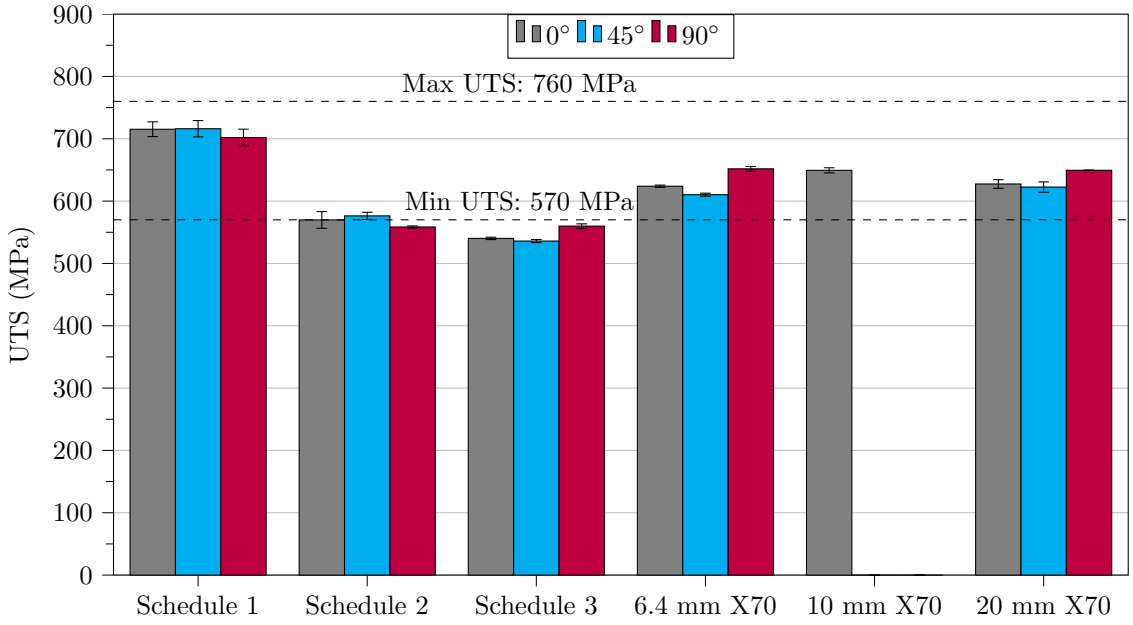

Figure 5.38: Combined UTS of industry supplied and laboratory rolled samples.

Ratio of $\sigma_{0.5}$/UTS

The ratio of $\sigma_{0.5}$/UTS is an important safety factor for the design of pipeline steel and gives a minimum range in which the pipeline can experience plastic deformation without failing. The API 5L standard [27] specifies for grades X80 and lower, a maximum ratio of 0.93. As seen in Figure 5.39, with the exception of the 10 mm X70, all the other steel samples have $\sigma_{0.5}$/UTS below the specified maximum value of 0.93. The $\sigma_{0.5}$/UTS is a margin of safety against unplanned loads allowing the structure to yield and not fail catastrophically [232]. Whilst the maximum allowable $\sigma_{0.5}$/UTS for grades below X80 is 0.93, higher strength steels have a maximum ratio of 0.99 [27]. As modern high strength steels exhibit high toughness and ductility even with their increased strength, the low maximum $\sigma_{0.5}$/UTS ratio is unnecessary. In effect, the industry supplied samples have a lower safety factor, although, as seen in Figure 5.36, the ductility of industry supplied materials is still quite high despite this.

The yield ratio is influenced strongly by the magnitude of the yield stress where an increase in yield strength tends to increase the ratio. The 10 mm X70 has the highest measured yield strength of the investigated specimens and this is reflected in the highest

measured $\sigma_{0.5}$/UTS. As the microstructures in Schedules 2 and 3 are very similar to that found in both industry supplied samples, the coarser grain size is expected to result in a lower yield ratio. Conversely, although Schedule 1 has a high yield stress and a high ratio is expected, upper bainite tends to experience fast work hardening rates and hence results in higher UTS values and a lower yield ratio [139]. The laboratory rolled samples are in that respect superior to the industry supplied samples.

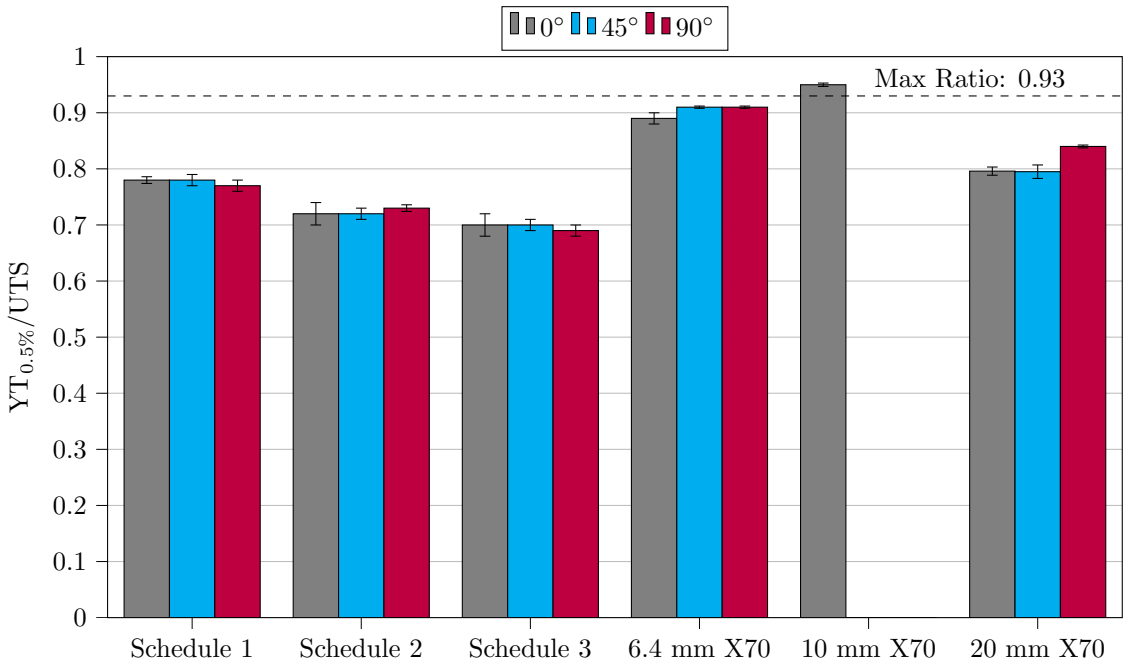

Figure 5.39: Combined $\sigma_{0.5}$/UTS of industry supplied and laboratory rolled samples.

Elongation

Elongation is a measure of ductility obtained from tensile testing. The total elongation, occurring after failure, and uniform elongation, occurring during deformation prior to the UTS, are required to be measured for pipelines. The minimum total elongation as specified by the API 5L standard was 13.4% and is calculated based on the tensile sample geometry and minimum tensile strength of pipe grade. The minimum total elongation is determined by Equation (5.4) found in Table 7 of the API 5L standard [233]. As stated in the API 5L standard [233], the total elongation is measured with regards to the gauge length and not the % area reduction.

$$A_f = C\frac{{A_{xc}}^{0.2}}{U^{0.9}} \tag{5.4}$$

Where:

A_f = Total Elongation

C = 1940 for SI units

A_{xc} = cross-sectional area of the test piece prior to testing to the nearest 10 mm^2

U = specified minimum tensile strength of the grade in MPa. As specified by the API 5L standard

As seen in Figure 5.40, all samples achieve the minimum elongation requirements for an X70 grade steel. Whilst samples rolled under Schedule 1 were the only laboratory rolled steel samples to achieve the minimum strength requirements for the X70 grade, it has the lowest total elongation of all the measured samples. The low total elongation is likely due to Schedule 1 being primarily composed of granular bainite and upper bainite, see Figure 5.27. Upper bainite in particular displays a reduction in total elongation with increasing concentrations [234]. Increasing the proportion of bainite tends to reduce the work hardenability of a steel, thereby lowering the overall ductility resulting in lower total elongation [235].

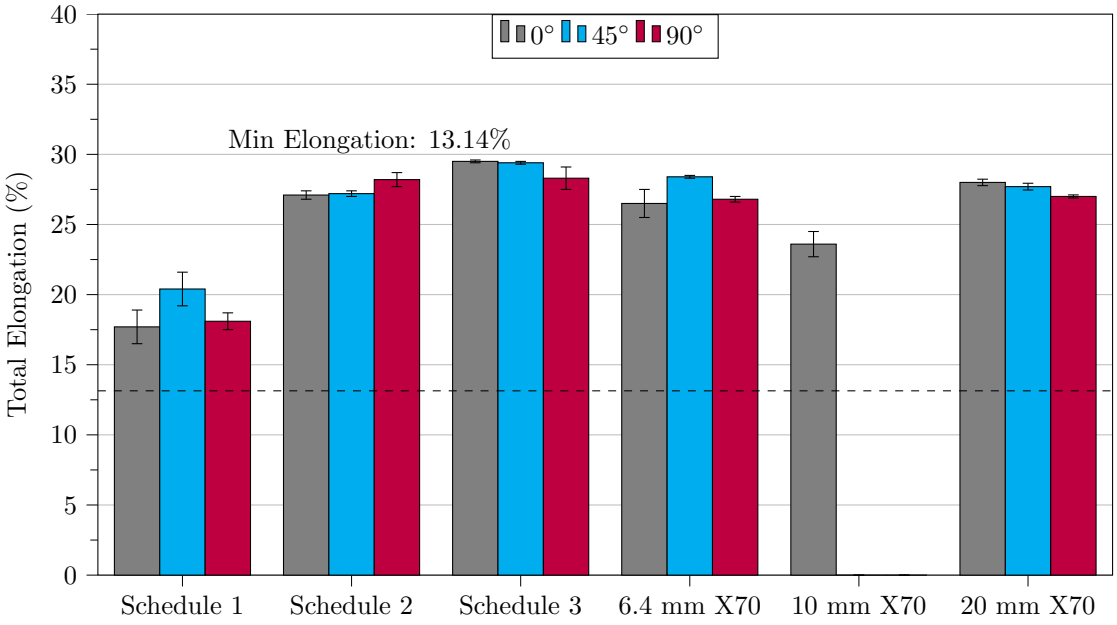

Figure 5.40: Combined total elongation of industry supplied and laboratory rolled samples.

The uniform elongation, while not specifically mentioned in the API 5L standard [27], is a property often specified by pipe owners during the manufacturing phase and specifies the minimum elongation the pipe can experience during tensile testing prior to necking. A value of 4% is often selected when specifying the minimum uniform elongation [236]. As seen in Figure 5.41, all samples meet the minimum uniform elongation requirements. Schedule 1 has the lowest uniform elongation whilst Schedules 2 and 3 have higher uniform elongations than the industry supplied samples. As Schedule 2 and Schedule 3 have higher proportions of ferrite (see Figures 5.29 and 5.31), higher uniform elongation is expected due to the higher work hardenability observed in steels containing lower proportions of bainite [235]. Schedule 1, containing primarily coarse upper bainite, is not expected to have a high uniform elongation as microstructures containing upper bainite tends to show lower total and uniform elongation compared to polygonal ferrite and granular bainite microstructures [72, 237].

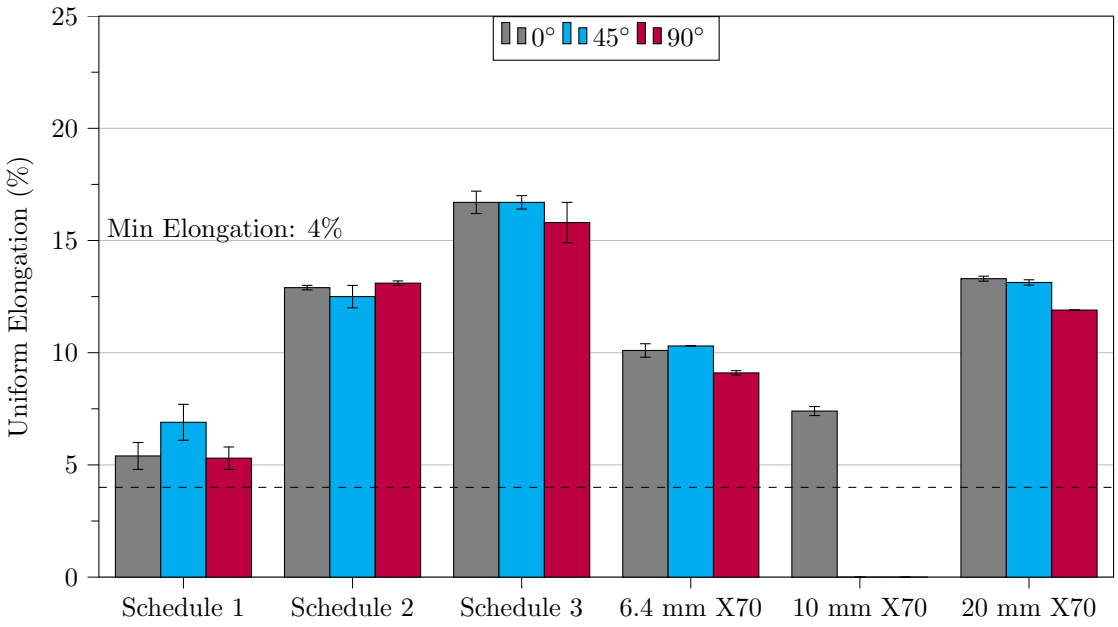

Figure 5.41: Combined uniform elongation of industry supplied and laboratory rolled samples.

5.4 Summary of Manufacturing Processes

Three rolling schedules designed to produce different crystallographic textures were designed and the resulting properties investigated. The rolling schedules consisted of a recrystallized rolling schedule where all rolling was conducted above T_{NR}, a hot rolling schedule where the finish rolling was conducted below T_{NR} and finally warm rolling where the finish rolling was conducted in the two phase region and deformation of ferrite occurred. The microstructures and mechanical properties were evaluated for these samples and compared to the industry supplied samples of X70. The main findings of this chapter are that each rolling schedule was successful in generating microstructures that were primarily bainitic and had similar properties overall to what is required of API 5L X70. The following chapter will explore the crystallographic texture developed in the rolled samples and how they compare to industry supplied samples.

Chapter 6

Results and Discussion - Crystallographic Texture

6.1 Introduction

The aim of the study was to investigate the role of controlled rolling on the formation of crystallographic texture in pipeline steel and the effect it had on stress corrosion cracking susceptibility. In order to generate sufficiently different crystallographic textures, sufficiently different rolling schedules were needed. As explored in Section 2.7.4, finish rolling at different temperatures is likely to produce different crystallographic textures. Therefore, three rolling schedules with difference temperature regimens were established to explore their effect on the generation of texture, see Chapter 5. This chapter covers the analyses of the crystallographic texture and explores the through-thickness texture of laboratory rolled and industry supplied samples.

The term crystallographic texture refers to the non-random distribution of crystal orientations within a polycrystalline material, in relation to an external set of axis. Certain crystallographic planes in a crystal (grain) align themselves in a preferred direction with respect to maximum strain direction, as influenced by either an external or internal force during manufacturing. For controlled rolling, the process parameters: rolling tempera-

tures, cooling rates, and reduction ratios can all be manipulated to develop steel structures with a range of crystallographic textures. A material is said to be strongly textured when a particular orientation is highly represented and is textureless when all orientations are equally represented. Textureless samples are usually only produced with metal powder. The texture of the laboratory rolled and industry supplied steel samples were determined through electron backscatter diffraction (EBSD) methods as described in Section 4.4.3.

6.2 Laboratory Rolled Samples

The texture of the laboratory rolled specimens is investigated in this section. The average orientation distribution function (ODF) plot from samples of each rolling schedule are investigated at each location and compared with literature to determine the textures produced from different rolling schedules. The laboratory rolled samples comprise of Schedules 1, 2 and 3 with the industry supplied samples compared in the next section. A summary of the rolling schedules is presented in Section 5.2.4 and presented here again in Figure 6.1 for the purpose of continuity and ease of comprehension of the text hereafter.

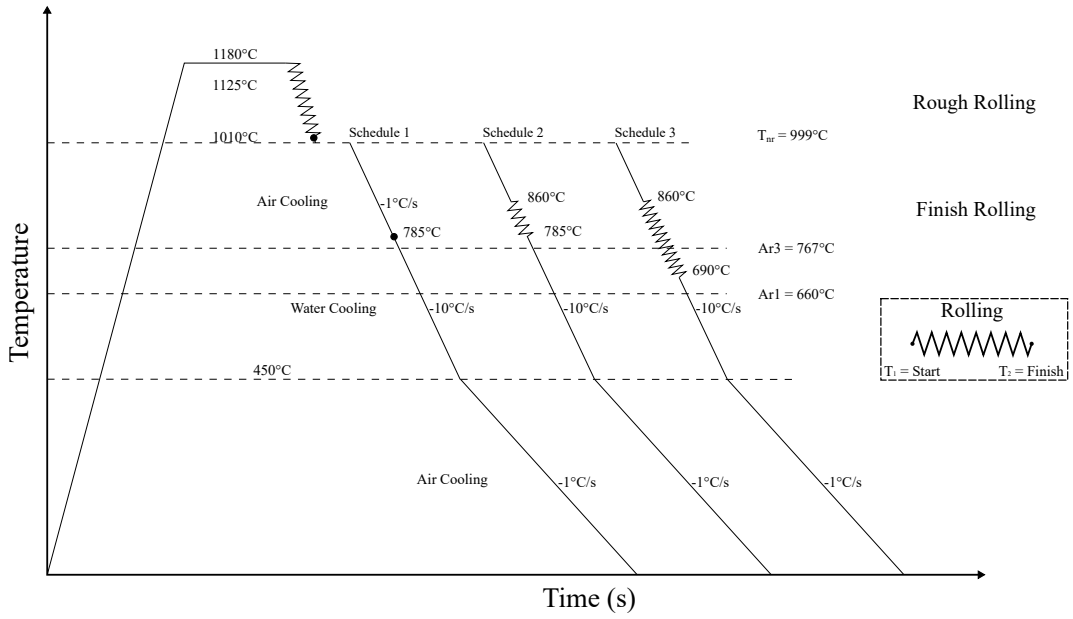

Figure 6.1: Summary of the laboratory rolling schedules.

6.2.1 Schedule 1

The ODF plots at the surface, quarter and centre planes are presented in Figure 6.2 with a key showing the textures present in each ODF Figure 6.2a.

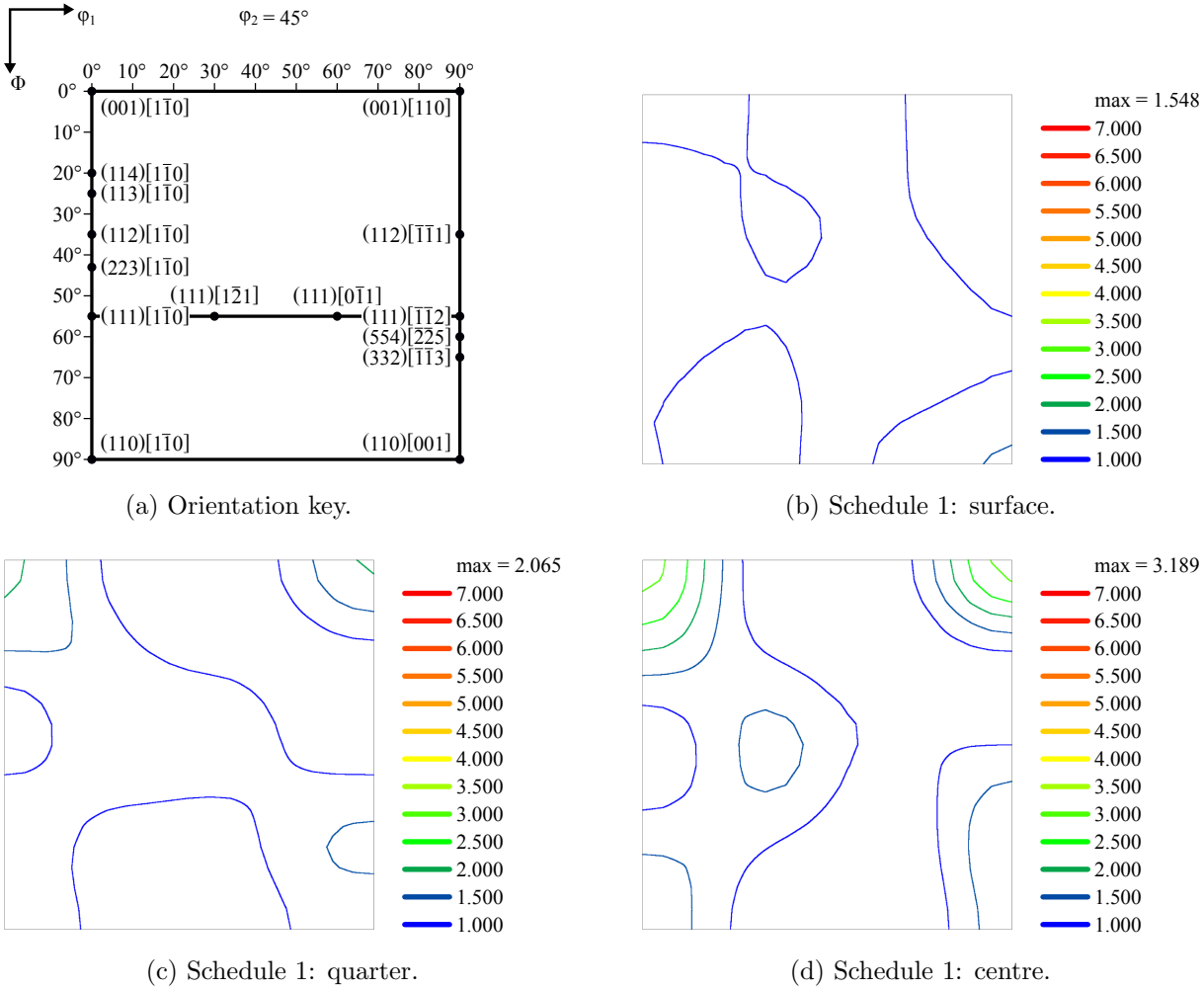

(a) Orientation key.

(b) Schedule 1: surface.

(c) Schedule 1: quarter.

(d) Schedule 1: centre.

Figure 6.2: ODFs at $\phi_2 = 45°$ of the textures identified in Schedule 1.

The crystallographic texture from the surface of samples manufactured through Schedule 1 is presented in Figure 6.2b. The ODF shows a maximum intensity of 1.548× random at the (110)[001] component. There are three minor textures at approximately (001)[1$\bar{1}$0], (001)[110] and near (110)[1$\bar{1}$0] at ($\varphi_1 = 20°$). Overall, the intensity of textures at the surface is quite weak.

The crystallographic texture at the quarter plane of samples manufactured by rolling

Schedule 1 is presented in Figure 6.2c. The crystallographic texture of the quarter plane shows the maximum intensity at (001)[1$\bar{1}$0] and (001)[110] of the rotated cube with weaker textures located at (110)[1$\bar{1}$0] and, near (110)[001]. The maximum texture intensity in the quarter plane is slightly higher than that observed in the surface at 2.065× random. There is a slightly lower intensity of the (332)[$\bar{1}\bar{1}$3] texture although, this may just be an artefact from averaging three scanned areas.

The crystallographic texture at the centre plane of samples manufactured by rolling Schedule 1 is presented in Figure 6.2d. Similar to the quarter plane, the centre plane has a maximum texture intensity at both (001)[1$\bar{1}$0] and (001)[110] of the rotated cube with a lower intensity of at (110)[1$\bar{1}$0] and (110)[001]. In addition, there is a slightly higher intensity of textures at approximately $(\varphi_1, \Phi, \varphi_2) = (30°,50°,45°)$.

Schedule 1, the recrystallised rolling schedule, had all deformation occur at temperatures above T_{NR} such that no strain accumulation could occur prior to transformation. As outlined in Section 2.7.4, recrystallization rolling tends to be influenced primarily by the cube texture in the prior austenite and the textures that develop upon transformation.

There are subtle differences between the textures that formed from the surface to the centre in Schedule 1. There appears to be an increase in the intensity of the rotated cube ((001)[1$\bar{1}$0] and (001)[110]) from the surface to the centre plane in addition to a slight increase in (110)[1$\bar{1}$0]. Texture at the surface tends to be influenced, at least moderately, by the interaction between the rollers and the material, whilst the centre experiences near plane strain [178, 179]. Shear texture at the surface can result in the preferential formation of (110)[001] textures whilst plane strain accentuates α-fibre and, (001)[1$\bar{1}$0] & (001)[110] textures in the centre plane [178].

The texture observed at the quarter plane of Schedule 1 shows strong rotated cube textures ((001)[1$\bar{1}$0] and (001)[110]) and a weaker intensity of (332)[$\bar{1}\bar{1}$3] orientations. This

is similar to the textures observed at the quarter plane of a X100 steel manufactured through recrystallized rolling by Nafisi et al. (2012) [180]. Whilst the intensity of textures is different, both the chemical composition and the texture measurement method were different (X-ray diffraction rather than EBSD) which would likely accounting for the observed differences. Bulk texture analysis of Nb steel that was water quenched post recrystallized rolling was undertaken by Ray et al. (1994) [21]. When accounting for chemical composition, the texture that developed was remarkably similar to that of the quarter and centre planes of Schedule 1.

There are few examples of low carbon pipeline steels control rolled above the T_{NR} in open literature that study the through-thickness texture. As such, there are few examples in open literature to which Schedule 1 can be compared. Although different steel alloys were investigated, those with chemical compositions similar to that of Schedule 1 are valid for these analyses.

6.2.2 Schedule 2

The ODF plots at the surface, quarter and centre planes are presented in Figure 6.3 with a key showing the textures present in each ODF.

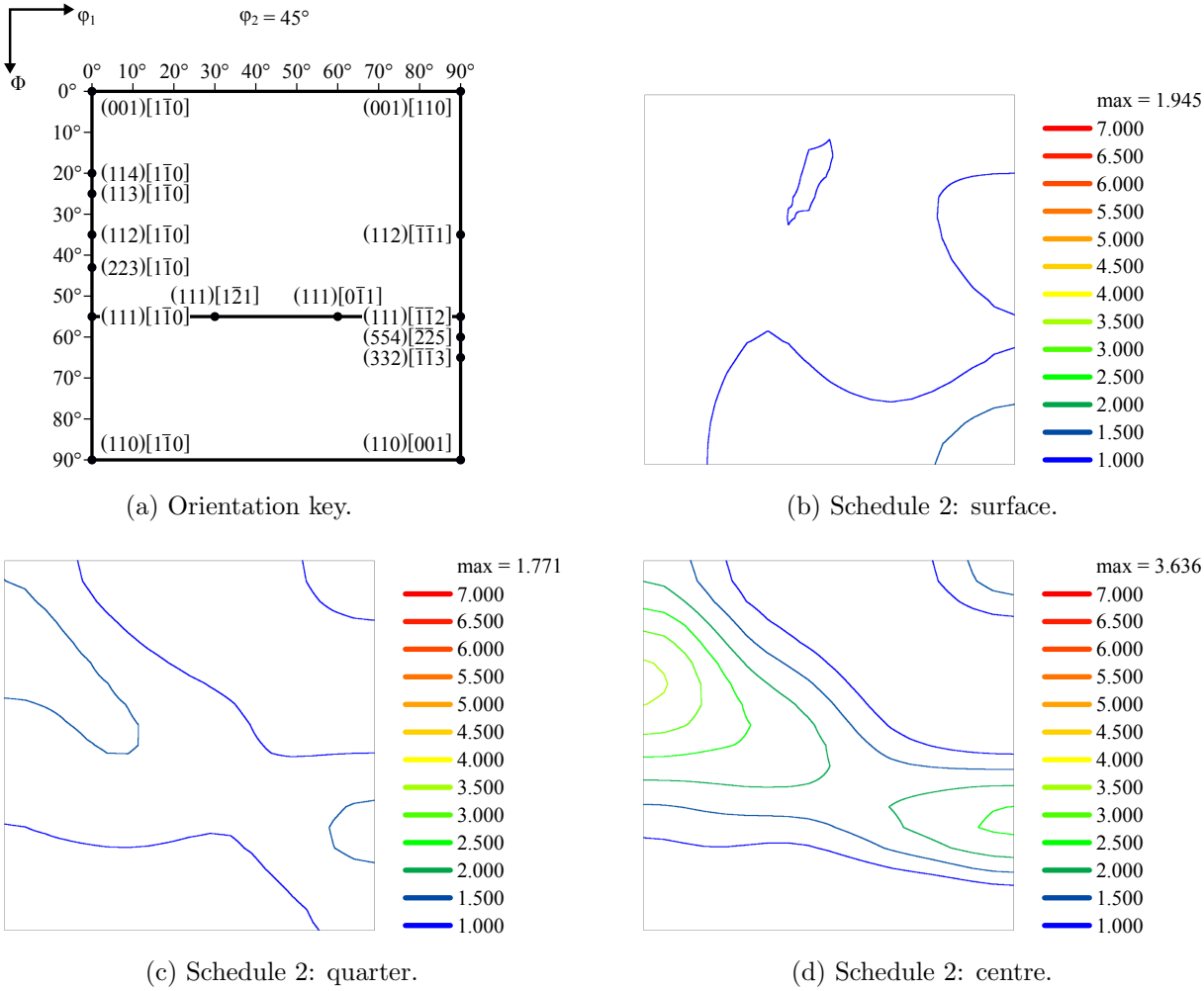

(a) Orientation key.

(b) Schedule 2: surface.

(c) Schedule 2: quarter.

(d) Schedule 2: centre.

Figure 6.3: ODFs at $\phi_2 = 45°$ of the textures identified in Schedule 2.

The crystallographic texture from the surface of samples manufactured through Schedule 2 is presented in Figure 6.3b. The texture with the strongest intensity is the (110)[001] orientation with a weaker component observed at (112)[$1\bar{1}\bar{1}$]. The maximum intensity at the surface is moderately strong with a maximum of 1.945× random. There is a weak texture component at $(\varphi_1, \Phi, \varphi_2) = (40°,20°,45°)$, however, it appears to be an artefact of combining the three constituent scans together. Two of the three constituent scans showed weak intensity of (001)[0$\bar{1}$0] textures and combining them together resulted in the

small portion remaining in Figure 6.3b.

The crystallographic texture of the quarter plane from samples manufactured through Schedule 2 are presented in Figure 6.3c. The textures identified in the quarter plane shows the highest intensity along the {114}//RP fibre ($\Phi \approx 19.5°$) (see Figure 2.18) with a weaker $(332)[\bar{1}\bar{1}3]$ intensity.

The crystallographic texture of the centre plane from samples manufactured through Schedule 2 are presented in Figure 6.3d. The main textures present in the centre are: between $(112)[1\bar{1}0]$ and $(113)[1\bar{1}0]$, at $(001)[110]$ and at $(332)[\bar{1}\bar{1}3]$. The maximum intensity exists between $(112)[1\bar{1}0]$ and $(113)[1\bar{1}0]$ because the constituent scans showed strong intensities at either $(112)[1\bar{1}0]$ or $(113)[1\bar{1}0]$ which was averaged when combined.

Schedule 2 was a hot rolling schedule where rough rolling occurred at temperatures above T_{NR} and was finish rolled below T_{NR}. As outlined in Section 2.7.4, finish rolling below T_{NR} results in strain accumulation, producing textures indicative of deformed austenite.

The aim of developing Schedule 2 was to finish roll below the T_{NR} such that strain accumulation would occur and a mixture of recrystallized and deformed austenite textures would develop. As seen in Figure 6.3, the textures from the surface to the centre in samples manufactured through Schedule 2 change from $(110)[001]$ dominant at the surface, to having a well defined γ-fibre in the centre plane. The formation of the strong $(110)[001]$ texture is commonly observed in hot rolled steels and is the result of the surface undergoing shear deformation due to the interaction between the material at the surface and the rollers [178, 179]. This texture is observed in hot rolled pipeline steels in the literature with Lavigne et al. (2016) [183] noting a high intensity of this texture at the surface of a hot rolled X65 steel. In samples of hot rolled X100 [238], and hot rolled X70 [239], the surface texture appears different, with stronger γ-fibre and a departure from $(110)[001]$ to a more even spread across the {110}//RP fibre. The difference in texture observed

between Schedule 2 and Zong et al. (2013) [238] could be due to the difference in deformation experienced by the two samples with the plate investigated by Zong et al. (2013) being commercially prepared and would have undergone more deformation than Schedule 2. The difference in observed texture between Schedule 2 and that from Masoumi and Abreu (2015) [239] could be due to their samples being quench and tempered as opposed to being control rolled like Schedule 2.

The textures of the quarter and centre planes are significantly different to the texture of the surface. A complete lack of (110)[001] and (112)$[\bar{1}\bar{1}1]$ orientations is observed in the quarter and centre planes. Similar textures to those developed in the quarter plane of Schedule 2 are present in the literature, although, slight differences in intensity, likely caused by differences in chemical composition in Masoumi et al. (2015) [137] and the rolling schedule in Nafisi et al. (2012) [180] were observed. The textures developed at the centre of Schedule 2 is a classic hot rolling texture and has been observed by many authors that developed similar textures through similar hot rolling schedules [181, 183–185]. As mentioned previously, with the development of texture in the quarter plane, depending on the exact rolling schedule and chemical composition of the investigated steel, some differences in texture can be observed despite being processed at similar temperatures [21, 137, 180].

6.2.3 Schedule 3

The ODF plots at the surface, quarter and centre planes are presented in Figure 6.4 with a key showing the textures present in each ODF.

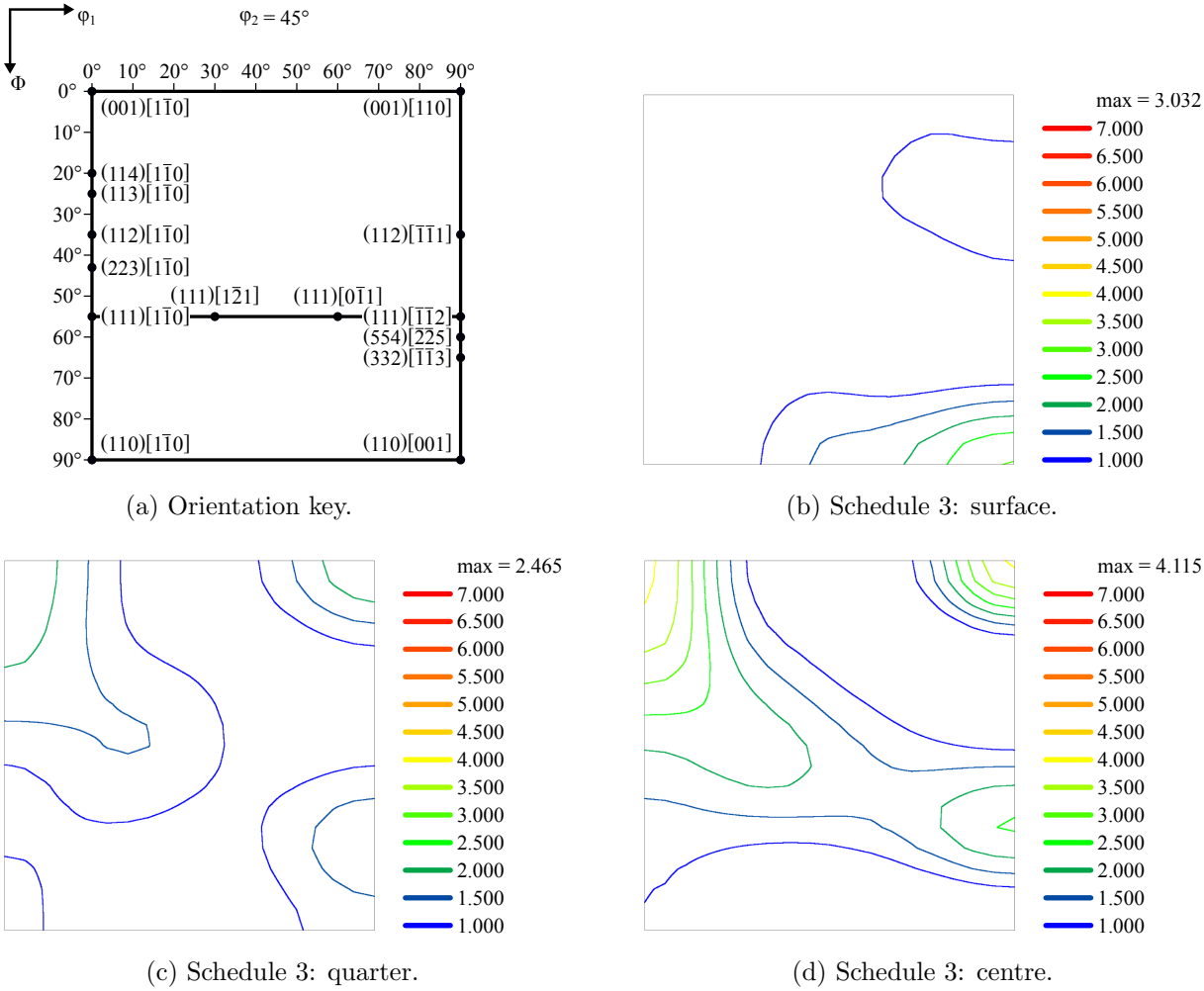

(a) Orientation key.

(b) Schedule 3: surface.

(c) Schedule 3: quarter.

(d) Schedule 3: centre.

Figure 6.4: ODFs at $\phi_2 = 45°$ of the textures identified in Schedule 3.

The crystallographic texture from the surface of samples manufactured through Schedule 3 is presented in Figure 6.4b. The two main textures identified at the surface of samples manufactured through Schedule 3 are the (110)[001] and (113)[$\bar{3}\bar{3}$2]. The surface has a maximum intensity of 3.032× random located at (110)[001] with the intensity of the (113)[$\bar{3}\bar{3}$2] orientation below 1.5× random.

The crystallographic texture at the quarter thickness plane of samples manufactured

through Schedule 3 is presented in Figure 6.4c. The quarter thickness plane has a high intensity of rotated cube textures ((001)[1$\bar{1}$0] and (001)[110]) and a moderately strong intensity of (332)[$\bar{1}\bar{1}$3] textures. A weak (110)[1$\bar{1}$0] is also observed, however, it is negligible. The highest texture is located at the rotated cube (001)[1$\bar{1}$0] with a maximum intensity of 2.465× random.

The crystallographic texture at the centre plane of samples manufactured through Schedule 3 is presented in Figure 6.4d. The centre plane of samples manufactured through Schedule 3 have the highest intensity of textures at the rotated cube with the (001)[1$\bar{1}$0] component having an intensity of 4.115× random. A moderately strong γ-fibre texture is present terminating at (332)[$\bar{1}\bar{1}$3] which has an intensity greater than 2.5× random.

Schedule 3 was a warm rolling schedule where rough rolling occurs at temperatures above T_{NR} and the finish rolling occurs in the two phase region where both austenite and ferrite exist. As outlined in Section 2.7.4 warm rolling concludes in the two phase region and results in slightly different textures than those formed through hot rolling as discussed in Section 2.7.4.

As outlined above, the aim of Schedule 3 was to develop warm rolling textures. The texture at the surface in Figure 6.4b shows a very similar texture to that of Schedule 2 Figure 6.3b. Authors Hölscher et al. (1991) [178] and, Lee and Lee (1998) [179] observed (110)[001] and (113)[$\bar{3}\bar{3}$2] textures at the surface of control rolled steel, and attributed the development to the shear between the rollers and the material surface. This may explain the textures developed at the surface of Schedules 2 and 3 that were manufactured using the same rolling mill. The intensity of the texture at the surface is considerably higher than that found at the surface of Schedule 1 or Schedule 2. A possible reason for this is that the surface of Schedule 3 contains some very large grains, as seen in Figure 5.31, that when scanned through EBSD would result in the texture of those few large grains being over represented; hence, the intensity would be greater. Similar results have been

discussed in the current authors' previous publications, where including only a small number of grains for texture analysis resulted in strong intensities [31].

The textures present in the quarter and centre planes are very similar in Schedule 3, as seen in Figures 6.4c and 6.4d. They both show dominant (001)[1$\bar{1}$0] & (001)[110] textures with slightly weaker (332)[$\bar{1}\bar{1}$3] orientations. The main difference is that the γ-fibre is more developed in the centre plane than the quarter plane. Warm rolling gives rise to deformed austenite and ferrite grains, with associated textures developing in both phases. The texture observed in samples of warm rolled low carbon steel, presented by author Shen et al. (2017) [187], showed that decreasing final rolling temperature changed the dominant texture from (112)[1$\bar{1}$0] to (001)[1$\bar{1}$0]. The change in finish rolling temperature between Schedule 2 and Schedule 3 shows a similar trend, with the texture at the quarter and centre showing stronger (001)[1$\bar{1}$0] texture in Schedule 3.

As observed by Nafisi et al. (2012) [180], at the quarter thickness plane, the texture of the warm rolled specimen is strongest at between (113)[1$\bar{1}$0] and (112)[1$\bar{1}$0]. The bulk texture of warm rolled steel as shown by Ray et al. (1994) [21] also tend to show stronger (112)[1$\bar{1}$0]/ (113)[1$\bar{1}$0] textures, although the chemical compositions of the steels are different compared to the pipe steel used in Schedule 3. One possible reason for the higher concentration of (001)[1$\bar{1}$0] in Schedule 3 is that the sample was not rolled significantly below the T_{NR} in the purely austenitic range. As a result deformed austenite textures did not develop and subsequent rolling instead strengthened the recrystallized textures, similar to that observed in Schedule 1.

6.2.4 Comparison of Laboratory Rolled Samples

When comparing the texture produced though the three rolling schedules, it is evident that the different rolling schedules produced different through-thickness texture profiles. A comparison of the surface, quarter plane and centre plane of the three rolled schedules

is undertaken below.

Surface Texture Comparison

The three surface textures of the laboratory rolled samples is presented in Figure 6.5. As seen in Figure 6.5, all three rolling schedules show the strongest intensity at the (110)[001] texture, which as discussed previously, is related to the shear stress induced in the surface of the steel during hot rolling. Other weak recrystallized textures are also present at the surface of Schedule 1, as seen in Figure 6.5a. As Schedule 1 was rolled above the T_{NR}, complete static recrystallization occurred between rolling passes so any strong shear texture that developed were likely weakened from recrystallization. Finish rolling, in both Schedules 2 and 3, occurred below T_{NR} hence, deformed grains were unable to undergo complete static recrystallization between passes and remained deformed prior to transformation to ferrite.

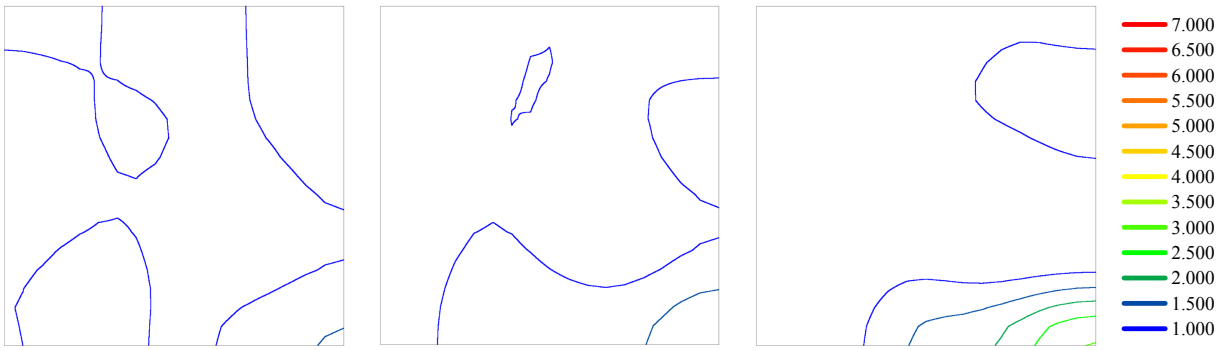

(a) Schedule 1: surface. (b) Schedule 2: surface. (c) Schedule 3: surface.

Figure 6.5: ODFs at $\phi_2 = 45°$ of the textures identified at the surface plane of the laboratory rolled schedules.

Quarter Texture Comparison

The quarter plane in Figure 6.6 show that similar textures in the three laboratory rolled samples samples with only slight differences between them. Schedule 1, in Figure 6.6a, appears to display homogeneous through-thickness texture by virtue of being rolled above

the T_{NR}. The textures that are observed in Schedule 1 are the result of the recrystallized cube texture ((100)[0$\bar{1}$0]) in austenite transforming to the rotated cube ((001)[1$\bar{1}$0] & (001)[110]), the Goss (110)[001] and rotated Goss (110)[1$\bar{1}$0] textures [21, 177]. When comparing Schedule 2 with Schedule 3 in Figures 6.6b and 6.6c, it is evident that each schedule has a different maximum texture intensity along the α-fibre. The strongest texture in Schedule 2 is present at (112)[1$\bar{1}$0] whilst in Schedule 3 it is located at (001)[1$\bar{1}$0]. This result is consistent with steel rolling literature that states the (112)[1$\bar{1}$0] is formed through transformation of deformed austenite texture whereas reducing the finish rolling temperature leads to increases in the (001)[1$\bar{1}$0] texture [21, 168, 240].

Whilst cosmetically, Schedules 2 and 3 appear almost identical to Schedule 1, there is a distinct lack of {223}//RP textures in Schedule 1 that are present in Schedules 2 and 3. {223}//RP textures are formed through transformation of deformed austenite and strengthens through deformation of ferrite [21, 240]. Hot and warm rolling can produce these textures, however, they can not be produced in high concentrations when rolling above T_{NR}.

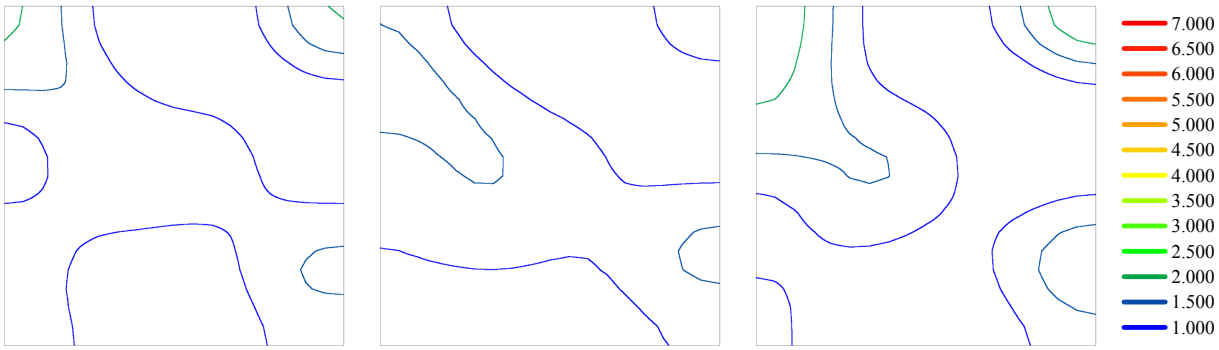

(a) Schedule 1: quarter. (b) Schedule 2: quarter. (c) Schedule 3: quarter.

Figure 6.6: ODFs at $\phi_2 = 45°$ of the textures identified at the quarter plane of the laboratory rolled schedules.

Centre Texture Comparison

When comparing the centre planes of Schedules 1, 2 and 3 in Figure 6.7 it is evident that there is a significant difference between the textures produced by the three rolling schedules. As discussed in Section 6.2.1, due to being rolled above the T_{NR}, complete static recrystallization occurred between passes in Schedule 1 resulting in a homogeneous through-thickness texture. When comparing Schedule 2 with Schedule 3, in Figures 6.7b and 6.7c, it is evident that along the α-fibre, the strongest intensity in Schedule 2 is at $(112)[1\bar{1}0]$ whilst in Schedule 3 it is at $(001)[1\bar{1}0]$. This result is consistent with steel rolling literature that states the $(112)[1\bar{1}0]$ is formed through transformation of deformed austenite texture whilst reducing the finish roll temperature leads to increases in the $(001)[1\bar{1}0]$ texture [21, 168, 240].

The difference in texture present in Schedules 2 and 3 could be due to the differences in rough and finish rolling temperatures. Whilst Schedule 2 was deformed in the entirely austenitic temperature range, Schedule 3 was finish rolled in the two phase region for all three passes. The additional ferrite deformation may have contributed to the stronger rotated cube textures present in Schedule 3. It has been reported in literature that {100}<110>orientations increase in strength with deformation [23, 240]. The {100}<110>recrystallization textures developed during rough rolling in Schedule 3 were strengthened during finish rolling and less deformation textures were produced due to rolling in the two phase region.

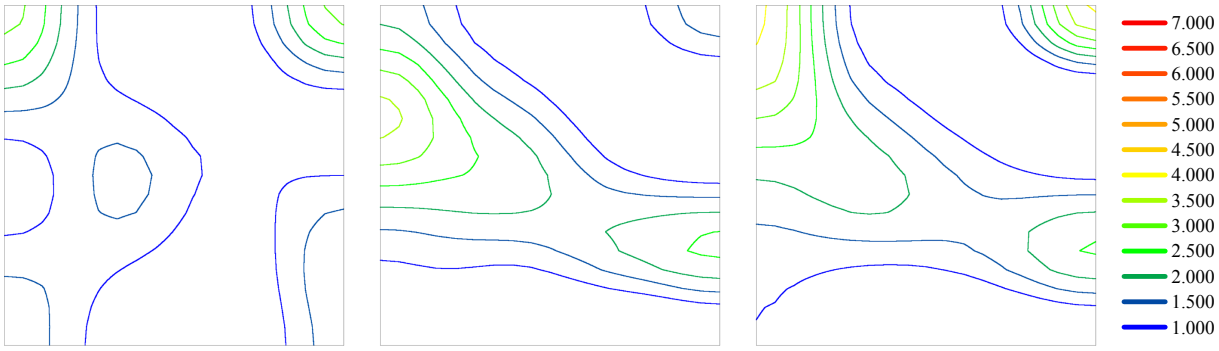

(a) Schedule 1: centre. (b) Schedule 2: centre. (c) Schedule 3: centre.

Figure 6.7: ODFs at $\phi_2 = 45°$ of the textures identified at the centre plane of the laboratory rolled schedules.

6.3 Industry Supplied Samples

To confirm the texture of the samples manufactured through the laboratory rolling schedules were comparable to those currently in-use, the industry supplied samples were characterised in the same manner for direct comparison. The industry supplied samples were prepared in an identical manner to the laboratory rolled samples with texture analysed at the surface, quarter, and centre planes. The textures produced in each sample is presented below with a comparison between the industry produced samples and the laboratory samples conducted thereafter.

6.3.1 20 mm X70 Plate

The 20 mm X70 plate is the as-received material for the laboratory rolled schedules and was manufactured and supplied by BAOSTEEL. No details regarding the manufacturing process were supplied, although it was specified that the material was thermomechanically formed as opposed to quench and tempered. The material was supplied unfinished, closer to transfer bar than finish rolled coil. The microstructure of the 20 mm samples, as explored in Section 5.1.1, had microstructures most similar to that of Schedule 2. Thus, it is expected that the rolling schedule used to manufacture the 20 mm X70 plate was

similar to the hot rolling schedule of Schedule 2. The ODF plots at the surface, quarter and centre planes are presented in Figure 6.8 with a key showing the textures present in each ODF.

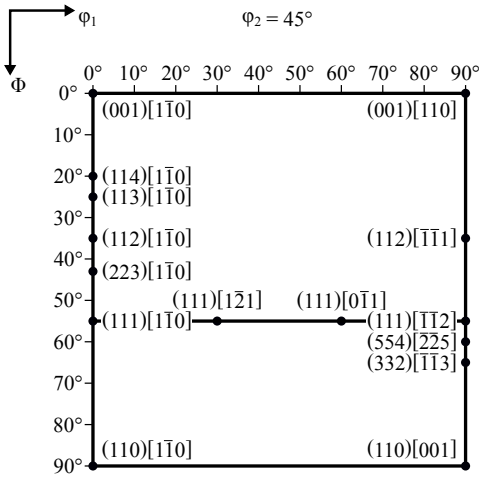

(a) Orientation key.

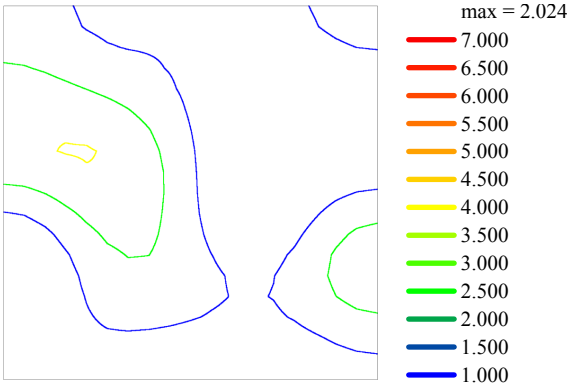

(b) 20 mm X70 plate: surface.

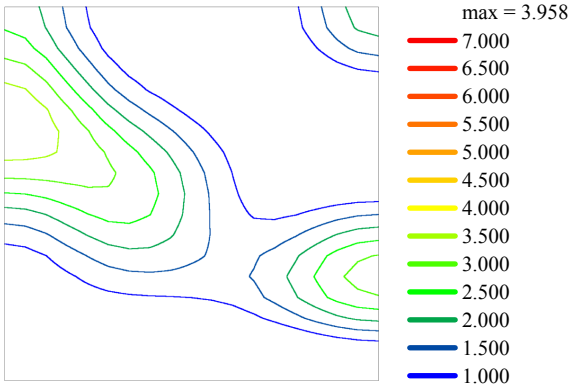

(c) 20 mm X70 plate: quarter.

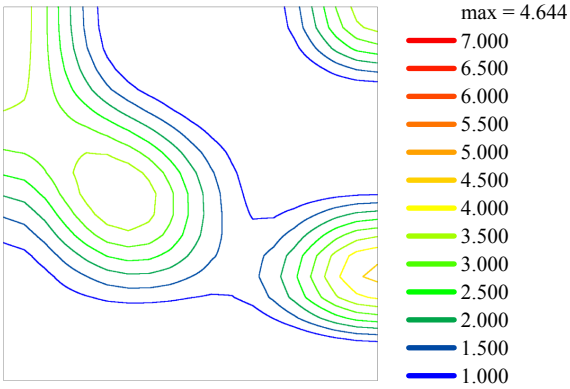

(d) 20 mm X70 plate: centre.

Figure 6.8: ODFs at $\phi_2 = 45°$ of the texture identified in the 20 mm X70 plate.

The crystallographic texture from the surface of 20 mm X70 plate samples is presented in Figure 6.8b. The surface texture shows a strong α-fibre texture between (112)[1$\bar{1}$0] and (223)[1$\bar{1}$0]. The maximum intensity of 2.024× random is found along the {112} RP fibre at $\varphi_1 = 20°$. Weaker textures are located at (554)[$\bar{2}\bar{2}$5] and (001)[110].

The crystallographic texture at the quarter thickness plane of 20 mm X70 plate samples is presented in Figure 6.8c. The quarter thickness plane shows a strong α-fibre texture with an intensity of 3.958× random centred between (112)[1$\bar{1}$0] and (113)[1$\bar{1}$0]. Both

(112)[1$\bar{1}$0] and (113)[1$\bar{1}$0] textures were present at similar intensities, likely explaining the highest intensity being centred between the two constituents. There is no strong intensity at either (332)[1$\bar{1}$3] or (001)[110]. The 20 mm X70 plate shows a developed γ-fibre that has the highest intensity at (111)[1$\bar{2}$1].

The crystallographic texture at the centre plane of 20 mm X70 plate samples is presented in Figure 6.8d. The centre plane has a maximum texture located at (332)[1$\bar{1}$3] with a maximum intensity of 4.644× random. There are slightly weaker intensities along the α-fibre with maximums at the rotated cube ((001)[1$\bar{1}$0] and (001)[110]). There was also a high intensity noted along the {223}//RP fibre centred at $\varphi_1 = 30°$.

The 20 mm X70 steel plate was the initial material of the laboratory rolled plate and as such the initial texture can provide some information of the rolling conditions that they initially underwent. The surface texture of the 20 mm X70 plate in Figure 6.8b is not commonly observed in the literature [96, 178, 179]. The surface texture is dominated by a α-fibre texture, between (112)[1$\bar{1}$0] and (223)[1$\bar{1}$0], with weaker textures at (554)[$\bar{2}\bar{2}$5] and (001)[110]. It is possible that the surface that developed in the 20 mm X70 plate was because the material was supplied unfinished unlike the laboratory rolled specimens and literature in general.

The quarter and centre thickness planes of the 20 mm X70 plate have very similar textures, both displaying strong α and γ-fibre textures and, a pronounced (001)[110] component. Where the quarter plane, in Figure 6.8c, has the highest intensity at approximately the (112)[1$\bar{1}$0] component, the centre plane, in Figure 6.8d, has the highest intensity at the (001)[1$\bar{1}$0] component. The difference in texture between the quarter and centre planes may be due to the centre plane experiencing nearly plane strain that increases the proportion of the (001)[1$\bar{1}$0] & (001)[110] textures [178]. The texture of the 20 mm X70 plate at the quarter plane appears almost identical to that observed in the quarter plane of samples manufactured through Schedule 2. The main difference is that the intensity of

the 20 mm X70 plate is more than twice that of samples manufactured through Schedule 2.

6.3.2 10 mm X70 Pipe

The 10 mm X70 pipe supplied by Jemena was a 500 mm long section of a ⌀500 mm pipe. Samples for texture analysis were sectioned from the 3 o'clock position of the pipe (weld at 12 o'clock position) to avoid the Heat Affected Zone (HAZ) near the weld and the centre of the roll where segregation concentrates, per Section 4.1. The rolling schedule used to manufacture the 10 mm X70 pipe was not provided although, based on the microstructure in Section 5.1.2, it was likely a thermomechanical process as opposed to a quench and tempered method. Quench and tempering steels result in equiaxed structures, often with the addition of tempered martensite, as seen in laboratory produced samples of X70 manufactured by Masoumi et al. (2015) [137], and Masoumi et al. (2016) [241] [1]. The microstructure appears most similar to that of Schedule 2 and it is likely that the texture will also be similar. The ODF plots at the surface, quarter and centre planes are presented in Figure 6.9 with a key showing the textures present in each ODF.

[1]The API 5L standard has allowed for grades up to X80 to be produced through quench and tempered methods [233]

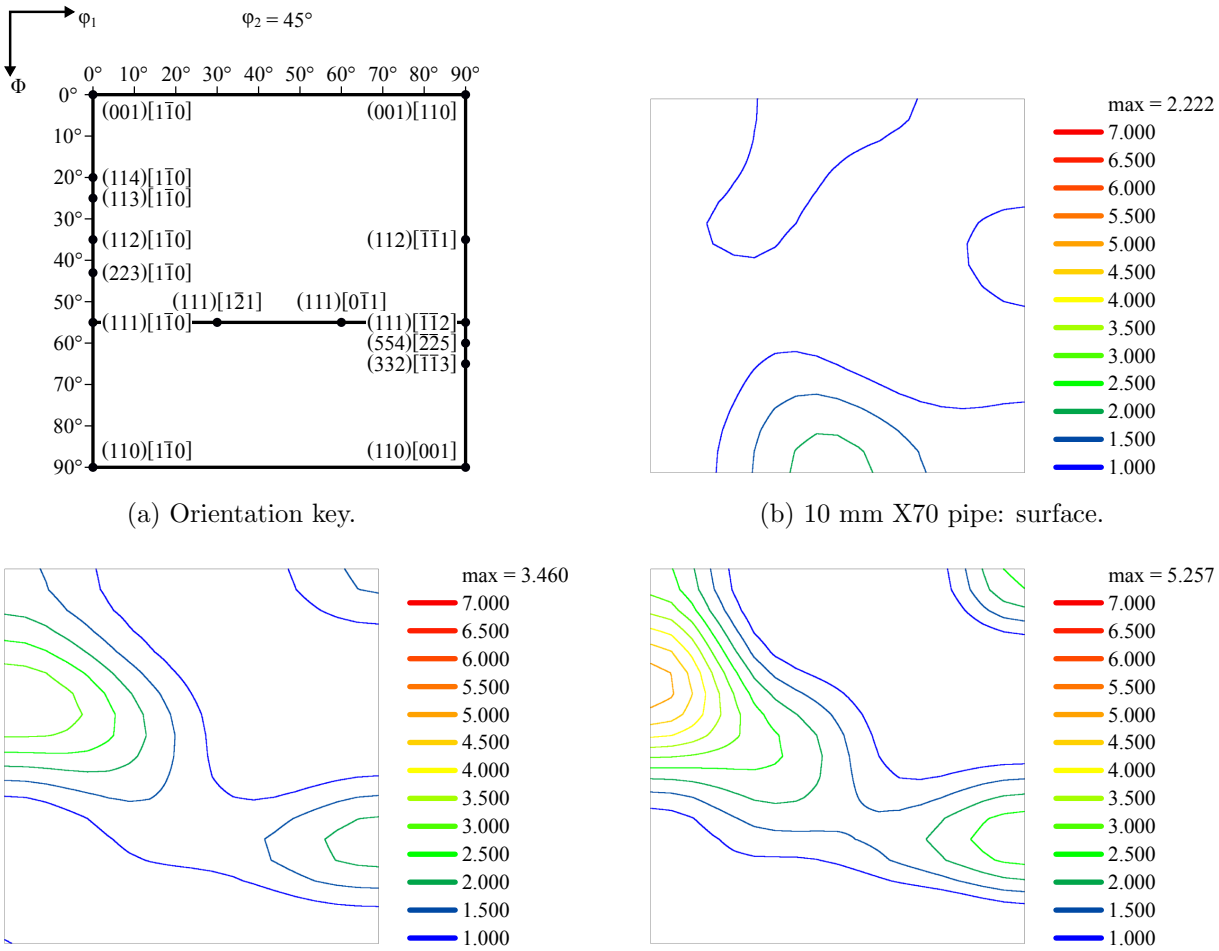

(a) Orientation key.

(b) 10 mm X70 pipe: surface.

(c) 10 mm X70 pipe: quarter.

(d) 10 mm X70 pipe: centre.

Figure 6.9: ODFs at $\phi_2 = 45°$ of the texture identified in the 10 mm X70 pipe.

The crystallographic texture from the surface of 10 mm X70 pipe samples is presented in Figure 6.9b. The surface texture shows a high intensity of 2.222× random along the {110}//RP fibre centred at $\varphi_1 = 45°$. In addition, there are two lower intensity components noted at (112)[$\bar{1}\bar{1}$1] and at approximately (001)[0$\bar{1}$0].

The crystallographic texture at the quarter thickness plane of 10 mm X70 pipe samples is presented in Figure 6.9c. The strongest intensity observed in the quarter plane 3.460× random is observed at the (112)[1$\bar{1}$0] component, scarcely joined along the γ-fibre to a marginally weaker (332)[$\bar{1}\bar{1}$3] orientation. The final orientation present in Figure 6.9c is a weak (001)[110] orientation.

The crystallographic texture at the centre plane of 10 mm X70 pipe samples is presented in

Figure 6.9d. The centre plane displays a strong α-fibre texture with a maximum intensity of 5.257× random, concentrated between (112)[1$\bar{1}$0] and (113)[1$\bar{1}$0]. The intensity being centred between (112)[1$\bar{1}$0] and (113)[1$\bar{1}$0] is an artefact from combining three constituent areas as each was concentrated at either (112)[1$\bar{1}$0] or (113)[1$\bar{1}$0]. Strong (332)[$\bar{1}\bar{1}$3] and (001)[110] textures with a well defined γ-fibre are also observed. The highest intensity of textures present along the γ-fibre is the (111)[1$\bar{2}$1] orientation.

The 10 mm X70 pipe sample was sourced from industry to benchmark against the laboratory rolled samples. As such the textures that developed were expected to be similar to those observed in the samples manufactured through Schedule 2. The surface plane, in Figure 6.9b, shows a strong {110}//RP fibre texture that has developed at approximately $\varphi = 45°$. The Goss (110)[001] texture is associated with textures at the surface of rolled material; typically formed by shear from the rollers [21, 168, 178]. The approximately (110)[3$\bar{3}$4] component present in the 10 mm X70 plate was not identified in any of the laboratory rolled samples, nor the 20 mm X70 plate. A possible reason for the difference in texture at the surface of the 10 mm pipe is the pipe forming and coating process the pipe underwent. The texture at the surface of bare plate is altered significantly during pipe forming and coating with an observable shift from (110)[001] to (110)[3$\bar{3}$4] observed by Li et al. (2017) [242].

The quarter and centre plane of the 10 mm X70 pipe sample in Figures 6.9c and 6.9d have very similar textures profiles with intensity of the main components the only difference. The main textures that formed in these two planes were the (112)[1$\bar{1}$0], (113)[1$\bar{1}$0], (001)[110] and the (332)[$\bar{1}\bar{1}$3] orientations. The textures observed in the 10 mm X70 pipe were typical of hot rolled low carbon steels published in the literature [137, 183, 185, 238]. The absence of the (001)[1$\bar{1}$0] orientation is likely due to the specifics of the rolling schedule; crystal variant selection favours (332)[$\bar{1}\bar{1}$3] production compared with (001)[1$\bar{1}$0] orientations with less severe rolling deformation in the austenitic region [240].

6.3.3 6.4 mm X70 Plate

The 6.4 mm X70 plate was supplied by Jemena and was sectioned from a hot rolled coil. Samples for this analysis were sectioned from $\frac{1}{4}$ of the width of the supplied plate, for consistency and, to ensure the flame cut edge did not influence the results. Per Section 5.1.3, the 6.4 mm plate was finish rolled at approximately 840°C, hence it is considered hot rolled and is expected to develop hot rolling textures. The ODF plots at the surface, quarter and centre planes are presented in Figure 6.10 with a key showing the textures present in each ODF.

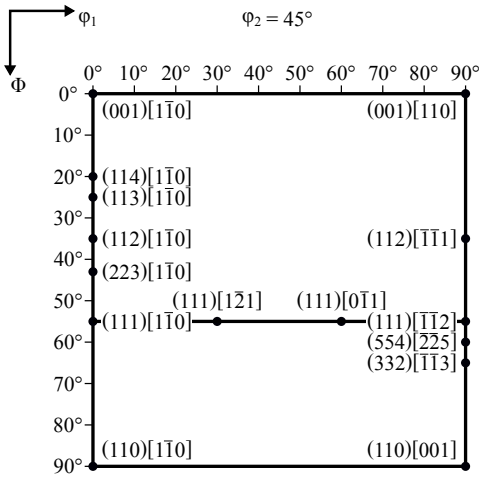

(a) Orientation key.

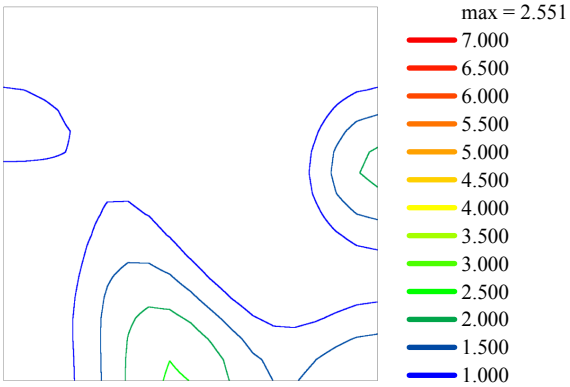

(b) 6.4 mm X70 plate: surface.

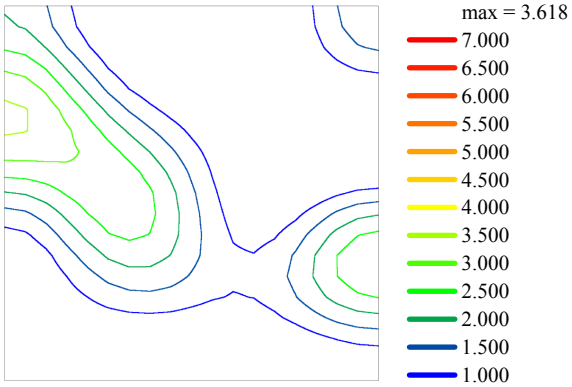

(c) 6.4 mm X70 plate: quarter.

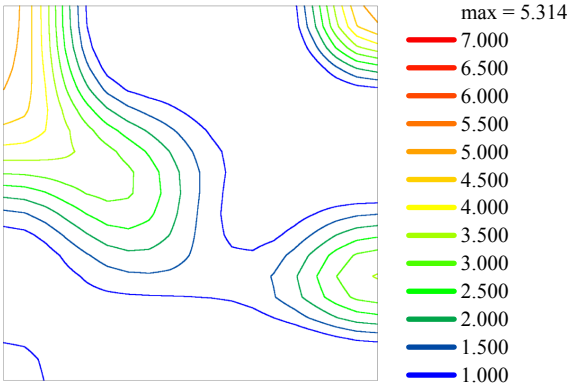

(d) 6.4 mm X70 plate: centre.

Figure 6.10: ODFs at $\phi_2 = 45°$ of the texture identified in the 6.4 mm X70 plate.

The crystallographic texture from the surface of 6.4 mm X70 plate samples is presented in Figure 6.10b. The component observed at the surface of the 6.4 mm X70 plate the highest intensity of 2.551× random, was along the {110}//RP fibre at approximately $\varphi_1 = 40°$.

Additionally, a moderately strong (112)[$\bar{1}\bar{1}$1] and, negligible (113)[1$\bar{1}$0] components were observed at the surface.

The crystallographic texture at the quarter thickness plane of the 6.4 mm X70 plate samples is presented in Figure 6.10c. The texture from the quarter plane shows a strong α-fibre texture with an intensity of 3.618× random at (113)[1$\bar{1}$0]. A strong (554)[$\bar{2}\bar{2}$5] orientation, only slightly weaker in intensity than the (113)[1$\bar{1}$0], is also observed. A weak (001)[110] component is present, as is the γ-fibre, although scarcely joined.

The crystallographic texture of the centre plane is presented in Figure 6.10d. The texture from the centre plane is strongest at (001)[1$\bar{1}$0] and (001)[110] where the maximum intensity 5.314× random at (001)[1$\bar{1}$0]. Two additional components at (332)[$\bar{1}\bar{1}$3] and (110)[1$\bar{1}$0] are also observed. The γ-fibre is partially defined with a maximum intensity at the (111)[1$\bar{2}$1] component.

The 6.4 mm X70 plate was the final industry sample intended to benchmark against the laboratory rolled specimens. It had the closest thickness to the 7 mm thick laboratory rolled specimens, and was supplied as hot rolled coil. The surface of the coil shows a similar texture profile to that identified in the surface of the 10 mm X70 pipe. The act of pipe forming appears to create this texture, and the typical surface (110)[001] component is rotated to the (110)[3$\bar{3}$4] component [242]. While this sample did not have any pipe forming operations carried out on it, it was uncoiled and flattened prior to receiving, a considerable deformation process. A weak (110)[001] orientation is present at the surface of the 6.4 mm X70 plate, not observed in the surface of the 10 mm X70 pipe. This feature may be present in the 6.4 mm X70 plate due to the lack of pipe forming and coating. This feature has been observed to disappear due to those additional processes in a sample of X70 steel as reported by Li et al. (2017) [242].

The textures at the quarter and centre plane are very similar with both displaying strong

α and γ-fibre textures and, a pronounced (001)[110] orientation. The main difference between them is the quarter plane, in Figure 6.10c, has the highest intensity at approximately (113)[1$\bar{1}$0], whilst the centre plane, in Figure 6.10d, has the highest intensity at (001)[1$\bar{1}$0]. The results may be due to the centre plane experiencing rolling as nearly perfect plane strain which increases the proportion of the (001)[1$\bar{1}$0] & (001)[110] textures [178]. The 6.4 mm X70 plate was stated in Section 5.1.3 to have been produced through hot rolling, with finish rolling conducted above the A_3 temperature. The textures observed in the 6.4 mm X70 plate appear to be consistent with those identified in hot rolling literature [137, 183, 185, 238]; however, the centre plane more closely resembles Schedule 3.

6.3.4 Comparison of Industry Supplied Samples

When comparing the texture measured in the three industry supplied samples, it is evident that there is a consistent texture produced in industry. A comparison of the surface, quarter and centre planes of the industry supplied samples is undertaken below.

Surface Texture Comparison

The textures identified at the surface of the industry supplied samples are presented in Figure 6.11. The textures at the surface of the 10 mm X70 pipe and 6.4 mm X70 plate samples in Figures 6.11b and 6.11c are almost identical. They were likely formed due to cold deformation from the coiling, uncoiling, and pipe forming. The 20 mm X70 plate, in Figure 6.11a, displays a surface texture more reminiscent of a quarter plane. The reason behind this may be because the 20 mm X70 plate was supplied unfinished, not subjected to coiling and is significantly thicker than the other investigated specimens. This significant deviation from the other two industry supplied samples likely contributed to the texture differences observed at the surface.

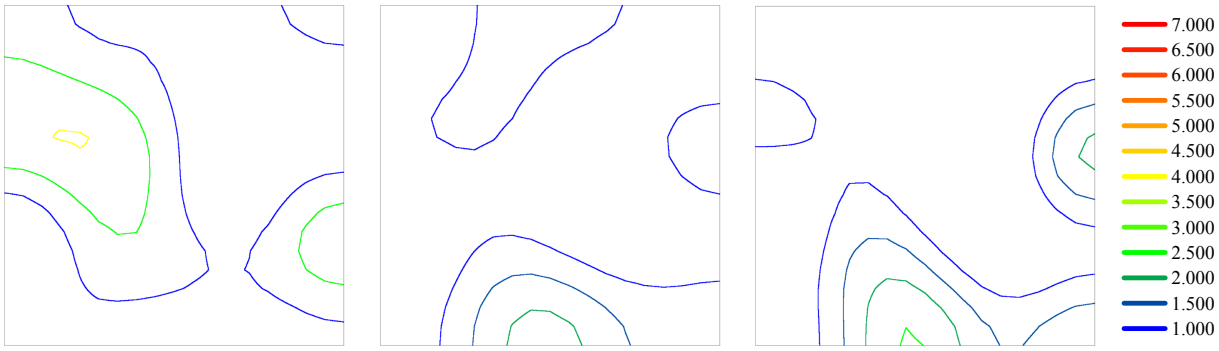

(a) 20 mm X70 plate: surface.

(b) 10 mm X70 pipe: surface.

(c) 6.4 mm X70 plate: surface.

Figure 6.11: ODFs at $\phi_2 = 45°$ of the textures identified at the surface of the industry supplied samples.

Quarter Texture Comparison

The texture at the quarter plane are presented in Figure 6.12. As seen in Figure 6.12, the three industry samples have similar textures, indicative of hot rolling. The industry samples display strong (112)/(113)[1$\bar{1}$0] and (332)[$\bar{1}\bar{1}$3] orientations with the beginnings of a well defined γ-fibre.

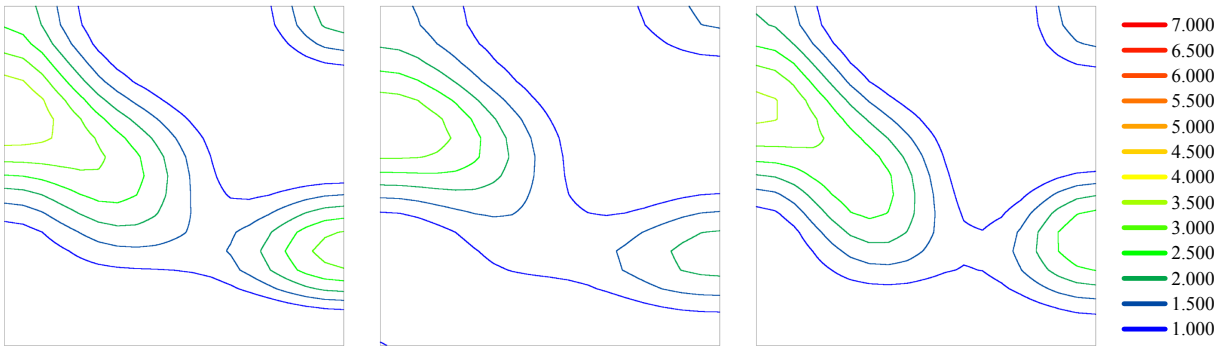

(a) 20 mm X70 plate: quarter.

(b) 10 mm X70 pipe: quarter.

(c) 6.4 mm X70 plate: quarter.

Figure 6.12: ODFs at $\phi_2 = 45°$ of the textures identified at the quarter of the industry supplied samples.

Centre Texture Comparison

The texture at the centre plane is presented in Figure 6.13. The 20 mm X70 plate and 6.4 mm X70 plate samples, in Figures 6.13a and 6.13c, are almost identical, with the exception of the 20 mm samples having a higher intensity of the {223}//RP fibre at $\varphi_1 = 30°$. The 10 mm X70 pipe sample has the highest intensity between the (112)[1$\bar{1}$0] and (113)[1$\bar{1}$0] orientations whereas, the 20 mm and 6.4 mm X70 plates display the highest intensity at the (001)[1$\bar{1}$0] component. The difference in texture between the 10 mm X70 pipe and the 20 mm and 6.4 mm X70 plates may be due to the pipe forming process. It has been observed in literature that pipe forming can strengthen (112)/(113)[1$\bar{1}$0] textures and weaken (001)[1$\bar{1}$0] textures, reported by Li et al. (2017) [242].

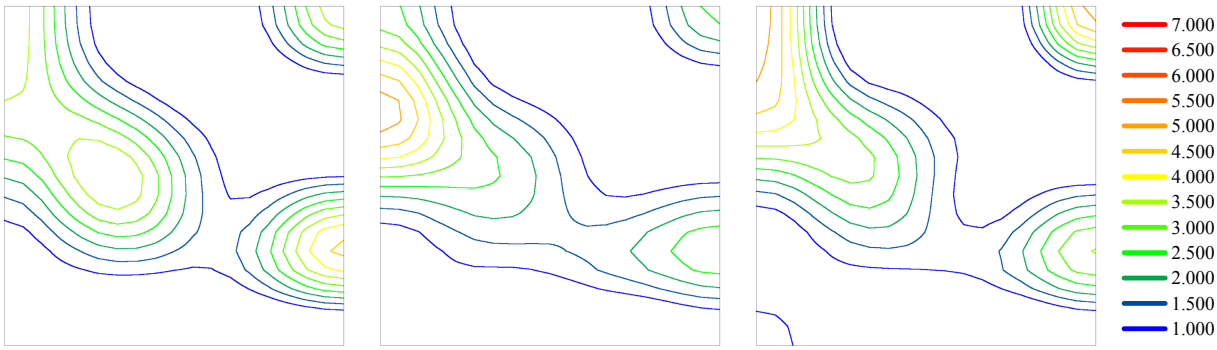

(a) 20 mm X70 plate: centre. (b) 10 mm X70 pipe: centre. (c) 6.4 mm X70 plate: centre.

Figure 6.13: ODFs at $\phi_2 = 45°$ of the textures identified at the centre of the industry supplied samples.

6.4 Comparison Between Laboratory Rolled and Industry Supplied Samples

The texture produced in the laboratory rolled samples were compared to studies in literature to confirm the textures that developed were representative of those studies. For further clarification, the initial material and two industry supplied X70 samples, of similar wall thickness to the final laboratory rolled X70 plates, were analysed to provide a direct comparison of textures. The following section contains a comparison of the tex-

tures developed in the laboratory rolled samples to those of the industry supplied samples.

Surface Texture Comparison

When comparing the surface textures of the laboratory rolled samples, in Figure 6.5, with the surface textures of the industry supplied samples, in Figure 6.11, some differences become apparent. Whilst the laboratory rolled samples, in Figure 6.5, show strong (110)[001] orientations at the surface, the 6.4 mm X70 plate and 10 mm X70 pipe, in Figures 6.11b and 6.11c, display primarily the (110)[$3\bar{3}4$] orientation. As outlined in Section 6.3.2, the different surface texture of the 10 mm X70 pipe is likely due to pipe forming processes [242]. In the case of the 6.4 mm X70 plate, as described in Section 6.3.3, whilst no pipe forming processes were undertaken on this sample, the act of uncoiling could result in a change in surface texture as uncoiling and pipe forming are inextricably linked in the manufacture of the 6.4 mm X70 plate. The laboratory rolled specimens were not coiled or deformed post rolling, hence different surface textures are expected. The 20 mm X70 plate has an unusual texture at the surface plane that does not align with classic literature, nor the other two industry supplied specimens. The likely reason for the unusual texture observed in the 20 mm X70 plate was that it was supplied unfinished and would likely require additional rolling to meet the thickness requirements, further altering the surface texture.

Quarter Texture Comparison

The textures observed at the quarter plane of the laboratory rolled samples, in Figure 6.6, are compared with the industry supplied samples, in Figure 6.12. It is evident that, whilst the industry supplied samples are more strongly textured, the textures that developed are very similar to Schedule 2, Figure 6.6b. As each of the industry supplied samples were expected to have been manufactured through hot rolling, it is not a surprise that the conventionally hot rolled laboratory sample had a similar texture profile.

The recrystallized rolling regimen of Schedule 1, Figure 6.6a, has a homogeneous through-thickness texture, likely because the processing conditions were so unlike conventional TMCP rolling [243]. This difference provides another texture to test the susceptibility of SCC to and strongly accentuates the textures that are seen as detrimental to SCC in literature (Section 2.7.5).

The warm rolling regimen of Schedule 3, Figure 6.6c, has a texture very similar to that of Schedule 1 with the main exception that it developed a higher intensity of $(112)[1\bar{1}0]$ orientations. The increased intensity provides an additional texture profile to test SCC susceptibility. The texture observed in samples manufactured through Schedule 3 is dissimilar to the industry supplied samples likely developed due to the warm rolling regimen used to manufacture it. As discussed in Section 6.2.3, the rotated cube {100}<110>textures are strengthened by deformation of transformed ferrite [102, 244].

Centre Texture Comparison

The centre textures of the laboratory rolled samples, in Figure 6.7, were compared to the industry supplied samples, in Figure 6.13. The textures observed in the industry supplied samples were most similar to the textures developed in Schedules 2 and 3, Figures 6.7b and 6.7c. As Schedule 1 was a recrystallized rolling schedule it developed homogeneous texture through-thickness. As discussed in Section 6.4, the recrystallized rolling schedule is not expected to develop textures similar to those identified in literature for hot or warm rolling.

6.5 Summary

The aim of the study was to investigate the role of controlled rolling on the formation of crystallographic texture in pipeline steel, and the effect it had on stress corrosion crack-

ing susceptibility. To achieve that, samples of 20 mm X70 plate were thermomechanically control rolled under the rolling schedules outlined in Section 5.2.4 with the aim of developing different textures to test their SCC susceptibility.

This chapter encompassed measuring textures developed in the rolling schedules and comparing them to the textures present in the industry supplied X70 samples. It is evident, in Section 6.4, that the laboratory rolling schedules were able to both mimic the texture of pipeline steel in service today as well as develop different textures such that SCC susceptibility could be evaluated in. Whilst the surface textures, due to rolling conditions, were almost identical, the quarter thickness plane had enough variability to test the subsequent SCC susceptibility of the rolling specimens.

One main finding is that the development of texture is not always predictable, and due to the multitude of transformation products that share common roots, it can be difficult to confirm where and by what process textures originated from. Therefore, the influence of rolling schedule on texture evolution in the industry supplied samples was not the focus of this chapter. It is not a simple matter to determine the manufacturing process based on the crystallographic texture due to the multiple paths through which texture can form. As all temperatures and rolling conditions of the laboratory rolled schedules were known, literature concerning texture transformation in steels was able to be linked to the expected conditions. The following chapter will explore the SCC susceptibility of the laboratory rolled and industry supplied specimens to determine the effect of crystallographic texture on SCC.

Chapter 7

Results and Discussion - SCC in Pipeline Steel

This chapter presents and discusses the results obtained from SCC testing to determine the susceptibility of both the laboratory rolled and industry supplied samples. SCC susceptibility is evaluated using the Linearly Increasing Stress Test (LIST) apparatus. As discussed in Section 2.5.2, the LIST applies a cyclic load to a tensile specimen immersed in a corrosive environment to simulate the conditions faced by pipelines in the field. Laboratory testing allows for the same environmental and stress conditions to be applied to the differently manufactured samples to investigate the role of manufacturing route on SCC susceptibility. LIST specimens were subjected to a $1N$ solution of sodium carbonate and bicarbonate ($0.5M\ Na_2CO_3 + 1M\ NaHCO_3$) held at 75°C and loaded between 0.9 - 0.95% of their yield stress for 10 cycles at a constant loading rate per Section 4.6.1. The resulting specimens were sectioned to identify the number and length of the cracks that formed over the testing period and the resulting measurements gave insight into the SCC susceptibility.

A total of 21 SCC specimens were tested, 12 laboratory rolled and 9 industry supplied with each sectioned into three parts to enable the determination of SCC susceptibility. The two measures of SCC susceptibility were the total number of cracks that formed in

the gauge length of the LIST specimen and the crack velocity (crack length normalised by the testing time). The number of cracks that form provides a measurement of the crack initiation susceptibility with more cracks indicating a higher SCC initiation susceptibility. The crack velocity is an indication of SCC crack propagation susceptibility and is found by normalising the maximum crack length with the testing time such that the speed of crack propagation can be compared between specimens.

As outlined in Section 4.6.3, the samples were sectioned from the quarter thickness plane of both the laboratory rolled and industry supplied samples due to the lack of texture variation identified in the surface of the laboratory rolled specimens observed in Figure 6.5.

The laboratory rolled samples and the industry supplied samples were subjected to the same environmental conditions along with the same stress profiles. The laboratory rolled samples were manufactured from the same raw material with the same nominal chemical composition to prevent differences in chemical composition from influencing SCC susceptibility. The three laboratory rolled samples and the 20 mm X70 plate with the same chemical composition could be directly compared, however, the 10 mm X70 pipe and 6.4 mm X70 plate with different nominal chemical compositions, could not be directly compared. As an additional bench mark, in the field, SCC cracks in an API 5L X65 grow on average at a rate of 0.25 mm/year or 7.93×10^{-9} mm/s.

The two parameters investigated are the crack velocity and a tally of the number of cracks identified in the gauge length of the LIST samples as described in Section 4.6.3. The crack velocity is calculated from the longest crack observed in the LIST specimen divided by the total time in the apparatus. The cracks are imaged using optical microscopy at 1000$\times$ magnification. The measuring system was calibrated using a stage micrometer prior to use that had a resolution of 10 μm.

The cracks were tallied with the aid of a digital tally counter in each of the LIST speci-

mens. The live view of the optical microscope had high enough resolution and magnification that cracks could easily be observed at the surface. To ensure pits or other surface defects were not included in the count, a crack must have an aspect ratio greater than 10 (depth:width) i.e. be at least 10× longer than it is wide, and be connected to the surface such that plate forming defects are not counted. In the event that multiple branches are observed along a single crack, only one crack is counted. A summary of defects that are considered cracks in this study is presented in Figure 7.1. The defects that are arrowed in Figure 7.1 are defined as cracks with any defect not arrowed not being defined as a crack. Pits in the samples investigated appeared to have aspect ratios less than 2 (depth:width) so were readily distinguishable from cracks. Due to the limitations of optical microscopy, sub-micron cracks were not included in the count as they could not be reliably detected nor distinguished from non corrosion related surface defects.

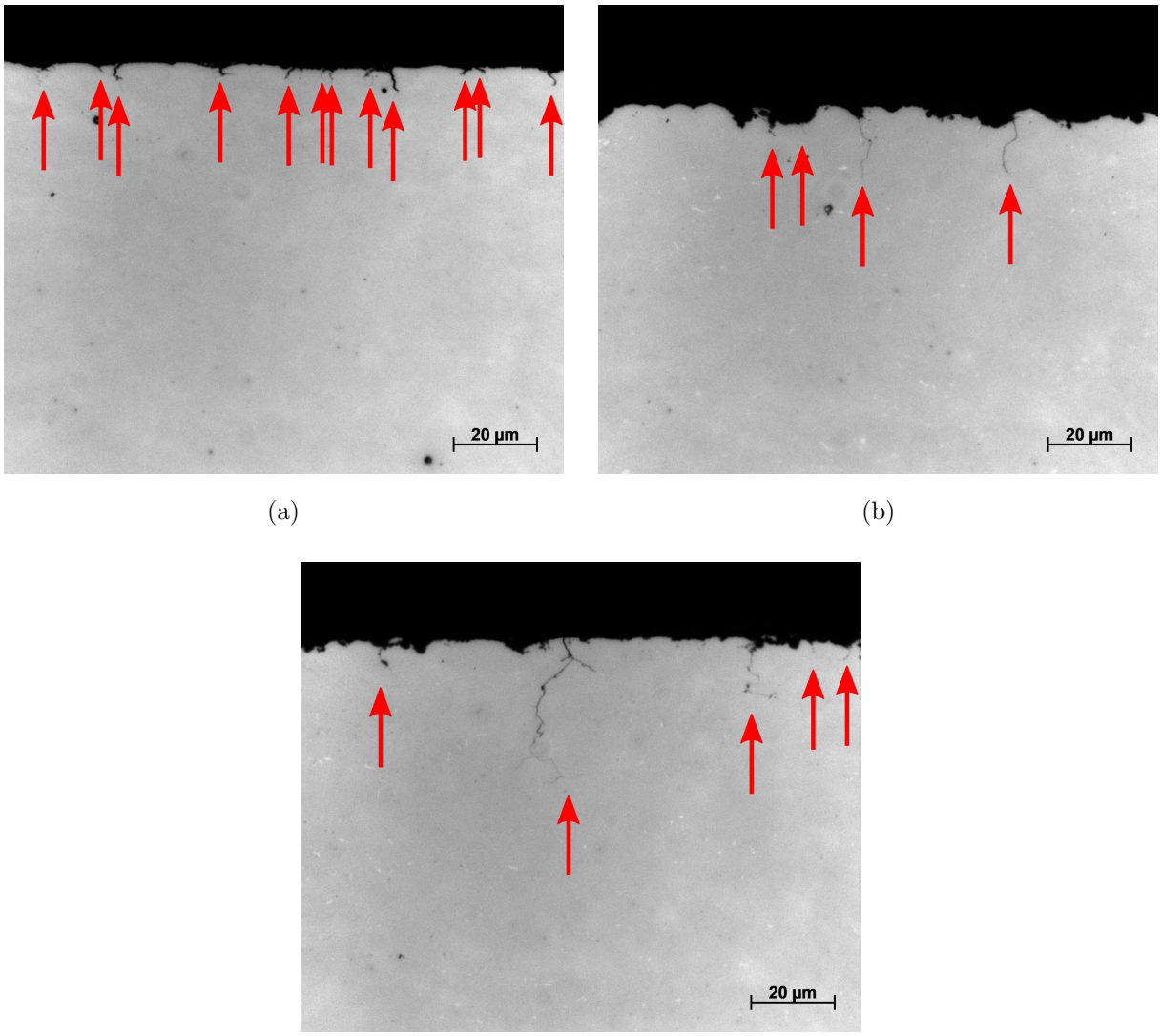

(a) (b)

(c)

Figure 7.1: Surface defects (arrowed) that are defined as cracks in this study.

7.1 SCC Susceptibility of Industry Supplied and Laboratory Rolled Samples

This section contains the results of SCC testing from the three industry supplied samples of X70 pipe and plate as well as the three investigated rolling schedules. As the 6.4 mm X70 and 10 mm X70 have slightly different chemical compositions as compared to the laboratory rolled samples and the 20 mm X70 plate, the SCC results may not directly comparable. The industry supplied samples are included to benchmark the laboratory

rolled sample SCC susceptibility in terms of crack velocity and number of cracks detected. The industry supplied samples also provide the opportunity to determine what level of SCC can be expected in current pipe stock.

7.1.1 6.4 mm X70 Plate

The 6.4 mm X70 plate was an industry supplied X70 plate used to manufacture 6.4 mm thick, ⌀300 mm pipe for gas transmission. The plate was supplied uncoated with the factory scale adhered to the surface of the material. The microstructure of the 6.4 mm X70 plate was primarily a mixture of granular bainite and polygonal ferrite as seen in Figure 5.11 with some dark phases associated with degenerated pearlite; see Figure 5.12. The average grain size of the 6.4 mm X70 plate at the quarter thickness plane was 9.0 ± 5.3 μm as measured through EBSD. The SCC susceptibility results of 6.4 mm X70 plate are presented in Table 7.1 where the time spent in the LIST, total number of cracks, maximum crack length and the crack velocity of all the tested specimens are compared.

Table 7.1: SCC susceptibility results of 6.4 mm X70 plate samples.

Sample	**Time in LIST (s)**	**Cracks Identified**	**Crack Length (μm)**	**Crack Velocity (mm/s)**
6.4.1	367700	4951	8.93	2.43×10^{-8}
6.4.2	374000	10429	16.70	4.46×10^{-8}
6.4.3	384000	6383	12.05	3.14×10^{-8}
Average	375233	7254	12.56	3.34×10^{-8}
STD	7279	2319	3	8.44×10^{-9}

The average crack velocity of the 6.4 mm X70 plate is approximately 3.34×10^{-8} mm/s corresponding to a crack rate of 1.05 mm/ year. The average number of cracks initiated from the surface was 7254, corresponding to approximately 73 cracks per mm (based on

50 mm gauge length with two initiating faces). Typical SCC cracks in the 6.4 mm X70 plate is presented in Figure 7.2. The three main cracks that formed in the 6.4 mm X70 plate were formed from the base of what appears to be deep pits. As seen in Figure 7.2a and at a higher magnification in Figure 7.2b, the three cracks are highly branched with many small cracks originating from the main crack. There appears to be a fracture in the surface oxide layer directly above where the cracks initiated, as seen in Figure 7.2b. An oxide layer prevents SCC whilst intact, however, when fractured as was the case here, it brings the surface into contact with the fluid which can allow SCC to initiate as also reported by Beavers et al. (1998) [47].

EBSD analysis was undertaken on the cracks and presented in Figures 7.2c and 7.2d. Whilst the crack appears to be mostly intergranular in nature in the Inverse Pole Figure (IPF), when observing the grain map with a grain boundary threshold of 15°, it appears as though cracking is both intergranular and transgranular. As seen in Figure 7.2d, both cracks 1 and 2 initially propagate intergranularly, however, they change to transgranular propagation near the crack tip. As the samples were removed from the LIST apparatus prior to failure, it is not possible to determine whether the cracks were arrested or would continue propagating with additional testing time. Small amounts of transgranular propagation is expected due to the surface of the LIST specimens being polished leading to a stressed deformed surface layer. The effect of the deformed layer on crack propagation method was observed by Wang and Atrens (2003) [245]. The deformed surface layer was reported by Wang and Atrens (2003) [245] to increase the levels of dislocations at the grain boundaries such that cracks were no longer constrained by grain boundaries and transgranular propagation becomes possible.

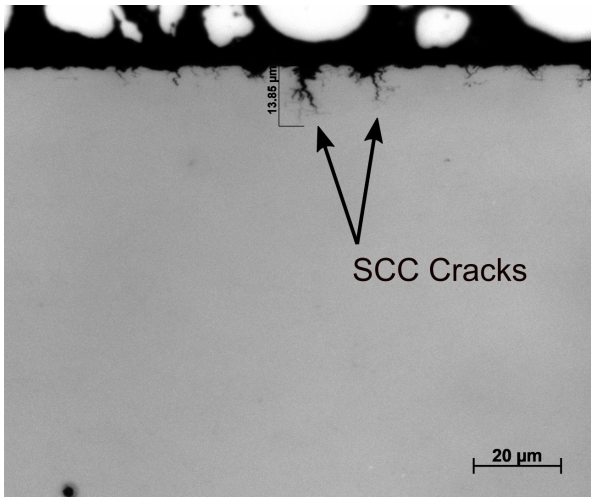

(a) Optical Micrograph

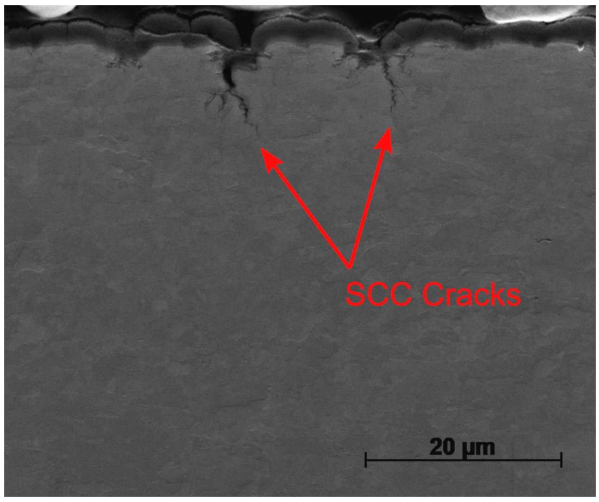

(b) SEM Micrograph

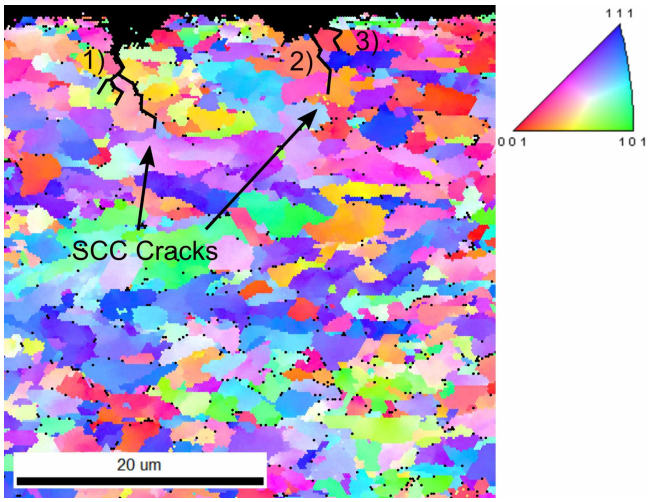

(c) EBSD IPF

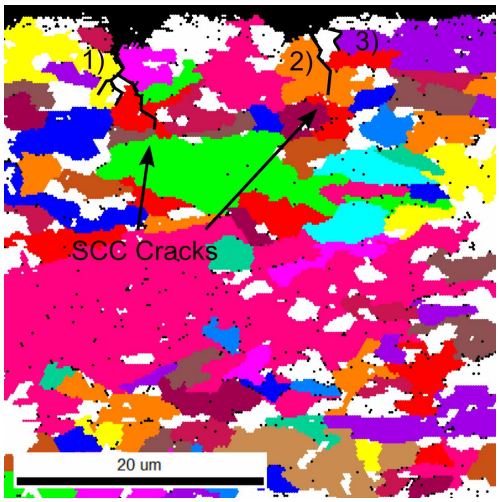

(d) EBSD Grain Map

Figure 7.2: Summary of cracks identified in the 6.4 mm X70 plate samples.

7.1.2 10 mm X70 Pipe

The 10 mm X70 pipe supplied by industry was a section of pipe stored by the pipe owners to use as a replacement in the event the current pipeline was damaged. The pipe was supplied coated in a dual layer epoxy with the end of the pipe bare to facilitate welding. The microstructure of the 10 mm X70 pipe was primarily a mixture of granular bainite and polygonal ferrite as seen in Figure 5.7 with dark secondary phases associated with degenerated pearlite and M/A constituents; see Figure 5.8. The average grain size of the 10 mm X70 pipe at the quarter thickness plane was 8.3 $\pm$ 3.8 μm as measured through

EBSD and was the smallest grain size measured out of all the test samples investigated. The SCC susceptibility results of the 10 mm X70 are presented in Table 7.2 where the time spent in the LIST, total number of cracks, maximum crack length and the crack velocity of all the tested specimens are compared.

Table 7.2: SCC susceptibility results of 10 mm X70 pipe samples.

Sample	**Time in LIST (s)**	**Cracks Identified**	**Crack Length (μm)**	**Crack Velocity (mm/s)**
10.1	367700	5015	17.63	4.29×10^{-8}
10.2	374000	5210	15.06	3.69×10^{-8}
10.3	384000	5355	16.81	4.17×10^{-8}
Average	375233	5193	16.5	4.05×10^{-8}
STD	7279	139	1	2.6×10^{-9}

The average crack velocity of the 10 mm X70 pipe is approximately 4.05×10^{-8} mm/s, corresponding to a crack rate of approximately 1.28 mm/year. The average number of cracks that initiated from the surface was 5193, corresponding to approximately 52 cracks per mm (based on 50 mm gauge length with two initiating faces). Typical SCC cracks observed in the 10 mm X70 pipe are presented in Figure 7.3. The cracks that formed in the 10 mm X70 were typically very thin, highly irregular and had minimal branching. An optical micrograph at 1000× magnification is presented in Figure 7.3a whilst SEM imaging of the same cracks are presented at higher magnification in Figure 7.3b. Whilst unetched, the colloidal silica used to polish the SEM sample reveals some faint grain structures surrounding the crack in Figure 7.3b showing what appears to be intergranular propagation.

Entirely intergranular propagation was confirmed in the EBSD imaging observed in Figures 7.3c and 7.3d, the EBSD IPF and grain maps respectively. The grain map in Figure 7.3d shows that with a grain boundary threshold of 15°, all cracks propagate entirely

intergranularly. The crack propagation observed in the 10 mm X70 pipe is compared to the mixed transmission observed in the 6.4 mm X70 plate in Figure 7.2d. Whilst both samples were prepared to the same nominal surface roughness, it appears as though the grain boundaries in the 10 mm X70 pipe were better able to constrain the crack to propagating intergranularly. As seen in Figure 7.2c, there is a higher proportion of very small deformed grains at the surface of the 6.4 mm X70 as compared to the surface of the 10 mm X70 cracks in Figure 7.3c. The lower deformation in the 10 mm X70 pipe likely resulted in a lower risk of transgranular propagation. This was hypothesised by Wang and Atrens (2003) [245] that deformation at the surface could result in transgranular cracking initially.

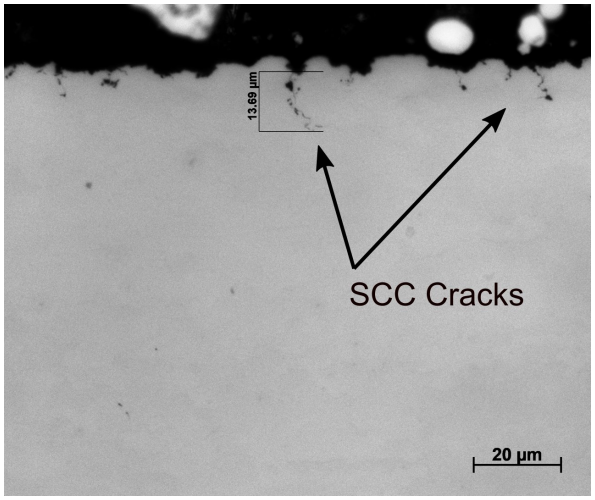

(a) Optical Micrograph

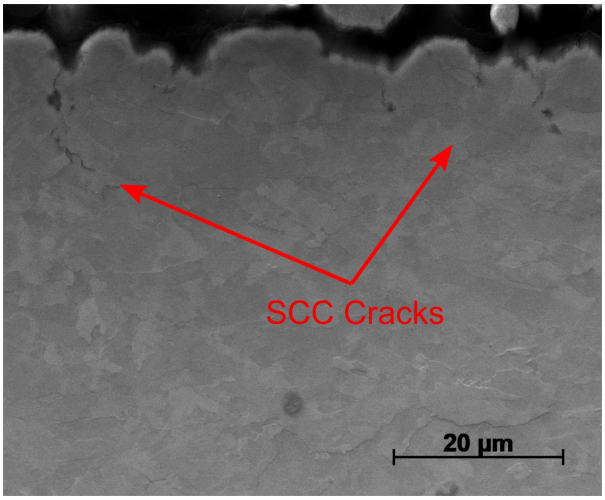

(b) SEM Micrograph

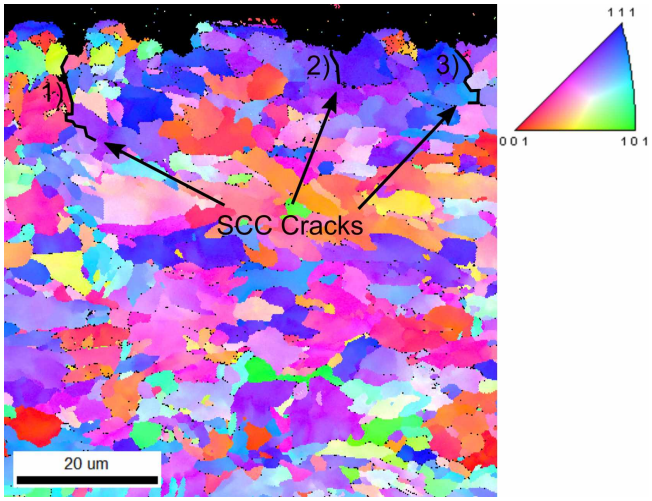

(c) EBSD IPF

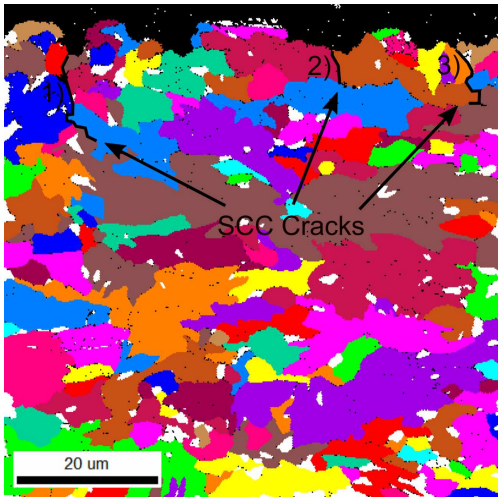

(d) EBSD Grain Map

Figure 7.3: Summary of cracks identified in the 10 mm X70 pipe samples.

7.1.3 20 mm X70 Plate

The 20 mm X70 plate was supplied by industry in the as rolled condition for use in laboratory testing. The 20 mm X70 plate was the starting material for the laboratory rolled steel sections preparation and, as such has the same nominal chemical composition. The microstructure of the 20 mm X70 plate was primarily granular bainite with some instances of polygonal ferrite as seen in Figure 5.2. Some secondary phases containing degenerated pearlite and M/A constituent were also present in the 20 mm X70 plate; see Figure 5.3. The 20 mm X70 plate had an average grain size of 9.5 ± 5.7 μm as measured through EBSD and had the largest average grain size of the three industry supplied samples. The SCC susceptibility results of the 20 mm X70 plate are presented in Table 7.3 where the time spent in the LIST, total number of cracks, maximum crack length and the crack velocity of all the tested specimens are compared.

Table 7.3: SCC susceptibility results of 20 mm X70 plate samples

Sample	**Time in LIST (s)**	**Cracks Identified**	**Crack Length (μm)**	**Crack Velocity (mm/s)**
20.1	345860	4063	14.40	4.16×10^{-8}
20.2	363710	2881	12.81	3.52×10^{-8}
20.3	357560	4465	15.61	4.37×10^{-8}
Average	355712	3803	14.27	4.02×10^{-8}
STD	7404	672.3	1.15	3.60×10^{-9}

The average crack velocity of the 20 mm X70 plate is approximately 4.02×10^{-8} mm/s, corresponding to a crack rate of approximately 1.27 mm/year. The average number of cracks that initiated from the surface was 3803, corresponding to approximately 39 cracks per mm (based on 50 mm gauge length with two initiating faces). Typical SCC cracks that grew in the 20 mm X70 plate are presented in Figure 7.4, where three main cracks are observed. Optical micrographs of the three cracks are presented in Figure 7.4a and

higher resolution SEM images in Figure 7.4b. As observed in Figure 7.4b, the three cracks initiated from the base of deep pits as well as the ground surface of the LIST specimen. There is no thick oxide present at the surface in this image as seen through SEM imaging.

EBSD IPF and grain maps were produced from this section and are displayed in Figures 7.4c and 7.4d. As seen clearly in Figure 7.4d the three cracks observed in the 20 mm X70 appear to have a mixed propagation of intergranular and transgranular cracking. Crack 1 in Figure 7.4d appears to propagate entirely transgranularly whereas crack 2 is entirely intergranular. Crack 3 is initially intergranular before it changes to transgranular propagation. Cracks 1 and 3 appear to grow transgranularly until they are blocked by perpendicular grain boundaries that appears to prevent additional cracking. LIST cracks that grow from ground surfaces often show transgranular propagation early on because the surface is highly deformed and offers low resistance to SCC within the grain [245]. As seen in the first crack, before it is blocked by the perpendicular grain boundary it begins to crack intergranularly, which was predicted by Wang and Atrens (2003) [245]. As discussed previously, as these samples were removed prior to failure it is not known whether SCC had halted or more time in the LIST would have allowed for continued propagation.

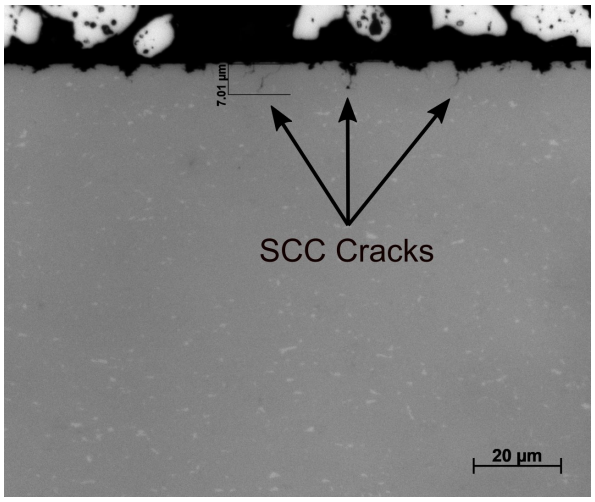

(a) Optical Micrograph

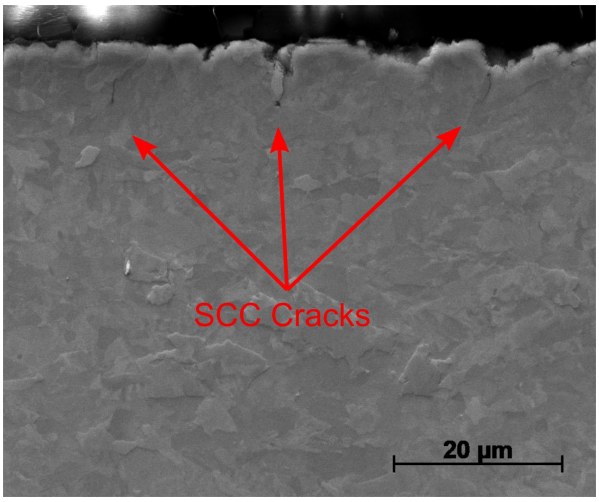

(b) SEM Micrograph

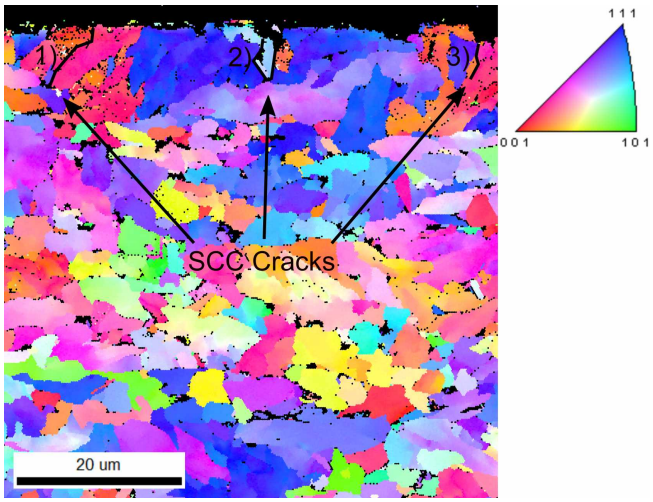

(c) EBSD IPF

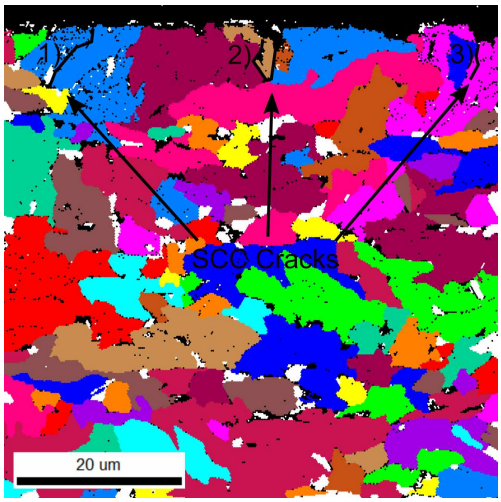

(d) EBSD Grain Map

Figure 7.4: Summary of cracks identified in the 20 mm X70 plate samples.

7.1.4 Schedule 1

Schedule 1 was the recrystallized rolling schedule that was formed by finish rolling above the T_{NR}, air cooling to just above A_{r3} (768°C), and then water cooled to 450°C at a rate of 10°C/s. The samples was subsequently air cooled to room temperature. The microstructure of Schedule 1 as outlined in Section 5.3.2 was a combination of granular and upper bainite, see Figure 5.27. Schedule 1 had a grain size of 12.6 ± 10.1 μm at the quarter thickness plane, as measured through EBSD. The SCC susceptibility results of Schedule 1 are presented in Table 7.4, where the time spent in the LIST, total number of cracks,

maximum crack length and the crack velocity of all the tested specimens are compared.

Table 7.4: SCC susceptibility results of Schedule 1

Sample	**Time in LIST (s)**	**Cracks Identified**	**Crack Length (μm)**	**Crack Velocity (mm/s)**
S1.1	380600	1515	80.28	2.11×10^{-7}
S1.2	333300	4973	62.86	1.88×10^{-7}
S1.3	376500	2344	117.14	3.11×10^{-7}
S1.4	433500	2053	86.30	1.99×10^{-7}
Average	380975	2721	86.63	2.27×10^{-7}
STD	35542	1333	20.00	4.89×10^{-8}

The average crack velocity of Schedule 1 is approximately 2.27×10^{-7} mm/s, corresponding to a crack rate of approximately 7.16 mm/year. The average number of cracks that initiated from the surface of Schedule 1 LIST specimens was 2721, corresponding to approximately 28 cracks per mm (based on 50 mm gauge length with two initiating faces). An SCC crack representative of SCC observed in the LIST samples of Schedule 1 is presented in Figure 7.5. An optical micrograph and SEM image are presented in Figures 7.5a and 7.5b, respectively, while EBSD IPF and grain images are presented in Figures 7.5c and 7.5d respectively.

As observed in the EBSD images in Figures 7.5c and 7.5d, the crack propagates primarily intergranularly. There appears to be a single small instance (arrowed) of transgranular cracking between two upper bainite sheaves. Overall, the cracks observed in Schedule 1 were the longest of all the investigated samples and appeared mostly intergranular in nature. The crack in Figure 7.5 appears to propagate with minimal branching, and follows a path perpendicular to the sample surface (perpendicular to the highest stress). The upper bainite observed in Schedule 1 differentiates it from the other investigated samples that have microstructures consisting of granular bainite and ferrite (polygonal and quasi

polygonal). The grain sizes observed in the grain map in Figure 7.5d is significantly larger than any other test specimen and shows straighter grain boundaries. Schedule 1 had the highest SCC susceptibility of all the samples tested. As established in Section 4.7, Schedule 1 was the only process to produce upper bainite. The presence of upper bainite is likely a contributing factor to the high SCC susceptibility observed in Schedule 1. It has been observed in literature that upper bainite has worse SCC resistance, as compared to bainite and ferrite mixed microstructures like those found in the other tested samples [14, 74].

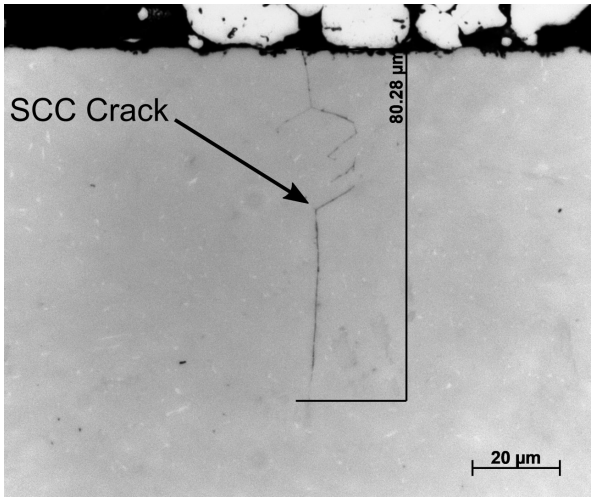

(a) Optical Micrograph

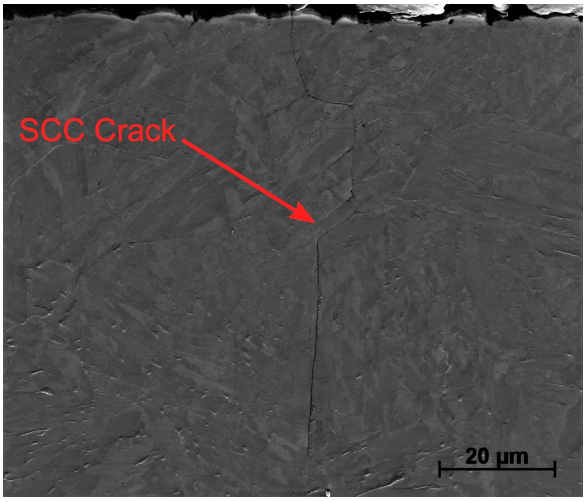

(b) SEM Micrograph

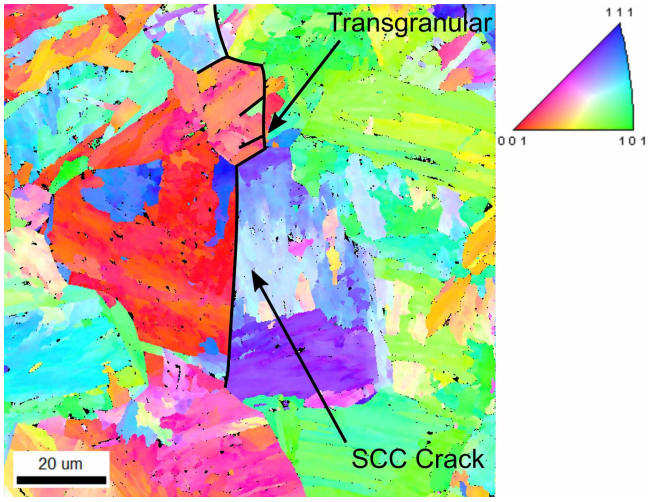

(c) EBSD IPF

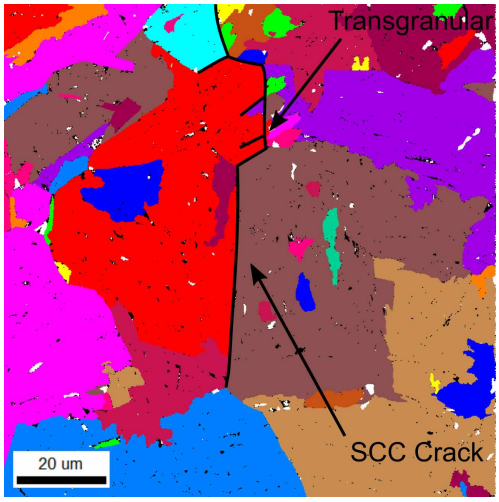

(d) EBSD Grain Map

Figure 7.5: Summary of cracks identified in Schedule 1.

It is believed the difference in microstructure for Schedule 1 is a major factor in having the

worst SCC resistance compared to the other tested samples. As observed in Figures 7.5c and 7.5d the grains in Schedule 1 samples are considerably more uniform in size and shape than those observed in the 6.4 mm X70 plate, the 10 mm pipe or the 20 mm X70 plate. As observed in the left branched crack in Figure 7.5c, a grain boundary perpendicular to the propagation direction of the crack halted its progression. As described by Wang and Atrens (2003) [245], when the crack encounters a grain boundary perpendicular to it is travel direction it is more likely to be halted. As the grains in Schedule 1 are uniform and less randomly oriented than the industry supplied samples, it has less potential sites to halt crack progression, allowing longer cracks to form.

7.1.5 Schedule 2

Schedule 2 was an example of a hot rolled manufacturing process where rough rolling occurred above T_{NR} and finish rolling was undertaken below T_{NR} in the austenite range before water cooling to 450°C at a rate of 10°C/s and subsequently air cooling to room temperature. The microstructure produced through this rolling schedule was primarily granular bainite with polygonal ferrite interspersed throughout, as seen in Figure 5.29; with an average grain size, as determined through EBSD, of 10 $\pm$ 5.7 μm. The SCC susceptibility results of Schedule 2 are presented in Table 7.5 where the time spent in the LIST, total number of cracks, maximum crack length and the crack velocity of all the test specimens are compared.

Table 7.5: SCC susceptibility results of Schedule 2

Sample	**Time in LIST (s)**	**Cracks Identified**	**Crack Length (μm)**	**Crack Velocity (mm/s)**
S2.1	260400	6090	45.45	1.75×10^{-7}
S2.2	262400	5505	27.27	1.04×10^{-7}
S2.3	247400	207	20.27	8.19×10^{-8}
S2.4	246500	1853	25.41	1.03×10^{-7}
Average	254175	3414	29.60	1.16×10^{-7}
STD	7279	2462	9.50	3.5×10^{-8}

The average crack velocity of the LIST samples manufactured from Schedule 2 material was 1.16×10^{-7} mm/s which, while lower than the crack velocity observed in Schedule 1, is still considerably greater than that of the industry supplied samples. The average number of cracks that initiated from the surface of the LIST specimens was 3414, corresponding to approximately 35 cracks per mm (based on 50 mm gauge length with two initiating faces). The number of cracks that formed in Schedule 2 is slightly higher than that of Schedule 1 but is still considerably lower than the average number that formed in the industry supplied samples. SCC cracks typical of those found in Schedule 2 LIST specimens are presented in Figure 7.6. An optical micrograph showing 1000 $\times$ magnification is observed in Figure 7.6a, whilst a higher magnification SEM image is presented in Figure 7.6b. EBSD IPF and grain maps are presented in Figures 7.6c and 7.6d, respectively.

As observed in the EBSD images, the three cracks propagate entirely intergranularly in the LIST specimens manufactured from Schedule 2 material. While the cracks appear to be blocked from further propagation by grain boundaries perpendicular to the direction of travel, as these cracks were not sourced from a fractured specimen, it is possible that should the LIST sample have been returned to the apparatus, it would have continued cracking. There does not appear to be any highly deformed grains at the polished surface and that may be why no transgranular propagation was observed initially as opposed to

that identified in the industry supplied samples.

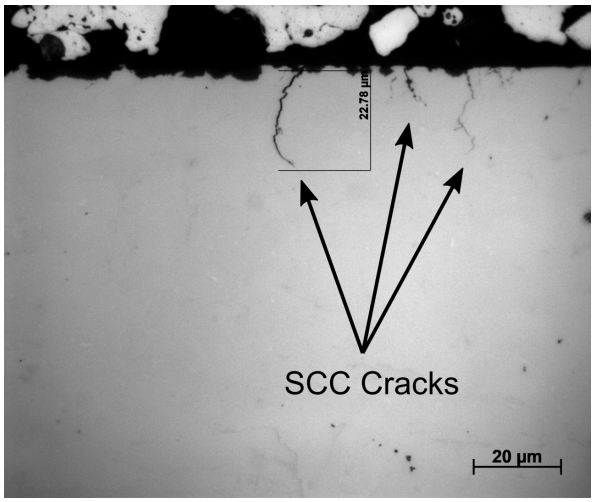

(a) Optical Micrograph

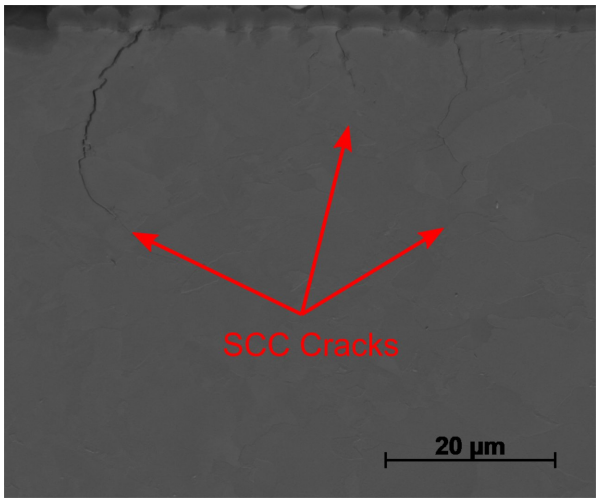

(b) SEM Micrograph

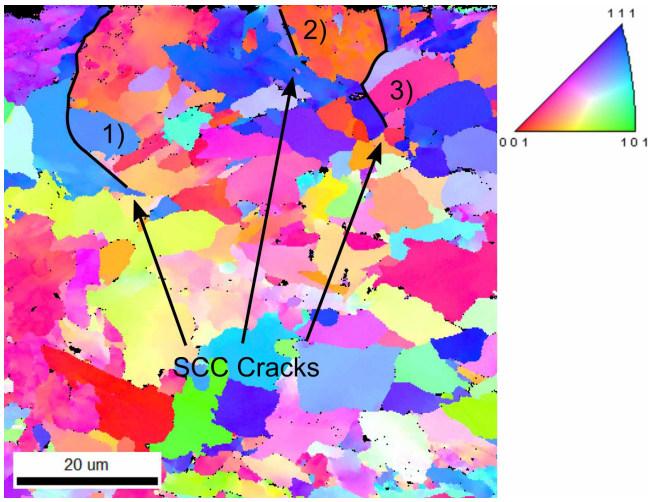

(c) EBSD IPF

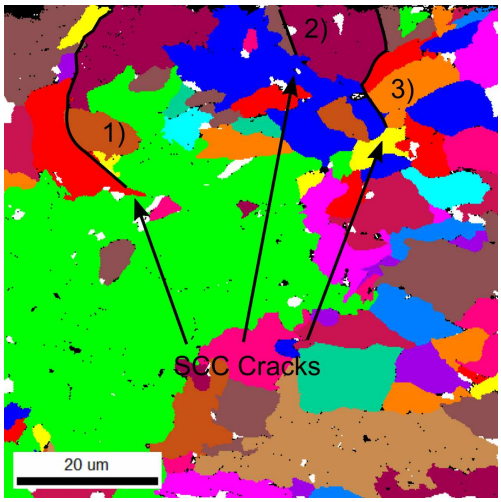

(d) EBSD Grain Map

Figure 7.6: Summary of cracks identified in Schedule 2.

Whilst the microstructures present in Schedule 2 appear the most similar to those of the industry supplied samples, there is a significant difference in the crack velocity that resulted. It is likely that the difference in grain size is a contributing factor to why there is an observed difference in SCC susceptibility between Schedule 2 and the industry supplied samples, as grain size has been observed in literature to influence the SCC susceptibility in a range of materials [17–19]. Although the average grain size of the samples as measured through EBSD is quite similar, as observed in the literature the average grain

size does not show the full extent of the grain size distribution as discussed in a previous publication by the current author [31].

7.1.6 Schedule 3

Schedule 3 was an example of a warm rolled manufacturing process, where rough rolling occurred above T_{NR} and finish rolling occurred below A_{r3} of 768°C, such that both austenite and ferrite were present. The samples were then water cooled to 450°C at a rate of 10°C/s and subsequently air cooled to room temperature. The microstructure produced through this rolling schedule was primarily polygonal ferrite and granular bainite interspersed throughout as observed in Figure 5.29 with an average grain size, as determined through EBSD, of 10.9 ± 5.6 μm. The SCC susceptibility results of Schedule 3 are presented in Table 7.6 where the time spent in the LIST, total number of cracks, maximum crack length and the crack velocity of all the tested specimens are compared.

Table 7.6: SCC susceptibility results of Schedule 3

Sample	**Time in LIST (s)**	**Cracks Identified**	**Crack Length (μm)**	**Crack Velocity (mm/s)**
S3.1	282900	3125	22.73	8.03×10^{-8}
S3.2	266000	4409	36.58	1.38×10^{-7}
S3.3	248100	868	11.45	4.61×10^{-8}
S3.4	244900	1330	20.54	8.39×10^{-8}
Average	260475	2433	22.83	8.70×10^{-8}
STD	15241	1419	9	3.27×10^{-8}

The average crack velocity of the LIST samples manufactured using Schedule 3 material was calculated to be 8.70×10^{-8} mm/s, which was the lowest of the laboratory rolled samples. In addition, the number of cracks tallied to have initiated at the surface of the

LIST specimens was 2433, which correlates to approximately 25 cracks per mm (based on 50 mm gauge length with two initiating faces). The number of cracks counted in Schedule 3 was the lowest of all the tested specimens, industry supplied and laboratory rolled. It appears that overall there are less instances of cracks forming in the laboratory rolled specimens as compared to the industry supplied samples, however, the average crack velocity of Schedule 3 is more than twice that of the fastest cracking industry supplied sample.

Characteristic cracks that formed in Schedule 3 LIST specimens are presented in Figure 7.7, with an optical micrograph at 1000 × magnification presented in Figure 7.7a and higher magnification SEM image in Figure 7.7b. It is clear that there is a thick surface oxide layer present above the cracks in Figure 7.7b, with slight evidence of a fracture corresponding to the location of crack initiation. EBSD IPF and grain maps are presented in Figures 7.7c and 7.7d respectively. The EBSD maps show that cracks 1 and 2 both propagate entirely intergranularly, however, crack 3 appears to propagate mostly transgranularly. It appears that there is some deformation present at the surface of the transgranular cracked grains, indicated by the arrow in Figure 7.7c. Crack 1 appears sheltered from the deformation by initiating from the base of a pit and avoiding an initial transgranular propagation mechanism. As previously discussed, deformation at the surface can lead to transgranular cracking in polished LIST samples [245]. It is shown clearly in Figure 7.7c that, when the crack initiated in a deformed grain (cracks 2 and 3), it is transgranular but, when sheltered from the deformed layer (crack 1), the propagation mechanism is intergranular.

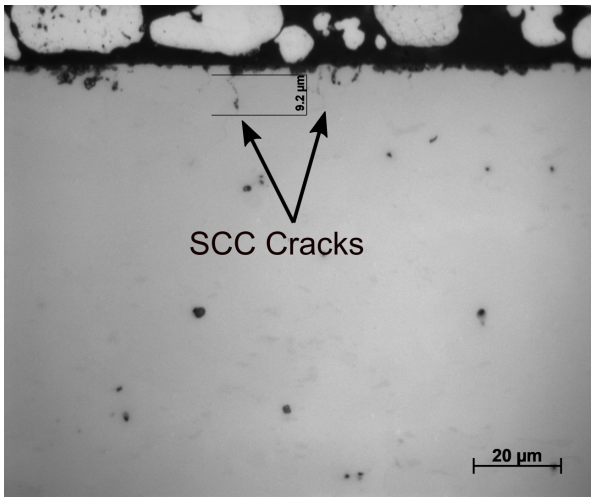

(a) Optical Micrograph

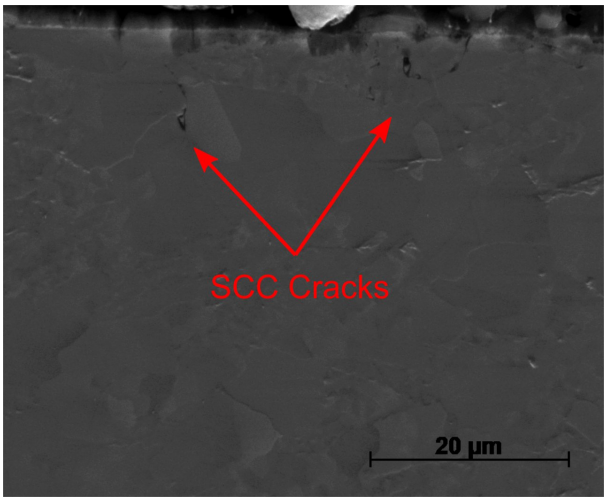

(b) SEM Micrograph

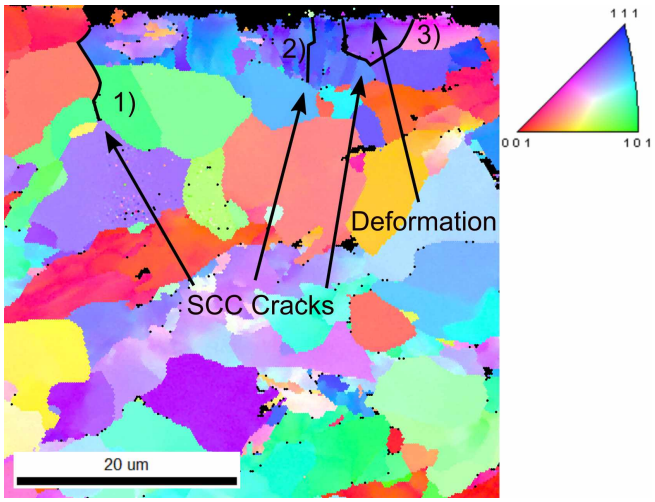

(c) EBSD IPF

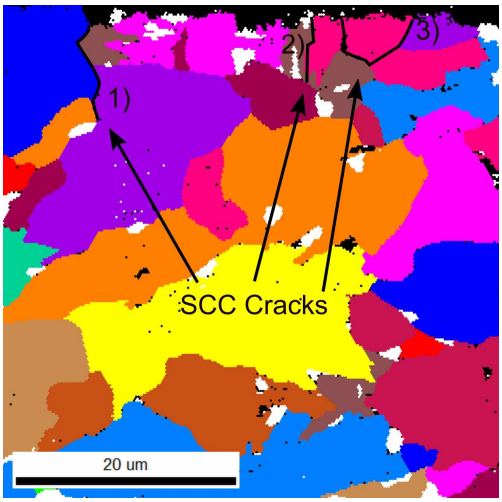

(d) EBSD Grain Map

Figure 7.7: Summary of cracks identified in Schedule 3.

7.1.7 Summary of Results

Table 7.7: Summary of SCC susceptibility results of the industry supplied and laboratory rolled samples.

Sample	Average Cracks Identified	Average Crack Velocity (mm/s)
6.4 mm X70 Plate	7254 ± 2319	$3.34 \times 10^{-8} \pm 8.44 \times 10^{-9}$
10 mm X70 Pipe	5193 ± 139	$4.05 \times 10^{-8} \pm 2.6 \times 10^{-9}$
20 mm X70 Plate	3803 ± 672	$4.02 \times 10^{-8} \pm 3.60 \times 10^{-9}$
Schedule 1	2721 ± 1333	$2.27 \times 10^{-7} \pm 4.89 \times 10^{-8}$
Schedule 2	3414 ± 2462	$1.16 \times 10^{-7} \pm 3.5 \times 10^{-8}$
Schedule 3	2433 ± 1419	$8.70 \times 10^{-8} \pm 3.27 \times 10^{-8}$

A summary of the average crack velocities and the number of cracks that developed during LIST testing of all test specimens is provided in Table 7.7, and graphically in Figures 7.8 and 7.9. As seen in Figure 7.8, of the laboratory rolled samples, Schedule 1 appears to have a significantly higher overall crack velocity compared to Schedules 2 and 3. Whilst Schedule 3 has a lower average crack velocity than Schedule 2, the spread of their values show considerable overlap. Schedule 1 was produced through a recrystallized rolling schedule that results in a considerably different crystallographic texture, microstructure and material properties compared to Schedule 2 and 3 which are, in contrast, very similar. It is likely that a combination of these factors result in the significantly higher crack velocity, which will be explored in the next section.

When observing the average crack velocity of the industry supplied samples, it is evident that, despite the difference in chemical composition, the crack velocity between the three samples is both very uniform and significantly lower (almost 7× slower) than that observed in the laboratory rolled samples. It is not surprising that the industry supplied samples have very similar SCC cracking velocities as they have very similar microstructures, mechanical properties and crystallographic textures at the regions investigated.

Whilst Schedule 2 was produced with similar microstructures to the industry supplied samples (compare Figures 5.2, 5.7 and 5.11 with Figure 5.29), the grain size appeared significantly larger in optical microscopy.

Another factor that may influence the crack growth rate is the propagation mechanism. Whilst cracks observed in laboratory rolled samples appeared to propagate nearly entirely intergranularly, there was mixed propagation observed in the industry supplied samples. It is expected that intergranular cracking would result in higher crack velocities compared with transgranular cracking due to fracture of grain boundaries requiring lower energy as compared to the fracture of a grain. This has been observed in the literature and offers a partial explanation to the differences in crack velocity of the industry and laboratory rolled samples [246]. Whilst near neutral pH conditions are typically required for transgranular cracking of low carbon steels according to Parkins et al. (1994) [247], it has been observed in literature that increased cold working can lead to mixed intergranular and transgranular SCC crack propagation [245, 248]. Surface deformation from polishing used to prepare the LIST samples may have influenced SCC cracking by making the initial propagation mechanism transgranular instead of intergranular as observed in Wang et al. (2003) [245]. Surface deformation appeared to influence the industry supplied samples more than the laboratory rolled samples.

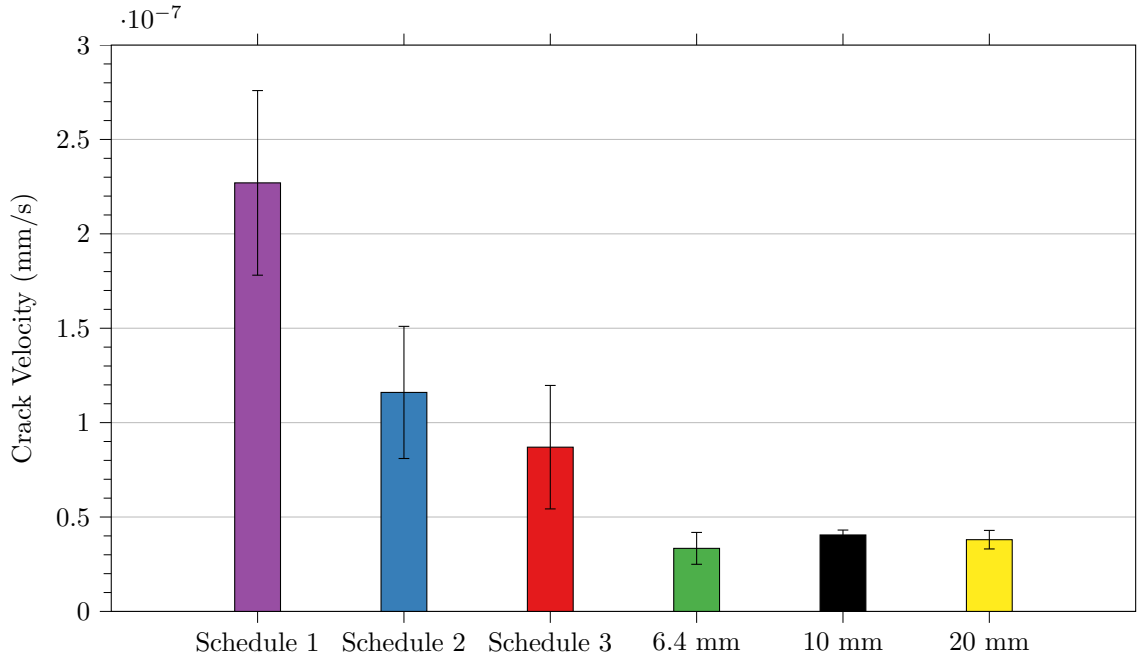

Figure 7.8: Comparison of SCC crack velocity in the industry supplied and laboratory rolled samples.

The number of cracks that initiated in the surface of the LIST specimens is presented in Figure 7.9 and shows the overall comparison between the laboratory rolled and industry supplied samples. Although the crack velocity was higher in the laboratory rolled samples, less cracks were observed in the surface compared to the industry supplied samples. The 6.4 mm X70 plate developed the most cracks out of the samples, with the 10 mm X70 pipe following closely behind. In contrast, the 20 mm X70 plate along with the three laboratory rolled samples developed considerably lower levels of cracks. The main difference between the industry supplied samples and the laboratory rolled specimens appears to be the grain size and the microstructures. It is possible that due to the smaller grain size, more crack initiation sites are present per unit length resulting in higher rates of crack initiation. This needs to be investigated further and will be covered in the following section. Whilst transgranular cracking in the industry supplied samples may have reduced the overall crack propagation rate, it does not adequately explain the significantly higher crack initiation rate. With initiation no longer bound to grain boundaries, it further increases the number of initiation sites per unit length. As is described by Wang et al. (2003) [245], it is likely that had samples been allowed to grow further in the solution,

they would have eventually transformed to intergranular cracks.

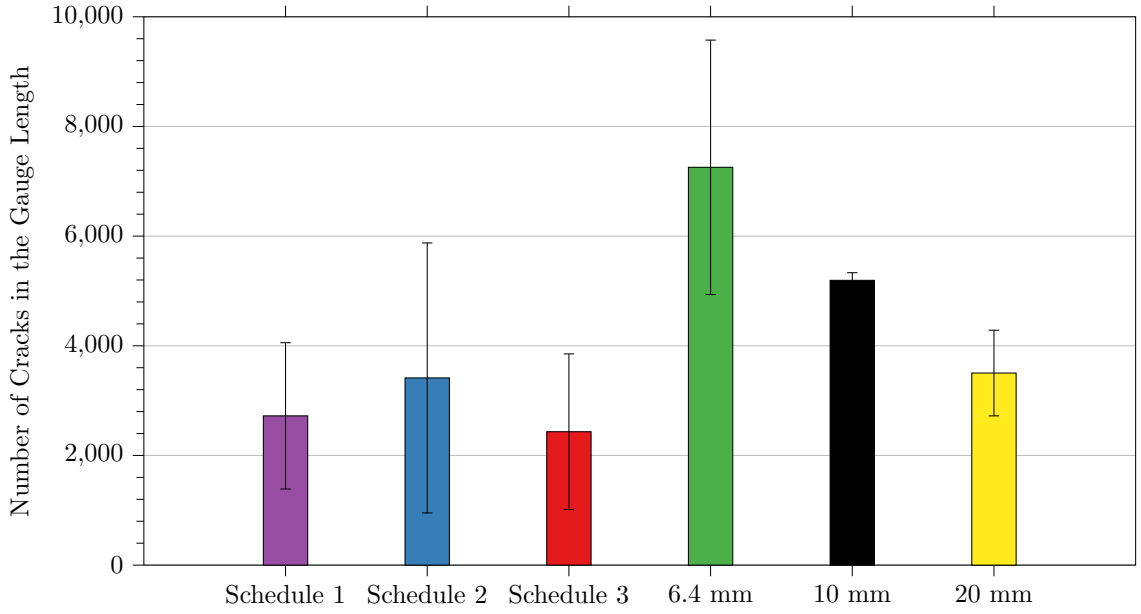

Figure 7.9: Comparison of the number of cracks that formed in the industry supplied and laboratory rolled samples.

7.2 Effect of Microstructural and Mechanical Properties on SCC

The following section outlines the effect of microstructural properties on the SCC susceptibility on the laboratory rolled and industry supplied samples. The microstructure of a steel is produced during manufacturing and is a function of the heating, cooling, deformation and time the material experiences during that process [249]. The microstructure is a fundamental aspect of any material and many properties, including mechanical, can be anticipated by the microstructure. Due to the interlinked nature of the microstructure and mechanical properties, the grain size, phases present and the yield strength will be investigated to find what effect they have on the SCC susceptibility.

The UTS was not considered in this analysis as SCC typically occurs at stresses below the yield and did not show a strong correlation with the SCC susceptibility. In addition,

properties that can be derived from the UTS, such as hardness, were not investigated .

7.2.1 Grain Size and SCC

The role of average grain size on the crack velocity is presented in Figure 7.10, where the average grain size taken from the cracked LIST samples are shown. A strong linear relationship between the average grain size and the SCC crack velocity is apparent in Figure 7.10, where an increase in average grain size appears to correspond to a faster crack velocity. It has been observed in the literature that increasing grain size increases the SCC susceptibility [17–19, 44, 250]. Although different reasons for the reduction in SCC susceptibility afforded by smaller grain size have been offered, a reason hypothesised by Lopez et al. (2006) [19] was that higher yield strength of fine grained materials strengthened the passive oxide film. This hypothesis does not seem reasonable, however, as an increase in yield strength tends to correlate to a decrease in the critical stress intensity factor for SCC which is, in effect, the fracture toughness of the passive oxide layer [251].

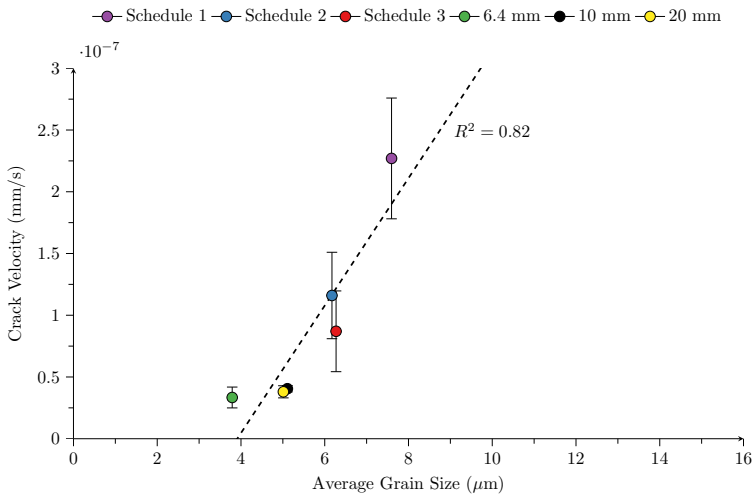

Figure 7.10: The effect of average grain size on SCC crack velocity.

Tsai et al. (1997) [17] hypothesised that the decrease of grain size in aluminium alloys corresponded to a more homogeneous slip mode and smaller grain boundary precipitate size, however, these findings may be specific to the SCC mechanism in aluminium and may

not translate exactly to the SCC mechanism in low carbon steels. There is little consensus in literature regarding why grain refinement reduces SCC susceptibility in steels. Ralston and Birbilis (2010) [18], proposed that oxide destabilisation could explain the corrosion improvement for both increases and decreases in grain size. As SCC fractures though grain boundary oxide layers as opposed to the parent metal as determined by Parkins (1996) [7], the critical stress intensity factor for SCC K_{ISCC} is typically lower than that of the parent metal [92, 93]. As discussed in Section 2.4.3, the K_{ISCC} corresponds to the fracture toughness of the oxide layer [11]. It was observed in literature that drastically altering the grain size did not have an appreciable impact on the overall K_{ISCC} as reported by Li et al. (2001) [251] so oxide destabilisation is not the likely reason for the increase in SCC susceptibility observed with increases in grain size. It is likely that grain refinement results in lower crack velocities because more distinct grain boundaries are required to fracture when the grain size is small as opposed to large. Simply put, large grains result in higher crack velocities because susceptible grain boundaries are longer and permit further propagation before the crack tip reaches another grain boundary.

Grain size does not appear to fully explain the crack velocity of the investigated samples, with Schedule 3 having a lower crack velocity than Schedule 2 despite it having a slightly larger average grain size. As the cracks that developed in the LIST specimens were on the order of 10 μm, the scan frame of the LIST samples were much smaller than that observed in the uncracked quarter plane leading to fewer grains investigated and potentially fewer large grains scanned.

The role of average grain size on the number of cracks that initiated in the LIST test section was investigated with the results displayed for the average LIST grain size in Figure 7.11. As seen in Figure 7.11, there appears to be a moderate trend linking the average grain size to the number of cracks that initiated in the LIST specimens. Smaller grains are likely more susceptible to crack initiation simply because there are more nucleation sites available. The number of cracks that formed in the laboratory rolled samples along

with the initial material, the 20 mm X70 plate, is clustered about the 3000 crack number.

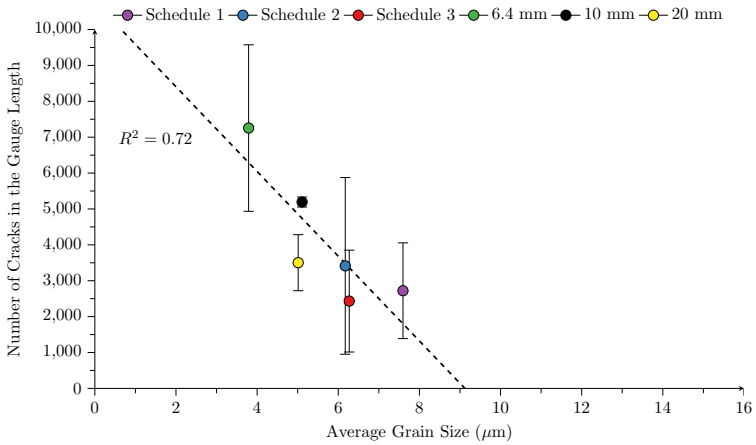

Figure 7.11: The effect of average grain size on the number of cracks that initiated.

Average grain size, while a useful tool, can obfuscate details surrounding the grain size distribution. In an effort to further analyse the role of grain size on SCC susceptibility, a grain size distribution for each of the LIST specimens was measured and the relationship with the crack velocity and number of cracks that developed investigated. A plot of the grain boundary distributions for each laboratory rolled schedule from the LIST specimens is presented in Figure 7.12. The plot shows that the industry supplied specimens have overall higher proportions of grains below 5 μm as compared to the laboratory rolled specimens. In the case of the 6.4 mm X70 plate, over 80% of grains are below 5 μm and 90% of grains in all the industry supplied samples are below 10 μm. The laboratory rolled samples have a higher proportions of grains with diameters larger than 10 μm.

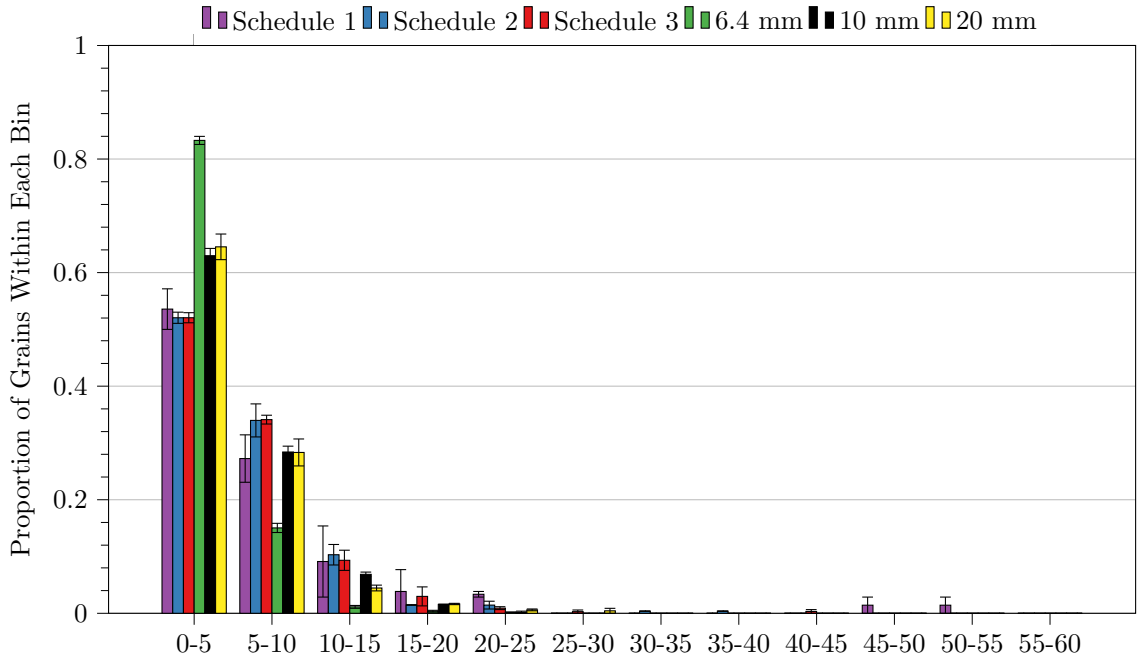

Figure 7.12: Grain size distribution as seen in the LIST samples.

The results of the grain size distribution from Figure 7.12 can be separated into individual bins to observe the effect different proportions have on the crack velocity. A series of plots are presented in Figure 7.13 that display the proportion of grains with diameters smaller than 5 μm, 10 μm and 20 μm vs. the crack velocity. It is interesting to note that as the overall grain diameter increases, the effect on the crack velocity becomes more linear. This result suggests that small grains below 5 μm do not appear to linearly impact the crack velocity, however, large grains appear to be more influential on the rate of crack propagation. As mentioned previously, it has been reported in the literature that increasing grain size increases the SCC susceptibility [17–19, 44, 250]; however, there is little consensus regarding why that is the case.

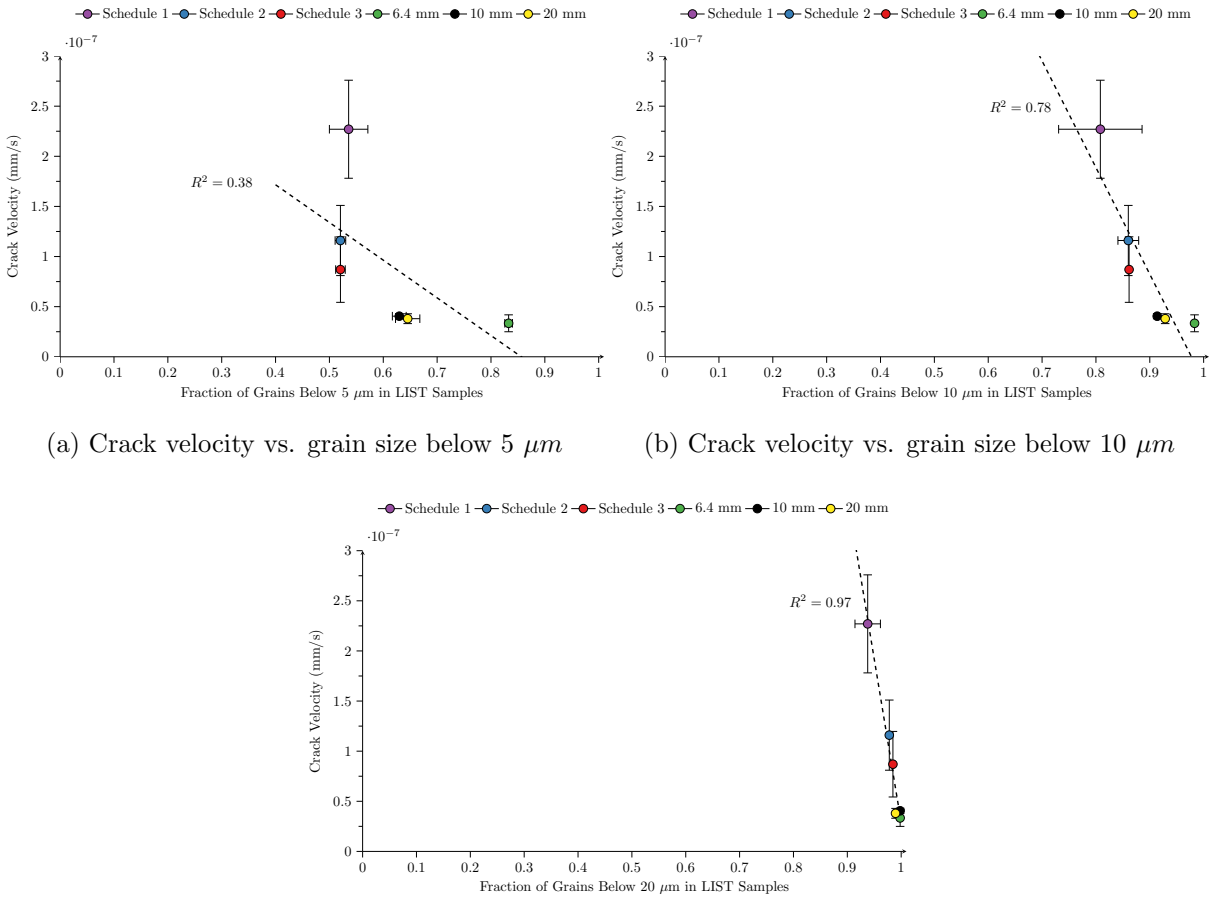

(a) Crack velocity vs. grain size below 5 μm

(b) Crack velocity vs. grain size below 10 μm

(c) Crack velocity vs. grain size below 20 μm

Figure 7.13: Crack velocity vs. the proportion of grains below varying thresholds.

As the number of cracks that initiated is another factor of SCC susceptibility, the effect that grain size had on the number of cracks that initiated needed to be determined. Similar to Figure 7.13, a series of plots relating the proportion of grains diameters smaller than 5 μm, 10 μm and 20 μm vs. the number of cracks that initiated in the LIST test sections are presented in Figure 7.14. The plots show that there exists a strong linear relationship between the number of grains with diameters smaller than 10 μm and number of cracks but dramatically diminished when including grains up to 20 μm. This may suggest that the number of cracks that initiate is related to the proportion of small grains present in the microstructure with grains smaller than 5 μm, as seen in Figure 7.14a, having the most impact on the crack initiation behaviour. This helps to explain why there was a significantly higher proportion of cracks that initiated in the industry supplied samples as compared to the laboratory rolled specimens. As seen in Figure 7.12,

the industry supplied specimens have significantly higher proportion of grains smaller than 5 μm compared to the laboratory rolled samples. This is supported by literature where SCC initiation occurred more frequently in materials with small grains compared to larger grains (10 μm compared to 100 μm) [73, 252]. An increase in the number of cracks that form with increased proportion of fine grains is not surprising as high pH SCC is an intergranular mechanism; increasing the number of grains in a a given area results in more grain boundaries exposed to the corrosive environment, leading to an increase in the number of potential sites for intergranular crack initiation as hypothesised by Parkins et al. (1993) [73].

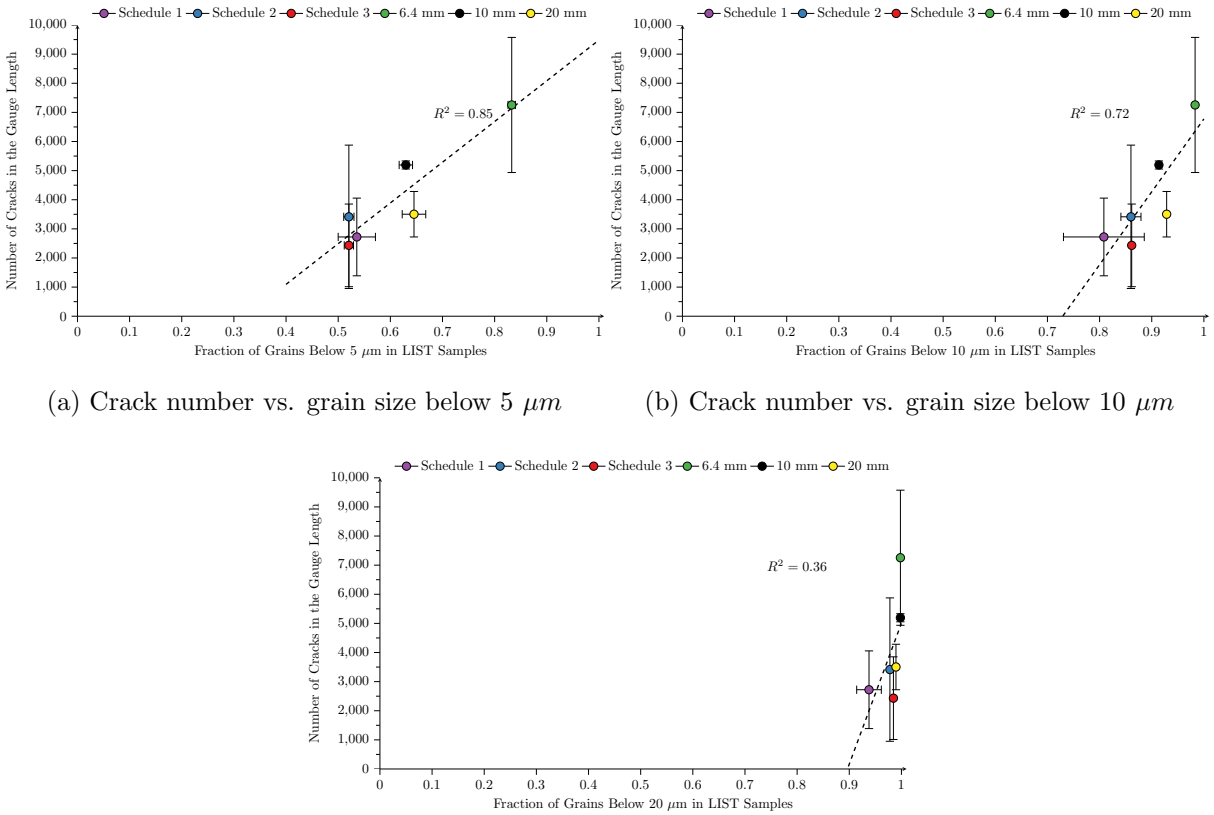

(a) Crack number vs. grain size below 5 μm

(b) Crack number vs. grain size below 10 μm

(c) Crack number vs. grain size below 20 μm

Figure 7.14: Crack number vs. the proportion of grains below varying thresholds.

7.2.2 SCC and Yield Stress

The role of 0.5% proof stress (yield stress) on crack velocity is presented in Figure 7.15. Whilst the yield stress was measured in three orientations, as presented in Section 5.3.4, the LIST specimens were loaded along the rolling direction and, hence, the 0° yield was evaluated. As seen in Figure 7.15, there appears to be a strong linear relationship between increasing the yield stress of the laboratory rolled specimens and increasing the crack velocity. Similarly, in the industry supplied samples, there is a slight upwards trend but due to the similarity in crack velocity between the samples it is not as defined as in the laboratory rolled samples.

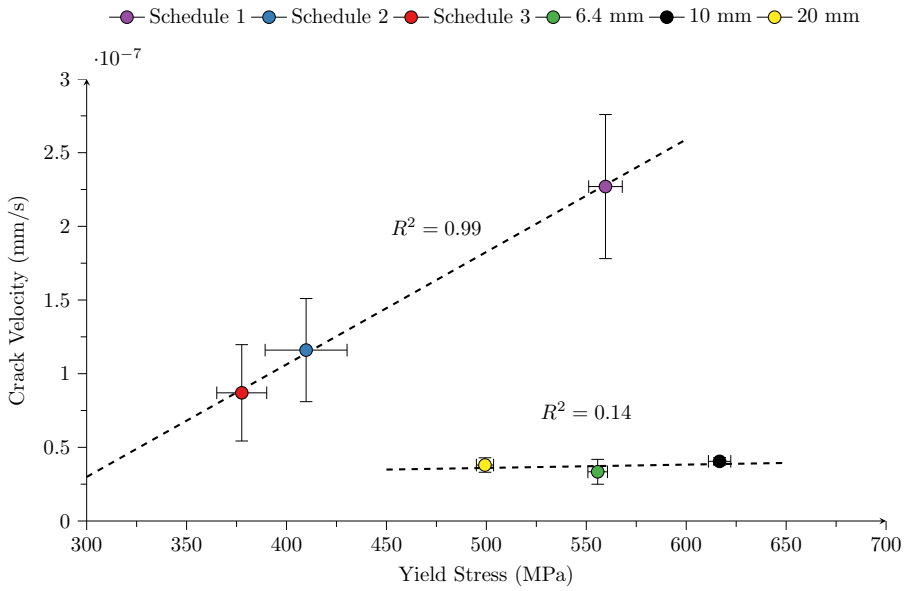

Figure 7.15: The effect of 0.5% yield stress on SCC crack velocity.

An increase in SCC (intergranular and transgranular) susceptibility with increasing yield stress has been reported in carbon steel by Eaglesham et al. (1988) [11], pipeline steels by Lu and Luo (2006) [74], and stainless steels by Andresen and Morra (2008) [253]. The work by Eaglesham et al. (1988) [11] was conducted on steels with far higher carbon contents with a minimum yield stress of 800 MPa, outside the range investigated here. In addition, the microstructures of the materials investigated by Eaglesham et al. (1988) [11] were likely different to those of the laboratory rolled and industry supplied samples, as they were quenched and tempered likely resulting in high proportions of martensite

and tempered martensite. The work carried out by Lu and Luo (2006) [74] was on transgranular SCC, however, the work carried out by Andresen and Morra (2008) [253] was on intergranualar cracking, hence the relationship appears to hold. In intergranular SCC, it has been observed that increases in yield strength correlate to a decrease in the critical stress intensity factor for SCC K_{ISCC} [11, 251]. The fracture toughness for SCC crack propagation is tied to the strength of the passive oxide layer, as SCC does not propagate through the parent metal but the corroded grain boundaries [7]. A decrease in the SCC stress intensity factor correlates to a weakening of the passive oxide layer, hence, a reduction in the stress required to fracture the oxide layer at the crack tip allowing anodic dissolution to propagate the SCC crack.

It is interesting that decreasing the grain size correlates to lower crack velocity as well as an increased yield strength, however, increased yield strength correlates to a decreased K_{ISCC} and hence a higher crack velocity. This contradiction is likely traced back to the heat treatment used in literature to alter the grain size and yield strength. Altering these properties often comes at the cost of changing the phases present in the microstructure; hence, when observing the effect of yield strength in Figure 7.15, the similar yield strength of Schedule 1 results in a far higher crack velocity than the 6.4 mm X70 plate. It is evident from the results that when comparing similar microstructures, there is a limit to the amount that increases to the yield stress will increase the crack velocity. This is because the K_{ISCC} does not decrease indefinitely with increased yield strength [11, 251].

The number of cracks that initiated as a result of the yield stress was plotted and presented in Figure 7.16. As can be observed, there is no strong evidence that increases in yield strength have any impact on the number of cracks that initiated in Figure 7.16a, however, when removing Schedule 1 from the data as carried out previously, a stronger trend appears. Whilst it is tempting to suggest that removing Schedule 1 from the equation results in a better relationship between the yield stress and the number of cracks that develop, the variance between the measured values and the initial plot is lower than the

variance between the measured values and the new plot, suggesting a poorer fit overall. In high strength steels, such as the ones tested, SCC tends to initiate below the yield stress [37]. As initiation occurs below the yield stress, the correlation between initiation and stress is harder to observe when surface defects such as pits and general roughness appear to have a greater effect on initiation [8, 37].

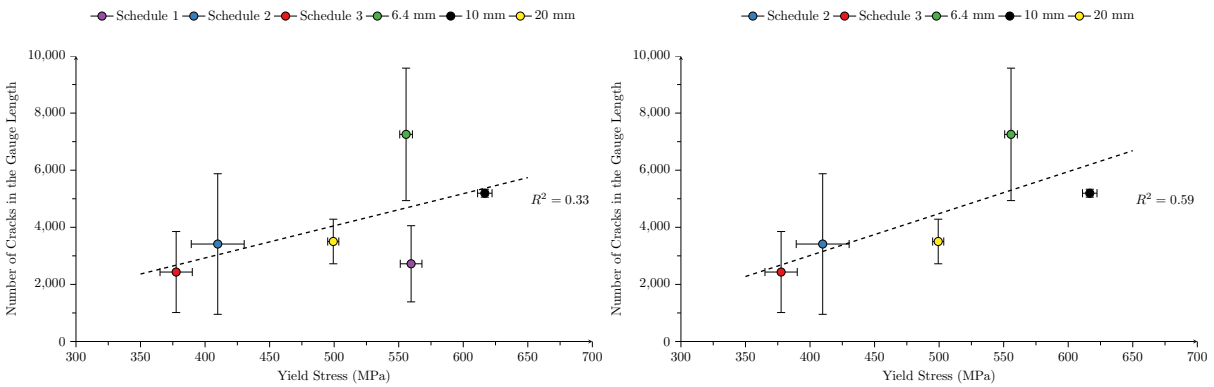

(a) Crack number vs. 0.5% yield stress

(b) Crack number vs. 0.5% yield stress without Schedule 1

Figure 7.16: The effect of 0.5% yield stress on the number of cracks that initiated.

7.2.3 SCC and Microstructure

As discussed in Section 4.7, all phases present in the investigated samples were identified and classified. At the quarter thickness plane where the LIST specimens were sectioned from, it was observed that Schedule 1 contained primarily granular bainite with some proportions of upper bainite as observed in Figure 5.27. Schedules 2, 3 and the industry supplied samples contained varying levels of granular bainite with either polygonal or quasi-polygonal ferrite as observed in Figures 5.29 and 5.31, respectively. Samples manufactured from Schedule 1 experienced the fastest crack velocity of all the tested specimens. Large, equiaxed bainitic microstructures such as those produced through quenching and tempering have been identified in literature as being more susceptible than other phases, including bainite formed through thermomechanical rolling [4, 13–16].

As microstructure change cannot be altered without also changing grain size and mechanical properties, those changes also need to be taken into account when discussing the impact of microstructure on SCC susceptibility. When comparing the microstructure of Schedule 2 to the industry supplied samples (Figure 5.29 vs. Figures 5.2, 5.7 and 5.11), they were observed to be almost identical with the exception of grain size. Despite the similarity in phases present in those samples, they experienced significantly different crack velocities under the same conditions. As explored by Lu and Luo (2006) [74], yield stress linearly influenced the SCC susceptibility, however, only when comparing similar microstructures. Differences in microstructure appear to influence the rate at which SCC can propagate but, as seen in the example of Schedule 2 and the industry supplied samples, other factors of mechanical and physical properties need to be taken into account.

7.2.4 Effect of Texture on SCC

Much like the microstructure and the mechanical properties, the crystallographic texture is produced in steel as a result of the manufacturing process and is influenced by the same factors. The crystallographic texture can be considered as another aspect of the microstructure, albeit one which can only be determined though diffraction methods. The following aspects of texture have been investigated for the role they play in SCC susceptibility; the overall texture, the texture surrounding SCC cracks and the grain boundary properties of SCC cracks.

Effect of Bulk Texture on SCC

The crystallographic texture of the laboratory rolled and industry supplied specimens was investigated in Section 5.4 and the produced textures were compared to those found in literature. A brief summary of the bulk textures followed by their impact on SCC susceptibility will follow. It is important to note that whilst the following texture plots

were carried out using EBSD, a sufficiently large number of grains were sampled which has been shown in literature to approximate the macro texture found through XRD [97]

ODF plots of the textures observed at the quarter plane (same plane as where the LIST specimens were sourced) is presented in Figure 7.17. An in-depth analysis on the textures that were produced due to the different rolling schedules is provided in Section 6.4, this section will focus on the role that the textures present in each sample plays on SCC susceptibility. It is evident from the ODF plots presented in Figure 7.17 that stronger crystallographic textures are developed in the industry supplied samples compared with the laboratory rolled. Despite that difference, the hot rolled Schedule 2, which most closely approximates the rolling schedules of the industry supplied samples, show strong similarities indicating a strong process dependent nature of texture development. Whilst Schedule 1 and Schedule 3 appear similar some key differences in texture strength are observed that serve to differentiate the two processes.

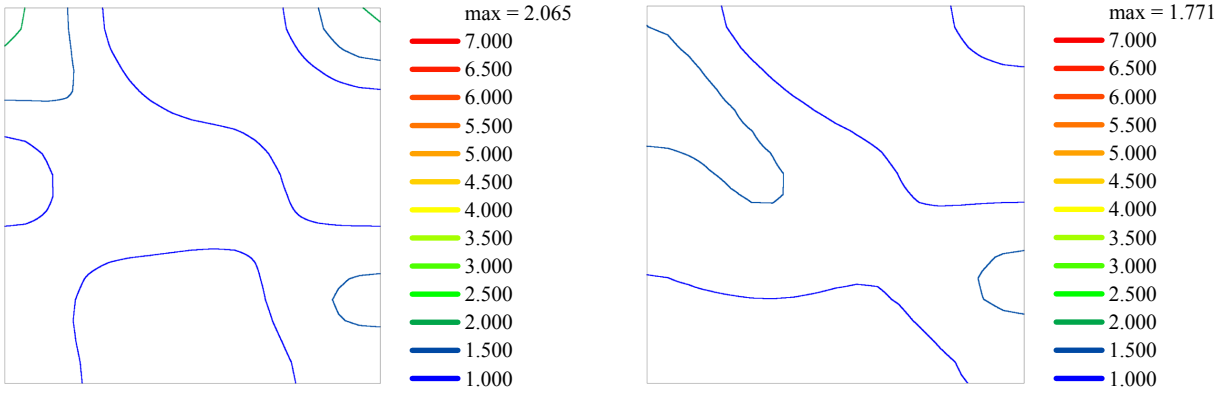

(a) Schedule 1 Quarter ODF

(b) Schedule 2 Quarter ODF

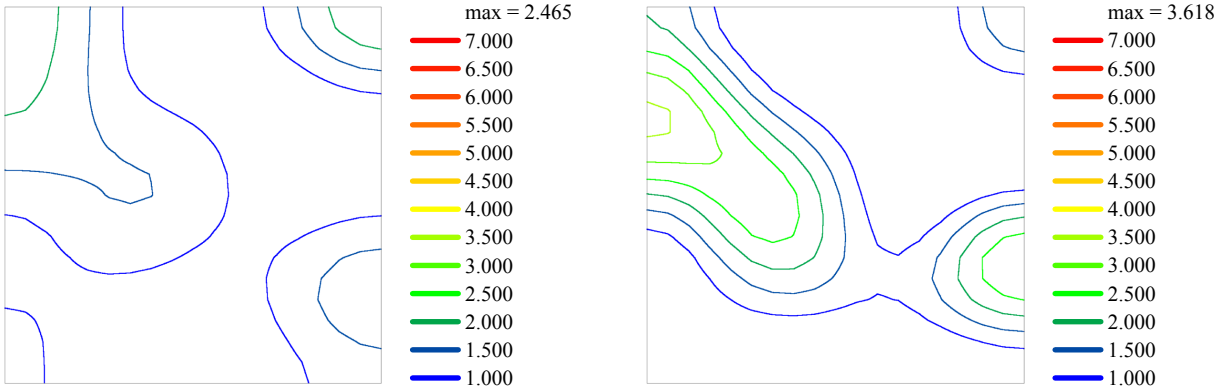

(c) Schedule 3 Quarter ODF

(d) 6.4 mm X70 Plate Quarter ODF

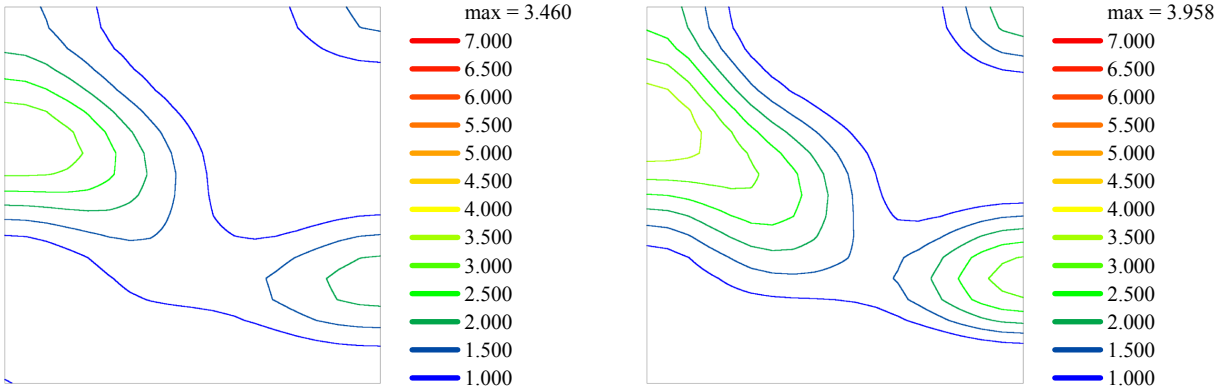

(e) 10 mm X70 Plate Quarter ODF

(f) 20 mm X70 Plate Quarter ODF

Figure 7.17: Bulk texture of the laboratory rolled and industry supplied specimens at the quarter thickness plane.

When comparing the shapes of the contours in Figure 7.17 it is not possible to comment on the role that texture has on SCC susceptibility. The reason for this is that there are broad similarities in texture that result in significantly different SCC susceptibilities. For example, the textures of Schedule 1 and Schedule 3 are very similar but Schedule 1 has an average crack velocity more than 2.5× that of Schedule 3. To determine the role bulk

texture has on SCC susceptibility, an analysis of the concentration of specific textures was undertaken.

Concentration of Specific Textures

As explored in Section 2.6.1, the $\varphi_2 = 45°$ component of Bunge notation ODF's encompasses textures components that are important for steels. The most important fibres and their locations are presented in Figure 7.18 and show the position and what textures the α-fibre, γ-fibre and ε-fibres encompass.

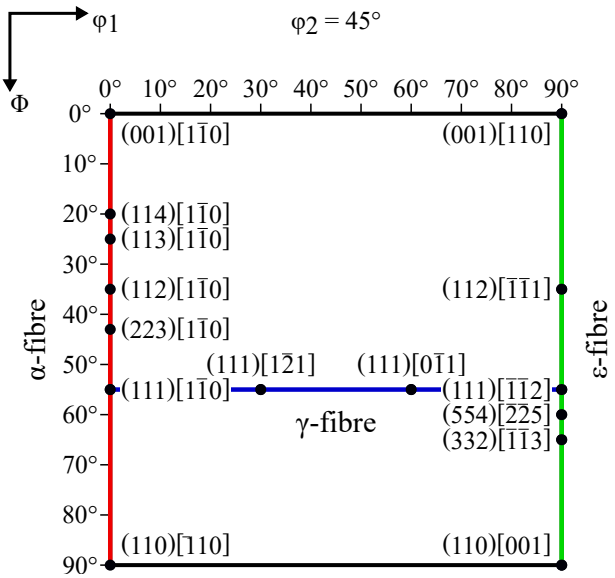

Figure 7.18: ODF of $\varphi_2 = 45°$ showing important fibres. Adapted from [168].

The three main fibre textures and the strength of each main component is presented in Figure 7.19. To determine which textures have the most impact on SCC susceptibility, regions that show the largest differences in texture concentration were identified. Regions with low texture concentration variation were ignored because they suggest that they had little influence on the final SCC susceptibility since there were significant differences between the laboratory rolled and industry supplied samples. Observing the graph of the α-fibre in Figure 7.19a, it becomes apparent that the largest deviation in texture occurs between the (113)[1$\bar{1}$0] and (112)[1$\bar{1}$0] textures, with coherent differences observed at

$(110)[1\bar{1}0]$. The graph of the γ-fibre in Figure 7.19b shows the largest difference in texture component strength at $(111)[1\bar{2}1]$ and $(111)[\bar{1}\bar{1}2]$. The graph of the ε-fibre in Figure 7.19c shows the largest degree of variation in texture at $(111)[\bar{1}\bar{1}2]$, $(554)[\bar{2}\bar{2}5]$, $(332)[\bar{1}\bar{1}3]$ and $(110)[001]$.

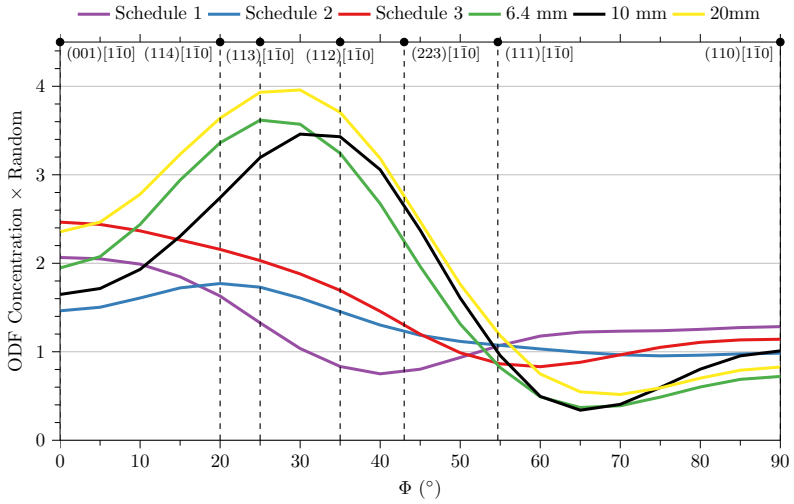

(a) α-fibre

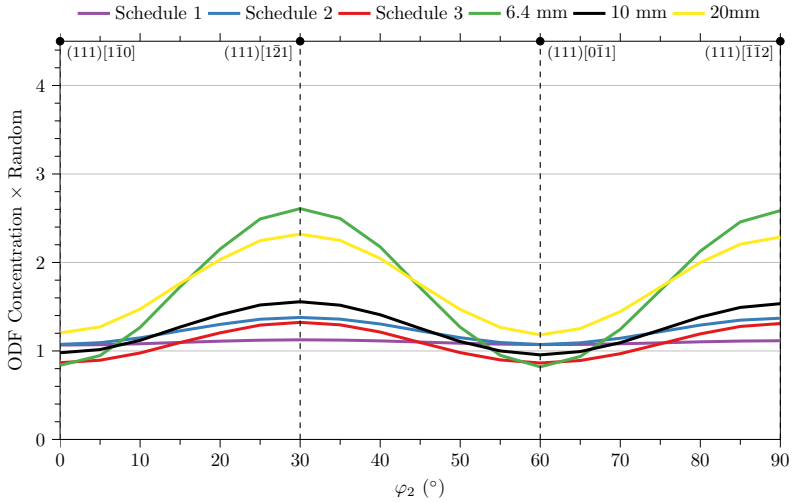

(b) γ-fibre

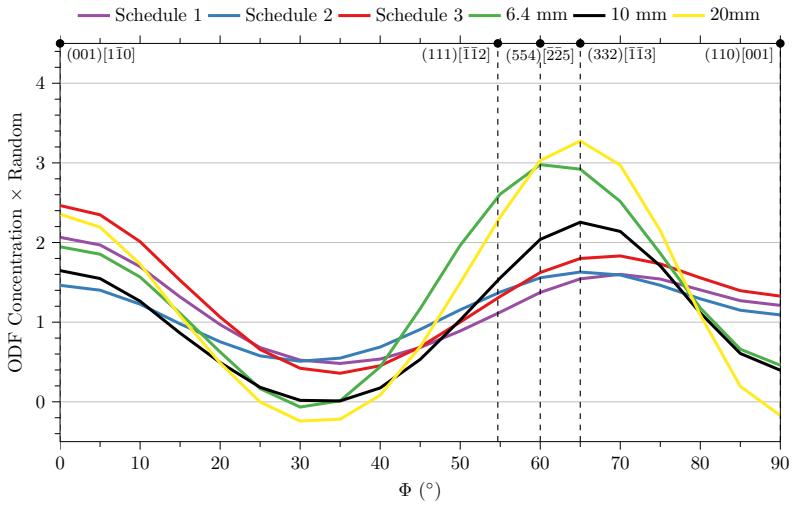

(c) ε-fibre

Figure 7.19: The strength of texture present in the investigated samples of the three main fibres.

As detailed in the previous paragraph, the textures with the largest deviation in concentration between the investigated samples appear most likely to influence the SCC susceptibility. The textures that have the highest likelihood of influencing susceptibility are as follows: (113)[1$\bar{1}$0], (112)[1$\bar{1}$0], (110)[001], (110)[1$\bar{1}$0], (111)[0$\bar{2}$1], (111)[$\bar{1}\bar{1}$2], (554)[$\bar{2}\bar{2}$5] and (332)[$\bar{1}\bar{1}$3] texture components. As explained in Section 2.7.4, these textures developed during transformation from austenite to ferrite during the manufacturing process of steel. The (332)[$\bar{1}\bar{1}$3] component originate from the Brass ({110}<112>) texture in austenite and through additional deformation forms the (111)[$\bar{1}\bar{1}$2]/[1$\bar{2}$1] and (554)[$\bar{2}\bar{2}$5] components [21]. The (113)[1$\bar{1}$0] forms through additional deformation of the (112)[1$\bar{1}$0] texture although it is common to see both components present [21, 184]. The (110)[001] and (110)[1$\bar{1}$0] textures are formed from the transformation of the cube texture in austentie to ferrite [168]. The concentration of these textures will be compared to the crack velocity and the number of cracks that initiated to determine what impact they have on SCC susceptibility.

(110)[1$\bar{1}$0] & (110)[001] Orientations

The effect that (110)[1$\bar{1}$0] and (110)[001] textures had on crack velocity and number of cracks that developed was plotted and presented in Figure 7.20. It was observed in Figure 7.20a that an increase in the concentration of (110)[1$\bar{1}$0] textures corresponded to an increase in crack velocity. Conversely, in Figure 7.20c, an increase in the concentration of (110)[1$\bar{1}$0] texture resulted in a lower number of cracks forming in the LIST specimens. The role of the (110)[001] texture on SCC susceptibility is presented in Figures 7.20b and 7.20d. An increase in (110)[001] texture appears to result in an increase in crack velocity, much like what was observed for (110)[1$\bar{1}$0] textures. In addition, increases in concentration of the (110)[001] texture also appeared to result in a lower number of cracks that formed in the LIST specimens. In both cases, weaker trends were observed for (110)[001] textures as opposed to (110)[1$\bar{1}$0] textures. The presented graphs appear to suggest that despite increasing the crack velocity, a lower number of cracks develop overall with increased concentrations of (110)[1$\bar{1}$0] textures. The observed behaviour sug-

gests that high proportions of (110)[1$\bar{1}$0] and (110)[001] textures reduce the initiation susceptibility, however, they did not appear to provide a high resistance to SCC propagation. A potential reason for this behaviour is that (110)[1$\bar{1}$0] and (110)[001] textures have highly variable grain boundary strengths depending on what orientations they are paired with. As observed by Rath and Bernstein (1971) [189], (110) grain boundaries are highly cohesive when paired together but form very weak grain boundaries when paired with other orientations. As was observed by Lavigne et al. (2014) [29], a higher proportion of (110)[001] textures at the surface resulted in a lower incidence of cracks forming under field conditions, although under laboratory testing, lower crack velocities were observed with increased concentration.

The study by Lavigne et al. (2014) [29] was carried out on the surface in the absence of other strong textures, which increases the likelihood of strong {110}-{110} grain boundaries. As this study was carried out on the quarter thickness plane, an increase in (110)[001] and (110)[1$\bar{1}$0] textures increased the likelihood of weak {110}-{hkl} grain boundaries, hence, increasing susceptibility. Arafin and Szpunar (2009) [24] identified that (110)[1$\bar{1}$0] textured grains were associated with halting cracks in a similar grade of low carbon steel to what was investigated by Lavigne et al. (2014) [29]. This observation was based partly on the assumption that high proportions of (110)[1$\bar{1}$0] textures ahead of the crack caused the crack to halt propagation. This assumption was questioned by the current author as there was no evidence of failure, it was likely the crack would continue propagation had the pipe been returned to service [31]. In addition, (110) oriented grains were identified surrounding cracks by the current author Roccisano et al. (2019) [31], which would indicate that the presence of (110) oriented grains alone is not enough to lower SCC susceptibility.

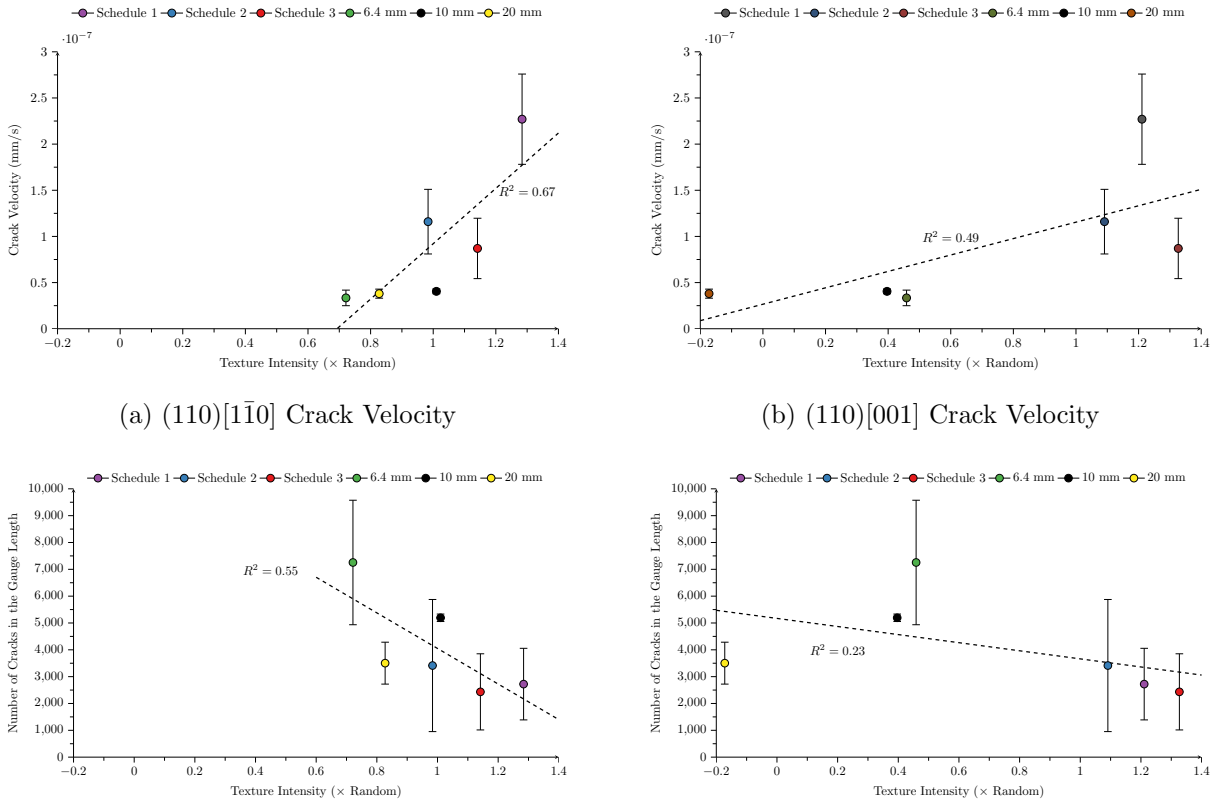

(a) (110)[1$\bar{1}$0] Crack Velocity

(b) (110)[001] Crack Velocity

(c) (110)[1$\bar{1}$0] Crack Number

(d) (110)[001] Crack Number

Figure 7.20: SCC susceptibility of the investigated samples compared to the concentration of (110) texture components.

(112)[1$\bar{1}$0] & (113)[1$\bar{1}$0] Orientations

The effect of the (112)[1$\bar{1}$0] and (113)[1$\bar{1}$0] texture components on crack velocity and the number of cracks that developed in the gauge length of the LIST specimen was plotted and is presented in Figure 7.21. As observed in both Figures 7.21a and 7.21b with increasing concentrations of (112)[1$\bar{1}$0] and (113)[1$\bar{1}$0] textures, there is a decrease in crack velocity. A strong linear trend is observed in the laboratory rolled samples in both Figures 7.21a and 7.21b but is weaker in the industry supplied samples, particularly in Figure 7.21b. The number of cracks that developed in the gauge length of the LIST specimens was presented in Figures 7.21c and 7.21d. A very weak linearly increasing trend is observed in both Figures 7.21c and 7.21d where increases to the intensity of (112)[1$\bar{1}$0] and (113)[1$\bar{1}$0] textures appears to show a weak association with a higher number of cracks that developed in the LIST specimens. In Figure 7.21c, the industry supplied samples show a negative trend to increases in the intensity of (112)[1$\bar{1}$0] textures whilst in both Figures 7.21c and 7.21d, the

laboratory rolled samples do not appear to show any significant increase in the number of cracks that develop with an increase in (112)[1$\bar{1}$0] and (113)[1$\bar{1}$0] intensities. This result is the opposite of that observed for (110)[1$\bar{1}$0], where an increase in intensity was associated with an increase in crack velocity and decrease in the number of cracks that initiated.

The behaviour observed in Figure 7.21 indicates that, with an increase in intensity of both (112)[1$\bar{1}$0] and (113)[1$\bar{1}$0] textures, there is a resulting decrease in SCC crack velocity and a weak association appears to show an increase in the number of cracks that developed. Due to the weak association between (112)[1$\bar{1}$0] and (113)[1$\bar{1}$0] texture intensity and the number of cracks that developed in the LIST specimens, the effect of these textures can likely be ignored. It would appear that increased intensity of (112)[1$\bar{1}$0] and (113)[1$\bar{1}$0] textures are resistant to cracking, likely because they are low-index planes that create strong grain boundaries. Rath and Bernstein (1971) [189] suggested that {112} oriented grains were low-index and formed coherent boundaries, although not to the same level at {110} boundaries. The role of (112)[1$\bar{1}$0] and (113)[1$\bar{1}$0] texture components on SCC of steel has not been widely reported in literature. In an EBSD study of SCC cracks by the current author, {112}//RP oriented grains were present in high concentrations surrounding SCC cracks [31]. In addition, when observing instances of transgranular cracking along the typically intergranular crack path, (112) oriented grains were present in up to 25% of instances [31]. HIC of pipe line steels also found that cracks propagated transgranularly through {112}//RP oriented grains [193, 194]. Whilst it appears that {112}//RP oriented grains are associated with environmental cracking, the orientations appear more inclined to fracture transgranulalrly than intergranularly.

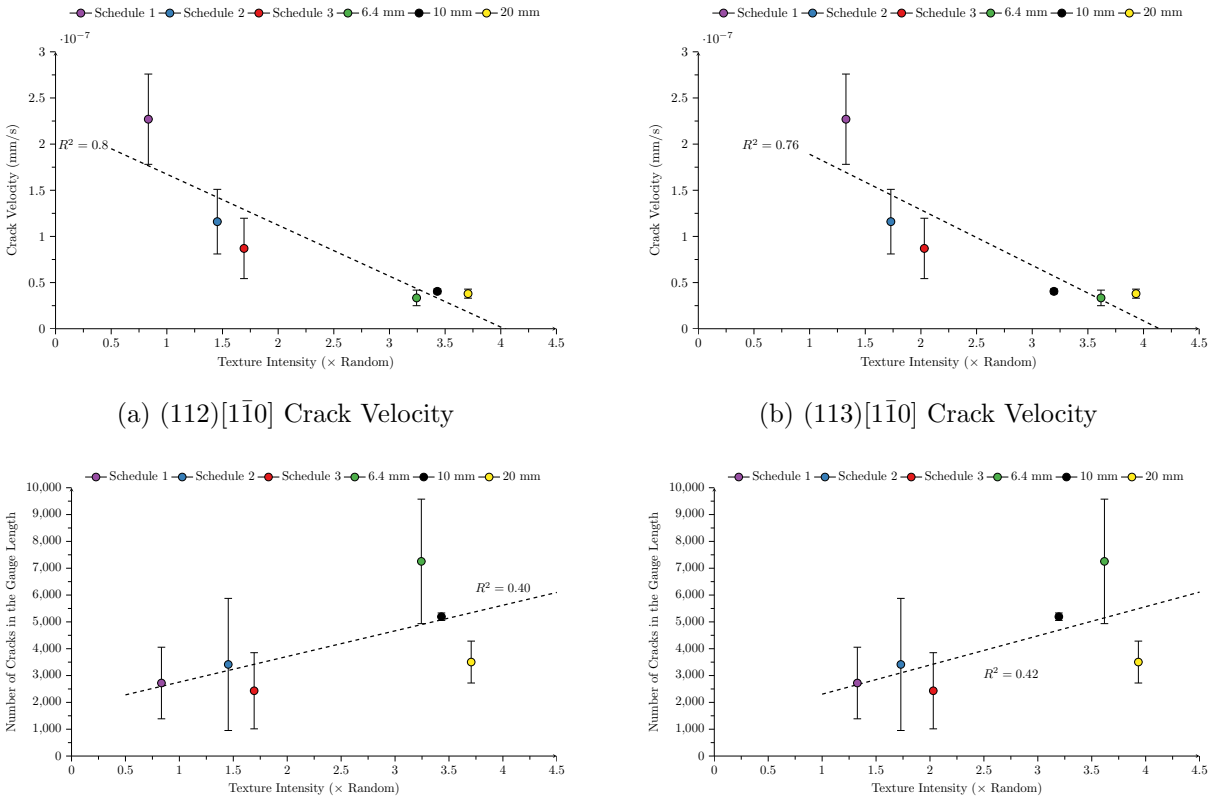

(a) (112)[1$\bar{1}$0] Crack Velocity

(b) (113)[1$\bar{1}$0] Crack Velocity

(c) (112)[1$\bar{1}$0] Crack Number

(d) (113)[1$\bar{1}$0] Crack Number

Figure 7.21: SCC susceptibility of the investigated samples compared to the concentration of (112) and (113) texture components.

(332)[$\bar{1}\bar{1}$3] & (554)[$\bar{2}\bar{2}$5] Orientations

The role that intensity of (332)[$\bar{1}\bar{1}$3] and (554)[$\bar{2}\bar{2}$5] textures has on crack velocity and the number of cracks that initiated in the LIST specimens was plotted and presented in Figure 7.22. There are weak linear trends that suggest that increased intensity of both (332)[$\bar{1}\bar{1}$3] and (554)[$\bar{2}\bar{2}$5] results in lower crack velocities, as observed in Figures 7.22a and 7.22b. It is apparent that Schedule 1 is an outlier compared to the other samples and has a significantly higher crack velocity than the intensity of (332)[$\bar{1}\bar{1}$3] or (554)[$\bar{2}\bar{2}$5] would predict. The microstructure of Schedule 1 is significantly different compared to the other samples as discussed above and can have a strong impact on the base SCC susceptibility. As discussed by Lu and Luo (2006) [74] different properties can linearly impact the SCC susceptibility, however, the microstructure was the differentiating factor. The number of cracks that developed in the LIST test sections with respect to the concentration of (332)[$\bar{1}\bar{1}$3] and (554)[$\bar{2}\bar{2}$5] textures are presented in Figures 7.22c and 7.22d. Similar to

what was identified in (112)[1$\bar{1}$0] and (113)[1$\bar{1}$0] texture components, there appears to be a weak association to an increase in the overall number of cracks that initiated in the test sections with increasing proportions of both (332)[$\bar{1}\bar{1}$3] and (554)[$\bar{2}\bar{2}$5] textures. These trends are very weak, however, and do not provide enough evidence that (332)[$\bar{1}\bar{1}$3] and (554)[$\bar{2}\bar{2}$5] intensities impact the number of cracks that develop in the LIST specimens. It is likely that (332)[$\bar{1}\bar{1}$3] and (554)[$\bar{2}\bar{2}$5] textures decrease SCC susceptibility because of their beneficial impact on mechanical strength and toughness isotropy. (332)[$\bar{1}\bar{1}$3] and (554)[$\bar{2}\bar{2}$5] textures have, relative to other typical orientations, good mechanical isotropy and have been long known to improve strength and toughness in high strength steel [21, 254]. It was determined for HIC that reducing mechanical anisotropy resulted in lower sensitivity to HIC, which may translate to SCC based corrosion [255]. There has not been any significant research on the role that (332)[$\bar{1}\bar{1}$3] and (554)[$\bar{2}\bar{2}$5] textures play on SCC susceptibility. This is likely due to texture assessments being conducted at the surface of pipes unaffected by SCC of which neither (332)[$\bar{1}\bar{1}$3] nor (554)[$\bar{2}\bar{2}$5] textures typically form as discussed in Section 5.4 [20, 24]. It is thought that due to the beneficial impact on mechanical properties, (332)[$\bar{1}\bar{1}$3] and (554)[$\bar{2}\bar{2}$5] textures may also result in lower SCC crack velocities.

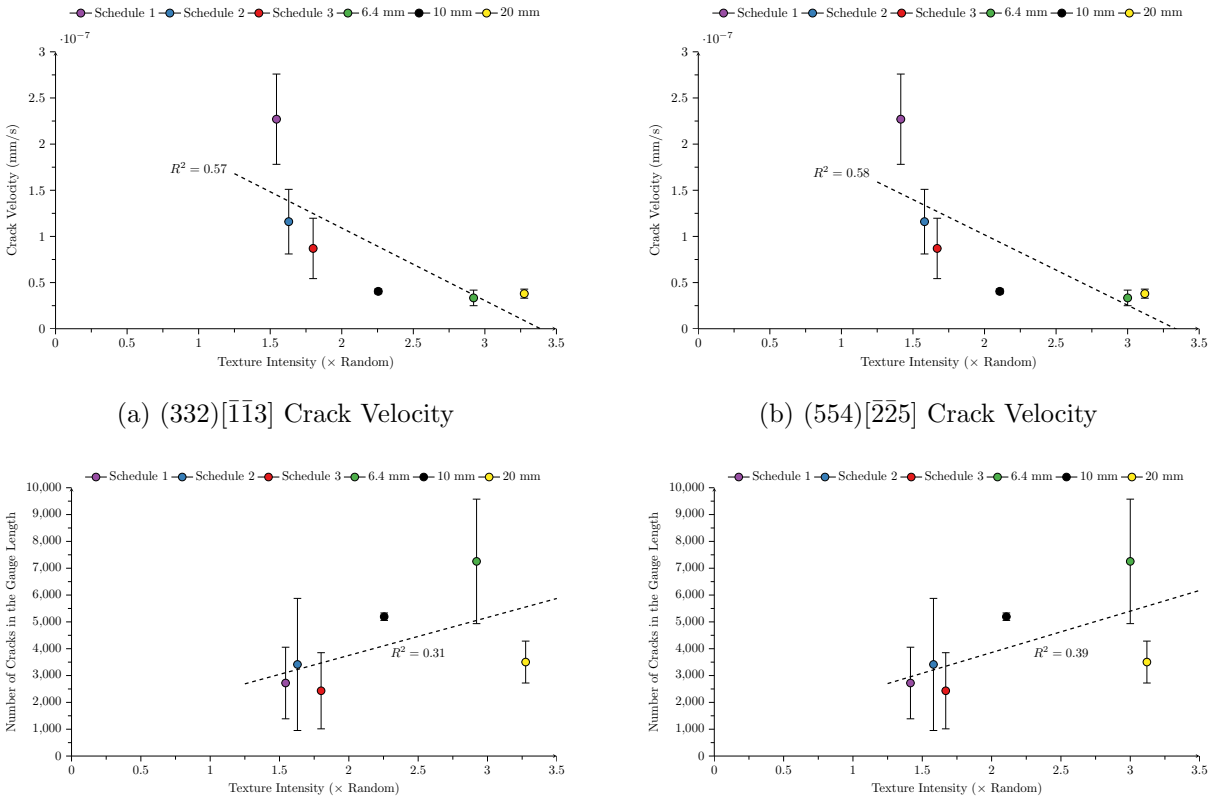

(a) (332)[$\bar{1}\bar{1}3$] Crack Velocity

(b) (554)[$\bar{2}\bar{2}5$] Crack Velocity

(c) (332)[$\bar{1}\bar{1}3$] Crack Number

(d) (554)[$\bar{2}\bar{2}5$] Crack Number

Figure 7.22: SCC susceptibility of the investigated samples compared to the concentration of (332) and (554) texture components.

(111)[$\bar{1}\bar{1}2$] & (111)[$1\bar{2}1$] Orientations

The effect that (111)[$\bar{1}\bar{1}2$] and (111)[$1\bar{2}1$] textures had on the SCC crack velocity and the number of cracks that formed in LIST test sections are presented in Figure 7.23. The (111)[$\bar{1}\bar{1}2$] and (111)[$1\bar{2}1$] are equivalent {111}<112> orientations, however, there are some slight differences between their values so both will be plotted. In both Figures 7.23a and 7.23b, there appears to be a weak correlation between an increase in (111)[$\bar{1}\bar{1}2$] and (111)[$1\bar{2}1$] intensities and a decrease in crack velocity. Similarly, as seen in Figures 7.23c and 7.23d there appears to be a weak correlation between a higher intensity of (111)[$\bar{1}\bar{1}2$] and (111)[$1\bar{2}1$] textures and higher number of cracks that initiated in the LIST specimens. Much like the (332)[$\bar{1}\bar{1}3$] and (554)[$\bar{2}\bar{2}5$] textures, it is likely that increasing the proportion of (111)[$\bar{1}\bar{1}2$] and (111)[$1\bar{2}1$] textures correlates with a lower crack velocity due to the isotropic strength and toughness these textures provide, as well their low energy configurations. {111}<112> orientations result in very isotropic mechanical

strength and toughness and, as explored for (332)[$\bar{1}\bar{1}$3] and (554)[$\bar{2}\bar{2}$5] textures previously, HIC susceptibility is reduced with reduced mechanical anisotropy [255]. With respect to SCC susceptibility, it has been observed that increases in {111}//RP textures lower SCC susceptibility by Arafin and Szpunar (2009) [24], however, this finding was based on the assumption that the area ahead of the crack was crack resistant which the current author disputes [31]. There is some evidence that increases in {111}<112> textures can correspond to higher levels of transgranular cracking [31, 256]. This may contribute to the higher number of cracks that formed in the industry supplied materials which, as observed previously in Figures 7.2 and 7.4 contained a mixed propagation mechanism of intergranular and transgranular cracking.

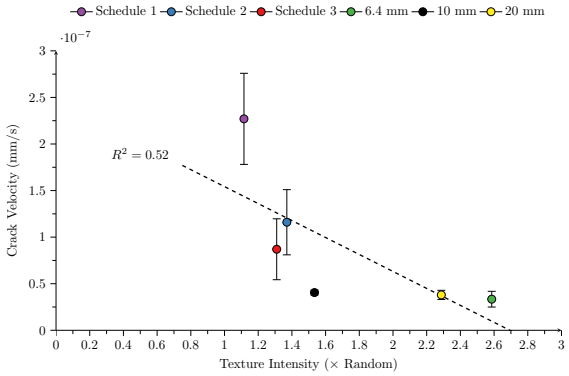

(a) (111)[$\bar{1}\bar{1}$2] Crack Velocity

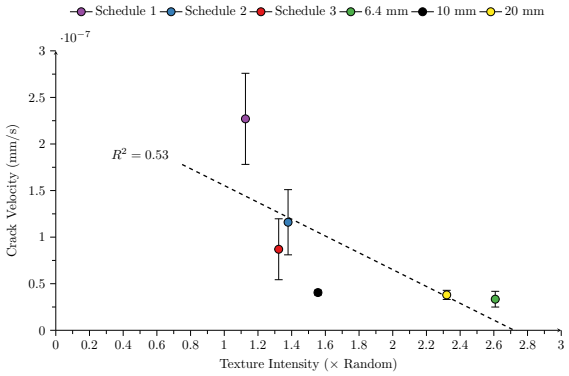

(b) (111)[$1\bar{2}1$] Crack Velocity

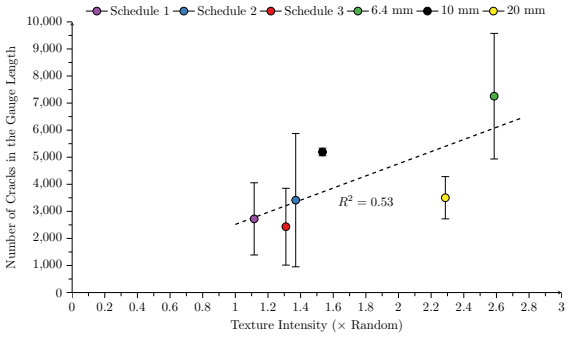

(c) (111)[$\bar{1}\bar{1}$2] Crack Number

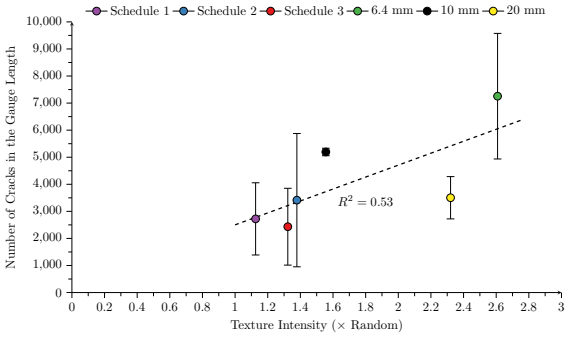

(d) (111)[$1\bar{2}1$] Crack Number

Figure 7.23: SCC susceptibility of the investigated samples compared to the concentration of (112) and (113) texture components.

(001)[1$\bar{1}$0] & (001)[110] Orientations

The role of (001)[1$\bar{1}$0] and (001)[110] textures on the SCC crack velocity and the number

of cracks that developed in the LIST specimens is presented in Figure 7.24. The effect of (001)[1$\bar{1}$0] and (001)[110] on crack velocity is presented in Figures 7.24a and 7.24b. There is no strong evidence to suggest that increasing the proportion of (001)[1$\bar{1}$0] or (001)[110] textures in terms of bulk texture has any impact on the crack velocity. When observing the effect intensity of (001)[1$\bar{1}$0] and (001)[110] textures had on the number of cracks that developed in the LIST specimens in Figures 7.24c and 7.24d, it is evident that there was no strong indication that any link exists. It is likely that bulk texture does not translate to microtexture behaviour and (001)[1$\bar{1}$0] and (001)[110] textures do contribute to susceptibility more than these results suggest. This finding is not surprising because, when observing field-grown SCC cracks in literature, there was no strong link identified between the bulk texture and the incidence of SCC cracking [20, 31]. This is likely due to SCC initiating from the surface where uniform (110)[001] textures were present with absence of strong (001)[1$\bar{1}$0] and (001)[110] orientations [20, 31]. It is only when observing micro texture immediately surrounding cracks, that cracking was linked to {001} textured grains in SCC by Arafin and Szpunar (2009) [24] and HIC by Venegas et al. (2007)[193]. The role of microtexture needs to be observed before the susceptibility of (001)[1$\bar{1}$0] and (001)[110] orientations can be concluded.

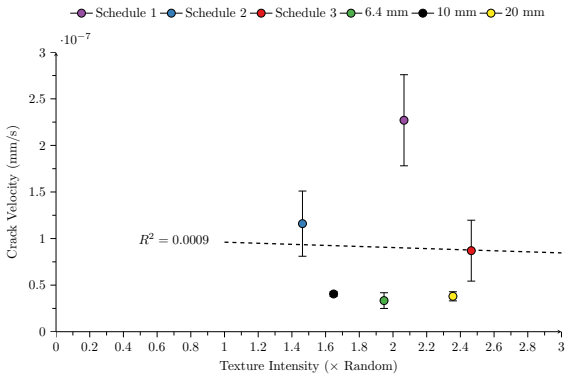

(a) (001)[1$\bar{1}$0] Crack Velocity

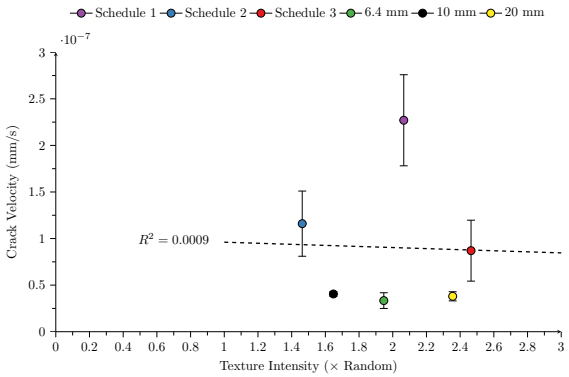

(b) (001)[110] Crack Velocity

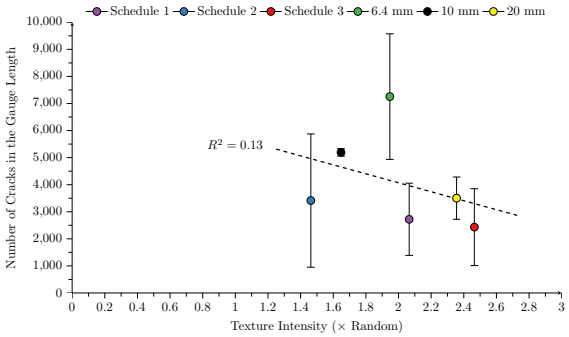

(c) (001)[1$\bar{1}$0] Crack Number

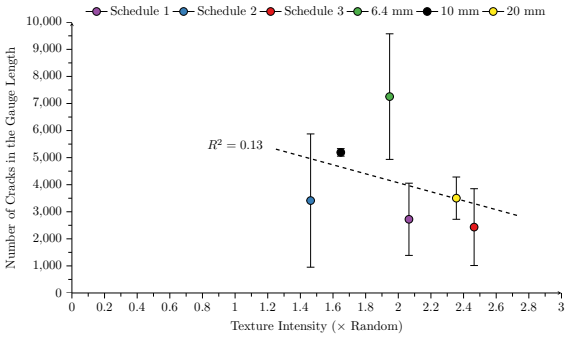

(d) (001)[110] Crack Number

Figure 7.24: SCC susceptibility of the investigated samples compared to the concentration of (001) texture components.

The role of different bulk texture components on the crack velocity and the number of cracks that initiated in the LIST specimens was investigated to determine what link existed between them. There is little evidence that crystallographic texture has any strong impact on the number of cracks that formed, however, the role on crack velocity was often more pronounced. It appears that higher concentrations of (110)[1$\bar{1}$0] textures are associated with higher crack velocities, as observed in Figure 7.20a. There is a good association that higher intensities of (112)[1$\bar{1}$0] and (113)[1$\bar{1}$0] textures result in lower crack velocities, as observed in Figure 7.21. To a lesser extent, as observed in Figures 7.22 and 7.23, the role of (332)[$\bar{1}\bar{1}$3], (554)[$\bar{2}\bar{2}$5] and {111}<112> textures appeared to have beneficial impacts on the overall crack velocity. Based on the results presented in Figure 7.24, there does not appear to be any evidence that higher or lower levels of {001}<110> bulk textures has any effect on either the crack velocity or the number of cracks that formed in the LIST specimens.

Texture Surrounding SCC Cracks

As discussed by the current author Roccisano et al. (2019) [31], the main issue with measuring texture of SCC cracks is that in any given frame, the crack only passes through a very small fraction of the total number of grain boundaries. As observed in Figure 7.24, bulk texture results were unable to find the link between (001)[1$\bar{1}$0] and (001)[110] textures and SCC susceptibility that were reported in literature concerning microtexture [24]. To remedy this, a series of LIST cracks were investigated with EBSD and the texture of the grains directly surrounding the crack separated from the unaffected grains to determine what textures were present.

A summary of the textures surrounding the cracks that developed in the LIST specimens of the laboratory rolled samples are presented in Figure 7.25 with the industry samples presented in Figure 7.26. As seen in Figures 7.25 and 7.26, {001}//RP textures are the most dominant orientations present in both the laboratory rolled and industry supplied specimens; appearing as the strongest texture in half of the investigated regions. {001}//RP textures are present in the highest concentrations in Schedule 1 in Figures 7.25a and 7.25b, Schedule 3 in Figure 7.25f, the 10 mm X70 pipe in Figure 7.26c and in the 20 mm X70 plate in Figures 7.26e and 7.26f. In the remaining half of the cropped cracks, the {113}//RP fibre in Figures 7.25d, 7.25e and 7.26b, the {332}//RP fibre in Figures 7.25c and 7.26a and at (223)[1$\bar{1}$0] in Figure 7.26d are dominant. When removing samples that experienced both intergranular and transgranular cracking (Schedule 3, 6.4 mm X70 plate and the 20 mm X70 plate), {001}//RP textures are still dominant in half of the remaining samples and no strong trend is present with the non {001}//RP. Overall, {001}//RP textures were present in high concentrations surrounding the SCC cracks in half of the investigated samples. It is likely that the grain boundaries produced by {001}//RP textured grains act as local stress concentrators as they permit cleavage fracture both transgranulalrly and intergranularly, leading to a greater SCC susceptibil-

ity; as was discussed by Venegas et al. (2007) [193] for HIC of pipeline steels.

Whilst the {001}//RP orientation did not appear to contribute significantly to SCC susceptibility in terms of the bulk texture, Figure 7.24, the orientation is the most common directly surrounding the SCC cracks. One likely explanation for the difference between bulk and microtexture results is the high concentrations of beneficial $(112)[1\bar{1}0]$, $(113)[1\bar{1}0]$, $(332)[\bar{1}\bar{1}3]$, $(554)[\bar{2}\bar{2}5]$ and {111}<112> textures mitigated the detrimental effect of {001}//RP textures on SCC susceptibility. This is evident when observing the difference in SCC susceptibility of Schedules 1 and 3. Despite having very similar crystallographic textures, as seen in Figure 7.17, they have dramatically different crack velocities, with Schedule 1 cracking approximately 2.6× faster than Schedule 3. Schedule 1 and 3 are differentiated by the intensity of the $(001)[1\bar{1}0]$ and the $(112)[1\bar{1}0]$ as observed in Figure 7.19. Schedule 1 has a higher intensity of the $(001)[1\bar{1}0]$ orientation and a lower intensity of the beneficial $(112)[1\bar{1}0]$ orientation, whilst Schedule 3 is the opposite. It is likely that the higher $(112)[1\bar{1}0]$ texture in Schedule 3 mitigated the detrimental impact of $(001)[1\bar{1}0]$ on the SCC susceptibility. This has been observed in literature when investigating the effect of crystallographic texture on mechanical properties; beneficial and detrimental crystallographic textures could be negated in the presence of sufficiently high intensities of their opposite [180, 257].

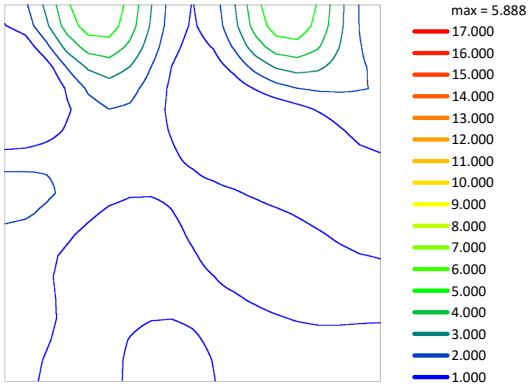

(a) Schedule 1 Cropped Frame ODF 1

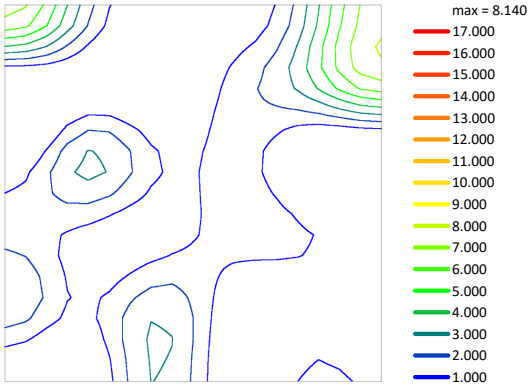

(b) Schedule 1 Cropped Frame ODF 2

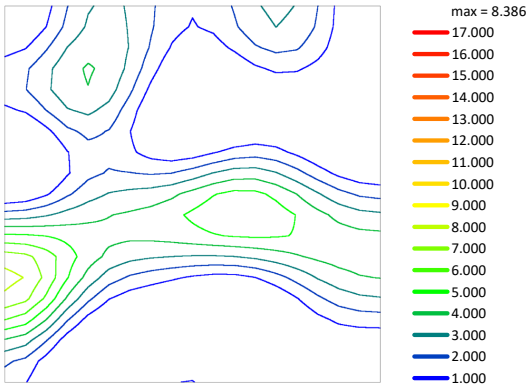

(c) Schedule 2 Cropped Frame ODF 1

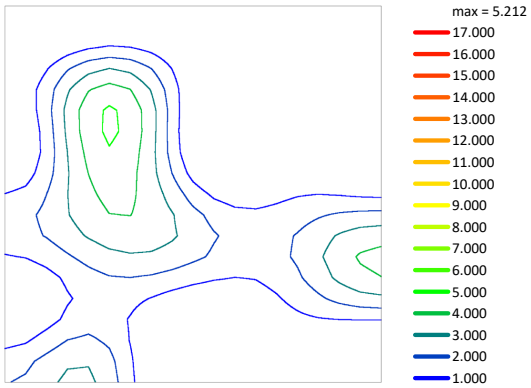

(d) Schedule 2 Cropped Frame ODF 2

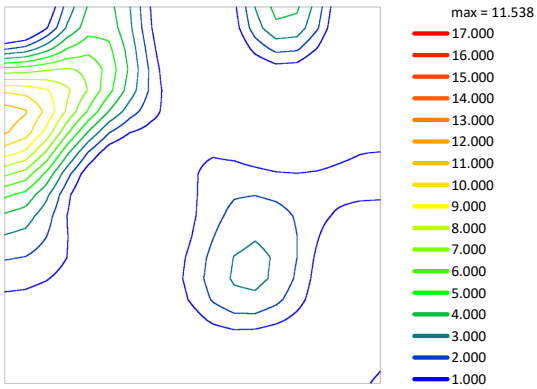

(e) Schedule 3 Cropped Frame ODF 1

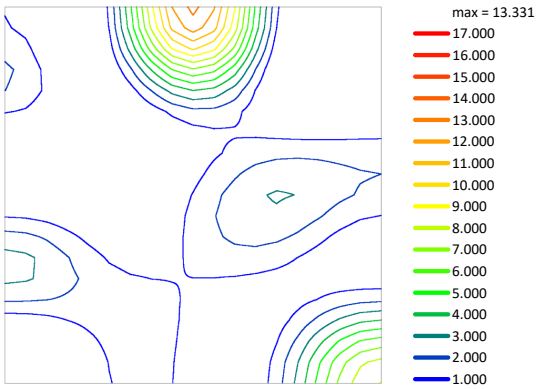

(f) Schedule 3 Cropped Frame ODF 2

Figure 7.25: Cropped SCC crack textures in the laboratory rolled samples.

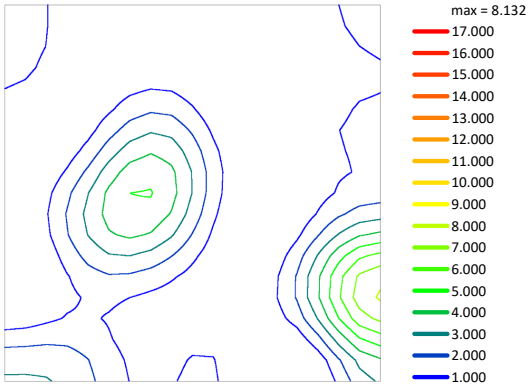

(a) 6.4 mm Cropped Frame ODF 1

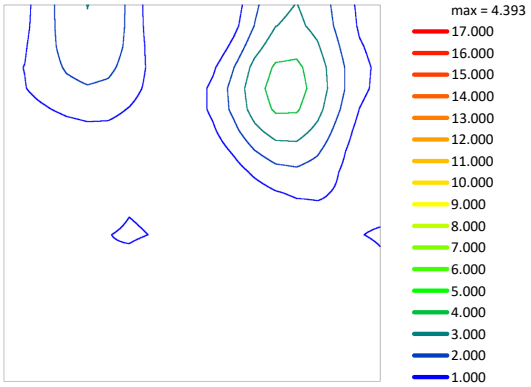

(b) 6.4 mm Cropped Frame ODF 2

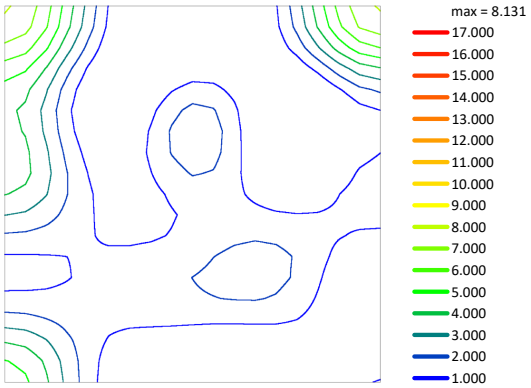

(c) 10 mm Cropped Frame ODF 1

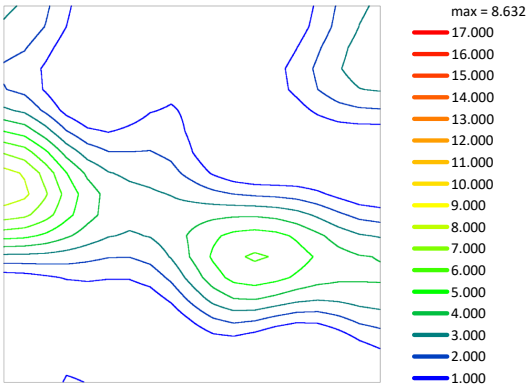

(d) 10 mm Cropped Frame ODF 2

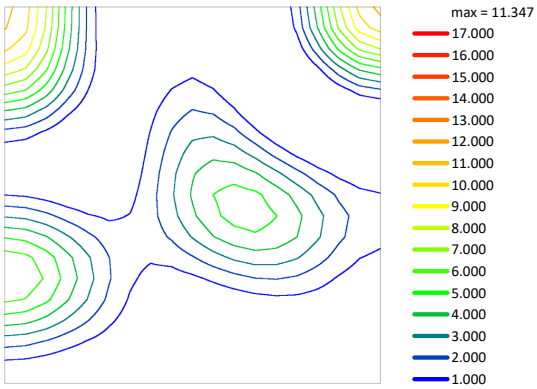

(e) 20 mm Cropped Frame ODF 1

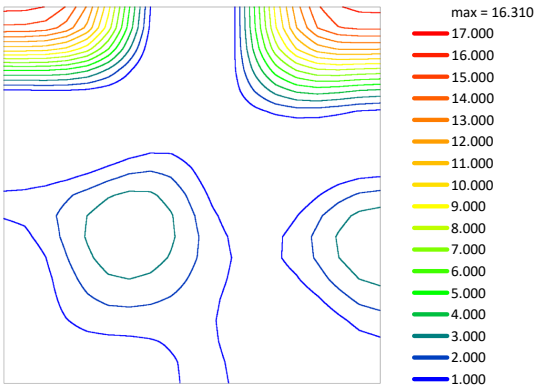

(f) 20 mm Cropped Frame ODF 2

Figure 7.26: Cropped SCC crack textures in the industry supplied samples.

7.3 Summary of SCC Susceptibility in Pipeline Steels

The SCC results show that in terms of crack velocity, the laboratory rolled specimens performed worse than the industry supplied samples they were benchmarked against. However, in terms of the number of cracks that initiated in the test specimens, the num-

ber that developed in the laboratory rolled samples was lower than the industry supplied samples. In order to explain this behaviour, microstructural and mechanical properties were investigated to determine what role they may have had on the overall SCC susceptibility of the test specimens.

As discussed in Section 7.2, the crack velocity appears to be strongly linked to the grain size with larger grains resulting in faster crack velocities. In contrast, the proportion of very small grains appears to correlate well with the number of cracks that initiated, however, the velocity was similarly reduced. It appears that the microstructure has a large role on the SCC susceptibility, however, none resulted in SCC immunity. Increases in the yield stress resulted in increases in the crack velocity of the laboratory rolled samples (approximately 1.4×10^{-7} mm/s increase corresponding to an approximately 180 MPa yield strength increase), however, there was only a minimal increase in the crack velocity linked to higher yield stresses in the industry supplied materials (approximately 3×10^{-10} mm/s increase corresponding to an approximately 120 MPa yield strength increase). The increase in yield stress appeared to have the strongest influence on SCC susceptibility in the laboratory rolled samples of all the mechanical parameters tested.

The crystallographic texture was also investigated to determine what effect it had on the SCC crack susceptibility of the samples. As seen in the bulk texture results in Section 7.2.4, it appears that there is strong evidence that the SCC crack velocity decreases with increased concentration of $(112)[1\bar{1}0]$ and $(113)[1\bar{1}0]$ textures. There is weaker evidence that the SCC crack velocity decreases with increased concentration of $(332)[\bar{1}\bar{1}3]$, $(554)[\bar{2}\bar{2}5]$ and $\{111\}\langle 112\rangle$ textures. In contrast, it appears as though there is some evidence that increasing the proportion of $(110)[1\bar{1}0]$ textures increases crack velocity. There was no strong evidence that the concentration of $\{001\}\langle 110\rangle$ bulk textures had any effect on the crack velocity. In terms of the number of cracks that developed in the test specimens, there was generally poor evidence that the bulk texture concentration of textures had any real impact on the number of cracks that initiated in the LIST specimens.

The texture of grains directly surrounding SCC cracks showed that {001}<110> appeared in disproportionally high concentrations surrounding cracks that the bulk texture results would have suggested. The likely cause of this is that overall weak {001}<110> bulk textures were mitigated by the impact of beneficial orientations. It is apparent that regardless of the bulk texture concentration of of {001}<110> orientations, they are highly susceptible orientations in the investigated steels but additions of $(112)[1\bar{1}0]$ and $(113)[1\bar{1}0]$, $(332)[\bar{1}\bar{1}3]$, $(554)[\bar{2}\bar{2}5]$, $(111)[\bar{1}\bar{1}2]$ and $(111)[1\bar{2}1]$ textures may mitigate their detrimental impact.

Chapter 8

Conclusion

The research carried out in this thesis was aimed at providing some understanding to what role manufacturing has on crystallographic texture development in pipeline steels, and quantifying the subsequent SCC susceptibility of those manufactured steels. Whilst the role manufacturing has on crystallographic texture is well studied, the role crystallographic texture has on SCC is somewhat less clear; with no previous research on the direct link between the three factors of manufacturing, crystallographic texture and SCC susceptibility. Based on literature regarding these three factors, the specific research aims were developed to fulfil the gaps identified in literature, namely to:

- Develop different rolling schedules that would simulate pipeline rolling procedures to generate different crystallographic textures.
- Determine the crystallographic texture developed from the different rolling schedules.
- Determine the high pH SCC susceptibility of the manufactured schedules.
- Identify the role that manufacturing has on the crystallographic texture and the subsequent high pH SCC susceptibility.

The first goal was achieved and presented in Chapter 5 where a series of three rolling schedules were developed with their microstructural and mechanical properties fully characterised. In addition, a series of analogous pipeline steel samples were sourced from

industry to act as the benchmark of the laboratory rolled samples with their mechanical and microstructural properties fully characterised. The results of the microstructural and mechanical properties identified that the hot and warm rolling schedules developed microstructures akin to samples sourced from industry whilst recrystallized rolling was significantly different. In terms of mechanical properties, only the recrystallized rolling schedule resulted in mechanical properties appropriate for the intended API 5L X70 grade. The primary reason for this was upper bainite formed through recrystallized rolling is intrinsically stronger than the granular bainite and polygonal/ quasi-polygonal ferrite formed through hot and warm rolling. The stronger phase developed through recrystallized rolling compensated for the lack of grain refinement due to laboratory scale rolling. The mechanical properties of the hot and warm rolled steels did not meet the requirements of an API 5L X70. The stronger upper bainitic phase present in recrystallized rolling compensated for the lack of grain refinement which is a highly effective strengthening mechanism. The result of Chapter 5 is both a theoretical and practical method of developing different textures for analysis that can be adapted to other pipe and steel grades in general.

The second goal was achieved in Chapter 6 where a detailed analysis of the through-thickness texture for each manufacturing process highlighted the similarities and differences with manufacturing processes identified in literature. The textures developed by the hot and warm rolling schedules were commonly identified in literature as well as in the benchmark industry supplied samples. One finding was the surface texture that developed was near identical regardless of the rolling schedule used to manufacture the samples. The similarity was likely due to the interaction between the material and the rollers. Similar surface textures were identified in the laboratory rolled samples further indicating a process dependent reason for the texture development. The results of Chapter 6 showed that the different rolling schedules developed different crystallographic textures in the rolled materials at the quarter and centre planes which can be used for SCC testing.

The third and fourth goals were achieved in Chapter 7 where the SCC susceptibility of each manufacturing process was carried out under comparable conditions to determine what impact the manufacturing process had on the SCC susceptibility. The SCC susceptibility was subsequently compared to the crystallographic texture as well as mechanical and microstructural properties to determine which properties had the strongest impact on the overall SCC susceptibility. The result showed that the recrystallized rolling schedule had the highest SCC susceptibility and the warm rolled material had the lowest susceptibility of the laboratory rolled samples. The level of crack initiation very similar between the three laboratory rolled samples. The laboratory rolled samples had significantly worse SCC susceptibility than any of the industry supplied samples with the recrystallized rolling schedule having an average crack velocity more than 5× that of the lowest industry supplied sample.

In terms of the physical properties, it was determined that SCC susceptibility was strongly linked to the grain size with larger average grain sizes resulting in higher crack velocities. In addition, high proportions of grains smaller than 5 μm was strongly linked to the number of cracks that initiated. With regards to mechanical properties, higher yield strengths strongly correlated in higher crack velocities in the laboratory rolled samples. The microstructure is likely a strong indicator of SCC susceptibility, however, aside from the recrystallized rolling schedule the other samples had very similar microstructures so a comparison between microstructures was not possible.

The crystallographic texture appeared to impact the SCC results and in terms of bulk textures, SCC crack velocity appeared to decrease with increased concentration of $(112)[1\bar{1}0]$, $(113)[1\bar{1}0]$, $(332)[\bar{1}\bar{1}3]$, $(554)[\bar{2}\bar{2}5]$, $(112)[\bar{1}\bar{1}2]$ and $(111)[1\bar{2}1]$ textures. There was an indication from SCC testing that increases in $(110)[1\bar{1}0]$ and, to a lesser extent, $(110)[001]$ textures increases crack velocity, however, as this result is contrary to what has been reported in literature, further investigation is required. Altering levels of $\{001\}\langle 110\rangle$ textures did not appear to have any impact on the crack velocity. In terms of the number

of cracks that initiated in the surface of the test specimens, increased concentration of $(112)[1\bar{1}0]$, $(113)[1\bar{1}0]$, $(332)[\bar{1}\bar{1}3]$, $(554)[\bar{2}\bar{2}5]$, $(112)[\bar{1}\bar{1}2]$ and $(111)[1\bar{2}1]$ textures resulting in more cracks initiating. Similarly increasing the concentration of $(110)[1\bar{1}0]$ and, to a lesser extent, (110)[001] textures decreased the number of cracks that initiated. Again there was no evidence that {001}<110> textures had any effect on the number of cracks that initiated.

Whilst it is tempting to recommend that increasing the overall proportions of the crystallographic textures that were seen as beneficial to SCC susceptibility is the answer to reducing the rate at which SCC initiates, these beneficial textures appear linked to higher SCC initiation. As crystallographic texture is, in essence, just another aspect of the microstructure, the role that it plays on SCC susceptibility must be tempered by the multitude of other microstructural properties. As with the mechanical properties, whilst it is apparent that increasing the yield strength results in higher SCC susceptibility in the laboratory rolled specimens, the effect of grains size and phases in each samples cannot be discounted and also play an overall role in the SCC susceptibility behaviour of the investigated samples. Whilst it would appear that crystallographic texture plays a role in determining the SCC susceptibility in steel, it is also true that the more strongly textured samples also happened to have on average smaller grain sizes, hence, only when all aspects of the materials are the same, then crystallographic texture becomes a leading factor. The roles of the other properties simply cannot be ignored.

Based on the results of the laboratory rolled samples, the warm rolling schedule used in Schedule 3 has resulted in the lowest SCC susceptibility. This appears to be linked to all the investigated microstructural properties studied. Beginning with the microstructure, the strain accumulation that occurred during finish rolling resulted in a primarily polygonal ferrite and granular bainite microstructure. In addition as the microstructure contained lower levels of granular bainite as compared to a hot rolling regime such as in Schedule 2, it had a lower yield strength than the recrystallized rolling or hot rolling

schedule. When comparing the textures that developed, the warm rolling process resulted in the highest concentration of $(332)[\bar{1}\bar{1}3]$, $(554)[\bar{2}\bar{2}5]$, $(112)[1\bar{1}0]$ and $(113)[1\bar{1}0]$ textures that were identified as being beneficial to SCC crack velocity. It is the sum of these factors that resulted in the low susceptibility of Schedule 3.

The study provided a highly experimental analysis on the role that different rolling schedules has on the mechanical and microstructural properties (including crystallographic texture) and what role those in unison have on the SCC susceptibility. It is apparent from the results that no single rolling schedule was perfectly suited to every situation. It is apparent that, because SCC susceptibility does not solely depend on a single property, it is likely that different recrystallized, hot and warm rolling schedules could result in better or worse SCC susceptibility depending on which properties are altered. It is this multitude of factors where the main limitation of this study lays; there is no standard rolling schedule as there are many methods available that achieve similar results.

The results presented in the thesis provide two different management strategies: 1) manufacture the steel to limit propagation; or 2) manufacture the steel to limit initiation. Typical SCC management relies on the results of many NDT investigations to determine the effective growth rate of defects in the pipe surface. It is unclear which management strategy would be more desirable, however, it is clear that highly detrimental SCC cracks develop in both instances. The specific implications to industry are presented in the following section.

8.1 Implications for Industry

The aim of the project at its core is to provide industry with a series of guidelines that they can use when specifying, during pipe procurement, the desired material properties of the steel that increases resistance to SCC. Whilst the pipe manufacturing processes utilised in this project develop pipe with properties similar to those industrially manufac-

tured, the rolling schedules used within this thesis should only be seen as representative rolling schedules and not optimised rolling schedules. In addition, as the primary aim of the project was to develop steels with different crystallographic textures, as opposed to generating pipe grade steels for industry, ensuring the material properties were within the minimum limits specified by AS2885 [60] or API 5L [27] standards was not a primary concern.

This project deals with the propagation behaviour of SCC as opposed to the initiation behaviour and as such effects of coatings and surface conditions were not investigated. There is a wealth of knowledge regarding proper coating, surface preparation and composition controls to limit the initiation of SCC and those findings should not be discarded in lieu of texture control. The implications to industry will consist of recommendations that industry can use to guide them when designing new pipelines and how the data collected can be used to improve knowledge of SCC susceptibility in general.

8.1.1 SCC Background

Before providing results regarding the SCC susceptibility of the different controlled rolling schedules, it is necessary to benchmark laboratory testing against real world SCC crack growth to provide background on what crack susceptibility is likely to be observed. The maximum theoretical crack velocity of SCC, if limited by dissolution rate and hence Faradays Law, is of the order of 10^{-6} mm/s corresponding to crack growth of 31.5 mm/year [7]. In practice this level of crack growth will never be achieved even under the worst possible laboratory conditions because SCC tends to be limited by the rate of film fracture rather than dissolution rate. SCC tends to have growth rates of between 10^{-9} - 10^{-7} mm/s or between 0.0315 - 3.15 mm/year [7, 36]. Under Australian conditions, SCC grows on average 0.25 mm/year which is within the expected range (APA Group estimates).

For SCC to occur, a susceptible material must be exposed to a corrosive medium whilst

experiencing a tensile stress. In the case of pipeline steels, a susceptible pipe must be exposed to a sufficiently high concentration of aqueous carbonate and bicarbonate ions [1]. As a result of wet and dry climate cycles, this concentration is not possible at all times of the year. During wet seasons, the concentration of carbonate and bicarbonate ions is diluted due to the increased moisture content in the soil surrounding the pipe, and during the dry season there is typically not enough moisture for aqueous solutions to exist [6]. As a result, high pH SCC only tends to occur between these weather extremes where the solution can achieve these high concentrations without drying out or becoming dilute. The magnitudes of SCC crack velocity derived from laboratory testing should only be considered as the most extreme crack growth rate that can occur when comparable conditions for SCC are present in the field. Each site will behave differently, however, the magnitude of the crack growth rate is comparable and materials with lower measured crack growth rates will not fail as quickly as materials with higher crack growth rates.

One of the primary concerns with SCC in pipeline steel is the loss of product and the cost for fixing pipes when SCC is observed in the pipe wall. When SCC is identified in a section of pipe and is of an actionable size, it can cost between $20,000 - $45,000 AUD (APA Group estimates) to excavate, assess and address the defect, depending on the pipe diameter. Any pipe technology that can delay or reduce the number of digs required over the lifetime of a pipeline results in substantial cost savings to pipe operators and overall lower running costs.

8.1.2 Project Results

This project was tasked with investigating the role crystallographic texture has on SCC susceptibility in terms of SCC propagation. Previous projects in the Energy Pipeline CRC RP2 program have determined that pipelines containing SCC tend to have different crystallographic textures than those that do not contain cracks [20]. To help industry purchase pipe with lower incidence of SCC, this project aimed to test three different rolling

schedules that would produce three different crystallographic textures and then undertake analysis to determine which rolling schedule results in the lowest SCC susceptibility. To remove any external effect aside from crystallographic texture, SCC testing conditions were the same between runs and each sample was produced from the same base material so the nominal chemical compositions were the same. In addition the grain size and microstructures at the levels tested were similar, further reducing the role of other factors on SCC susceptibility. The three rolling schedules tested and their SCC growth rates are:

- Schedule 1: recrystallized rolling, 2.27×10^{-7} mm/s (7.16 mm/yr)
- Schedule 2: hot rolling, 1.16×10^{-7} mm/s (3.66 mm/yr)
- Schedule 3: warm rolling, 8.70×10^{-8} mm/s (2.74 mm/yr)

Recrystallised Rolling is rolling that takes place entirely above the non-recrystallisation temperature of steel such that when the material cools it develops equiaxed grains with no elongation [180]. Hot Rolling is the more typical pipeline rolling procedure used in industry where finish rolling occurs below the non-recrystallization temperature of steel such that some elongation is retained in the resulting material and anisotropy of the material properties is expected [102]. Warm Rolling is a hybrid of Hot Rolling and Cold Rolling where finish rolling occurs in the two phase region of steel prior to cooling and develops properties similar to those of Hot Rolling [102]. More detailed information is provided in the literature review in Chapter 2 of the thesis.

SCC testing of the three different rolling schedules revealed that Schedule 3 (warm rolling) had the lowest SCC susceptibility closely followed by Schedule 2 (hot rolling) and finally Schedule 1 (recrystallized rolling) which had the highest SCC susceptibility. When presenting the crack velocities in terms of actual pipe dimensions, assuming a pipe wall thickness of 8.3 mm and that the pipe requires 7 mm of crack penetration for rupture, a pipe will be expected to last approximately one year under the worst possible conditions had it been manufactured through recrystallized rolling, approximately 2 years for hot rolling and approximately 2.5 years had it been manufactured under warm rolling. While

these extreme conditions used in the lab experiments are not likely to be experienced in the field, under the worst possible conditions warm rolling would allow an additional six months of operation over a hot rolling regime and over 18 months additional operation to a recrystallized rolling regime, allowing more time to repair the SCC.

As can be observed from the experimental results obtained here, the SCC susceptibility of the three rolling schedules are an order of magnitude higher than what is typically observed in the field. Whilst field observations give the best indication to SCC susceptibility, the decade long test durations are unworkable, especially when the end goal is to compare relative susceptibility. In addition, the field environment is more variable due to changes in temperature, pressure fluctuations, soil moisture content and resulting solution concentration. These random factors are not able to be easily mimicked in a laboratory setting in a repeatable manner, hence simpler conditions are necessary for laboratory testing. The overall findings from the laboratory testing undertaken in this study can be used to compare the relative susceptibility to SCC, which is the primary goal of this project.

8.1.3 Implications for Industry

When planning a new pipeline, SCC is typically not of primary concern for pipe owners with the physical dimensions and resulting gas throughput generally being of greater importance. Warm rolling, while providing the highest SCC resistance, also produces the lowest mechanical properties and in fact resulted in the lowest yield stress and UTS of the three schedules tested. This would suggest that warm rolled material may only be suitable for lower pipe grades unless alloy and rolling design is carried out such that microstructures correlated with high strength can be produced when finish rolled in the two phase region. Alteration of the chemistry and rolling schedule to improve the mechanical properties could potentially remedy these shortcomings but is beyond the scope of this project.

Hot Rolling, such as that used for the Schedule 2 sample in this sample, tends to be the

primary method of pipe manufacturing currently used in industry. While warm rolling and recrystallized rolling schedules have been designed to provide the required strength levels in pipeline steel, they are not commonly used processes. As Hot Rolling is the preferred method of producing pipe there may be some difficulty procuring warm rolled pipe from suppliers who may not be equipped to manufacture pipe of sufficiently high grade through warm rolling. One key recommendation to industry would be that when sourcing high grade pipe from rolling mills, avoid pipe manufactured solely through recrystallized rolling as the SCC susceptibility is likely to be higher than both current and historical manufactured pipe.

As one of the most effective methods for preventing SCC is to ensure adequate coating of pipes and careful installation such that coating defects do not occur, the use of warm rolling may be best suited to cases where SCC is a primary concern and the potentially lower strength substitute can be accommodated. This may not be a disadvantage as a lower pipe grade necessitates a higher wall thickness to allow for higher internal transport pressures, likely further increasing the long-term integrity because a crack would need to propagate through more material before a breach is possible. This will likely result in higher upfront capital expenditure and should be reserved for areas with extreme SCC susceptibility.

The use of hot rolled pipe grades is not associated with a significant increase in SCC susceptibility compared to warm rolling, with the overall difference being quite small (3.66 vs. 2.74 mm/year maximum growth rate). As mentioned previously, the rolling schedules produced in this study represent only a single representative example of each process and other hot rolling schedules with different reduction cycles and rolling temperatures may result in lower SCC susceptibility and higher mechanical properties.

8.1.4 Guidelines

As the primary aim of this research is to help pipeline operators with pipe selection when building new gas pipelines and in relation to the likelihood of SCC development in existing pipelines, the following guidelines have been produced to help pipe owners make more informed decisions regarding overall SCC protection:

- SCC susceptibility is linked to the crystallographic texture formed through different manufacturing processes and should be considered during manufacturing. However, other parameters such as yield strength, grain size and microstructure play some role.
- Pipe should be produced through warm rolling in areas where SCC is prominent as it has the lowest measured SCC susceptibility.
- Improving SCC susceptibility may come at the cost of lower mechanical properties so may only be practical for projects that can accommodate lower grade pipe.
- Hot rolling which is, compared to warm rolling, the most commonly used process, has only a marginally higher SCC susceptibility so pipe manufactured through this process does not warrant action beyond what is currently employed.
- Recrystallized rolling has the worst SCC susceptibility and should not be used for pipe manufacturing in locations where SCC is likely.

The incidence of SCC in gas pipelines is typically due to a coating failure that brings the SCC forming environment into contact with the surface of the pipe. These guidelines do not supersede previous SCC initiation research and preventing the corrosive environment from reaching the bare pipe through appropriate coatings should still be considered the first defence against SCC.

8.1.5 Future Industry Work

Whilst this research has provided industry with a series of recommendations concerning the role that manufacturing can have on SCC susceptibility, there still remains some unanswered questions that could further benefit industry. The rolling schedules investigated represent a single representative example of each rolling regime i.e. a single recrystallized rolling schedule, a single hot rolling schedule and a single warm rolling schedule. For these particular schedules, warm rolling has the lowest SCC susceptibility followed by hot rolling and recrystallized rolling, however, changing the rolling parameters could potentially optimise the SCC resistances further leading to lower susceptibilities in each rolling process. Further investigation of the rolling parameters is beyond the scope of this current project. As touched upon earlier, as industry moves towards higher strength pipe grades, warm rolling may not continue to be a suitable process to use for developing high strength steel. As such, optimising the rolling process could help to reduce SCC susceptibility in future pipe grades.

Whilst the primary aim of this work was to develop a series of different crystallographic textures in a manner similar to those used in industry pipe making to test the final SCC susceptibility, the data that has been collected could be of further use to industry with little additional work. With the upcoming goal of making gas distribution more renewable, the addition of hydrogen to natural gas lines appears to be inevitable. With the addition of hydrogen to the gas supply there come new challenges for maintaining the integrity of pipe structure as the likelihood of Hydrogen Induced Cracking (HIC) increases. As touched upon in the Literature Review section of the thesis, the initial work linking crystallographic texture to corrosion mechanisms in pipeline steels was carried out initially on the HIC corrosion mechanism. Future projects wanting to test the effect crystallographic texture has on HIC could adapt the rolling schedules developed in this project for other laboratory rolling tests and determine the resulting HIC susceptibility based on the crystallographic textures developed.

Another potential route to build upon this project in the future could be to improve the correlation between laboratory grown SCC rates to field grown SCC rates. Whilst SCC cracks are able to be reliably produced under laboratory conditions, correlating laboratory results to observations in the field can still be improved upon. Laboratory testing tends to overpredict the growth rate of SCC in pipeline steels and is not able to model the multitude of variables pipelines are exposed to in the field, including: concentration change of the electrolyte, cathodic protection effectiveness, pressure fluctuation and temperature change. Improving the link between laboratory measured susceptibility and field susceptibility would enable pipe owners to know with a higher degree of certainty how long it will take for a crack to grow and thus reduce the number of unnecessary digs.

8.2 Future Work

Whilst this thesis has added significant knowledge to the literature, it is clear that new gaps and future research directions have developed. These gaps could help to answer new questions regarding SCC and steel rolling in general. This section seeks to illuminate these new avenues of research.

8.2.1 Gaps in Knowledge

This thesis has provided some additional information regarding the role that manufacturing has on texture development and the eventual SCC susceptibility. As touched upon in the previous section, this thesis presents three rolling schedules finish rolled above the T_{NR}, finished rolled below the T_{NR} and finish rolled in the two phase region. It is not clear whether altering, for instance, the hot rolling schedule to develop properties similar to those developed in the warm rolling schedule would result in different SCC susceptibility.

Whilst there has been significant research related to the specific grain boundaries through

which SCC propagates through, there is still some ambiguity over why certain grain boundaries crack preferentially compared to others. Whilst work by Arafin and Szpunar (2009) [24] sought to explain cracking behaviour, recent work by Roccisano et. al. (2019) [31] found many instances of SCC cracks propagating through resistant grain boundaries. There is still an underlying mechanism or group of mechanisms that determines the exact SCC propagation path that is still uncertain. It is likely that the stress state of the grains prior to fracturing could have in some way facilitated SCC, however, after cracking it is not possible to determine what state the grain boundaries were initially under.

Another gap that has become clear is that it is unknown what exact effect pipe forming and coating has on the crystallographic texture in a pipe. An initial investigation has been completed by [242] but only one grade and thickness of pipeline steel was tested. As the work carried out in this thesis was undertaken on the as-rolled material with no additional pipe forming or coating, the textures could be altered, altering the SCC susceptibility.

8.2.2 Research Directions

There are some experiments that present themselves as viable candidates to help fill some of the gaps identified in the previous section. Some of the experiments can potentially fill multiple gaps but their primary role is to answer the questions identified in the previous section.

To understand the role that the specific per pass deformation had on microstructure development and eventual SCC susceptibility, additional rolling schedules with different per pass reductions in each finish temperature regime would provide a more complete understanding on what textures develop due to the reduction and would enable more granular SCC susceptibility results. To conduct this experiment, a series of rolling schedules with varying rolling reductions per pass would be developed and samples with identical chem-

ical composition would be manufactured to those specifications. The samples would then be fully characterised and SCC susceptibility tests carried out on them. In addition to SCC susceptibility, many other corrosion phenomena could be investigated with the same raw material including HIC or Stress Sulphide Cracking (SSC). In addition, the different rolling schedules could be used to determine the role of manufacturing on different mechanical properties depending on the grade selected.

To enable a clearer understanding of why cracks selectively propagate through the grain boundaries they do, an understanding of the initial stress state of the material prior to cracking would be a useful. To achieve this, a series of pre cracked compact tensile samples would be produced with their faces highly polished such that EBSD could be undertaken and an understanding of the region ahead of the pre crack could be achieved. Following this initial EBSD, the samples would be cracked using the LIST apparatus and then re polished lightly to determine which grain boundaries the SCC cracks propagated through. This experiment could enable a new experimental method for determining crack propagation in a variety of situations and corrosion mechanisms.

To understand the role that pipe forming and coating has on the crystallographic texture of pipeline steels,It is not clear whether altering, a series of texture examinations using XRD could be undertaken to determine what effect each process has on the macrotexture of the sample. As only macrotexture is being investigated a high speed XRD would enable the most grains sampled and hence the most representative texture. A series of plate, uncoated pipe and coated pipe sections with different wall thickness and grade would be sourced from an industry partner where they would then be sectioned into surface, quarter, centre, 3 quarter and inner surface sections which would then be analysed to determine what the role of each process had on the texture.

This thesis has provided insight into the role that different rolling schedules have on the material properties, microstructure and crystallographic texture and the role they have

on the SCC susceptibility. The identified gaps build upon the work that has been undertaken in this thesis and the research directions provide experiments to help answer the questions raised by those gaps.

The role that manufacturing has on SCC is not a burgeoning field but this thesis serves to link properties that are not typically linked. A series of rolling schedules were developed for the purpose of creating different crystallographic textures such that the role that manufacturing had on texture and the subsequent effect on SCC could be determined. This aim has been achieved and the results have be disseminated through publications to industry and the broader community at large. This work serves as a template for testing the role that manufacturing has on different corrosion phenomena and it is hoped that it will be used to create safer infrastructure in the future.

Appendix A

API Standards

This appendix contains a summary of the chemical and strength requirements for API 5L pipe steels. The grades investigated are thermomechanically formed as opposed to seamless or quench and tempered and they require slightly different chemical compositions. These particular tables were sourced from the API 5L pipe specification standard from 2013 [27].

A.1 Chemical Composition Limits for API 5L Pipe Grades

The chemical composition presented in Appendix A.1 are for PSL 2 pipe with thickness ⩽25 mm. PSL 2 pipe is a higher grade than PSL 1 grade and has stricter standards for chemical composition.

Table A.1: Chemical composition limits outlined in the API 5L standard (w.t. %). Adapted from [27].

Grade	C	Si	Mn	P	S	V	Nb	Ti	Cu	Ni	Cr	Mo	B
L290 or X42	0.22	0.45	1.30	0.025	0.015	0.05	0.05	0.04	0.50	0.30	0.50	0.15	
L320 or X46	0.22	0.45	1.30	0.025	0.015	0.05	0.05	0.04	0.50	0.30	0.50	0.15	
L360 or X52	0.22	0.45	1.40	0.025	0.015	a	a	a	0.50	0.30	0.50	0.15	
L390 or X56	0.22	0.45	1.40	0.025	0.015	a	a	a	0.50	0.30	0.50	0.15	
L415 or X60	0.12	0.45	1.60	0.025	0.015	a	a	a	0.50	0.50	0.50	0.50	
L450 or X65	0.12	0.45	1.60	0.025	0.015	a	a	a	0.50	0.50	0.50	0.50	
L485 or X70	0.12	0.45	1.70	0.025	0.015	a	a	a	0.50	0.50	0.50	0.50	
L555 or X80	0.12	0.45	1.85	0.025	0.015	a	a	a	0.50	1.0	0.50	0.50	
L625 or X90	0.10	0.55	2.10	0.020	0.010	a	a	a	0.50	1.0	0.50	0.50	
L690 or X100	0.10	0.55	2.10	0.020	0.010	a	a	a	0.50	1.0	0.50	0.50	0.004
L830 or X120	0.10	0.55	2.10	0.020	0.010	a	a	a	0.50	1.0	0.50	0.50	0.004

a) The sum of the niobium, vanadium and titanium concentrations shall be $\leq 0.15\%$

A.2 Strength Limits API 5L Pipe Grades

The mechanical strength limits presented in Appendix A.2 are for PSL 2 welded or seamless pipes, for all manufacturing processes.

Table A.2: Strength limits for PSL 2 API 5L standard. Adapted from [27].

Grade	**Yield Stress (MPa)**		**Tensile Stress (MPa)**		**Ratio**
	Minimum	Maximum	Minimum	Maximum	Maximum
L290 or X42	290	495	415	760	0.93
L320 or X46	320	525	435	760	0.93
L360 or X52	360	530	460	760	0.93
L390 or X56	390	545	490	760	0.93
L415 or X60	415	565	520	760	0.93
L450 or X65	450	600	535	760	0.93
L485 or X70	485	635	570	760	0.93
L555 or X80	555	705	625	825	0.93
L625 or X90	625	775	695	915	0.95
L690 or X100	690	840	760	990	0.97
L830 or X120	830	1050	915	1145	0.99

A.3 Allowable Pipe Manufacturing Processes for API 5L Grades

The allowable manufacturing processes for the various API 5L pipe grades is presented in Table A.3. Higher grade pipes require more advanced manufacturing processes with lower grades allowing simpler processes.

Table A.3: API 5L permissible manufacturing methods for PSL2 grade pipeline steel. Adapted from [27].

Delivery Condition	**Pipe/ Steel Grade**
As Rolled	L245R or BR
Normalizing rolled, normalizing formed,	L245N or BN
normalized or normalized and tempered	L290N or X42N
	L320N or X46N
	L360N or X52N
	L390N or X56N
	L415N or X60N
Quenched and tempered	L245Q or BQ
	L290Q or X42Q
	L320Q or X46Q
	L360Q or X52Q
	L390Q or X56Q
	L415Q or X60Q
	L450Q or X65Q
	L485Q or X70Q
	L555Q or X80Q
Thermomechanical rolled or	L245M or BM
thermomechanical formed	L290M or X42M
	L320M or X46M
	L360M or X52M
	L390M or X56M
	L415M or X60M
	L450M or X65M
	L485M or X70M
	L555M or X80M
Thermomechanical rolled	L625M or X90M
	L690M or X100M
	L830M or X120M

A.4 Strength Calculations for API 5L Grades

When calculating the yield stress in the API 5L pipeline grades, the standard uses the 0.5% total extension yield strength as opposed to the 0.2% offset yield strength. A functional difference between calculating the two of these is presented in Figure A.1.

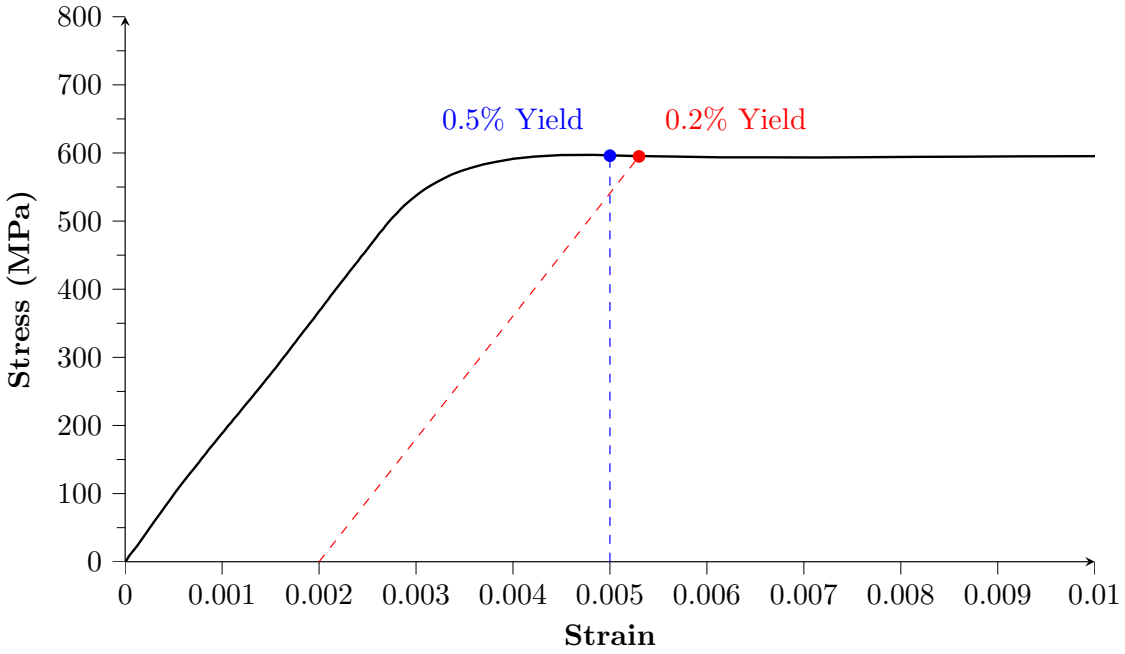

Figure A.1: Difference between the 0.5% and 0.2% yield strengths.

Appendix B

Polishing Procedure

This polishing procedure covers the polishing of low carbon and mild steels in general. The polishing guide presented in this Appendix was used during this project for all steel specimens. As stated in Section 3.3, polishing was carried out on a Sturers Tegramin 25 polisher. The procedure was carried out on 25 mm mounted specimens but can be used on larger samples with adjustments to the force.

Table B.1: Polishing procedure for low to medium carbon steels.

Step	**Time (min)**	**RPM Head/Body**	**Rotation**	**Force (psi)**	**Abrasive**
1	3.00	150/300	Co-Rotation	35	220 grit diamond disk
2	3.00	150/150	Co-Rotation	35	500 grit diamond disk
3	5.00	150/150	Co-Rotation	30	1200 grit diamond disk
4	5.00	150/150	Co-Rotation	25	9 μm diamond suspension
5	3.00	150/150	Co-Rotation	20	3 μm diamond suspension
6	3.00	150/150	Co-Rotation	20	1 μm diamond suspension
7	Variable	150/150	Counter	15	0.04 μm Colloidal Silica

The time spent polishing the specimens using colloidal silica (step 7) depends on the final analysis technique. For optical microscopy colloidal silica is not strictly necessary, how-

ever, if there is some residual contamination on the 1 μm pad a final polish for 3 minutes with colloidal silica can remove the fine scratches. SEM characterisation of etched samples benefit from a 10 minute polish with colloidal silica prior to etching as it removes all fine scratches. For EBSD analysis upwards of 30 minutes is necessary to remove all damage caused by prior polishing. Excessive polishing with colloidal silica causes surface relief so significantly more than 30 minutes can damage the surface.

Between the different polishing stages, the samples were rinsed with water and then placed in a container of ethanol in an ultrasonic cleaner. The samples are cleaned for for 2 minutes (or more depending on the level of contamination) before being rinsed under running water and dried with ethanol and hot air. In the event the suspension is not removed from the surface through ultrasonic cleaning, samples are placed under running water and rubbed with a cotton bud (moving in only one direction to prevent excessive scratching) until cleaned before being placed back in the ultrasonic cleaner. To ensure cross contamination of the different suspensions does not occur, the polisher is cleaner as is the rotating head to remove all traces of the previous diamond grit.

Appendix C

Etching Procedure

This Appendix covers the etching procedure used for optical microscopy of the low carbon, pipe grade steels used during this project. Over the course of the project two main etchants were used, 2% Nital and saturated aqueous Picric acid. The 2% Nital was used to expose grain boundaries and general microstructure whilst the saturated aqueous Picric acid was used to expose prior austenite grain boundaries.

C.1 Nital Etchant

C.1.1 Solution Chemistry

2% Nital Solution	
2 mL	Concentrated nitric acid
98 mL	Ethanol (95%)

C.1.2 Etching Procedure

To ensure a uniform etch over the surface, ethanol was first pipetted onto the surface of the sample to completely wet it. Approximately 3 mL of 2% Nital was then pipetted over the layer of ethanol and allowed to etch, on average 20 seconds, until the surface

changed from reflective to dull. The sample was immediately rinsed with ethanol to halt the reaction was then rinsed with water to remove all traces of acid from the surface. The sample was then dried with ethanol and subsequently hot air to ensure water marks remained. The application of ethanol to the surface prior to the 2% Nital allowed for a gentle and very uniform etch that was easily controllable and repeatable.

C.2 Aqueous Picric Acid Etch

C.2.1 Solution Chemistry

Aqueous Picric Acid Etch	
10 g	Picric acid
100 mL	Water
1 g	Sodium dodecylbenzene sulfonate
2 drops	HCl (Optional)

Measure out 10 g of Picric acid and thoroughly mix with plastic or glass stirring rods to ensure all a completely dissolved solution. *N.B. Pure sodium dodecylbenzene sulfonate was not available at the time of carrying out the prior austenite grain boundary investigations so a 5 g of Earth Choice Dishwash Liquid – Lemon Fresh was substituted due to it containing between 10-30% sodium dodecylbenzene sulfonate at the time of purchase. See Appendix H for an SDS of the dishwashing liquid.*

C.2.2 Etching Procedure

To reveal the prior austenite grain boundaries, the samples were immersed in a beaker of Aqueous Picric Acid heated to $65°C$ in a water bath for 10 minutes. After 10 minutes the samples were removed from the solution and rinsed in a waiting beaker of RO water.

The samples were then rinsed with running water and swabbed with a clean cotton bud to remove the black film formed during etching. Once clean, samples were sprayed with ethanol to displace the water and dried with hot air. The addition of 2 drops of concentrated HCl was not beneficial to revealing prior austenite grain boundaries and when tested revealed cementite boundaries.

Appendix D

Prior Austenite Grain Size Determination

Presented in this appendix are the prior austenite grain micrographs of the 20 mm X70 plate for the purpose of measuring the prior austenite grain size. The prior austenite grain size was determined by soaking samples of the 20 mm X70 plate at $1180°C$ in a furnace and taking each sample out at 60, 120, 150 and 180 minutes and quenching them in room temperature water. Each sample was sectioned and mounted in the transverse (TRD) orientation and etched with aqueous picric acid (see Section 8.2.2) to reveal the prior austenite grain boundaries. The grain size was determined through the boundary intercept method presented below per ASTM E112 [200].

D.1 60 Minute Soak

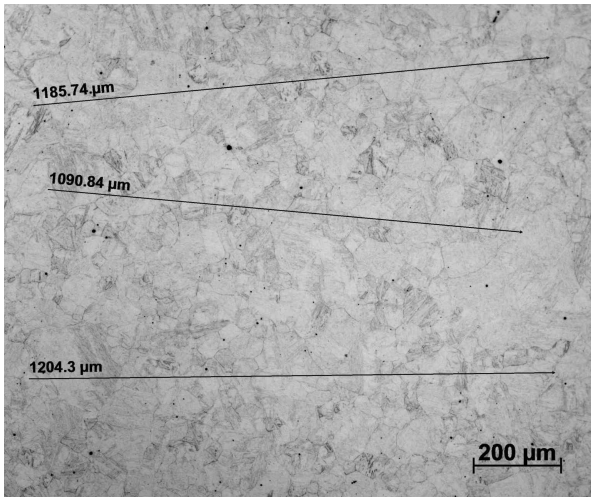

(a) Location 1.

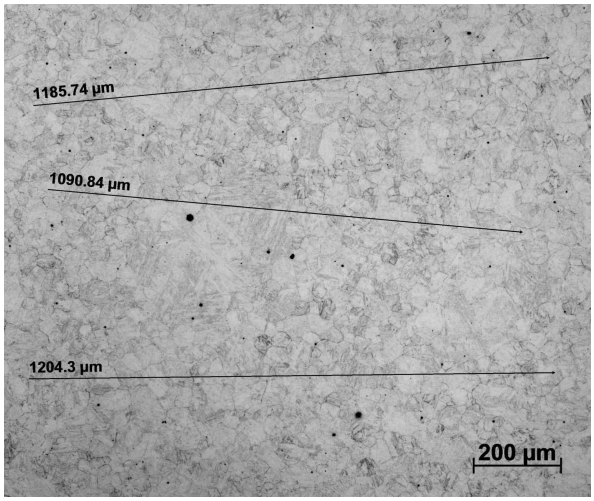

(b) Location 2.

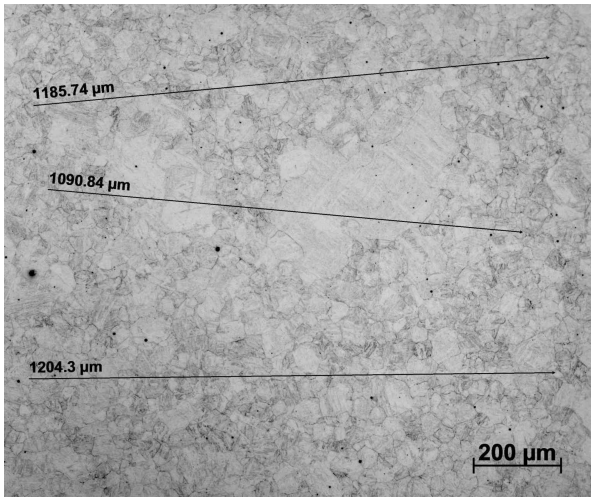

(c) Location 3.

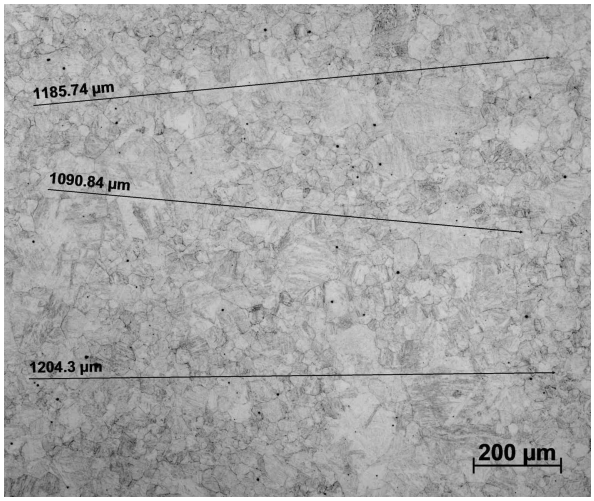

(d) Location 4.

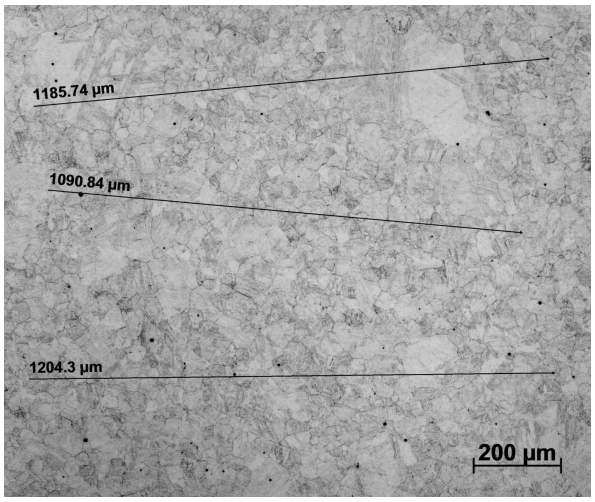

(e) Location 5.

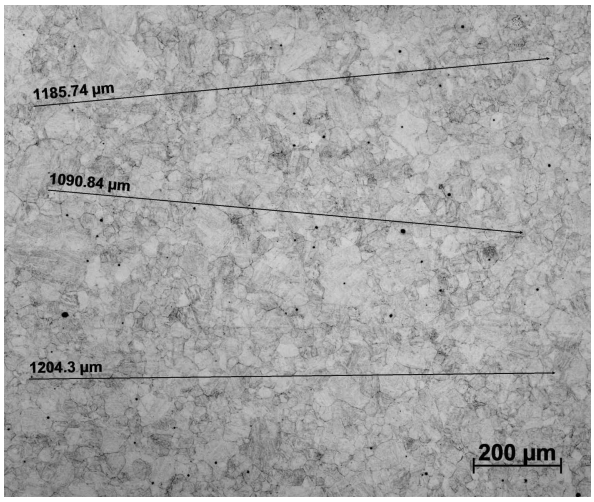

(f) Location 6.

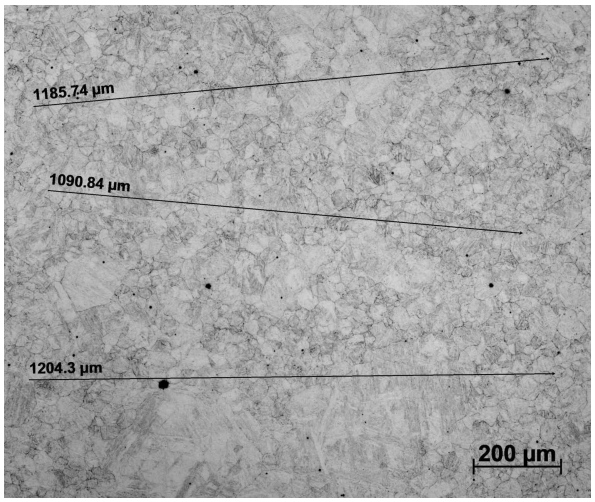

(g) Location 7.

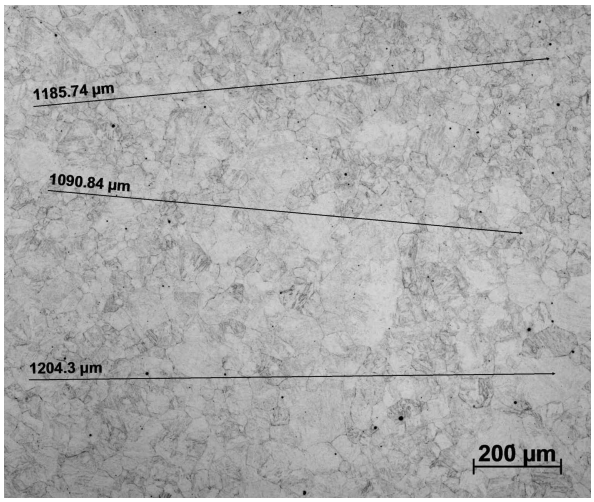

(h) Location 8.

Figure D.1: Prior austenite grain size after soaking for 60 minutes.

Table D.1: Number of intercepts identified in the 60 minute sample.

	Number of Intercepts		
Location	**Line 1** ($\mathbf{1185.74\,\mu m}$)	**Line 2** ($\mathbf{1090.84\,\mu m}$)	**Line 3** ($\mathbf{1204.3\,\mu m}$)
1	14	19	20
2	27	20	28
3	27	15	31
4	32	21	30
5	23	24	23
6	28	23	29
7	27	18	28
8	26	26	30

Table D.2: Average grain sizes identified in the 60 minute sample.

	Grain Diameter			
Image	**Line 1** ($\boldsymbol{\mu m}$)	**Line 2** ($\boldsymbol{\mu m}$)	**Line 3** ($\boldsymbol{\mu m}$)	**Average** ($\boldsymbol{\mu m}$)
1	84.7	57.4	60.2	67.4
2	43.9	54.5	43.0	47.2
3	43.9	72.7	38.8	51.8
4	37.1	51.9	40.1	43.0
5	51.6	45.5	52.4	49.8
6	42.3	47.4	41.5	43.8
7	43.9	60.6	43.0	49.2
8	45.6	42.0	40.1	42.6
			Average	49.3
			STD	8.1

D.2 120 Minute Soak

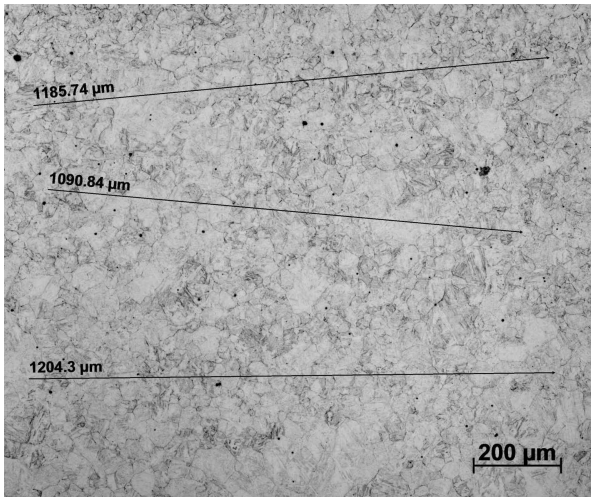

(a) Location 1.

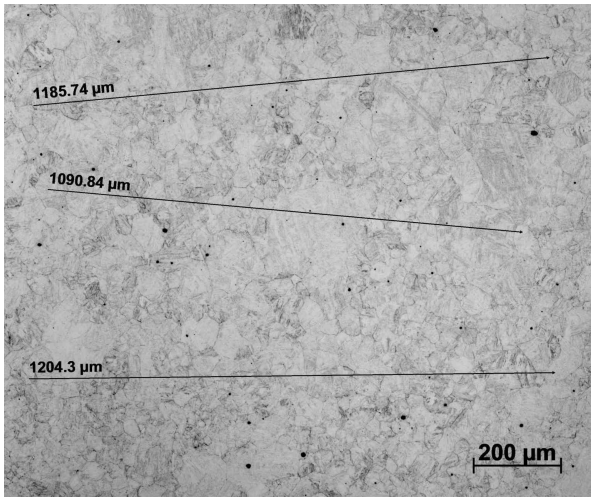

(b) Location 2.

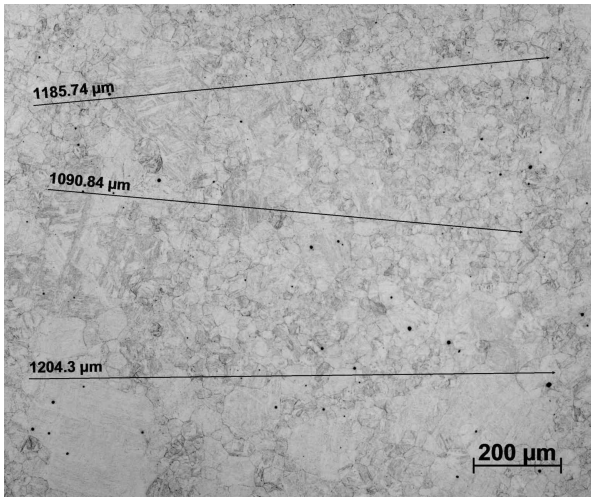

(c) Location 3.

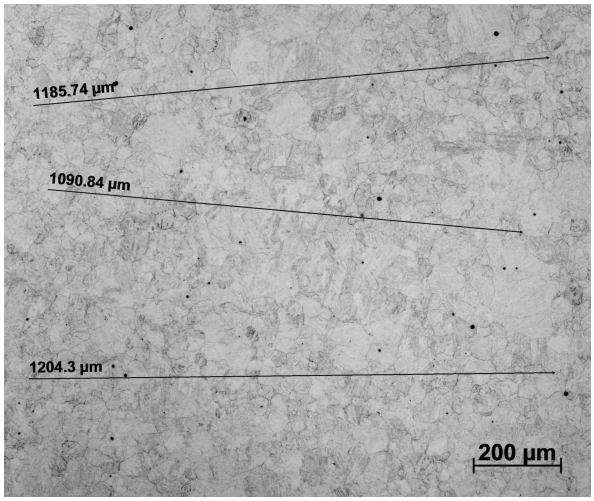

(d) Location 4.

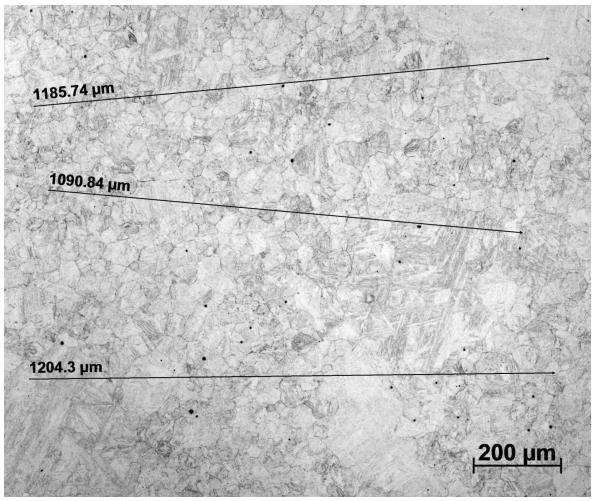

(e) Location 5.

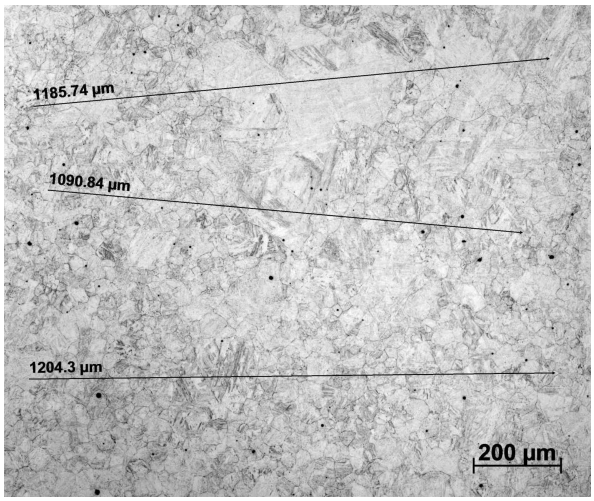

(f) Location 6.

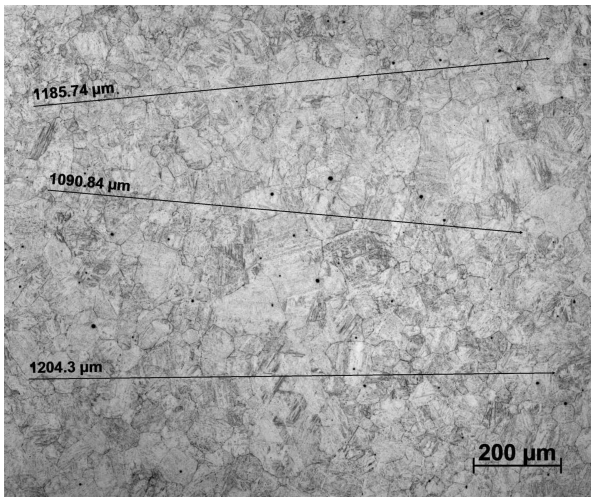

(g) Location 7.

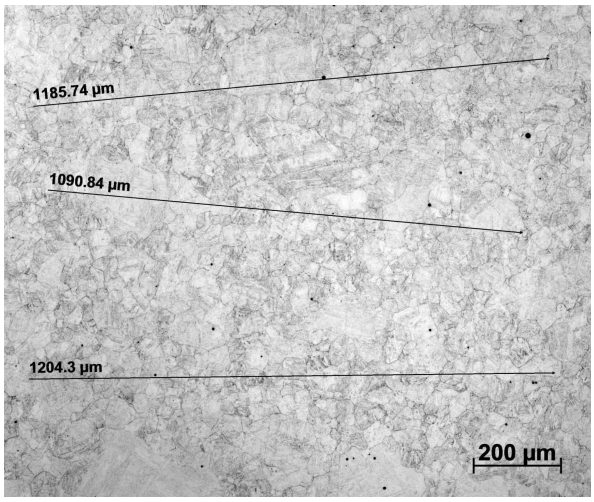

(h) Location 8.

Figure D.2: Prior austenite grain size after soaking for 120 minutes.

Table D.3: Number of intercepts identified in the 120 minute sample.

	Number of Intercepts		
Location	**Line 1** ($\mathbf{1185.74\,\mu m}$)	**Line 2** ($\mathbf{1090.84\,\mu m}$)	**Line 3** ($\mathbf{1204.3\,\mu m}$)
1	24	26	33
2	19	20	29
3	25	20	26
4	20	19	34
5	19	17	15
6	17	17	24
7	21	16	20
8	26	23	29

Table D.4: Average grain sizes identified in the 120 minute sample.

	Grain Diameter			
Image	**Line 1** (μm)	**Line 2** (μm)	**Line 3** (μm)	**Average** (μm)
1	49.4	42.0	33.1	41.5
2	62.4	54.5	37.6	51.5
3	47.4	54.5	42.0	48.0
4	59.3	57.4	32.1	49.6
5	62.4	64.2	72.7	66.4
6	69.7	64.2	45.5	59.8
7	56.5	68.2	54.5	59.7
8	45.6	47.4	37.6	43.5
			Average	52.5
			STD	8.7

D.3 150 Minute Soak

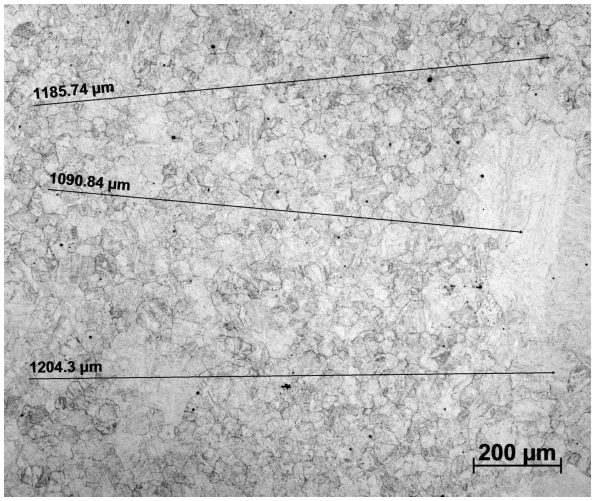

(a) Location 1.

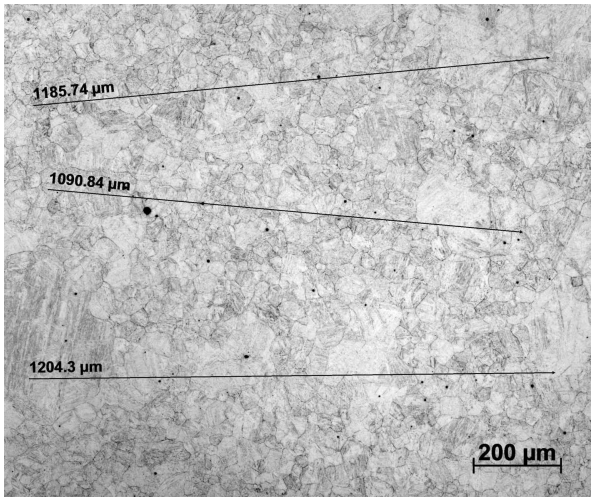

(b) Location 2.

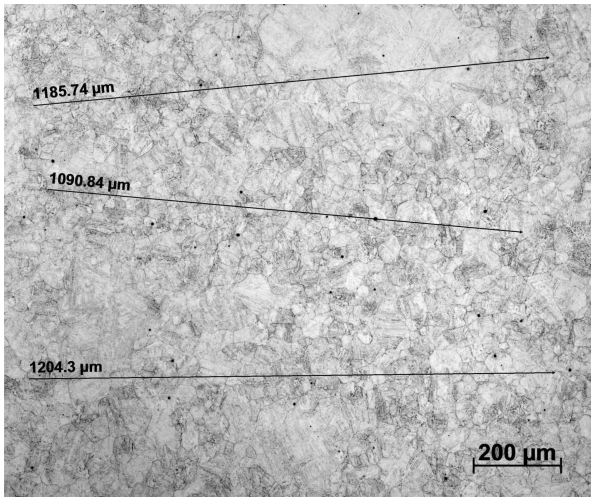

(c) Location 3.

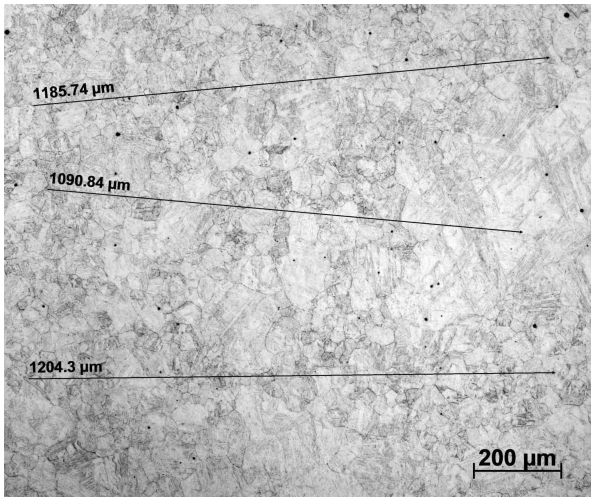

(d) Location 4.

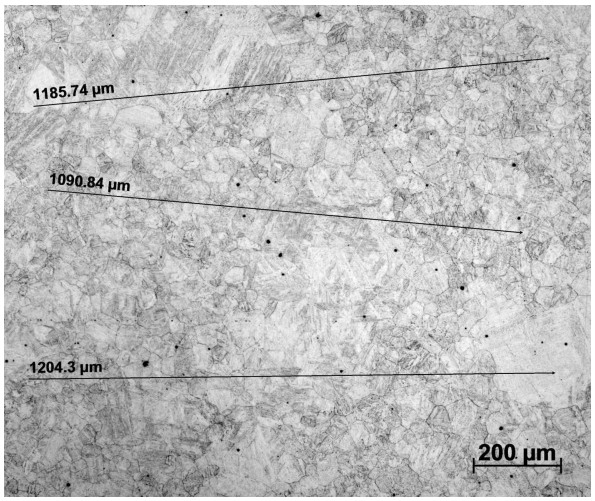

(e) Location 5.

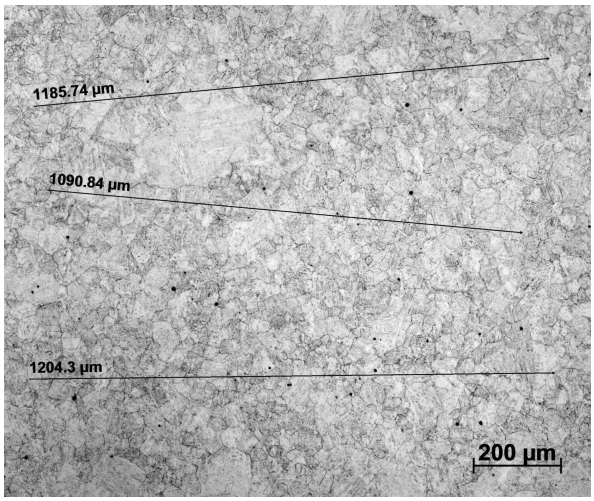

(f) Location 6.

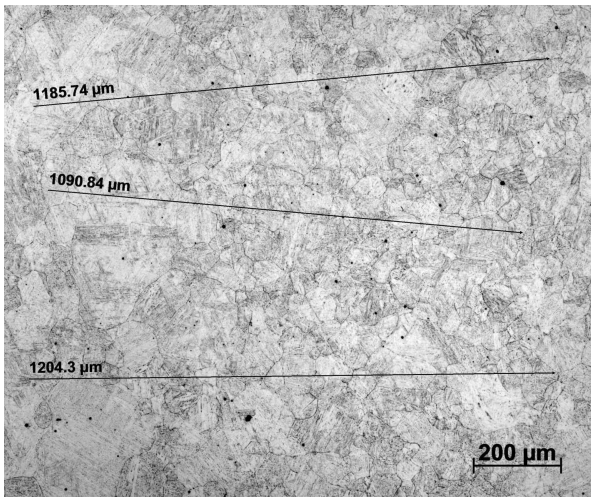

(g) Location 7.

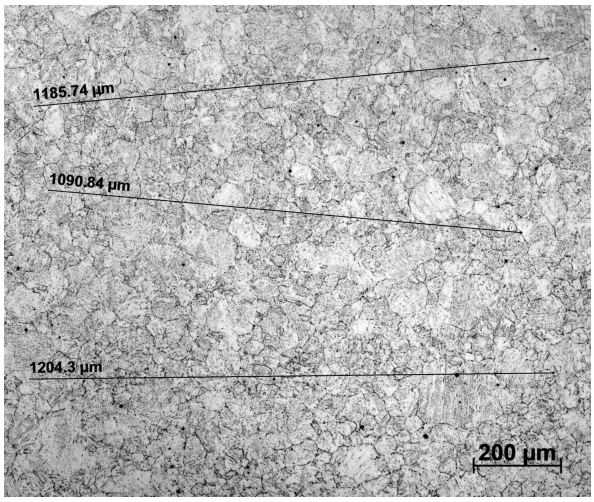

(h) Location 8.

Figure D.3: Prior austenite grain size after soaking for 150 minutes.

Table D.5: Number of intercepts identified in the 150 minute sample.

	Number of Intercepts		
Location	**Line 1** ($\mathbf{1185.74\,\mu m}$)	**Line 2** ($\mathbf{1090.84\,\mu m}$)	**Line 3** ($\mathbf{1204.3\,\mu m}$)
1	32	22	34
2	26	28	23
3	19	27	29
4	22	18	19
5	13	17	16
6	23	18	22
7	12	10	15
8	15	19	16

Table D.6: Average grain sizes identified in the 150 minute sample

	Grain Diameter			
Image	**Line 1** (μm)	**Line 2** (μm)	**Line 3** (μm)	**Average** (μm)
1	37.1	49.6	35.4	40.7
2	45.6	39.0	52.4	45.6
3	62.4	40.4	41.5	48.1
4	53.9	60.6	63.4	59.3
5	91.2	64.2	75.3	76.9
6	51.6	60.6	54.7	55.6
7	98.8	109.1	80.3	96.1
8	79.0	57.4	75.3	70.6
			Average	61.6
			STD	18.6

D.4 180 Minutes Soak

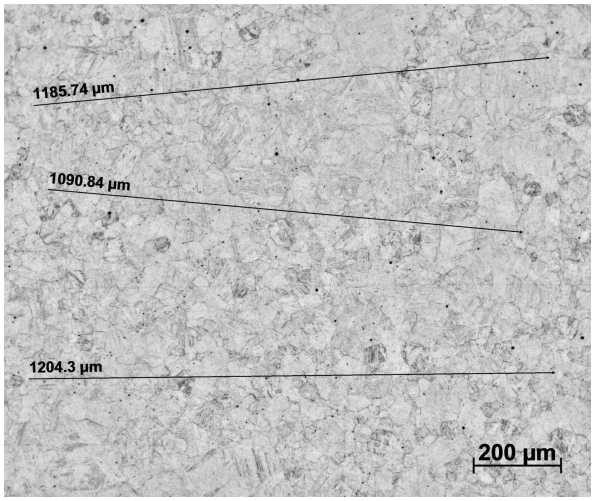

(a) Location 1.

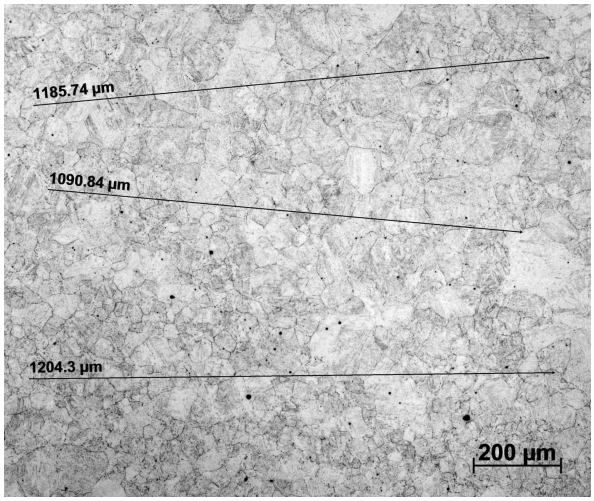

(b) Location 2.

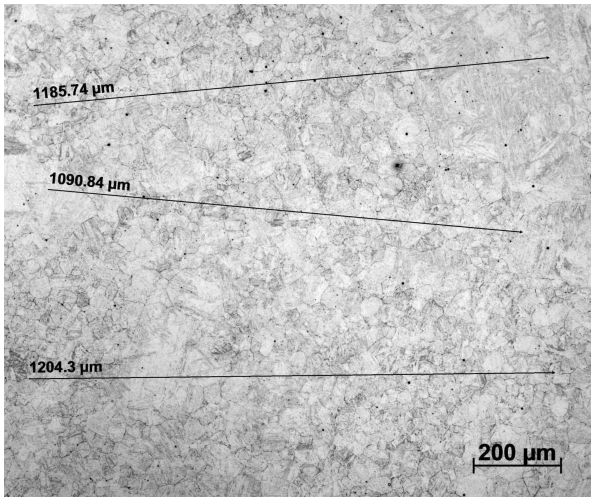

(c) Location 3.

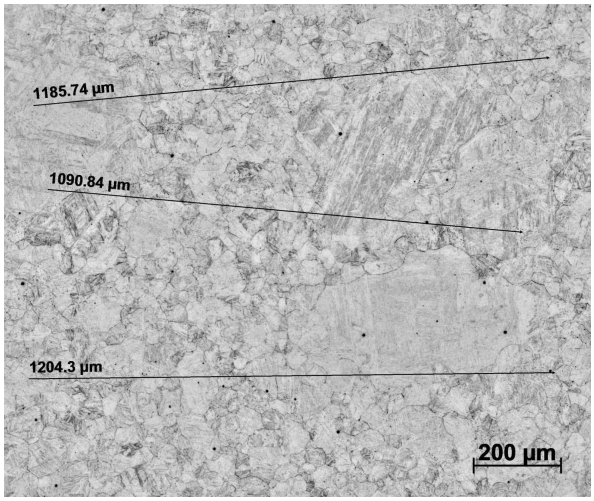

(d) Location 4.

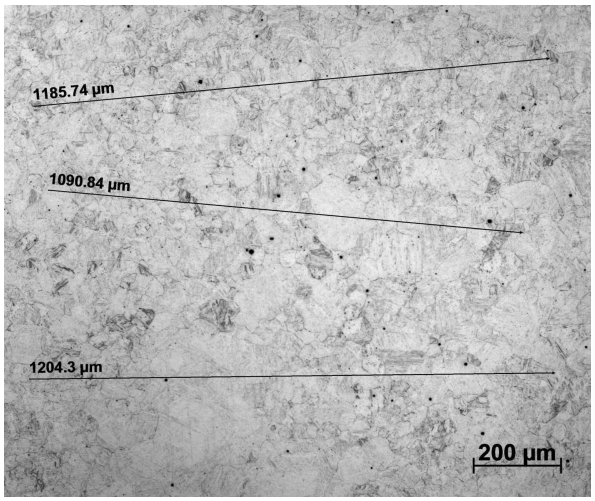

(e) Location 5.

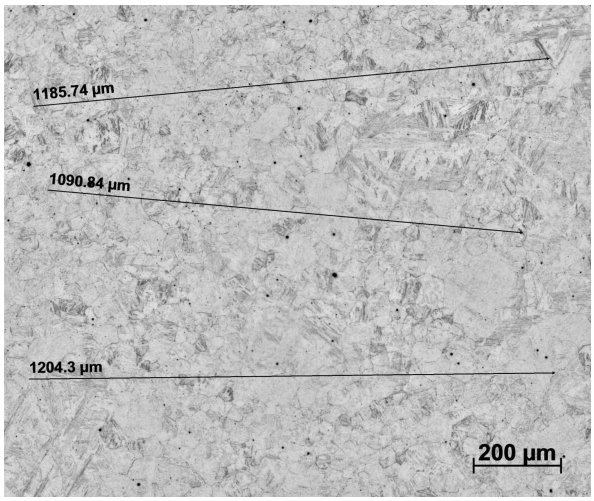

(f) Location 6.

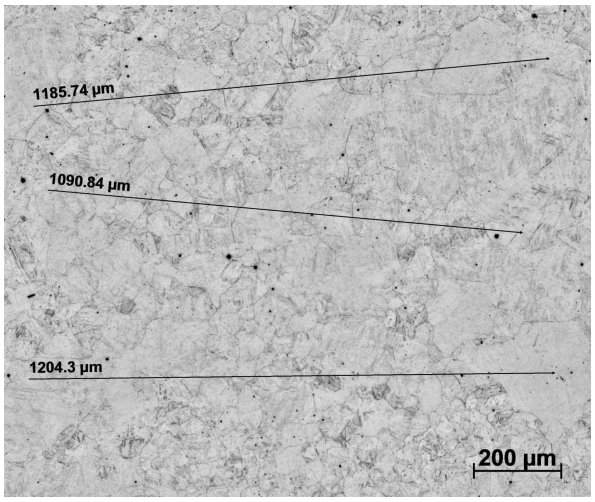

(g) Location 7.

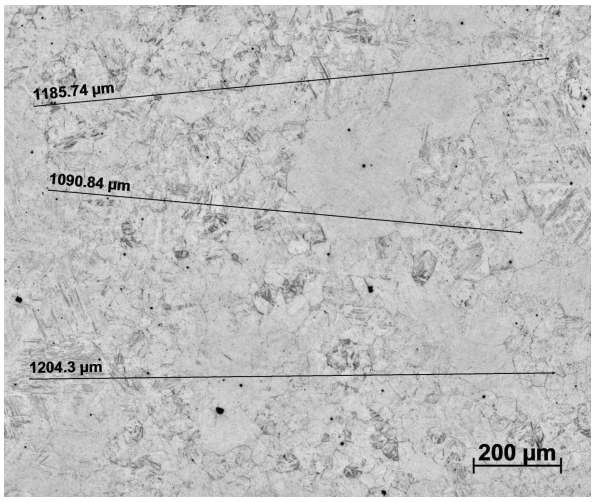

(h) Location 8.

Figure D.4: Prior austenite grain size after soaking for 180 minutes.

Table D.7: Number of Intercepts Identified in the 180 Minute Sample

	Number of Intercepts		
Location	**Line 1** ($\mathbf{1185.74\,\mu m}$)	**Line 2** ($\mathbf{1090.84\,\mu m}$)	**Line 3** ($\mathbf{1204.3\,\mu m}$)
1	13	17	21
2	19	21	22
3	21	20	22
4	16	17	15
5	20	13	15
6	16	20	17
7	17	11	13
8	12	11	19

Table D.8: Average Grain Sizes Identified in the 180 Minute Sample

	Grain Diameter			
Image	**Line 1** (μm)	**Line 2** (μm)	**Line 3** (μm)	**Average** (μm)
1	91.2	64.2	57.3	70.9
2	62.4	51.9	54.7	56.4
3	56.5	54.5	54.7	55.2
4	74.1	64.2	80.3	72.9
5	59.3	83.9	80.3	74.5
6	74.1	54.5	70.8	66.5
7	69.7	99.2	92.6	87.2
8	98.8	99.2	63.4	87.1
			Average	71.3
			STD	12.1

Appendix E

EBSD Procedure

Electron backscatter diffraction (EBSD) datasets can provide useful information regarding orientation and phase of a variety of materials and was a cornerstone of this thesis. While EBSD systems have become more sophisticated and simple to use, to obtain meaningful results, care during both acquisition and analysis stages is required.

E.1 EBSD Acquisition

The acquisition of EBSD is a two step process by which an SEM image is first acquired and the EBSD data is subsequently captured for later analysis.

E.1.1 SEM Acquisition

To obtain the highest quality EBSD image, there needs to be a high concentration of backscattered electrons reaching the EBSD detector. To facilitate this the EBSD samples were tilted to 70° using a fixed angle stub and the aperture size was increased from 30 μm to 50 μm.

The settings that were used to obtain the EBSD images in this thesis are displayed in Table E.1. The settings were selected through consultation with EDAX engineers and

adjusted to suit the samples being examined. Some SEM specific software settings were used to generate the best possible image including tilt correction and dynamic focus to account for the highly tilted sample.

Table E.1: SEM settings for EBSD acquisition.

SEM Setting	**Value**
Voltage	25 keV
Spot Size	5
Aperture	50 μm
Working Distance	10 - 15 mm

E.1.2 EBSD Capture Variables

To capture high quality diffraction patterns that the system can translate into orientation data, the system needs a method of differentiating the diffraction pattern of the point of interest with the rest of the sample. To do this, the overall background of the sample needs to be quantified and then removed from pattern recognition. On recommendation from EDAX software engineers, 500 frames of the background were fist acquired and then removed from subsequent scans through background subtraction, dynamic background subtraction and by normalising intensity. Following this, the basic EBSD settings are selected as shown in Table E.2.

Table E.2: EBSD settings for pattern acquisition.

EBSD Setting	**Value**
Binning	5×5
Exposure	4 ms
Gain	500

Binning is a method of combining adjacent pixels together and averaging the readings to get a more sensitive but lower resolution image. Binning is used to speed up acquisition by strengthening the signal to noise ratio and lowering the computing power necessary to decode each image. There is a limit to the amount of binning that can be undertaken to result in an accurate representation of the pattern. 5×5 binning is utilised because it outputs a 96×96 pixel pattern and the Hough pattern requires a 96×96 pixel pattern. As recommended by EDAX engineers, 5×5 binning has the best signal to noise ratio.

Exposure is how long the backscatter electrons are exposed to the phosphor screen before the image is captured. As exposure is measured in seconds the longer the exposure, the longer the overall scan takes. Shorter exposure time increases the overall frames per second that can be evaluated with 4 ms corresponding to approximately 250 frames able to be evaluated per second. Gain is applied amplification of the signal to improve the pattern quality without increasing the exposure time. Increasing gain increases noise and if used to much will obscure the true pattern. To translate diffraction patterns into orientation data, a function known as the Hough is tuned.

Hough Patterns

The Hough is the mathematical function that translates the diffraction patterns into orientation data. As touched upon in Section 4.4.3, the Hough settings that were used for carrying out this work were provided in Figure 4.22. The hough transform is technique that can extract the line data from diffraction lines and outputs it as a two-dimensional function as seen in Figure E.1. A brief explanation of what the individual settings mean is provided in this section. A summary of the Hough settings utilised is shown in Table E.3.

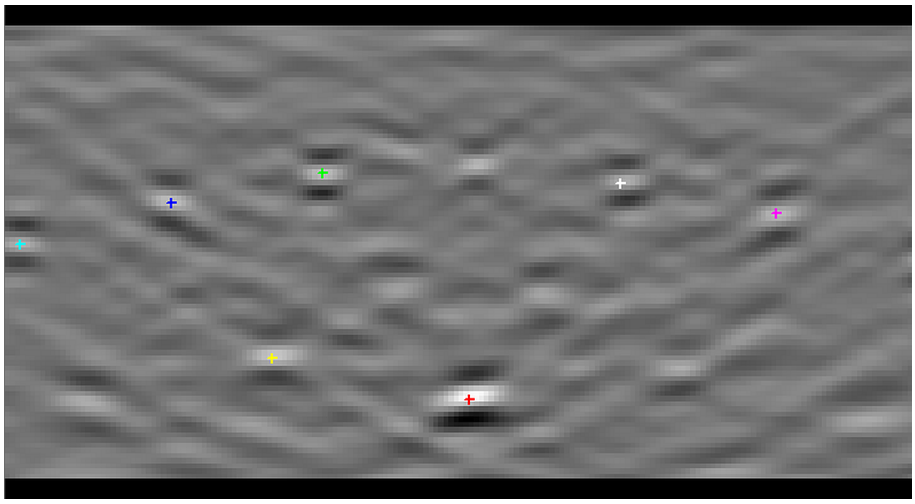

Figure E.1: Hough diagram used in EBSD pattern detection.

Table E.3: Hough settings for EBSD pattern acquisition.

Hough Setting	**Value**
Binned Pattern Size	96
Theta Step Size	1°
Rho Fraction	90%
Max Peak Count	9
Min Peak Count	3
Convolution Mask	9×9
Min Peak Magnitude	5
Min Peak Distance	15
Peak Symmetry	0.5

Binned Pattern Size

The Binned Pattern Size is a measurement of the compression used on the pattern image to calculate the Hough transform from. It is physically the resolution of the vertical component of the Hough Pattern.

Theta Step Size

Theta step size is a parameter used to control the angular fit of detected bands. This is the horizontal resolution of the Hough pattern and the higher the resolution the higher the certainty regarding the location of the peaks output by the hough transform.

Rho Fraction

This value controls how much of the pattern image is used in the calculation of the Hough transform with 90% meaning a circle with a radius 90% of the total circles radius. In general a value of either 90-95% is used for Hough pattern detection and it is not altered unless phantom bands are identified.

Peak Count

The min and max peak count controls how many peaks the software will try to find. If the software detects less than the minimum count it will count the point as unindexed. The more peaks the software is allowed to detect the more likely you are to get phantom bands. A minimum of 3 and a maximum of 9 was the recommended value provided by EDAX engineers.

Convolution Mask

This value determines which bands are preferred to be indexed with higher values of the convolution mask leading to thicker bands being preferred. If you set this to 1×1 you get the hough pattern with no compression. The lower the compression the slower the orientation is identified but the more accurate it is. A 9×9 Convolution mask was recommended by EDAX engineers.

Min Peak Magnitude

This value is used to limit on what is considered a point in the Hough transform. A lower value relaxes this requirement and a higher value is more particular.

Min Peak Distance

This setting is used more when scanning a sample which produces a number of false peaks close to real peaks. It results in ignoring potentially strong false peaks close to real peaks and seeks out weaker real peaks further away.

Peak Symmetry

This setting is used to control how close to the ideal pattern a measured pattern has to be to be before considering it to be correct. A value of 0 means no symmetry needed and a value of 1 means it has to perfectly match the ideal pattern.

E.2 EBSD Analysis

After acquiring an EBSD scan, the resulting data requires data processing to correlate all the orientation data. Analysis of EBSD data was undertaken using OIM Analysis 7 where data processing was used to clean the data, set grain boundary parameters and ensure it was in the correct orientation for texture analysis.

E.2.1 Cleaning Data

When carrying out an EBSD scan the identification of points, the accuracy of a potential match is determined by the points confidence index. The Confidence index is a rating from 0-1 that determines how accurate the system rates it's identification of a point. If the value is 0 then the point is unindexed whereas a value of 1 is a perfect match. To

accurately determine grain sizes and orientation data, unindexed and low index points need to be removed from the scan data to increase the overall accuracy of the EBSD scan. Whilst there are many cleaning algorithms that can clean EBSD data, the two that are recommended by EDAX that don't alter any scan points are the confidence index standardisation and filtering of low index points from the scan. In confidence index standardisation the system determines the size of grains within the scan and standardises the confidence index of all points within the grain to the point that has the highest confidence index. Filtering the scan data again doesn't alter any grains but instead removes grains that have confidence indices lower than 0.1 from the scan data. Filtering also has the benefit of highlighting grain boundaries and cracks.

E.2.2 Rotating Data

Depending on the manufacturing process of an investigated material, some frames may be of higher physical importance than others and are more desirable to analyse than others, for example a drawn wire sample is most commonly analysed perpendicular to the drawing direction. Depending on the sample properties, it may not be possible to scan the sample in the most desirable orientation. To account for this the data can be analysed as if it were from the intended plane by rotating the data such that it aligns with the correct plane. The default orientation for rolled samples in OIM is observed in Figure E.2a where the rolling direction (RD) has the label Axis 1. In the samples scanned from the ND-TD plane, the orientation is seen in Figure E.2b. As discussed with EDAX engineers, to orientate the data such that it is in the same frame as the preferred orientation, a rotation of 90° about Axis 2 is all that is required.

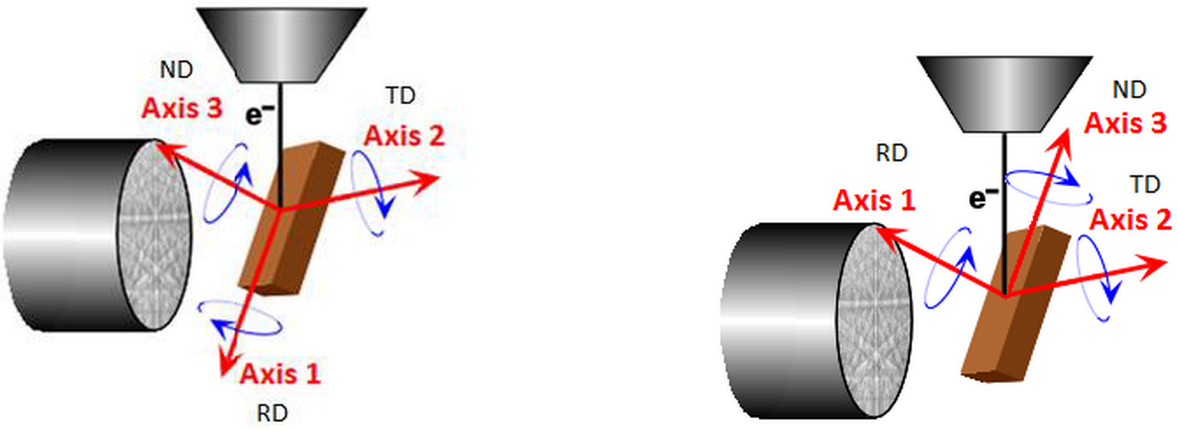

(a) Default orientation of EBSD acquisition.

(b) Rotated orientation of EBSD acquisition.

Figure E.2: Sample orientation in OIM with respect to the EBSD detector and electron gun.

E.2.3 Grain Size Determination

The grain size of EBSD scans can be determined by any threshold you select and as such requires consistent and careful consideration to avoid getting incorrect results. The threshold between low angle grain boundaries and high angle grain boundaries varies somewhat depending on the varies depending on the crystal orientation of the selected grains and the material, however it is often quoted as being 15° which was the values selected for this work. According to ASTM E2627 [202] the minimum pixel count for considering what constitutes a grain should be set to 100 pixel with scans undertaken with a step size fine enough to allow for this.

E.2.4 Texture Analysis

ODF plots were created in Bunge notation (ϕ_1, Φ, ϕ_2) with the main focus being the plane in Euler space with the parameters $(\phi_1 = 0 - 90°, \Phi = 0 - 90°, \phi_2 = 45°)$. The ODF is produced using a harmonic series expansion with a series rank of 10 and Gaussian Half-Width of 5°.

Appendix F

Rolling Length Calculations

F.1 Theory

The development of rolling schedules was in part influenced by the length samples would be rolled to and how they would fit in the furnaces. When calculating the initial and final length of rolled specimens, as the volume remains the same, the equation for determining length can be linked to the volume equation:

$$L_1 W_1 T_1 = L_2 W_2 T_2 \tag{F.1}$$

Where L is the length, W is the initial width and T is the thickness. The vertical compression of the sample thickness due to rolling is translated into an elongation in the rolling direction and does not increase the sample width. Hence, as the width of the samples does not change significantly the initial width is equal to the final width in Equation (F.1)

$$W_1 = W_2 \tag{F.2}$$

therefore,

$$L_1 T_1 = L_2 T_2 \tag{F.3}$$

The final thickness is found by the following equation

$$L_2 = \frac{L_1 T_1}{T_2} \tag{F.4}$$

F.2 Length Calculations

The rolling specimens had an initial length of 200 mm with a width of 120 mm and initial thickness of 20 mm. The final thickness is required to be 7 mm giving a total reduction of 65%. The final thickness as found by Equation (F.4) would be 571.4 mm, however, as there is a 50 mm wedge machined out of the leading edge it overestimated the final length. The lead was machined into the sample to ensure the rolling mill could pull the sample into the rolling mill. As the lead removes material from the specimen, deformation is no longer occurring on a uniform volume so the initial volume needs to be calculated to include the wedge. $V_1 = 441000$ mm^3 is the initial volume of the specimen hence:

$$V_1 = L_2 W_2 T_2 \tag{F.5}$$

the final length is calculated:

$$L_2 = \frac{V_1}{W_2 T_2} \tag{F.6}$$

As the final width is the same as the initial width, the final length of samples with a wedge machined into the lead, the final length was calculated to be 525 mm.

F.3 Schedule Length Calculations

The following section contains a summary of the rolling schedules 1, 2 and 3. The tables contain, in addition to the length calculations, the schedule parameters including rolling temperatures, % reduction and cooling rates/ methods at each stage. *N.B.: T_i is the initial thickness of the plate and T_f is the final thickness of the plate.*

Schedule 1

Table F.1: Schedule 1 sample length calculations.

Schedule 1	**Temperature** (°C)	T_i (mm)	T_f (mm)	**Reduction** (%)	**Length** (mm)	**Cooling Parameters** (°C/s)
Pass 1	1180-1010	20	17	15	216.18	
Pass 2	1180-1010	17	13.6	20	270.22	
Pass 3	1180-1010	13.6	10.2	25	360.29	
Pass 4	1180-1010	10.2	7	31.4	525	
Cooling 1	1010-785					1 °C/s (Air)
Cooling 2	785-450					10 °C/s (Water)
Cooling 3	450-RT					1 °C/s (Air)

Schedule 2

Table F.2: Schedule 2 sample length calculations.

Schedule 2	**Temperature** (°C)	T_i (mm)	T_f (mm)	**Reduction** (%)	**Length** (mm)	**Cooling Parameters** (°C/s)
Pass 1	1125-1010	20	17.5	12.5	210	
Pass 2	860-785	17.5	12.25	30	300	
Pass 3	860-785	12.25	9.2	25	400	
Pass 4	860-785	9.2	7	23.8	525	
Cooling 1	785-450					10 °C/s (Water)
Cooling 2	450-RT					1 °C/s (Air)

Schedule 3

Table F.3: Schedule 3 sample length calculations.

Schedule 3	**Temperature** (°C)	T_i (mm)	T_f (mm)	**Reduction** (%)	**Length** (mm)	**Cooling Parameters** (°C/s)
Pass 1	1125-1010	20	14	30	262.5	
Pass 2	860-690	14	10.36	26	354.7	
Pass 3	860-690	10.36	8.24	20.5	446.2	
Pass 4	860-690	8.24	7	15	525	
Cooling 1	690-450					10 °C/s (Water)
Cooling 2	450-RT					1 °C/s (Air)

Appendix G

Vickers Hardness Determination

Vickers hardness is a measure of a materials resistance to plastic deformation. A Vickers hardness indenter applies a constant load over a prescribed time period (between 10-15 seconds according to the ASTM E384 [204]. A Vickers hardness tester uses an indenter that has four triangular faces with an included angle of 136° as seen in Figure G.1a. The resulting indent is a square with diagonals d_1 and d_2 as seen in Figure G.1b.

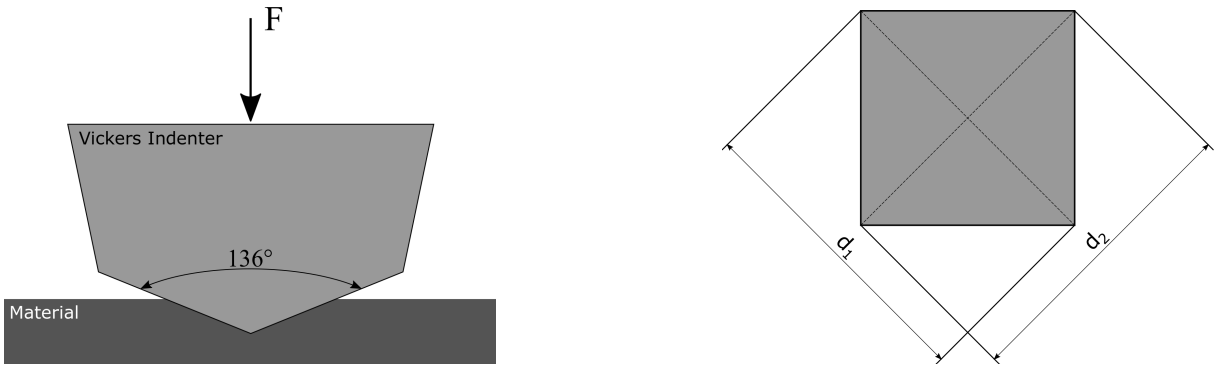

(a) Vickers Indenter Schematic Diagram

(b) Vickers Hardness Indent

Figure G.1: Schematic diagram of a Vickers hardness indenter and the indent produced.

Vickers hardness is measuring the amount of deformation produced in the material as a result of the applied force, hence the unit for the Vickers hardness number is in MPa. To determine the Vickers hardness number, the Force and Area need to be calculated. The area of the indent is calculated from the average of the length of the diagonals d_1 and d_2

$$A = \frac{d^2}{2sin(136°/2)}[mm^2] \tag{G.1}$$

The force is found from the applied load used during hardness testing, typically less than $1kg$ for microhardness measurements and between 1 kg and 100 kg for macrohardness testing. Hence:

$$HV = \frac{F}{A} = \frac{F \times 2sin(136°/2)}{d^2}[kgf/mm^2] \tag{G.2}$$

$$HV \approx \frac{0.1891 \times F}{d^2}[N/mm^2] \tag{G.3}$$

Where F is in Newtons and d is in mm.

Appendix H

Chemical Grades

coregas

CERTIFICATE OF CONFORMANCE

NITROGEN 4.0 D

Product Code: 224110

This is to certify that quality verification tests have been performed on representative samples of Nitrogen 4.0 from Coregas' approved production plants and the results of the tests comply with the requirements of the Nitrogen 4.0 specification.

Component	Chemical Formula	Specification	Unit
Nitrogen	N_2	≥ 99.99	%
Moisture	H_2O	≤ 10	ppm
Oxygen	O_2	≤ 10	ppm

Cylinder connection as per AS2473	50	
Cylinder pressure	20,000 kPa	at 15°C
Package content	1.8 m³	at 15°C, 101 kPa

Remarks: -

Approved by:

National Quality and Compliance Manager

Date of issue: 1 November 2017

Certified System ISO 9001

Complies with requirements
of ISO 9001:2008
Certificate number: QEC0889

Coregas Pty Ltd
66 Loftus Road, Yennora NSW 2161, Australia
Phone (+61) 1800 807 203 | coregas.com.au

Product Specification

Product Name: SODIUM CARBONATE Anhydrous LR

Alternate Name(s) Soda ash; washing soda; soda; dry alkali; sal soda; calcined soda; carbonic acid, disodium salt; solvay soda; bisodium carbonate.

Description

Grayish white powder or lumps. Hygroscopic.

Properties

Chemical Formula: Na_2CO_3

Molecular Weight: 105.99

Product Code: SL099

CAS No. 497-19-8

General Information:

Soluble in glycerol. Insoluble in alcohol. Corrodes aluminium and zinc. Incompatible with strong acids and alkaline earth metals in powder form.

Hazard and Safety Data

UN Group: None Allocated
Class: None Allocated
UN Number: None Allocated
Hazchem code: None Allocated
CS MSDS Code: 1CH68
Poison schedule: S5
Emergency Procedure Guide No.: N/A

Quality Specification

Assay: 99.16% min.

Specific Properties and Impurities [Typical levels]:

Density	0.89 - 1.09 kg/L
On 30 mesh (> 600 micron)	≤ 5.0%
On 100 mesh (>150 micron)	> 85.0%
Through 200 Mesh (<75 micron)	≤ 3.0%
Sodium chloride (NaCl)	≤ 0.50%
Sodium sulfate (Na2SO4)	≤ 0.20%
Iron (Fe)	≤ 0.002%
Total Alkalinity as Na2O	≤ 58.02%

Chem-Supply Pty Ltd - An ISO 9001:2008 Accredited Company

38 - 50 Bedford Street, Gillman SA 5013, Australia ABN 19 008 264 211 PO Box 201, Port Adelaide SA 5015, Australia
Telephone +61 8 8440 2000 Fax +61 8 8440 2001 E-mail: sales@chemsupply.com.au Web: www.chemsupply.com.au

Rev. No: 4

Product Specification

Product Name: SODIUM HYDROGEN CARBONATE LR

Alternate Name(s) Baking soda; bicarbonate of soda; sodium acid carbonate; sodium bicarbonate.

Description

White powder or crystalline lumps; cooling slightly alkaline taste. M.P. loses carbon dioxide at 270 °C.

Properties

Chemical Formula: $NaHCO_3$

Molecular Weight: 84.01

Product Code: SL001

CAS No. 144-55-8

General Information:

Insoluble in alcohol. Slowly decomposes in moist air. Incompatible with acids. Non combustible.

Quality Specification

Assay: 99.0% min.

Specific Properties and Impurities [Typical levels]:

Solubility in Water	95.5 g/L (20 °C)
Specific Gravity	2.159
Melting Point	270 °C
Chloride (Cl)	≤ 0.015%
Heavy metals (as Pb)	≤ 0.005%
Ammonium (NH4)	≤ 0.002%
Arsenic (As)	≤ 0.001%
Iron (Fe)	≤ 0.002%

Hazard and Safety Data

UN Group:	None Allocated
Class:	None Allocated
UN Number:	None Allocated
Hazchem code:	None Allocated
CS MSDS Code:	1CH6E
Poison schedule:	Not Scheduled
Emergency Procedure Guide No.:	N/A

Chem-Supply Pty Ltd - An ISO 9001:2008 Accredited Company

38 - 50 Bedford Street, Gillman SA 5013, Australia ABN 19 008 264 211 PO Box 201, Port Adelaide SA 5015, Australia
Telephone +61 8 8440 2000 Fax +61 8 8440 2001 E-mail: sales@chemsupply.com.au Web: www.chemsupply.com.au

Rev. No: 3

MATERIAL SAFETY DATA SHEET

1. IDENTIFICATION OF THE MATERIAL AND SUPPLIER

Product Name:	Earth Choice Dishwash Liquid – Lemon Fresh and Aloe Fresh
Other Name(s):	Lemon: FP1041 (ECD), Aloe: FP1040 (EDA)
Recommended Use:	Hand dishwashing detergent.
Supplier:	Natures Organics Pty Ltd
Address:	31 Cornhill Street Ferntree Gully VIC 3156
Telephone:	+613 9759 0300
Emergency Telephone:	+613 9759 0300 (8 am to 5 pm EST)

2. HAZARDS IDENTIFICATION

Hazard Classification:	Not classified as hazardous according to criteria of Worksafe Australia. Non dangerous goods.
Risk Phrases:	None
Safety Phrases:	S25 Avoid contact with eyes.

3. COMPOSITION/INFORMATION ON INGREDIENTS

Chemical Name	CAS Number	Proportion (%)
Water	7732-18-5	> 60
Sodium Dodecylbenzene Sulfonate	25155-30-0	10 - 30
Sodium Laureth Sulfate	68603-42-9	< 10
Cocamide DEA	61790-63-4	< 10
Sodium Citrate	6132-04-3	< 10
Aloe Vera Extract	85507-69-3	< 10
Fragrance	-	< 10
Benzisothiazolinone	2634-33-5	< 10
CI 42090	3844-45-9	< 10

4. FIRST AID MEASURES

Ingestion:	Rinse mouth with water. Do not induce vomiting. Give plenty of water to drink. If irritation persists, seek medical advice or contact the Poisons Information Centre (phone 13 1126).
Eye:	Immediately hold eyes open and flush with water for at least 15 minutes. If irritation persists, seek medical advice.
Skin:	Wipe off excess with tissue or towel. Remove contaminated clothing. Wash well with water. If irritation occurs, seek medical advice.
Inhaled:	Not applicable.
First Aid Facilities:	Workcover recommended first aid facilities appropriate to the size of the workplace.
Advice to Doctor:	Treat symptomatically.

5. FIRE FIGHTING MEASURES

Extinguishing media:	Water spray or fog, foam, dry chemical powder, carbon dioxide.
Hazards from combustion products:	This mixture is not combustible under normal conditions. However, it will break down under fire conditions and the hydrocarbon component will burn. In a large fire, heating may produce toxic fumes containing carbon monoxide, carbon dioxide, sulfur dioxide and nitrogen oxides.
Personal protective equipment:	Fire fighters to wear self-contained breathing apparatus and suitable protective clothing.
Hazchem code:	None assigned.

6. ACCIDENTAL RELEASE MEASURES

Emergency procedures:	Slippery when spilt. Avoid accidents, clean up immediately. Wear personal protective equipment during cleanup.
Methods and materials for containment and clean up:	Contain spill to prevent contamination of drains / waterways. Use absorbent material such as sand or earth. Collect and seal in properly labelled containers for disposal in accordance with local regulations. Wash area down with water to remove residual material.

7. HANDLING AND STORAGE

Precautions for safe handling:	Avoid eye contact.
Conditions for safe storage:	Store in original containers in a cool (below 30°C), dry, well ventilated area and out of direct sunlight. Store away from foodstuffs, foodstuff containers and incompatible materials such as oxidising agents.
Storage incompatibility:	None known.

8. EXPOSURE CONTROLS/PERSONAL PROTECTION

National exposure standards:	No exposure standard applies for this product.	
Biological limit values:	Not available	
Engineering controls:	Use in well ventilated areas.	
Personal protective equipment:	Eyes:	Not normally required.
	Hands:	Wear suitable gloves for prolonged exposure.
	Respiratory:	Not normally a hazard due to the non-volatile nature of the product.
	Other:	Always wash hands before smoking, eating, drinking or using the toilet.

9. PHYSICAL AND CHEMICAL PROPERTIES

Appearance	Clear slightly viscous liquid. The Lemon Fresh variant is a pale yellow colour. The Aloe Fresh variant is a pale green colour.
Odour	The Lemon Fresh variant has a lemon fragrance. The Aloe Fresh variant has a floral fragrance.
pH (5% solution)	7.0 – 8.0
Vapour Pressure (kPa)	Not available

Boiling Point (°C)	Approximately 100°C (water)
Melting Point (°C)	Not available
Solubility in Water	Readily soluble
Specific Gravity	Approximately 1.027 @ 20°C
Flash Point (°C)	Not applicable
Flammability Limits	Not flammable
Ignition Temperature	Not available
Specific Heat Value	Not available
VOC Content	< 1%
Evaporation Rate	Not available
Viscosity (cps)	Approximately 1000 cps
Volatile Component	Not available
Saturated Vapour Pressure	Not available
Decomposition Temperature	Not available

10. STABILITY AND REACTIVITY

Chemical stability:	Stable under normal conditions.
Conditions to avoid:	Excessive heat and direct sunlight.
Incompatible materials:	Strong oxidising agents.
Hazardous decomposition products:	Thermal degradation may produce carbon monoxide, carbon dioxide, sulfur dioxide and nitrogen oxides.
Hazardous reactions:	None known.

11. TOXICOLOGICAL INFORMATION

Potential health effects:

Acute	
Swallowed:	May cause irritation if directly introduced to the mouth, throat and stomach. Symptoms may include abdominal pain, nausea, vomiting and diarrhoea.
Oral LD50 (rat):	Not available.
Eye:	Irritating if directly introduced into eyes.
Skin:	Repeated or prolonged skin contact may lead to irritation.
Inhaled:	Not normally a hazard due to non-volatile nature of product.
Chronic	No information available.

12. ECOLOGICAL INFORMATION

Avoid contaminating waterways.

13. DISPOSAL CONSIDERATIONS

Waste disposal:	Dispose of by incineration or burial in an approved landfill in accordance with Commonwealth, State and Local Government regulations.

14. TRANSPORT INFORMATION

Not classified as Dangerous Goods according to the Australian Code for the Transport of Dangerous Goods by Road and Rail.

UN Number:	None
Proper Shipping Name:	None
Dangerous Goods Class:	None
Subsidiary Risk:	None
Pack Group:	None
Hazchem Code:	None
Marine Pollutant:	No
Special precautions for user:	None

15. REGULATORY INFORMATION

Poisons Schedule: None.

All components of this product are listed on the Australian Inventory of Chemical Substances (AICS).

16. OTHER INFORMATION

This product is made from readily biodegradable surfactants according to Australian Standard AS 4351.

For Emergencies:	Australian Poisons Information Centre – phone 13 1126
Issued By:	Greg Bryant Chief QC Chemist
Issue Date:	21/06/2013

This MSDS summarises to our best knowledge the health and safety hazard information of the product and general guidance on how to safely handle the product in the workplace. Each user must, prior to usage, assess and control the risks arising from its use of the product in the workplace, including in conjunction with other products.

Appendix I

Publications

Statement of Authorship

Title of Paper	Stress Corrosion Cracking Observed in Ex-service Gas Pipelines: A Comprehensive Study
Publication Status	☑ Published ☐ Accepted for Publication ☐ Submitted for Publication ☐ Unpublished and Unsubmitted work written in manuscript style
Publication Details	Roccisano, A., Nafisi, S. and Ghomashchi, R., 2020. Stress Corrosion Cracking Observed in Ex-service Gas Pipelines: A Comprehensive Study. *Metallurgical and Materials Transactions A*, *51*(1), pp.167-188.

Principal Author

Name of Principal Author (Candidate)	Anthony Roccisano		
Contribution to the Paper	Conducted all the experiments, analysed all the data and wrote the majority of the paper.		
Overall percentage (%)	70%		
Certification:	This paper reports on original research I conducted during the period of my Higher Degree by Research candidature and is not subject to any obligations or contractual agreements with a third party that would constrain its inclusion in this thesis. I am the primary author of this paper.		
Signature		Date	16/04/2020

Co-Author Contributions

By signing the Statement of Authorship, each author certifies that:

i. the candidate's stated contribution to the publication is accurate (as detailed above);

ii. permission is granted for the candidate in include the publication in the thesis; and

iii. the sum of all co-author contributions is equal to 100% less the candidate's stated contribution.

Name of Co-Author	Shahrooz Nafisi		
Contribution to the Paper 25%	Provided guidance and supervision from concept to submission. Assisted in the analysis of all data and contributed a paragraph regarding bulk crystallographic texture. Helped to revise the paper.		
Signature		Date	17/04/2020

Name of Co-Author	Reza Ghomashchi		
Contribution to the Paper 5%	Provided guidance and supervision from concept to submission and helped to revise the paper.		
Signature		Date	16/04/2020

Please cut and paste additional co-author panels here as required.

Stress Corrosion Cracking Observed in Ex-service Gas Pipelines: A Comprehensive Study

A. ROCCISANO, S. NAFISI, and R. GHOMASHCHI

The properties affecting stress corrosion cracking (SCC) in ex-service API 5L X42 and X65 pipeline steels were investigated to determine the differences between the two grades. Field-grown sections of SCC affected pipelines were studied to determine what effect the physical properties had on SCC growth. Using electron backscatter diffraction (EBSD) and a newly developed technique, SCC affected grains were separated from unaffected grains to determine the microstructural properties influencing SCC. It was confirmed in both grades that cracks primarily propagated between high angle grain boundaries and most coincident site lattice boundaries didn't offer increased resistance to SCC. Σ3, Σ7, and Σ11 boundaries were present in higher proportions in uncracked grain boundaries than cracked in both grades. Crack arrest locations typically had high levels of {110}//RP (rolling plane) and {111}//RP textured grains ahead of cracks whilst cracked grain boundaries tended to contain both {110}//RP and {112}//RP textured grains. Uncracked outer surfaces of pipe in both grades contained mostly {110}//RP textured grains. Transgranular cracking was observed in both grades in isolated locations and tended to occur in {100}//RP and {111}⟨112⟩ textures.

https://doi.org/10.1007/s11661-019-05496-3

I. INTRODUCTION

WHILST the consequences of catastrophic failure of oil and gas pipelines due to stress corrosion cracking (SCC) can be severe,[1] there still remains some uncertainty over the crack propagation mechanism in widely used pipe grades. SCC is an insidious form of environmental induced cracking that causes failure in pipelines, often, with little warning. SCC can occur in pipelines when three conditions are met[2,3];

1. The pipe is subject to an applied or residual tensile stress,
2. Exposure to a corrosive environment, and
3. The material is susceptible to SCC

SCC defects form in steel pipelines when coating disbondment occurs in cathodically protected pipes. When a sufficiently high cathodic potential is applied, water is dissociated to form hydroxyl ions, (OH^-), that create a localized, low pH region capable of combining CO_2 dissolved in groundwater present in surrounding soil to form carbonate and bicarbonate ions.[4] Solutions with a pH greater than 9.3 cause the intergranular, high pH form of SCC, whereas a lower pH between 5.5 and 7.5 tends to encourage the transgranular, near neutral form of SCC.[4–6] The primary propagation mechanism for high pH SCC (SCC hereafter) is anodic dissolution of the steel pipe combined with passive film fracture at the crack tip.[7,8] Anodic dissolution occurs at the grain boundaries until cathodic protection forms a passive film at the crack tip that halts corrosion. When the film fractures due to the applied or residual tensile stress, anodic dissolution between grain boundaries can occur again.

To mitigate failure in pipelines, there has been considerable research into the risk factors controlling the susceptibility of steels to SCC. Since SCC requires a tensile or residual stress, corrosive environment, and susceptible material to be present concurrently, removing any of these conditions prevents SCC. The magnitude and direction of the residual stress at the surface caused by manufacturing can dramatically alter the resistance to SCC as for instance tensile residual stresses at the surface can lead to increased SCC activity.[9,10] In addition, the replacement of failed pipeline coatings with modern coatings can dramatically reduce the SCC growth rate.[6] However, it is important to note, that recoating of pipelines may not halt crack propagation entirely as fatigue cracking can become the dominant mechanism in recoated pipes under load.[11] Steel composition,[12–14] surface roughness,[15,16] and microstructure [17–19] can also affect SCC susceptibility.

A. ROCCISANO and R. GHOMASHCHI are with the The University of Adelaide, Adelaide, SA 5005, Australia. Contact e-mail: a.roccisano@adelaide.edu.au S. NAFISI is with the The University of Adelaide and also with the University of Alberta, Edmonton, Alberta T6G 1H9, Canada.

Manuscript submitted March 15, 2019.

Published online: 21 October 2019

Recent investigation has focused on exploring the link between SCC susceptibility and crystallographic texture from both macro- and micro-texture viewpoints.[10,20,21]

There are limited investigations available in the open literature that have attempted to link SCC susceptibility to crystallographic texture in pipeline steels[10,20–22]; however, the investigation of intergranular cracking and the effect of grain boundary type on susceptibility is extensive.[23–29] It has been identified in the available literature that intergranular SCC is more likely to propagate through High Angle Boundaries (HAB's) with misorientation $\theta \geq 15$ deg as compared to Low Angle Boundaries (LAB's) with misorientation $\theta < 15$ deg. In addition, there is some evidence that grains with orientations belonging to the {111}//RP (Rolling Plane) and {110}//RP fiber are more resistant to SCC than randomly oriented grains.[10,20,21] In comparison, when cracking occurred between grains with similar angular misorientation, there was a tendency for cracks to grow between grains that had $\{100\}\langle 110\rangle$ orientations.[10,20,21] $\Sigma 11$ and $\Sigma 13b$ coincidence site lattice (CSL) boundaries were present in higher concentrations at crack tips and other crack arrest points, inferring those boundaries provide increased resistance to SCC.[20] Following from previous work carried out by the authors,[22] it is the aim of this study to further explore the cracking behavior of ex-service X42 and X65 pipes and compare the mechanical and microstructural properties of each to develop an in-depth understanding of SCC in these pipe grades.

II. EXPERIMENTAL PROCEDURE

The samples investigated were ex-service gas transmission pipes manufactured from API 5L X42 and X65 steels[30] with composition outlined in Table I (carbon and nitrogen were measured using LECO and ELTRA combustion analyzers respectively). Table II shows the reported mechanical properties of the as-received pipe sections. The pipe samples are sourced from ex-service sections deemed, during regular inspection, to contain irreparable levels of SCC.

The X42 pipe was in service for approximately 39 years before extraction and had a nominal diameter of 168.3 mm and a nominal wall thickness of 4.4 mm. It was manufactured from center-slit strip and welded through the electrical resistance welding (ERW) process. PVC tape wrap over a rubberized layer coated the X42 pipe which was removed prior to receiving. The X65 was in service for approximately 30 years before extraction, had a nominal diameter of 864 mm and, a nominal wall thickness of 8.3 mm. The X65 was manufactured from steel plate through the "UOE" process (U'ing press, O'ing press and expansion mandrel). The X65 pipe was coated in the field with coal tar enamel that was removed prior to receiving. Figure 1 shows the typical pipe regions where SCC cracks formed in both grades, highlighted through Magnetic Particle Inspection (MPI).

Two significant cracks (length > 10 pct wall thickness) in each pipe grade were selected for electron backscatter diffraction (EBSD) analysis. An additional two cracks in each pipe grade were used for optical and scanning electron microscopy (SEM). SCC cracks were sectioned transverse to the rolling direction and finish polished with colloidal silica. SEM analysis was undertaken on a FEI Quanta 450 and EBSD analysis was carried out on an FEI Inspect F50 SEM equipped with EDAX Hikari EBSD detector using OIM software. SEM voltage was 25 kV and an aperture of 50 μm. The step size and frame size were kept consistent for areas directly compared.

Hardness measurements on the pipe transverse section, from the outer surface to the inner surface, were conducted using a Vickers microhardness indenter (LECO LM-700AT) according to ASTM E384.[31] Three sets of microhardness measurements were conducted at 500 μm intervals from the outer surface towards the inner surface of the pipe utilizing a 500 g (4.9 N) load.

III. RESULTS

A. *Microstructural Characterization*

Optical micrographs of the X42 and X65 pipes were taken from three locations to give an overall view of the microstructure of the pipe transverse section from the outer surface to the center of the pipe. The micrographs were taken from the outer surface, one quarter of the wall thickness and the center of the wall thickness, transverse to the rolling direction, presented in Figure 2. The X42 pipe in Figures 2(a), (c), and (e) was primarily composed of polygonal ferrite and degenerate pearlite in levels that remained constant through thickness. The X65 in Figures 2(b), (d), and (f) shows a more typical low carbon steel microstructure consisting of polygonal ferrite with 9 ± 1 pct pearlite as measured by quantitative optical microscopy through thickness. The pearlite concentration increases from the surface to the

Table II. Mechanical Properties of X42 and X65 Pipe

	0.2 Pct Yield (MPa)	UTS (MPa)	Elongation (Pct)
X42	341	431	28
X65	457	577.5	25.5

Table I. Chemical Compositions of Pipe Samples (Weight Percent)

	C	Mn	S	P	Si	Al	Ni	Cu	Mo	V	Nb	Ti	Cr	N
X42	0.21	1.34	0.017	0.015	0.20	0.003	0.015	0.012	0.004	0.002	0.004	0.001	0.03	0.006
X65	0.09	1.40	0.005	0.015	0.28	0.025	0.025	0.180	0.007	0.003	0.045	0.002	0.27	0.009

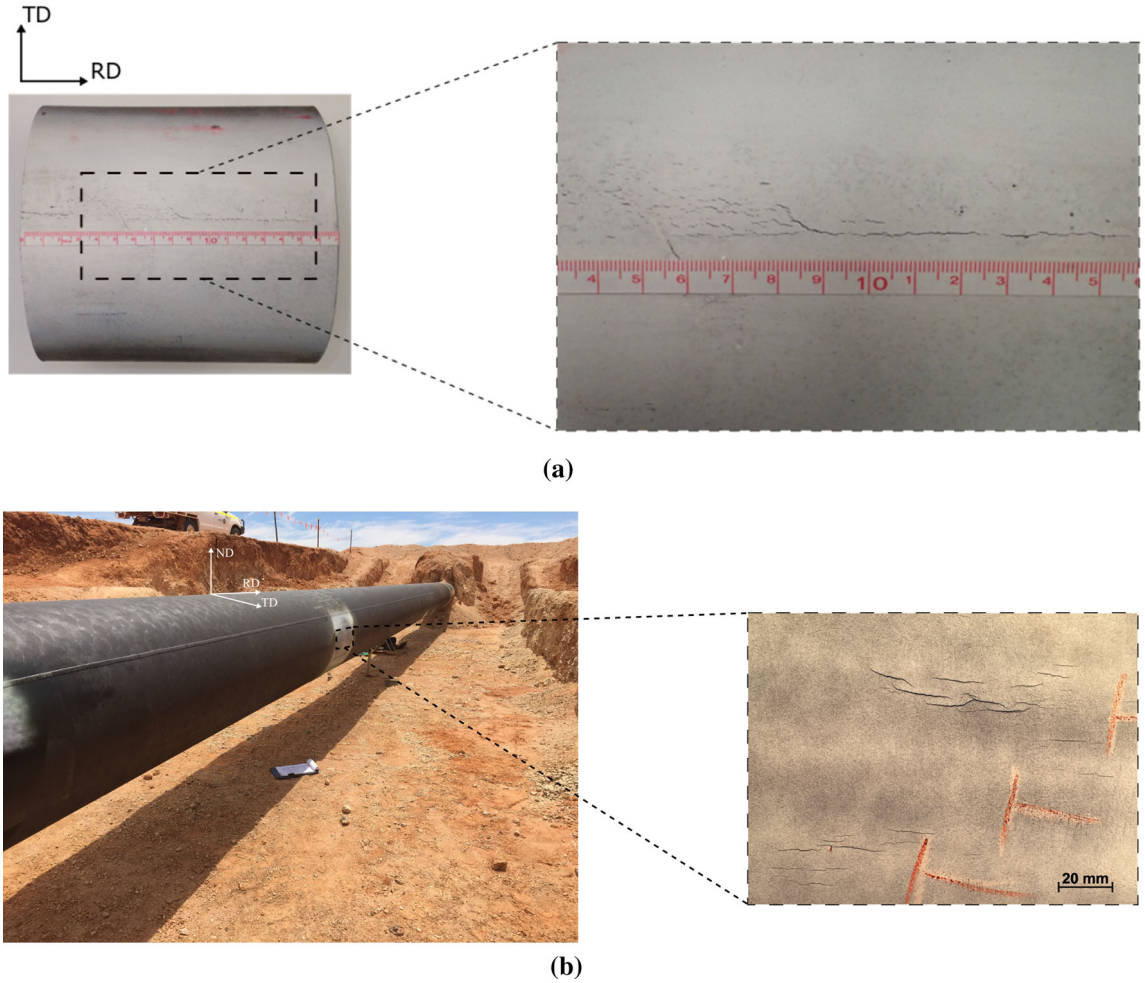

Fig. 1—A section of SCC affected pipe and a magnified view of the cracks highlighted through MPI (*a*) X42 (scale in mm), (*b*) X65. (*ND* normal direction, *RD* rolling direction, *TD* transverse direction).

center with segregation banding identified at the center plane Figure 2(f).

Figure 3 shows SEM images taken from the quarter thickness plane, transverse to the rolling direction. The degenerate pearlite, characterized by discrete cementite particles, is widely distributed throughout the X42 pipeline. There is some lamellar cementite near grain boundaries but the majority of the cementite particles are discrete. The pearlite grains in X65 have the appearance of densely packed cementite lamella that are intact and much finer than those seen in the X42 (note that different magnifications were necessary to resolve the lamellae in X42 and X65).

Grain size distributions were determined through direct area measurement from EBSD maps of uncracked areas taken at three locations, *i.e.*, from 200 μm below the surface, quarter plane, and center plane (Figure 4). The average grain size for X42 and X65 are 17.8 $\pm$ 1 and 8.2 $\pm$ 1 μm, respectively. Grain size in both the X42 and X65 pipe steels showed a normal distribution that is slightly skewed right. In the X42, there was not strong statistical significance between the grain sizes along the pipe transverse cross-section at different distances from the surface with 83 pct of grains having a diameter between 5 and 30 μm. In X65, the surface has the smallest grain size, increasing towards the center plane. Greater than 90 pct of all grains had a diameter less than 15 μm. The grains in the X42 showed a highly varied distribution of grain sizes that did not change significantly from the surface to the center of the pipe. The grains in the X65, however, were more uniform and smaller as compared to the X42 grain size, with a noticeable increase in grain size from the surface of the pipe to the center.

B. *Hardness Measurement*

Figures 5(a) and (b) show the average results of three sets of through-thickness microhardness measurements in X42 and X65 pipe samples taken near the weld bead, outside the heat affected zone. The average through-thickness hardness of the X42 was 183 $\pm$ 6 HV, whilst the average through-thickness hardness of the X65 was higher at 223 $\pm$ 6 HV. The centerline segregation in X42 as labeled in Figure 5c, presents as a dark line at the center of the pipe that extends towards the outer and inner surface of the pipe in the etched cross-section. The X42 was manufactured from

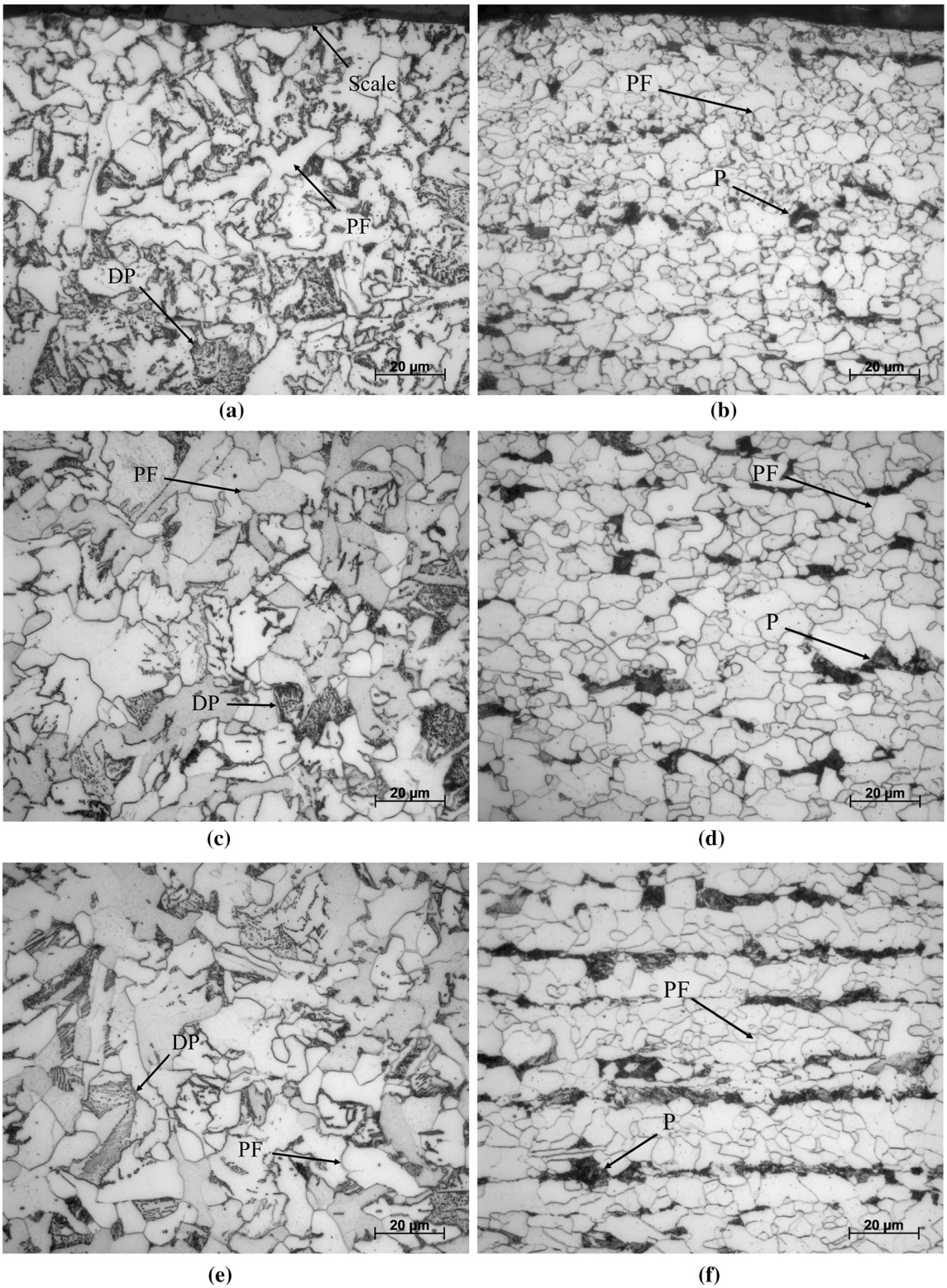

Fig. 2—Optical micrographs of X42 and X65 pipe samples taken from the surface (*a*) X42 and (*b*) X65, quarter plane (*c*) X42 and (*d*) X65 and the center plane (*e*) X42 and (*f*) X65 (*PF* polygonal ferrite, *P* pearlite, *DP* degenerate pearlite).

center-slit strip so the segregation only appears on one side of the weld. The graph of the through-thickness hardness in X42 (Figure 5(a)) shows a peak hardness at the center of the pipe on the segregated side of the weld whilst on the unsegregated side there was a slight drop in hardness at the center. The X65 as seen in Figure 5(d) does not appear to have any centerline segregation either side of the weld bead and hence the

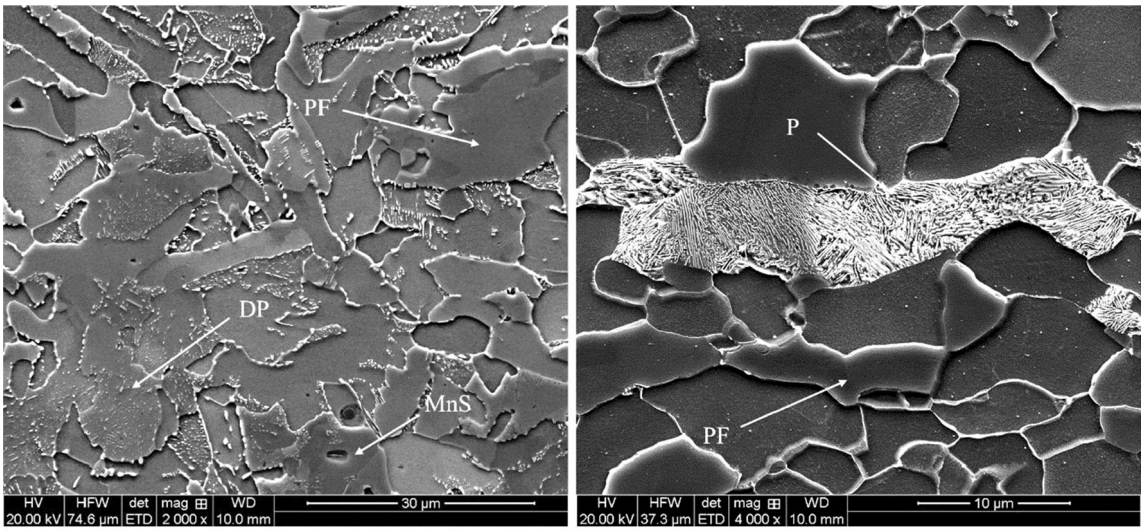

Fig. 3—SEM images taken from the quarter thickness in (*a*) X42 and (*b*) X65 showing pearlite in each grade (2 pct nital etch).

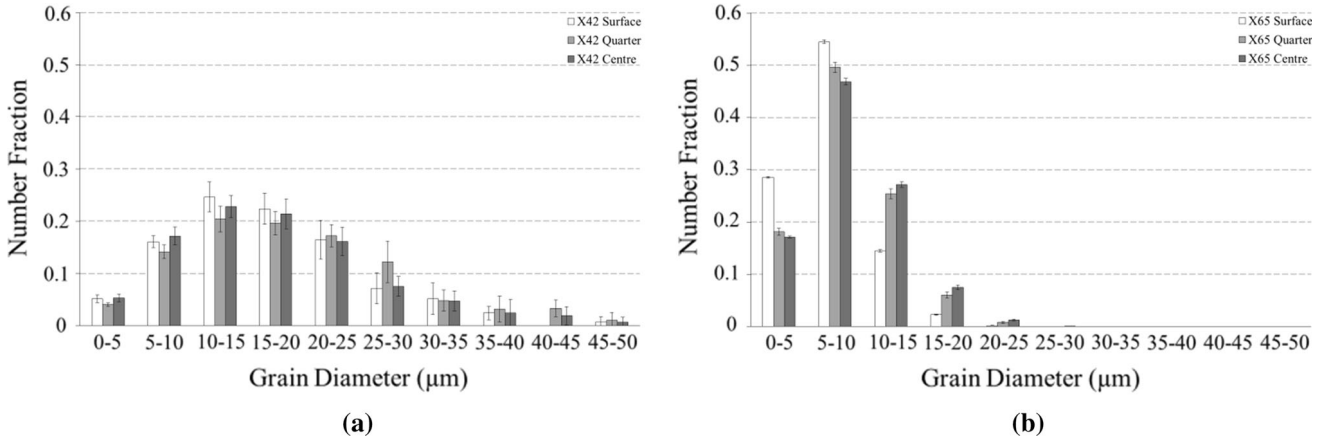

Fig. 4—Grain size distribution from EBSD data in (*a*) X42 and (*b*) X65 taken from 200 μm below the surface, quarter thickness and the center plane.

through-thickness hardness does not have any obvious peak at the center of the pipe (Figure 5(b)).

The hardness differences (due to segregation) on either side of the weld in X42 pipe steel did not appear to influence the severity of SCC damage as cracks were observed on both sides of the weld in the X42. The X42 had similar hardness at the surface on both sides of weld and no crack grew deep enough to be exposed to the segregation zone. This means hardness had no effect on initiation nor propagation of the SCC crack. The same was observed for X65.

C. *Characterization of SCC Cracks*

SCC cracks grow along the rolling direction (RD) along the pipe surface as shown in Figure 6 due to the internal gas pressure creating a maximum stress in the hoop direction (transverse direction "TD"). SCC in X42 tended to form as singular cracks near the weld seam as seen in Figure 6(a). SCC in the case of the X65 formed in colonies (Figure 6(b)) around the entire circumference of the pipe with no strong preference for proximity to the seam weld. The cracks investigated in X65 were from a large colony with the first cracks located 150 mm from the seam weld. SCC often forms under defects in pipe coatings, growing from the outer surface towards the inner surface, perpendicular to the direction of greatest stress, characteristics identified in both the X42 and X65 samples.

X42 and X65 display different crack morphologies when sectioned along the transverse direction. Whilst both cracks showed branching and having a jagged appearance with intergranular path, the X42 generally grew perpendicular from the outer surface towards the inner surface of the pipe (Figure 7(a)). The X65, however, grew perpendicular for approximately 200 μm before inclining to an angle of approximately 45 deg to the pipe surface (Figure 7(b)), typical of inclined SCC in Australia.[32] Inclination can be the result of crack tip plasticity, the electrochemistry at the crack tip, residual

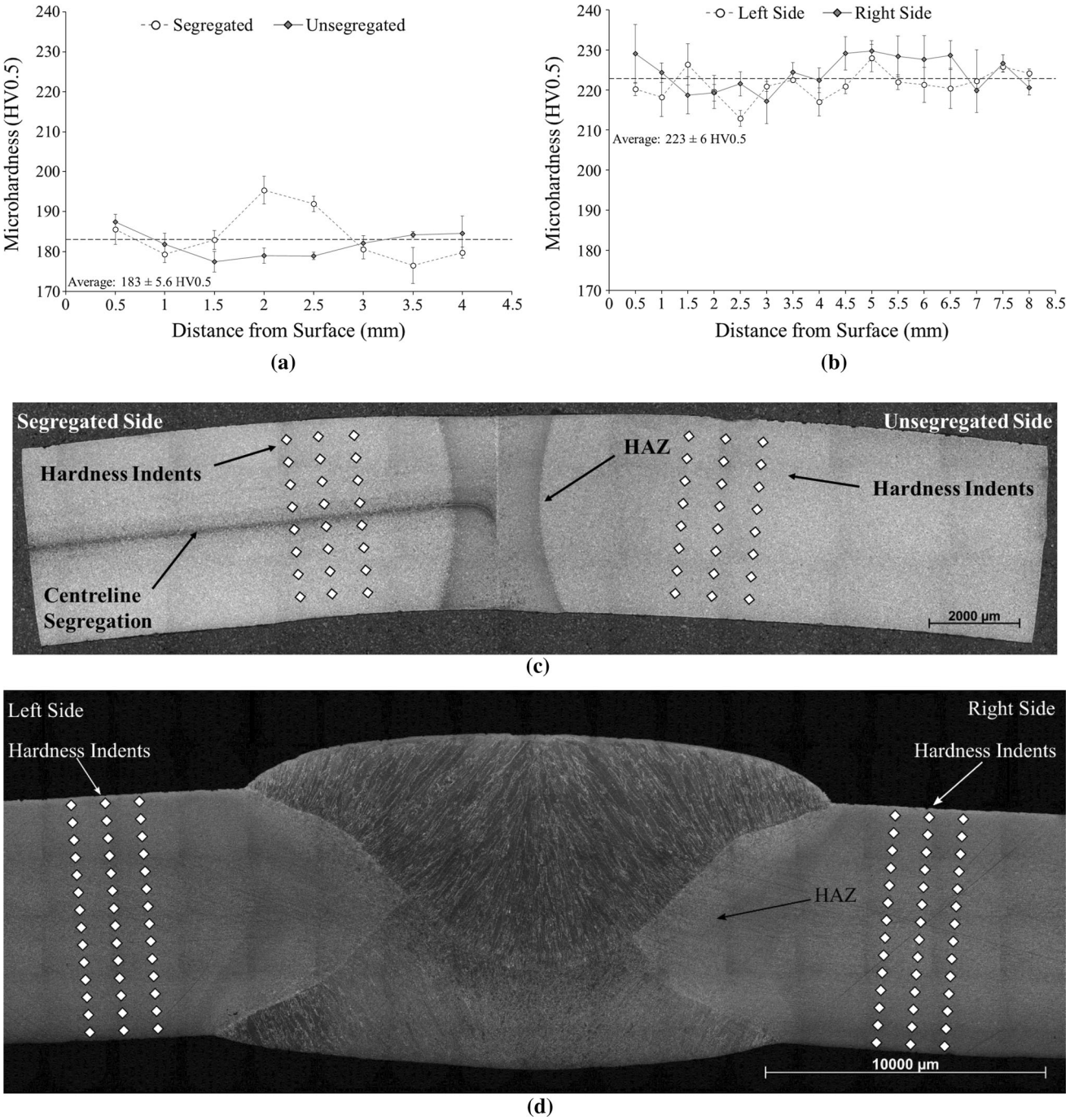

Fig. 5—Average through-thickness microhardness from (*a*) X42 pipe and (*b*) X65 pipe. (*c*) Difference in centerline segregation either side of the weld bead in X42. (*d*) Lack of segregation either side of the weld in X65 (hardness indents highlighted).

stresses, and texture anisotropy.[32–34] The crack lengths in X42 and X65 varied considerably with the longest crack in X42 found to be 1.5 mm in length (34 pct wall thickness) whilst the longest crack in X65 was 3.6 mm (43 pct wall thickness).

Both pipes received field-applied coal tar enamel coatings during installation, but the coating appeared to have failed to prevent the corrosive environment from contacting the surface and thus initiating SCC. This is believed to be due to disbondment which may have caused by either incorrect application or degradation in service. Coal tar enamel coatings are more susceptible to disbondment and cathodic shielding than modern epoxy coatings that increased the likelihood of SCC formation.[35]

The surfaces of the affected pipes, whilst mostly unblemished and uniform, contained areas with significant levels of mill scale and deep pitting. As seen in

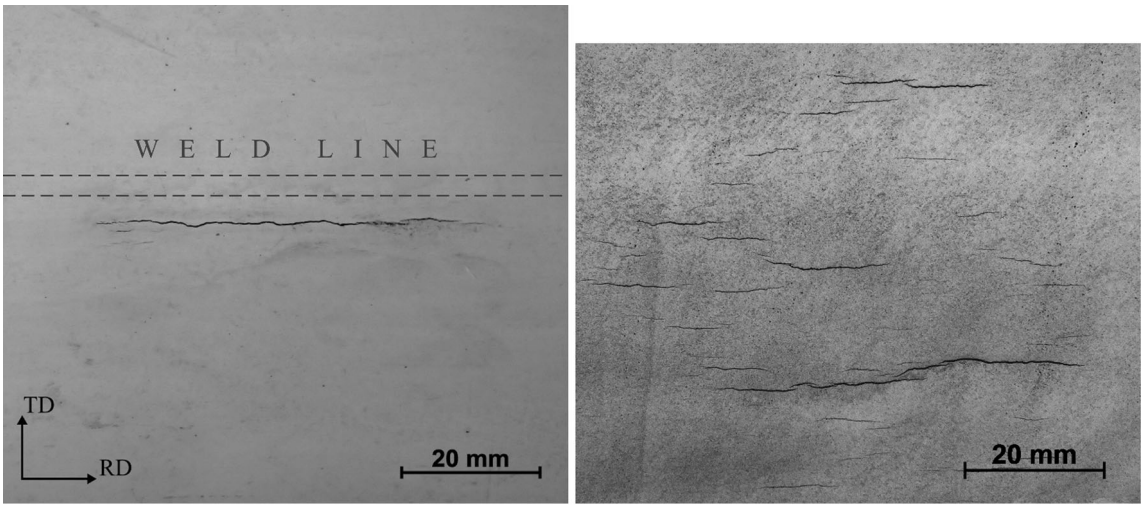

Fig. 6—Crack appearances at the surface of the pipes: (*a*) X42 and (*b*) X65.

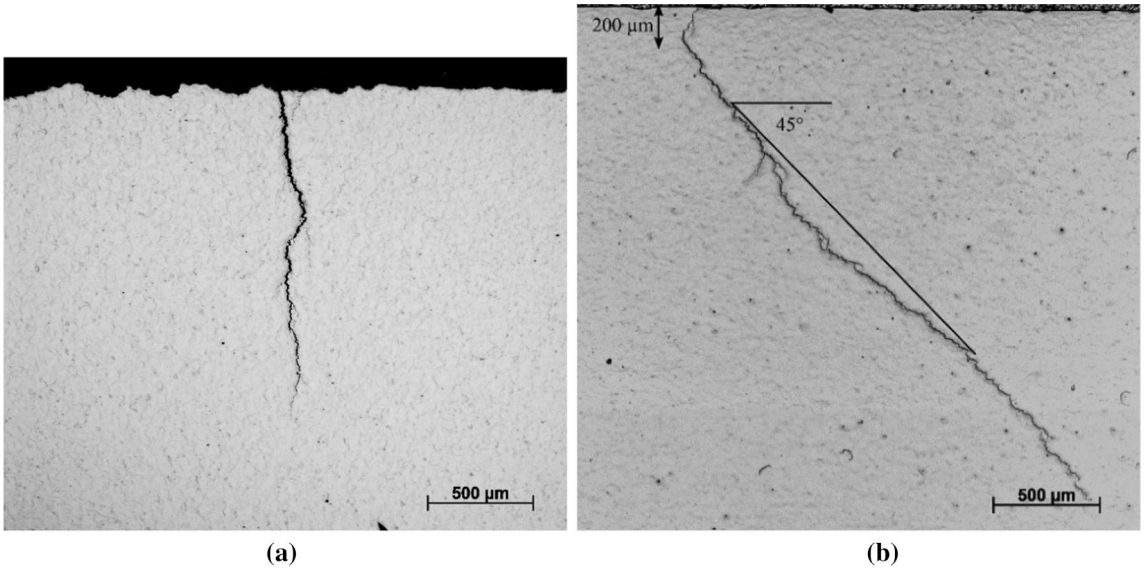

Fig. 7—Typical unetched images of SCC cracks in (*a*) X42 and (*b*) X65.

Figures 8(a) and (b), SCC cracks formed extensively in regions of heavy pitting and mill scale in both pipe grades. Pitting likely occurred prior to the pipe being exposed to high pH conditions and can act as a stress concentrator, particularly if the pit is deep relative to the overall wall thickness.[2]

At higher magnifications (Figures 8(c) and (d)), the cracks seem to form directly beneath regions where the oxide had fractured. Like disbonded coatings, mill scale can shield the surface from cathodic protection, shifting the applied potential to one conducive for SCC formation.[15]

Pipes were supplied with the coating removed and white background paint applied for magnetic particle inspection (MPI). As excessive scale can prevent defect detection with MPI, some scale may have been mechanically removed prior to investigation.

D. *EBSD Analysis*

Recent work on SCC in pipeline steels has explored the effect of grain boundary orientation and crystallographic texture on SCC susceptibility.[10,20,21] SCC affected pipes were investigated through EBSD to determine the role of grain boundary misorientation, CSL boundaries and crystallographic texture on SCC propagation. It has been reported that in X65 SCC tends to propagate through mainly high angle grain boundaries and when the crack front approaches a junction where it could propagate through either a high or a low angle grain boundary, the crack tends to fracture the high angle grain boundary.[20] In regards to CSL boundaries, cracks appear to not propagate through Σ11 or Σ13b boundaries whilst other boundaries do not show significant SCC resistance.[20] One important factor to note is these boundaries were considered

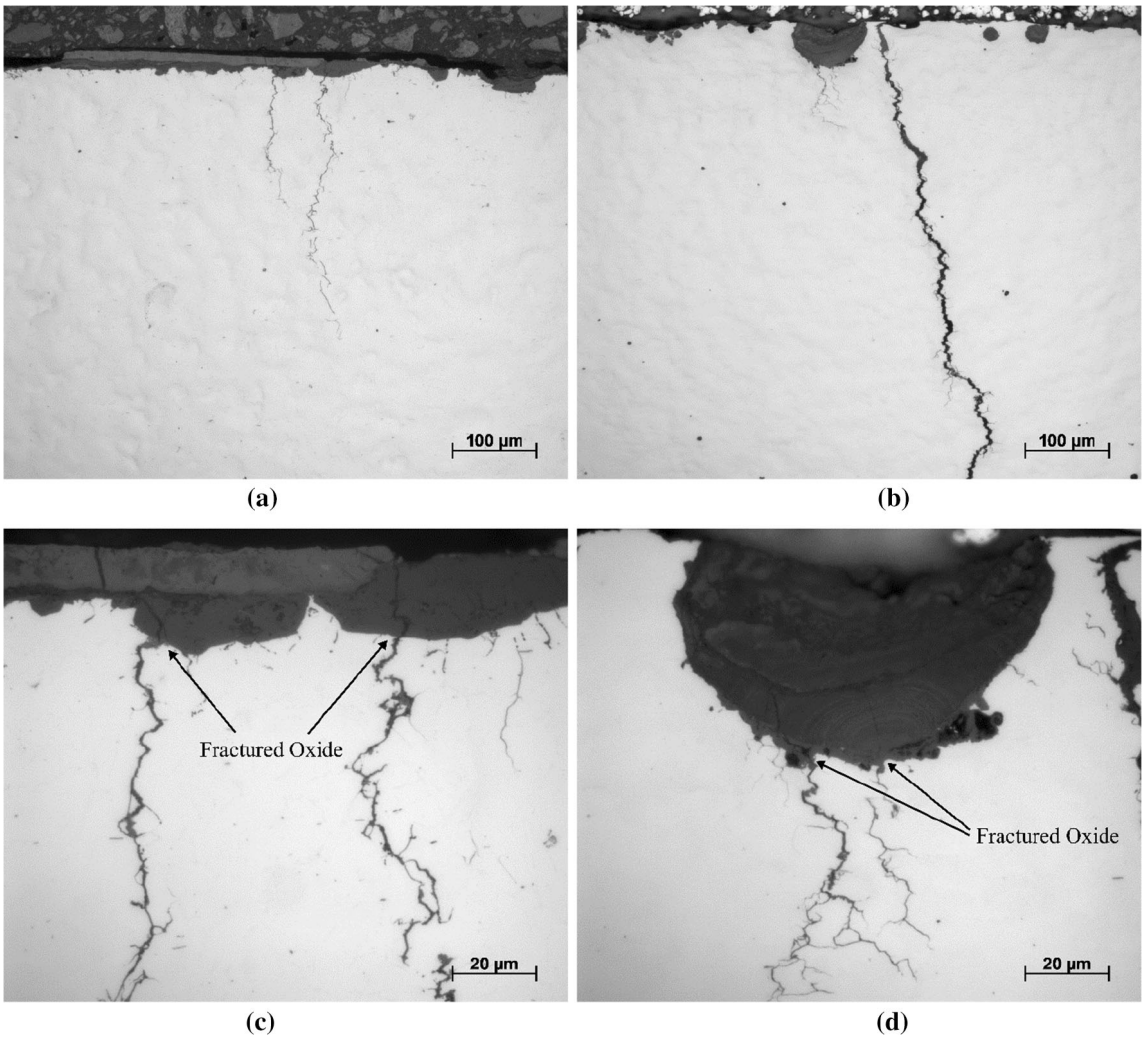

Fig. 8—Surface of cracked (*a*) X42 and (*b*) X65 and magnified sections showing cracks originating from surface pits in (*c*) X42 and (*d*) X65.

resistant by the authors of Reference 20 based on their presence at the crack tip and some uncracked junctions but were not found in high enough proportions to derive statistically valid information. EBSD analysis relating to grain boundary misorientation and CSL boundaries has only been carried out on X65 and has not repeated in X42 grade pipes.

1. *Grain boundary distribution*

As high pH SCC propagates intergranually, grain boundaries must be more susceptible to anodic dissolution than the transgranular path. It has been presented in the literature that cracks tend to propagate between HAB's due to their higher energy state compared to that of LAB's and CSL boundaries.[20] As a result of that, the majority of cracked grain boundaries should be high angle. As the crack accounts for only a small proportion of the overall grain boundaries present in an EBSD scan, a method to remove the unaffected grain boundaries from the calculation was required. Initial trials involved cropping and measuring of the crack out of the main frame but were found to be dependent on the area of the selection and did not result in repeatable results.

The only method able to differentiate between the cracked and uncracked grain boundaries was through direct measurement of the misorientation between grains bordering the crack. As shown in Figure 9(a), manual misorientation is undertaken by measuring grain misorientation across and along the crack in uniform steps. The results of misorientations calculated manually and compared to the full frame are seen in Figure 9(b). The results show that the cracked grain boundaries (across the crack) comprise mostly of HAB's, in line with intergranular crack behavior, and along the crack there is still mostly HAB's; however, there is an increase in LAB's that tend to be more resistant to cracking. The use of manual misorientations allows for the grain boundary properties present along and across the crack to be differentiated. This is a simple method of confirming the preferred grain boundary for an SCC crack propagation path.

The methodology was applied over the entire length of the four SCC cracks analyzed (two in X42 and two in X65) in the regions across the crack and along the crack. The grain boundaries along the crack are uncracked whilst across the crack are by definition cracked grain

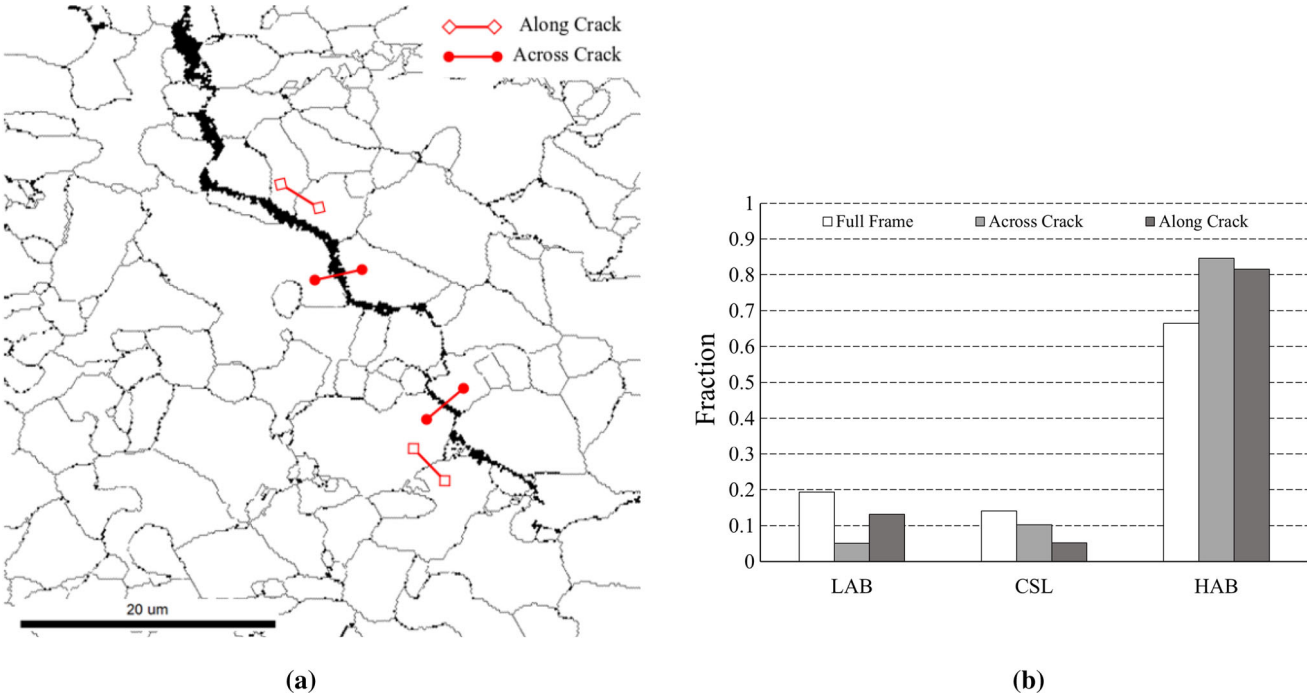

Fig. 9—Schematic diagram of misorientation investigation in X65 sample showing (*a*) interactive misorientation investigation along and across cracked grains and (*b*) comparison of the grain boundary characteristics identified through manual misorientations along and across the crack.

boundaries. A comparison of the grain boundaries present along and across the crack offer insight into the characteristics of high pH SCC.

In both X42 and X65 (Figures 10(b) and (c)), there was a significantly greater proportion of HAB's present across the cracked boundaries as compared to uncracked boundaries along the crack path. This is consistent with intergranular cracking behavior and expected from high pH SCC in steel. There is, however, a significant proportion of LAB's present in both X42 and X65 across the crack indicative of transgranular cracking, surprising for an intergranular corrosion phenomenon. There are statistically significant differences between the levels of LAB's present in X42 across the crack as compared to along the crack with a higher proportion of LAB's found along the crack as compared to across the crack. This suggests that in X42 there are more LAB's in the vicinity of the crack, yet, the crack preferentially propagates through HAB's. Similarly, in X65, there are almost twice the amount of LAB's present along the crack as compared to across the crack with the same outcome as X42. In terms of CSL boundaries, there is no real statistically significant difference between levels present in X42 or X65 in any category.

A CSL distribution chart for X42 and X65 is given in Figure 11 with CSL boundaries ranging from Σ3 to Σ29. Boundaries below Σ29 are considered low sigma CSL's whilst those greater than Σ29 are considered random[36] and are not included in the analysis. In the X42 samples Σ3, Σ7, Σ11, Σ19b, Σ21b, Σ23, Σ25a, and Σ27b boundaries were present in higher proportions along the main SCC crack than across whilst in the X65 sample Σ3, Σ7, Σ9, Σ11, Σ13a, Σ13b, Σ17a, and Σ25a CSL boundaries were present in higher proportions along the main SCC crack than across. It is thought that since these CSL boundaries were present in higher proportions along the main SCC crack than across, that these boundaries may offer higher resistance to SCC than other CSL boundaries. Only the Σ3, Σ7 and Σ11 CSL boundaries are common in the X42 and X65. Despite being reported as one of the main CSL boundaries resistant to SCC cracking in Reference 20 the overall proportion of Σ13b boundaries in the X42 and X65 (Figure 11) samples was below 5 pct and did not appear to contribute significantly to SCC resistance. It is important to note that the proportion of CSL boundaries identified in the X42 and X65 samples was less than 20 pct of the total boundaries identified in each orientation and was hence not a large constituent of present boundaries. Therefore, it is not possible to draw a confident conclusion about the role played by CSL boundaries on SCC resistance.

2. *Crack tip*

The crack tip as defined in Figure 10(a) is the uncracked area immediately ahead of the crack which is thought of as being comprised of resistant grains.[20,21,24] To determine whether there were any special properties of the area ahead of the crack that halted SCC propagation, the grain boundary distribution was compared between six regions adjacent to the crack tip and the full frame. This is because the previous investigations[20,21] considered the crack tip to contain resistant microstructures as the crack did not propagate further into the material.

The grain boundary distribution was determined for a series of reduced regions in line with the crack tip as shown in Figure 12(a) along with the full frame and the results compared in Figures 12(b) and (c) for X42 and

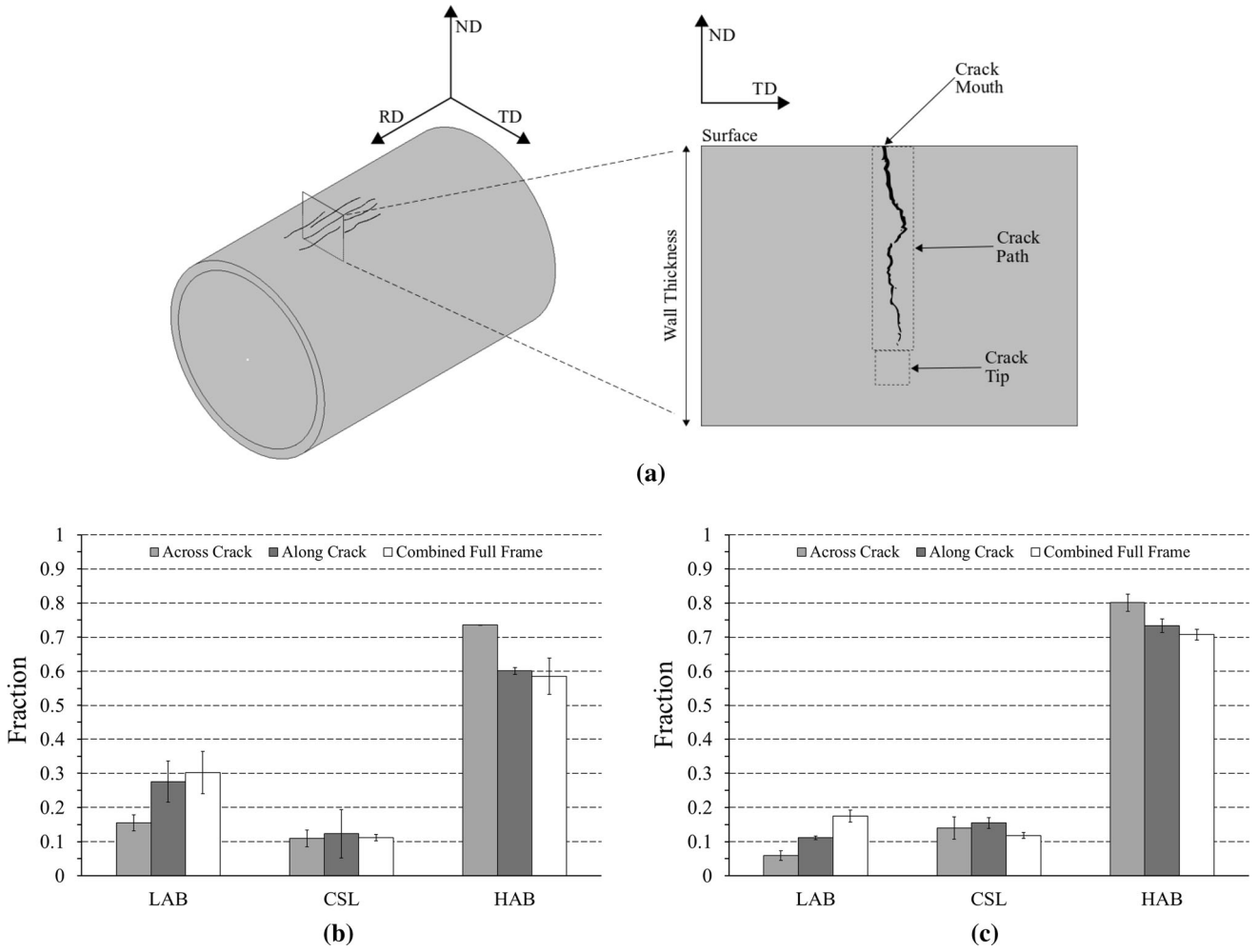

Fig. 10—(*a*) Schematic diagram to show crack formation on pipe surface (along rolling direction) and its propagation through pipe thickness along transverse direction. The crack tip is also shown. (*b*) and (*c*) are distribution of LAB's, CSL's and HAB's (b) X42 and (c) X65.

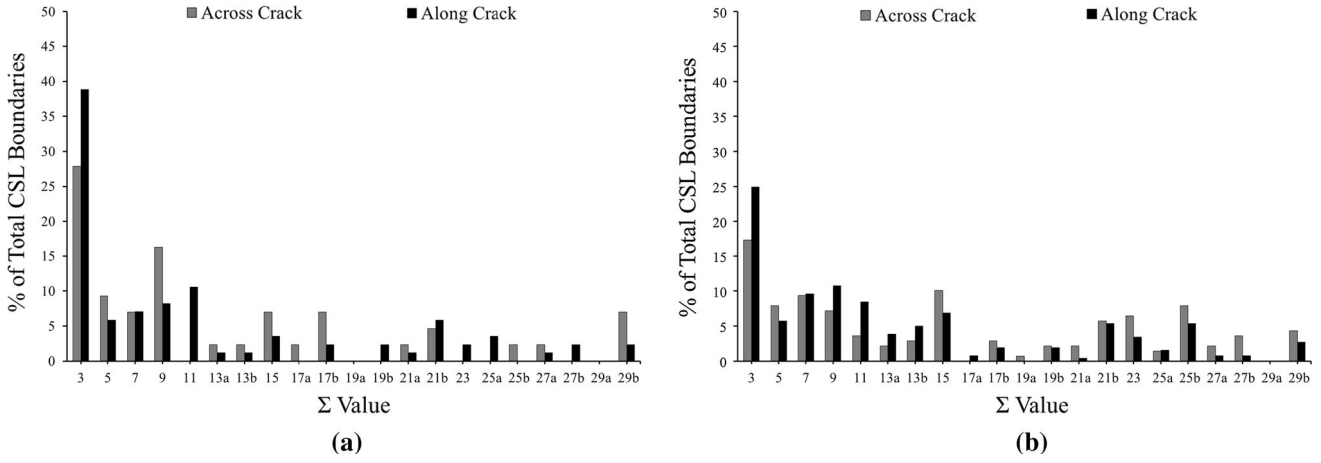

Fig. 11—CSL boundary distribution made through manual misorientations in (*a*) X42 and (*b*) X65.

X65 respectively. The results show that the crack tip has a very similar grain boundary distribution to areas 1 to 6 not directly at the tip of the crack. A comparison of the crack tip and areas 1 to 6 was made to the full frame grain boundary characteristics. The results showed that not only did the crack tip and areas 1 to 6 contain near identical levels of LAB's, HAB's, and CSL boundaries, they contained levels nearly identical to the full frame. The crack tip does not appear to be unique in terms of grain boundary distribution and appears to just be

representative (in terms of grain boundary distribution) to the larger full frame. In other words, it does not appear that the grain boundary character at the crack tip prevented the crack from propagating.

3. *Crack propagation, branching, and deflection behavior*

In selected cracks found in both X42 and X65, SEM, EBSD Image Quality (IQ), grain map (each grain has a different color), and Taylor factor maps* were extracted to clarify the role of grain boundaries on crack behavior with grains of interest numbered and presented in Figures 13(a) through (h). Figures 13(i) and (j) show selected triple junctions and the direction the crack took when presented with two grain boundaries ahead of the crack front. The SEM images provided the highest quality image of the crack whilst the IQ map is able to distinguish grain boundaries better. Grain maps present each individual grain as a different color from its neighbors to better distinguish the grains from each other. Intergranular cracking may be more likely when the Taylor factors of adjacent grains have significant differences in their values, hence it is presented to give additional indications of crack propagation behavior.[38] Misorientation between grains surrounding cracks as well as texture measurements were calculated to develop a better understanding of what features promoted and halted cracking in each steel grade.

*The Taylor factor shows the expected yield behavior of a grain based on its crystal orientation and the characteristics of the applied stress.[37]

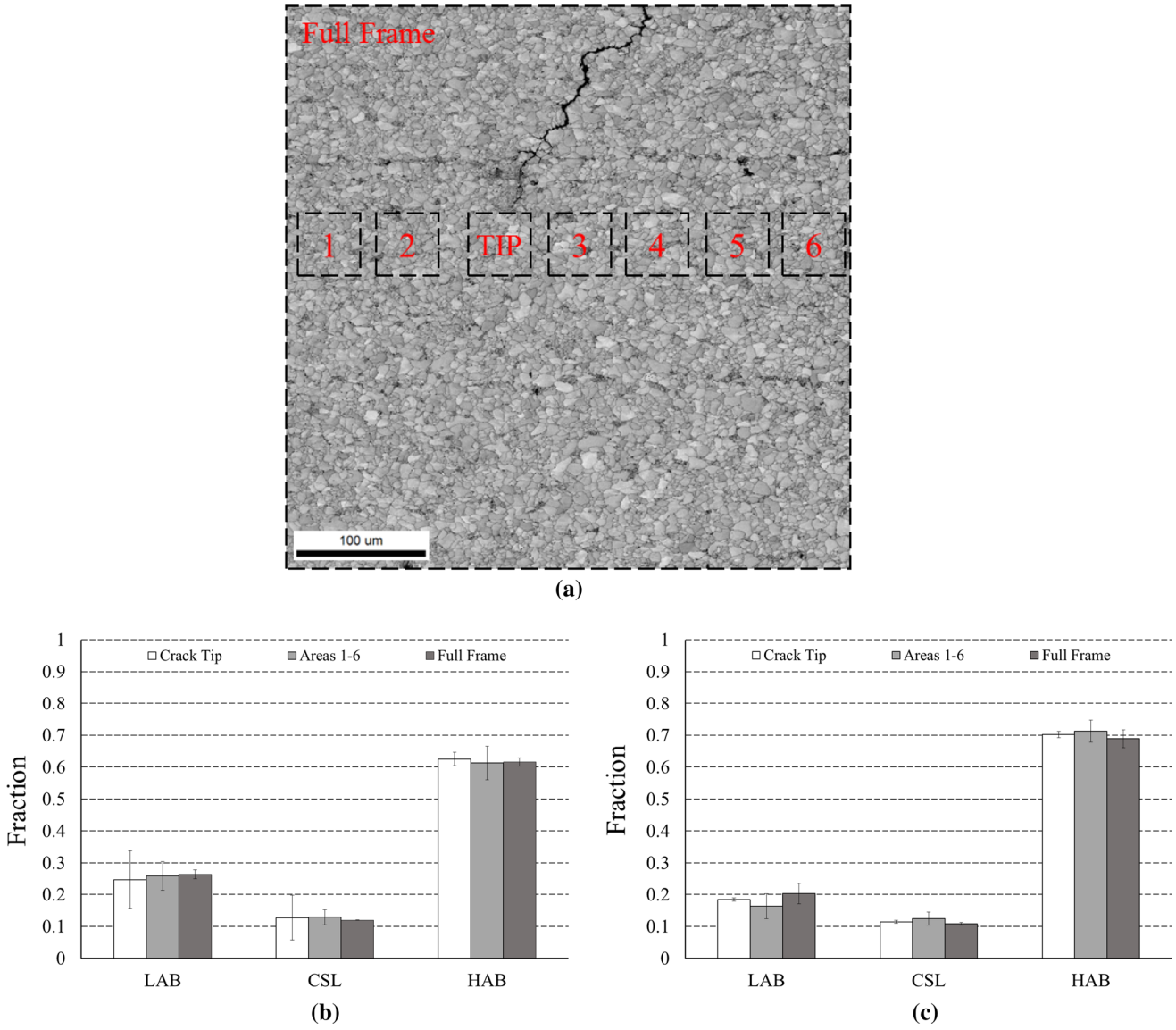

Fig. 12—(*a*) Image quality map to show the analyzed areas around the crack tip (TIP) and surrounding areas (1 to 6). (*b*) X42 and (*c*) X65 show the distribution of all boundaries in the nominated areas and the full frame.

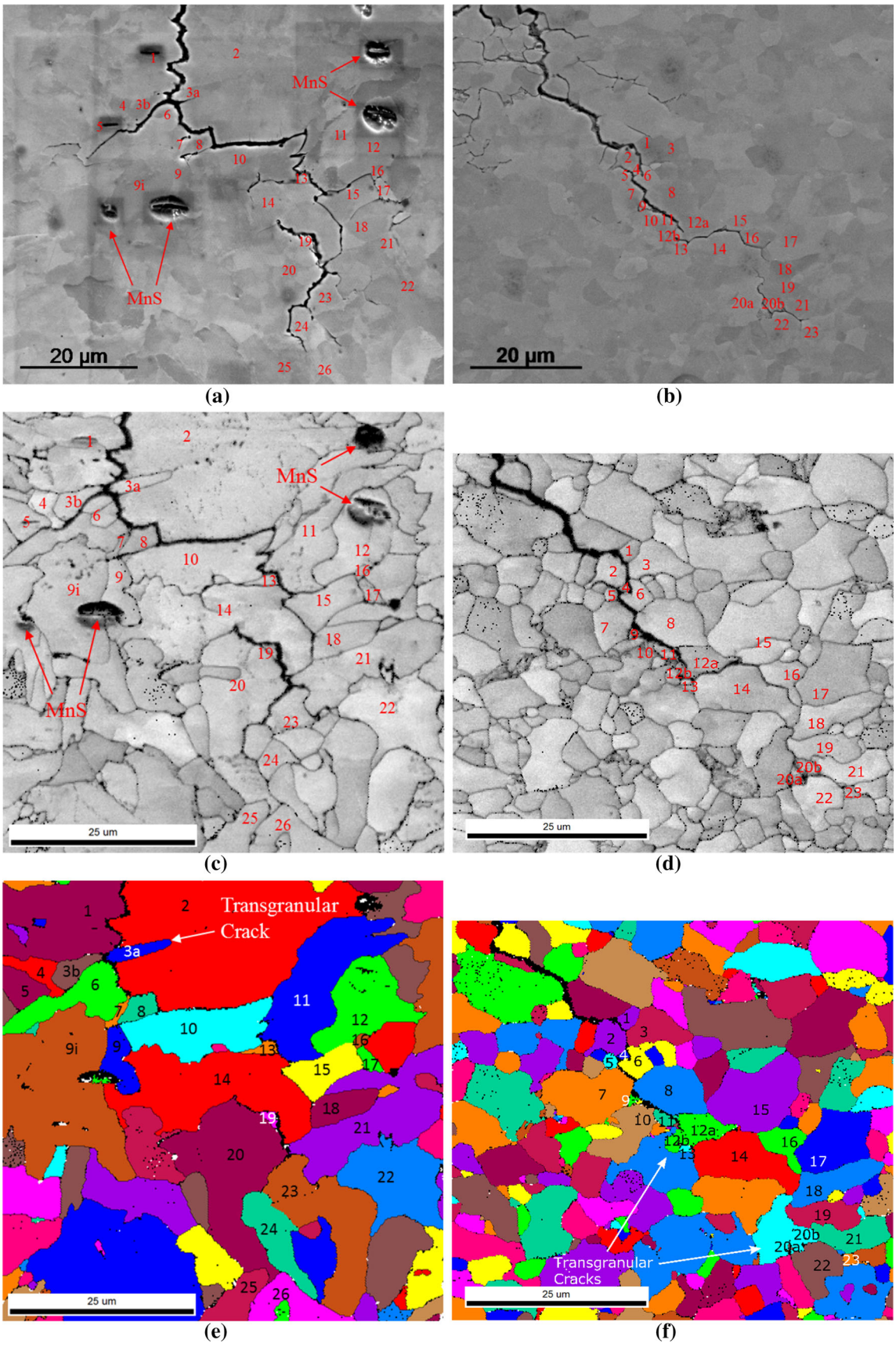

Fig. 13—(*a*) and (*b*) SEM, (*c*) and (*d*) IQ, (*e*) and (*f*) grain map, (*g*) and (*h*) Taylor factor, and (*i*) and (*j*) triple junction schematic diagram for X42 (a, c, e, g, i) and X65 (b, d, f, h, j).

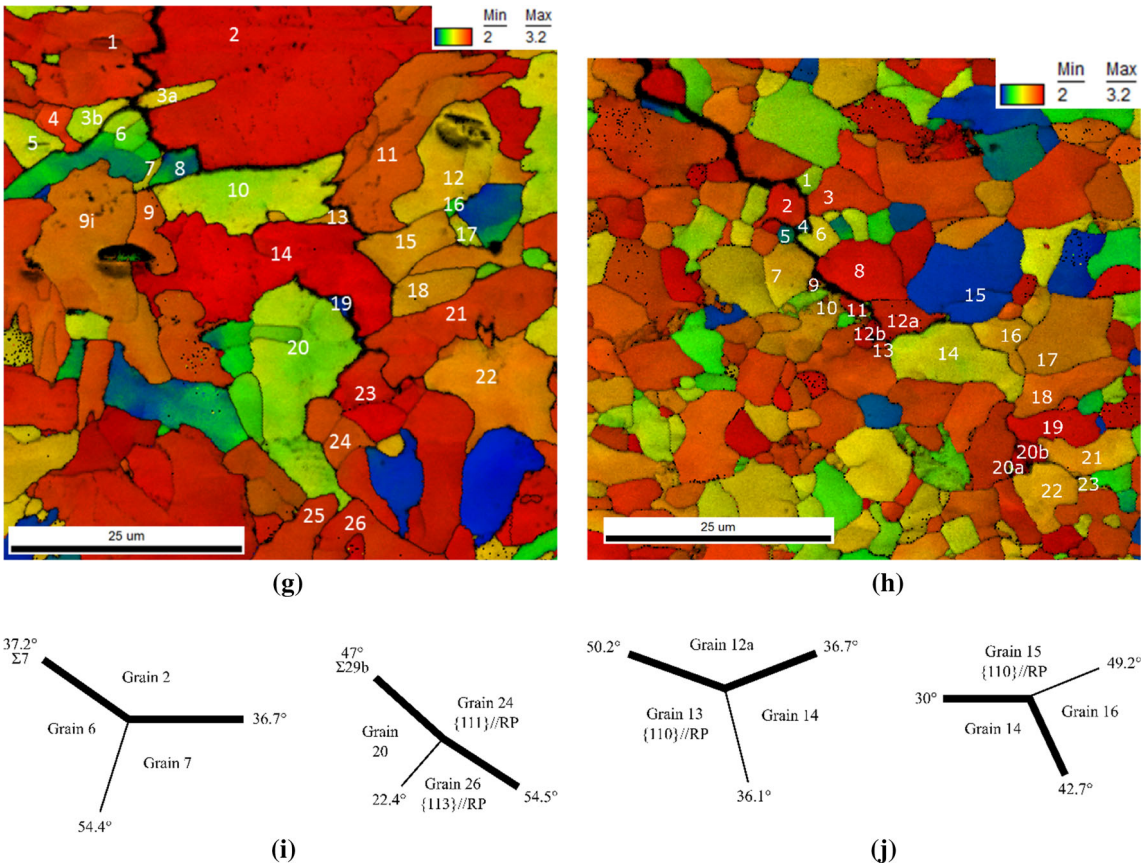

Fig. 13—continued.

a. X42 crack example The X42 crack presented in Figure 13(a) is a section of a main crack near the crack tip. MnS inclusions were identified surrounding the crack and confirmed through EDX. The MnS inclusions don't appear to encourage SCC to grow closer to them and in fact the crack appears to bypass the areas MnS inclusions are present. Whilst MnS may encourage SCC cracks forming due to increased pitting when located at the surface,[39] no cracking occurred through inclusions. The grains of interest surrounding the crack in the EBSD IQ map in Figure 13(c) were numbered and the misorientation between the grains calculated. Once the crack propagated intergranually between grains 1 to 2 (44.6 deg misorientation), the crack then propagated through grain 3 transgranularly evidenced by the misorientation between grain 3a to 3b equal to 2.7 deg. Note that the grain map in Figure 13(e) shows 3a and 3b as a different color. The software is not able to recognize 3a and 3b as a transgranularly cracked grain because they are completely separated. Grain 3 was a highly elongated grain with crystallographic texture aligned to the {100}//RP which is claimed to promote transgranular cracks in Body Centered Cubic (BCC) materials.[23] A triple junction is a location where three grain boundaries intersect and a crack propagating through one boundary could then propagate through either of the two adjoining boundaries depending on which grain boundary was more susceptible to cracking.[20] After the crack progressed between grains 2 to 6 (37.2 deg and Σ7 boundary), the crack reached a junction where it could have propagated between grains 6 to 7 (54.4 deg) but instead propagated between grains 2 to 7 (36.7 deg). This is summarized in the illustration in Figure 13(i). Whilst the misorientation is lower, total grain boundary energy is not only determined by the misorientation; but also grain boundary plane orientation.[40] The Taylor factor differential between grain 2 to 7 is higher than between grains 6 to 7 which would suggest intergranular cracking is more likely between the two grains as a higher Taylor factor differential is indicative of a higher likelihood of fractured grain boundaries.[38,41] The crack appears to halt when encountering the grain boundary created by grains 24 to 26 (54.5 deg) summarized in Figure 13(i). Whilst the boundary misorientation categorizes it as a high angle grain boundary, the crystallographic texture measured for grain 24 is {111}//RP and grain 26 is close to the {113}//RP texture which may produce a resistant grain boundary due to being low index plane *i.e.*, the lower

the miller index of the bordering crystals, the closer packed the resulting boundary will be.[26]

b. X65 crack example The X65 crack in EBSD IQ map Figure 13(d) was intergranular with two instances of transgranular cracking through grains 12 and 20 highlighted in Figure 13(f). There are no inclusions in this cracked section and the sample has the finer grain size expected for X65. The first instance of a triple junction occurred after the crack propagated transgranularly through grain 12. The crack could have propagated between grains 13 to 14 (36.1 deg) or grains 12a to 14 (36.7 deg) shown in Figure 13(h). In this case, both the grain misorientation and the Taylor factor differential Figure 13(h) between the two boundaries were almost identical with the crack growing through boundary 12a to 14; potentially due to the measured texture of grain 13 being {110}//RP oriented which has been found in literature to be resistant to SCC.[20] The next triple junction occurred when the crack encountered grains 14 to 16 (42.7 deg) and 15 to 16 (49.2 deg) shown in Figure 13(h). In this case, the crack began to grow between grains 15 to 16 but it appeared to halt and instead propagated between grains 14 to 16. The boundary between grains 15 to 16 should be more susceptible due to there being a higher Taylor Factor differential than between grains 14 to 16; however, this was not the case. Grain 15 was measured to be {110}// RP textured which has been suggested by literature as being more resistant to SCC.[20] After the crack propagated between grains 21 to 22 (56.9 deg), it seems to diverge around grain 23 before crack growth halted (note that the crack arrest is based on a 2D polished section of a 3D phenomenon) Figure 13(d). It is unclear from the microstructure why the crack halted as grain 23 is {100}//RP textured and grain boundaries 21 to 23 (45.9 deg) and 22 to 23 (31.8 deg) were both high angle boundaries. The halted crack propagation was likely due to the pipe being removed from service in this case as opposed to microstructural circumstances. When comparing the two pipe samples, it is evident that most cracked grain boundaries were high angle (with the exception of the transgranularly cracked grains). When triple points occurred it appears that when misorientation is similar, boundaries with low index crystallographic orientations seem to be more resistant to SCC propagation.[26] In addition, whilst the low index crystallographic orientations seem to take precedence, the Taylor factor appears to provide some additional information regarding the likelihood of cracking when there is a high mismatch. A distinction between the examined regions in X42 and X65 is the level of inclusions present surrounding the cracks. The crack in X42 was surrounded by inclusions whilst the X65 crack was free from inclusions, although this is likely just a characteristic of the materials with X65 pipe steel being of a better quality (cleanliness). However, it is imperative to point out that crystallographic texture appears more important on SCC crack propagation than weak and incoherent interface between the steel matrix and inclusion for crack propagation.

4. *Micro-texture surrounding SCC cracks*

The main challenge with EBSD datasets is often the cracked regions comprise only a small portion of the scan frame so the uncracked grain boundaries obscure the properties of the cracked grain boundaries. By applying a similar technique used previously to investigate the grain misorientation of cracks, the unaffected grains can be removed from analysis so only cracked grains are investigated. To get data only associated with cracked grains, the data set was cropped such that the surrounding, uncracked grains were removed from analysis. As an example, Figure 14(a) shows a scan of an Inverse Pole Figure (IPF) map of an SCC crack, when cropping around the crack including only grains attached to cracked grain boundaries, you get the map presented in Figure 14(b). Cropping datasets allows analysis of the entire crack path to occur without surrounding grains influencing the findings.

The effect of cropping the dataset and excluding additional grains is quite dramatic. Figure 15 shows Orientation Distribution Function plots (ODF plots) comparing the initial full frame EBSD scans and the cropped regions. Whilst the X42 shows a weak overall texture, the cropped frame has a peak concentration higher than the full frame located along the {112}//RP fiber at φ_1 = 40 to 50 deg and an increase of (113) [1$\bar{1}$0] textured grains. The X65 shows a dramatic change in contour from having a very weak texture in the full frame where all fiber textures are present in equal proportions to the cropped frame where the overall maximum texture increased. The cropped frame presents with the highest concentration of texture along the {112}//RP fiber and an increase in texture near (110)[001] with no significant texture identified along the {100}//RP fiber. This approach allows dominant features of cracked and uncracked regions to be accurately distinguished. In both the X42 and X65 areas in Figure 15, there are higher proportion of {112} and {113}//RP textured grains in the cropped areas whilst a slight decrease in levels of {100}//RP textured grains was identified in the X65. {112}//RP textures have been linked to transgranular cracking in ferritic-pearlitic steels[23] in literature whilst in X65 grade pipe, {100}// RP textured grains were more susceptible to SCC and {111}//RP fiber and {110}//RP fibers were more resistant to SCC.[10,20–22]

a. Crack tip Additional crack tips have been analyzed and the results presented in Figure 16. The crack tip in X42 (Figure 16(a)) shows a high proportion of both {111}//RP and {110}//RP textured grains with some lesser proportion of {113}//RP textured grains. In comparison the crack tip in X65 shows the highest concentration along the {332}//RP fiber. The results are in line with literature which suggests the crack tip contains a high proportion of {110}//RP and {111}//RP thought to be responsible for halting crack propagation.[20] As the pipe sections were removed from service prior to failure, the cracks analyzed may have not necessarily reached their full length. It is possible that if the pipes had remained in service the cracks

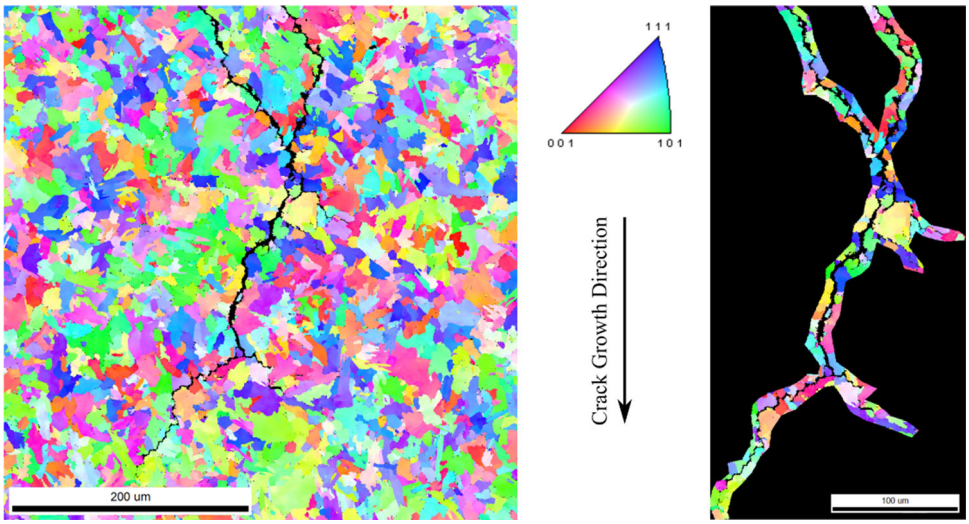

Fig. 14—Comparison between full frame EBSD scans (left) and the cropped scan (right) presented in an [001] IPF map of a crack in X42 pipeline.

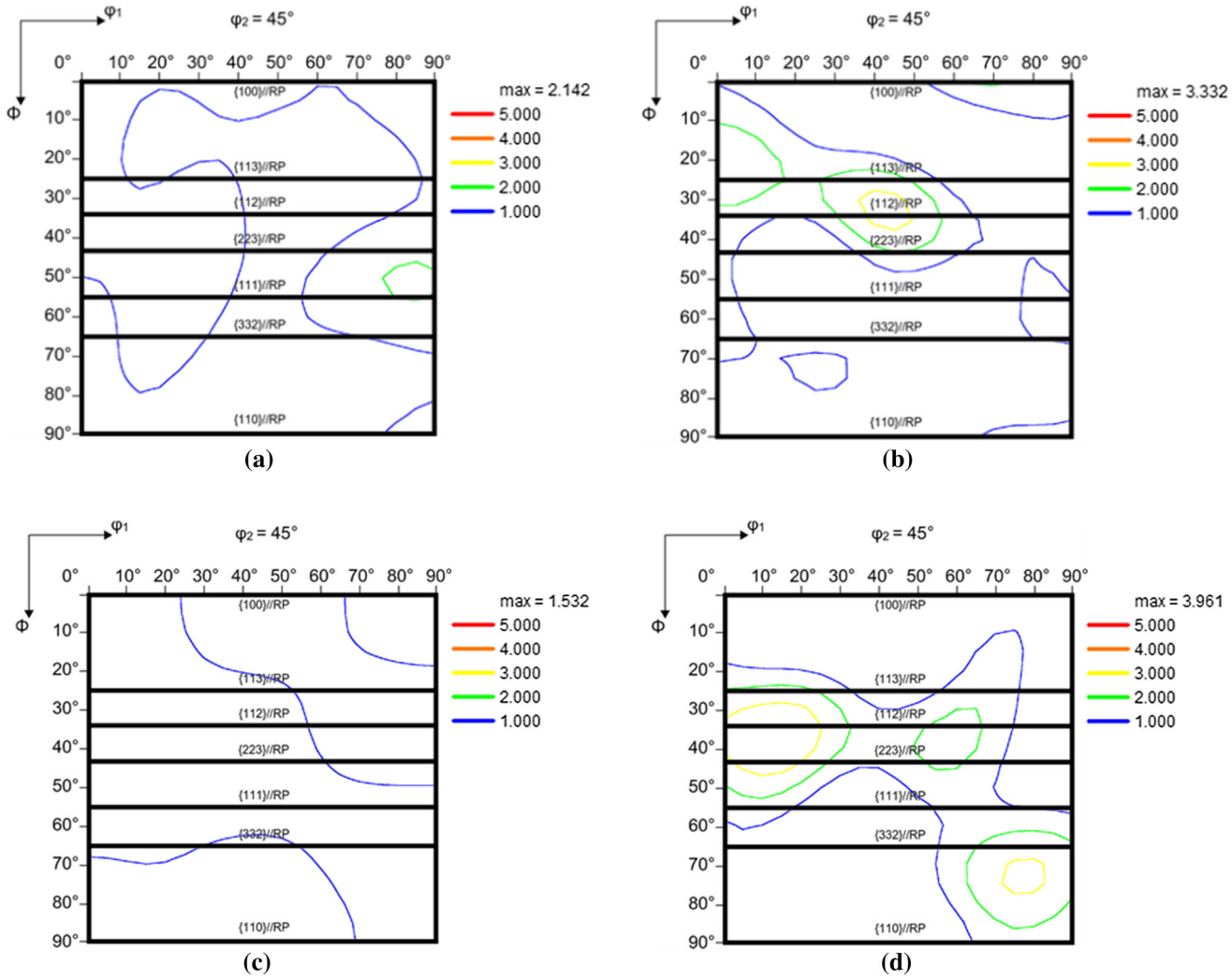

Fig. 15—Comparison of the full frame EBSD scans to the cropped area (*a*) full frame X42, (*b*) cropped X42, (*c*) full frame X65, and (*d*) cropped X65.

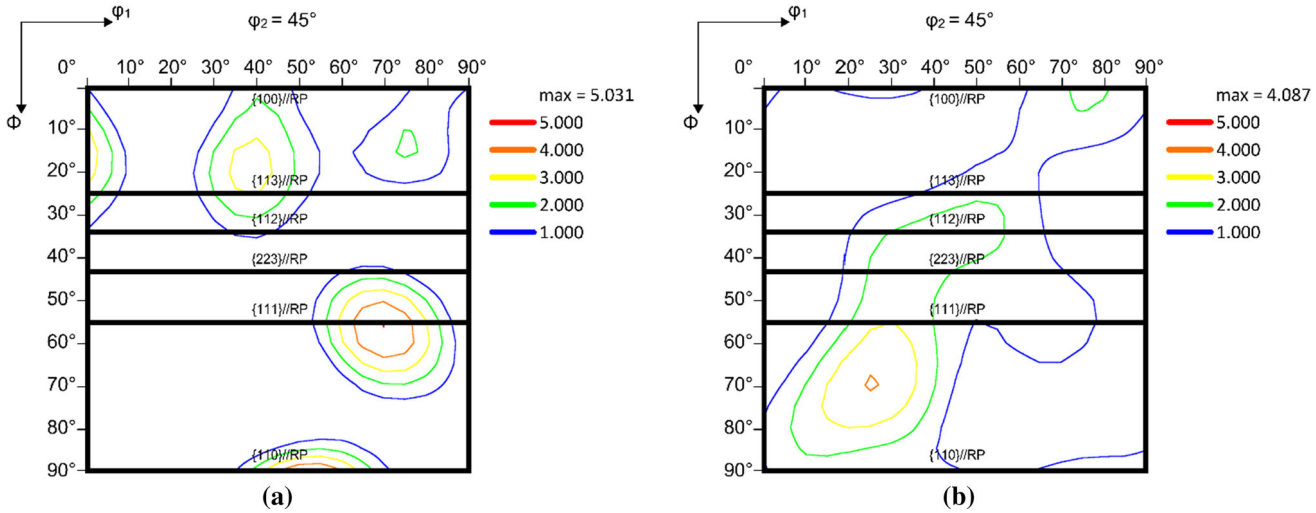

Fig. 16—Comparison of the texture found in crack tips in (*a*) X42 and (*b*) X65.

would have continued to propagate. One method to determine whether a crack tip is resistant is to grow an SCC crack in a compact tensile specimen, carry out EBSD on the sample crack tip, and then place the sample back in solution to determine whether the crack extends or not depending on the initial measured crystallographic texture.

b. Uncracked texture The sub-surface texture in both pipes is predominantly $\{110\}\langle 112\rangle$ and $\{112\}\langle 111\rangle$ which are brass and copper textures respectively. For High Strength Low Alloy (HSLA) steels, these texture components are the austenite rolling texture which usually transform into $\{332\}\langle 113\rangle$ and $\{113\}\langle 110\rangle$ textures after the $\gamma \rightarrow \alpha$ transformation.[42] It is worth noting that the transformation textures of the sub-surface region of the thermo-mechanically controlled processed (TMCP) steels will be quite different than the typical ferrite transformation texture due to the complex shear strain present in this region as a result of the friction between the roll and the steel surface.[43] However, in the present cases, it is obvious that the original austenite deformation texture is retained in the final microstructure near the surface. At quarter thickness for the X65 sample, the ferrite transformation textures $\{332\}\langle 113\rangle$ and $\{113\}\langle 110\rangle$ dominate the microstructure. However, some $\{100\}\langle 110\rangle$ grains also started to appear with the increase of the depth which are known to be detrimental for the toughness of the steel.[44,45] ODFs at the center plane of the steels (Figures 17(e) through (f)) showed that the intensity of $\{100\}\langle 110\rangle$ increased significantly at the expense of $\{332\}\langle 113\rangle$ and $\{113\}\langle 110\rangle$ texture. Therefore, it is obvious that the texture in X42 and X65 steels are inhomogeneous through the thickness. The fact that there is a significant amount of $\{100\}\langle 011\rangle$ grains (highest texture intensity) present in the mid-thickness region of the steel suggests that the parent austenite grains prior to accelerated cooling had $\{100\}\langle 001\rangle$ recrystallized textured grains which eventually transformed into $\{100\}\langle 011\rangle$ ferrite transformation textures.[42]

E. *Transgranular Cracking*

As seen in Figure 18, SEM analysis revealed isolated instances of transgranular cracking rather than intergranular crack. An investigation to determine whether EBSD could clarify why certain grains cracked transgranularly whilst neighboring grains cracked intergranually was undertaken.

Whilst the majority of transgranular cracking occurred sporadically, the longest X65 crack (3.59 mm) was transgranular near the tip of the crack as shown in Figure 19(a). The change in propagation behavior from intergranular to transgranular with a straight line path may suggest the crack propagation mechanism is different in this section of the crack. Work carried out by Gamboa *et al.*[11] on fatigue of SCC suggests the change in the crack from inclined and intergranular to straight and transgranular was due to the dominant cracking mechanism shifting from SCC to fatigue and is likely the reason for the change in this sample. Crystallographic texture of the transgranular region surrounding the crack, as seen in Figure 19(b), showed dominant {100}// RP texture consistent with transgranular cracking in pipeline steel.[23] Investigation of the individual transgranular cracked grains was undertaken to determine if a dominant texture was present in these grains. A survey of 31 instances of transgranular cracking in X42 and 33 in X65 was undertaken and the results presented in Figure 19(c). In X42 transgranular cracking occurs in grains with {111}//RP and {110}//RP fiber texture greater than 50 pct of the time. In X65, the dominant fibers present in transgranularly cracked grains are the {100}//RP, {112}//RP, and {110}//RP fibers.

Taylor factor analysis was undertaken on the transgranularly cracked grains section of X65 presented in Figure 19(a). The Taylor analysis revealed that while most transgranularly cracked grains presented with high

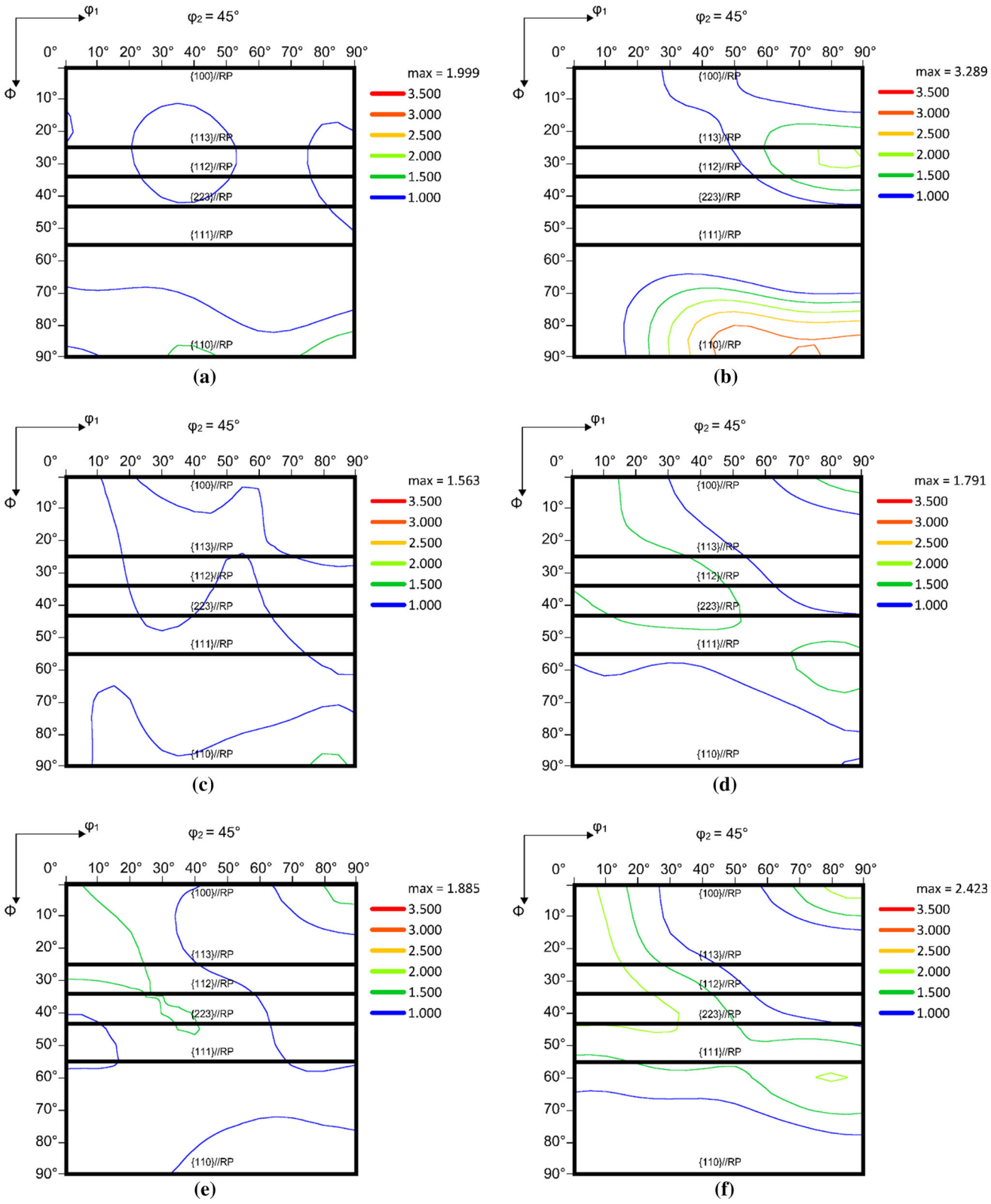

Fig. 17—ODF φ_2 = 45 deg of uncracked samples in X42 and X65 (*a*) X42 surface, (*b*) X65 surface, (*c*) X42 quarter thickness, (*d*) X65 quarter thickness, (*e*) X42 center, (*f*) X65 center.

Taylor factors, there was a high proportion that had relatively low Taylor factors. This can be seen in Figure 20 where the circled cracked grains (with misorientation < 15 deg confirming transgranular cracking) show that there is a range of Taylor factors present in transgranular cracking. This is somewhat at odds

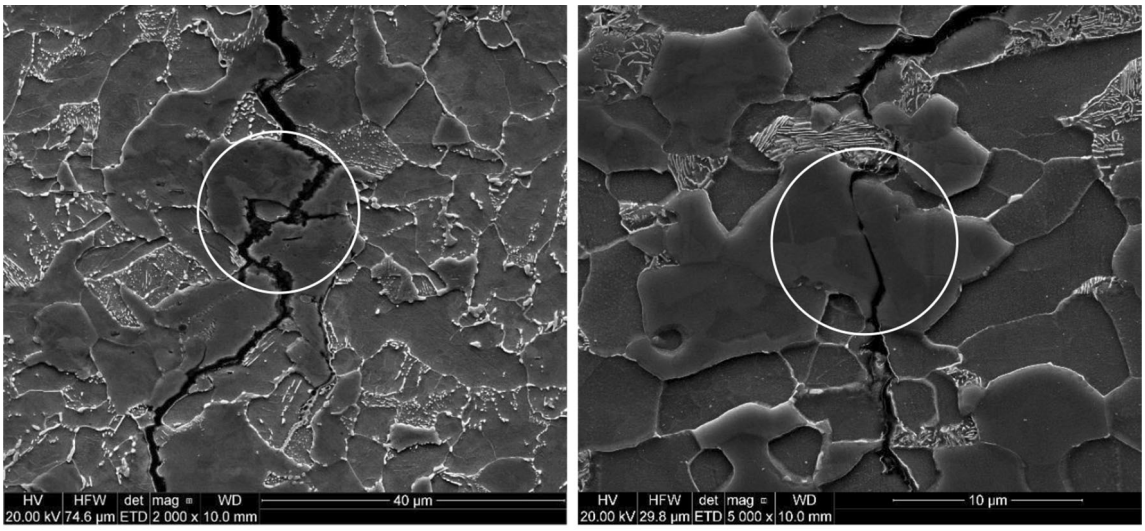

(a) **(b)**

Fig. 18—SEM instances of transgranular cracking (circled) in (*a*) X42 and (*b*) X65.

with literature where transgranular cracking was more often associated with grains with high Taylor factors.[38,41]

Further analysis of the individually transgranularly cracked grains identified along the crack path in both X42 and X65 specimens was carried out with the results presented in Figure 21. Whilst the majority of transgranularly cracked grains had high Taylor factors *i.e.*, the color was orange or red corresponding to a Taylor factor of greater than 2.75, a significant proportion (nearly 25 pct of transgranularly cracked grains in X42 and 30 pct of grains in X65) had Taylor factors below 2.75. Whilst high Taylor factors are more commonly identified in transgranularly cracked grains, a high Taylor factor alone doesn't appear to be a reliable indicator of transgranular cracking due to the significant proportion of transgranularly cracked grains having low Taylor factors.

IV. DISCUSSION

A. *Effect of Grain Boundary Distribution on SCC*

The cropped regions surrounding the SCC crack tended to present a different grain boundary distribution as compared to the full frame EBSD scan (Figure 9). This isn't necessarily unexpected as the full frame EBSD scan contained mostly uncracked grain boundaries which were not in the direct vicinity of the SCC crack. As SCC is a primarily intergranular corrosion mechanism, it was expected that the SCC affected grain boundaries would present with a higher proportion of high angle grain boundaries than the surrounding area. As evidenced in both X42 and X65 in Figures 10(b) and (c), there was a higher proportion of HAB's present across the cracked grain boundaries as compared to the full frame EBSD scans, an example of which is presented in Figure 9(d). The higher proportion of HAB's resulting from SCC cracked grain boundaries highlights high pH SCC's selective nature with high angle boundaries being the most susceptible. When analyzing the grain boundaries which SCC did not propagate through *i.e.*, along the crack, it is clear that along the crack there was a higher proportion of low angle grain boundaries (particularly in X42) and a subsequently lower proportion of HAB's. As SCC is an intergranular cracking mechanism, the sub-grain boundaries (LAB's) along the crack offered higher resistance to SCC and their presence tended to shape the crack by deflecting it through less resistant HAB boundaries.

When investigating the role that misorientation between high angle grain boundaries has on SCC it is tempting to conclude that higher misorientation results in higher SCC susceptibility; however, as seen in Figure 13, this wasn't necessarily the case. In Figure 13(i) the crack propagated through grain boundary made by grains 2 to 7 (36.7 deg) that had lower misorientation than the boundary between grains 6 to 7 (54.4 deg) and in Figure 13(j) the crack propagated through boundary of grains 14 to 16 (42.7 deg) with the lower misorientation as opposed to boundary of grains 15 to 16 (49.2 deg). The likelihood of a crack propagation through any boundary is strongly determined by the grain boundary energy with higher energy corresponding to higher chance of fracture.[27] Grain boundary energy is not simply determined by grain boundary misorientation hence it is not possible to simply use grain boundary misorientation alone to explain the susceptibility behavior of grain boundaries when cracked by SCC.[26]

The total fraction of CSL boundaries remained relatively constant surrounding the main SCC crack with the number of boundaries observed across the crack were at similar levels to those observed along the crack. There is a slightly higher proportion of $\Sigma 3$, $\Sigma 7$, and $\Sigma 11$ boundaries present in uncracked boundaries along the main SCC crack in both X42 and X65. In X65,

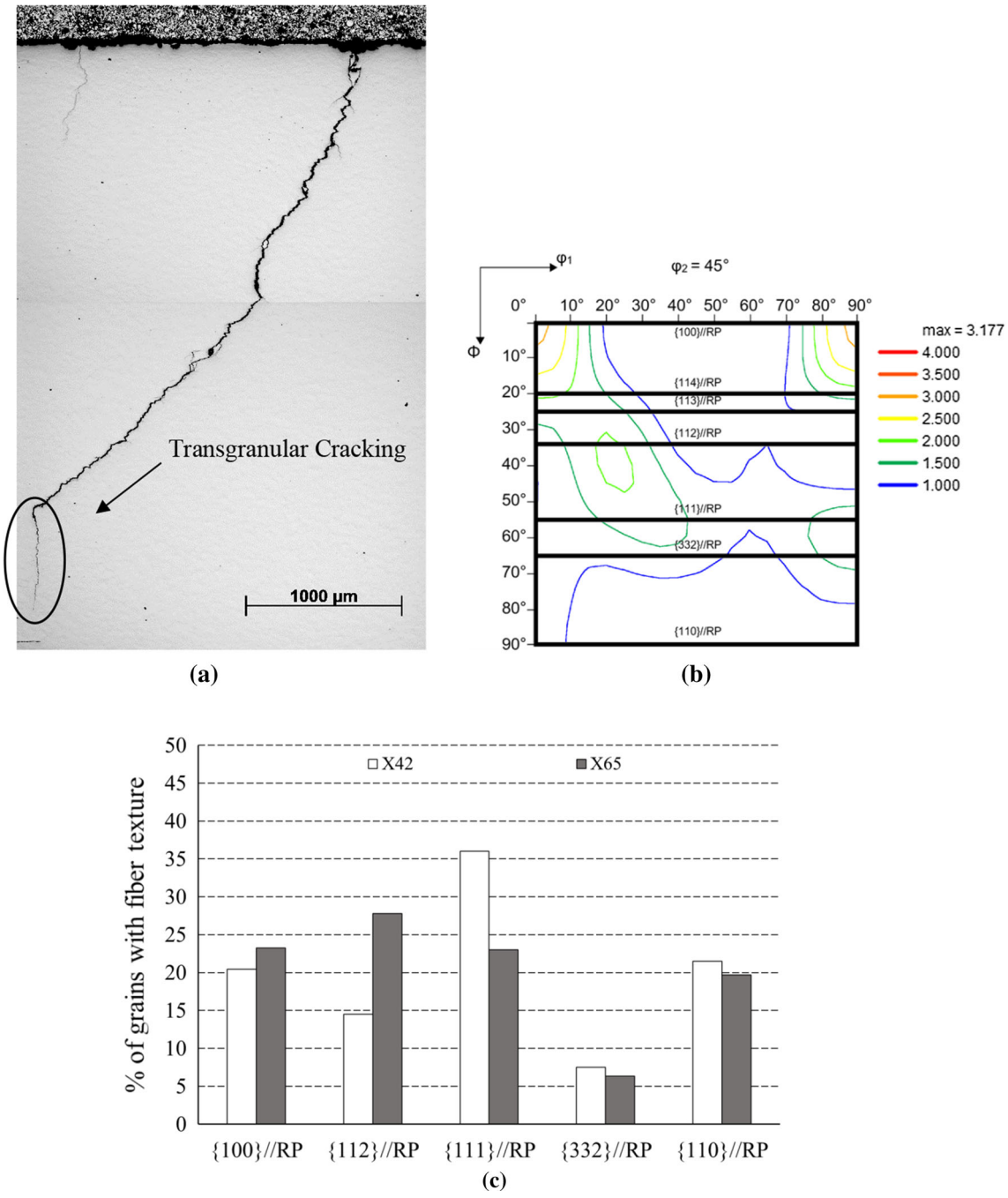

Fig. 19—(*a*) X65 crack which transitions from intergranular to transgranular (circled), (*b*) ODF of transgranularly cracked grains at the end of the crack, (*c*) fraction of fiber textures present in transgranularly cracked grains.

Σ3, Σ7, Σ9, Σ11, Σ13a, Σ13b, Σ17a, and Σ25a boundaries are present in higher proportions along the crack than across the main SCC crack whilst in X42, Σ3, Σ7, Σ11, Σ19b, Σ21b, Σ23, Σ25a, and Σ27b boundaries are present in higher proportions along the main SCC crack than across the crack. With the exception of Σ3 boundaries, other CSL boundaries identified as resistant to SCC cracking were present in very low concentrations and their resistance properties should not be overstated. Arafin and Szpunar[20] found that Σ11 and Σ13b boundaries showed resistance to SCC in X65 whilst Venegas[24] found Σ11, Σ13b, and Σ29a may be resistant to HIC in X46 and ASTM A106 steels. It should be noted that in each case the overall number of boundaries tested in these studies was quite low and may not be representative of the overall mechanism. From the results we obtained it does not appear that CSL boundaries significantly impact SCC propagation resistance in the low proportions identified here.

There is consensus in literature that Σ3 boundaries are highly resistant to cracking in many materials,[28,29,46] although this appears to be a special case with most

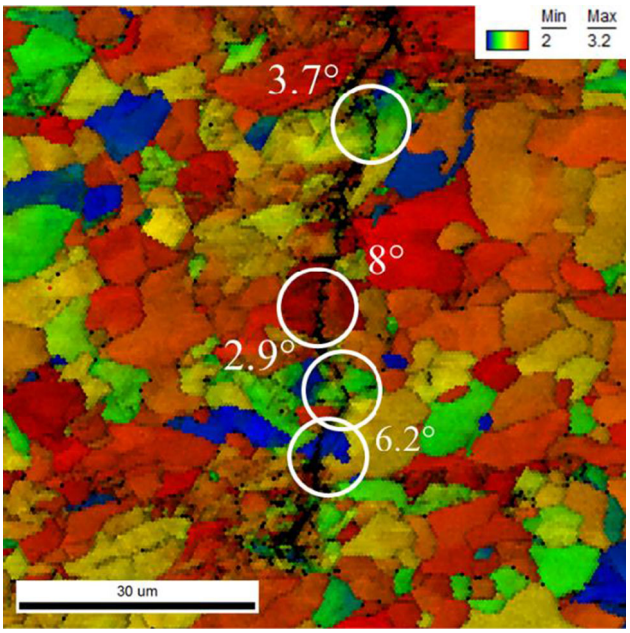

Fig. 20—Taylor factor map of transgranularly cracked region in X65.

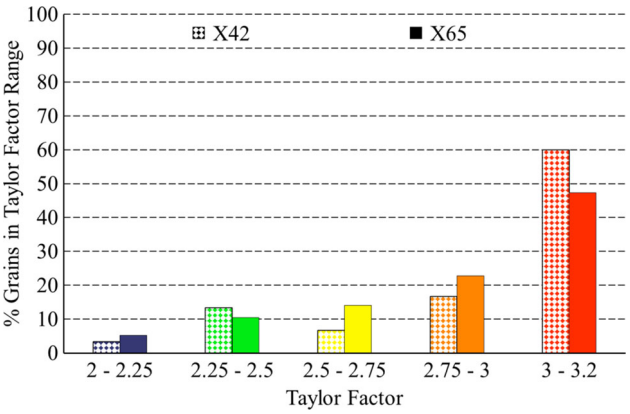

Fig. 21—Range of Taylor factors present in transgranularly cracked grains (range 2 to 3.2).

other CSL boundaries not reported as especially resistant.[47] This is somewhat at odds with the observation that an increase in CSL boundaries in general can increase resistance to intergranular cracking in many materials.[48–50] The initiation of SCC is reduced through increasing the proportion of CSL boundaries[49] although application of strain prior to SCC testing reduces the immunity of CSL boundaries significantly.[50] We do not have any information regarding the SCC crack initiation with CSL boundaries as these samples were not adequate to test this point. Further work is currently underway on X70 to test control rolled pipe steel to establish whether CSL boundaries formed during rolling has any effect on initiation.

B. *Effect of Texture on SCC Propagation*

The effect of texture on SCC propagation is not as clear when analyzing full crack lengths as it is when analyzing individual grains along the crack path. It appears that while in some situations high proportions of {100}//RP textures increase likelihood of cracking, in other situations it would appear that {110}//RP, {112}//RP grains are present along the cracked path. It is not certain whether {100}//RP textured grains play a significant role in all intergranular crack propagation as they do not appear to be a dominant constituent in all scans surrounding cracks. It is noted that the results are different to those presented previously.[22] In previous works the limited number of tests showed a more dominant contribution of {100}//RP textured grains; however, work presented in this article is the result of a significantly higher number of regions along the cracks being investigated with the new results more representative of cracking behavior. Current findings show a higher proportion of {110}//RP and {112}//RP textures present in the cracked regions. Decreasing proportions of {110}//RP and {112}//RP textures may result in higher resistance to SCC in pipeline steels.

The most dominant textures in transgranular cracking were the {100}//RP, {112}//RP, {111}//RP, and {110}//RP textured grains in X42 and X65. The presence of grains with {100}//RP fiber textures has been found to crack through cleavage during transgranular cracking whilst the {112}//RP and {110}//RP fibers through slip.[23,24] The reduction of these textures would likely reduce the instances of transgranular cracking in X42 and X65. Whilst the {111}//RP fiber is not often associated with transgranular cracking in low carbon steels, the majority of the cracked grains with {111}//RP fiber textures had ⟨112⟩ rotation axes. {111}//RP grains with ⟨112⟩ rotation axes have been found to be susceptible to transgranular cracking.[51] Whilst {112}//RP, {110}//RP fibers, and {111}//RP fibers are inherent in hot rolled steels, it would appear that reducing the {100}//RP fiber and {111}⟨112⟩ textures may reduce overall susceptibility to transgranular cracking in X42 and X65 grade steels undergoing high pH SCC.

C. *Role of Crack Tips on Halting SCC*

The role that the crack tip has on halting SCC cracks is not as clear as has been reported previously in literature. In terms of the grain boundary distribution, the proportion of HABs, LABs, and CSL boundaries at the crack tip in Figure 12 doesn't appear to be any different from those in regions adjacent to the crack tip. As such, simply measuring the grain boundary distribution does not provide any insight on whether the crack was halted due to the material properties or simply because the load was removed.

The crystallographic texture present in the crack tip in Figure 16 contains high proportions of both {111}//RP and {110}//RP textured grains with some smaller

proportion of {113}//RP textured grains. Whilst crystallographic texture observed in the crack tips are similar to those reported in literature as resistant to cracking,[10,20] one important point of consideration is that the pipe sections were removed from service prior to failure and the resulting cracks did not lead to rupture. It is likely that if the pipes were returned to service under the same conditions, the cracks would continue to propagate. It does not appear that the crack tip can provide a reliable indication of what characteristics are responsible for halting crack growth because it is unknown whether the crack was halted or the pipe was removed from service prematurely.

V. CONCLUSION

Sections of X42 and X65 ex-service pipe underwent optical and scanning electron microscopy followed by EBSD and texture analysis to determine the SCC behavior in each grade. Initial investigations found that the pipes had similar microstructures; however, the X65, which was manufactured later, contained a finer grain structure and more uniform grain size. SCC formed under cracked mill scale or at the base of deep pits in both grades likely due disbondment of the field-applied coatings.

An approach was developed that made it possible to distinguish cracked and uncracked regions by removing the influence of grains not bordering the SCC crack. Previous works have been carried out on either full frame scans which typically contain more uncracked grain boundaries than cracked, or on individual cracked grains which may not be representative of the failure. SCC propagated primarily through high angle grain boundaries and CSL boundaries (although some transgranular cracking was observed at isolated sections along the crack path). There was some evidence that $\Sigma 3$, $\Sigma 7$, and $\Sigma 11$ CSL in both X42 and X65 resisted cracking at a higher rate than other CSL boundaries; however, the overall proportion of these boundaries was very low and would not likely enhance SCC resistance overall unless the proportion was significantly increased. Each grade had additional CSL boundaries identified as potentially crack resistant; however, the number of boundaries identified for these other CSL boundaries was too low to draw any significant conclusions. The majority of CSL boundaries didn't appear to have a net positive effect on SCC susceptibility and the incredibly limited proportion of beneficial boundaries didn't appear to prevent crack propagation.

Texture investigation was able to identify that {112}// RP textures tended to be dominant surrounding cracked grain boundaries. Comparing the full frame textures with the cropped, cracking tended to occur in textures that were least dominant. Uncracked regions showed strong singular {110}//RP textures at the surface which seems to prevent cracks from propagating. More investigation in different pipe grades is required to conclude on the effect texture has on intergranular SCC.

Transgranular cracking occurred at roughly the same frequency in both X42 and X65 with 50 pct of cracked grains having either {100}//RP or $\{111\}\langle 112\rangle$ textures. Reducing levels of {100}//RP textured or $\{111\}\langle 112\rangle$ textured grains may reduce the likelihood of transgranular cracking in X42 and X65.

Transgranular cracking tended to be indicated by high Taylor factors; however, a significant proportion of transgranularly cracked grains had low Taylor factors so measuring the Taylor factor alone is an ineffective method of determining the likelihood of transgranular cracking.

ACKNOWLEDGMENTS

This work was funded by the Energy Pipelines CRC, supported through the Australian Government's Cooperative Research Centres Program. The funding and in-kind support from the APGA RSC is gratefully acknowledged. The authors also acknowledge the facilities, and the scientific and technical assistance, of the Australian Microscopy & Microanalysis Research Facilities at the University of Adelaide and Flinders University. The Authors would like to acknowledge the support of Dr. Erwin Gamboa of TransCanada (former lecturer at The University of Adelaide) and the technical assistance of the applications engineers at EDAX particularly Matt Nowell.

REFERENCES

1. Transportation Research Board and National Academies of Sciences, Engineering, Medicine: *Safely Transporting Hazardous Liquids and Gases in a Changing U.S. Energy Landscape*, The National Academies Press, Washington, DC, 2018. https://doi.org/10.17226/24923.
2. R.N. Parkins: *CORROSION 2000*. 2000.
3. A. King, G. Johnson, D. Engelberg, W. Ludwig, and J. Marrow: *Science*, 2008, vol. 321 (5887), pp. 382–85.
4. B. Fang, A. Atrens, J. Wang, E.-H. Han, Z. Zhu, and W. Ke: *J. Mater. Sci.*, 2003, vol. 38 (1), pp. 127–32.
5. J.G. Gonzalez-Rodriguez, M. Casales, V.M. Salinas-Bravo, J.L. Albarran, and L. Martinez: *Corrosion*, 2002, vol. 58 (7), pp. 584–90.
6. National Energy Board: *Public Inquiry Concerning Stress Corrosion Cracking on Canadian Oil and Gas Pipelines: Report ofthe Inquiry*, Technical Report no. MH-2-95, National Energy Board, Calgary, AB, 1996. http://publications.gc.ca/pub?id=9.646397&sl=0.
7. F. Song: *CORROSION 2008*. 2008.
8. R.N. Parkins: *Corrosion*, 1996, vol. 52 (5), pp. 363–74.
9. G. Van Boven, W. Chen, and R. Rogge: *Acta Mater.*, 2007, vol. 55 (1), pp. 29–42.
10. O. Lavigne, E. Gamboa, W. Costin, M. Law, V. Luzin, and V. Linton: *Eng. Fail. Anal.*, 2014, vol. 45, pp. 283–91.
11. E. Gamboa, V. Linton, and M. Law: *Int. J. Fatigue*, 2008, vol. 30 (5), pp. 850–60.
12. J.H. Bulloch: *Theoret. Appl. Fract. Mech.*, 1991, vol. 16 (1), pp. 1–17.
13. M.A. Eaglesham, J.U. Gaum, and J.H. Bulloch: *Theoret. Appl. Fract. Mech.*, 1988, vol. 10 (2), pp. 97–109.
14. R. Parkins: in *5th Symp. Line Pipe Research L*. 1974. p. 30174.
15. J.A. Beavers, T.K. Christman, and R.N. Parkins: *Mater. Perform.*, 1988, vol. 27 (4), pp. 22–26.
16. P. Kentish: *Corros. Sci.*, 2007, vol. 49 (6), pp. 2521–33.

17. H. Asahi, T. Kushida, M. Kimura, H. Fukai, and S. Okano: *Corrosion*, 1999, vol. 55 (7), pp. 644–52.
18. J. Li, M. Elboujdaini, B. Fang, R. Revie, and M.W. Phaneuf: *Corrosion*, 2006, vol. 62 (4), pp. 316–22.
19. Z.Y. Liu, X.G. Li, C.W. Du, G.L. Zhai, and Y.F. Cheng: *Corros. Sci.*, 2008, vol. 50 (8), pp. 2251–57.
20. M.A. Arafin and J.A. Szpunar: *Corros. Sci.*, 2009, vol. 51 (1), pp. 119–28.
21. M.A. Arafin and J.A. Szpunar: *ICF12, Ottawa 2009*, 2009.
22. A. Roccisano, S. Nafisi, and R. Ghomashchi: in *Iron Steel Technol. Conf., AISTech 2018*, 2018.
23. V. Venegas, F. Caleyo, J.L. González, T. Baudin, J.M. Hallen, and R. Penelle: *Scripta Mater.*, 2005, vol. 52 (2), pp. 147–52.
24. V.C. Venegas, F. Hallen, J.M. Baudin, and T. Penelle: *Metall. Mater. Trans. A*, 2007, vol. 38A (5), pp. 1022–31.
25. V. Venegas, F. Caleyo, T. Baudin, J.H. Espina-Hernández, and J.M. Hallen: *Corros. Sci.*, 2011, vol. 53 (12), pp. 4204–12.
26. B. Rath and I. Bernstein: *Metall. Trans.*, 1971, vol. 2 (10), pp. 2845–51.
27. T. Watanabe: *Res Mech.*, 1984, vol. 11 (1), pp. 47–84.
28. H. Lin and D. Pope: *Acta Metall. Mater.*, 1993, vol. 41 (2), pp. 553–62.
29. P. Lin, G. Palumbo, U. Erb, and K.T. Aust: *Scr. Metall. Mater.*, 1995, vol. 33 (9), pp. 1387–92.
30. American Petroleum Institute: *API 5L: Specification for Line Pipe*, 43rd edn., API Publishing Services, Washington, DC, 2004.
31. A. ASTM: *ASTM Stand*, 2012, pp. 1–43.
32. O. Lavigne, E. Gamboa, J. Griggs, V. Luzin, M. Law, and A. Roccisano: *Mater. Sci. Technol.*, 2016, vol. 85, pp. 26–35.
33. E. Gamboa: *Corr. Eng. Sci. Technol.*, 2015, vol. 50 (3), pp. 191–95.
34. O. Lavigne, E. Gamboa, V. Luzin, and M. Law: *Eng. Fail. Anal.*, 2018, vol. 85, pp. 26–35.
35. J. Beavers and N. Thompson: *ASM Handbook*, Cleveland, ASM International, 2006, pp. 1015–25.
36. F.J. Humphreys, G.S. Rohrer, and A.D. Rollett: in *Recrystallization and related annealing phenomena*, chap. 4, Elsevier, Amsterdam, 2017, p. 118.
37. J.H. Shen, Y.L. Li, and Q. Wei: *Mater. Sci. Eng. A*, 2013, vol. 582, pp. 270–275.
38. EDAX: Electron Backscatter Diffraction (EBSD) Analysis of Cracking in Polycrystalline Materials, Technical Note, 2015. https://www.edax.com/resources/applications-literature?requestedmedia=/-/media/ametekedax/files/ebsd/technical_notes/ebsd%20analysis%20of%20cracking%20in%20polycrystalline%20materials.pdf&EmailRequired=yes.
39. J. Kuniya, H. Anzai, and I. Masaoka: *Corrosion*, 1992, vol. 48 (5), pp. 419–25.
40. G.S. Rohrer: *J. Mater. Sci.*, 2011, vol. 46 (18), pp. 5881–95.
41. M.A. Mohtadi-Bonab, J.A. Szpunar, R. Basu, and M. Eskandari: *Int. J. Hydrogen Energy*, 2015, vol. 40 (2), pp. 1096–1107.
42. R. Ray, J. Jonas, M. Butron-Guillen, and J. Savoie: *ISIJ Int.*, 1994, vol. 34 (12), pp. 927–42.
43. O. Engler, M.Y. Huh, and C.N. Tome: *Metall. Mater. Trans. A*, 2000, vol. 31A (9), pp. 2299–15.
44. N.S. Mourino, R. Petrov, J.H. Bae, K. Kim, and L.A.I. Kestens: *Adv. Eng. Mater.*, 2010, vol. 12 (10), pp. 973–80.
45. S. Nafisi, M.A. Arafin, L. Collins, and J. Szpunar: *Metall. Mater. Trans. A*, 2012, vol. 531A, pp. 2–11.
46. H. Kurishita, A. Oishi, H. Kubo, and H. Yoshinaga: *J. Jpn. Inst. Metals*, 1983, vol. 47, p. 546.
47. V.Y. Gertsman and S.M. Bruemmer: *Acta Mater.*, 2001, vol. 49 (9), pp. 1589–98.
48. B. Alexandreanu, B. Capell, and G.S. Was: *Mater. Sci. Eng. A*, 2001, vol. 300 (1–2), pp. 94–104.
49. D.C. Crawford and G.S. Was: *Metall. Mater. Trans. A*, 1992, vol. 23A (4), pp. 1195–1206.
50. B. Alexandreanu and G.S. Was: *Scripta Mater.*, 2006, vol. 54 (6), pp. 1047–52.
51. A. Boumaiza, T. Baudin, N. Rouag, and R. Penelle: *Chin. Phys. Lett.*, 2007, vol. 24 (6), p. 1759.

Statement of Authorship

Title of Paper	Texture Study of Stress Corrosion Cracking in Ex-Service Pipeline Steels
Publication Status	☑ Published ☐ Accepted for Publication ☐ Submitted for Publication ☐ Unpublished and Unsubmitted work written in manuscript style
Publication Details	Roccisano, A., Nafisi, S. and Ghomashchi, R., 2018. Texture Study of Stress Corrosion Cracking in Ex-Service Pipeline Steels *AISTech 2018 Proceedings*, pp.2763-2774.

Principal Author

Name of Principal Author (Candidate)	Anthony Roccisano		
Contribution to the Paper	Conducted all the experiments, analysed all the data and wrote the majority of the paper.		
Overall percentage (%)	70%		
Certification:	This paper reports on original research I conducted during the period of my Higher Degree by Research candidature and is not subject to any obligations or contractual agreements with a third party that would constrain its inclusion in this thesis. I am the primary author of this paper.		
Signature		Date	16/04/2020

Co-Author Contributions

By signing the Statement of Authorship, each author certifies that:

i. the candidate's stated contribution to the publication is accurate (as detailed above);

ii. permission is granted for the candidate in include the publication in the thesis; and

iii. the sum of all co-author contributions is equal to 100% less the candidate's stated contribution.

Name of Co-Author	Shahrooz Nafisi		
Contribution to the Paper 25%	Provided guidance and supervision from concept to submission. Assisted in the analysis of data and helped to revise the paper.		
Signature		Date	17/04/2020

Name of Co-Author	Reza Ghomashchi		
Contribution to the Paper 5%	Provided guidance and supervision from concept to submission and helped to revise the paper.		
Signature		Date	16/04/2020

Please cut and paste additional co-author panels here as required.

Texture Study of Stress Corrosion Cracking in Ex-Service Pipeline Steels

A. Roccisano[1*], S. Nafisi[1, 2], R. Ghomashchi[1]

[1] The University of Adelaide, Adelaide, South Australia, 5005, Australia
Email: a.roccisano@adelaide.edu.au

[2] University of Alberta, Edmonton, Alberta, T6G 1H9, Canada

Keywords: Ex-service, Pipeline, SCC, Texture, EBSD, X42, X65

ABSTRACT

Stress Corrosion Cracking (SCC) is a particularly insidious form of environmentally induced cracking which affects a wide range of gas pipelines around the world. Samples of API 5L X42 and X65 ex-service pipes containing SCC were analyzed using Electron BackScatter Diffraction (EBSD) techniques to investigate the crack behavior between these two grades. The results showed that cracks primarily propagated between High Angle Boundaries (HAB's) and a high density of Low Angle Boundaries (LAB's) was important for crack resistance. There was no evidence that a greater density of Coincidence Site Lattice (CSL) boundaries increased resistance to SCC but certain CSL boundaries may be more resistant than others. An in-depth study of cracked grains showed a greater concentration of {100}//RP (Rolling Plane) texture while uncracked areas had a greater overall concentration of {111}//RP and {110}//RP textures.

INTRODUCTION

Whilst the risk of Stress Corrosion Cracking (SCC) has long been a concern in the pipeline industry, uncertainty remains over the exact mechanism by which cracks propagate in widely used pipe grades. SCC is a form of environmentally induced cracking which requires 3 main components, i.e. a tensile or residual stress, corrosive environment, and a susceptible material to be in place simultaneously to occur [1, 2]. Pipeline steels tend to be in the ideal environment for SCC to occur as the cathodic protection applied to the pipe can, in exposed pipe, create the corrosive environment necessary for SCC to occur. The cathodic protection system creates a high pH solution at the pipe surface which absorbs CO_2 dissolved in the soil to form the carbonate and bicarbonate ions, which are necessary for SCC to occur [3-5]. Solutions with a pH of between 9-11 cause the intergranular, high pH form of SCC, whereas a lower pH of between 5.5-7.5 tends to encourage the transgranular, near neutral form of SCC to occur [6]. In high pH SCC, the crack propagates through periodic anodic dissolution at the crack tip which occurs from the tensile stress fracturing the protective oxide layer, formed by the cathodic protection, and allowing anodic dissolution to corrode the exposed grain boundary before the cathodic protection system can reform the oxide at the crack tip [7].

There has been a small number of investigations available in the open literature for identifying the effect crystallographic texture has on SCC in pipeline steels [8-11]. Based on studies available, it has been identified that cracks are more likely to progress through High Angle Boundaries (HAB's) with a misorientation $\theta>15°$ as expected for an intergranular phenomenon. It was found that when cracking occurred in grains with similar angular misorientation, there was a greater tendency for cracks to pass between grains which had {100} <110> orientations [8, 10, 12]. In addition, there is some evidence that grains with orientations belonging to the γ-fiber {111}//RP (Rolling Plane) and {110}//RP fiber are more resistant than randomly oriented grains which would stall crack growth [8-10, 12]. It was found that Σ11 and Σ13b Coincidence Site Lattice (CSL) boundaries were present in higher concentrations at crack tip regions and crack arrest points which is proposed to be because those boundaries provide increased resistance to SCC [8, 9, 13]. The previously identified studies have only considered X65 steels, there has been no studies carried out on other pipe grades. In addition, there was a limited number of cracks investigated so it is unclear whether the results are universal or not [8-10].

The aim of this study is to investigate the SCC cracking behavior of X42 and X65 pipes to determine whether the cracking behavior is the same between grades. In addition, this paper seeks to explore the options available for analyzing cracks in Electron BackScatter Diffraction (EBSD) datasets and the methodology to isolate the relevant grain boundaries.

EXPERIMENTAL PROCEDURE

The investigation of SCC in pipeline steels was carried out to determine the impact of crystallographic texture on stress corrosion cracking. Samples of API 5L X42 and X65 ex-service pipes containing SCC were examined [14]. The X42, with chemistry shown in Table 1, was extracted from the field after 39 years of operation when it was found to contain SCC. The pipe has a nominal wall thickness of 4.4 mm, a nominal pipe diameter of 168 mm and was manufactured by ERW process (Electrical Resistance Welding) [15]. The X65 with chemistry also shown in Table 1 was extracted from the field after approximately 30 years of service. The pipe has a nominal wall thickness of 8.3 mm and a nominal pipe diameter of 864 mm [10] which was manufactured by "UOE" process (U'ing and O'ing formed pipe) [16]. Both pipes were coated and connected to a cathodic protection system. The X65 was coated over the ditch with coal tar enamel and the X42 was coated with a PVC tape wrap.

Samples of SCC cracks in both X42 and X65 were sectioned along the TD-ND plane in the manner viewed in Figure 1 and prepared for EBSD analysis. EBSD was carried out on an FEI Inspect F50 Scanning Electron Microscope (SEM) equipped with EDAX Hikari EBSD detector and OIM 7.3 collection software. Each sample was analyzed at 25 keV with a spot size of 5 and an aperture of 50 µm. The scan frame size in all X42 and X65 samples was 435x435 µm with a step size of 0.5 µm.

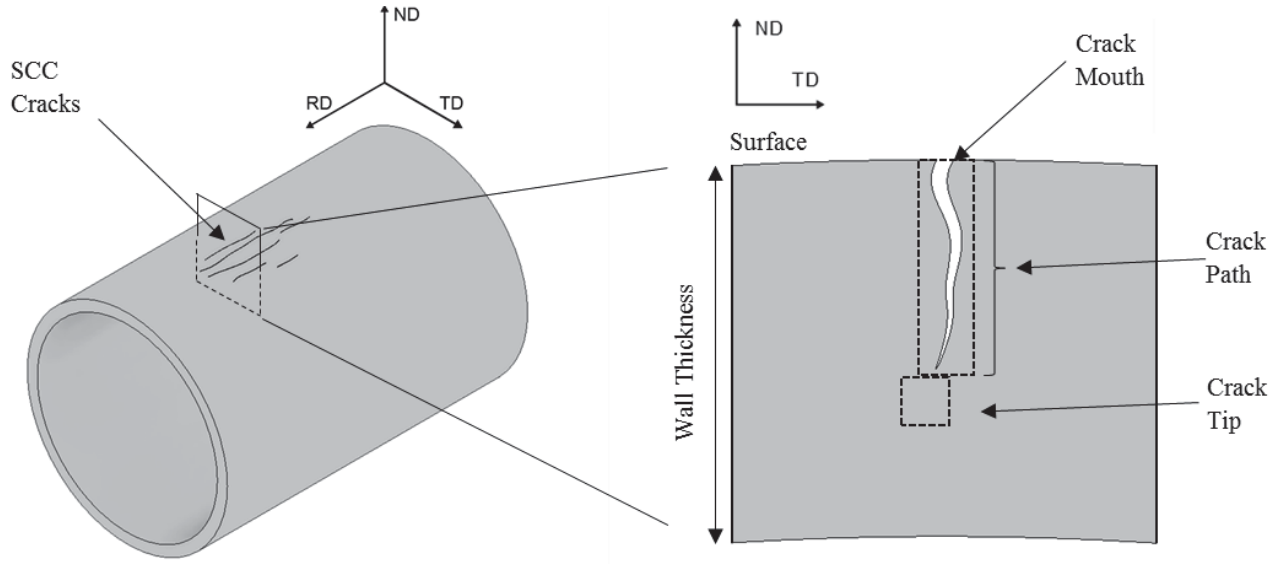

(a) (b)

Figure 1: (a) typical orientation of SCC cracks in pipelines, (b) crack path nomenclature (ND: Normal Direction, RD: Rolling Direction and TD: Transverse Direction)

Table 1. Chemical Compositions of pipe samples (wt%)

	C	Mn	Si	Ni	Cu	Al	Mo	V	Nb	Ti	Cr	P	S	N
X42	0.21	1.34	0.20	0.015	0.012	0.003	0.004	0.002	0.004	0.0008	0.03	0.015	0.017	0.0058
X65	0.09	1.40	0.28	0.025	0.18	0.025	0.007	0.003	0.045	0.002	0.27	0.015	0.005	0.0091

RESULTS AND DISCUSSION

Characterization of Pipes

Optical micrographs of the pipelines taken from the quarter thickness plane sectioned transverse to the rolling direction are presented in Figure 2. The X42 contains a mixture of polygonal ferrite (PF) with degenerate pearlite (DP). The X65 contains a finer grain structure of polygonal ferrite and pearlite (P) with banding present in the center plane. The volume fraction of pearlite in the X65 is less than that in the X42 which is expected from the lower carbon content as compared to the X42 pipe. Grain size was also measured at quarter thickness based on EBSD analyses. In both samples, the grain size distribution curves

were normally distributed (i.e. no bimodal distribution). It was calculated that over 80% of grain size was populated between 5-30 microns and 0-15 microns in X42 and X65 respectively. The difference in grain size also contributes to the microstructure in X65 being harder to resolve with the comparatively low magnification of optical microscopy.

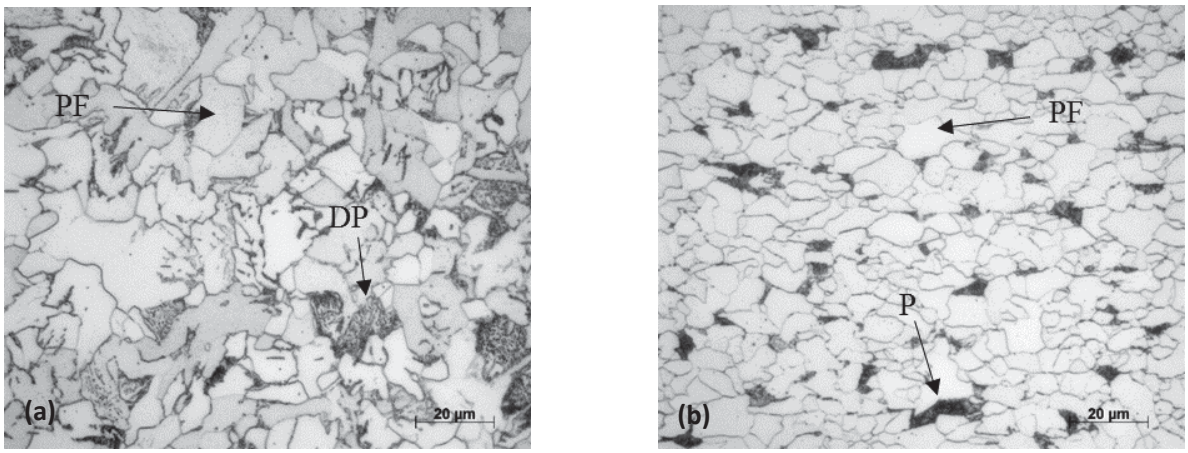

Figure 2: Optical micrographs taken from quarter thickness in (a) X42 and (b) X65
(PF: polygonal ferrite, P: pearlite, DP: degenerate pearlite)

Figure 3 shows SEM images of the X42 and X65 pearlitic structures taken from transverse sections at the quarter thickness with the pearlite colony clearly visible. The cementite lamellae of pearlite colony in the X42 appear to be broken in the center of the image with some intact lamella present at the edge of the grain. In contrast, the pearlitic cementite lamella in the X65 appear to be intact and are much finer than those seen in the X42 which accounts for the higher magnification necessary in the X65 image.

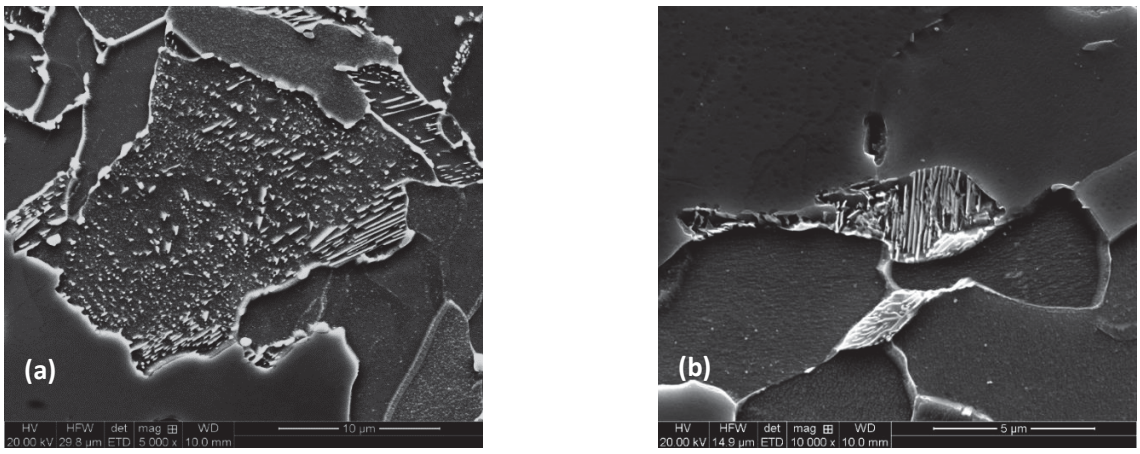

Figure 3: SE images taken from the quarter thickness (a) X42 and (b) X65

Presentation of SCC

SCC in pipelines is caused by the interaction of three components; a corrosive environment, an applied or residual tensile stress and a susceptible material [1, 2]. SCC cracks grow from the outer surface of the pipe towards the inner surface in the direction specified in Figure 1a. Stress is at a maximum from the internal pressure along the transverse direction and as a result, causes cracks to grow parallel to the rolling direction. Cracks often grow outside the Heat Affected Zone (HAZ) of seam welds in pipes due to a combination of increased hardness, residual stress, and difference in chemical composition caused by the interaction of the parent material and the weld [17, 18]. In the case of the samples analyzed, SCC in the X42 occurred in the parent material just outside the HAZ of the seam weld and the SCC in X65 occurred in the parent material far from the weld seam.

The SCC cracks investigated in both X42 and X65 were of significant length (>10% of wall thickness) and four cracks were chosen for EBSD analysis. The others were used for optical and SEM characterization of the crack paths. The typical shapes of the cracks are shown in Figure 4 where a distinct difference between the cracks in X42 and X65 is observed. The X42 cracks

tend to grow perpendicular to the pipe surface with minimal branching, whilst the X65 grows straight for about 500 µm before inclining. The difference in the shape of the crack is believed to be the result of the differences in manufacturing process, operating conditions (e.g. pressure) and residual stresses in the X42 and X65 pipes [15, 19].

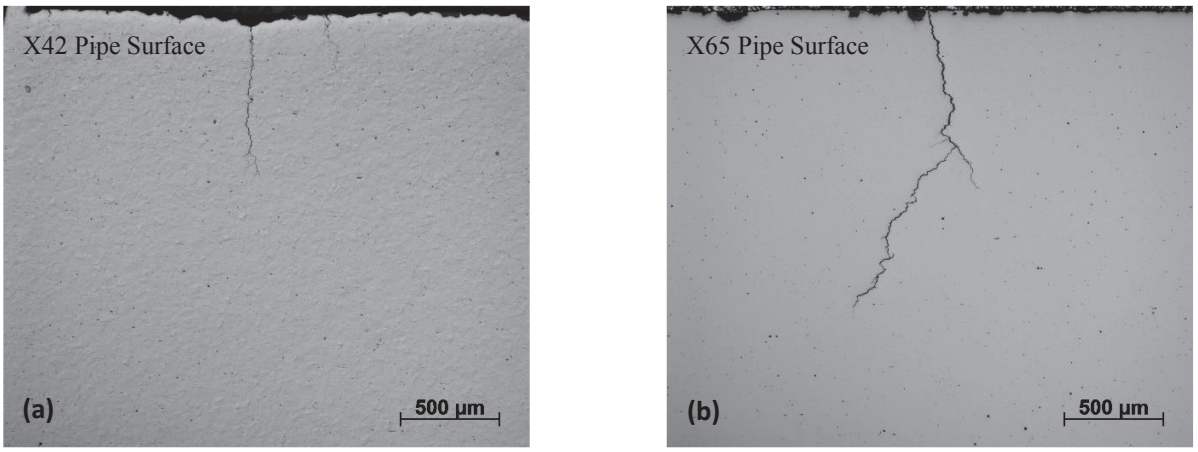

Figure 4: Optical unetched images of SCC cracks in (a) X42 and (b) X65

It was initially expected that the crack path would be exclusively intergranular due to the irregular path it took towards the inner wall of the pipe and the thin crack width. Upon etching, it was found that most of the cracking was indeed intergranular in nature, however, some instances of transgranular crack propagation was observed along the crack path in both X42 and X65. An instance of intergranular and transgranular crack propagation is shown in Figure 5 where there is intergranular cracking near the crack tip of the X42 seen in Figure 5a whilst the crack tip shows transgranular cracking in an X65 sample in Figure 5b. Instances of transgranular cracking in a high pH environment is not fully understood currently and it unlikely to be the result of a change in pH forcing the crack mechanism to favor transgranular propagation but possibly another fracture mechanism.

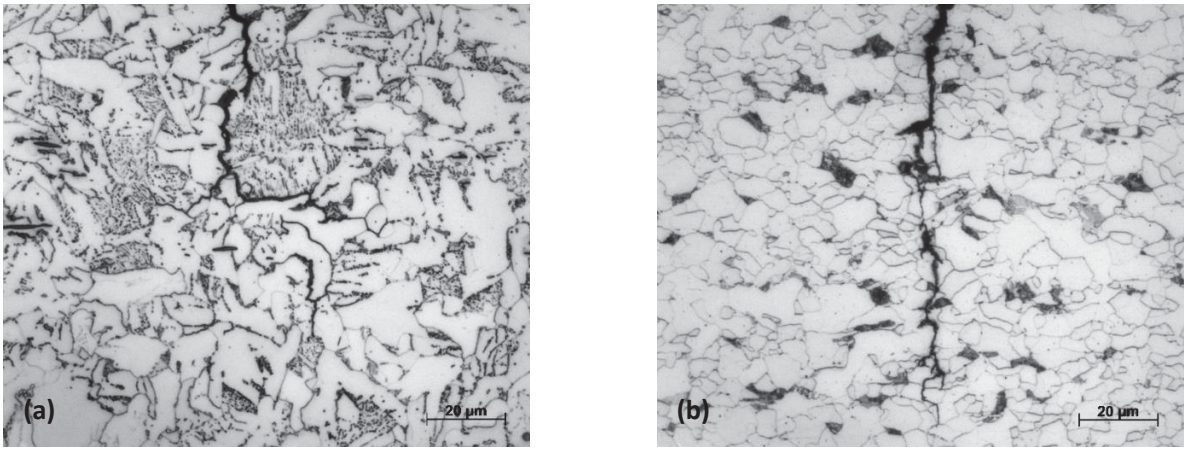

Figure 5: Etched images of the crack path in (a) X42 showing intergranular cracking near the crack tip and (b) X65 showing transgranular cracking near the crack tip

It was investigated whether transgranular cracking occurred at a greater rate in pearlite or ferrite with the hypothesis that pearlites lamellar cementite structure offered lower resistance than grain boundaries when the crack tip encountered them. Whilst there has been observation that intergranular cracks will preferentially turn transgranular when encountering pearlite colonies in X52 grade pearlitic/ ferritic steels [20], this phenomenon was not witnessed in the X42 and X65 presented. Although transgranular cracking was observed through pearlite colonies in X65, transgranular cracking was also observed in ferrite so the transgranular cracking behavior is not necessarily related to the presence of pearlite colonies. This can be seen in Figure 6b where the crack has sheared through a pearlite grain in the top right corner in the same region that ferrite grains were also cracked. There was no transgranular cracking through pearlite grains identified in X42 and as seen in Figure 6a, the crack preserved an intergranular character when encountering pearlite grains. The exact cause of the transgranular propagation is an

area of continued interest with the crystallographic texture being considered a potential method to determine the cause but is not the overall aim of this study.

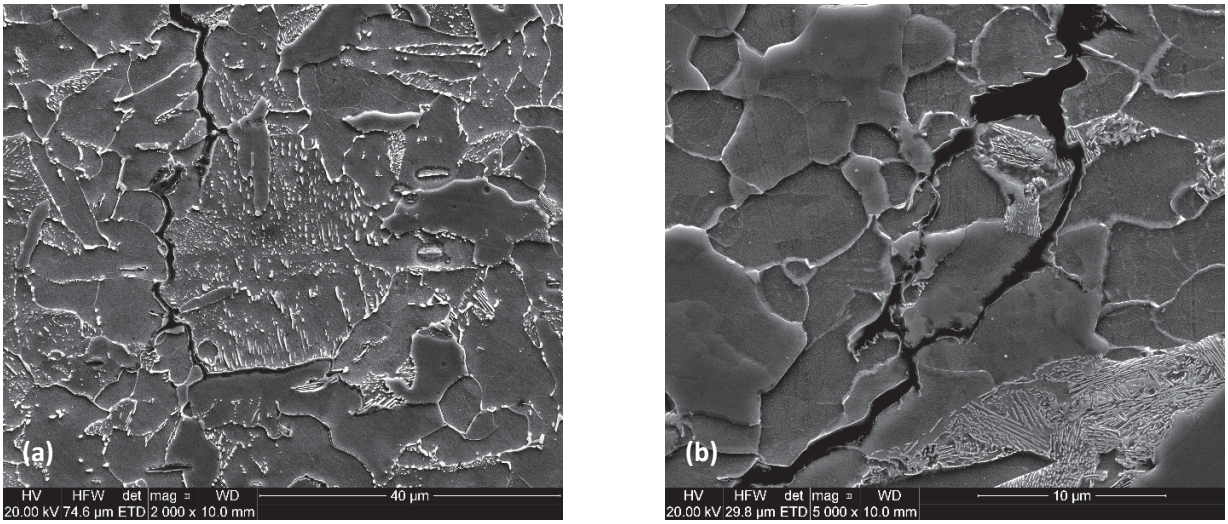

Figure 6: Examples of crack propagation surrounding pearlite with
(a) intergranular propagation around the pearlite in X42 and (b) transgranular propagation in X65.

Crystallographic Texture

As already detailed in literature, microtexture can play a significant role in the crack behavior observed in pipeline steels [8-10]. As there has been no clear explanation and methodology in open literature to date, there was significant study by the authors to isolate the properties of the material which contributed to crack propagation.

The investigated cracks were split up into discreet sections and were scanned at regular intervals from the crack mouth to the crack tip (see Figure 1). The scan areas were 435x435 µm which encompassed the crack as well as a large amount of surrounding, i.e. unaffected grains. Initially, entire scan areas were investigated, and the texture was output in the form of an Orientation Distribution Function (ODF) plot (in Bunge notation). These initial results were unsuitable as they included a larger portion of unaffected grains than cracked ones which served to dilute the influence of susceptible textures. To separate the unaffected grains from the cracked grains, the scan areas were cropped such that only grains which were directly bordering the crack were included for analysis, the result of which can be seen in Figure 7 as an example.

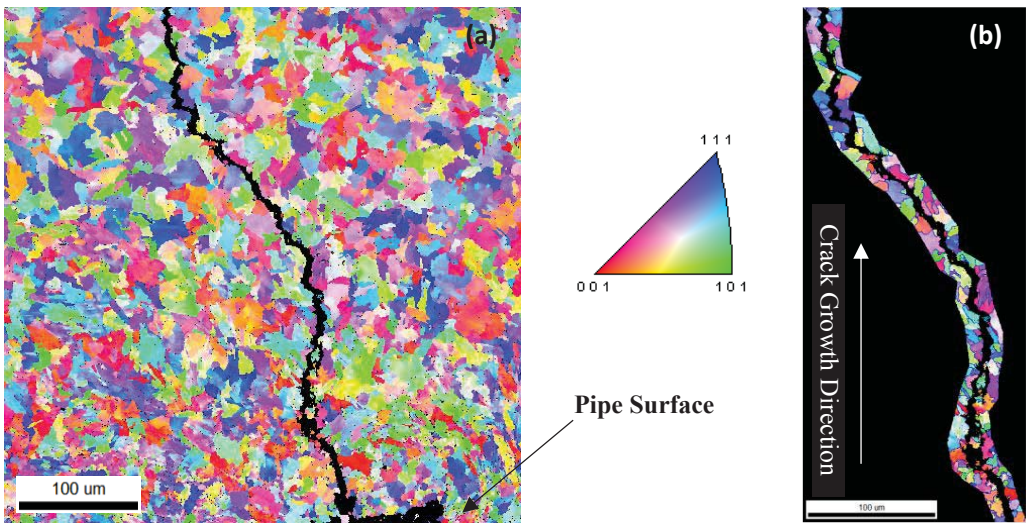

Figure 7: (a) Original scan area Inverse Pole Figure (IPF) and (b) cropped scan area to isolate only the affected grains
Note: The crack is upside down due to the coordinate system in the SEM

The result of filtering unnecessary information was the development of a plot which displayed only the textures associated with cracked grains. An example is shown in Figure 8 where maps (a) and (c) display the weak texture of the overall structure whereas (b) and (d) show the sharper, more specific texture surrounding the cracks in both X42 and X65. The difference in the textures between the X42 and X65 samples could be due to many reasons including the rolling schedule and cooling rate.

Limited literature suggests that there is a greater tendency for cracks to pass through {100}//RP textured grains whilst {110}//RP and {111}//RP textured grains tended to have better resistance to SCC [8, 10, 12]. As seen in Figure 8b, along the crack path, there is a strong texture along the {100}//RP fiber compared to the overall section texture in Figure 8a. There also appears to be a higher concentration of texture along the {112}//RP fiber and along the α fiber (φ_1=0°, ϕ=0-90°). In Figure 8d, there appears to be a small increase of texture along the {100}//RP fiber as compared to the texture seen in Figure 8c. There is also a higher proportion along the {112}//RP fiber but minimal change in concentration of the {111}//RP fiber. Literature reports {100}//RP being a susceptible texture in X65 [8, 9], and based on results from Figures 8b and 8d, the cracked sections have a moderate amount of this texture. There is a dramatic sharpening of texture when comparing the overall section to the cropped area and it would appear that cropping around the crack is a valid method to analyze texture dependency of SCC.

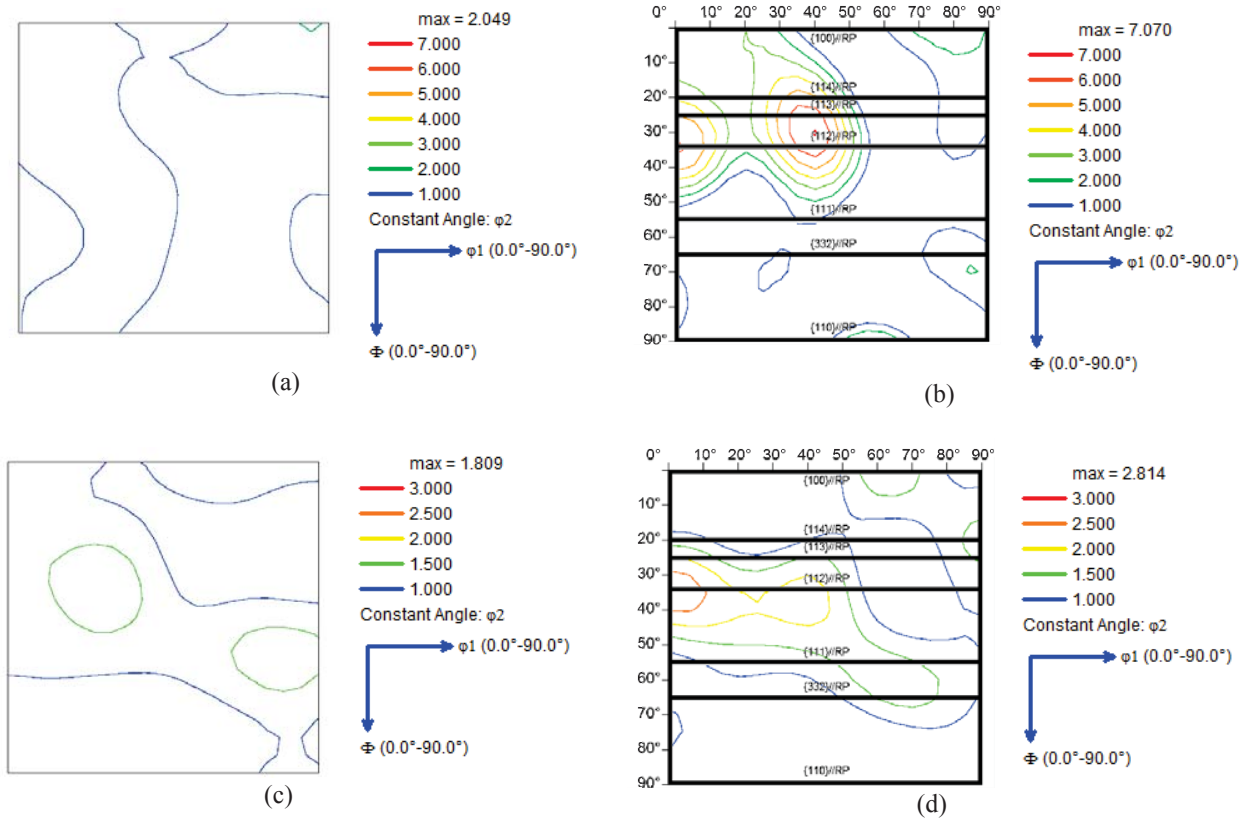

Figure 8: ODF φ_2=45° of cracked sample in (a) X42 overall area around the crack path, (b) X42 surrounding only the crack path, (c) X65 overall area around the crack path, (d) X65 surrounding only the crack path

As reported elsewhere [8], the crack tip area immediately ahead of the crack path is expected to contain a high proportion of {110}//RP and {111}//RP textured grains which are thought to halt the progression of SCC. Two crack tip regions ahead of an X42 and X65 cracks were investigated and displayed as examples in Figure 9. In Figure 9a, the crack tip region ahead of the X42 crack shows a low proportion of {100}//RP and {112}//RP textures in addition to a high concentration of {111}//RP and {332}//RP textures. The crack tip ahead of the X65 crack in Figure 9b shows the highest concentration of texture between the {111}//RP and {112}//RP texture fibers. There is a comparatively lower concentration of {100}//RP textures and no discernable concentration of texture along the {110}//RP fiber. Comparing these results to the literature [8, 9], it is evident that the investigated samples of X42 and X65 show a high concentration of {111}//RP fibers which may be responsible for halting the cracks progression in these samples.

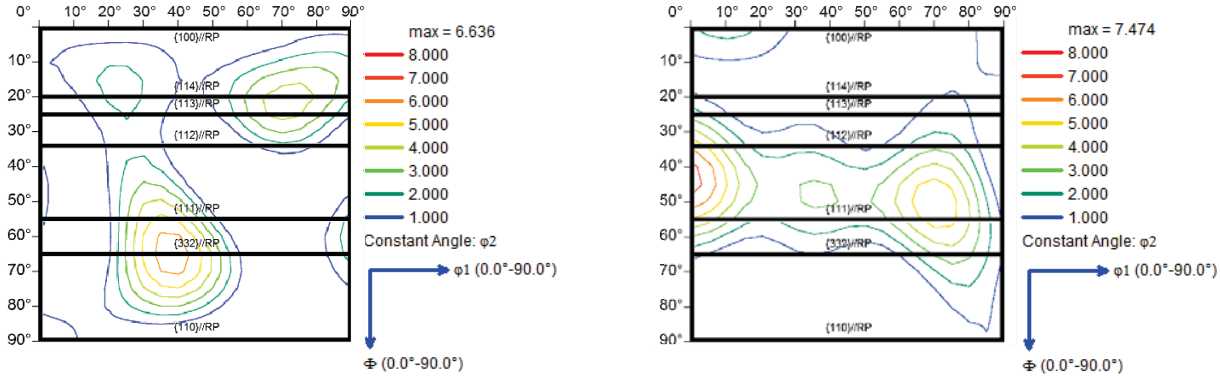

(a) (b)

Figure 9: ODF φ_2=45° of cracked sample at the crack tip area immediately ahead of the cracks in (a) X42, (b) X65

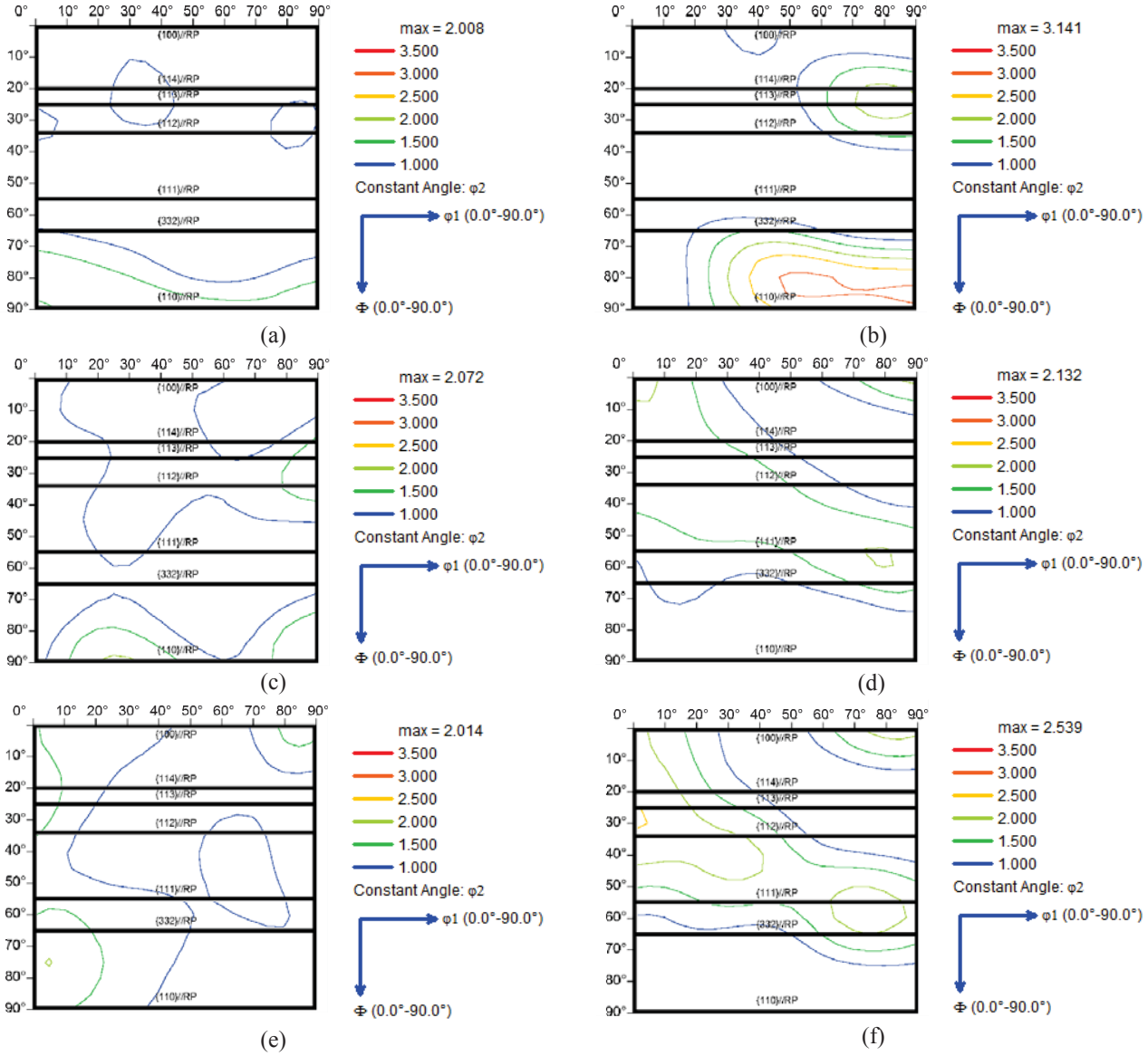

(a) (b) (c) (d) (e) (f)

Figure 10: ODF φ_2=45° of uncracked samples in X42 and X65 (a) X42 surface, (b) X65 surface, (c) X42 quarter thickness, (d) X65 quarter thickness, (e) X42 center, (f) X65 center

In addition to texture examinations of the cracks and cracks' tips, the microtexture of uncracked regions (i.e. far from cracked areas) was investigated to determine what textures are present in uncracked areas as well as to investigate the change in texture through thickness. Each pipe was scanned at three depths, 400 µm below the surface, quarter of the pipe thickness, and at the centerline with the texture at each region identified. It has been reported in the open literature that a high proportion of {110}//RP macrotexture at the surface enhances crack prevention [10, 12]. Based on Figures 10a and 10b, both uncracked surfaces contain a relatively high proportion of texture along the {110}//RP fiber which agrees with literature. The change in through thickness texture appears to be a function of the pipe thickness. The through thickness texture in X65 seems to have a strong {110}//RP fiber texture at the surface and a strengthening {111}//RP fiber texture as it progresses into the center plane to be more typical of texture evolution found in hot rolled steels which are finished at relatively low temperatures. The X42 seems to have a far weaker overall texture which seems more typical of steels finish rolled at high temperatures where recrystallization can have a large effect on texture [21-23].

Grain Misorientation

As indicated in the introduction, high pH SCC propagates through a primarily intergranular cracking mechanism. It is inferred that cracks will tend to propagate between HAB's due to their higher energy state compared to that of LAB's and CSL boundaries [8]. To examine if this was the case in the X42 and X65 pipe samples, a survey of misorientations around the crack path was undertaken.

Initial results aimed to carry out a measurement of every misorientation present in the area around the crack path, but due to a high proportion of LAB's within grains away from the crack path, the results were artificially skewed to incorrectly report a large proportion of LABs. As a solution, an interactive method of grain misorientation was undertaken which allowed for grains across the crack and grains along the crack to be analyzed; a schematic diagram of which can be found in Figure 11.

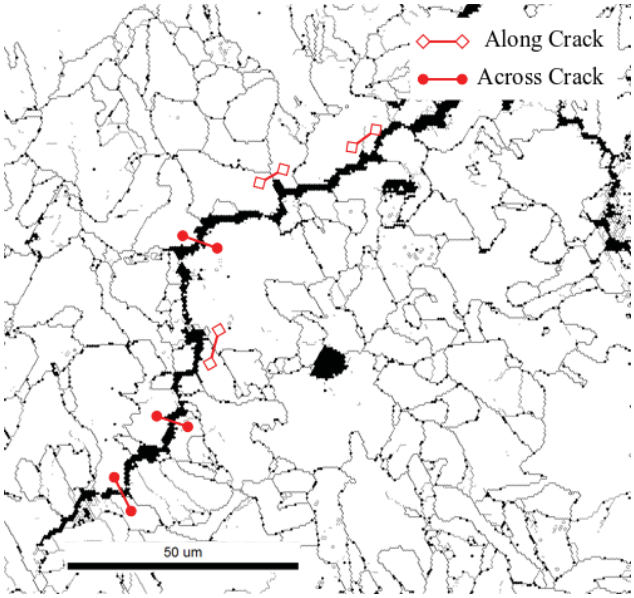

Figure 11: Schematic diagram of interactive misorientation investigation along and across cracked grains showing the manual interactive grain selection

Results of the aforementioned logic are presented in Figure 12. In both samples, there was a significantly greater proportion of HAB's present across the cracked boundaries and both samples showed a greater proportion of LAB's in the crack tip area. The fraction of CSL boundaries remained relatively constant along and across the crack path, and the crack tip. The results conform to literature in that the cracks in both X42 and X65 seemed to propagate preferentially through high angle grain boundaries [8]. Additionally, the uncracked sections (along the crack and the crack tip) contained a greater proportion of LAB's compared to across the crack. Based on Figure 12, it does not appear there is a greater proportion of CSL boundaries present in uncracked sections when compared to the cracked grain boundaries which was contrary to the literature which reported a high proportion of CSL boundaries was present in crack arrest areas as compared to cracked regions [8, 13].

It was determined in the open literature for Hydrogen Induced Cracking (HIC), there was a distinct difference in the CSL boundaries found between cracked and uncracked grains [13]. Similarly, in SCC studies, it was reported a strong preference

for Σ11 and Σ13b CSL boundaries in the crack tip area [8, 9]. Based on Figure 12, it does not appear there is a greater proportion of CSL boundaries present in uncracked sections when compared to the cracked grain boundaries which is contrary to the existing literature which showed a high proportion of CSL boundaries in crack arrest areas [8, 9, 13]. This does not necessarily mean CSL boundaries are not resistant but it would appear they are not the primary crack arresting feature in the X42 and X65 examined.

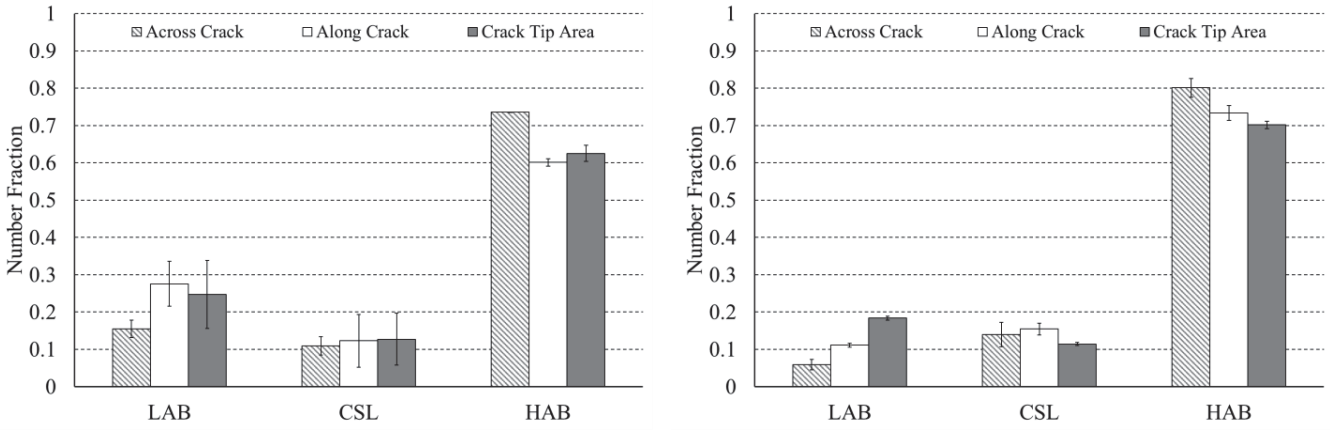

Figure 12: Grain boundary fraction of LAB's, CSL's and HAB's in sample of (a) X42 and (b) X65 across crack, along crack, and crack tip areas

Interactive Crack Path

To clarify the role of grain boundaries on the cracking behavior, EBSD IQ (Image Quality) maps were generated from two crack branches in X42 and X65 (Figure 13). The grains bordering the cracks were numbered and the angular misorientation between them was calculated to determine the misorientation between grains the crack passed through and those it did not. In both cases, the crack is primarily intergranular in nature with transgranular instances labeled in Figures 13c and 13d.

In Figure 13a, the X42 crack propagated almost entirely intergranually with the exception of grains such as 6 and 14 which were transgranular cracks (see grain map in Figure 13c). As seen in Figure 13a, there are three branched cracks growing from the main crack starting through grains 2-6a, 14a-18 and 18-21. These branched cracks are growing in the same direction towards a large, alumina-manganese sulfide inclusion. The inclusion seems to act as a stress concentrator which draws the cracks towards it. When analyzing the crack path, it was of interest to observe the crack behavior at triple junctions where the crack could grow equally through two paths. The first triple junction occurs after the crack propagated between grains 4-12 (27.9°). The crack could have propagated between either grains 11-12 (58.8°) or 4-11 (48.8°) but propagated through the boundary with greater misorientation 11-12 shown in Figure 13e. The next triple junction occurs after the crack propagates between grains 14b-18 (51.9°). The crack could have either propagated between grains 14b-19 (42.1°) but instead propagated through grain 18-19 (55.6°) which had the greater misorientation. The final triple junction occurs when the crack could propagate between grains 19-20 (48.9°) or 18-20 (17.3°). While it was thought the crack would pass through grain 19-20 which had the greater misorientation, the crack traveled between grains 18-20 shown in Figure 13e. This could be due to grain boundary 19-20 being a CSL Σ11 boundary which has been shown in literature to be somewhat resistant to cracking [8, 9]. It would appear that the main crack is halted once it propagated through grains 20-21 (56.1°). Grain 20 was found to be {111}//RP textured and grain 21 was found to be {110}//RP textured which would imply the crack progression was possibly halted due to the texture of these grains.

In Figure 13b, the X65 crack was generally an intergranular crack with two instances of transgranular cracking through grains 12 and 20 shown in Figure 13d. There are not any inclusions visible in this cracked section and X65 sample has a finer grain size as described earlier. It was of interest to investigate the crack path to determine the cracking behavior when the crack reached triple junctions. The first instance of a triple junction occurred after the transgranular propagation through grain 12 where the crack could have propagated between grains 13-14 (36.1°) or grains 12a-14 (36.7°) shown in Figure 13f. In this case, the grain misorientation between the two boundaries were almost identical with the crack grew through boundary 12a-14 potentially due to grain 13 being {110}//RP oriented. The next triple junction occurred when the crack encountered grains 14-16 (42.7°) and 15-16 (49.2°) shown in Figure 13f. In this case, the crack began to grow between grains 15-16 but it appeared to halt and instead propagated between grains 14-16. The main difference between the two grains was that grain 15 was {110}//RP textured which could have stalled crack growth through boundary 15-16. After the crack propagated between grains

21-22 (56.9°), it seems to diverge around grain 23 before the crack growth halts (note that the crack arrest is assumed based on the 2D polished section). It is not clear why the crack halted as grain 23 is {100}//RP textured and grain boundaries 21-23 (45.9°) and 22-23 (31.8°) were both susceptible high angle boundaries.

Based on initial interactive crack path investigation, when the crack is faced with two grain boundaries at a similar orientation to the crack growth direction, the crack generally will pass through the grain boundary which has the greater misorientation. In the event the crack avoids the boundary with higher misorientation, it appears grains with orientations {110}//RP and {111}//RP and potentially Σ11 boundaries may resist cracking.

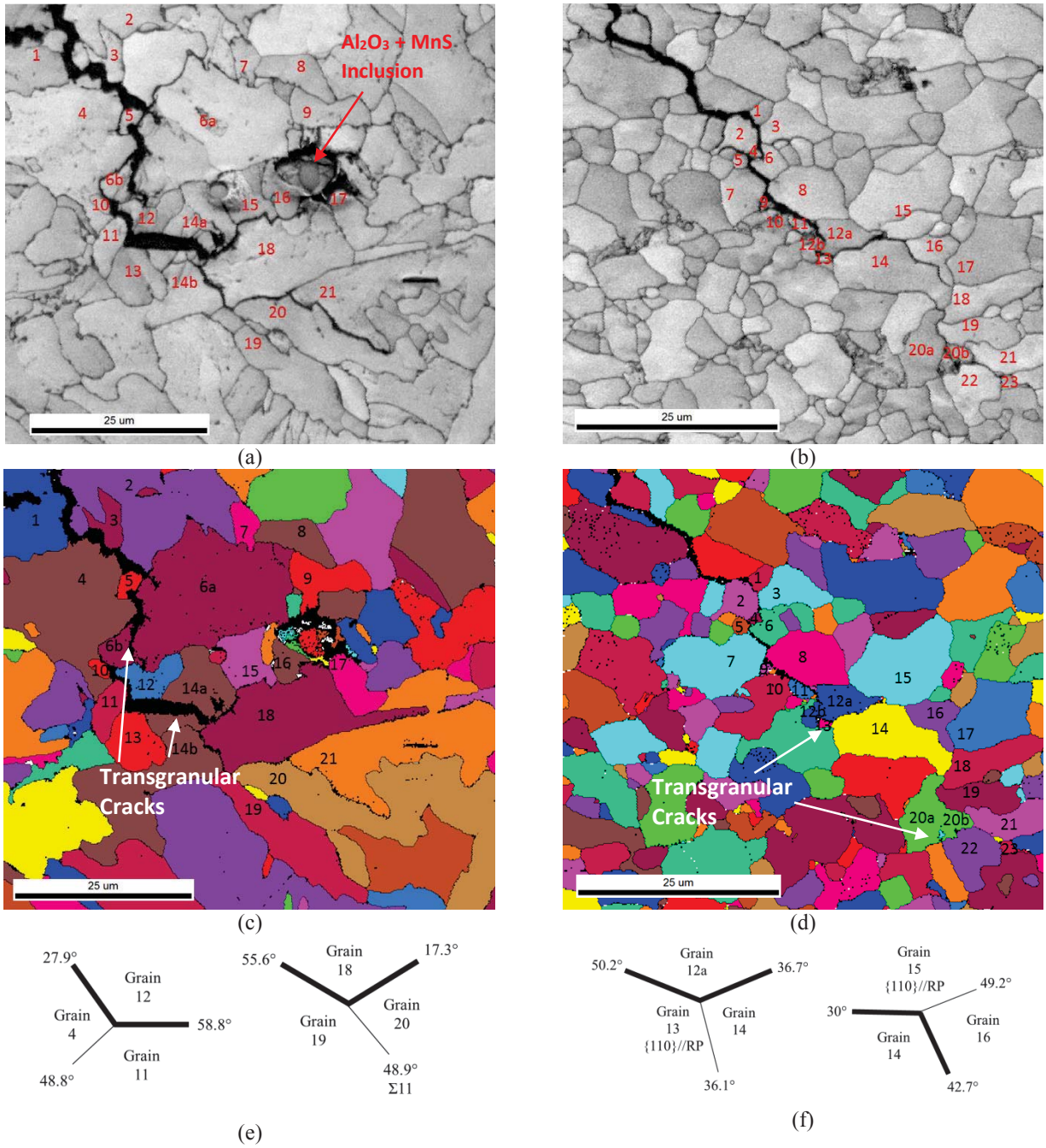

Figure 13: (a) IQ crack image in X42 (b) IQ crack image in X65, (c) grain map of crack in X42 and (d) grain map of crack in X65

CONCLUSIONS

Two sections of API X42 pipe (39 years in service, 4.4 mm wall thickness, 168 mm OD, ERW) and API X65 pipe (30 years in service, 8.3 mm wall thickness, 864 mm OD, UOE) with SCC were characterized via optical and electron microscopy followed by EBSD and texture analyses. Preliminary investigation showed that in both X42 and X65 steels, SCC was a primarily intergranular cracking mechanism. The cracks tended to follow HAB's and were halted by LAB's but there was no evidence that increased concentration of CSL boundaries in general increased resistance to SCC.

In terms of texture analysis, it was found that generally {100}//RP textures are susceptible to cracking in both X42 and X65. While {112}//RP textures are present in high concentrations around cracks, they are also present in uncracked pipe sections; further study is necessary before being able to conclude on their impact. In the uncracked regions of pipes, it was found that there was a greater proportion of {111}//RP and {110}//RP textures present as compared to cracked sections in both pipe samples.

Preliminary results from this investigation indicated that increasing the proportion of LAB's and a greater proportion of {111}//RP and {110}//RP textures through the pipe as well as reducing the amount of {100}//RP textures can lead to increased resistance to SCC in both pipes.

ACKNOWLEDGMENTS

This work was funded by the Energy Pipelines CRC, supported through the Australian Government's Cooperative Research Centers Program. The funding and in-kind support from the APGA RSC is gratefully acknowledged. The authors also acknowledge the facilities, and the scientific and technical assistance, of the Australian Microscopy & Microanalysis Research Facilities at the University of Adelaide and Flinders University. The Authors would like to acknowledge the support of Dr. Erwin Gamboa of TransCanada (former lecturer at The University of Adelaide) and the technical assistance of the application engineers at EDAX especially Matt Nowell.

REFERENCES

1. R.N. Parkins. "A review of stress corrosion cracking of high pressure gas pipelines". in *CORROSION 2000*. 2000. NACE International.
2. A. King, G. Johnson, D. Engelberg, W. Ludwig, and J. Marrow, "Observations of intergranular stress corrosion cracking in a grain-mapped polycrystal". *Science*, 2008. 321(5887): p. 382-385.
3. J. Sutcliffe, R. Fessler, W. Boyd, and R. Parkins, "Stress corrosion cracking of carbon steel in carbonate solutions". *Corrosion*, 1972. 28(8): p. 313-320.
4. J.A. Beavers and B.A. Harle, "Mechanisms of high-pH and near-neutral-pH SCC of underground pipelines". *Journal of Offshore Mechanics and Arctic Engineering-Transactions of the Asme*, 2001. 123(3): p. 147-151.
5. B. Fang, A. Atrens, J. Wang, E.-H. Han, Z. Zhu, and W. Ke, "Review of stress corrosion cracking of pipeline steels in "low" and "high" pH solutions". *Journal of materials science*, 2003. 38(1): p. 127-132.
6. J.G. Gonzalez-Rodriguez, M. Casales, V.M. Salinas-Bravo, J.L. Albarran, and L. Martinez, "Effect of Microstructure on the stress corrosion cracking of X-80 pipeline steel in diluted sodium bicarbonate solutions". *Corrosion*, 2002. 58(7): p. 584-590.
7. R. Parkins. "The controlling parameters in stress corrosion cracking". in *5th Symp. Line Pipe Research L*. 1974.
8. M.A. Arafin and J.A. Szpunar, "A new understanding of intergranular stress corrosion cracking resistance of pipeline steel through grain boundary character and crystallographic texture studies". *Corrosion Science*, 2009. 51(1): p. 119-128.
9. M.A. Arafin and J.A. Szpunar. "Grain Boundary Engineering to Control the Intergranular Stress Corrosion Cracking of Pipeline Steel". in *ICF12, Ottawa 2009*. 2013.
10. O. Lavigne, E. Gamboa, W. Costin, M. Law, V. Luzin, and V. Linton, "Microstructural and mechanical factors influencing high pH stress corrosion cracking susceptibility of low carbon line pipe steel". *Engineering Failure Analysis*, 2014. 45: p. 283-291.
11. Y.A. Perlovich, M. Isaenkova, O. Krymskaya, N. Morozov, F. Chinesta, E. Cueto, and E. Abisset-Chavanne. "Layer texture of hot-rolled BCC metals and its significance for stress-corrosion cracking of main gas pipelines". in *AIP Conference Proceedings*. 2016. AIP Publishing.
12. Y. Perlovich, O. Krymskaya, M. Isaenkova, N. Morozov, I. Ryakhovskikh, and T. Esiev. "Effect of Layer-by-Layer Texture Inhomogeneity on the Stress Corrosion of Gas Steel Tubes". in *Materials Science Forum*. 2017. Trans Tech Publ.
13. V.C. Venegas, F. Hallen, J. M. Baudin, T. Penelle, R., "Role of crystallographic texture in hydrogen-induced cracking of low carbon steels for sour service piping". *Metallurgical and Materials Transactions a-Physical Metallurgy and Materials Science*, 2007. 38A(5): p. 1022-1031.

14. American Petroleum Institute: Specification for Line Pipe, API SPECIFICATION 5L, API, USA, (2013).
15. O. Lavigne, E. Gamboa, V. Luzin, and M. Law, "Analysis of intergranular stress corrosion crack paths in gas pipeline steels; straight or inclined?". *Engineering Failure Analysis*, 2018. 85: p. 26-35.
16. M.D. Herynk, S. Kyriakides, A. Onoufriou, and H.D. Yun, "Effects of the UOE/UOC pipe manufacturing processes on pipe collapse pressure". *International Journal of Mechanical Sciences*, 2007. 49(5): p. 533-553.
17. M. Baker Jr, "Inc., Stress Corrosion Cracking Studies–Final Report, DOT-Research and Special Programs Administration, Office of Pipeline Safety". 2005, Technical Report No. TTO-8.
18. B. Lu, J.-L. Luo, and D.G. Ivey, "Near-Neutral pH Stress Corrosion Cracking Susceptibility of Plastically Prestrained X70 Steel Weldment". *Metallurgical and Materials Transactions A*, 2010. 41(10): p. 2538-2547.
19. J. Griggs, E. Gamboa, and O. Lavigne, "2D modelling of inclined intergranular stress corrosion crack paths". *Fatigue & Fracture of Engineering Materials & Structures*, 2017. 40(4): p. 543-555.
20. J. Li, M. Elboujdaini, B. Fang, R. Revie, and M.W. Phaneuf, "Microscopy study of intergranular stress corrosion cracking of X-52 line pipe steel". *Corrosion*, 2006. 62(4): p. 316-322.
21. O. Engler, M.Y. Huh, and C.N. Tome, "A study of through-thickness texture gradients in rolled sheets". *Metallurgical and Materials Transactions a-Physical Metallurgy and Materials Science*, 2000. 31(9): p. 2299-2315.
22. R. Ray, J. Jonas, M. Butron-Guillen, and J. Savoie, "Transformation textures in steels". *ISIJ International*, 1994. 34(12): p. 927-942.
23. S. Nafisi, M.A. Arafin, L. Collins, and J. Szpunar, "Texture and mechanical properties of API X100 steel manufactured under various thermomechanical cycles". *Materials Science and Engineering a-Structural Materials Properties Microstructure and Processing*, 2012. 531: p. 2-11.

Statement of Authorship

Title of Paper	Correlation Between EBSD Quantification and Dilatometry Examination of an X70 Steel
Publication Status	☑ Published ☐ Accepted for Publication ☐ Submitted for Publication ☐ Unpublished and Unsubmitted work written in manuscript style
Publication Details	Roccisano, A., Nafisi, S. and Ghomashchi, R., 2019. Correlation Between EBSD Quantification and Dilatometry Examination of an X70 Steel. *MS&T19 Proceedings,* pp.423-430.

Principal Author

Name of Principal Author (Candidate)	Anthony Roccisano		
Contribution to the Paper	Conducted all the experiments, analysed all the data and wrote the majority of the paper.		
Overall percentage (%)	70%		
Certification:	This paper reports on original research I conducted during the period of my Higher Degree by Research candidature and is not subject to any obligations or contractual agreements with a third party that would constrain its inclusion in this thesis. I am the primary author of this paper.		
Signature		Date	16/04/2020

Co-Author Contributions

By signing the Statement of Authorship, each author certifies that:

i. the candidate's stated contribution to the publication is accurate (as detailed above);

ii. permission is granted for the candidate in include the publication in the thesis; and

iii. the sum of all co-author contributions is equal to 100% less the candidate's stated contribution.

Name of Co-Author	Shahrooz Nafisi		
Contribution to the Paper 25%	Provided guidance and supervision from concept to submission. Assisted in the analysis of data and helped to revise the paper.		
Signature		Date	17/04/2020

Name of Co-Author	Reza Ghomashchi		
Contribution to the Paper 5%	Provided guidance and supervision from concept to submission and helped to revise the paper.		
Signature		Date	16/04/2020

Please cut and paste additional co-author panels here as required.

Contributed Papers from Materials Science and Technology 2019 (MS&T19)
September 29–October 3, 2019, Oregon Convention Center, Portland, Oregon, USA

DOI 10.7449/2019/MST_2019_423_430

CORRELATION BETWEEN EBSD QUANTIFICATION AND DILATOMETRY EXAMINATION OF AN X70 STEEL

Anthony Roccisano[1*], Shahrooz Nafisi[1,2], Reza Ghomashchi[1]

[1] The University of Adelaide, South Australia, 5005, Australia

[2] University of Alberta, Edmonton, Alberta, T6G 1H9, Canada

Keywords: CCT Diagram, API 5L, X70, EBSD, Microstructure

Abstract

In order to design controlled rolling schedules, it is critically important to understand phase transformation and to have detailed transformation temperatures of the phases to achieve the desired microstructure. Samples of API 5L X70 pipeline steel were soaked at 1100°C for 5 minutes in a dilatometer and then continuously cooled at constant rates from 0.5 to 100°C/s to develop a range of different microstructures. The microstructures of all specimens were examined by optical and electron microscopy (SEM). Three specimens with different cooling rates were further analyzed through EBSD to better differentiate the microstructures to enable the development of a CCT diagram for the design of rolling schedules.

Introduction

Control over microstructural development during thermomechanical processing of high strength low alloy steels is critically important to produce steels with superior mechanical properties (strength, toughness and ductility) for use in the pipeline industry. As industrial processes typically use continuous cooling during the later stages of thermomechanical treatment to achieve the desired microstructure through phase transformation, CCT diagrams were acknowledged as useful tool to predict the microstructures developed through different cooling rates. Modern high-grade pipeline steels use bainitic microstructures to leverage the high strength and ductility afforded by the microstructure [1, 2]. Classifying mixed bainitic microstructures can be challenging for researchers, especially in low carbon steels where different forms could be developed due to variation in manufacturing conditions [3-5]. Electron BackScatter Diffraction (EBSD) is common tool used to simplify phase identification, and in some cases, quantify the proportion of different microstructures in steels [5-7]. The use of EBSD to aid in phase determination in steel was trailed in this paper.

The primary aim of this paper is to explore the characterization of steel microstructure to better understand phase transformations in low carbon steels with the resulting knowledge used for the development of a CCT diagram.

Experimental Procedure

The CCT diagram was developed on a sample of 20 mm thick API 5L X70 plate with chemistry shown in Table 1. The X70 plate was evaluated in the as supplied condition and no pipe forming operations were carried out prior to this investigation.

Table 1. Chemical Composition of 20 mm X70

C	Mn	Si	Ni	Cu	Al	Mo	V	Nb	Ti	Cr	P	S	N
0.059	1.57	0.19	0.187	0.157	0.049	0.174	0.028	0.046	0.01	0.032	0.011	<0.002	0.0042

Dilatometry curves were produced on a TA Instruments DIL 805 A/D quenching and deformation dilatometer. Samples were sectioned from the quarter thickness plane of the 20 mm thick X70 plate. Dilatometer samples of dimensions ø4 × 10 mm were machined conventionally to the specified dimensions, taking care not to introduce excessive heat into the specimens. Prior to dilatometry, the specimens were uniformly polished with fine silicon carbide sandpaper to ensure a uniform surface, degreased with ethanol and the physical dimensions measured. Samples were heated at a rate of 3°C/s to the austenitizing temperature of 1100°C where they were soaked for 5 minutes. Samples were then continuously cooled to room temperature with cooling rates of 0.5, 1, 3, 5, 10, 20, 30, 50 and 100°C/s as shown in the schematic diagram in Figure 1.

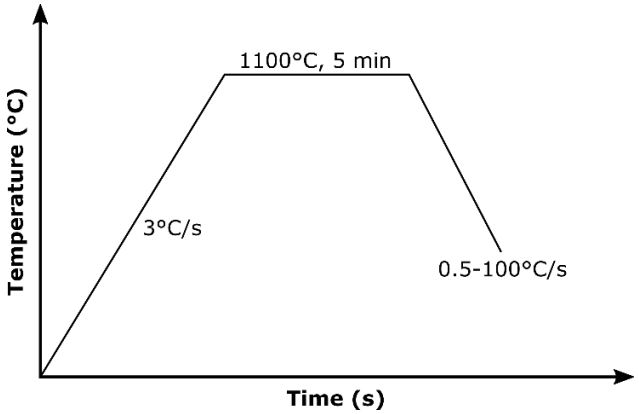

Figure 1: Heat Treatments for Dilatometry Measurement

The CCT metallographic specimens were prepared conventionally down to 1 μm diamond paste, etched with 2% Nital and examined through optical microscopy (Zeiss AXIO Imager.M2m) and Scanning Electron Microscopy (FEI Quanta 450 SEM). For EBSD (FEI Inspect F50 SEM with an EDAX Hikari detector) analysis, the sample preparation is critically important and was conducted in a manner reported previously [8]. Four 150 × 150 μm regions were scanned with EBSD per sample, all carried out with a step size of 0.2 μm. The presented EBSD results were averaged from the four areas to provide greater certainty of the results. Hardness measurements were carried out on a LECO LM700AT microhardness tester at a force of 500gf (~4.9N) and dwell time of 15 s and the result averaged over five locations.

Results and Discussion

Microstructure Characterization

During the course of this experiment, three distinct and dominant microstructures were identified in the samples tested depending on the cooling rate. The three dominant microstructures were a ferrite / bainite mixture, granular bainite dominant, and upper bainite dominant with cooling rates of 0.5, 10 and 50°C/s respectively.

i) Optical microscopy

The optical micrographs of the as-received material and samples of the three distinct microstructures identified during dilatometry are presented in Figure 2. The as-received X70 steel microstructure (Figure 2a) consisted primarily of granular bainite (GB) and polygonal ferrite (PF). The microstructure of the 0.5°C/s cooling rate samples (Figure 2b) consisted primarily of quasi-polygonal ferrite (QF) and some instances of granular bainite with light and dark grey secondary phases not able to be resolved through optical microscopy. The microstructure of the 10°C/s samples as seen in Figure 2c consists of primarily granular bainite with some lath like structures starting to form but not yet clearly defined. The final microstructure presented in Figure 2d was formed by cooling at a rate of 50°C/s and has clearly defined laths of bainitic ferrite separated by cementite, consistent with upper bainite (UB) [3, 4].

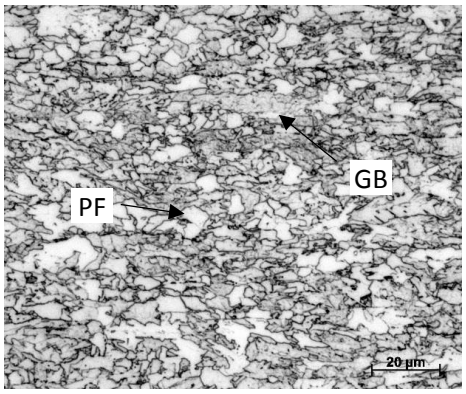

(a) Initial Microstructure

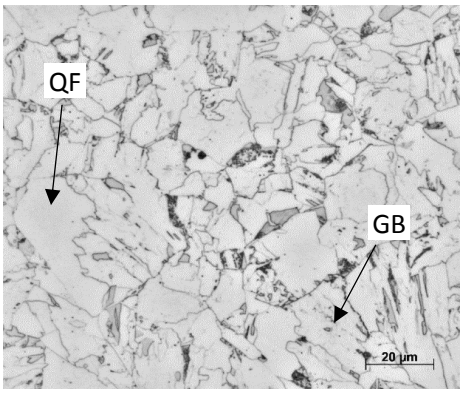

(b) 0.5°C/s

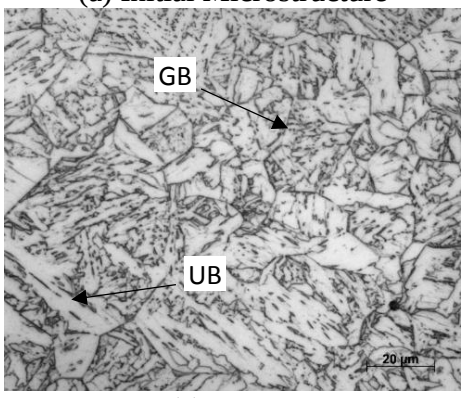

(c) 10°C/s

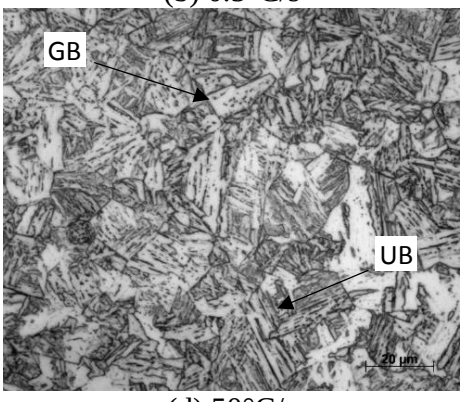

(d) 50°C/s

Figure 2: Optical Micrographs of the steel studied at different cooling rates (PF: Polygonal Ferrite, QF: Quasi-Polygonal Ferrite, GB: Granular Bainite, UB: Upper Bainite)

ii) Electron microscopy

SEM analysis was employed to determine the nature and morphology of the secondary phases that formed in the 0.5, 10 and 50°C/s samples (Figure 3). For the 0.5°C/s cooling rate specimen, two secondary structures of, martensite/austenite (M/A) constituent and degenerated pearlite were identified. M/A constituents formed either within quasi-polygonal ferrite or as seen in Figure 3a, between larger quasi-polygonal ferrite grains [5]. Degenerated pearlite formed, similarly to the M/A constituent either within quasi-polygonal ferrite grains as seen in Figure 3b or separately between larger quasi-polygonal ferrite grains [5]. Degenerate pearlite forms at cooling rates between pearlite and granular bainite where higher transformation temperatures allow cooperative growth of ferrite and cementite but reduced diffusion interrupts the regular formation of pearlite lamellae [5, 9].

The microstructure identified in the 10°C/s cooling rate material was primarily granular bainite. Within the granular bainite, secondary phases were primarily M/A constituents as seen in Figure 3c although some instances of debris of cementite formed within the granular bainite grains. Granular bainite forms through the same mechanism as upper bainite, however, due to the higher transformation temperature, when carbon is partitioned out from the ferrite, it stabilizes the austenite instead of forming cementite leading to austenite being present post transformation [3]. The microstructure in the 50°C/s material was identified as upper bainite and as seen in Figure 3d the ferrite laths are separated by cementite with no cementite identified within the ferrite laths that would indicate lower bainite formation [5]. Bainite is formed through the diffusionless transformation of austenite to bainitic ferrite followed by the diffusion of carbon from the ferrite into the austenite [3]. At high temperatures, carbon can diffuse into the surrounding austenite rapidly precipitating as iron carbide outside the ferrite plate forming upper bainite. At lower transformation temperatures, carbon cannot diffuse out completely and iron carbide precipitates within the bainitic ferrite before cementite in the enriched austenite forms outside leading to the formation of lower bainite [3]. Some instances of granular bainite were observed within the 50°C/s sample, however, upper bainite remained the dominant microstructure.

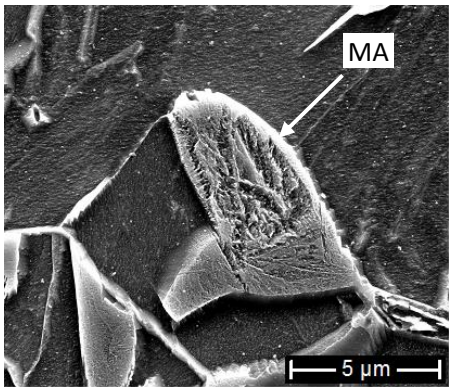

(a) M/A Constituent in 0.5°C/s

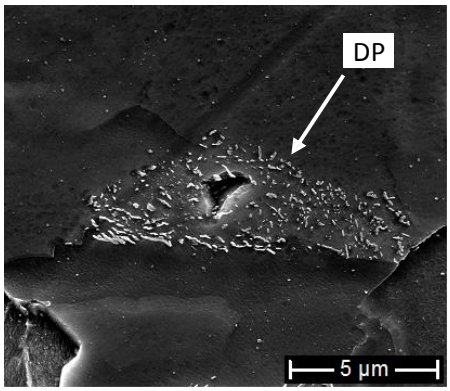

(b) Degenerated Pearlite in 0.5°C/s

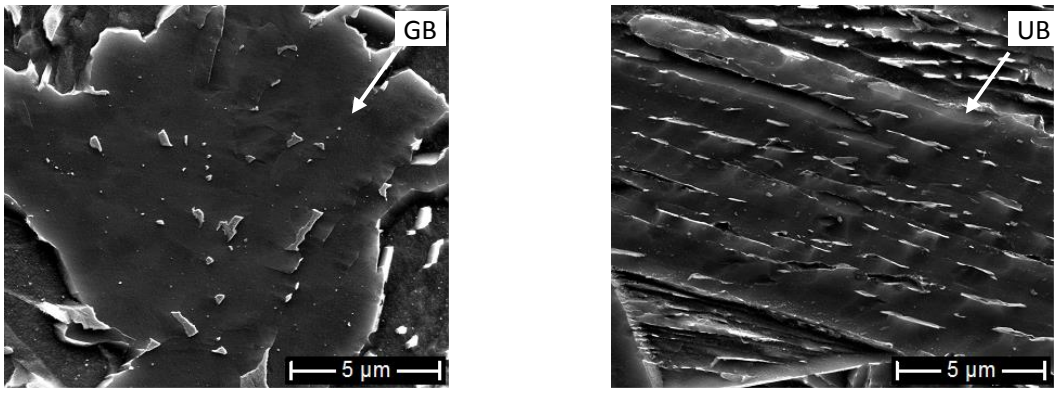

(c) Granular Bainite in 10°C/s (d) Upper Bainite in 50°C/s

Figure 3: SEM Images for Phase Identification
(MA: martensite/austenite constituent, DP: Degenerated Pearlite)

EBSD Quantification

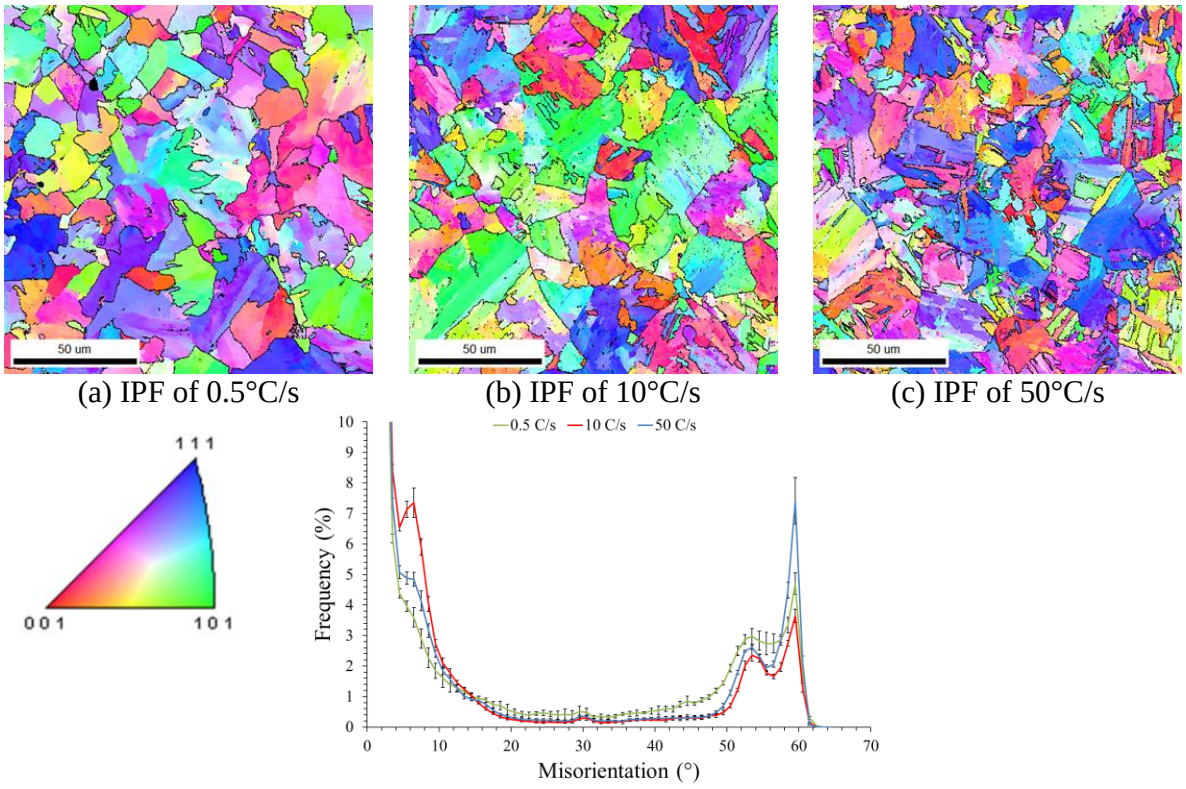

(a) IPF of 0.5°C/s (b) IPF of 10°C/s (c) IPF of 50°C/s

(d) Combined Misorientation Maps

Figure 4: IPF and Misorientation Maps of 0.5, 10 and 50°C/s Cooling Rate Materials

To better differentiate the microstructures generated in each of the samples, the three selected cooling rates were analyzed through EBSD with the Inverse Pole Figures (IPF) presented in Figure 4a – 4c. To compare the properties of the different microstructures developed over the three cooling rates, a plot highlighting the distribution of grain boundary misorientations is presented in Figure 4d. One method of classifying mixed microstructures is by comparing the features of misorientation plots as different microstructures result in different misorientation profiles [5, 10,

11]. The transformation of austenite to ferrite often follows the Kurdjumov-Sachs (KS) $\{111\}_\gamma//\{110\}_\alpha$ and $<110>_\gamma//<111>_\alpha$ or Nishiyama-Wasserman (NW) $\{111\}_\gamma//\{110\}_\alpha$ and $<112>_\gamma//<110>_\alpha$ orientation relationships although some debate exists on which is more applicable due to the small angular differences between them [12]. Due to crystal symmetry, different ferrite orientations can form within a single austenite grain with 24 such variants existing in the KS orientation relationship and 12 in the NW [13, 14]. These variants produce different misorientations depending on the transformation conditions and cause microstructures to have different misorientation profiles [11, 13, 15].

The misorientation profiles presented in Figure 4d show that the majority of misorientations present in the samples exist below 20° and above 50°. The 0.5°C/s sample, with microstructure comprised of quasi-polygonal ferrite and granular bainite, had two small peaks at 53° and 60° and a slight increase of misorientations between 4–8°. This misorientation profile is similar to that identified previously in literature of quasi-polygonal ferrite and granular bainite formed through continuous cooling [6]. The proportion of misorientations between 20° and 50° was almost double that of the 10 and 50°C/s samples with a higher variance. Ferritic microstructures tend to have higher proportions of misorientations present between 20-50° [6], although, due to inconsistent scaling the effect tends to be exaggerated in literature.

The 10°C/s (granular bainite dominant) sample in Figure 4d has a significant peak between 4–8° with two smaller peaks identified at 53° and 60°. Granular bainite and polygonal ferrite mixtures have been shown to have a more random misorientation distribution [5], however, as the 10°C\s sample investigated contains primarily granular bainite with upper bainite, the misorientation profile appears to follow that of high temperature upper bainite. Upper bainite formed at high temperatures has a high proportion of V1/V4, V1/V8 and V1/V11 variant (KS) boundaries that have measured misorientations between 6.1 and 10.9° with a lower proportion of variants with misorientations higher than 50° [13]. As granular bainite forms similarly to upper bainite, although at higher transformation temperatures, the variant production at high transformation temperatures may account for the high proportion of these misorientations in the 10°C/s sample.

The 50°C/s (upper bainite dominant) sample in Figure 4d has the highest proportion of misorientations above 50° with an especially prominent peak at 60° along with a slight peak in misorientations between 4–8°. As shown in literature, when transformation temperature in upper bainite reduces i.e. when cooling rate increases, the proportion of the V1/V2 (KS) variant that has a misorientation of 60° increases whilst misorientations between 6.1 and 10.9° reduce resulting in a high peak at 60° and a reduction in misorientations between 4-8° [13].

Grain Size Determination

A comparison of the grain size distribution and average grain size of the three cooling rates was made in Figure 5 using EBSD with a grain misorientation parameter of 15°. The minimum number of pixels for a grain to be considered in the grain size statistics was selected as 100 pixels in accordance with ASTM E2627 [16] which removed some smaller laths from the 50°C/s sample meaning a higher proportion of grains existed below 5 μm that was reported. As seen in Figure 5b the 0.5°C/s had an average grain size of 9.0 μm, the 10°C/s sample had an average grain size of

6.7 μm and the 50°C/s samples had an average grain size of 5.4 μm. The reduction in mean grain size with increasing cooling rate has been identified in other continuous cooling experiments [6, 17]. As seen in Figure 5a over 90% of grains had diameters less than 15 μm in all three cooling rates tested with the 50°C/s sample having the highest proportion below 5 μm.

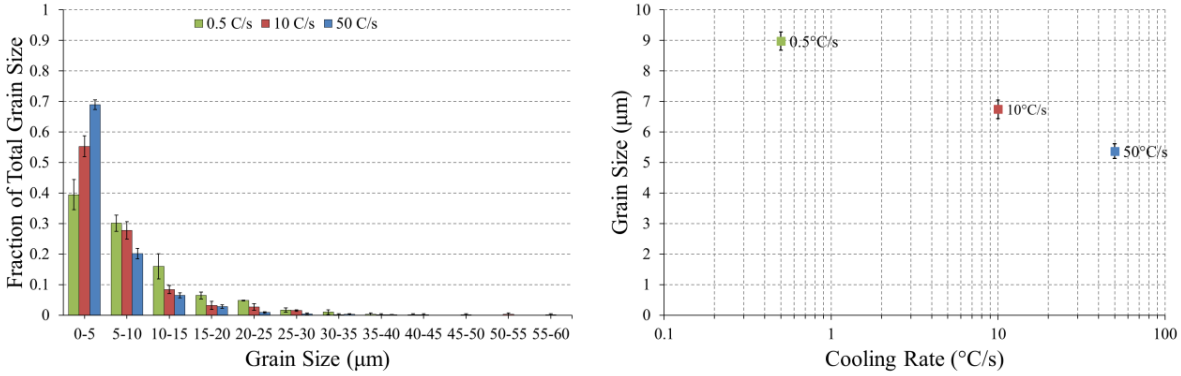

(a) Grain Size Distribution (b) Average Grain Size

Figure 5: Grain Size Distribution

CCT Diagram

The CCT diagram in Figure 6 obtained from the dilatometer experiments represents a CCT diagram where no deformation was undertaken on the dilatometer specimens during or prior to cooling. The presence of quasi-polygonal ferrite was restricted to cooling rates below 3°C/s with the remaining austenite transforming into a mixture of granular bainite and M/A constituents. The presence of granular bainite was confirmed over most of the cooling rates employed with the only exception of the very fastest rate of 100°C/s; not displaying any obvious presence of granular bainite. The knee in the 100°C/s cooling curve is believed to be the result of recalescence which is the release of latent heat during phase change and is present, although less noticeably in the 50, 30 and 20°C/s samples [18].

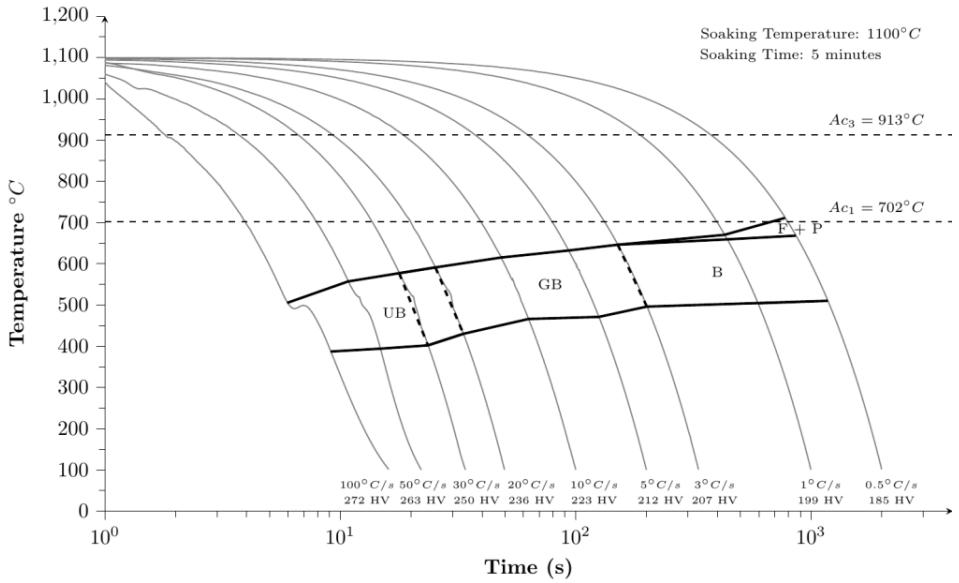

Figure 6: CCT Diagram of the X70 Steel

Conclusions

In order to be able to design controlled rolling schedule for an X70 pipeline steel having bainitic structure, a CCT diagram was constructed using dilatometry. The formation of phases at a range of cooling rates were analyzed metallographically using optical and electron microscopy. The resulting CCT diagrams intended use is for the production of different rolling schedules that will be used to study the effect of manufacturing on the susceptibility of linepipe steel to stress corrosion cracking.

Three distinct microstructures were identified in the samples tested at different cooling rates. They were ferrite /bainite mixture, granular bainite, and upper bainite, although SEM analyses confirmed the formation of M/A and degenerate pearlite as minor constituents. The application of EBSD and analysis of grain boundary misorientation provide useful information to identify the complex and sometimes difficult to resolve morphologies of bainitic phases. The cooling rate plays an important role on the morphology of bainite;

1- Granular bainite confirmed over most of the cooling rates except the fastest rate of 100°C/s
2- Quasi-polygonal ferrite was restricted to cooling rates below 3°C/s
3- The misorientation profile may be used to differentiate different bainitic morphologies in support of previously reported findings in the open literature.

References

1. Yoo, J.-Y., et al., Materials and Manufacturing Processes, 2011. **26**(1): p. 154-160.
2. Nafisi, S., et al., Materials Science and Engineering a-Structural Materials Properties Microstructure and Processing, 2012. **531**: p. 2-11.
3. Bhadeshia, H. and R. Honeycombe, *Steels: microstructure and properties: microstructure and properties*. 2011: Butterworth-Heinemann.
4. Krauss, G., *Steels: processing, structure, and performance*. 2015: Asm International.
5. Zajac, S., et al. *Materials Science Forum*. 2005. Trans Tech Publ.
6. Cizek, P., et al., Metallurgical and Materials Transactions A, 2015. **46**(1): p. 407-425.
7. Shrestha, S.L., et al., Ultramicroscopy, 2014. **137**: p. 40-47.
8. Nafisi, S., et al., Metals, 2019. **9**(5).
9. Matrosov, M.Y., et al., Steel in Translation, 2012. **42**(1): p. 84-93.
10. Long, X.Y., et al., Materials & Design, 2014. **64**: p. 237-245.
11. Gourgues, A.-F., et al., Materials Science and Technology, 2000. **16**(1): p. 26-40.
12. Verbeken, K., et al., ISIJ international, 2009. **49**(10): p. 1601-1609.
13. Takayama, N., et al., Acta Materialia, 2012. **60**(5): p. 2387-2396.
14. Suikkanen, P.P., et al., Journal of Materials Science & Technology, 2013. **29**(4): p. 359-366.
15. Furuhara, T., et al., Materials Science and Engineering: A, 2006. **431**(1-2): p. 228-236.
16. ASTM, *E2627-13,"Standard Practice for Determining Average Grain Size Using Electron Backscatter Diffraction (EBSD) in Fully Recrystallized Polycrystalline Materials.", ASTM International, West Conshohocken, PA, 2013*. 2013.
17. Isasti, N., et al., Metallurgical and Materials Transactions A, 2013. **44**(8): p. 3552-3563.
18. Vander Voort, G.F., *Atlas of time-temperature diagrams for irons and steels*. 1991: ASM international.

Bibliography

[1] RN Parkins. "A review of stress corrosion cracking of high pressure gas pipelines". In: *CORROSION 2000*.

[2] R. R. Fessler. "Combination of Conditions causes stress corrosion cracking". In: *Oil Gas J.;(United States)* 74 (1976).

[3] BY Fang, A Atrens, JQ Wang, En-Hou Han, ZY Zhu, and W Ke. "Review of stress corrosion cracking of pipeline steels in "low" and "high" pH solutions". In: *Journal of materials science* 38.1 (2003), pp. 127–132. ISSN: 0022-2461.

[4] J. G. Gonzalez-Rodriguez, M. Casales, V. M. Salinas-Bravo, J. L. Albarran, and L. Martinez. "Effect of Microstructure on the stress corrosion cracking of X-80 pipeline steel in diluted sodium bicarbonate solutions". In: *Corrosion* 58.7 (2002), pp. 584–590.

[5] NE Board. "Public Inquiry Concerning Stress Corrosion Cracking on Canadian Oil and Gas Pipelines". In: (1996).

[6] Fengmei Song. "Overall mechanisms of high pH and near-neutral pH SCC, models for forecasting SCC susceptible locations, and simple algorithms for predicting high pH SCC crack growth rates". In: *CORROSION 2008*. NACE International.

[7] R. N. Parkins. "Mechanistic aspects of intergranular stress corrosion cracking of ferritic steels". In: *Corrosion* 52.5 (1996), pp. 363–374. ISSN: 0010-9312.

[8] Peter Kentish. "Stress corrosion cracking of gas pipelines – Effect of surface roughness, orientations and flattening". In: *Corrosion Science* 49.6 (2007), pp. 2521–

2533. ISSN: 0010-938X. DOI: http://dx.doi.org/10.1016/j.corsci.2006.12.014.

[9] G. Sandoz. "The effects of alloying elements on the susceptibility to stress-corrosion cracking of martensitic steels in salt water". In: *Metallurgical Transactions* 2.4 (1971), pp. 1055–1063. ISSN: 1543-1916. DOI: 10.1007/BF02664236.

[10] BE Wilde and JS Armijo. "Influence of silicon and manganese on corrosion behavior of austenitic stainless steels". In: *Corrosion* 24.12 (1968), pp. 393–402. ISSN: 1938-159X.

[11] M. A. Eaglesham, J. U. Gaum, and J. H. Bulloch. "The Role of Carbon Level on the Stress-Corrosion Cracking Characteristics of Steel". In: *Theoretical and Applied Fracture Mechanics* 10.2 (1988), pp. 97–109. ISSN: 0167-8442. DOI: Doi10.1016/0167-8442(88)90002-X.

[12] J. H. Bulloch. "Stress-Corrosion Cracking of Low-Alloy Steels in Natural Seawater Environment - the Influence of Carbon Level". In: *Theoretical and Applied Fracture Mechanics* 16.1 (1991), pp. 1–17. ISSN: 0167-8442. DOI: Doi10.1016/0167-8442(91)90036-J.

[13] Jeffrey Bulger and Jingli Luo. "Effect of microstructure on near-neutral-pH SCC". In: *2000 3rd International Pipeline Conference*. American Society of Mechanical Engineers.

[14] Z. Y. Liu, X. G. Li, C. W. Du, G. L. Zhai, and Y. F. Cheng. "Stress corrosion cracking behavior of X70 pipe steel in an acidic soil environment". In: *Corrosion Science* 50.8 (2008), pp. 2251–2257. ISSN: 0010938X. DOI: 10.1016/j.corsci.2008.05.011.

[15] H Asahi, T Kushida, M Kimura, H Fukai, and S Okano. "Role of microstructures on stress corrosion cracking of pipeline steels in carbonate-bicarbonate solution". In: *Corrosion* 55.7 (1999), pp. 644–652. ISSN: 0010-9312.

[16] Takahiro Kushida, Koichi Nose, H. Asahi, Mitsuo Kimura, Yasuyoshi Yamane, Shigeru Endo, and Haruya Kawano. *Effects of Metallurgical Factors and Test Conditions on Near Neutral pH SCC of Pipeline Steels*. Conference Paper. 2001.

[17] TC Tsai and TH Chuang. "Role of grain size on the stress corrosion cracking of 7475 aluminum alloys". In: *Materials Science and Engineering: A* 225.1-2 (1997), pp. 135–144. ISSN: 0921-5093.

[18] KD Ralston and N Birbilis. "Effect of grain size on corrosion: a review". In: *Corrosion* 66.7 (2010), pp. 075005–075005–13. ISSN: 0010-9312.

[19] HF Lopez, MM Cisneros, H Mancha, O Garcia, and MJ Pérez. "Grain size effects on the SCC susceptibility of a nitrogen steel in hot NaCl solutions". In: *Corrosion science* 48.4 (2006), pp. 913–924. ISSN: 0010-938X.

[20] O. Lavigne, E. Gamboa, W. Costin, M. Law, V. Luzin, and V. Linton. "Microstructural and mechanical factors influencing high pH stress corrosion cracking susceptibility of low carbon line pipe steel". In: *Engineering Failure Analysis* 45 (2014), pp. 283–291. ISSN: 1350-6307. DOI: DOI10.1016/j.engfailanal.2014.07.011.

[21] RK Ray, JJ Jonas, MP Butron-Guillen, and J Savoie. "Transformation textures in steels". In: *ISIJ International* 34.12 (1994), pp. 927–942. ISSN: 0915-1559.

[22] A. Haldar and R. K. Ray. "Microstructural and textural development in an extra low carbon steel during warm rolling". In: *Materials Science and Engineering a-Structural Materials Properties Microstructure and Processing* 391.1-2 (2005), pp. 402–407. ISSN: 0921-5093. DOI: DOI10.1016/j.msea.2004.09.014.

[23] L. S. Toth, J. J. Jonas, D. Daniel, and R. K. Ray. "Development of Ferrite Rolling Textures in Low-Carbon and Extra Low-Carbon Steels". In: *Metallurgical Transactions a-Physical Metallurgy and Materials Science* 21.11 (1990), pp. 2985–3000. ISSN: 0360-2133. DOI: Doi10.1007/Bf02647219.

[24] M. A. Arafin and J. A. Szpunar. "A new understanding of intergranular stress corrosion cracking resistance of pipeline steel through grain boundary character

and crystallographic texture studies". In: *Corrosion Science* 51.1 (2009), pp. 119–128. ISSN: 0010938X. DOI: 10.1016/j.corsci.2008.10.006.

[25] M. A. Arafin and J. A. Szpunar. "Grain Boundary Engineering to Control the Intergranular Stress Corrosion Cracking of Pipeline Steel". In: *ICF12, Ottawa 2009*. 2009.

[26] G. Palumbo, P. J. King, K. T. Aust, U. Erb, and P. C. Lichtenberger. "Grain boundary design and control for intergranular stress-corrosion resistance". In: *Scripta Metallurgica et Materialia* 25.8 (1991), pp. 1775–1780. ISSN: 0956-716X. DOI: http://dx.doi.org/10.1016/0956-716X(91)90303-I.

[27] American Petroleum Institute. *Specification For Line Pipe*. Standard. 2013.

[28] J. Griggs, E. Gamboa, and O. Lavigne. "2D modelling of inclined intergranular stress corrosion crack paths". In: *Fatigue & Fracture of Engineering Materials & Structures* 40.4 (), pp. 543–555. ISSN: 8756-758x. DOI: 10.1111/ffe.12514.

[29] O. Lavigne, E. Gamboa, V. Luzin, M. Law, M. Giuliani, and W. Costin. "The effect of the crystallographic texture on intergranular stress corrosion crack paths". In: *Materials Science and Engineering a-Structural Materials Properties Microstructure and Processing* 618 (2014), pp. 305–309. ISSN: 0921-5093. DOI: DOI10.1016/j.msea.2014.09.038.

[30] Olivier Lavigne, Erwin Gamboa, Vladimir Luzin, and Michael Law. "Analysis of intergranular stress corrosion crack paths in gas pipeline steels; straight or inclined?" In: *Engineering Failure Analysis* 85 (2018), pp. 26–35. ISSN: 13506307. DOI: 10.1016/j.engfailanal.2017.12.004.

[31] A. Roccisano, S. Nafisi, and R. Ghomashchi. "Stress Corrosion Cracking Observed in Ex-service Gas Pipelines: A Comprehensive Study". In: *Metallurgical and Materials Transactions A* (2019). ISSN: 1543-1940. DOI: 10.1007/s11661-019-05496-3.

[32] A. P. Jivkov. "Strain-induced passivity breakdown in corrosion crack initiation". In: *Theoretical and Applied Fracture Mechanics* 42.1 (2004), pp. 43–52. ISSN: 0167-8442. DOI: https://doi.org/10.1016/j.tafmec.2004.06.004.

[33] RL Wenk. "Field Investigation of Stress Corrosion Cracking". In: *5th symposium on line pipe research*.

[34] Facundo Varela, Mike Yongjun Tan, and Maria Forsyth. "An overview of major methods for inspecting and monitoring external corrosion of on-shore transportation pipelines". In: *Corrosion Engineering, Science and Technology* 50.3 (2015), pp. 226–235. ISSN: 1478-422X.

[35] C. Manfredi and J. L. Otegui. "Failures by SCC in buried pipelines". In: *Engineering Failure Analysis* 9.5 (2002), pp. 495–509. ISSN: 1350-6307. DOI: PiiS1350-6307(01)00032-2Doi10.1016/S1350-6307(01)00032-2.

[36] A. Atrens, C. C. Brosnan, S. Ramamurthy, A. Oehlert, and I. O. Smith. "Linearly Increasing Stress Test (List) for SCC Research". In: *Measurement Science & Technology* 4.11 (1993), pp. 1281–1292. ISSN: 0957-0233. DOI: Doi10.1088/0957-0233/4/11/017.

[37] Z. F. Wang and A. Atrens. "Initiation of stress corrosion cracking for pipeline steels in a carbonate-bicarbonate solution". In: *Metallurgical and Materials Transactions A* 27.9 (1996), pp. 2686–2691. ISSN: 1543-1940. DOI: 10.1007/BF02652362.

[38] R. N. Parkins. "Stress corrosion cracking". In: (1988).

[39] TR Baker, RN Parkins, and GG Rochfort. "Investigations Relating to Stress Corrosion Cracking on the Pipeline Authority's Moomba-to-Sydney Pipeline". In: *Proc. 7th Symp. Line Pipe Research, Catalog*, pp. 27–1.

[40] Canadian Energy Pipeline Association. *CEPA Recommended Practices for Managing Near-neutral pH Stress Corrosion Cracking*. Report. 2015.

[41] JM Sutcliffe, RR Fessler, WK Boyd, and RN Parkins. "Stress corrosion cracking of carbon steel in carbonate solutions". In: *Corrosion* 28.8 (1972), pp. 313–320. ISSN: 1938-159X.

[42] JA Beavers and RG Worthingham. "The influence of soil chemistry on SCC of underground pipelines". In: *2002 4th International Pipeline Conference*. American Society of Mechanical Engineers, pp. 1671–1678.

[43] RN Parkins. "Realistic stress corrosion crack velocities for life prediction estimates". In: (1991).

[44] RN Parkins and RR Fessler. "Stress corrosion cracking of high-pressure gas transmission pipelines". In: *International Journal of Materials in Engineering Applications* 1.2 (1978), pp. 80–96. ISSN: 0141-5530.

[45] RB Rebak, Z Xia, R Safruddin, and Z Szklarska-Smialowska. "Effect of solution composition and electrochemical potential on stress corrosion cracking of X-52 pipeline steel". In: *Corrosion* 52.5 (1996), pp. 396–405. ISSN: 0010-9312.

[46] RN Parkins. "The controlling parameters in stress corrosion cracking". In: *5th Symp. Line Pipe Research L*. Vol. 30174.

[47] John A Beavers, Carolyn L Durr, and Burke S Delanty. "High-pH SCC: temperature and potential dependence for cracking in field environments". In: *1998 2nd International Pipeline Conference*. American Society of Mechanical Engineers, pp. 423–437.

[48] R. N. Parkins. "Factors Influencing Stress-Corrosion Crack-Growth Kinetics". In: *Corrosion* 43.3 (1987), pp. 130–139. ISSN: 0010-9312.

[49] TN Baker, GG Rochfort, and RN Parkins. "Postrupture analyses reveal probable future line failures". In: *Oil Gas J.;(United States)* 85.2 (1987).

[50] X. Chen, X. G. Li, C. W. Du, and Y. F. Cheng. "Effect of cathodic protection on corrosion of pipeline steel under disbonded coating". In: *Corrosion Science* 51.9 (2009), pp. 2242–2245. ISSN: 0010-938X. DOI: http://dx.doi.org/10.1016/j.corsci.2009.05.027.

[51] F Latino, Facundo Varela, MYJ Tan, and Maria Forsyth. "An overview on cathodic shielding produced by disbonded coatings". In: *AC Assosiation, Corrosion & Prevention 2016 Conference, Auckland, New Zealand*.

[52] John A. Beavers and Neil G. Thompson. *Corrosion Beneath Disbonded Coatings: A Review*. Conference Paper. 1996.

[53] Ian Thompson and Janardhan Rao Saithala. "Review of pipeline coating systems from an operators perspective". In: *Corrosion Engineering, Science and Technology* 51.2 (2016), pp. 118–135. ISSN: 1478-422X.

[54] F. Hasan, J. Lqbal, and F. Ahmed. "Stress corrosion failure of high-pressure gas pipeline". In: *Engineering Failure Analysis* 14.5 (2007), pp. 801–809. ISSN: 1350-6307. DOI: DOI10.1016/j.engfailanal.2006.11.002.

[55] J. A. Beavers, T. K. Christman, and R. N. Parkins. "Effects of Surface Condition on the Stress-Corrosion Cracking of Line Pipe Steel". In: *Materials Performance* 27.4 (1988), pp. 22–26. ISSN: 0094-1492.

[56] Mimoun Elboujdaini, Yong-Zhi Wang, R. Yong-Zhi Wang, Winston Revie, M. T. Shehata, and Redvers N. Parkins. *Stress Corrosion Crack Initiation Processes: Pitting and Microcrack Coalescence*. Conference Paper. 2000.

[57] G. T. Burstein and P. C. Pistorius. "Surface-Roughness and the Metastable Pitting of Stainless-Steel in Chloride Solutions". In: *Corrosion* 51.5 (1995), pp. 380–385. ISSN: 0010-9312. DOI: Doi10.5006/1.3293603.

[58] R. R. Fessler, A. J. Markworth, and R. N. Parkins. "Cathodic Protection Levels under Disbonded Coatings". In: *CORROSION* 39.1 (1983), pp. 20–25. ISSN: 0010-9312. DOI: 10.5006/1.3580809.

[59] BN Leis and RJ Eiber. "Stress-corrosion cracking on gas-transmission pipelines: history, causes, and mitigation". In: *First International Business Conference on Onshore Pipelines, Berlin*, p. 7.

[60] Standards Australia Limited. *AS2885 Pipelines-Gas and Liquid Petroleum*. Standard. 2012.

[61] B. Saleem, F. Ahmed, M. A. Rafiq, M. Ajmal, and L. Ali. "Stress corrosion failure of an X52 grade gas pipeline". In: *Engineering Failure Analysis* 46 (2014), pp. 157–165. ISSN: 1350-6307. DOI: DOI10.1016/j.engfailanal.2014.08.011.

[62] W. Chen, S. H. Wang, R. Chu, F. King, T. R. Jack, and R. R. Fessler. "Effect of precyclic loading on stress-corrosion-cracking initiation in an X-65 pipeline steel exposed to near-neutral pH soil environment". In: *Metallurgical and Materials Transactions a-Physical Metallurgy and Materials Science* 34a.11 (2003), pp. 2601–2608. ISSN: 1073-5623. DOI: DOI10.1007/s11661-003-0019-y.

[63] S Beckinsale, CE Mallinson, and H Moore. "The season-cracking of brass and other copper alloys". In: *J INST MET* 25 (1921), pp. 35–126.

[64] T. Hemmingsen, H. Hovdan, P. Sanni, and N. O. Aagotnes. "The influence of electrolyte reduction potential on weld corrosion". In: *Electrochimica Acta* 47.24 (2002), pp. 3949–3955. ISSN: 0013-4686. DOI: PiiS0013-4686(02)00366-3Doi10.1016/S0013-4686(02)00366-3.

[65] S. J. Kim, M. Okido, and K. M. Moon. "The electrochemical study on mechanical and hydrogen embrittlement properties of HAZ part as a function of post-weld heat treatment in SMAW". In: *Surface & Coatings Technology* 169 (2003), pp. 163–167. ISSN: 0257-8972. DOI: PiiS0257-8972(03)00219-6Doi10.1016/S0257-8972(03)00219-6.

[66] K. M. Moon, M. H. Lee, K. J. Kim, and S. J. Kim. "The effect of post-weld heat treatment affecting corrosion resistance and hydrogen embrittlement of HAZ part in FCAW". In: *Surface & Coatings Technology* 169 (2003), pp. 675–678. ISSN: 0257-8972. DOI: PiiS0257-8972(03)00060-4Doi10.1016/S0257-8972(03)00060-4.

[67] M Law, H Prask, V Luzin, and T Gnaeupel-Herold. "Residual stress measurements in coil, linepipe and girth welded pipe". In: *Materials Science and Engineering: A* 437.1 (2006), pp. 60–63. ISSN: 0921-5093.

[68] Jun-Young Nam, Duck-hee Seo, Sang-yun Lee, Woong-Ki Hwang, and Bo-Young Lee. "The effect of residual stress on the SCC using ANSYS". In: *Procedia Engineering* 10 (2011), pp. 2609–2614. ISSN: 1877-7058. DOI: https://doi.org/10.1016/j.proeng.2011.04.435.

[69] J Flis. "Action of carbon in stress corrosion cracking of mild steel in nitrate solutions". In: *Corrosion* 29.1 (1973), pp. 37–46. ISSN: 1938-159X.

[70] JAS Green and RN Parkins. "Electrochemical properties of ferrite and cementite in relation to stress corrosion of mild steels in nitrate solutions". In: *Corrosion* 24.3 (1968), pp. 66–69. ISSN: 1938-159X.

[71] A. Roccisano, S. Nafisi, and R. Ghomashchi. *Texture Study of Stress Corrosion Cracking in Ex-Service Pipeline Steels*. Conference Paper. 2018.

[72] S. Y. Shin, B. Hwang, S. Lee, N. J. Kim, and S. S. Ahn. "Correlation of microstructure and charpy impact properties in API X70 and X80 line-pipe steels". In: *Materials Science and Engineering a-Structural Materials Properties Microstructure and Processing* 458.1-2 (2007), pp. 281–289.

[73] R. N. Parkins, E. Belhimer, and W. K. Blanchard. "Stress Corrosion Cracking Characteristics of a Range of Pipeline Steels in Carbonate-Bicarbonate Solution". In: *CORROSION* 49.12 (1993), pp. 951–966. ISSN: 0010-9312. DOI: 10.5006/1.3316023.

[74] BT Lu and JL Luo. "Relationship between yield strength and near-neutral pH stress corrosion cracking resistance of pipeline steels—an effect of microstructure". In: *Corrosion* 62.2 (2006), pp. 129–140. ISSN: 0010-9312.

[75] G. H. Koch. "Tests for Stress-Corrosion". In: *Advanced Materials & Processes* 159.8 (2001), pp. 36–38.

[76] JA Beavers and GH Koch. "Limitations of the slow strain rate test for stress corrosion cracking testing". In: *Corrosion* 48.3 (1992), pp. 256–264. ISSN: 0010-9312.

[77] ASTM International. *G129, Standard Practice for Slow Strain Rate Testing to Evaluate the Susceptibility of Metallic Materials to Environmentally Assisted Cracking*. Generic. 2006.

[78] International Organization for Standardization. *ISO 7539-7:2005 Corrosion of metals and alloys — Stress corrosion testing — Part 7: Method for slow strain rate testing*. Standard. 2005.

[79] NACE International. *Slow Strain Rate Test Method for Screening Corrosion-Resistant Alloys (CRAs) for Stress Corrosion Cracking in Sour Oilfield Service*. Standard. 2016.

[80] T. N. Baker, C. G. Rochfort, and R. N. Parkins. "Pipeline Rupture .2. Studies of Line Failure Focus on Cracking Conditions". In: *Oil & Gas Journal* 85.4 (1987), pp. 77–83. ISSN: 0030-1388.

[81] Michael J. Danielson, R. H. Jones, and Kevin Krist. *Effect of Microstructure and Microchemistry on the SCC Behavior of Pipeline Steels in a High pH Environment*. Conference Paper. 2000.

[82] R. N. Parkins. "Predictive Approaches to Stress-Corrosion Cracking Failure". In: *Corrosion Science* 20.2 (1980), pp. 147–. ISSN: 0010-938x. DOI: Doi10.1016/0010-938x(80)90128-6.

[83] RN Parkins and BS Greenwell. "The interface between corrosion fatigue and stress-corrosion cracking". In: *Metal Science* 11.8-9 (1977), pp. 405–413. ISSN: 0306-3453.

[84] Cortest. *CERT/SSRT LOAD FRAMES*. Web Page. 2017.

[85] N. Winzer, A. Atrens, W. Dietzel, G. Song, and K. U. Kainer. "Comparison of the linearly increasing stress test and the constant extension rate test in the evaluation of transgranular stress corrosion cracking of magnesium". In: *Materials Science and Engineering a-Structural Materials Properties Microstructure and Processing* 472.1-2 (2008), pp. 97–106. ISSN: 0921-5093. DOI: 10.1016/j.msea.2007.03.021.

[86] J Salmond and A Atrens. "SCC of copper using the linearly increasing stress test". In: *Scripta metallurgica et materialia* 26.9 (1992), pp. 1447–1450. ISSN: 0956-716X.

[87] Ernesto Villalba and Andrej Atrens. "Metallurgical aspects of rock bolt stress corrosion cracking". In: *Materials Science and Engineering: A* 491.1-2 (2008), pp. 8–18. ISSN: 0921-5093.

[88] Ernesto Villalba and Andrej Atrens. "Hydrogen embrittlement and rock bolt stress corrosion cracking". In: *Engineering Failure Analysis* 16.1 (2009), pp. 164–175. ISSN: 1350-6307.

[89] Jeffrey Venezuela, Qinglong Liu, Mingxing Zhang, Qingjun Zhou, and Andrej Atrens. "The influence of hydrogen on the mechanical and fracture properties of some martensitic advanced high strength steels studied using the linearly increasing stress test". In: *Corrosion Science* 99 (2015), pp. 98–117. ISSN: 0010-938X.

[90] Qian Liu, Bartolomeus Irwanto, and Andrej Atrens. "The influence of hydrogen on 3.5 NiCrMoV steel studied using the linearly increasing stress test". In: *Corrosion Science* 67 (2013), pp. 193–203. ISSN: 0010-938X.

[91] Erwin Gamboa and Andrej Atrens. "Environmental influence on the stress corrosion cracking of rock bolts". In: *Engineering Failure Analysis* 10.5 (2003), pp. 521–558. ISSN: 1350-6307.

[92] Sarvesh Pal and R. K. Singh Raman. "Determination of threshold stress intensity factor for stress corrosion cracking (KISCC) of steel heat affected zone". In: *Corrosion Science* 51.10 (2009), pp. 2443–2449. ISSN: 0010-938X. DOI: `https://doi.org/10.1016/j.corsci.2009.06.032`.

[93] R. N. Ibrahim, R. Rihan, and R. K. Singh Raman. "Validity of a new fracture mechanics technique for the determination of the threshold stress intensity factor for stress corrosion cracking (KIscc) and crack growth rate of engineering materials". In: *Engineering Fracture Mechanics* 75.6 (2008), pp. 1623–1634. ISSN: 0013-7944. DOI: `https://doi.org/10.1016/j.engfracmech.2007.06.007`.

[94] Satyam Suwas and Ranjit Kumar Ray. *Crystallographic Texture of Materials*. Springer, 2014. ISBN: 1447163141.

[95] A. Haldar, S. Suwas, and D. Bhattacharjee. *Microstructure and Texture in Steels: and Other Materials*. Springer, 2009. ISBN: 9781848824546.

[96] B. Gardiola, M. Humbert, C. Esling, G. Flemming, and K. E. Hensger. "Determination and prediction of the inherited ferrite texture in a HSLA steel produced by compact strip production". In: *Materials Science and Engineering a-Structural Materials Properties Microstructure and Processing* 303.1-2 (2001), pp. 60–69. ISSN: 0921-5093. DOI: Doi10.1016/S0921-5093(00)01887-6.

[97] Stuart I. Wright and Matthew M. Nowell. "A Comparison of Texture Measurements Via EBSD and X-RAY". In: *Materials Processing and Texture*. John Wiley & Sons, Inc., 2008, pp. 357–364. ISBN: 9780470444191. DOI: 10.1002/9780470444191.ch40.

[98] Michael T Hutchings, Philip J Withers, Thomas M Holden, and Torben Lorentzen. *Introduction to the characterization of residual stress by neutron diffraction*. CRC press, 2005. ISBN: 0203402812.

[99] Bernard Dennis Cullity and Stuart R Stock. *Elements of X-ray Diffraction*. Vol. 3. Prentice hall New Jersey, 2001.

[100] Anthony Kelly and Kevin M Knowles. *Crystallography and crystal defects*. John Wiley & Sons, 2012. ISBN: 0470750146.

[101] R. K. Ray and J. J. Jonas. "Transformation textures in steels". In: *International Materials Reviews* 35.1 (1990), pp. 1–36. ISSN: 0950-6608. DOI: 10.1179/095066090790324046.

[102] R. K. Ray, J. J. Jonas, and R. E. Hook. "Cold rolling and annealing textures in low carbon and extra low carbon steels". In: *International Materials Reviews* 39.4 (1994), pp. 129–172. ISSN: 0950-6608.

[103] R. K. Ray, M. P. Butronguillen, J. J. Jonas, and G. E. Ruddle. "Effect of Controlled Rolling on Texture Development in a Plain Carbon and a Nb Microalloyed Steel". In: *Isij International* 32.2 (1992), pp. 203–212. ISSN: 0915-1559. DOI: DOI10.2355/isijinternational.32.203.

[104] Donald R Askeland and Pradeep Prabhakar Phulé. *The Science and Engineering of Materials*. Springer, 2003. ISBN: 0534393934.

[105] PJE Forsyth, R King, GJ Metcalfe, and B Chalmers. "Grain boundaries in metals". In: *Nature* 158.4024 (1946), p. 875. ISSN: 1476-4687.

[106] Van Vlack. *Elements Of Material Science And Engineering, 6/E*. Pearson Education India, 1959. ISBN: 8131706001.

[107] Tadao Watanabe. "An Approach to Grain Boundary Design for Strong and Ductile Polycrystals". In: *Res Mechanica* 11.1 (1984), pp. 47–84.

[108] AP Sutton, EP Banks, and AR Warwick. "The five-dimensional parameter space of grain boundaries". In: *Proc. R. Soc. A* 471.2181 (2015), p. 20150442. ISSN: 1364-5021.

[109] Myrjam Winning, AD Rollett, Günter Gottstein, DJ Srolovitz, A Lim, and LS Shvindlerman. "Mobility of low-angle grain boundaries in pure metals". In: *Philosophical Magazine* 90.22 (2010), pp. 3107–3128. ISSN: 1478-6435.

[110] D. G. Brandon. "The structure of high-angle grain boundaries". In: *Acta Metallurgica* 14.11 (1966), pp. 1479–1484. ISSN: 0001-6160. DOI: https://doi.org/10.1016/0001-6160(66)90168-4.

[111] W. T. Read and W. Shockley. "Dislocation Models of Crystal Grain Boundaries". In: *Physical Review* 78.3 (1950), pp. 275–289. ISSN: 0031-899x. DOI: DOI10.1103/PhysRev.78.275.

[112] EDAX. *OIM Analysis 7 User Manual*. Generic. 2013.

[113] E. M. Lehockey, G. Palumbo, P. Lin, and A. M. Brennenstuhl. "On the relationship between grain boundary character distribution and intergranular corrosion". In: *Scripta Materialia* 36.10 (1997), pp. 1211–1218. ISSN: 1359-6462. DOI: Doi10.1016/S1359-6462(97)00018-3.

[114] P. Lin, G. Palumbo, U. Erb, and K. T. Aust. "Influence of Grain-Boundary-Character-Distribution on Sensitization and Intergranular Corrosion of Alloy-600". In: *Scripta Metallurgica Et Materialia* 33.9 (1995), pp. 1387–1392. ISSN: 0956-716x. DOI: Doi10.1016/0956-716x(95)00420-Z.

[115] M Michiuchi, H Kokawa, ZJ Wang, YS Sato, and K Sakai. "Twin-induced grain boundary engineering for 316 austenitic stainless steel". In: *Acta materialia* 54.19 (2006), pp. 5179–5184. ISSN: 1359-6454.

[116] M Shimada, H Kokawa, ZJ Wang, YS Sato, and I Karibe. "Optimization of grain boundary character distribution for intergranular corrosion resistant 304 stainless steel by twin-induced grain boundary engineering". In: *Acta Materialia* 50.9 (2002), pp. 2331–2341. ISSN: 1359-6454.

[117] Jonathan D French, Junhong Zhao, Martin P Harmer, Helen M Chan, and Gary A Miller. "Creep of duplex microstructures". In: *Journal of the American Ceramic Society* 77.11 (1994), pp. 2857–2865. ISSN: 0002-7820.

[118] S Lartigue, C Carry, and L Priester. "Grain boundaries in high temperature deformation of yttria and magnesia co-doped alumina". In: *Le Journal de Physique Colloques* 51.C1 (1990), pp. C1–985–C1–990. ISSN: 0449-1947.

[119] EM Lehockey and G Palumbo. "On the creep behaviour of grain boundary engineered nickel 1". In: *Materials Science and Engineering: A* 237.2 (1997), pp. 168–172. ISSN: 0921-5093.

[120] H Yoshida, K Okada, Y Ikuhara, and T Sakuma. "Improvement of high-temperature creep resistance in fine-grained Al2O3 by Zr4+ segregation in grain boundaries". In: *Philosophical magazine letters* 76.1 (1997), pp. 9–14. ISSN: 0950-0839.

[121] Yong Gao, RO Ritchie, Mukul Kumar, and RK Nalla. "High-cycle fatigue of nickel-based superalloy ME3 at ambient and elevated temperatures: role of grain-boundary engineering". In: *Metallurgical and Materials Transactions A* 36.12 (2005), pp. 3325–3333. ISSN: 1073-5623.

[122] Shigeaki Kobayashi, Toshiyuki Inomata, Hiroyuki Kobayashi, Sadahiro Tsurekawa, and Tadao Watanabe. "Effects of grain boundary-and triple junction-character on intergranular fatigue crack nucleation in polycrystalline aluminum". In: *Journal of Materials Science* 43.11 (2008), pp. 3792–3799. ISSN: 0022-2461.

[123] Harshad Kumar Dharamshi Hansraj Bhadeshia. *Bainite in steels: theory and practice*. CRC Press, 2019. ISBN: 1351574817.

[124] LCD Fielding. "The bainite controversy". In: *Materials Science and Technology* 29.4 (2013), pp. 383–399. ISSN: 0267-0836.

[125] Stanislaw Zajac, Volker Schwinn, and KH Tacke. "Characterisation and quantification of complex bainitic microstructures in high and ultra-high strength linepipe steels". In: *Materials Science Forum*. Vol. 500. Trans Tech Publ, pp. 387–394. ISBN: 0878499814.

[126] Zhixiong Zhu, Jian Han, and Huijun Li. "Influence of heat input on microstructure and toughness properties in simulated CGHAZ of X80 steel manufactured using high-temperature processing". In: *Metallurgical and Materials Transactions A* 46.11 (2015), pp. 5467–5475. ISSN: 1073-5623.

[127] Y. M. Kim, S. K. Kim, Y. J. Lim, and N. J. Kim. "Effect of microstructure on the yield ratio and low temperature toughness of linepipe steels". In: *Isij International* 42.12 (2002), pp. 1571–1577. ISSN: 0915-1559. DOI: DOI10.2355/isijinternational.42.1571.

[128] Luis F Ramos, David K Matlock, and George Krauss. "On the deformation behavior of dual-phase steels". In: *Metallurgical Transactions A* 10.2 (1979), pp. 259–261. ISSN: 0360-2133.

[129] G. T. Van Rooyen. "Basic factors which influence the Lüders strain during discontinuous yielding". In: *Materials Science and Engineering* 7.1 (1971), pp. 37–48. ISSN: 0025-5416. DOI: https://doi.org/10.1016/0025-5416(71)90059-0.

[130] Koji Shibata and Kentaro Asakura. "Transformation behavior and microstructures in ultra-low carbon steels". In: *ISIJ international* 35.8 (1995), pp. 982–991. ISSN: 0915-1559.

[131] H. K. Sung, S. S. Sohn, S. Y. Shin, S. Lee, N. J. Kim, S. H. Chon, and J. Y. Yoo. "Effects of finish rolling temperature on inverse fracture occurring during drop weight tear test of API X80 pipeline steels". In: *Materials Science and Engineer-*

ing a-Structural Materials Properties Microstructure and Processing 541 (2012), pp. 181–189. ISSN: 0921-5093. DOI: 10.1016/j.msea.2012.02.019.

[132] ASME B31.3. *Process Piping*. Generic. 2016.

[133] H Yajima, M Tada, and K Kajimoto. "Extensive application of TMCP-manufactured high tensile steel plates to ship hulls and offshore structures". In: *Mitsubishi Heavy Industries Technical Review* 24.1 (1987). ISSN: 0026-6817.

[134] EA Goli-Oglu, LI Éfron, and Yu D Morozov. "Effect of deformation regime in main stages of controlled rolling on pipe steel microstructure". In: *Metal Science and Heat Treatment* 55.5-6 (2013), p. 294. ISSN: 0026-0673.

[135] S. Vervynckt, K. Verbeken, P. Thibaux, and Y. Houbaert. "Evaluation of the Austenite Recrystallization by Multideformation and Double Deformation Tests". In: *Steel Research International* 82.4 (2011), pp. 369–378. ISSN: 1611-3683. DOI: 10.1002/srin.201000167.

[136] T Tanaka. "Science and technology of hot rolling process of steel". In: *Proceedings of the International Conference Microalloyed*. Vol. 95, pp. 165–181.

[137] Mohammad Masoumi, Luis Flavio Gaspar Herculano, and Hamilton Ferreira Gomes de Abreu. "Study of texture and microstructure evaluation of steel API 5L X70 under various thermomechanical cycles". In: *Materials Science and Engineering: A* 639 (2015), pp. 550–558. ISSN: 0921-5093.

[138] B. Hwang, Y. G. Kim, S. Lee, Y. M. Kim, N. J. Kim, and J. Y. Yoo. "Effective grain size and charpy impact properties of high-toughness X70 pipeline steels". In: *Metallurgical and Materials Transactions a-Physical Metallurgy and Materials Science* 36a.8 (2005), pp. 2107–2114.

[139] Y. M. Kim, S. K. Kim, Y. J. Lim, and N. J. Kim. "Effect of microstructure on the yield ratio and low temperature toughness of linepipe steels". In: *Isij International* 42.12 (2002), pp. 1571–1577.

[140] I. Olivares, M. Alanis, R. Mendoza, B. Campillo, and J. A. Juarez-Islas. "Development of microalloyed steel for pipeline applications". In: *Ironmaking & Steelmaking* 35.6 (2008), pp. 452–457.

[141] Harry Bhadeshia and Robert Honeycombe. *Steels: microstructure and properties: microstructure and properties*. Butterworth-Heinemann, 2011. ISBN: 0080462928.

[142] B. K. Panigrahi. "Processing of low carbon steel plate and hot strip—An overview". In: *Bulletin of Materials Science* 24.4 (2001), pp. 361–371. ISSN: 0973-7669. DOI: 10.1007/BF02708632.

[143] JY Koo, MJ Luton, NV Bangaru, RA Petkovic, DP Fairchild, CW Petersen, H Asahi, T Hara, Y Terada, and M Sugiyama. "Metallurgical design of ultra high-strength steels for gas pipelines". In: *International Journal of Offshore and Polar Engineering* 14.01 (2004). ISSN: 1053-5381.

[144] Xiao-Long Yang, Yun-Bo Xu, Xiao-Dong Tan, and Di Wu. "Relationships among crystallographic texture, fracture behavior and Charpy impact toughness in API X100 pipeline steel". In: *Materials Science and Engineering: A* 641 (2015), pp. 96–106. ISSN: 0921-5093. DOI: http://dx.doi.org/10.1016/j.msea.2015.06.029.

[145] Jang-Yong Yoo, Seong-Soo Ahn, Dong-Han Seo, Woo-Hyun Song, and Ki-Bong Kang. "New development of high grade X80 to X120 pipeline steels". In: *Materials and Manufacturing Processes* 26.1 (2011), pp. 154–160. ISSN: 1042-6914.

[146] Karl-Heinz Brensing and B Sommer. "Steel tube and pipe manufacturing processes". In: *Salzgitter Mannersmann Rohrenwerke* (2008).

[147] ID Simpson, Z Tritsiniotis, and LG Moore. "Steel cleanness requirements for X65 to X80 electric resistance welded linepipe steels". In: *Ironmaking & Steelmaking* 30.2 (2003), pp. 158–164. ISSN: 0301-9233.

[148] M. D. Herynk, S. Kyriakides, A. Onoufriou, and H. D. Yun. "Effects of the UOE/UOC pipe manufacturing processes on pipe collapse pressure". In: *International Journal of Mechanical Sciences* 49.5 (2007), pp. 533–553. ISSN: 0020-7403. DOI: DOI10.1016/j.ijmecsci.2006.10.001.

[149] M Atkins. "Atlas of continuous cooling transformation diagrams for engineering steels". In: *American Society for Metals, 1980* (1980), p. 260.

[150] American Society for Metals. *Atlas of isothermal transformation and cooling transformation diagrams*. American Society for Metals, 1977.

[151] William D Callister and David G Rethwisch. *Materials science and engineering*. Vol. 5. John Wiley & Sons NY, 2011.

[152] SK Mandal. *Steel Metallurgy: Properties, Specifications and Applications*. McGraw-Hill Education, 2015. ISBN: 0071844619.

[153] Ming-Chun Zhao, Ke Yang, Fu-Ren Xiao, and Yi-Yin Shan. "Continuous cooling transformation of undeformed and deformed low carbon pipeline steels". In: *Materials Science and Engineering: A* 355.1 (2003), pp. 126–136. ISSN: 0921-5093. DOI: https://doi.org/10.1016/S0921-5093(03)00074-1.

[154] E. B. Hawbolt, B. Chau, and J. K. Brimacombe. "Kinetics of austenite-pearlite transformation in eutectoid carbon steel". In: *Metallurgical Transactions A* 14.9 (1983), pp. 1803–1815. ISSN: 1543-1940. DOI: 10.1007/bf02645550.

[155] Y. E. Smith and C. A. Siebert. "Continuous cooling transformation kinetics of thermomechanically worked low-carbon austenite". In: *Metallurgical Transactions* 2.6 (1971), pp. 1711–1725. ISSN: 1543-1940. DOI: 10.1007/BF02913897.

[156] Frederick John Humphreys and Max Hatherly. *Recrystallization and related annealing phenomena*. Elsevier, 2012. ISBN: 008098388X.

[157] R. D. Doherty, D. A. Hughes, F. J. Humphreys, J. J. Jonas, D. Juul Jensen, M. E. Kassner, W. E. King, T. R. McNelley, H. J. McQueen, and A. D. Rollett. "Current issues in recrystallization: a review". In: *Materials Science and Engineering: A* 238.2 (1997), pp. 219–274. ISSN: 0921-5093. DOI: https://doi.org/10.1016/S0921-5093(97)00424-3.

[158] Stephanie Vervynckt, Kim Verbeken, B Lopez, and JJ Jonas. "Modern HSLA steels and role of non-recrystallisation temperature". In: *International Materials Reviews* 57.4 (2012), pp. 187–207. ISSN: 0950-6608.

[159] Caryn Nicole Homsher. "Determination of the non-recrystallization Temperature (Tnr) in multiple Microalloyed steels". Thesis. 2013.

[160] E. J. Palmiere, C. I. Garcia, and A. J. DeArdo. "The influence of niobium supersaturation in austenite on the static recrystallization behavior of low carbon microalloyed steels". In: *Metallurgical and Materials Transactions A* 27.4 (1996), pp. 951–960. ISSN: 1543-1940. DOI: 10.1007/BF02649763.

[161] Yun Bo Xu, Yong Mei Yu, Bao Liang Xiao, Zhen Yu Liu, and Guo Dong Wang. "Modelling of microstructure evolution during hot rolling of a high-Nb HSLA steel". In: *Journal of Materials Science* 45.10 (2010), pp. 2580–2590. ISSN: 1573-4803. DOI: 10.1007/s10853-010-4229-6.

[162] D. Q. Bai, S. Yue, W. P. Sun, and J. J. Jonas. "Effect of Deformation Parameters on the No-Recrystallization Temperature in Nb-Bearing Steels". In: *Metallurgical Transactions a-Physical Metallurgy and Materials Science* 24.10 (1993), pp. 2151–2159. ISSN: 0360-2133. DOI: Doi10.1007/Bf02648589.

[163] F Boratto, R Barbosa, S Yue, and JJ Jonas. "Effect of chemical composition on the critical temperatures of microalloyed steels". In: *International Conference on Physical Metallurgy of Thermomechanical Processing of Steels and Other Metals. THERMEC-88.* Vol. 1, pp. 383–390.

[164] F Fletcher. "Meta-analysis of Tnr measurements: Determining new empirical models based on composition and strain". In: *Austenite Processing Symposium (Internal company presentation)*, pp. 1–14.

[165] D Bai, RL Bodnar, J Ward, J Dorricott, and S Sanders. "Development of discrete X80 line pipe plate at SSAB Americas". In: *Proceedings of AIST 2011 International Symposium on the Recent Developments in Plate Steels.*

[166] J. Calvo, I. H. Jung, A. M. Elwazri, D. Bai, and S. Yue. "Influence of the chemical composition on transformation behaviour of low carbon microalloyed steels". In: *Materials Science and Engineering: A* 520.1–2 (2009), pp. 90–96. ISSN: 0921-5093. DOI: http://dx.doi.org/10.1016/j.msea.2009.05.027.

[167] Kim Verbeken, Liesbeth Barbé, and Dierk Raabe. "Evaluation of the crystallographic orientation relationships between FCC and BCC phases in TRIP steels". In: *ISIJ international* 49.10 (2009), pp. 1601–1609. ISSN: 0915-1559.

[168] John J. Jonas. "Transformation Textures Associated with Steel Processing". In: Microstructure and Texture in Steels. Springer London, 2009, pp. 3–17. ISBN: 978-1-84882-454-6.

[169] Edgar C Bain and NY Dunkirk. "The nature of martensite". In: *trans. AIME* 70.1 (1924), pp. 25–47.

[170] H Inagaki. "Effect of the alloying element on the development of the rolling texture in high purity Iron". In: *Z. Metallkd.* 79.3 (1988), pp. 164–173. ISSN: 0044-3093.

[171] Hirosuke Inagaki. "Formation of transformation textures in control-rolled low carbon steels". In: *Z. Metallkd.* 75.7 (1984), pp. 510–516. ISSN: 0044-3093.

[172] D Raabe. "Texture and microstructure evolution during cold rolling of a strip cast and of a hot rolled austenitic stainless steel". In: *Acta Materialia* 45.3 (1997), pp. 1137–1151. ISSN: 1359-6454.

[173] GV Kurdjumov and G Sachs. "Over the mechanisms of steel hardening". In: *Z. Phys* 64 (1930), pp. 325–343.

[174] Z Nishiyama. "X-ray investigation of the mechanism of the transformation from face-centerd cubic lattice to body-centerd cubic lattice". In: *Sci. Tohoku Univ.* 23 (1934), p. 638.

[175] G Wassermann. "Influence of the α-γ-transformation of an irreversible Ni steel onto crystal orientation and tensile strength". In: *Arch. Eisenhüttenwes* 126 (1933), p. 647.

[176] S. Vervynckt, K. Verbeken, P. Thibaux, M. Liebeherr, and Y. Houbaert. "Austenite Recrystallization-Precipitation Interaction in Niobium Microalloyed Steels". In: *Isij International* 49.6 (2009), pp. 911–920. ISSN: 0915-1559.

[177] MP Butron-Guillen, CS Da Costa Viana, and JJ Jonas. "A variant selection model for predicting the transformation texture of deformed austenite". In: *Metallurgical and Materials Transactions A* 28.9 (1997), pp. 1755–1768. ISSN: 1073-5623.

[178] Martin Hölscher, Dierk Raabe, and Kurt Lücke. "Rolling and recrystallization textures of bcc steels". In: *steel research international* 62.12 (1991), pp. 567–575. ISSN: 1869-344X.

[179] Sang Heon Lee and Dong Nyung Lee. "Shear rolling and recrystallization textures of interstitial-free steel sheet". In: *Materials Science and Engineering: A* 249.1–2 (1998), pp. 84–90. ISSN: 0921-5093. DOI: http://dx.doi.org/10.1016/S0921-5093(98)00588-7.

[180] S. Nafisi, M. A. Arafin, L. Collins, and J. Szpunar. "Texture and mechanical properties of API X100 steel manufactured under various thermomechanical cycles". In: *Materials Science and Engineering a-Structural Materials Properties Microstructure and Processing* 531 (2012), pp. 2–11. ISSN: 0921-5093. DOI: DOI10.1016/j.msea.2011.09.072.

[181] Jae Young Park, Kyu Hwan Oh, and Hyung Yong Ra. "Texture and deformation behavior through thickness direction in strip-cast 4.5 wt% Si steel sheet". In: *ISIJ international* 40.12 (2000), pp. 1210–1215. ISSN: 0915-1559.

[182] O. Engler, M. Y. Huh, and C. N. Tome. "A study of through-thickness texture gradients in rolled sheets". In: *Metallurgical and Materials Transactions a-Physical Metallurgy and Materials Science* 31.9 (2000), pp. 2299–2315. ISSN: 1073-5623. DOI: DOI10.1007/s11661-000-0146-7.

[183] O. Lavigne, E. Gamboa, J. Griggs, V. Luzin, M. Law, and A. Roccisano. "High-pH inclined stress corrosion cracking in Australian and Canadian gas pipeline X65 steels". In: *Materials Science and Technology* (2016), pp. 1–7. ISSN: 0267-0836. DOI: 10.1080/02670836.2015.1132030.

[184] D. Raabe. "Microstructure and Crystallographic Texture of Strip-Cast and Hot-Rolled Austenitic Stainless-Steel". In: *Metallurgical and Materials Transactions*

a-Physical Metallurgy and Materials Science 26.4 (1995), pp. 991–998. ISSN: 1073-5623. DOI: Doi10.1007/Bf02649096.

[185] C. Zong, G. H. Zhu, and W. M. Mao. "Effect of Crystallographic Texture on Anisotropy of Yield Strength in X100 Pipeline Steel". In: *Journal of Iron and Steel Research International* 20.8 (2013), pp. 66–71. ISSN: 1006-706x. DOI: Doi10.1016/S1006-706x(13)60143-0.

[186] B. Hutchinson. "Deformation microstructures and textures in steels". In: *Philosophical Transactions of the Royal Society a-Mathematical Physical and Engineering Sciences* 357.1756 (1999), pp. 1471–1485. ISSN: 1364-503x. DOI: DOI10.1098/rsta.1999.0385.

[187] X. J. Shen, S. Tang, Y. J. Wu, X. L. Yang, J. Chen, Z. Y. Liu, R. D. K. Misra, and G. D. Wang. "Evolution of microstructure and crystallographic texture of microalloyed steel during warm rolling in dual phase region and their influence on mechanical properties". In: *Materials Science and Engineering: A* 685 (2017), pp. 194–204. ISSN: 0921-5093. DOI: https://doi.org/10.1016/j.msea.2016.12.108.

[188] Barnett MR and Jonas JJ. "Distinctive aspects of the physical metallurgy of warm rolling". In: *ISIJ international* 39.9 (1999), pp. 856–873. ISSN: 0915-1559.

[189] BB Rath and IM Bernstein. "The relation between grain-boundary orientation and intergranular cracking". In: *Metallurgical Transactions* 2.10 (1971), pp. 2845–2851. ISSN: 0026-086X.

[190] Hiroaki Kurishita, Akira Oishi, Haruyoshi Kubo, and Hideo Yoshinaga. "Grain Boundary Fracture in Molybdenum Bicrystals with Various (110) Symmetric Tilt Boundaries By Hiroaki Kurishita, Akira Gishi, Haruyoshi Kubo and Hideo Yoshinaga". In: *J. Japan Inst. Metals* 47 (1983), p. 546.

[191] Hui Lin and DP Pope. "The influence of grain boundary geometry on intergranular crack propagation in Ni3Al". In: *Acta metallurgica et materialia* 41.2 (1993), pp. 553–562. ISSN: 0956-7151.

[192] V. Venegas, F. Caleyo, J. L. González, T. Baudin, J. M. Hallen, and R. Penelle. "EBSD study of hydrogen-induced cracking in API-5 L-X46 pipeline steel". In: *Scripta Materialia* 52.2 (2005), pp. 147–152. ISSN: 1359-6462. DOI: http://dx.doi.org/10.1016/j.scriptamat.2004.09.015.

[193] V. Venegas, F. Caleyo, J. M. Hallen, T. Baudin, and R. Penelle. "Role of crystallographic texture in hydrogen-induced cracking of low carbon steels for sour service piping". In: *Metallurgical and Materials Transactions a-Physical Metallurgy and Materials Science* 38A.5 (2007), pp. 1022–1031. ISSN: 1073-5623. DOI: DOI10.1007/s11661-007-9130-9.

[194] V. Venegas, F. Caleyo, T. Baudin, J. H. Espina-Hernández, and J. M. Hallen. "On the role of crystallographic texture in mitigating hydrogen-induced cracking in pipeline steels". In: *Corrosion Science* 53.12 (2011), pp. 4204–4212. ISSN: 0010-938X. DOI: http://dx.doi.org/10.1016/j.corsci.2011.08.031.

[195] MA Mohtadi-Bonab, JA Szpunar, and SS Razavi-Tousi. "Hydrogen induced cracking susceptibility in different layers of a hot rolled X70 pipeline steel". In: *International Journal of Hydrogen Energy* 38.31 (2013), pp. 13831–13841. ISSN: 0360-3199.

[196] M. A. Mohtadi-Bonab, M. Eskandari, and J. A. Szpunar. "Texture, local misorientation, grain boundary and recrystallization fraction in pipeline steels related to hydrogen induced cracking". In: *Materials Science and Engineering a-Structural Materials Properties Microstructure and Processing* 620 (2015), pp. 97–106. ISSN: 0921-5093. DOI: DOI10.1016/j.msea.2014.10.009.

[197] M. A. Mohtadi-Bonab, J. A. Szpunar, R. Basu, and M. Eskandari. "The mechanism of failure by hydrogen induced cracking in an acidic environment for API 5L X70 pipeline steel". In: *International Journal of Hydrogen Energy* 40.2 (2015), pp. 1096–1107. ISSN: 0360-3199. DOI: http://dx.doi.org/10.1016/j.ijhydene.2014.11.057.

[198] ASM International. "ASM Handbook Vol 13: Corrosion". In: *Metals Park, OH* 811 (1987).

[199] Chiaki Ouchi and Tomoyoshi Okita. "Austenitic grain refinement through static recrystallization immediately after hot rolling". In: *Transactions of the Iron and Steel Institute of Japan* 24.9 (1984), pp. 726–733. ISSN: 0021-1583.

[200] ASTM International. *ASTM E112-13-Standard Test Methods for Determining Average Grain Size*. Generic. 2013.

[201] Serope Kalpakjian. *Manufacturing processes for engineering materials*. Pearson Education India, 1984. ISBN: 8131705668.

[202] ASTM International. *E2627-13,"Standard Practice for Determining Average Grain Size Using Electron Backscatter Diffraction (EBSD) in Fully Recrystallized Polycrystalline Materials.", ASTM International, West Conshohocken, PA, 2013*. Generic.

[203] ASTM International. *ASTM E8-16-Standard Test Methods for Tension Testing of Metallic Materials*. Generic. 2016.

[204] ASTM International. "E384: Standard Test Method for Knoop and Vickers Hardness of Materials". In: *ASTM Stand* (2012), pp. 1–43.

[205] Warrick Fletcher and Pubudu Gunawardena. *Design & Construction of a Test Rig For Stress Corrosion Cracking Testing*. Report. The University of Adelaide, 2006.

[206] David Liew. *LIST Machine Control System Manual*. Report. The University of Adelaide, 2011.

[207] M. P. Staiger, B. Jessop, P. D. Hodgson, A. Brownrigg, and C. H. J. Davies. "Effect of Nitrogen on Formation of Martensite-Austenite Constituent in Low Carbon Steels". In: *ISIJ International* 39.2 (1999), pp. 183–190. DOI: 10.2355/isijinternational.39.183.

[208] Lei Zheng, Mingzhuo Bai, Bei Zhang, Tiancheng Cui, and Haishen Xu. "Research and Development of X70 Large Diameter UOE Linepipe With High Deformability for Strain-Based Design Pipeline". In: *2012 9th International Pipeline Conference*. American Society of Mechanical Engineers, pp. 367–373.

[209] Houman Alipooramirabad, Anna Paradowska, Reza Ghomashchi, and Mark Reid. "Investigating the effects of welding process on residual stresses, microstructure and mechanical properties in HSLA steel welds". In: *Journal of Manufacturing Processes* 28 (2017), pp. 70–81. ISSN: 1526-6125. DOI: https://doi.org/10.1016/j.jmapro.2017.04.030.

[210] Lihong Su, Huijun Li, Cheng Lu, Jintao Li, Leigh Fletcher, Ian Simpson, Frank Barbaro, Lei Zheng, Mingzhuo Bai, and Jianlan Shen. "Transverse and z-direction CVN impact tests of X65 line pipe steels of two centerline segregation ratings". In: *Metallurgical and Materials Transactions A* 47.8 (2016), pp. 3919–3932. ISSN: 1073-5623.

[211] Y. M. Kim, S. Y. Shin, H. Lee, B. Hwang, S. Lee, and N. J. Kim. "Effects of molybdenum and vanadium addition on tensile and charpy impact properties of API X70 linepipe steels". In: *Metallurgical and Materials Transactions a-Physical Metallurgy and Materials Science* 38a.8 (2007), pp. 1731–1742. ISSN: 1073-5623. DOI: 10.1007/s11661-007-9197-3.

[212] Matthias Militzer, E Bruce Hawbolt, T Ray Meadowcroft, and Alan Giumelli. "Austenite grain growth kinetics in Al-killed plain carbon steels". In: *Metallurgical and Materials Transactions A* 27.11 (1996), pp. 3399–3409. ISSN: 1073-5623.

[213] John G. Lenard. "Introduction". In: *Primer on Flat Rolling (Second Edition)*. Ed. by John G. Lenard. Oxford: Elsevier, 2014, pp. 1–15. ISBN: 978-0-08-099418-5. DOI: https://doi.org/10.1016/B978-0-08-099418-5.00001-9.

[214] J. Fernández, S. Illescas, and J. M. Guilemany. "Effect of microalloying elements on the austenitic grain growth in a low carbon HSLA steel". In: *Materials Letters* 61.11 (2007), pp. 2389–2392. ISSN: 0167-577X. DOI: https://doi.org/10.1016/j.matlet.2006.09.021.

[215] M. Kang, H. Kim, S. Lee, and S. Y. Shin. "Effects of Dynamic Strain Hardening Exponent on Abnormal Cleavage Fracture Occurring During Drop Weight Tear Test of API X70 and X80 Linepipe Steels". In: *Metallurgical and Materials Trans-*

actions a-Physical Metallurgy and Materials Science 45a.2 (2014), pp. 682–697. ISSN: 1073-5623. DOI: 10.1007/s11661-013-2046-7.

[216] S. Nafisi, M. Arafin, R. Glodowski, L. Collins, and J. Szpunar. "Impact of Vanadium Addition on API X100 Steel". In: *Isij International* 54.10 (2014), pp. 2404–2410. DOI: DOI10.2355/isijinternational.54.2404.

[217] R. Shukla, S. K. Ghosh, D. Chakrabarti, and S. Chatterjee. "Characterisation of Microstructure, Texture and Mechanical Properties in Ultra Low-Carbon Ti-B Microalloyed Steels". In: *Metals and Materials International* 21.1 (2015), pp. 85–95. ISSN: 1598-9623. DOI: DOI10.1007/s12540-015-1010-z.

[218] Lin-na Duan, Ji-man Wang, Qing-you Liu, Xin-jun Sun, and Jian-chun Cao. "Austenite grain growth behavior of X80 pipeline steel in heating process". In: *Journal of Iron and Steel Research International* 17.3 (2010), pp. 62–66. ISSN: 1006-706X.

[219] A Al Shahrani, Thomas Schambron, Ali Dehghan-Manshadi, James G Williams, and Elena V Pereloma. "Effects of processing parameters on microstructure development in X70 pipeline steel". In: *Materials Science Forum*. Vol. 654. Trans Tech Publ, pp. 298–301. ISBN: 0878492550.

[220] Thomas Schambron, Andrew W Phillips, David M Obrien, Joshua Burg, Elena V Pereloma, Chris C Killmore, and Jim A Williams. "Thermomechanical processing of pipeline steels with a reduced Mn content". In: *ISIJ international* 49.2 (2009), pp. 284–292. ISSN: 0915-1559.

[221] Raymond Edward Smallman. *Modern physical metallurgy*. Elsevier, 2016. ISBN: 1483105970.

[222] P Cizek, BP Wynne, CHJ Davies, and PD Hodgson. "The effect of simulated thermomechanical processing on the transformation behavior and microstructure of a low-carbon Mo-Nb linepipe steel". In: *Metallurgical and Materials Transactions A* 46.1 (2015), pp. 407–425. ISSN: 1073-5623.

[223] Harshad Kumar Dharamshi Hansraj Bhadeshia and JW Christian. "Bainite in steels". In: *Metallurgical transactions A* 21.3 (1990), pp. 767–797. ISSN: 0360-2133.

[224] FG Caballero, H Roelofs, St Hasler, C Capdevila, J Chao, J Cornide, and C Garcia-Mateo. "Influence of bainite morphology on impact toughness of continuously cooled cementite free bainitic steels". In: *Materials Science and Technology* 28.1 (2012), pp. 95–102. ISSN: 0267-0836.

[225] Carlos Garcia-Mateo, Caballero FG, and Bhadeshia HKDH. "Development of hard bainite". In: *ISIJ international* 43.8 (2003), pp. 1238–1243. ISSN: 0915-1559.

[226] Elena Pereloma and David V Edmonds. *Phase transformations in steels: Diffusionless transformations, high strength steels, modelling and advanced analytical techniques*. Elsevier, 2012. ISBN: 0857096117.

[227] RY Zhang and JD Boyd. "Bainite transformation in deformed austenite". In: *Metallurgical and Materials Transactions A* 41.6 (2010), pp. 1448–1459. ISSN: 1073-5623.

[228] Pavel Cizek, BP Wynne, CHJ Davies, Barrington C Muddle, and Peter D Hodgson. "Effect of composition and austenite deformation on the transformation characteristics of low-carbon and ultralow-carbon microalloyed steels". In: *Metallurgical and Materials Transactions A* 33.5 (2002), pp. 1331–1349. ISSN: 1073-5623.

[229] M. S. Joo, D. W. Suh, J. H. Bae, and H. K. D. H. Bhadeshia. "Toughness anisotropy in X70 and X80 linepipe steels". In: *Materials Science and Technology* 30.4 (2014), pp. 439–446. ISSN: 0267-0836. DOI: 10.1179/1743284713y.0000000371.

[230] J. Bauer, P. Flüss, E. Amoris, and V. Schwinn. "Microstructure and properties of thermomechanical controlled processing steels for linepipe applications". In: *Ironmaking & Steelmaking* 32.4 (), pp. 325–330. ISSN: 03019233. DOI: 10.1179/174328105X48025.

[231] P. Mohseni, J. K. Solberg, M. Karlsen, O. M. Akselsen, and E. Østby. "Investigation of mechanism of cleavage fracture initiation in intercritically coarse grained heat affected zone of HSLA steel". In: *Materials Science and Technology* 28.11 (2012), pp. 1261–1268. ISSN: 0267-0836. DOI: 10.1179/1743284712Y.0000000056.

[232] AC Bannister and SJ Trail. "The significance of the yield stress/tensile stress ratio to structural integrity". In: *British Steel plc, Sub task* 2.1 (1996).

[233] American Petroleum Institute. *Specification For Line Pipe*. Standard. 2007.

[234] Khodamorad Abbaszadeh, Hassan Saghafian, and Shahram Kheirandish. "Effect of bainite morphology on mechanical properties of the mixed bainite-martensite microstructure in D6AC steel". In: *Journal of Materials Science & Technology* 28.4 (2012), pp. 336–342. ISSN: 1005-0302.

[235] Xiaoyong Zhang, Huilin Gao, Xueqin Zhang, and Yan Yang. "Effect of volume fraction of bainite on microstructure and mechanical properties of X80 pipeline steel with excellent deformability". In: *Materials Science and Engineering: A* 531 (2012), pp. 84–90. ISSN: 0921-5093.

[236] Canadian Standards Association. *CSA Z245.1 : 2014*. Standard. 2014.

[237] Yasuhiro Shinohara, Takuya Hara, Eiji Tsuru, Hitoshi Asahi, Yoshio Terada, Naoshi Ayukawa, and Masahiko Murata. "Development of a high strength steel line pipe for strain-based design applications". In: *The Seventeenth International Offshore and Polar Engineering Conference*. International Society of Offshore and Polar Engineers.

[238] C Zong, G Zhu, and W Mao. "Effect of crystallographic texture on the anisotropy of Charpy impact behavior in pipeline steel". In: *Materials Science and Engineering: A* 563 (2013), pp. 1–7. ISSN: 0921-5093.

[239] Mohammad Masoumi and Hamilton Ferreira Gomes de Abreu. *Textural analysis through thickness of api x70 steel after hot rolling and post heat treatment*. Conference Paper. 2015.

[240] P. Chapellier, R. K. Ray, and J. J. Jonas. "Prediction of Transformation Textures in Steels". In: *Acta Metallurgica Et Materialia* 38.8 (1990), pp. 1475–1490. ISSN: 0956-7151. DOI: Doi10.1016/0956-7151(90)90116-X.

[241] Mohammad Masoumi, Cleiton Carvalho Silva, and Hamilton Ferreira Gomes de Abreu. "Effect of crystallographic orientations on the hydrogen-induced cracking resistance improvement of API 5L X70 pipeline steel under various thermomechanical processing". In: *Corrosion Science* (2016). ISSN: 0010938X. DOI: 10.1016/j.corsci.2016.05.003.

[242] Jintao Li, Lihong Su, Cheng Lu, Huijun Li, and Dongzhi Luo. "The evolution of microtexture of pipeline steel from strip to bare pipe to coated pipe". In: *Procedia Engineering* 207 (2017), pp. 1844–1849. ISSN: 1877-7058. DOI: https://doi.org/10.1016/j.proeng.2017.10.949.

[243] Nobuo Shikanai, Shinji Mitao, and Shigeru Endo. "Recent development in microstructural control technologies through the thermo-mechanical control process (TMCP) with JFE steel's high-performance plates". In: *JFE Steel, Tokyo, Japan, JFE Technical Report* 11 (2008), pp. 011–02.

[244] U. von Schlippenbach, F. Emren, and K. Lücke. "Investigation of the development of the cold rolling texture in deep drawing steels by ODF-analysis". In: *Acta Metallurgica* 34.7 (1986), pp. 1289–1301. ISSN: 0001-6160. DOI: http://dx.doi.org/10.1016/0001-6160(86)90015-5.

[245] J.Q. Wang and A. Atrens. "SCC initiation for X65 pipeline steel in the "high" pH carbonate/bicarbonate solution". In: *Corrosion Science* 45.10 (2003), pp. 2199–2217. ISSN: 0010938X. DOI: 10.1016/s0010-938x(03)00044-1.

[246] Vimal H. Desai. *Mechanistic Differences In Transgranular And Intergranular Cracking Of Austenitic Stainless Steels*. Conference Paper. 1997.

[247] R. N. Parkins, W. K. Blanchard, and B. S. Delanty. "Transgranular Stress-Corrosion Cracking of High-Pressure Pipelines in Contact with Solutions of near Neutral Ph". In: *Corrosion* 50.5 (1994), pp. 394–408. ISSN: 0010-9312. URL: <GotoISI>://WOS:A1994NJ40000009.

[248] C García, F Martín, P De Tiedra, JA Heredero, and ML Aparicio. "Effects of prior cold work and sensitization heat treatment on chloride stress corrosion cracking in

type 304 stainless steels". In: *Corrosion science* 43.8 (2001), pp. 1519–1539. ISSN: 0010-938X.

[249] William D. Callister. *Materials science and engineering : an introduction*. 6th ed. Includes bibliographical references and index. New York, NY: John Wiley & Sons, 2003.

[250] M Henthorne and RN Parkinst. "Some aspects of the influence of structure upon stress-corrosion cracking and grain boundary corrosion in mild steels". In: *British Corrosion Journal* 2.5 (1967), pp. 186–192. ISSN: 0007-0599.

[251] Hui Lu Li, Wu Yang Chu, Ke Wei Gao, and Li Jie Qiao. "Stress corrosion cracking of high-strength steels". In: *Steel research* 72.9 (2001), pp. 366–370. ISSN: 0177-4832.

[252] Koji Arioka. "2014 WR Whitney Award Lecture: Change in Bonding Strength at Grain Boundaries Before Long-Term SCC Initiation". In: *Corrosion* 71.4 (2015), pp. 403–419. ISSN: 0010-9312.

[253] Peter L. Andresen and Martin M. Morra. "IGSCC of non-sensitized stainless steels in high temperature water". In: *Journal of Nuclear Materials* 383.1 (2008), pp. 97–111. ISSN: 0022-3115. DOI: https://doi.org/10.1016/j.jnucmat.2008.08.005.

[254] Hirosuke Inagaki, Kiwami Kurihara, and Isao Kozasu. "Influence of crystallographic texture on the strength and toughness of control-rolled high tensile strength steel". In: *Transactions of the Iron and Steel Institute of Japan* 17.2 (1977), pp. 75–81. ISSN: 0021-1583.

[255] JI Verdeja, J Asensio, and JA Pero-Sanz. "Texture, formability, lamellar tearing and HIC susceptibility of ferritic and low-carbon HSLA steels". In: *Materials characterization* 50.1 (2003), pp. 81–86. ISSN: 1044-5803.

[256] A Boumaiza, T Baudin, N Rouag, and R Penelle. "Electron backscattered diffraction of transgranular crack propagation in soft steel". In: *Chinese Physics Letters* 24.6 (2007), p. 1759. ISSN: 0256-307X.

[257] Xiao-Long Yang, Yun-Bo Xu, Xiao-Dong Tan, and Di Wu. "Influences of crystallography and delamination on anisotropy of Charpy impact toughness in API X100 pipeline steel". In: *Materials Science and Engineering: A* 607 (2014), pp. 53–62. ISSN: 0921-5093. DOI: https://doi.org/10.1016/j.msea.2014.03.121. URL: http://www.sciencedirect.com/science/article/pii/S0921509314004122.